

ABSTRACT

GAWRYS, KEITH LOUIS. How Asphaltenes Aggregate: Role of Chemistry and Solvent.
(Under the direction of Peter K. Kilpatrick)

Asphaltenes from three crude oils were separated on a preparatory-scale into 20 - 30 discrete subfractions by sequential precipitation from mixtures of n-heptane and toluene. The earliest fractions precipitated were characterized by lower than average aromaticity and atomic N/C ratios and contained significant amounts of co-precipitated inorganic solids or metal atoms bound to functional groups intrinsic to the asphaltenes. The subfractions isolated in the regime where asphaltene solubility changed significantly with slight changes in the solvent were characterized by atomic H/C ratios that varied significantly with the yield of precipitated asphaltenes. Atomic N/C ratios decreased and O/C ratios increased systematically with increasing precipitated asphaltene yield in this solvent regime. The higher yield fractions were generally the most aromatic and formed the largest aggregates in solution, suggesting that asphaltene solubility and aggregation behavior is dominated by π -bonding interactions between the aromatic moieties. After precipitation of ~ 80 % (w/w) of the asphaltenes, the remaining fractions were more “resin-like” in terms of chemical composition and aggregation behavior.

SANS has proven useful for deducing the sizes and morphologies of asphaltenic aggregates in solution. Selection of an appropriate form factor model that closely approximates the structure of asphaltenic aggregates is important for determining the radius of gyration, molar mass, apparent fractal dimension, and second virial coefficients (A_2) of the aggregates. SANS measurements were performed on solutions of asphaltenes dispersed in perdeuterated solvents with a broad range of solute and solvent chemical compositions.

Comparison of various geometric form factor models to the asphaltene scattering spectra suggested that the shape of asphaltenic aggregates is best described by an oblate cylinder model with radius polydispersity. The polydisperse cylinder model provided typical values of the particle thicknesses from 5 to 32 Å, the average particle radius from 25 to 125 Å, and ~ 30 % radius polydispersity. Subsequent calculation of average aggregate molar masses suggested a range of solvent entrainment from 30 to 50 % (v/v) within the aggregates that was consistent with previous viscosity measurements.

Changes in the apparent aggregate molar mass with concentration indicated deviations from ideal solution behavior (i.e., non-interacting aggregates plus solvent), which were quantified through the determination of aggregate A_2 values. Aggregate A_2 values varied significantly with solvent conditions, concentration, and chemical composition (e.g., atomic H/C ratio) of the solute. These results suggested that interactions of asphaltenes, resins, and solvent are strongly dominated by dispersion and π -bonding interactions. The magnitude of the experimentally measured A_2 values generally under-predicted or agreed with the values calculated from an excluded volume model, suggesting that energetic interactions of the solute and entrained solvent are significant.

A UV-vis spectroscopic technique was developed to determine the solubility of polynuclear aromatic compounds in binary solvent mixtures with the intention of extending the analyses to more complex multi-component mixtures, such as petroleum asphaltenes. Binary solvent mixtures were selected to probe specific intermolecular interactions between the solvent and solute (i.e., dispersion, polar, and hydrogen bond interactions). The solubility data were fit to a three-dimensional solubility parameter model based on regular solution theory. The model provided accurate solubility predictions for two solutes in several binary

solvent mixtures with less than 30 % error, but the predictive capability of the model decreased significantly when the polar and/or hydrogen-bonding contributions to the solvent solubility parameter deviated significantly from that of the solute. Additional experiments measured the solubility behavior of a multi-component solute mixture of ACA and PHD in 2-butanol. The results suggested the need to modify the existing model to account for aggregation.

**HOW ASPHALTENES AGGREGATE:
ROLE OF CHEMISTRY AND SOLVENT**

by

KEITH LOUIS GAWRYS

A dissertation submitted to the Graduate Faculty of
North Carolina State University
in partial fulfillment of the
requirements for the Degree of
Doctor of Philosophy

CHEMICAL ENGINEERING

Raleigh

2005

APPROVED BY:



Peter K. Kilpatrick
Chair of Advisory Committee



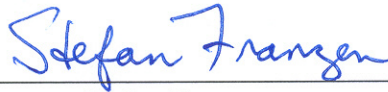
Saad A. Khan



Jan Genzer



Richard J. Spontak



Stefan Franzen

BIOGRAPHY

KEITH LOUIS Gawrys was born on November 19, 1974, in Middlefield, Ohio but spent most of his childhood on the Florida Space Coast. In 1993, he graduated as valedictorian from Titusville High School in Titusville, Florida. He attended his freshman year at Davison College in Davidson, North Carolina and transferred the following year to Florida State University in Tallahassee, Florida. He graduated Summa Cum Laude from Florida State University in 1998 with dual Bachelor of Science degrees in Chemistry and Chemical Engineering. From 1998 to 2005, he attended North Carolina State University in Raleigh, North Carolina, and graduated with a Ph.D. in Chemical Engineering. After completing his doctoral work, he accepted a position as a Senior Engineer with Nalco Energy Services Division, Refinery Process and Fuel Additives Research group in Sugar Land, Texas.

ACKNOWLEDGEMENTS

I would like to thank my advisor and mentor Dr. Peter Kilpatrick for providing sound advice and direction for my thesis research. He has helped me develop patience, a positive attitude, and confidence in my ability to succeed that will benefit the rest of my life.

I have enjoyed the opportunity of working with many fellow graduate students, postdoctoral associates and undergraduate assistants. Andrew Sullivan, Matthew Spiecker, Nael Zaki, Jihong Tong, Xiaoli Yang, Tian-xi Zhang, Marit-Helen Ese, George Blankenship, Maria Lupe Marques, Matthew Smith, and Vinnie Verruto have all provided useful intellectual input or experimental assistance with various aspects of the experimental research.

I would like to thank the staff of the Chemical Engineering Department whose assistance and friendship was greatly appreciated-- particularly Courtney Smith, Kit Yeung, Sheila Hayes, Natalie Worth, and Sandra Doby.

I would like to thank my parents, Bill and Judy Gawrys, for providing a stable and nurturing environment during my childhood and for providing continued love and support in my adulthood. I credit my wife, Jennifer Day-Gawrys, for much of my happiness.

This research was supported by the Petroleum Environmental Research Forum, ExxonMobil, Shell, Equilon, ChevronTexaco, Nalco Energy Services Division, Champion Technologies, National Science Foundation Grants (CTS981727), and the National Science Foundation Graduate Research Fellowship Program. This work benefited from the use of facilities in the Intense Pulsed Neutron Source and the Chemistry Division, which is funded by the U. S. Department of Energy, Office of Basic Energy Sciences under contract W-31-109-ENG-38 to the University of Chicago. I would particularly like to thank Pappannan

Thiyagarajan and Denis Wozniak of the Intense Pulsed Neutron Source Division at Argonne National Laboratory for their assistance on the SAND instrument. I also acknowledge the support of the National Institute of Standards and Technology, U.S. Department of Commerce, in providing the neutron research facilities used in this work and Min Lin for his assistance on the NG1 and NG3 beamlines.

TABLE OF CONTENTS

	Page
List of Tables	x
List of Figures	xiii
Chapter 1. Introduction	1
1.1 Petroleum Production Challenges	1
1.2 Asphaltene Chemistry	1
1.3 Asphaltene Subfractionation	3
1.3.1 Subfractionation Procedures	3
1.3.2 Coarse Fractionations	3
1.3.3 Fine Fractionations	5
1.4 Asphaltene Aggregate Structure	6
1.5 Instrumental Techniques	8
1.5.1 Near-Infrared Spectroscopy	8
1.5.2 Pulsed Field Gradient Spin Echo NMR	9
1.5.3 Vapor Pressure Osmometry	10
1.5.4 Viscosity Measurements	11
1.5.5 Small-Angle Scattering	12
1.5.5.1 Guinier and Zimm Approximations	13
1.5.5.2 Monodisperse Form Factors	14
1.5.5.3 Polydisperse Form Factors	14
1.6 Overview of Dissertation	16
1.7 References	19
Abstract: Asphaltenic Aggregates are Polydisperse Oblate Cylinders	28
Chapter 2. Asphaltenic Aggregates are Polydisperse Oblate Cylinders	
2.1 Introduction	29
2.2 Experimental	34
2.2.1 Asphaltene Precipitation	34
2.2.2 Chemical Characterization	35
2.2.3 SANS Sample Preparation	35
2.2.4 SANS Measurements	35
2.3 Model Fitting	37
2.3.1 Geometry Independent Scattering Models	37
2.3.2 Form Factor Models	38
2.4 Results and Discussion	41
2.5 Conclusions	47
2.6 Acknowledgements	49
2.7 Appendix: Polydisperse Radius Oblate Cylinder Model	50
2.8 References	53

Abstract: On Distribution Functions of Chemical Properties and Aggregation of Solubility Fractions in Asphaltenes	65
Chapter 3. On Distribution Functions of Chemical Properties and Aggregation of Solubility Fractions in Asphaltenes	
3.1 Introduction	66
3.2 Experimental	72
3.2.1 Materials	72
3.2.2 Asphaltene Precipitation	72
3.2.3 Desalting of B6 Asphaltenes	73
3.2.4 Asphaltene Fine Fractionation	74
3.2.5 Chemical Characterization	75
3.2.6 SANS Measurements	75
3.3 Results	77
3.4 Discussion	83
3.5 Conclusions	87
3.6 Acknowledgements	88
3.7 References	89
Abstract: Solvent Entrainment in and Flocculation of Asphaltenic Aggregates Probed by Small-Angle Neutron Scattering	107
Chapter 4. Solvent Entrainment in and Flocculation of Asphaltenic Aggregates Probed by Small-Angle Neutron Scattering	
4.1 Introduction	108
4.2 Experimental	112
4.2.1 Asphaltene Precipitation	112
4.2.2 Chemical Characterization	113
4.2.3 SANS Sample Preparation	113
4.2.4 SANS Measurements	114
4.2.5 SANS Model Fitting	115
4.3 Results and Discussion	117
4.3.1 Model Fit Parameters	117
4.3.2 Solvent Entrainment	123
4.3.3 Asphaltene Flocculation	129
4.4 Conclusions	130
4.5 Acknowledgements	132
4.6 References	133
Abstract: Second Virial Coefficients of Asphaltenic Aggregates in Varying Solvents Probed by Small-Angle Neutron Scattering	148
Chapter 5. Second Virial Coefficients of Asphaltenic Aggregates in Varying Solvents Probed by Small-Angle Neutron Scattering	
5.1 Introduction	149
5.2 Experimental	152

5.2.1	Asphaltene and Resin Isolation	152
5.2.2	Chemical Characterization	154
5.2.3	SANS Sample Preparation	154
5.2.4	SANS Measurements	155
5.2.5	SANS Model Fitting	156
5.3	Results and Discussion	158
5.4	Conclusions	167
5.5	Acknowledgements	169
5.6	References	169
Abstract: Estimation of the Three-Dimensional Solubility Parameters for Polyaromatic Compounds by UV-Vis Spectroscopy		179
Chapter 6. Estimation of the Three-Dimensional Solubility Parameters for Polyaromatic Compounds by UV-Vis Spectroscopy		
6.1	Introduction	180
6.2	Theory	182
6.2.1	Solubility Parameter Theory	182
6.2.2	Three-Dimensional Solubility Parameters	186
6.3	Experimental	188
6.3.1	Materials	188
6.3.2	Physical Property Data	188
6.3.3	Solubility Experiments	189
6.4	Results and Discussion	190
6.4.1	Estimation of Solubility Parameters for ACA and PHD	190
6.4.2	Pure Solute Solubility Modeling	192
6.4.3	Solubility of Mixed Solutes	195
6.5	Conclusions	197
6.6	Acknowledgements	198
6.7	References	198
Chapter 7. Conclusions and Future Work		214
6.1	Conclusions	214
6.2	Future Work	218
Appendix A. Aggregation and Solubility Behavior of Asphaltenes and Their Subfractions		224
A.1	Abstract	224
A.2	Introduction	225
A.3	Experimental	230
A.3.1	Asphaltene Source	230
A.3.2	Asphaltene Precipitation	230
A.3.3	Asphaltene Solubility Determination	231
A.3.4	Chemical Characterization	231
A.3.5	Small Angle Neutron Scattering: 25°C	232

A.3.6 Small Angle Neutron Scattering: 80°C	234
A.4 Data Handling	234
A.5 Results and Discussion	235
A.5.1 Asphaltene Fractionation	236
A.5.2 Asphaltene Fraction Chemistry	238
A.5.3 Vapor pressure osmometry of asphaltenes and their fractions	240
A.5.4 Small Angle Neutron Scattering: 25°C	241
A.5.5 Small Angle Neutron Scattering: 80°C	245
A.6 Conclusions	247
A.7 Acknowledgements	249
A.8 References	250
 Appendix B. Effects of Petroleum Resin on Asphaltene Aggregation and Water-in-Oil Emulsion Formation	 272
B.1 Abstract	272
B.2 Introduction	273
B.3 Experimental	275
B.3.1 Asphaltene Precipitation and Fractionation	275
B.3.2 SARA Fractionation	276
B.3.3 Asphaltene and Resin Solubility	277
B.3.4 Small-Angle Neutron Scattering	277
B.3.5 Resin-Asphaltene Emulsions	279
B.4 Results and Discussions	279
B.4.1 Asphaltene-Resin Solubility	279
B.4.2 SANS: Asphaltenes and Resins in Heptol	280
B.4.3 Asphaltene-Resin Emulsion Stability: Effect of varied R/A ratio	283
B.4.4 Asphaltene (Soluble, Whole, Precipitate)-Resin Emulsion Stability	285
B.5 Conclusions	288
B.6 Acknowledgements	290
B.7 References	290
 Appendix C. The Role of Asphaltene Solubility and Chemistry on Asphaltene Aggregation	 308
C.1 Abstract	308
C.2 Introduction	308
C.3 Experimental	312
C.3.1 Asphaltene Precipitation and Fractionation	312
C.3.2 SARA Fractionation	313
C.3.3 Asphaltene and Resin Solubility	313
C.3.4 Small-Angle Neutron Scattering	313
C.4 Results and Discussion	315
C.4.1 Asphaltene-Resin Solubility	315
C.4.2 SANS: Aggregate Size Analysis	317

C.4.3 SANS: Molecular Weight and Fractal Dimension Analysis	320
C.5 Conclusions	322
C.6 Acknowledgements	323
C.7 References	323
Appendix D. Asphaltene Aggregation: Techniques for Analysis	342
D.1 Introduction	342
D.2 Instrumental Techniques	343
D.2.1 Near-Infrared (NIR) Spectroscopy	343
D.2.2 Pulsed-Field Gradient Spin Echo Nuclear Magnetic Resonance (PFG-SE NMR)	343
D.2.3 Vapor Pressure Osmometry (VPO)	344
D.2.4 Small-Angle Neutron Scattering (SANS)	345
D.3 Conclusions	346
D.4 References	347
Appendix E. Synthesis and Characterization of Substituted Triphenylenes to Mimic the Solubility Behavior and Interfacial Activity of Asphaltenes	351
E.1 Introduction	351
E.2 Proposed Synthesis Reactions	352
E.3 Preliminary Results	354
E.4 References	354
Appendix F. SANS Dopant Data	363
Appendix G. Prediction of Resin Partitioning into Asphaltenic Aggregates	376
G.1 Abstract	376
G.2 Introduction	376
G.3 Experimental	380
G.3.1 Sample Preparation and Characterization	380
G.3.2 Small-Angle Neutron Scattering	380
G.3.3 Data Analysis	381
G.4 Results and Discussion	385
G.5 Acknowledgements	387
G.6 References	387
Appendix H. Asphaltene Emulsions	403

LIST OF TABLES

	Page
Table 2.1 Elemental composition of asphaltene samples.	58
Table 2.2 Comparison of Fit Parameters obtained from the Guinier approximation and small-particle mass-fractal models.	58
Table 2.3 Comparison of fit parameters obtained from various monodisperse and polydisperse form factor models.	59
Table 3.1 Crude oil and whole asphaltene properties.	94
Table 3.2 Log-normal distribution of chemical compositions (atomic) for asphaltenic fine fractions.	94
Table 3.3 Log-normal distribution of aggregate sizes.	94
Table 4.1 Ranges of chemical compositions (molar ratios) for asphaltene fractions.	138
Table 4.2 Model fitting parameters for Hondo asphaltenes in 40:60 d-heptane: d-toluene (v/v).	138
Table 4.3 Estimation of solvent entrainment for HO and GC asphaltenes in mixtures of deuterated toluene and hydrogenated toluene.	138
Table 4.4 Volume fraction of micro-particles from SANS for various asphaltene fractions in mixtures of d-heptane and d-toluene with comparison to precipitated volume fraction from gravimetric experiments.	139
Table 5.1 Elemental composition (atomic) of asphaltenes and resins.	173
Table 5.2 Summary of aggregate size parameters for HO1 asphaltenes in toluene as a function of concentration.	173
Table 5.3 Summary of aggregate molar masses, second virial coefficients, and percent solvent entrainment values for mixtures of asphaltenes and resins in various solvents.	173
Table 6.1 Hansen partial solubility parameter values of various solvents.	203
Table 6.2 Phase change data and ideal mole fraction solubility for anthracene and PHD.	203
Table 6.3 Molar extinction coefficients for ACA and PHD in 2-butanol at	203

selected wavelengths.	
Table 6.4 Hansen partial solubility parameters of ACA and PHD and corresponding weighting coefficients from regression analyses.	204
Table 6.5 Mole fraction solubility of ACA in binary solvent mixtures.	204
Table 6.6 Mole fraction solubility of PHD in binary solvent mixtures.	205
Table A.1 Typical Values of Elemental Compositions in Asphaltenes.	257
Table A.2 Crude oil properties.	257
Table A.3 Asphaltene fractionation results (wt%).	258
Table A.4 Asphaltene fraction composition in wt.%, except H/C ratio (atomic).	259
Table A.5 Metals analysis (ppm).	259
Table A.6 Correlation length (Å) of Whole, Soluble and Precipitate asphaltenes in heptol at 25 and 80°C: 1 wt %.	260
Table A.7 Correlation length (Å) of asphaltenes in 1-methylnaphthalene and toluene (80°C).	261
Table B.1 Crude oil properties	297
Table B.2 Asphaltene fraction composition in wt %, except H/C	297
Table B.3 Resin composition in wt %, except H/C (O by difference)	297
Table C.1 Crude oil properties	328
Table C.2 Asphaltene fraction composition in wt %, except H/C	328
Table C.3 Resin composition in wt %, except H/C (O by difference)	328
Scheme E.1 Synthesis of 2,3,6,7,10,11-hexahexyloxytriphenylene (HAT6)	356
Scheme E.2 Synthesis of branched alkoxytriphenylenes via oxidative trimerization	356
Scheme E.3 Variation of alkyl-chain length and extent of branching via (a) Mixed trimerization of 2 or more precursors and (b) Direct trimerization of asymmetric dialkoxybenzenes	357

Scheme E.4 Synthesis of polar functionalized triphenylenes	358
Table G.1 Chemical composition and coherent neutron scattering length density (ρ) of asphaltenes and resins. Scattering length density calculation assumes asphaltene mass density of 1.1 g/cm ³ and resin mass density of 1.0 g/cm ³ .	393
Table G.2 Summary of modified Lorentzian fit parameters to pure resin scattering curves.	393
Table G.3 Summary of Teixeira fit parameters to pure resin and mixed asphaltene-resin scattering curves before and after subtraction of resin scattering contributions. (Key: B6W60 = B6 Whole asphaltenes in 60 % toluene; B6P100 = B6 Precipitate asphaltenes in 100 % toluene; CSW60 = CS Whole asphaltenes in 60 % toluene; B6R100 = B6 resins in 100 % toluene; B6R60 = B6 resins in 60 % toluene).	394
Table H.1 Composition, Sauter mean droplet diameter, and stability of water-in-model oil emulsions. The aqueous phase consisted of brine at pH = 12 and the model oil phase consisted of 0.5 % (w/w) HO asphaltenes in 45:55 Heptane/Toluene. The volume ratio of oil: water was 1:1.	406

LIST OF FIGURES

	Page
<p>Figure 2.1 Low Q power law correction and small-particle mass-fractal fits to Hondo asphaltenes in mixed solvents. Legend: (Δ) Hondo asphaltenes in 40:60 d-heptane: d-toluene; (-----) low Q power law fit to 40:60 d-heptane: d-toluene; (\circ) power law subtracted data for 40:60 d-heptane: d-toluene; (\square) Hondo asphaltenes in 90:10 d-toluene: d-methanol; (—) small-particle mass-fractal fits with constant background.</p>	60
<p>Figure 2.2 Schematic representation of an asphaltene monomer and an asphaltenic aggregate consisting of four monomers.</p>	61
<p>Figure 2.3 Fits of monodisperse sphere (\times), monodisperse prolate cylinder (\bullet), and monodisperse oblate cylinder (—) models to Hondo asphaltenes (\square) in 90:10 d-toluene: d-methanol.</p>	62
<p>Figure 2.4 Reduced chi-squared values at various polydispersity parameters for fits of (\circ) polydisperse length oblate cylindrical and (\square) polydisperse radius oblate cylindrical models to Hondo asphaltenes in 90:10 d-toluene: d-methanol.</p>	63
<p>Figure 2.5 Fits of a polydisperse radius oblate cylinder form factor to Hondo asphaltenes in (\circ) 40:60 d-heptane: d-toluene and (\square) 90:10 d-toluene: d-methanol. Solid lines represent the model fits.</p>	64
<p>Figure 3.1 Schematic representation of the fine fractionation procedure for the preparation of N fractions. Whole asphaltenes (W) are dispersed in mixtures of heptane and toluene (H/T) at fixed solute concentration. After filtration of the equilibrated solution, the filter cake (P1) and filtrate (S1) are recovered and dried. The S1 fraction is dispersed in a H/T mixture with a higher volume fraction to recover a second precipitated fraction (P2). The sequential fractionation of the soluble fraction (S2) continues until N fractions are isolated. The final precipitated fraction (PN) and soluble fraction (SN) are isolated from pure heptane.</p>	95
<p>Figure 3.2 Cumulative % asphaltenes precipitated as function of volume % toluene in n-heptane-toluene mixtures, so-called differential solubility profiles, for (Δ) CS, (\square) HO, and (\circ) B6 asphaltenes in mixtures of heptane and toluene.</p>	96
<p>Figure 3.3a-c Histograms of atomic (a) hydrogen, (b) nitrogen, and (c) sodium contents for Hondo asphaltene solubility fractions. The solid lines represent fits of the data to log-normal distributions.</p>	97

Figure 3.4 Variation in atomic hydrogen: carbon ratio for (Δ) CS, (\square) HO, and (\circ) B6 asphaltenic fractions.	98
Figure 3.5 Variation in atomic nitrogen: carbon ratio for (Δ) CS, (\square) HO, and (\circ) B6 asphaltenic fractions.	99
Figure 3.6 Variation in atomic (\circ) oxygen and (\bullet) sulfur contents for B6 asphaltenic fractions.	100
Figure 3.7 Variation in atomic sodium: carbon ratio for (Δ) CS, (\square) HO, and (\circ) B6 asphaltenic fractions.	101
Figure 3.8 Variation in atomic (\circ) calcium, (\square) potassium, and (Δ) magnesium contents for B6 asphaltenic fractions.	102
Figure 3.9 Variation in atomic vanadium: carbon ratio for (Δ) CS, (\square) HO, and (\circ) B6 asphaltenic fractions.	103
Figure 3.10 Variation in atomic (\circ) aluminum, (\square) iron, and (Δ) nickel contents for B6 asphaltenic fractions.	104
Figure 3.11 Variation in atomic aggregate size for (\circ) B6 asphaltenic fractions in 90:10 d-methylnaphthalene: d-methanol, (\bullet) B6 asphaltenic fractions in toluene, and (\square) HO asphaltenic fractions in 90:10 d-toluene: d-methanol.	105
Figure 3.12a-b Histograms of aggregate size values for 1% (w/w) solutions of (a) Hondo asphaltenic fractions in 90:10 d-toluene: d-methanol and (b) B6 asphaltenic fractions in 90:10 d-methylnaphthalene: d-methanol. The solid lines represent fits of the data to log-normal distributions.	106
Figure 4.1 Example model fits to scattering curve for Hondo asphaltenes (1% wt) in 40:60 d-heptane: d-toluene (v/v). Legend: (Δ) raw data, (dashed line) power law fit, (\circ) power law corrected data, (black line) mass fractal fit, (grey line) polydisperse cylinder fit.	140
Figure 4.2 Comparison of (a) I_0 and (b) $\langle R_G \rangle$ parameters obtained from polydisperse oblate cylinder and Guinier fits. Dashed lines represent parity lines.	141
Figure 4.3 Correlation of apparent fractal dimension with aggregate size parameters obtained from the mass-fractal model. Filled triangles represent fractions dissolved in mixtures of d-heptane and d-toluene. Open circles represent fractions dissolved in mixtures of d-toluene (or d-methylnaphthalene) and d-methanol.	142

- Figure 4.4 Correlation of particle aspect ratio with average aggregate size parameters obtained from the polydisperse cylinder model. Filled triangles represent fractions dissolved in mixtures of d-heptane and d-toluene. Open circles represent fractions dissolved in mixtures of d-toluene (or d-methylnaphthalene) and d-methanol. 143
- Figure 4.5 Correlation of radius polydispersity with aggregate size parameters obtained from the polydisperse cylinder model. Filled triangles represent fractions dissolved in mixtures of d-heptane and d-toluene. Open circles represent fractions dissolved in mixtures of d-toluene (or d-methylnaphthalene) and d-methanol. 144
- Figure 4.6 Parity plot comparing apparent molecular weight calculated from the moments of the particle volume (eq. 15) and from I_0 measurements (eq. 14) assuming (○) no solvent entrainment and (□) solvent entrainment. The dashed line represents the parity line. 145
- Figure 4.7 Variation in percentage solvent entrainment with aggregate size. Filled triangles represent fractions dissolved in mixtures of d-heptane and d-toluene. Open circles represent fractions dissolved in mixtures of d-toluene (or d-methylnaphthalene) and d-methanol. 146
- Figure 4.8 Average aggregate molecular weight (dry) for the assumption of solvent entrainment compared to the average aggregate molecular weight for the assumption of no solvent entrainment. Solid line represents best-fit line through the data. 147
- Figure 5.1 SANS scattering curves for HO1 asphaltenes in d-toluene as a function of concentration: (○) 4.38 % w/w, (□) 1.98 % w/w, (△) 1.49 % w/w, (▽) 1.02 % w/w, (◇) 0.51 % w/w, and (x) 0.25 % w/w. Solid lines represent fits to polydisperse radius cylinder model. 174
- Figure 5.2 Comparison of calculated I_0 values (Equation 10) with those obtained from polydisperse cylinder fits for a concentration series of HO1 asphaltenes in d-toluene assuming various values of solvent entrainment. Legend: (□) no entrainment, slope = 2.75; (○) 10 % (v/v), slope = 2.26; (△) 20 % (v/v), slope = 1.81; (▽) 30 % (v/v), slope = 1.41; and (◇) 41 % (v/v), slope = 1.02. 175
- Figure 5.3 Concentration dependence of apparent molar mass (Equation 14) for mixtures of HO1 asphaltenes and B6 resins in 176

- d-toluene at various resin: asphaltene mass ratios (R/A).
Legend: (□) no resins; (○) R/A = 1.02; (△) R/A = 4.94.
- Figure 5.4 Second virial determination for mixtures of HO1 asphaltenes and B6 resins in d-toluene (R/A = 4.94). Parameters for best linear fit (solid line) through the data: slope = $2.0 \times 10^{-4} \pm 4 \times 10^{-5}$, intercept = $2.3 \times 10^{-5} \pm 2 \times 10^{-6}$, $R^2 = 0.9632$. 177
- Figure 5.5 Correlation of A_2 values to atomic H/C ratio for (□) asphaltenes, (○) resins, and (△) mixtures of asphaltenes and resins in d-toluene. The dashed line represents the best fit of the data to an exponential function. 178
- Figure 6.1 Molecular structures of 9-anthracenecarboxylic acid (ACA), phenanthridine (PHD), and a representative asphaltene molecule with molecular formula $C_{77}H_{89}NO_2S$ and molar mass of 1093 amu. 206
- Figure 6.2 UV-vis absorption spectra for (—) ACA and (---) PHD in 2-butanol. 207
- Figure 6.3 Beer-Lambert calibration curve for ACA in 2-butanol at $\lambda_{\max} = 381.0$ nm. The dashed line represents the best linear fit through the data. 208
- Figure 6.4a-d Solubility of ACA in mixed solvents. Solid lines represent solubility calculated from three-dimensional solubility parameter model. Legend: (■) Solvent 1: MN, Solvent 2: IBA; (□) Solvent 1: MN, Solvent 2: MB; (●) Solvent 1: DPK, Solvent 2: IBA; (○) Solvent 1: BBZ, Solvent 2: NBB; (▲) Solvent 1: IPA, Solvent 2: AN; (△) Solvent 1: H, Solvent 2: T; (◆) Solvent 1: EA, Solvent 2: PC. 209
- Figure 6.5a-d Solubility of PHD in mixed solvents. Solid lines represent solubility calculated from three-dimensional solubility parameter model. Legend: (■) Solvent 1: MN, Solvent 2: IBA; (□) Solvent 1: MN, Solvent 2: MB; (●) Solvent 1: DPK, Solvent 2: IBA; (○) Solvent 1: BBZ, Solvent 2: NBB; (▲) Solvent 1: IPA, Solvent 2: AN; (△) Solvent 1: H, Solvent 2: T; (◆) Solvent 1: EA, Solvent 2: PC. 210
- Figure 6.6 Correlation of % error in calculated mole fraction solubility to square of difference in hydrogen bonding parameters of ACA and IBA:DPK solvent blends. 211
- Figure 6.7 Correlation of % error in calculated mole fraction solubility to weighted sum of squared differences in solubility parameters of ACA 212

and (●) EA:PC and (□) MN:IBA solvent blends.

Figure 6.8	Solubility of ACA in solutions of 2-butanol with varying initial concentrations of PHD. The solid line represents ACA solubility calculated from the three-dimensional solubility parameter model assuming PHD modifies the solvent solubility parameters.	213
Figure A.1	Solubility profiles of Whole asphaltenes in heptol.	262
Figure A.2	Solubility profiles of Whole, Soluble and Precipitate asphaltenes in heptol.	263
Figure A.3	VPO molar masses of B6 asphaltenes (Soluble, Whole and Precipitate) in toluene at 53°C	264
Figure A.4	VPO molar masses of CS (Whole and Precipitate) asphaltenes in toluene at 53°C.	265
Figure A.5	SANS curves of B6 Whole asphaltenes in mixtures of d-heptane and d-toluene at 1 wt%, 25°C.	266
Figure A.6	SANS fits using Lorentzian line shapes. a.) AH Soluble asphaltenes: 1 wt %, 50 % (v/v) toluene in heptane, 25°C; $I_0 = 1.27 \pm 0.02$, $\xi = 29.9 \pm 0.3$, $R^2 = 0.9987$; b.) B6 Whole asphaltenes: 1 wt %, 60 % (v/v) toluene in heptane, 25°C; $I_0 = 6.7 \pm 0.1$, $\xi = 79 \pm 1$, $R^2 = 0.9974$. Note: Every other point displayed.	267
Figure A.7	Correlation lengths of Whole asphaltenes in heptol determined by SANS: 1 wt %, 25°C. The vertical dashed lines represent the solubility limit for a 1 wt% asphaltene solution in heptol.	268
Figure A.8	Correlation lengths of (a) Soluble and (b) Precipitate asphaltenes in heptol by SANS: 1 wt %, 25°C.	269
Figure A.9	Comparison of scattering intensities for HO Whole asphaltenes in toluene (I_w) and the weight-averaged summation of scattering intensities from HO Soluble and Precipitate fractions in toluene (I_{sum}). Fits of the scattering curves to Lorentzian lineshapes appear as solid lines with parameters for I_w given as $I_0: 2.12 \pm 0.05$, $\xi: 41 \pm 2$, $R^2: 0.9573$ and parameters for I_{sum} given as $I_0: 5.4 \pm 0.1$, $\xi: 74 \pm 2$, $R^2: 0.9964$. Note: Every other point displayed.	270
Figure A.10	SANS curves of asphaltenes (1% wt.) in heptol: a.) B6 Soluble in 50 % toluene; b.) B6 Whole in 60 % toluene; c.) B6 Precipitate in 100 % toluene.	271

Figure B.1 Schematic illustration of archipelago model of asphaltene monomers, asphaltenic aggregate in absence of resins, and asphaltenic aggregate in presence of resins.	298
Figure B.2 Solubility of 0.75 % (w/v) Whole asphaltenes and their more and less soluble subfractions in heptol with and without resins. Half filled markers denote systems without resins. R/A ratio was fixed at 1:1 by mass. (a) AH; (b) B6; (c) CS; (d) HO	299
Figure B.3 SANS fits (2 mm path length) using Lorentzian lineshapes. Canadon Seco Whole asphaltenes at 25°C in 60 % toluene with: a) No Resins: $I_0: 11.7 \pm 0.4$, $\xi: 101 \pm 3$, $R^2: 0.9958$; b) 0.5 wt% B6 Resins: $I_0: 6.9 \pm 0.1$, $\xi: 70 \pm 1$, $R^2: 0.9962$; c) 2 wt% B6 Resins: $I_0: 4.56 \pm 0.06$, $\xi: 48.5 \pm 0.8$, $R^2: 0.9967$; d) 4 wt% B6 Resins: $I_0: 3.80 \pm 0.03$, $\xi: 36.9 \pm 0.5$, $R^2: 0.9970$; e) 6 wt% B6 Resins: $I_0: 4.02 \pm 0.05$, $\xi: 31.1 \pm 0.6$, $R^2: 0.9940$; f) 10 wt% B6 Resins: $I_0: 3.30 \pm 0.04$, $\xi: 22.5 \pm 0.4$, $R^2: 0.9922$ Note: Every 2 nd data point plotted above $Q = 0.006$.	300
Figure B.4 Correlation length (ξ) of 1 wt % B6 Whole asphaltenic aggregates with AH and B6 Resins in pure toluene and 60 % toluene at 80°C determined from SANS (5 mm path length). Legend displayed as (resin type, % toluene).	301
Figure B.5 Emulsion stability (% water resolved) and aggregate ξ of CS Whole asphaltenes in 60 % toluene with added resins. R/A represents mass ratio of resins to asphaltenes. Emulsions tested using CS resins, 0.5 wt % asphaltenes. SANS ξ measured at 25°C using B6 resins, 1 wt % asphaltenes, 2 mm path length.	302
Figure B.6 Emulsion stability (% water resolved) and aggregate ξ of B6 Precipitate asphaltenes in toluene with B6 resins. Emulsions tested at 0.5 wt % and ξ determined by SANS at 25°C, 1 wt % asphaltenes, and 2 mm path length.	303
Figure B.7 Emulsion stability (% water resolved) and aggregate ξ of B6 Precipitate asphaltenes in 30 % toluene with B6 resins. Emulsions tested at 0.5 wt % and ξ determined by SANS at 25°C, 1 wt % asphaltenes, and 2 mm path length.	304
Figure B.8 Emulsion stability (% water resolved) of AH asphaltenes in heptol with AH resins. Emulsions tested at 0.5 wt %, 25°C. a) Soluble: 30, 60 % toluene; b) Whole: 30, 55 % toluene; c) Precipitate: 30, 60 % toluene	305
Figure B.9 Emulsion stability (% water resolved) of CS asphaltenes in heptol with CS resins. Emulsions tested at 0.5 wt %, 25°C.	306

- a) Soluble: 40, 50, 60 % toluene; b) Whole: 30, 45, 60 % toluene;
c) Precipitate: 50, 100 % toluene
- Figure B.10 Emulsion stability (vol % water resolved) and solubility (wt % precipitated) of B6 asphaltenes in heptol with B6 resins. Emulsions tested at 0.5 wt %, 25°C. a) B6 Soluble: 10, 30, 60 % toluene; b) B6 Whole: 40, 60, 100 % toluene; c) B6 Precipitate: 30, 60, 100 % toluene; d) HO Precipitate: 30, 60, 100 % toluene 307
- Figure C.1 Solubility of 0.75 % (w/v) CS Whole asphaltenes and their more and less soluble subfractions in heptol with and without resins. Half filled markers denote systems without resins. R/A ratio was fixed at 1:1 by mass. 329
- Figure C.2 Schematic illustrating the likeliest molecular structure of asphaltene and resin monomers, asphaltenic aggregates in the absence of solvating resins, and asphaltenic aggregates in the presence of solvating resins. The jagged lines represent aliphatic hydrocarbon moieties, the grey shaded regions represent aromatic or fused aromatic rings, and the black dots represent polar functional groups. 330
- Figure C.3 SANS curves of HO Whole asphaltenes in mixtures of d-heptane and d-toluene at 1 wt%, 25°C, 5 mm path length. 331
- Figure C.4 SANS fits (2 mm path length) using Lorentzian lineshapes. CS Precipitate asphaltenes at 25°C in pure toluene with: a) No Resins: Background: -0.12 ± 0.07 , I_0 : 15 ± 1 , I_1 : $1.94E-8 \pm 8.E-10$, ξ : 110 ± 8 ; b) 0.5 wt% B6 Resins: Background: -0.06 ± 0.06 , I_0 : 14.8 ± 0.9 , I_1 : $1.39E-8 \pm 5.E-10$, ξ : 103 ± 6 ; c) 2 wt% B6 Resins: Background: -0.02 ± 0.03 , I_0 : 6.9 ± 0.2 , I_1 : $1.22E-8 \pm 2.E-10$, ξ : 63 ± 2 ; d) 4 wt% B6 Resins: Background: 0.01 ± 0.06 , I_0 : 5.0 ± 0.2 , I_1 : $1.53E-8 \pm 3.E-10$, ξ : 47 ± 3 ; e) 6 wt% B6 Resins: Background: 0.09 ± 0.05 , I_0 : 4.3 ± 0.1 , I_1 : $1.44E-8 \pm 2.E-10$, ξ : 41 ± 2 ; f) 10 wt% B6 Resins: Background: 0.2 ± 0.1 , I_0 : 3.6 ± 0.2 , I_1 : $8.4E-9 \pm 4.E-10$, ξ : 38 ± 5 . Note: Every 2nd data point plotted above $Q = 0.006$ 332
- Figure C.5 Correlation lengths of B6 solubility fractions in heptol determined by SANS: 1 wt %, 25°C, 5 mm path length. 333
- Figure C.6 Correlation length ξ of B6 Whole asphaltene aggregates with B6 resins in pure toluene and 60 % toluene determined from SANS: 1 wt % asphaltenes, 80°C, 5 mm path length. 334
- Figure C.7 Correlation length ξ of CS Precipitate asphaltene aggregates with B6 resins in pure toluene and 50 % toluene determined from SANS: 1 wt % asphaltenes, 25°C, 2 mm path length. 335

- Figure C.8 Correlation length ξ of B6 Precipitate asphaltene aggregates with B6 resins in pure toluene and 30 % toluene determined from SANS: 1 wt % asphaltenes, 25°C, 2 mm path length. 336
- Figure C.9 Weight average molecular weight of B6 asphaltene solubility fractions in heptol determined by SANS: 1 wt %, 25°C, 5 mm path length. 337
- Figure C.10 Weight average molecular weight of CS Precipitate asphaltenes in heptol determined by SANS at various neutron path lengths: 1 wt %, 25°C . 338
- Figure C.11 Weight average molecular weight of CS Precipitate asphaltenes in pure toluene and 50 % toluene with added resins determined by SANS: 1 wt % asphaltenes, 25°C, 2 mm path length 339
- Figure C.12 Variation of aggregate molecular weight with ξ in all Whole asphaltenes and their sub-fractions dissolved in heptol: a) AH: slope of best fit line = 1.7 ± 0.1 , intercept = 5.2 ± 0.4 , $R^2 = 0.931$; b) B6: slope of best fit line = 1.91 ± 0.09 , intercept = 4.1 ± 0.4 , $R^2 = 0.938$; c) CS: slope of best fit line = 1.85 ± 0.07 , intercept = 4.6 ± 0.3 , $R^2 = 0.970$; d) HO: slope of best fit line = 2.12 ± 0.05 , intercept = 3.3 ± 0.2 , $R^2 = 0.989$. 340
- Figure C.13 Variation of aggregate molecular weight with ξ in all asphaltenes solvated with resins: slope of best fit line = 2.7 ± 0.1 , intercept = 0.1 ± 0.5 , $R^2 = 0.888$. 341
- Figure D.1 VPO molar masses of Athabasca C7-asphaltenes in 1,2-dichlorobenzene. [Reproduced with permission from *Ind. Eng. Chem. Res.* **2000**, 39(8), 2916-2924. Copyright 2000 Am. Chem. Soc.]. 348
- Figure D.2 Schematic illustration depicting (a) an asphaltene monomer; (b) an asphaltene aggregate with size ca. 3-4 nm, molecular weight ca. 20-25 kDa, and apparent “fractal” dimension between 1-2; and (c) an asphaltene aggregate with size ca. 12-15 nm, molecular weight ca. 200-400 kDa, and apparent “fractal” dimension between 2-2.5. 349
- Figure D.3 Aggregate sizes B6 Soluble (■), Whole (●), and Precipitate (◆) asphaltene fractions (1% wt) as a function of d-heptane content in d-toluene. Correlation length (ξ) scales with radius of gyration (R_g) according to the relation: $\xi = R_g / \sqrt{3}$. 350

Figure E.1 Representative 2D and 3D structures of a plausible asphaltene molecule with a structural formula of $C_{84}H_{98}N_2S_2O_3$, a molecular weight of 1248 amu, and an H/C ratio of 1.18. The 3D side view shows the flat, planar shape of the aromatic core.	359
Figure E.2 H^1 -NMR spectra and elemental analysis results for HAT6.	360
Figure E.3 H^1 -NMR spectra and mass spectroscopy results for HAT4-OH.	361
Figure E.4 H^1 -NMR spectra for HAT4-iso.	362
Figure F.1 Africa resins in d-toluene (ANL, 2 mm, 25°C).	363
Figure F.2 B6 P asphaltenes (1% wt.) and Africa resins in d-toluene (ANL, 2 mm, 25°C).	364
Figure F.3 B6 P asphaltenes (1% wt.) and d-methanol in d-toluene (ANL, 2 mm, 25°C).	364
Figure F.4 B6 P asphaltenes (1% wt.) and PHD in d-toluene (NIST, 5 mm, 80°C).	365
Figure F.5 B6 P asphaltenes (1% wt.) and B6 resins in d-toluene (ANL, 2 mm, 25°C).	365
Figure F.6 B6 P asphaltenes (1% wt.) and B6 resins in d-toluene (NIST, 5 mm, 80°C).	366
Figure F.7 B6 P asphaltenes (1% wt.) and B6 resins in 70:30 d-H:T (ANL, 2 mm, 25°C).	366
Figure F.8 B6 P asphaltenes (1% wt.) and B6 resins in d-MN (ANL, 2 mm, 25°C).	367
Figure F.9 B6 resins in 40:60 d-H:T (ANL, 2 mm, 25°C).	367
Figure F.10 B6 W asphaltenes (1% wt.) and B6 resins in 40:60 d-H:T (ANL, 2 mm, 25°C).	368
Figure F.11 B6 W asphaltenes (1% wt.) and B6 resins in d-toluene (ANL, 2 mm, 25°C).	368
Figure F.12 B6 W asphaltenes (1% wt.) and EBA in d-toluene (NIST, 5 mm, 80°C).	369
Figure F.13 B6 W asphaltenes (1% wt.) and Africa resins in 40:60 d-H:T	369

(ANL, 2 mm, 25°C).	
Figure F.14 CS P asphaltenes (1% wt.) and B6 resins in d-toluene (ANL, 2 mm, 25°C).	370
Figure F.15 CS P asphaltenes (1% wt.) and PHD in d-toluene (NIST, 5 mm, 80°C).	370
Figure F.16 CS P asphaltenes (1% wt.) and THC in d-toluene (NIST, 5 mm, 80°C).	371
Figure F.17 CS P asphaltenes (1% wt.) and B6 resins in 50:50 d-H:T (ANL, 2 mm, 25°C).	371
Figure F.18 CS W asphaltenes (1% wt.) and PHD in d-toluene (NIST, 5 mm, 80°C).	372
Figure F.19 CS W asphaltenes (1% wt.) and B6 resins in 40:60 d-H:T (ANL, 2 mm, 25°C).	372
Figure F.20 CS W asphaltenes (1% wt.) and B6 resins in 40:60 d-H:T (NIST, 5 mm, 80°C).	373
Figure F.21 CS W asphaltenes (1% wt.) and PHD in 40:60 d-H:T (NIST, 5 mm, 80°C).	373
Figure F.22 HO W asphaltenes (1% wt.) and B6 resins in d-toluene (NIST, 5 mm, 80°C).	374
Figure F.23 HO W asphaltenes (1% wt.) and B6 resins in 40:60 d-H:T (NIST, 5 mm, 80°C).	374
Figure F.24 HO W asphaltenes (1% wt.) and CA in 40:60 d-H:T (ANL, 2 mm, 25°C).	375
Figure G.1 Schematic illustration of an asphaltene monomer, resin monomer, asphaltenic aggregate in the absence of resins, and asphaltenic aggregate in the presence of resins.	395
Figure G.2 SANS scattering intensity curves for B6 Whole asphaltenes (1 % wt.) in 60 % toluene with: (□) no resins; (○) 2 % wt. B6 resins; (△) 6 % wt. B6 resins; and (◇) 10 % wt. B6 resins.	396
Figure G.3 Example fit of SANS scattering curve for B6 resins (10% wt.) in 60% toluene to a modified Lorentzian lineshape with additional terms to account for incoherent scattering and low Q upturn: $I_1 = 7.91E-6$;	397

$n = 2.07$; $I_0 = 0.521 \text{ cm}^{-1}$; $\xi = 11.0 \text{ \AA}$; $\text{bkg} = 0.0043 \text{ cm}^{-1}$; $R^2 = 0.9990$.
 Note: Every 2nd data point displayed.

- Figure G.4 SANS scattering intensity curves and Teixeira fits for solutions of B6 Whole asphaltenes (1% wt.) and B6 resins (4% wt.) in 60% toluene: (\square) Asphaltene-resin mixture, $I_{0AR} = 3.56 \pm 0.04 \text{ cm}^{-1}$, $D_{AR} = 1.62 \pm 0.05$, $\xi_{AR} = 43 \pm 2 \text{ \AA}$, $R^2 = 0.9993$; (\circ) Resin only solution, $I_{0R} = 0.343 \pm 0.001 \text{ cm}^{-1}$, $D_R = 1.86 \pm 0.05$, $\xi_R = 13.7 \pm 0.3 \text{ \AA}$, $R^2 = 0.9981$; (\triangle) Asphaltene only solution, $I_{0A} = 6.2 \pm 0.2 \text{ cm}^{-1}$, $D_A = 2.05 \pm 0.05$, $\xi_A = 64 \pm 3 \text{ \AA}$, $R^2 = 0.9993$; (\diamond) Residual scattering curve after resin subtraction, $I_{0Res} = 3.19 \pm 0.04 \text{ cm}^{-1}$, $D_{Res} = 1.87 \pm 0.05$, $\xi_{Res} = 40 \pm 2 \text{ \AA}$, $R^2 = 0.9991$. Note: Every 2nd data point displayed. 398
- Figure G.5 Molecular weight (M_R) values for B6 resins as a function of concentration in pure toluene (\blacksquare) and 60% toluene (\bullet). 399
- Figure G.6 Molecular weight values for solutions of asphaltenes (1% wt.) with B6 resins at various concentrations: a) B6 Whole asphaltenes in 60% toluene (\blacksquare); b) B6 Precipitate asphaltenes in 100% toluene (\bullet); c) CS Whole asphaltenes in 60% toluene (\blacktriangle). The solid, dashed, and dotted lines represent the weight-averaged summation of molecular weights for the individual scattering components by three different methods. d) Values of the asphaltene (x_A , \blacklozenge) and asphaltene-resin (x_{AR} , \blacktriangledown) mass fractions as a function of resin content. 400
- Figure G.7 Correlation length (half-filled symbols) and fractal dimension (filled symbols) values for B6 and CS Whole asphaltenes (1% wt.) in 60% toluene with various concentrations of phenanthridine added as a dopant. SANS scattering curves were collected at 80°C in 5 mm pathlength cells. 401
- Figure G.8 Correlation length (\blacksquare) and fractal dimension (\blacksquare) values for HO Whole asphaltenes (1% wt.) in 100% toluene with various concentrations of β -cholanic acid added as a dopant. 402
- Figure H.1 Schematic representation of a water droplet in an oil continuous emulsion according to a core-shell model. Legend: r_{core} = core radius; ρ_{core} = scattering length density of water phase; t = shell thickness; ρ_{shell} = scattering length density of shell; ρ_{oil} = scattering length density of oil phase. 407
- Figure H.2 SANS scattering intensity curves for mixed CA and asphaltene emulsions. 408
- Figure H.3 Fits of emulsions E8 to a polydisperse core-shell model. 409

Figure H.4 Fit of the polydisperse core-shell model to emulsion E1.

410

CHAPTER 1

INTRODUCTION

1.1 Petroleum Production Challenges

The tendency of petroleum asphaltenes to associate in solution and adsorb at interfaces can cause significant problems during the production, recovery, pipeline transportation, and refining of crude oil. For example, a common method of increasing oil production involves the injection of miscible agents (e.g., carbon dioxide or natural gas) into underground reserves to displace the oil. This practice may result in the formation asphaltenic deposits that tend to plug up the reservoir wells and pipelines [1,2]. Similarly, asphaltene-stabilized water-in-crude oil (w/o) emulsions are formed during various stages of the production, such as by turbulent flow of fluids up a bore hole, with the addition of “wash water” during the desalting operation, and by wave agitation of crude oil spills on water [3-11]. The propensity of asphaltenes to adsorb at interfaces is related to the extent of asphaltene aggregation and the solvating power of the crude oil media [12]. Asphaltenes maintain a delicate balance between solvency, aggregation, and interfacial activity in solution that must ultimately be related to the chemical composition of the participating components.

1.2 Asphaltene Chemistry

Asphaltenes are operationally defined as the portion of crude oil insoluble in light n-alkanes (e.g., n-heptane or n-pentane), but soluble in aromatic solvents (e.g., benzene or toluene) [13]. The quantity, chemical composition, and molar mass distribution of the asphaltene “solubility class” varies significantly with the source of the crude oil and with the method of precipitation [14-16]. Asphaltenes comprise the most polar fraction of the crude

oil and consist of polyaromatic condensed rings with short aliphatic side chains and polar heteroatom-containing functional groups [17-21]. Asphaltenes are polydisperse in terms of chemical composition, with typical atomic H/C ratios varying between 1.0 to 1.3 and N, S, and O contents of a few weight percent [12,22-24]. FTIR studies have shown that sulfur is evenly distributed among the acidic, basic, and neutral fractions of asphaltenes [25-28]. X-ray absorption near-edge structure spectroscopy (XANES) reveals that sulfur exists predominantly as thiophenic heterocycles (65-85%) and sulfidic groups [29]. The thiophenic groups are only slightly polar and are not likely to contribute to intermolecular associations, such as hydrogen bonding. Unlike sulfur, oxygen and nitrogen containing moieties in asphaltenes are generally polar and capable of participating in strong intermolecular associations. For example, FTIR and XANES spectroscopy reveal several polar functional groups, such as carboxylic acids, carbonyls, phenols, pyrroles, and pyridines, that are capable of participating in proton donor-acceptor interactions [28,30,31]. Mingyuan et al. [32] used diffuse reflectance FTIR to show that the interfacially active components of fractionated asphaltenes contained significant concentrations of acidic and open chain carbonyl groups. They suggested that the elastic nature of open chained carbonyls (as opposed to carbonyls in ring systems) introduces a strong hydrogen bonding contribution to the mechanical film strength that prevents water droplet coalescence.

Various metals (e.g., Ni, V, Fe, Al, Na, Ca, and Mg) have also been shown to accumulate in the asphaltenic fraction of crude oil, typically in concentrations < 1 % (w/w) [12,15,33,34]. Vanadium and nickel are generally the most abundant of the trace metals, are present mainly as chelated porphyrin complexes, and have been linked to catalyst poisoning during upgrading of heavy oils [35-37]. The concentrations of other trace metals not bound

in porphyrin structures (e.g., Fe, Al, Na, Ca, and Mg) have also been reported to vary in deposits as a function of well depth [38] and among asphaltene subfractions [12,34].

1.3 Asphaltene Subfractionation

1.3.1 Subfractionation Procedures

Several of the above-described problems encountered during petroleum production may be related to a particular subfraction of the total asphaltenes. Separation of the total asphaltenes into subfractions is often motivated by an attempt to probe the relationship between the chemical composition, solubility, aggregation behavior, and emulsion-stabilizing properties of discrete portions of the asphaltene fraction. Previous methods of separating asphaltenes into subfractions include gel permeation chromatography [39], sequential elution solvent chromatography [40], liquid-liquid extraction [41], dialysis fractionation [42], ultra-centrifugation [43], and precipitation by the addition of flocculants [12,20,31,33-34,41,44-47].

1.3.2 Coarse Fractionations

Two different experimental methods are common for the separation of asphaltenes into subfractions by precipitation and will be referred to as the “coarse” and “fine” fractionation methods. The solvent/anti-solvent combination used and exact procedure for isolation of the precipitated asphaltenes generally varies between researchers; however, in both methods the total asphaltene fraction is typically dispersed in a “good” solvent (e.g., toluene) at a fixed solute concentration and a flocculating solvent (e.g., n-heptane) is added to induce partial precipitation. During a coarse fractionation, two asphaltenic fractions (i.e.,

insolubles and solubles) are generated by asphaltene precipitation at a given solvent condition. Typically, the ratio of flocculant to solvent is varied so that several pairs of more and less soluble fractions are generated. For example, Yarranton and Masliyah studied the solubility behavior and molar mass distribution from vapor pressure osmometry (v.p.o.) and interfacial tension measurements of several Athabasca n-C₇ asphaltenic coarse fractions precipitated from mixtures of hexane and toluene [48]. Andersen et al. generated several coarse fractions of Boscan n-C₇ asphaltenes by precipitation in mixtures of heptane and toluene [41,46]. Spiecker et al. studied the solubility and aggregation behavior by SANS of coarse asphaltenic fractions precipitated from various parent asphaltenes by a similar procedure [12]. In each of the above studies, the aromaticity and N/C content of the less soluble fractions generally decreased with increasing yield of precipitated asphaltenes (i.e., higher flocculant/solvent ratios) and corresponded with an increase in aggregate size. Sulfur and oxygen contents were typically distributed evenly throughout the fractions. Furthermore, the less soluble fractions were generally more aromatic, had a higher N/C content, and formed larger aggregates in toluene and pyridine than the more soluble fractions. The various studies offered differing results concerning the isolation of trace metal species. UV-vis and HPLC-SEC measurements on Boscan asphaltenes indicated that metalloporphyrins were preferentially extracted in the more soluble fraction and contents decreased with decreasing asphaltene yield of the insoluble fraction [41,46]. In contrast, higher concentrations of various trace metals (e.g., Fe, Ni, V, Na) were observed in the less soluble fractions compared to the more soluble fractions as determined by the inductively coupled plasma (ICP) technique [12].

1.3.3 Fine Fractionations

Instead of generating only two fractions, one of which represents at least half of the original asphaltene by mass, the fine fractionation procedure separates the total asphaltene into several discrete subfractions by a step-wise increase in the concentration of the flocculating solvent. During each precipitation step, a small amount of asphaltene material is precipitated and isolated, the soluble filtrate is recovered, and the next fraction is precipitated after a change in solvent conditions. The major difference between the coarse and fine fractionation methods is that the coarse fractions precipitated at higher flocculant contents likely contain the entire subset of chemical species present in fractions precipitated at lower flocculant contents; whereas each fine fraction should represent the discrete subset of asphaltene that precipitate between the ranges of two solvent conditions. For example, Yang et al. isolated six asphaltene subfractions from Athabasca bitumen by step-wise increasing the ratio of n-heptane to bitumen (H/B) [34]. The first fraction to precipitate was the most aromatic and had the highest concentration of Fe, Ca, Mg, and Al. Atomic H/C ratio was observed to increase and metalloporphyrin contents decrease systematically as the fractionation proceeded (i.e., at higher H/B ratios). Unlike the previous analyses of coarse fractions by SANS and v.p.o. [12,45], no significant variations in aggregate molar mass were observed v.p.o. for the fractions dissolved in toluene at 50°C. Groenzin et al. isolated six subfractions of n-C₅ asphaltene by sequential precipitation in mixtures of n-pentane and toluene [20]. Fluorescence depolarization measurements on solutions of the asphaltene fractions in toluene indicated that the less soluble fractions emitted at higher wavelengths than more soluble fractions, suggesting the less soluble fraction possibly contained a higher population of large chromophores.

Buenrostro-Gonzalez et al. compared the chemical composition of subfractions generated by step-wise increasing the amount of flocculant (i.e., acetone or n-heptane) added to a 2.3 % (w/w) solution of Mayan n-C₇ asphaltenes in toluene [31]. Ten discrete fractions were generated for each solvent mixture, but not enough material was precipitated during the first few fractionations (i.e., the least soluble asphaltenic fractions) to perform subsequent chemical analyses. There were no apparent trends in atomic H/C, N/C, S/C, or O/C with the order of fractionation for the heptane-toluene fractions analyzed. Similarly, there were no apparent trends in atomic H/C, N/C, or S/C for the acetone-toluene fractions; however, O/C content appeared to increase continuously for the third through sixth fraction. These results suggested that polar interactions dominated the solubility behavior at low acetone contents, while dispersion interactions dominated the solubility behavior at high acetone contents and for the heptane-toluene fractions. Similar polar fractionations were performed by sequentially increasing the amount of n-pentane flocculant to a mixture of Mobil and Venezuelan n-C₇ asphaltenes in methylene chloride [33,44]. Marked differences in physical appearance, crystallinity, and solubility behavior (in dodecylbenzene sulfonic acid) were observed between the most polar and least polar fractions. Similarly, the more polar fractions had higher metals contents (i.e., Fe, Ni, and V) than the less polar fractions.

1.4 Asphaltene Aggregate Structure

The aggregation mechanism for asphaltenes is primarily governed by van der Waals dispersion interactions, electrostatic interactions between molecular charges, hydrogen bonding of polar moieties, and orientation dependent repulsive steric interactions with lesser contributions stemming from intermolecular charge transfer and weak inductive interactions

[49]. A recent proposal based on a review of the current literature suggests that strong specific forces, such as interactions between polar heteroatoms or π -bonding between aromatic moieties, drive asphaltene aggregation while weaker non-specific dispersion forces dominate asphaltene precipitation [50].

Although the intermolecular interactions that drive asphaltene aggregation are generally accepted, debate still exists over the orientation of heteroatom, alkyl, and aromatic moieties within the molecular framework. For example, two different models have been adopted in the literature to account for the degree of aromatic condensation within the fused ring backbone of asphaltenes, but both models are consistent with monomer masses between 500 to 1000 amu. One is the so-called “continental” model of asphaltenes [51], which posits a monomer molecular structure consisting of a large, highly condensed aromatic core surrounded by an aliphatic periphery, as inferred from X-ray diffraction and fluorescence depolarization experiments [20,52-56]. Interactions of “continental” monomers would likely form dense-packed aggregates through stacking interactions of the aromatic cores [55,56]. Alternatively, the so-called “archipelago” model [51] was proposed in which individual asphaltene monomers are comprised of clusters of polycondensed groups consisting of 5 to 7 aromatic rings connected by short aliphatic side chains, possibly containing polar heteroatom bridges [18,19,55,57,58]. The “archipelago” model is supported by chemical and thermal degradation studies which concluded that the extent of aromatic condensation in asphaltenes is significantly lower than generally believed [58]. Furthermore, molecular simulation studies on a proposed Athabasca asphaltene structure suggested that the presence of long aliphatic bridges gives asphaltenes the capacity to fold themselves into a complex three-dimensional globular structure with self-similar internal structure [55]. If the archipelago-

like structure is valid, it seems probable that asphaltenic aggregates possess a porous, reticulated microstructure susceptible of entraining significant amounts of surrounding solvent.

1.5 Instrumental Techniques

Various experimental techniques have previously been applied to study the aggregation behavior of asphaltenes in solution including: near-infrared spectroscopy [59,60], pulsed-field gradient spin echo nuclear magnetic resonance [61,62], vapor pressure osmometry [12,48,63], viscosity measurements [64-67], small-angle X-ray scattering (SAXS) [43,63,65,68-72], and small-angle neutron scattering (SANS) [11,12,63,64,69-71,73-85].

1.5.1 Near-Infrared Spectroscopy

The near-infrared (NIR) spectroscopic region of the electromagnetic spectrum spans the wavelength range from 780-2500 nm. The most prominent absorption bands in this region are associated with the overtones or combinations of stretching vibrations from carbon-hydrogen bonds. Such vibrational modes are described theoretically using an anharmonic oscillator model. NIR spectra also possess a background elevation due to light scattering by particles and aggregates. NIR experiments are relatively simple, time efficient, and non-invasive. The NIR technique can be quickly and accurately exploited to generate a large amount of information; however, it is still unclear whether or not it can quantitatively predict aggregate sizes [59,60]. For example, Auflem et al. performed NIR experiments to study the disintegration of North Sea asphaltenes (0.125% wt) dissolved in 70/30 n-

heptane/toluene by adding various amphiphiles and naphthenic acids as a function of concentration [59]. Changes in asphaltene aggregate size were observed as a decrease in the optical density at 1600 nm. Aske et al. pressurized North Sea crude oil (~0.8% wt asphaltenes) to 300 bar and then depressurized in incremental steps with NIR spectra recorded at each pressure [60]. The aggregation onset pressures, as well as changes in the fluid compressibility and aggregate size, were determined from multivariate analysis of the NIR spectra. Furthermore, re-pressurization showed reversibility of the crude oil aggregates to their original aggregate size after 72 hours at 300 bar.

1.5.2 Pulsed-Field Gradient Spin Echo Nuclear Magnetic Resonance

Pulsed-field gradient spin echo nuclear magnetic resonance (PFG-SE NMR) is a non-invasive, relatively fast instrumental technique to probe molecular self-diffusion coefficients using magnetic field gradients of varying strength to effect large signal attenuation. Asphaltene polydispersity can be accounted for in the data analysis by assuming a log-normal distribution of diffusion coefficients. A log-normal distribution is reasonable because diffusion coefficients are positive-definite and may vary over several orders of magnitude. Deuterated solvents are typically used to prevent signal attenuation from proton spin-spin relaxation. Östlund et al. studied the self-diffusion of Venezuelan asphaltenes (0.044 to 5% wt) in d-toluene [61]. Fitting the signal attenuation in the range from 0.7 to 1.9 ppm provided a polydispersity ($\sigma \sim 0.6$) that was concentration independent. A median diffusion coefficient, D_m , on the order of 1×10^{-10} to 2×10^{-10} m²/s monotonically decreased with increasing concentration, indicating an increase in the average aggregate size. Model fitting of the diffusion coefficients based on particle geometry and concentration suggested that

asphaltene aggregates could not be spherical in shape, because of large obstruction effects. Instead, a disc-like structure was proposed. In another study, deuterated n-pentane and n-heptane ($\leq 30\%$ wt) were added to Venezuelan asphaltenes (3.7% wt) in d-toluene and d-ethylbenzene [62]. Non-linear increases in D_m with flocculant concentration were observed that could not be attributed to changes in the solvent viscosity alone. For example, D_m of asphaltenes in toluene increased from ca. 1.15×10^{-10} m²/s with no flocculant added to 1.35×10^{-10} m²/s at 30% pentane. The polydispersity of the solute increased from $\sigma = 0.6$ to 0.7 at the highest flocculant concentration, further suggesting that n-alkane addition was inducing flocculation. Sjöblom et al. showed that PFG-SE NMR is applicable to study the interactions of asphaltenes with various additives, such as naphthenic acids, which serve to solvate asphaltenes and decrease aggregate sizes [86].

1.5.3 Vapor Pressure Osmometry

Vapor pressure osmometry (v.p.o.) takes advantage of the change in vapor pressure when a small amount of solute is added to a pure solvent. The v.p.o. measuring chamber consists of a solvent reservoir with two wicks providing a saturated solvent atmosphere around two thermistors. Condensation of solvent from the atmosphere into an asphaltene solution placed at one thermistor releases heat and increases the thermistor temperature until the solution vapor pressure matches the pure solvent. Subsequent small voltage changes induced at the thermistor are related to the number-averaged molar mass of the solute. Vapor pressure osmometry measurements are limited to single solvent solutions and are impractical for the study of whole crudes. Yarranton et al. observed the molar masses of Athabasca and Cold Lake bitumen asphaltenes in toluene and 1,2-dichlorobenzene increased with

concentration to a limiting value of 10-20 g/L (~ 1-2 wt %) [48]. Linear extrapolation of apparent molar mass versus solute concentration below 3 g/L suggested monomer molar masses of ca. 1000 g/mol. The molar mass at high concentration approached 6000 g/mol, a value indicative of an aggregate with approximately six monomers. The degree of asphaltene association varied with solvent polarity and temperature with no clear indication that asphaltenes were completely dissociated in the low concentration limit. Spiecker et al. performed v.p.o. measurements on whole asphaltenes and their more and less soluble subfractions in toluene at 53°C [12]. The apparent molar masses (12,000-17,000 g/mole) of the less soluble fraction of B6 crude oil were substantially higher than the corresponding unfractionated asphaltenes and more soluble fractions (2500-3500 g/mole) due to significant polar and H-bonding interactions among the asphaltene monomers in the absence of the solvating character of the complementary more soluble fraction.

1.5.4 Viscosity Measurements

Low shear viscosity measurements are often performed to complement other experimental methods, because the geometry-dependent intrinsic viscosity is often coupled with other contributions, such as interparticle interactions and solvation [66]. In fact, solvation of asphaltenes by the surrounding solvent is suggested to modify the aggregate geometry. For example, viscosity measurements on Khafji asphaltenes in benzene described four alternative means of modeling the hydrodynamic shape of solvated and unsolvated asphaltenic aggregates depending on assumptions made concerning the thickness of the solvation layer [67]. The extent of solvation for Ratawi and Hassi Messaoud asphaltenes in toluene was quantified by measuring the relative viscosity as a function of solute

concentration [66,87]. Similar calculations of solvent entrainment were obtained from viscosity measurements performed on natural and synthetic Ratawi vacuum residue [88]. The results from these studies suggested that the solvated volume of the asphaltenic aggregates was 1.7 to 2.7 times the unsolvated or “dry” asphaltene volume, implying a volumetric entrainment of about 40-60%. Similar attempts to quantify the extent of solvation of Safaniya asphaltenes in mixtures of heptane and toluene were performed by a combination of SANS and viscosity measurements [64]; however, poor agreement of the effective asphaltene volume fraction within the aggregates calculated from the two methods suggested the need to include polydispersity or to modify the assumed aggregate shape.

1.5.5 Small-Angle Scattering

In a typical scattering experiment, radiation is elastically scattered by a sample and the resulting scattering pattern is used to deduce various colloidal properties of the aggregates in solution, such as the aggregate radius of gyration (R_g), molar mass, apparent “fractal” dimension, and second virial coefficients (A_2). Molar masses are weight-averaged and may be biased toward the presence of a small number of high mass aggregates in solution. Small-angle neutron scattering (SANS) and small-angle x-ray scattering (SAXS) methods differ in the type of incident radiation used. Subsequently, scattering of x-rays is caused by differences in electron density while scattering of neutrons is caused by differences in scattering length density of various nuclei. SANS studies typically employ selective solvent deuteration to maximize the coherent scattering contrast between the solvent and solute. Perhaps the major drawback of SANS is the monetary cost of deuterated solvents and the limited availability of beamtime at national laboratories.

A wide variety of intra-particle structure factors have previously been applied to the SAXS and SANS scattering spectra of asphaltene solutions, often with limited information concerning the quality of the fits and the data range over which the models were applied. Due to the wide range of particle geometries included in the model fits, it is unlikely that every model describes accurately the structure of asphaltenic aggregates. However, it is reasonable to assume that the asphaltenic aggregate structure could change with concentration, solvent conditions, temperature, and solute chemical composition.

1.5.5.1 Guinier and Zimm Approximations

In the absence of a geometric model that describes the colloidal structure of asphaltenic aggregates, the Guinier approximation has been applied to estimate the radius of gyration (R_G) and zero-Q scattering intensity (I_0) of the aggregates [74,83]. For example, X-ray scattering experiments performed by on Mexican oil and deposit asphaltenes dissolved in toluene and tetrahydrofuran showed a decrease in Guinier R_G values as a function of aging time (fresh to one month) [83]. A similar non-geometric data treatment is the Zimm approximation [89] in which the scattering intensity in the low Q limit is described by a Lorentzian lineshape. Several studies applied the Zimm approximation to solutions of asphaltenes to determine changes in aggregate R_G and apparent molar mass with changes in solvent conditions [64], source crude [72], temperature and concentration [81], fractionation of the asphaltenes [12,43], and with the addition of selective solvating agents [11,65]. Similar studies were performed on the compatible and incompatible blending of crude oil mixtures [84]. Application of both the Guinier and Zimm approximations are limited to the data range where $Q_{\max}R_G \leq 1$.

1.5.5.2 Monodisperse Form Factors

Various monodisperse form factors previously fit to asphaltene scattering data included spheres, ellipsoids, and cylinders. For example, Tanaka et al [82] inferred a change in the aggregate morphology of Maya, Khafji, and Iranian Light asphaltenes (5% wt. in decalin, 1-methylnaphthalene, and quinoline) from monodisperse prolate ellipsoids to monodisperse spheres as the solution temperature increased from 25°C to 350°C. Ravey et al. [73] suggested the SANS scattering spectra for Safaniya asphaltenes (1% wt. in tetrahydrofuran) were consistent with a thin disk model of typical dimensions 7 x 150 Å (thickness x radius). Similarly, Espinat et al. [69] suggested the scattering spectra for Safaniya asphaltenes (2% wt.) in toluene were consistent with an oblate ellipsoid of dimensions 6 x 92 Å (thickness x radius). X-ray diffraction experiments on Ratawi and Kuwaiti asphaltenes indicated an average stack height of 20 to 30 Å with an average distance of 3.5 to 3.7 Å between the aromatic sheets [90], suggesting that aggregates contain 7 to 10 aromatic sheets within a stacked cluster. The monodisperse form factor fits described above are inconsistent with the X-ray diffraction results and suggest that average clusters of aromatic moieties within the aggregates occur as dimers. Furthermore, considering that asphaltene molecules are polydisperse in terms of chemical composition, one would expect the aggregates formed from the interactions of individual molecules to be polydisperse as well. Therefore, it is unlikely that any monodisperse form factor model accurately describes the morphology of asphaltenic aggregates.

1.5.5.3 Polydisperse Form Factors

Other researchers have introduced polydispersity analyses into model fits during the analyses of scattering spectra from asphaltene solutions. For example, Sheu et al. [76] modeled the scattering behavior of asphaltenes in toluene (1 to 20% wt.) assuming polydisperse spheres with a Schultz distribution of radii. Similar polydisperse sphere analyses performed on the SAXS spectra of Athabasca asphaltenes in toluene (5 to 15% wt.) showed a Schultz-like distribution of radii with $R_{\text{avg}} = 33 \text{ \AA}$ and a second distribution peak around 140 \AA for the 5% wt. dispersion (90 \AA for the 15% wt. dispersion) [70]. Barre et al. [71] analyzed SAXS scattering curves for Safaniya vacuum resid asphaltenes (5% wt. in toluene) using polydisperse spherical, ellipsoidal, and cylindrical form factors with a log-normal distribution of radii. Subsequent comparison of the fit parameters suggested a range in polydispersity values from 50 to 60% and variation in the average particle volume from 340 to 440 nm^3 depending on the model used. Other researchers have modeled the aggregation behavior of asphaltenes as polydisperse mass-fractal aggregates [77, 80].

Depending on the aspect ratio of particle radius to length, different geometric models that include polydispersity in the aggregate size parameters appear accurate. In some cases, the scattering spectra were modeled as oblate cylinders with polydispersity in the particle radius. For example, Herzog et al. [68] observed the X-ray scattering intensity distribution for Grenada and Pematang asphaltenes in benzene was consistent with a thin disk model (thickness = 3.4 \AA) with a power law distribution of radii ($13 \text{ \AA} \leq R \leq 800 \text{ \AA}$). Bardon et al. [63] approximated the scattering intensity curves for Safaniya asphaltenes (2% wt. in toluene) as flat disks with a log-normal distribution of radii. Size parameters obtained from SANS measurements indicated an average particle radius, radius spread, and thickness of 51 \AA , 19 \AA , and 8 \AA , respectively. Assuming an average distance of 3.5 \AA between the aromatic

sheets, the particle thicknesses obtained from the above model fits suggest that stacks of aromatic moieties within the aggregates are one or two monomers thick. These thicknesses do not appear credible considering the previously described X-ray diffraction results [90]. In other cases, the scattering spectra were modeled as prolate cylinders with polydispersity in the particle length. For example, Thiyagarajan et al. [78] performed SANS experiments on 5% wt. Maya asphaltenes in 1-methylnaphthalene as a function of solution temperature from 20°C to 400°C and analyzed the corresponding scattering curves using a maximum entropy technique. Under the maximum entropy technique, a cylinder form factor was convoluted with an instrument resolution function to extract the polydispersity in the radius and length of the particles. Measurements performed at 20°C suggested that the aggregates were best represented as prolate cylinders with a radius of 18 Å and a distribution of lengths from 100 to 500 Å. Lin et al. [79] applied a polydisperse cylinder model with a Schultz distribution of radii to 2.5% wt. asphaltenes in 1-methylnaphthalene (60°C). The average radius, standard deviation in the radius, and thickness of the aggregate were 14 Å, 12.9 Å, and 20 Å, respectively.

1.6 Overview of Dissertation

To help the petroleum industry improve the conversion of crude oil into useful product, it is necessary to better understand the factors that contribute to the aggregation behavior and interfacial activity of asphaltenes. An in-depth knowledge of the distribution of chemical compositions of the asphaltenic subfractions, as well as elucidation of asphaltene aggregate structures and aggregate interactions with the surrounding solvent media is a vital part of these efforts.

In Chapter 2, several form factor models are applied to the SANS scattering intensity curves of asphaltene solutions in three different solvents. Criteria are established to assess the quality of each model fit in an effort to determine the general shape of asphaltenic aggregates. As it is well known that asphaltene molecules are chemically polydisperse, one would expect the aggregates formed from the interactions of individual molecules to also be polydisperse. Thus, a polydisperse radius oblate cylinder model is introduced to characterize asphaltene aggregation behavior. In subsequent chapters, the model is used to calculate various physical properties from the scattering data, such as the average aggregate radius of gyration, molar mass, second virial coefficients, and percentage of solvent entrapment within asphaltenic aggregates.

In Chapter 3, asphaltenes from three different crude sources are separated on a preparatory-scale into 20 to 30 discrete subfractions by sequential precipitation in mixtures of heptane and toluene. Combustion elemental analyses and ICP metals analyses are performed to measure the carbon, hydrogen, nitrogen, sulfur, oxygen, and trace metals contents of each subfraction. SANS measurements are performed on subfractions dissolved in mixtures of d-toluene (or d-methylnaphthalene) and d-methanol and the resulting scattering intensity curves are fit using a polydisperse oblate cylinder form factor to determine the average radius of gyration of the aggregates. The preparatory-scale separation of the asphaltenes into several discrete subfractions allows the development of the first ever chemical and colloidal distribution functions for petroleum asphaltenes.

Chapter 4 demonstrates the applicability of the polydisperse oblate cylinder model to the SANS scattering curves of asphaltene solutions possessing a wide diversity of solute chemical compositions and solvent qualities. Typical ranges of aggregate size parameters are

discussed in relation to the contending “continental” and “archipelago” models describing the molecular framework of asphaltenes. Discrepancies between average aggregate molar masses obtained by two independent means suggest the need to include the solvation effects in the calculations. The amount of solvent entrained within the asphaltenic aggregates is quantified and compared to results obtained from earlier viscosity measurements. The calculated solvent entrainment values are also used to estimate the relative proportions of micro-scale and nano-scale aggregates in solution with limited accuracy.

Chapter 5 builds on the previous calculations of average aggregate molar masses and extents of solvent entrainment to discuss the interactions of asphaltenic aggregates in solutions. Changes in the apparent aggregate mass with solute concentration indicate deviations from ideal solution behavior (i.e., non-interacting aggregates plus solvent), which are quantified through the determination of aggregate second virial coefficients. Second virial coefficient values were previously reported or inferred from SANS and VPO experiments studying asphaltenes in toluene and 1,2-dichlorobenzene; however, this study is the first to investigate the roles of source crude, chemical composition, solvent conditions, and the influence of selective solvating agents on asphaltene second virial coefficient values.

A UV-vis spectroscopic technique is developed in Chapter 6 to determine the solubility of poly-nuclear aromatic compounds in binary solvent mixtures with the intention of extending the analyses to more complex multi-component mixtures, such as petroleum asphaltenes. Binary solvent mixtures are selected to probe specific intermolecular interactions between the solvent and solute (i.e., dispersion, polar, and hydrogen bond interactions). The solubility data are fit to a three-dimensional solubility parameter model based on regular solution theory with a Flory-Huggins correction for non-zero entropy of

mixing. The predictive capability of the model is tested for two poly-nuclear aromatic compounds in several binary solvent mixtures. Additional experiments apply the solubility parameter model to a multi-component solute mixture.

Chapter 7 summarizes the major findings in this study and contains suggestions for future work. This unified body of work examines the roles of chemical composition and solvency on the aggregation and solubility behavior of asphaltenes. Although small-angle neutron scattering has been used in the past to characterize the aggregation behavior of petroleum asphaltenes, many of these earlier studies assumed particle shapes that are not physically reasonable and/or neglected solvent entrainment and second virial effects in calculations of the aggregate molar masses. The petroleum industry can apply the findings of this research to better characterize the asphaltenes responsible for aggregation and interfacial adsorption and to enable the selection of more efficient dispersants or demulsifiers for petroleum mixtures.

1.8 References

1. A. Hammami, C. H. Phelps, T. Monger-McClure, T. M. Little, "Asphaltene precipitation from live oils: An experimental investigation of onset conditions and reversibility," *Energy & Fuels*, 2000, **14**(1): p. 14-18.
2. K. Karan, A. Hammami, M. Flannery, B. A. Stankiewicz, "Evaluation of asphaltene instability and a chemical control during production of live oils," *Petroleum Science and Technology*, 2003, **21**(3-4): p. 629-645.
3. S. D. Taylor, J. Czarnecki, J. Masliyah, "Disjoining pressure isotherms of water-in-bitumen emulsion films," *Journal of Colloid and Interface Science*, 2002, **252**(1): p. 149-160.
4. H. W. Yarranton, H. Hussein, J. H. Masliyah, "Water-in-hydrocarbon emulsions stabilized by asphaltenes at low concentrations," *Journal of Colloid and Interface Science*, 2000, **228**(1): p. 52-63.

5. K. Khristov, S. D. Taylor, J. Czarnecki, J. Masliyah, "Thin liquid film technique - application to water-oil-water bitumen emulsion films," *Colloids and Surfaces a-Physicochemical and Engineering Aspects*, 2000, **174**(1-2): p. 183-196.
6. T. E. Havre, J. Sjoblom, "Emulsion stabilization by means of combined surfactant multilayer (D-phase) and asphaltene particles," *Colloids and Surfaces a-Physicochemical and Engineering Aspects*, 2003, **228**(1-3): p. 131-142.
7. N. Aske, R. Orr, J. Sjoblom, H. Kallevik, G. Oye, "Interfacial properties of water-crude oil systems using the oscillating pendant drop. Correlations to asphaltene solubility by near infrared spectroscopy," *Journal of Dispersion Science and Technology*, 2004, **25**(3): p. 263-275.
8. N. Aske, H. Kallevik, J. Sjoblom, "Water-in-crude oil emulsion stability studied by critical electric field measurements. Correlation to physico-chemical parameters and near-infrared spectroscopy," *Journal of Petroleum Science and Engineering*, 2002, **36**(1-2): p. 1-17.
9. I. H. Auflem, H. Kallevik, A. Westvik, J. Sjoblom, "Influence of pressure and solvency on the separation of water-in-crude-oil emulsions from the North Sea," *Journal of Petroleum Science and Engineering*, 2001, **31**(1): p. 1-12.
10. P. M. Spiecker, P. K. Kilpatrick, "Interfacial rheology of petroleum asphaltenes at the oil-water interface," *Langmuir*, 2004, **20**(10): p. 4022-4032.
11. P. M. Spiecker, K. L. Gawrys, C. B. Trail, P. K. Kilpatrick, "Effects of petroleum resins on asphaltene aggregation and water-in-oil emulsion formation," *Colloids and Surfaces a-Physicochemical and Engineering Aspects*, 2003, **220**(1-3): p. 9-27.
12. P. M. Spiecker, K. L. Gawrys, P. K. Kilpatrick, "Aggregation and solubility behavior of asphaltenes and their subfractions," *Journal of Colloid and Interface Science*, 2003, **267**(1): p. 178-193.
13. D. L. Mitchell, J. G. Speight, "The Solubility of Asphaltenes in Hydrocarbon Solvents," *Fuel*, 1973, **52**(4): p. 149-152.
14. J. T. Miller, R. B. Fisher, P. Thiyagarajan, R. E. Winans, J. E. Hunt, "Subfractionation and characterization of Mayan asphaltene," *Energy & Fuels*, 1998, **12**(6): p. 1290-1298.
15. J. D. McLean, P. K. Kilpatrick, "Comparison of Precipitation and Extrography in the Fractionation of Crude Oil Residua," *Energy and Fuels*, 1997, **11**: p. 570-585.
16. G. Brons, J. M. Yu, "Solvent Deasphalting Effects on Whole Cold Lake Bitumen," *Energy & Fuels*, 1995, **9**(4): p. 641-647.

17. O. P. Strausz, P. Peng, J. Murgich, "About the colloidal nature of asphaltenes and the MW of covalent monomeric units," *Energy & Fuels*, 2002, **16**(4): p. 809-822.
18. J. M. Sheremata, M. R. Gray, H. D. Dettman, W. C. McCaffrey, "Quantitative molecular representation and sequential optimization of athabasca asphaltenes," *Energy & Fuels*, 2004, **18**(5): p. 1377-1384.
19. M. R. Gray, "Consistency of asphaltene chemical structures with pyrolysis and coking behavior," *Energy & Fuels*, 2003, **17**(6): p. 1566-1569.
20. H. Groenzin, O. C. Mullins, S. Eser, J. Mathews, M. G. Yang, D. Jones, "Molecular size of asphaltene solubility fractions," *Energy & Fuels*, 2003, **17**(2): p. 498-503.
21. U. Bergmann, H. Groenzin, O. C. Mullins, P. Glatzel, J. Fetzer, S. P. Cramer, "X-ray Raman spectroscopy - A new tool to study local structure of aromatic hydrocarbons and asphaltenes," *Petroleum Science and Technology*, 2004, **22**(7-8): p. 863-875.
22. M. A. Bestougeff, "Chemical Composition and Structure of Asphaltenes . Their Importance among Natural Organic Compounds," *Bulletin De La Societe Chimique De France*, 1967, (12): p. 4773-&.
23. M. M. Boduszynski, "Characterization of "Heavy" Crude Components," *Preprints ACS Division of Petroleum Chemistry*, 1985, **30**: p. 626-640.
24. M. M. Boduszynski, "Composition of Heavy Petroleums. 2. Molecular Characterization," *Energy & Fuels*, 1988, **2**(5): p. 597-613.
25. J. F. McKay, D. R. Latham, W. E. Haines, "Composition of Petroleum Heavy Ends. 3. Comparison of the Composition of High-Boiling Petroleum Distillates and Petroleum > 675 C Residues," *Fuel*, 1981, **60**(1): p. 27-32.
26. J. F. McKay, P. M. Harnsberger, R. B. Erickson, T. E. Cogswell, D. R. Latham, "Composition of Petroleum Heavy Ends. 2. Characterization of Compound Types in Petroleum >675 C Residues," *Fuel*, 1981, **60**(1): p. 17-26.
27. J. F. McKay, P. J. Amend, P. M. Harnsberger, T. E. Cogswell, D. R. Latham, "Composition of Petroleum Heavy Ends. 1. Separation of Petroleum > 675 C Residues," *Fuel*, 1981, **60**(1): p. 14-16.
28. M. M. Boduszynski, J. F. McKay, D. R. Latham, "Asphaltenes, Where Are You?," *Proceedings of the Association of Asphalt Paving Technologists*, 1980, **49**: p. 123-143.
29. O. C. Mullins, Sulfur and Nitrogen Molecular Structures in Asphaltenes and Related Materials Quantified by XANES Spectroscopy, *in* "Asphaltenes: Fundamentals and

- Applications" (E. Y. Sheu and O. C. Mullins, Eds.), Plenum Press, New York, 1995; pp 53-96.
30. S. Mitrakirtley, O. C. Mullins, J. Vanelp, S. J. George, J. Chen, S. P. Cramer, "Determination of the Nitrogen Chemical Structures in Petroleum Asphaltenes Using Xanes Spectroscopy," *Journal of the American Chemical Society*, 1993, **115**(1): p. 252-258.
 31. E. Buenrostro-Gonzalez, S. I. Andersen, J. A. Garcia-Martinez, C. Lira-Galeana, "Solubility/molecular structure relationships of asphaltenes in polar and nonpolar media," *Energy & Fuels*, 2002, **16**(3): p. 732-741.
 32. L. Mingyuan, A. Christy, J. Sjoblom, Water-in-Crude Oil Emulsions from the Norwegian Continental Shelf Part VI -- Diffuse Reflectance Fourier Transform Infrared Characterization of Interfacially Active Fractions from North Sea Crude Oil, in "Emulsions -- A Fundamental and Practical Approach" (J. Sjoblom, Eds.), Kluwer Academic Publishers, The Netherlands, 1992; pp 157-172.
 33. T. J. Kaminski, H. S. Fogler, N. Wolf, P. Wattana, A. Mairal, "Classification of asphaltenes via fractionation and the effect of heteroatom content on dissolution kinetics," *Energy & Fuels*, 2000, **14**(1): p. 25-30.
 34. X. L. Yang, H. Hamza, J. Czarnecki, "Investigation of subfractions of athabasca asphaltenes and their role in emulsion stability," *Energy & Fuels*, 2004, **18**(3): p. 770-777.
 35. M. F. Ali, H. Perzanowski, A. Bukhari, A. A. Al-Haji, "Nickel and Vanadyl Porphyrins in Saudi Arabian Crude Oils," *Energy & Fuels*, 1993, **7**(2): p. 179-184.
 36. C. Ovalles, I. Rojas, S. Acevedo, G. Escobar, G. Jorge, L. B. Gutierrez, A. Rincon, B. Scharifker, "Upgrading of Orinoco Belt crude oil and its fractions by an electrochemical system in the presence of protonating agents," *Fuel Processing Technology*, 1996, **48**(2): p. 159-172.
 37. M. E. Pena, A. Manjarrez, A. Campero, "Distribution of vanadyl porphyrins in a Mexican offshore heavy crude oil," *Fuel Processing Technology*, 1996, **46**(3): p. 171-182.
 38. E. Chouparova, A. Lanzirrotti, H. Feng, K. W. Jones, N. Marinkovic, C. Whitson, P. Philp, "Characterization of petroleum deposits formed in a producing well by synchrotron radiation-based microanalyses," *Energy & Fuels*, 2004, **18**(4): p. 1199-1212.
 39. N. Cyr, D. D. McIntyre, G. Toth, O. P. Strausz, "Hydrocarbon Structural Group Analysis of Athabasca Asphaltene and its G.P.C. Fractions by C-13 N.M.R.," *Fuel*, 1987, **66**: p. 1709-1714.

40. F. S. Jacobs, R. H. Filby, "Liquid Chromatographic Fractionation of Oil-Sand and Crude Oil Asphaltenes," *Fuel*, 1983, **62**(10): p. 1186-1192.
41. S. I. Andersen, A. Keul, E. Stenby, "Variation in composition of subfractions of petroleum asphaltenes," *Petroleum Science and Technology*, 1997, **15**(7-8): p. 611-645.
42. S. Acevedo, G. Escobar, M. A. Ranaudo, J. Pinate, A. Amorin, M. Diaz, P. Silva, "Observations about the structure and dispersion of petroleum asphaltenes aggregates obtained from dialysis fractionation and characterization," *Energy & Fuels*, 1997, **11**(4): p. 774-778.
43. D. Fenistein, L. Barre, "Experimental measurement of the mass distribution of petroleum asphaltene aggregates using ultracentrifugation and small-angle X-ray scattering," *Fuel*, 2001, **80**(2): p. 283-287.
44. V. Nalwaya, V. Tangtayakom, P. Piumsomboon, S. Fogler, "Studies on asphaltenes through analysis of polar fractions," *Industrial & Engineering Chemistry Research*, 1999, **38**(3): p. 964-972.
45. H. W. Yarranton, J. H. Masliyah, "Molar Mass Distribution and Solubility Modeling of Asphaltenes," *AIChE Journal*, 1996, **42**(12): p. 3533-3543.
46. S. I. Andersen, "Dissolution of Solid Boscan Asphaltenes in Mixed-Solvents," *Fuel Science & Technology International*, 1994, **12**(11-12): p. 1551-1577.
47. S. I. Andersen, "Effect of Precipitation Temperature on the Composition of N-Heptane Asphaltenes .2," *Fuel Science & Technology International*, 1995, **13**(5): p. 579-604.
48. H. W. Yarranton, H. Alboudwarej, R. Jakher, "Investigation of asphaltene association with vapor pressure osmometry and interfacial tension measurements," *Industrial & Engineering Chemistry Research*, 2000, **39**(8): p. 2916-2924.
49. J. Murgich, "Intermolecular forces in aggregates of asphaltenes and resins," *Petroleum Science and Technology*, 2002, **20**(9-10): p. 983-997.
50. G. Porte, H. G. Zhou, V. Lazzeri, "Reversible description of asphaltene colloidal association and precipitation," *Langmuir*, 2003, **19**(1): p. 40-47.
51. J. Murgich, "Molecular simulation and the aggregation of the heavy fractions in crude oils," *Molecular Simulation*, 2003, **29**(6-7): p. 451-461.

52. T. F. Yen, J. G. Erdman, S. S. Pollack, "Investigation of Structure of Petroleum Asphaltenes By X-Ray Diffraction," *Analytical Chemistry*, 1961, **33**(11): p. 1587-1594.
53. H. Groenzin, O. C. Mullins, "Asphaltene molecular size and structure," *Journal of Physical Chemistry A*, 1999, **103**(50): p. 11237-11245.
54. H. Groenzin, O. C. Mullins, "Molecular size and structure of asphaltenes from various sources," *Energy & Fuels*, 2000, **14**(3): p. 677-684.
55. J. Murgich, J. A. Abanero, O. P. Strausz, "Molecular recognition in aggregates formed by asphaltene and resin molecules from the Athabasca oil sand," *Energy & Fuels*, 1999, **13**(2): p. 278-286.
56. A. Sharma, H. Groenzin, A. Tomita, O. C. Mullins, "Probing order in asphaltenes and aromatic ring systems by HRTEM," *Energy & Fuels*, 2002, **16**(2): p. 490-496.
57. V. Calemma, P. Iwanski, M. Nali, R. Scotti, L. Montanari, "Structural Characterization of Asphaltenes of Different Origins," *Energy & Fuels*, 1995, **9**(2): p. 225-230.
58. O. P. Strausz, T. W. Mojelsky, E. M. Lown, "The Molecular-Structure of Asphaltene - an Unfolding Story," *Fuel*, 1992, **71**(12): p. 1355-1363.
59. I. H. Auflem, T. E. Havre, J. Sjoblom, "Near-IR study on the dispersive effects of amphiphiles and naphthenic acids on asphaltenes in model heptane-toluene mixtures," *Colloid and Polymer Science*, 2002, **280**(8): p. 695-700.
60. N. Aske, H. Kallevik, E. E. Johnsen, J. Sjoblom, "Asphaltene aggregation from crude oils and model systems studied by high-pressure NIR spectroscopy," *Energy & Fuels*, 2002, **16**(5): p. 1287-1295.
61. J. A. Ostlund, S. I. Andersson, M. Nyden, "Studies of asphaltenes by the use of pulsed-field gradient spin echo NMR," *Fuel*, 2001, **80**(11): p. 1529-1533.
62. J. A. Ostlund, J. E. Lofroth, K. Holmberg, M. Nyden, "Flocculation behavior of asphaltenes in solvent/nonsolvent systems," *Journal of Colloid and Interface Science*, 2002, **253**(1): p. 150-158.
63. C. Bardon, L. Barre, D. Espinat, V. Guille, M. H. Li, J. Lambard, J. C. Ravey, E. Rosenberg, T. Zemb, "The colloidal structure of crude oils and suspensions of asphaltenes and resins," *Fuel Science & Technology International*, 1996, **14**(1-2): p. 203-242.

64. D. Fenistein, L. Barre, D. Broseta, D. Espinat, A. Livet, J. N. Roux, M. Scarsella, "Viscosimetric and neutron scattering study of asphaltene aggregates in mixed toluene/heptane solvents," *Langmuir*, 1998, **14**(5): p. 1013-1020.
65. C. Giavarini, D. Mastrofini, M. Scarsella, L. Barre, D. Espinat, "Macrostructure and rheological properties of chemically modified residues and bitumens," *Energy & Fuels*, 2000, **14**(2): p. 495-502.
66. Y. Bouhadda, D. Bendedouch, E. Sheu, A. Krallafa, "Some preliminary results on a physico-chemical characterization of a Hassi Messaoud petroleum asphaltene," *Energy & Fuels*, 2000, **14**(4): p. 845-853.
67. W. Takeshige, "Hydrodynamic shape and size of Khafji asphaltene in benzene," *Journal of Colloid and Interface Science*, 2001, **234**(2): p. 261-268.
68. P. Herzog, D. Tchoubar, D. Espinat, "Macrostructure of Asphaltene Dispersions by Small-Angle X-Ray-Scattering," *Fuel*, 1988, **67**(2): p. 245-250.
69. D. Espinat, J. C. Ravey, V. Guille, J. Lambard, T. Zemb, J. P. Cotton, "Colloidal Macrostructure of Crude-Oil Studied by Neutron and X-Ray Small-Angle Scattering Techniques," *Journal De Physique Iv*, 1993, **3**(C8): p. 181-184.
70. Y. N. Xu, Y. Koga, O. P. Strausz, "Characterization of Athabasca Asphaltenes by Small-Angle X-Ray-Scattering," *Fuel*, 1995, **74**(7): p. 960-964.
71. L. Barre, D. Espinat, E. Rosenberg, M. Scarsella, "Colloidal structure of heavy crudes and asphaltene solutions," *Revue de l'Institut Francais du Petrole*, 1997, **52**(2): p. 161-175.
72. T. G. Savvidis, D. Fenistein, L. Barre, E. Behar, "Aggregated structure of flocculated asphaltenes," *Aiche Journal*, 2001, **47**(1): p. 206-211.
73. J. C. Ravey, G. Ducouret, D. Espinat, "Asphaltene Macrostructure by Small-Angle Neutron-Scattering," *Fuel*, 1988, **67**(11): p. 1560-1567.
74. R. E. Overfield, E. Y. Sheu, S. K. Sinha, K. S. Liang, "SANS Study of Asphaltene Aggregation," *Fuel Science & Technology International*, 1989, **7**(5-6): p. 611-624.
75. J. C. Ravey, D. Espinat, "Macrostructure of petroleum asphaltenes by small angle neutron scattering," *Progress in Colloid & Polymer Science*, 1990, **81**: p. 127-130.
76. E. Y. Sheu, K. S. Liang, S. K. Sinha, R. E. Overfield, "Polydispersity Analysis of Asphaltene Solutions in Toluene," *Journal of Colloid and Interface Science*, 1992, **153**(2): p. 399-410.

77. Y. C. Liu, E. Y. Sheu, S. H. Chen, D. A. Storm, "Fractal Structure of Asphaltenes in Toluene," *Fuel*, 1995, **74**(9): p. 1352-1356.
78. P. Thiyagarajan, J. E. Hunt, R. E. Winans, K. B. Anderson, J. T. Miller, "Temperature-Dependent Structural-Changes of Asphaltenes in 1-Methylnaphthalene," *Energy & Fuels*, 1995, **9**(5): p. 829-833.
79. M. Y. Lin, E. B. Sirota, H. Gang, "Neutron scattering characterization of asphaltene particles," *Abstracts of Papers of the American Chemical Society*, 1997, **213**: p. 66-FUEL.
80. M. Sahimi, H. Rassamdana, "Formation, growth and precipitation of fractal molecular aggregates in porous media," *Physica A*, 1997, **240**(3-4): p. 419-431.
81. J. N. Roux, D. Broseta, B. Deme, "SANS study of asphaltene aggregation: Concentration and solvent quality effects," *Langmuir*, 2001, **17**(16): p. 5085-5092.
82. R. Tanaka, J. E. Hunt, R. E. Winans, P. Thiyagarajan, S. Sato, T. Takanohashi, "Aggregates structure analysis of petroleum asphaltenes with small-angle neutron scattering," *Energy & Fuels*, 2003, **17**(1): p. 127-134.
83. A. Cosultchi, P. Bosch, V. H. Lara, "Small-angle X-ray scattering study of oil- and deposit-asphaltene solutions," *Colloid and Polymer Science*, 2003, **281**(4): p. 325-330.
84. T. G. Mason, M. Y. Lin, "Asphaltene nanoparticle aggregation in mixtures of incompatible crude oils," *Physical Review E*, 2003, **67**(5): p.
85. T. G. Mason, M. Y. Lin, "Time-resolved small angle neutron scattering measurements of asphaltene nanoparticle aggregation kinetics in incompatible crude oil mixtures," *Journal of Chemical Physics*, 2003, **119**(1): p. 565-571.
86. J. Sjoblom, N. Aske, I. H. Auflem, O. Brandal, T. E. Havre, O. Saether, A. Westvik, E. E. Johnsen, H. Kallevik, "Our current understanding of water-in-crude oil emulsions. Recent characterization techniques and high pressure performance," *Advances in Colloid and Interface Science*, 2003, **100**: p. 399-473.
87. E. Y. Sheu, M. M. Detar, D. A. Storm, "Rheological Properties of Vacuum Residue Fractions in Organic-Solvents," *Fuel*, 1991, **70**(10): p. 1151-1156.
88. D. A. Storm, E. Y. Sheu, "Rheological Studies of Ratawi Vacuum Residue at 366-K," *Fuel*, 1993, **72**(2): p. 233-237.
89. B. H. Zimm, "The Scattering of Light and the Radial Distribution Function of High Polymer Solutions," *Journal of Chemical Physics*, 1948, **16**(12): p. 1093-1099.

90. M. N. Siddiqui, M. F. Ali, J. Shirokoff, "Use of X-ray diffraction in assessing the aging pattern of asphalt fractions," *Fuel*, 2002, **81**(1): p. 51-58.

Asphaltenic Aggregates are Polydisperse Oblate Cylinders

Keith L. Gawrys and Peter K. Kilpatrick

ABSTRACT

Small-angle neutron scattering (SANS) has proven to be very useful for deducing the sizes and morphologies of asphaltenic aggregates in solution. A wide variety of intra-particle structure factors have previously been applied to SANS scattering spectra, but the studies often provided limited information concerning the quality of the fits and the Q-range over which the models were applied. Selection of an appropriate form factor that closely approximates the structure of asphaltenic aggregates is important for determining the properties of asphaltenic aggregates, such as the radius of gyration (R_G), molar mass, and apparent fractal dimension. This study evaluates various mono- and polydisperse intra-particle structure factor models as applied to four asphaltene scattering spectra. Agreement of the model fit parameters (I_0 and R_G) with those obtained from Guinier analyses suggests that such a form factor model is physically reasonable. Reduced chi-squared values for each non-linear least squares fit indicates how well a given model fits the entire Q-range studied for the scattering intensity distribution. In the polydispersity analyses, an analytical function is introduced to model the scattering behavior of oblate cylinders with a Schultz distribution of radii. Results indicate that the polydisperse radius oblate cylinder model best approximates the shape of asphaltenic aggregates.

CHAPTER 2

ASPHALTENIC AGGREGATES ARE POLYDISPERSE OBLATE CYLINDERS

2.1 Introduction

Because of their propensity to aggregate, flocculate, precipitate, and adsorb onto interfaces, the presence of asphaltenes in crude oil poses considerable challenges for the petroleum industry. Asphaltenes are generally defined as the toluene (or benzene) soluble, yet *n*-heptane (or *n*-pentane) insoluble, portion of crude oil [1-3]. This solubility class definition of asphaltenes suggests a broad distribution of asphaltene molecular structures that vary greatly among crude sources. In general, asphaltenes possess fused ring aromaticity, small aliphatic side chains, and polar heteroatom-containing functional groups (e.g., carboxylic acids, carbonyl, phenol, pyrroles, and pyridines) capable of donating or accepting protons inter- and intra-molecularly [4-8]. Atomic H/C ratios from 1.0 to 1.3 and nitrogen, sulfur, and oxygen contents of a few weight percent suggest that the asphaltene backbone mostly contains fused aromatic carbon interspersed with occasional polar functional groups [9-13]. The most plausible mechanisms of asphaltene aggregation involve van der Waals dispersion interactions between aromatic rings, hydrogen bonding between polar functional groups, and other charge transfer interactions [14]. Therefore, asphaltene aggregation behavior is likely controlled by the polydispersity, chemical composition, and steric arrangement or inter-connectivity of functional groups in the asphaltene monomers.

Various experimental techniques have previously been applied to study the aggregation behavior of asphaltenes in solution including: near-infrared spectroscopy [15,16], pulsed-field gradient spin echo nuclear magnetic resonance [17,18], vapor pressure

osmometry [19-21], viscosity measurements [22-25], small-angle X-ray scattering (SAXS) [19,23,26-31], and small-angle neutron scattering (SANS) [19,21,22,27-29,32-45]. Small-angle scattering methods, such as SAXS and SANS, have been useful for deducing the sizes of asphaltenic aggregates in solution based on assumed particle morphologies. However, a wide variety of intra-particle structure factors have previously been applied to the SAXS and SANS scattering spectra of asphaltene solutions, often with limited information concerning the quality of the fits and the data range over which the models were applied. Due to the wide range of particle geometries included in the model fits, it is unlikely that every model describes accurately the structure of asphaltenic aggregates. However, it is reasonable to assume that the asphaltenic aggregate structure could change with concentration, solvent conditions, temperature, and solute chemical composition.

In the absence of a geometric model that describes the colloidal structure of asphaltenic aggregates, the Guinier approximation has been applied to estimate the radius of gyration (R_G) and zero-Q scattering intensity (I_0) of the aggregates [33,43]. For example, X-ray scattering experiments performed by on Mexican oil and deposit asphaltenes dissolved in toluene and tetrahydrofuran showed a decrease in Guinier R_G values as a function of aging time (fresh to one month) [43]. A similar non-geometric data treatment is the Zimm approximation [46] in which the scattering intensity in the low Q limit is described by a Lorentzian lineshape. Several studies applied the Zimm approximation to solutions of asphaltenes to determine changes in aggregate R_G and apparent molar mass with changes in solvent conditions [22], source crude [31], temperature and concentration [40], fractionation of the asphaltenes [21,30], and with the addition of dopants [23,41]. Similar studies were performed on the compatible and incompatible blending of crude oil mixtures [44].

Application of both the Guinier and Zimm approximations are limited to the data range where $Q_{\max}R_G \leq 1$.

Various monodisperse form factors previously fit to asphaltene scattering data included spheres, ellipsoids, and cylinders. For example, Tanaka et al [42] inferred a change in the aggregate morphology of Maya, Khafji, and Iranian Light asphaltenes (5% wt. in decalin, 1-methylnaphthalene, and quinoline) from monodisperse prolate ellipsoids to monodisperse spheres as the solution temperature increased from 25°C to 350°C. Ravey et al. [32] suggested the SANS scattering spectra for Safaniya asphaltenes (1% wt. in tetrahydrofuran) were consistent with a thin disk model of typical dimensions 7 x 150 Å (thickness x radius). Similarly, Espinat et al. [27] suggested the scattering spectra for Safaniya asphaltenes (2% wt.) in toluene were consistent with an oblate ellipsoid of dimensions 6 x 92 Å (thickness x radius). X-ray diffraction experiments on Ratawi and Kuwaiti asphaltenes indicated an average stack height of 20 to 30 Å with an average distance of 3.5 to 3.7 Å between the aromatic sheets [47], suggesting that aggregates contain 7 to 10 aromatic sheets within a stacked cluster. The monodisperse form factor fits described above are inconsistent with the X-ray diffraction results and suggest that average clusters of aromatic moieties within the aggregates occur as dimers. Furthermore, considering that asphaltene molecules are polydisperse in terms of chemical composition, one would expect the aggregates formed from the interactions of individual molecules to be polydisperse as well. Therefore, it is unlikely that any monodisperse form factor model accurately describes the morphology of asphaltenic aggregates.

Other researchers have introduced polydispersity analyses into model fits during the analyses of scattering spectra from asphaltene solutions. For example, Sheu et al. [35]

modeled the scattering behavior of asphaltenes in toluene (1 to 20% wt.) assuming polydisperse spheres with a Schultz distribution of radii. Similar polydisperse sphere analyses performed on the SAXS spectra of Athabasca asphaltenes in toluene (5 to 15% wt.) showed a Schultz-like distribution of radii with $R_{\text{avg}} = 33 \text{ \AA}$ and a second distribution peak around 140 \AA for the 5% wt. dispersion (90 \AA for the 15% wt. dispersion) [28]. Barre et al. [29] analyzed SAXS scattering curves for Safaniya vacuum resid asphaltenes (5% wt. in toluene) using polydisperse spherical, ellipsoidal, and cylindrical form factors with a log-normal distribution of radii. Subsequent comparison of the fit parameters suggested a range in polydispersity values from 50 to 60% and variation in the average particle volume from 340 to 440 nm^3 depending on the model used. Other researchers have modeled the aggregation behavior of asphaltenes as polydisperse mass-fractal aggregates [36,39].

Depending on the aspect ratio of particle radius to length, different geometric models that include polydispersity in the aggregate size parameters appear accurate. In some cases, the scattering spectra were modeled as oblate cylinders with polydispersity in the particle radius. For example, Herzog et al. [26] observed the X-ray scattering intensity distribution for Grenada and Pematang asphaltenes in benzene was consistent with a thin disk model (thickness = 3.4 \AA) with a power law distribution of radii ($13 \text{ \AA} \leq R \leq 800 \text{ \AA}$). Bardon et al. [19] approximated the scattering intensity curves for Safaniya asphaltenes (2% wt. in toluene) as flat disks with a log-normal distribution of radii. Size parameters obtained from SANS measurements indicated an average particle radius, radius spread, and thickness of 51 \AA , 19 \AA , and 8 \AA , respectively. Assuming an average distance of 3.5 \AA between the aromatic sheets, the particle thicknesses obtained from the above model fits suggest that stacks of aromatic moieties within the aggregates are one or two monomers thick. These thickness do

not appear credible considering the previously described X-ray diffraction results [47]. In other cases, the scattering spectra were modeled as prolate cylinders with polydispersity in the particle length. For example, Thiagarajan et al. [37] performed SANS experiments on 5% wt. Maya asphaltenes in 1-methylnaphthalene as a function of solution temperature from 20°C to 400°C and analyzed the corresponding scattering curves using a maximum entropy technique. Under the maximum entropy technique, a cylinder form factor was convoluted with an instrument resolution function to extract the polydispersity in the radius and length of the particles. Measurements performed at 20°C suggested that the aggregates were best represented as prolate cylinders with a radius of 18 Å and a distribution of lengths from 100 to 500 Å. Min et al. [38] applied a polydisperse cylinder model with a Schultz distribution of radii to 2.5% wt. asphaltenes in 1-methylnaphthalene (60°C). The average radius, standard deviation in the radius, and thickness of the aggregate were 14 Å, 12.9 Å, and 20 Å, respectively.

This study compares various intra-particle structure factor models applied to scattering intensity curves obtained from solutions of Hondo, Canadon Seco, and Arab Heavy asphaltenes at different solvent conditions (i.e., a dispersive solvent and a flocculating solvent). A set of criteria is established to assess the quality of the data fits. The values of the non-linear least-squares fit parameters (I_0 and R_G) are compared to those obtained from the Guinier approximation to determine if the parameters obtained are molecularly reasonable. Furthermore, the reduced χ^2 values from each model fit are directly compared to assess the quality of each model with respect to other models. An analytical function is derived in the analyses to model the scattering behavior of polydisperse oblate cylinders with a Schultz distribution of radii. Once a model is determined to accurately describe the

structure of asphaltenic aggregates, additional parameters may be calculated from the scattering data, including aggregate molar masses, second virial coefficients, and percentage of solvent entrainment within aggregates [48,49].

2.2 Experimental

2.2.1 Asphaltene Precipitation

Asphaltenes were precipitated from Hondo (off-shore California) crude oil by the addition of excess n-heptane (40:1 v/v). All preparation solvents were obtained from Fisher Scientific and were HPLC grade. The crude oil/n-heptane mixture was allowed to equilibrate for 24 hours. During this period, the mixture was subjected to constant, gentle shaking to ensure that all of the material was completely dispersed. After this equilibration period, the precipitated asphaltenes were removed by gravimetric filtration through 18.5 cm diameter, Whatman 542 hardened ashless filter paper. The filter cake was washed with additional n-heptane via Soxhlet extraction to remove any co-precipitated maltenes. A second Soxhlet extraction was performed using toluene as the wash solvent to dissolve the asphaltenes from the filter paper, leaving behind any inorganic insolubles. Both extraction procedures continued until the overflow from the extractions became colorless. Most of the solvent was removed from the asphaltene solutions by rotary evaporation under partial vacuum at 60°C. Once nearly dry, the asphaltenes were moved into a nitrogen-flushed vacuum oven at 50°C for 24 h. The dry asphaltenes were transferred to glass jars and stored under argon to prevent oxidation. Additional asphaltenes were isolated from Canadon Seco (Argentina) and Arab Heavy crude oils by heptane precipitation using the procedure of Spiecker et al [21].

2.2.2 Chemical Characterization

The isolated asphaltenes were characterized by combustion elemental analysis at the University of Alberta (Department of Chemistry, Edmonton, Alberta, Canada) using a Carlo Erba instrument. Elemental analysis results for the isolated asphaltenes are presented in Table 2.1. Hondo asphaltenes were less aromatic with higher polar heteroatom content than the corresponding Canadon Seco and Arab Heavy asphaltenes.

2.2.3 SANS Sample Preparation

Two solutions with mass concentration of 1 % (w/w) were prepared by dissolving the Hondo asphaltenes in mixtures of 90:10 d-toluene: d-methanol (v/v) and 40:60 d-heptane: d-toluene (v/v). Two additional solutions with mass concentration of 1 % (w/w) were prepared by dissolving Canadon Seco and Arab Heavy asphaltenes in d-toluene. Solvents were obtained from CDN Isotopes and had > 99.9% chemical purity and >99.5% perdeuteration. During the sample preparation, d-toluene was initially added to the dry asphaltenes and the solution was subjected to constant, gentle shaking until the asphaltenes were completely dissolved. Upon dissolution of the asphaltenes, the second solvent (i.e., d-methanol or d-heptane) was added to the solutions. The solutions were allowed to equilibrate for at least one week prior to performing the scattering experiments.

2.2.4 SANS Measurements

SANS measurements were performed on the small-angle neutron diffractometer (SAND) at the Intense Pulsed Neutron Source (IPNS) Division of Argonne National Laboratory (Argonne, IL). Pulsed neutrons (30 Hz) with wavelengths ranging from 1 to 14

Å were generated by acceleration of H⁻ ions at a spallation target. Higher energy neutrons had lower wavelengths and reached the sample ahead of lower energy neutrons. Thus, the energy of each scattered neutron was determined by its time-of-flight to the detector. The sample-to-detector distance was fixed at 2 m. Neutrons were collected on an area detector (40 cm by 40 cm, 4 to 6 mm FWHM resolution). The instrument geometry and neutron wavelength values bound the operating Q range according to:

$$Q = \frac{4\pi}{\lambda} \sin \theta \quad (1)$$

where θ is half the scattering angle and λ is the neutron wavelength. The available Q range for the SAND instrument extended from 0.0035 to 2 Å⁻¹ and was adequate to yield scattering curves that cover the full Q-range for asphaltenic aggregates. Spectra were collected at 25°C in cylindrical quartz sample cells (NGS Precision) with a path length of 2 mm. A typical scattering experiment consisted of 15 minutes of detecting neutron transmission through the samples followed by 60 minutes of scattering. The absolute scattering intensity distribution, $I(Q)$, for each sample was obtained from the total detector counts corrected for background radiation, neutron transmission through the sample, scattering from the quartz cell, and detector sensitivity. Scattering intensity versus scattering angle ($I(Q)$ vs. Q) curves were fit to various intra-particle structure factor models using the macro functions authored by Kenneth Littrell and provided by Argonne National Laboratory for use with IgorPro software. The fitting function for polydisperse radius oblate cylinders was written by the authors.

2.3 Model Fitting

2.3.1 Geometry Independent Scattering Models

A variety of models can be applied to the scattering intensity distribution, $I(Q)$, of an asphaltene solution in order to obtain information concerning the morphology of the scattered particle. For example, the Guinier approximation [50] provides a means of estimating aggregate sizes without specifying the particle geometry as given by:

$$I(Q) = I_0 \exp(-Q^2 R_G^2 / 3) \quad (2)$$

where I_0 is the scattering intensity extrapolated to $Q = 0$. R_G is the radius of gyration defined as the root mean squared distance of all atoms from the center of mass of the particle. The zero- Q scattering intensity, I_0 , provides additional information concerning the particle geometry and is related to the weight-averaged molecular weight of the aggregates.

Another scattering function that describes the behavior of aggregates without specifying the particle geometry is the small-particle mass-fractal model [51] given by:

$$I(Q) = I_0 \frac{\sin[(D-1) \tan^{-1}(Q\xi)]}{(D-1)Q\xi(1+Q^2\xi^2)^{(D-1)/2}} \quad (3)$$

where D and ξ are the fractal dimension and exponential cut-off length for fractal aggregation, respectively. Mass fractals are defined by the scaling relationship between the total particle mass contained within a given radius, r , according to $M \sim r^D$. Equation (3) is a simplification of the mass-fractal model introduced by Chen and Teixeira [52] that describes the aggregates as a three-dimensional agglomeration consisting of elementary spherical particles with radius, R , and having a fractal-like nature. The small-particle mass-fractal

assumes that scattering from the elementary spherical particles is negligible (i.e., $\xi \gg R$ and $Q_{\max}R \ll 1$).

2.3.2 Form Factor Models

Alternatives to the Guiner and mass fractal analyses are those based on form factors. With a monodisperse system, the scattering intensity distribution is proportional to the product of an intra-particle structure factor, $P(Q)$, and an inter-particle structure factor, $S(Q)$, as given by:

$$I(\mathbf{Q}) = I_0 P(\mathbf{Q}) S(\mathbf{Q}) = I_0 |F(\mathbf{Q})|^2 S(\mathbf{Q}) \quad (4)$$

In the limit of low particle density, the solution becomes ideal and the inter-particle structure factor is assumed unity. All of the models presented in this study neglect interactions between particles. In the above equation, $|F(Q)|$ is the amplitude of the particle form factor defined by:

$$|F(\mathbf{Q})| = \int [\rho_p(\mathbf{r}) - \rho_s] \exp(i\mathbf{Q} \cdot \mathbf{r}) d\mathbf{r} \quad (5)$$

where $\rho_p(\mathbf{r})$ is the particle scattering length density at distance \mathbf{r} from the particle and ρ_s is the solvent scattering length density. The particle form factor is geometry dependent. Since particles are assumed to be randomly oriented, anisotropic particles must be averaged over spatial orientation. An extensive review of form factor models for various monodisperse particle shapes is provided by Pedersen [53].

The scattering intensity distribution for a polydisperse system is proportional to the ensemble average of the intra-particle structure factor (i.e., assuming no inter-particle interactions) as given by:

$$I(\mathbf{Q}) = \int_0^{\infty} I_0 P(\mathbf{Q}, x) f(x) dx \quad (6)$$

where $f(x)$ is a normalized distribution function for size parameter, x . Examples of size-distribution functions used to describe polydispersity in asphaltene aggregate sizes include the log-normal distribution [19,29] and the Schultz distribution [35]. The general formula for a log-normal distribution is given by:

$$f_{\ln}(x) = \frac{1}{\sqrt{2\pi}\sigma x} \exp\left(-\frac{1}{2}\left[\frac{\ln(x) - \ln(x_{avg})}{\sigma}\right]^2\right) \quad (7)$$

where σ and x_{avg} are the standard deviation and average size parameter value of the log-normal distribution, respectively. The general formula for a Schultz distribution is given by

$$f_s(x) = \frac{x^z}{\Gamma(z+1)} \left[\frac{z+1}{x_{avg}}\right]^{z+1} \exp\left(-\frac{(z+1)x}{x_{avg}}\right) \quad (8)$$

where $\Gamma(n)$ is the gamma function and z is the polydispersity parameter defined by:

$$z = \left(\frac{x_{avg}}{\sigma}\right)^2 - 1 \quad (9)$$

Both of the distribution functions are right-hand skewed, indicating the scattering intensity distributions are weighted more heavily by contributions from larger scatterers in solution. The polydisperse form factors presented in this study assume a Schultz distribution of particle sizes (e.g., polydisperse spheres and polydisperse length cylinders) which allows for direct analytical solutions to the integral in Eq. (6).

The various intra-particle structure factors applied to the SANS scattering intensity curves for asphaltene solutions in this study include: monodisperse spheres, monodisperse oblate cylinders, monodisperse prolate cylinders, polydisperse spheres, polydisperse length

oblate cylinders, and polydisperse radius oblate cylinders. The intra-particle structure factor for a homogeneous sphere with radius R is given by:

$$P_{sphere}(Q) = \left(\frac{3[\sin(QR) - QR \cos(QR)]}{(QR)^3} \right)^2 \quad (10)$$

Kotlarchyk and Chen [54] derived an analytical expression for a polydisperse intra-particle structure factor with a Schultz distribution of radii by combining Eqs. (6), (8) and (10). Sheu extended the analysis of polydisperse spheres to several other distribution functions [55] and justified the use of the Shultz spherical model for asphaltene solutions in toluene [35].

The intra-particle structure factor for a monodisperse cylinder (oblate or prolate) with radius R and length L is given by:

$$P_{cyl}(Q) = \int_{\beta=0}^{\pi/2} \left[\frac{2J_1(QR \sin \beta)}{QR \sin \beta} \frac{\sin((QL \cos \beta)/2)}{(QL \cos \beta)/2} \right]^2 \sin \beta d\beta \quad (11)$$

where $J_1(x)$ represents a first order Bessel function of the first kind and β is the orientational averaging angle. One simplification of Eq. (11) for a monodisperse flat disk (i.e., oblate cylinder) may be written as [56]:

$$P_{ob,1}(Q) = 2 \left[\frac{\sin(QL/2)}{QL/2} \right]^2 \left[\frac{1 - J_1(2QR)/QR}{(QR)^2} \right] \quad (12)$$

Alternatively, the high Q region of a monodisperse flat disk may also be described by an exponential approximation [50] given by:

$$P_{ob,2}(Q) = \frac{2}{(QR)^2} \exp\left(-\frac{(QL)^2}{12}\right) \quad (13)$$

Sheu [55] derived an explicit form of the intra-particle structure factor for a cylinder with a Schultz distribution of particle lengths by combining Eqs. (6), (8), and (11). Similar attempts

to model the intra-particle structure factor for a cylinder with a Schultz distribution of radii require numerical integration techniques (e.g., Gaussian quadrature) to solve the ensemble average integral in Eq. (6). A direct analytical solution for the case of polydisperse oblate cylinders with a Schultz distribution of radii is obtained by taking advantage of the flat disk approximations given in Eq. (12) and Eq. (13). Specific details concerning the model development are found in the Appendix at the end of this chapter.

2.4 Results and Discussion

Scattering intensity versus scattering angle ($I(Q)$ vs. Q) curves of 1% (w/w) solutions of Hondo asphaltenes in 90:10 d-toluene: d-methanol (v/v) and 40:60 d-heptane: d-toluene (v/v) are shown in Figure 2.1. The sharp rise in the scattering intensity at low Q values for Hondo asphaltenes in 40:60 d-heptane: d-toluene (Δ) indicated the presence of micron sized flocs in solution. A small percentage of Hondo asphaltenes are precipitated at this concentration of heptane and toluene [21]. Similar Porod-like power law behavior was observed for asphaltene solutions and crude oil blends [40,44]. For example, Roux et al. observed a low Q feature for Safaniya asphaltenes in toluene at 8 and 20°C that diminished in intensity with heating [40]. This observation suggests that an increase in solution temperature is effective in dissolving these flocs. It is not possible to determine the size of the flocs from these scattering experiments, because the Porod-like upturns do not exhibit a plateau behavior at the lowest scattering angles. The three lowest Q data points for this solution were fit to a power law function with an exponent of -4 (i.e., $I(Q) \sim Q^{-4}$). The corresponding power law fit appears as the dashed line in Figure 2.1. This power law function was subtracted from the original scattering data over the entire available Q range.

As seen in the figure, the resulting power law subtracted scattering curve (\circ) reveals the full Q-range of the scattering behavior from nano-scale aggregates in this solution. The various model fits were applied to this modified scattering curve in order to study the morphology of the nano-scale aggregates. A similar power law correction was applied to the scattering intensity distribution for Canadon Seco asphaltenes in d-toluene. The scattering intensity curves for Hondo asphaltenes in 90:10 d-toluene: d-methanol and Arab Heavy asphaltenes in d-toluene did not possess significant low Q features, indicating that the asphaltenic aggregates were completely soluble in these solvents and, hence, no power law corrections were needed for these samples prior to performing the model fits.

Initial estimates of the nano-particle I_0 and R_G parameters were obtained by applying the Guinier approximation (Eq. 2) to the modified scattering curves (see Table 2.2). The values of I_0 and R_G for Hondo asphaltenes in 90:10 d-toluene: d-methanol were 1.08 cm^{-1} and 43 \AA , respectively. As expected, larger I_0 (4.2 cm^{-1}) and R_G (71 \AA) values were observed as the solvent quality decreased to 40:60 d-heptane: d-toluene. It should be noted that the fits to the Guinier approximation were limited to 10 - 17 total data points and represented only the lowest Q-region of the scattering spectra. Additional estimates of the aggregate size are obtained from general models, such as the small-particle mass-fractal model, that fit the full range of Q values in the scattering spectra.

Fits of the small-particle mass-fractal model to the scattering intensity curves for both solutions of Hondo asphaltenes are shown as the solid lines in Figure 2.1. The Q range over which the small-particle mass fractal and subsequent model fits were applied was fixed between 0.01 and 0.52 \AA^{-1} . A constant background term was included in the model fits to account for incoherent scattering from all nuclei with non-zero spin in the solvent and solute.

The values of the incoherent background terms obtained from the small-particle mass-fractal fits were also fixed during the subsequent fits of the remaining intra-particle structure factors. The values of the fit parameters obtained from the small-particle mass-fractal model are shown in Table 2.2. The radius of gyration was determined from the model fit parameters by:

$$R_G^2 = D(D+1)\xi^2/2 \quad (14)$$

As indicated in the table, the I_0 values obtained from the mass-fractal model fits generally agreed with those obtained from the Guinier approximation within 12 %; however, the R_G values obtained from the mass-fractal fits generally over-predicted the corresponding Guinier values by approximately 20 to 30 %. As previously mentioned, the χ_{red}^2 parameter describes the quality of the model fit reduced by the number of degrees of freedom (n-1) and is defined by:

$$\chi_{red}^2 = \sum_{k=1}^n \left(\frac{I_k - I_{k,calculated}}{\delta I_k} \right)^2 / (n-1) \quad (15)$$

where I_k , δI_k , and $I_{k,calculated}$ are the experimentally observed scattering intensity, experimental uncertainty in the scattering intensity, and the calculated scattering intensity for data point k, respectively. In practical applications, values of the reduced chi-squared that approach unity suggest that the given model fits well to the experimental data.

The near unity values of the reduced chi-squared for the mass-fractal fits suggests that the small-particle mass-fractal model may be effectively used to model the aggregation behavior of asphaltenic aggregates in solution. However, relating the model to a physical description of the appearance of asphaltenic aggregates in solution is more difficult. For example, questions arise concerning the nature of the small-particles that compose the mass-

fractal asphaltene aggregate. Rassamdana and Sahimi [57] estimated that the mass-to-particle size scaling relationship for diffusion limited cluster-cluster aggregates with a nanoparticle fractal dimension of 2.5 is consistent with a primary particle size of ~ 5.8 Å. This prediction is supported by small-angle X-ray scattering [26] and gel permeation chromatography [58] data that modeled the molecular structure of asphaltenes as thin disks with approximate thickness of 4 Å. X-ray diffraction experiments on Ratawi and Kuwaiti asphaltenes [47] suggested an average layer diameter of aromatic sheets between 7 to 10 Å and an average distance between aromatic sheets between 3.5 to 3.7 Å. Considering these observations, the elementary particles constituting an asphaltene mass-fractal aggregate might consist of stacks of one to two aromatic sheets, possibly connected to similar aromatic moieties by short, aliphatic linkages. For example, a schematic representation of a possible asphaltene monomer and an asphaltenic aggregate consisting of four monomers is presented in Figure 2.2.

The values of the I_0 and R_G parameters obtained from the Guinier fits, as well as the quality of fit (reduced χ^2) parameter from the various intra-particle structure factor fits were used as a basis for assessing the particle geometry that best describes the geometric morphology of asphaltenic aggregates in solution. Example fits of monodisperse sphere, prolate cylinder, and oblate cylinder intra-particle structure factors to Hondo asphaltenes in 90:10 d-toluene: d-methanol are presented in Figure 2.3. The radius of gyration for a solid sphere is obtained from the value of the radius parameter as given by:

$$R_g^2 = \frac{3}{5} R^2 \quad (16)$$

The radius of gyration for a circular cylinder is obtained from the length and radius parameters as given by:

$$R_g^2 = \frac{L^2}{12} + \frac{R^2}{2} \quad (17)$$

Values of the fit parameters obtained from the various monodisperse and polydisperse form factors are shown in Table 2.3. As indicated in the table, the monodisperse sphere fits had the poorest fit quality and was observed to under-predict the values of the I_0 and R_G fit parameters obtained from the Guinier fits. The monodisperse prolate cylinder fit provided molecularly reasonable size parameters for Hondo asphaltenes in 90:10 d-toluene: d-methanol and Arab Heavy asphaltenes in d-toluene, but not for the more intensely scattering Hondo asphaltenes in 40:60 d-heptane: d-toluene or the Canadon Seco asphaltenes in d-toluene. The oblate cylinder model provided better agreement for the more intensely scattering samples to the Guinier parameters than the other monodisperse models. Likewise, the values of the reduced χ^2 parameter were minimized for the oblate cylinder model fits compared to other molecularly reasonable monodisperse fits. These results indicate that the morphologies of asphaltenic aggregates are likely similar to those of flat disks; however, the chemical polydispersity of asphaltenes suggests that the particle sizes of asphaltenic aggregates are likely polydisperse as well. The reduced χ^2 values for the Schultz polydisperse spheres show an improvement in fit quality over the monodisperse sphere model; however, the reduced χ^2 values are still larger than those for the monodisperse oblate cylinder fits. In addition, the average R_G values obtained from the polydisperse sphere fits under-predicted those obtained from the mass-fractal fits by two orders of magnitude. Since the oblate cylinder fits provided the lowest reduced χ^2 values of the various monodisperse

models, attempts were made to introduce Schultz distributions of particle lengths and radii for the oblate cylinder model.

Figure 2.4 presents reduced χ^2 values for fits of polydisperse length (\circ) and polydisperse radius (\square) oblate cylinders at fixed values of the polydispersity parameter for Hondo asphaltenes in 90:10 d-toluene: d-methanol. In this case, the polydispersity parameter, p , is defined by:

$$p = \frac{\sigma_x}{x_{avg}} \quad (18)$$

where σ_x and x_{avg} are the standard deviation and average size parameter values of the Schultz distribution, respectively. The value of the reduced χ^2 for the fit at polydispersity of zero represents the least-squares fit to a monodisperse oblate cylinder model. Figure 2.4 suggests that the incorporation of length polydispersity at fixed particle radius does not significantly improve the quality of the fit. For the case presented, the monodisperse oblate cylinder model fit the scattering intensity distribution better than the Schultz polydisperse length oblate cylinder model, regardless of the assumed polydispersity parameter. On the other hand, significant improvement in the quality of the model fits was observed when a Schultz distribution of particle radii were assumed for the aggregates at fixed particle length. As indicated in Figure 2.4, the value of the reduced χ^2 parameter was observed to decrease with increasing radius polydispersity with a minimum in the reduced χ^2 at a polydispersity value of 0.35. The quality of the model fits declined rapidly at values above the optimum polydispersity value. These results agree with the previous results of Herzog et al. [26] and Bardon et al. [19] that suggest the structure of asphaltenic aggregates may be represented using a distribution of thin disks of fixed thickness and polydisperse radii.

The optimum values of I_0 , the average radius, length, and radius spread for the two solutions of Hondo asphaltenes were determined by non-linear least-squares fitting of the scattering intensity curves to the Schultz polydisperse radius oblate cylinder model as shown in Figure 2.5. Unlike Figure 2.4, the constraint on the polydispersity parameter was relaxed for these fits. The values of the fit parameters obtained from the fits of the scattering spectra to the polydisperse radius oblate cylinder model are shown in Table 3. The radius of gyration for a system of polydisperse radius cylinders is given by [38]:

$$\langle R_g \rangle^2 = \frac{L^2}{3} + \frac{R_{avg}^2}{2} \frac{(z+6)(z+5)}{(z+1)^2} \quad (19)$$

As indicated in Tables 2.2 and 2.3, the fit quality of the Schultz polydisperse radius oblate cylinder model was consistently better than that of the other geometric form factor models. Furthermore, the values of the I_0 and average R_G parameters for the poly-radius cylinder agreed with the parameters obtained from the Guinier fits within the statistical uncertainty. Such agreement in the fit parameters was not observed with similar consistency for the other intra-particle structure factor models.

2.5 Conclusions

Various intra-particle structure factor models have been applied in the past to determine aggregate size and I_0 parameters from scattering intensity curves of asphaltene solutions, but not all of these models accurately reflected the morphology of the asphaltenic aggregates in solution. Here we applied several intra-particle structure factor models to the scattering intensity curves for solutions of asphaltenes in three different solvents. The reduced χ^2 values from the fits were used as a criterion to assess the quality of fit.

Comparison of I_0 and R_G values obtained from the fits to those obtained from Guinier analyses suggested if the obtained fit parameters were physically reasonable.

The fits of scattering intensity curves to the monodisperse models were useful in determining the general shape of the asphaltenic aggregates; however, it is well known that asphaltene molecules are polydisperse and one would expect the aggregates formed from the interactions of individual molecules to be polydisperse as well. In the cases studied, the monodisperse oblate cylinder model provided a better quality of fit and/or better agreement with the Guinier parameters than the other monodisperse models. When length and radius polydispersity was introduced to the oblate cylinder fits, only the inclusion of radius polydispersity was observed to significantly improve the fit quality over the monodisperse case. The inclusion of polydispersity tended to complicate the analyses of scattering intensity curves as an additional integral is introduced to calculate to ensemble average of the polydisperse size parameter within a distribution function. In many cases, the ensemble average integral must be solved using numerical techniques, such as Gaussian quadrature. The inclusion of numerical integration techniques often significantly increases the computing time for the non-linear least-squares regression. In this study, a direct analytical function was derived for the scattering of polydisperse radius oblate cylinders using approximations for the form factor of a flat disk, as well as a polynomial expansion of the first order Bessel function of the first kind. The new function fit well to the scattering intensity curves studied, both in terms of overall fit quality (i.e., reduced χ^2) and comparison to the Guinier parameters (i.e., I_0 and R_G). The observations that the parameters obtained from the polydisperse radius oblate cylinder and Guinier fits agreed within experimental uncertainty and that the reduced χ^2 values for the polydisperse cylinder fits were consistently lower than that of other geometric

form factors, regardless of the solute chemistry or solvent quality, suggests that the asphaltene aggregate structure is best described by a polydisperse flat disk (or polydisperse flat ellipsoid) model. The selection of an appropriate model for the macrostructure of asphaltenic aggregates is important for the calculation of additional parameters from the scattering data, such as the aggregate molecular weight, second virial coefficients, and percentage of solvent entrainment within asphaltenic aggregates.

2.6 Acknowledgements

This research is supported by the Petroleum Environmental Research Forum, ExxonMobil, Shell, Equilon, ChevronTexaco, Nalco Energy Services Division, Champion Technologies, National Science Foundation Grants (CTS981727), and the NSF Graduate Research Fellowship Program. This work benefited from the use of facilities in the Intense Pulsed Neutron Source and the Chemistry Division, which is funded by the U. S. Department of Energy, Office of Basic Energy Sciences under contract W-31-109-ENG-38 to the University of Chicago. We would particularly like to thank Pappannan Thiyagarajan and Denis Wozniak of the Intense Pulsed Neutron Source Division at Argonne National Laboratory for their assistance with the SAND instrument. We would also like to thank Matthew B. Smith, M. Lupe Marques, George Blankenship, and Vincent Verruto for helping with the sample preparation and SANS data collection.

2.7 Appendix: Polydisperse Radius Oblate Cylinder Model

The scattering intensity distribution for a system with radius polydispersity is proportional to the normalized average of the intra-particle structure factor (i.e., neglecting inter-particle interactions) as given by [55]:

$$I(Q) = \frac{\phi (\Delta\rho)^2 \langle V^2 \rangle}{\langle V \rangle} \langle P(Q) \rangle = I_0 \langle P(Q) \rangle \quad (\text{A.1})$$

where ϕ is the volume fraction of scatterers, $\Delta\rho$ is the scattering length density difference between the solvent and solute, $\langle V \rangle$ is the first moment of the particle volume, and $\langle V^2 \rangle$ is the second moment of the particle volume. The normalized average of the intraparticle structure factor is given by:

$$\langle P(Q) \rangle = \frac{\int_0^{\infty} P(Q, R) V^2 f(R) dR}{\int_0^{\infty} V^2 f(R) dR} \quad (\text{A.2})$$

where $f(R)$ is a normalized distribution function for the radius parameter, R . In the case presented, a Schultz distribution of radii is assumed:

$$f_s(R) = \frac{R^z}{\Gamma(z+1)} \left[\frac{z+1}{R_{\text{avg}}} \right]^{z+1} \exp\left(-\frac{(z+1)R}{R_{\text{avg}}}\right) \quad (\text{A.3})$$

where $\Gamma(n)$ is the gamma function, R_{avg} is the average particle radius, and z is the polydispersity parameter defined by:

$$z = \left(\frac{R_{\text{avg}}}{\sigma} \right)^2 - 1 \quad (\text{A.4})$$

The intra-particle structure factor for a monodisperse cylinder (oblate or prolate) with radius R and length L is given by:

$$P_{cyl}(Q) = \int_{\beta=0}^{\pi/2} \left[\frac{2J_1(QR \sin \beta) \sin((QL \cos \beta)/2)}{QR \sin \beta (QL \cos \beta)/2} \right]^2 \sin \beta d\beta \quad (A.5)$$

where $J_1(x)$ represents a first order Bessel function of the first kind and β is the orientational averaging angle. The monodisperse cylinder intra-particle structure factor may be separated into contributions from the radius (P_R) and length (P_L) terms as given by:

$$P_{cyl}(Q, R, L) = P_R(Q, R) P_L(Q, L) \quad (A.6)$$

In the limit that $R \gg L$, Pedersen [56] showed that the length contribution to the orientation integral in Eq. (A.4) was only significant when $\cos \beta = 1$. After subsequent substitution, the orientation integral only involves the particle radius. The intra-particle structure factor for an infinitely thin disk introduced by Kratky and Porod [59] is given by:

$$P_R(Q, R) = \frac{2}{(QR)^2} \left[1 - \frac{J_1(2QR)}{QR} \right] \quad (A.7)$$

Substitution of Eq. (A.7) in Eqs. (A.5) and (A.6) removes the contribution of the particle radius to the orientation integral. Therefore, the orientation integral is no longer dependent on either the particle radius or length and the intra-particle structure factor for a monodisperse flat disk (i.e., oblate cylinder) may be written as [56]:

$$P_{ob,1}(Q) = 2 \left[\frac{\sin(QL/2)}{QL/2} \right]^2 \left[\frac{1 - J_1(2QR)/QR}{(QR)^2} \right] \quad (A.8)$$

Alternatively, the high Q region of a monodisperse flat disk may also be described by an exponential approximation [50] given by:

$$P_{ob,2}(Q) = \frac{2}{(QR)^2} \exp\left(-\frac{(QL)^2}{12}\right) \quad (A.9)$$

Caution should be used when applying Eq. (A.9), as it does not exhibit plateau behavior in the low Q limit. For the ratio of R/L size parameter values observed in this study, Eq. (A.9) converges with Eq. (A.8) in the limited Q range roughly defined by $QR > 3$.

Because the radial dependence of the oblate cylinder form factor in Eq. (A.8) contains the Bessel function term, the combination of Eqs. (A.1) and (A.8) requires numerical techniques to solve the ensemble average integral. However, the $J_1(x)$ Bessel function may be expanded in a polynomial series given by:

$$J_1(x) = \sum_{n=0}^{\infty} \frac{(-1)^n \left(\frac{1}{2}x\right)^{2n+1}}{n! \Gamma(n+2)} \quad (\text{A.10})$$

Substitution of an 66-term polynomial series from Eq. (A.10) into Eq. (A.8) allows for a direct analytical solution to the ensemble average integral in Eq. (A.1) using the relation:

$$\int_0^{\infty} x^n \exp(-ax) dx = \frac{\Gamma(n+1)}{a^{n+1}} \quad (\text{A.11})$$

Because the 66-term polynomial expansion does not converge properly at higher Q values, the intra-particle structure factor in Eq. (A.8) is used for the polydisperse fits in the range $QR < 3.2$. In order to model the polydisperse radius oblate cylinders in the range $QR > 3.2$, the exponential approximation of the flat disk intra-particle structure factor is used in Eq. (A.1). Since the radius dependence in Eq. (A.9) is a polynomial, the ensemble average integral of the particle radius may be solved analytically using Eq. (A.11). The intra-particle structure factor used in this study to model polydisperse radius oblate cylinders thus takes the form:

$$\begin{aligned} \langle P(Q) \rangle &= \int_0^{\infty} P_{ob,1}(Q, R) f_S(R) dR \quad \{QR < 3 \\ \langle P(Q) \rangle &= \int_0^{\infty} P_{ob,2}(Q, R) f_S(R) dR \quad \{QR > 3 \end{aligned} \quad (\text{A.12})$$

The radius of gyration for a monodisperse circular cylinder is obtained from the length and radius parameters as given by:

$$R_g^2 = \frac{L^2}{12} + \frac{R^2}{2} \quad (\text{A.13})$$

The radius of gyration for a system of polydisperse radius cylinders is related to the sixth moment of the radius distribution give by [38]:

$$\langle R_g \rangle^2 = \frac{L^2}{3} + \frac{\langle R^6 \rangle}{2\langle R^4 \rangle} \quad (\text{A.14})$$

2.8 References

1. J. P. Pfeiffer, R. N. J. Saal, "Asphaltic Bitumen as Colloid System," *Journal of Physical Chemistry*, 1940, **44**: p. 139-149.
2. J. M. Swanson, "A Contribution to the Physical Chemistry of the Asphalts," *Journal of Physical Chemistry*, 1942, **46**: p. 141-150.
3. T. F. Yen, J. G. Erdman, S. S. Pollack, "Investigation of Structure of Petroleum Asphaltenes By X-Ray Diffraction," *Analytical Chemistry*, 1961, **33**(11): p. 1587-1594.
4. J. C. Petersen, "An Infra-red Study of Hydrogen Bonding in Asphalt," *Fuel*, 1967, **46**(4-5): p. 295-305.
5. R. V. Barbour, J. C. Petersen, "Molecular Interactions of Asphalt: An Infrared Study of the Hydrogen-Bonding Basicity of Asphalt," *Analytical Chemistry*, 1974, **46**(2): p. 273-277.
6. S. E. Moschopedis, J. G. Speight, "Investigation of Hydrogen Bonding by Oxygen Functions in Athabasca Bitumen," *Fuel*, 1976, **55**: p. 187-192.
7. T. Ignasiak, O. P. Strausz, D. S. Montgomery, "Oxygen Distribution and Hydrogen Bonding in Athabasca Asphaltene," *Fuel*, 1977, **56**: p. 359-365.
8. M. M. Boduszynski, J. F. McKay, D. R. Latham, "Asphaltenes, Where Are You?," *Proceedings of the Association of Asphalt Paving Technologists*, 1980, **49**: p. 123-143.

9. M. A. Bestougeff, P. Gendrel. *Study on the Structure of Asphaltenic Constituents by Combined Physical and Chemical Methods*. in *147th American Chemical Society Meeting*. 1964. Philadelphia, PA: ACS, Division of Petroleum Chemistry.
10. J. G. Speight, "A Structural Investigation of the Constituents of Athabasca Bitumen by Proton Magnetic Resonance Spectroscopy," *Fuel*, 1970, **49**: p. 76-90.
11. J. F. McKay, D. R. Latham, W. E. Haines, "Composition of Petroleum Heavy Ends. 3. Comparison of the Composition of High-Boiling Petroleum Distillates and Petroleum > 675 C Residues," *Fuel*, 1981, **60**(1): p. 27-32.
12. M. M. Boduszynski, "Characterization of "Heavy" Crude Components," *Preprints ACS Division of Petroleum Chemistry*, 1985, **30**: p. 626-640.
13. M. M. Boduszynski, "Composition of Heavy Petroleums. 2. Molecular Characterization," *Energy & Fuels*, 1988, **2**(5): p. 597-613.
14. J. Murgich, "Intermolecular forces in aggregates of asphaltenes and resins," *Petroleum Science and Technology*, 2002, **20**(9-10): p. 983-997.
15. N. Aske, H. Kallevik, E. E. Johnsen, J. Sjoblom, "Asphaltene aggregation from crude oils and model systems studied by high-pressure NIR spectroscopy," *Energy & Fuels*, 2002, **16**(5): p. 1287-1295.
16. I. H. Auflem, T. E. Havre, J. Sjoblom, "Near-IR study on the dispersive effects of amphiphiles and naphthenic acids on asphaltenes in model heptane-toluene mixtures," *Colloid and Polymer Science*, 2002, **280**(8): p. 695-700.
17. J. A. Ostlund, S. I. Andersson, M. Nyden, "Studies of asphaltenes by the use of pulsed-field gradient spin echo NMR," *Fuel*, 2001, **80**(11): p. 1529-1533.
18. J. A. Ostlund, J. E. Lofroth, K. Holmberg, M. Nyden, "Flocculation behavior of asphaltenes in solvent/nonsolvent systems," *Journal of Colloid and Interface Science*, 2002, **253**(1): p. 150-158.
19. C. Bardon, L. Barre, D. Espinat, V. Guille, M. H. Li, J. Lambard, J. C. Ravey, E. Rosenberg, T. Zemb, "The colloidal structure of crude oils and suspensions of asphaltenes and resins," *Fuel Science & Technology International*, 1996, **14**(1-2): p. 203-242.
20. H. W. Yarranton, H. Alboudwarej, R. Jakher, "Investigation of asphaltene association with vapor pressure osmometry and interfacial tension measurements," *Industrial & Engineering Chemistry Research*, 2000, **39**(8): p. 2916-2924.

21. P. M. Spiecker, K. L. Gawrys, P. K. Kilpatrick, "Aggregation and solubility behavior of asphaltenes and their subfractions," *Journal of Colloid and Interface Science*, 2003, **267**(1): p. 178-193.
22. D. Fenistein, L. Barre, D. Broseta, D. Espinat, A. Livet, J. N. Roux, M. Scarsella, "Viscosimetric and neutron scattering study of asphaltene aggregates in mixed toluene/heptane solvents," *Langmuir*, 1998, **14**(5): p. 1013-1020.
23. C. Giavarini, D. Mastrofini, M. Scarsella, L. Barre, D. Espinat, "Macrostructure and rheological properties of chemically modified residues and bitumens," *Energy & Fuels*, 2000, **14**(2): p. 495-502.
24. Y. Bouhadda, D. Bendedouch, E. Sheu, A. Krallafa, "Some preliminary results on a physico-chemical characterization of a Hassi Messaoud petroleum asphaltene," *Energy & Fuels*, 2000, **14**(4): p. 845-853.
25. W. Takeshige, "Hydrodynamic shape and size of Khafji asphaltene in benzene," *Journal of Colloid and Interface Science*, 2001, **234**(2): p. 261-268.
26. P. Herzog, D. Tchoubar, D. Espinat, "Macrostructure of Asphaltene Dispersions by Small-Angle X-Ray-Scattering," *Fuel*, 1988, **67**(2): p. 245-250.
27. D. Espinat, J. C. Ravey, V. Guille, J. Lambard, T. Zemb, J. P. Cotton, "Colloidal Macrostructure of Crude-Oil Studied by Neutron and X-Ray Small-Angle Scattering Techniques," *Journal De Physique Iv*, 1993, **3**(C8): p. 181-184.
28. Y. N. Xu, Y. Koga, O. P. Strausz, "Characterization of Athabasca Asphaltenes by Small-Angle X-Ray-Scattering," *Fuel*, 1995, **74**(7): p. 960-964.
29. L. Barre, D. Espinat, E. Rosenberg, M. Scarsella, "Colloidal structure of heavy crudes and asphaltene solutions," *Revue de l'Institut Francais du Petrole*, 1997, **52**(2): p. 161-175.
30. D. Fenistein, L. Barre, "Experimental measurement of the mass distribution of petroleum asphaltene aggregates using ultracentrifugation and small-angle X-ray scattering," *Fuel*, 2001, **80**(2): p. 283-287.
31. T. G. Savvidis, D. Fenistein, L. Barre, E. Behar, "Aggregated structure of flocculated asphaltenes," *AIChE Journal*, 2001, **47**(1): p. 206-211.
32. J. C. Ravey, G. Ducouret, D. Espinat, "Asphaltene Macrostructure by Small-Angle Neutron-Scattering," *Fuel*, 1988, **67**(11): p. 1560-1567.
33. R. E. Overfield, E. Y. Sheu, S. K. Sinha, K. S. Liang, "SANS Study of Asphaltene Aggregation," *Fuel Science & Technology International*, 1989, **7**(5-6): p. 611-624.

34. J. C. Ravey, D. Espinat, "Macrostructure of petroleum asphaltenes by small angle neutron scattering," *Progress in Colloid & Polymer Science*, 1990, **81**: p. 127-130.
35. E. Y. Sheu, K. S. Liang, S. K. Sinha, R. E. Overfield, "Polydispersity Analysis of Asphaltene Solutions in Toluene," *Journal of Colloid and Interface Science*, 1992, **153**(2): p. 399-410.
36. Y. C. Liu, E. Y. Sheu, S. H. Chen, D. A. Storm, "Fractal Structure of Asphaltenes in Toluene," *Fuel*, 1995, **74**(9): p. 1352-1356.
37. P. Thiyagarajan, J. E. Hunt, R. E. Winans, K. B. Anderson, J. T. Miller, "Temperature-Dependent Structural-Changes of Asphaltenes in 1-Methylnaphthalene," *Energy & Fuels*, 1995, **9**(5): p. 829-833.
38. M. Y. Lin, E. B. Sirota, H. Gang, "Neutron scattering characterization of asphaltene particles," *Abstracts of Papers of the American Chemical Society*, 1997, **213**: p. 66-70.
39. M. Sahimi, H. Rassamdana, "Formation, growth and precipitation of fractal molecular aggregates in porous media," *Physica A*, 1997, **240**(3-4): p. 419-431.
40. J. N. Roux, D. Broseta, B. Deme, "SANS study of asphaltene aggregation: Concentration and solvent quality effects," *Langmuir*, 2001, **17**(16): p. 5085-5092.
41. P. M. Spiecker, K. L. Gawrys, C. B. Trail, P. K. Kilpatrick, "Effects of petroleum resins on asphaltene aggregation and water-in-oil emulsion formation," *Colloids and Surfaces a-Physicochemical and Engineering Aspects*, 2003, **220**(1-3): p. 9-27.
42. R. Tanaka, J. E. Hunt, R. E. Winans, P. Thiyagarajan, S. Sato, T. Takanohashi, "Aggregates structure analysis of petroleum asphaltenes with small-angle neutron scattering," *Energy & Fuels*, 2003, **17**(1): p. 127-134.
43. A. Cosultchi, P. Bosch, V. H. Lara, "Small-angle X-ray scattering study of oil- and deposit-asphaltene solutions," *Colloid and Polymer Science*, 2003, **281**(4): p. 325-330.
44. T. G. Mason, M. Y. Lin, "Asphaltene nanoparticle aggregation in mixtures of incompatible crude oils," *Physical Review E*, 2003, **67**(5): p.
45. T. G. Mason, M. Y. Lin, "Time-resolved small angle neutron scattering measurements of asphaltene nanoparticle aggregation kinetics in incompatible crude oil mixtures," *Journal of Chemical Physics*, 2003, **119**(1): p. 565-571.
46. B. H. Zimm, "The Scattering of Light and the Radial Distribution Function of High Polymer Solutions," *Journal of Chemical Physics*, 1948, **16**(12): p. 1093-1099.

47. M. N. Siddiqui, M. F. Ali, J. Shirokoff, "Use of X-ray diffraction in assessing the aging pattern of asphalt fractions," *Fuel*, 2002, **81**(1): p. 51-58.
48. K. L. Gawrys, P. K. Kilpatrick, " Second virial coefficients of asphaltenic aggregates in varying solvents probed by small angle neutron scattering," *Energy & Fuels*, submitted.
49. K. L. Gawrys, G. A. Blankenship, P. K. Kilpatrick, " Solvent entrainment in and flocculation of asphaltenic aggregates probed by small-angle neutron scattering," *Langmuir*, submitted.
50. A. Guinier, G. Fournet, *Small Angle Scattering of X-rays*; John Wiley & Sons: New York, 1955.
51. X. J. Hu, K. Littrel, S. Ji, D. G. Pickles, W. M. Risen, "Characterization of silica-polymer aerogel composites by small-angle neutron scattering and transmission electron microscopy," *Journal of Non-Crystalline Solids*, 2001, **288**(1-3): p. 184-190.
52. S. H. Chen, J. Teixeira, "Structure and Fractal Dimension of Protein-Detergent Complexes," *Physical Review Letters*, 1986, **57**(20): p. 2583-2586.
53. J. S. Pedersen, "Analysis of small-angle scattering data from colloids and polymer solutions: modeling and least-squares fitting," *Advances in Colloid and Interface Science*, 1997, **70**: p. 171-210.
54. M. Kotlarchyk, S. H. Chen, "Analysis of Small-Angle Neutron-Scattering Spectra from Polydisperse Interacting Colloids," *Journal of Chemical Physics*, 1983, **79**(5): p. 2461-2469.
55. E. Y. Sheu, "Polydispersity Analysis of Scattering Data from Self-Assembled Systems," *Physical Review A*, 1992, **45**(4): p. 2428-2438.
56. J. S. Pedersen, "Form factors of block copolymer micelles with spherical, ellipsoidal and cylindrical cores," *Journal of Applied Crystallography*, 2000, **33**(1): p. 637-640.
57. H. Rassamdana, M. Sahimi, "Asphalt flocculation and deposition .2. Formation and growth of fractal aggregates," *AIChE Journal*, 1996, **42**(12): p. 3318-3332.
58. S. Acevedo, G. Escobar, M. A. Ranaudo, L. B. Gutierrez, "Discotic Shape of Asphaltenes Obtained from Gpc Data," *Fuel*, 1994, **73**(11): p. 1807-1809.
59. O. Kratky, G. Porod, "Diffuse Small-Angle Scattering of X-Rays in Colloid Systems," *Journal of Colloid Science*, 1949, **4**(1): p. 35-70.

Table 2.1 Elemental composition of asphaltene samples.

Asphaltene	wt % C	wt % H	wt % N	wt % S	wt % O	H/C (atomic)
Hondo	80.72	8.27	1.96	6.87	2.18	1.29
Canadon Seco	88.21	8.22	1.32	0.52	1.73	1.11
Arab Heavy	81.25	7.77	1.02	8.32	1.64	1.14

Table 2.2 Comparison of fit parameters obtained from the Guinier approximation and small-particle mass-fractal models

Asphaltene	Guinier Approximation			Small-Particle Mass-Fractal				
	I_0 (cm ⁻¹)	R_G (Å)	QR_G	I_0 (cm ⁻¹)	ξ (Å)	D	R_G (Å)	χ^2
Hondo (90:10 Tol:MeOD)	1.08 ± 0.03	43 ± 3	0.986	1.07 ± 0.02	23.9 ± 0.5	2.61 ± 0.02	52 ± 2	0.8091
Hondo (40:60 H:T)	4.2 ± 0.2	71 ± 5	1.005	4.15 ± 0.06	38.7 ± 0.6	2.52 ± 0.02	82 ± 2	1.6089
Canadon Seco (Toluene)	3.0 ± 0.1	58 ± 5	0.945	3.20 ± 0.05	34.3 ± 0.6	2.63 ± 0.02	75 ± 2	1.7325
Arab Heavy (Toluene)	1.48 ± 0.04	45 ± 3	0.990	1.49 ± 0.02	22.0 ± 0.5	2.76 ± 0.03	50 ± 2	0.9080

Table 2.3 Comparison of fit parameters obtained from various monodisperse and polydisperse form factor models.

Hondo Asphaltenes (90:10 Toluene:Methanol)							
Model Fit	I_0 (cm ⁻¹)	R_{avg} (Å)	σ_R (Å)	L_{avg} (Å)	σ_L (Å)	$\langle R_G^2 \rangle^{1/2}$ (Å)	χ^2
Monodisperse spheres	0.62 ± 0.01	35.7 ± 0.1	--	--	--	27.7 ± 0.1	48.381
Monodisperse prolate cylinders	1.12 ± 0.02	20.7 ± 0.1	--	186 ± 5	--	56 ± 2	9.5199
Monodisperse oblate cylinders	0.88 ± 0.01	52.8 ± 0.3	--	12.2 ± 0.6	--	38 ± 2	4.3489
Schultz polyradius spheres	0.91 ± 0.01	0.69 ± 0.02	2.40 ± 0.04	--	--	0.68 ± 0.02	4.9721
Schultz polylength oblate cylinders	0.88 ± 0.01	52.7 ± 0.3	--	12.1 ± 0.6	0.5	38 ± 2	4.3488
Schultz polyradius oblate cylinders	0.98 ± 0.01	42.6 ± 0.9	13.5 ± 0.3	15.1 ± 0.6	--	45 ± 4	1.3845
Hondo Asphaltenes (40:60 Heptane:Toluene)							
Model Fit	I_0 (cm ⁻¹)	R_{avg} (Å)	σ_R (Å)	L_{avg} (Å)	σ_L (Å)	$\langle R_G^2 \rangle^{1/2}$ (Å)	χ^2
Monodisperse spheres	1.61 ± 0.01	44.1 ± 0.1	--	--	--	34.2 ± 0.1	173.7
Monodisperse prolate cylinders	179 ± 1	7.6 ± 0.2	--	11280 ± 50	--	3260 ± 30	9.5825
Monodisperse oblate cylinders	3.29 ± 0.03	79.6 ± 0.4	--	20.3 ± 0.3	--	57 ± 1	12.833
Schultz polyradius spheres	2.92 ± 0.02	0.55 ± 0.04	2.52 ± 0.08	--	--	0.43 ± 0.03	26.086
Schultz polylength oblate cylinders	3.29 ± 0.03	79.5 ± 0.4	--	19.9 ± 0.3	2	83 ± 2	12.830
Schultz polyradius oblate cylinders	4.14 ± 0.04	69.4 ± 0.7	22.3 ± 0.1	20.5 ± 0.3	--	73 ± 2	5.7508
Canadon Seco Asphaltenes (Toluene)							
Model Fit	I_0 (cm ⁻¹)	R_{avg} (Å)	σ_R (Å)	L_{avg} (Å)	σ_L (Å)	$\langle R_G^2 \rangle^{1/2}$ (Å)	χ^2
Monodisperse spheres	1.43 ± 0.01	44.8 ± 0.1	--	--	--	34.7 ± 0.1	125.98
Monodisperse prolate cylinders	151 ± 1	8.4 ± 0.3	--	11260 ± 60	--	3300 ± 100	8.1415
Monodisperse oblate cylinders	2.56 ± 0.02	75.3 ± 0.4	--	20.5 ± 0.4	--	54 ± 1	11.548
Schultz polyradius spheres	2.48 ± 0.02	0.66 ± 0.05	2.8 ± 0.1	--	--	0.51 ± 0.04	13.895
Schultz polylength oblate cylinders	2.55 ± 0.02	74.7 ± 0.4	--	13.7 ± 0.8	7	53 ± 3	11.254
Schultz polyradius oblate cylinders	2.84 ± 0.03	60 ± 1	18.9 ± 0.3	25.6 ± 0.4	--	58 ± 5	2.9527
Arab Heavy Asphaltenes (Toluene)							
Model Fit	I_0 (cm ⁻¹)	R_{avg} (Å)	σ_R (Å)	L_{avg} (Å)	σ_L (Å)	$\langle R_G^2 \rangle^{1/2}$ (Å)	χ^2
Monodisperse spheres	0.88 ± 0.01	35.6 ± 0.1	--	--	--	27.6 ± 0.1	73.381
Monodisperse prolate cylinders	1.66 ± 0.03	21.2 ± 0.1	--	194 ± 5	--	58 ± 2	12.303
Monodisperse oblate cylinders	1.26 ± 0.01	52.6 ± 0.3	--	17.1 ± 0.4	--	38 ± 1	6.5966
Schultz polyradius spheres	1.33 ± 0.01	0.71 ± 0.04	2.47 ± 0.07	--	--	0.55 ± 0.03	4.2643
Schultz polylength oblate cylinders	1.26 ± 0.01	52.5 ± 0.3	--	16.6 ± 0.4	2	83 ± 2	6.5948
Schultz polyradius oblate cylinders	1.38 ± 0.01	41.4 ± 0.9	13.2 ± 0.2	20.8 ± 0.7	--	45 ± 3	1.8979

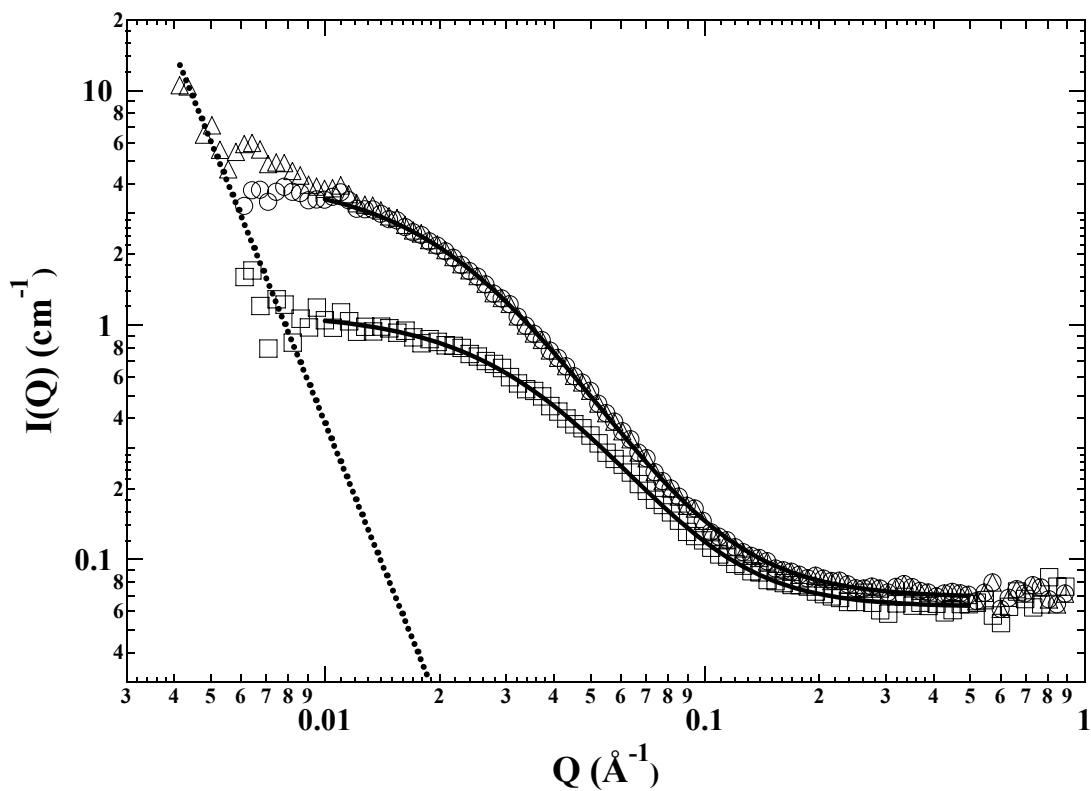


Figure 2.1 Low Q power law correction and small-particle mass-fractal fits to Hondo asphaltene in mixed solvents. Legend: (Δ) Hondo asphaltene in 40:60 d-heptane: d-toluene; (.....) low Q power law fit to 40:60 d-heptane: d-toluene; (\circ) power law subtracted data for 40:60 d-heptane: d-toluene; (\square) Hondo asphaltene in 90:10 d-toluene: d-methanol; (—) small-particle mass-fractal fits with constant background.

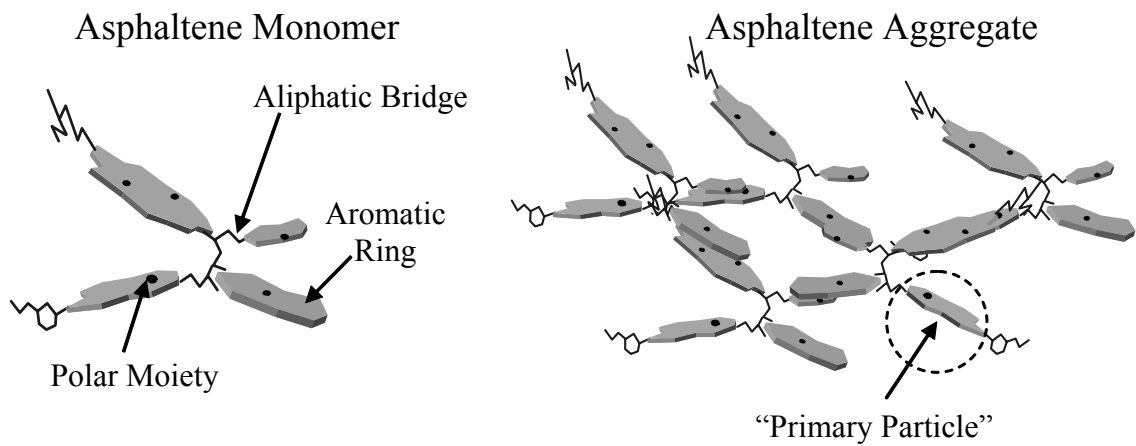


Figure 2.2 Schematic representation of an asphaltene monomer and an asphaltene aggregate consisting of four monomers.

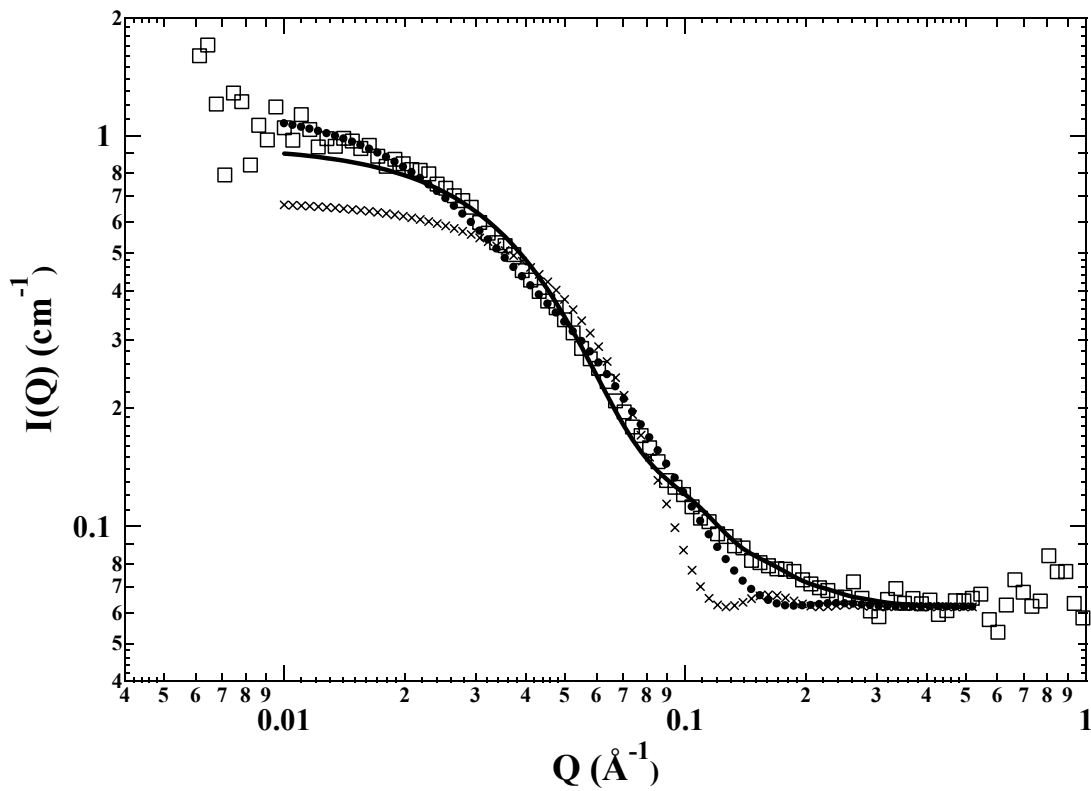


Figure 2.3 Fits of monodisperse sphere (x), monodisperse prolate cylinder (●), and monodisperse oblate cylinder (—) models to Hondo asphaltenes (□) in 90:10 d-toluene: d-methanol.

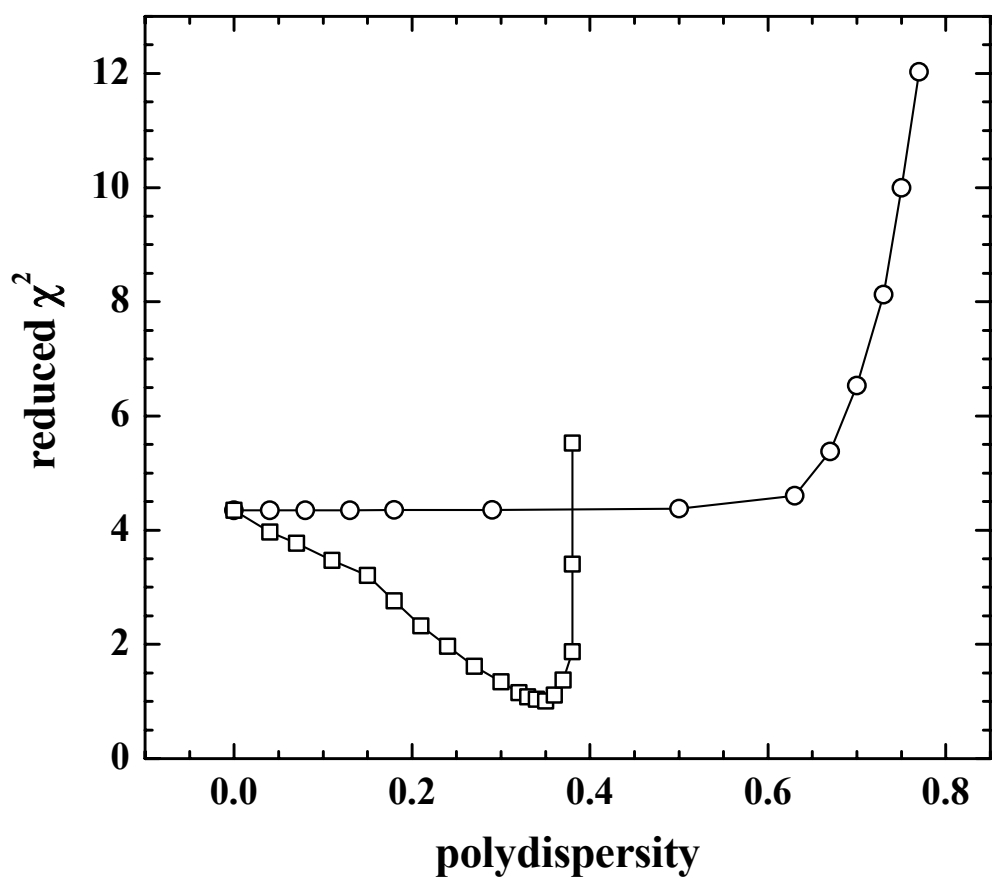


Figure 2.4 Reduced chi-squared values at various polydispersity parameters for fits of (\circ) polydisperse length oblate cylindrical and (\square) polydisperse radius oblate cylindrical models to Hondo asphaltenes in 90:10 d-toluene: d-methanol.

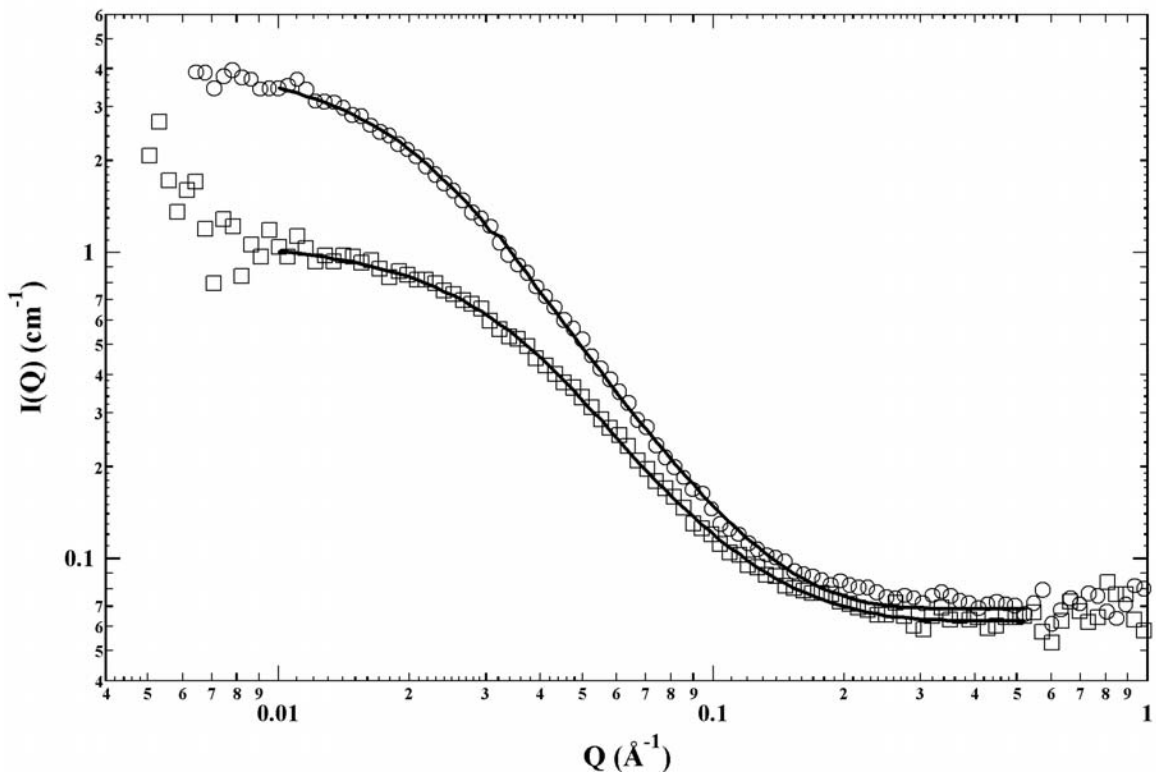


Figure 2.5 Fits of a polydisperse radius oblate cylinder form factor to Hondo asphaltenes in (○) 40:60 d-heptane: d-toluene and (□) 90:10 d-toluene: d-methanol. Solid lines represent the model fits.

**On Distribution Functions of Chemical Properties and Aggregation of Solubility
Fractions in Asphaltenes**

Keith L. Gawrys, George A. Blankenship, and Peter K. Kilpatrick

ABSTRACT

Asphaltenes from three crude oils were separated on a preparatory-scale into 20 - 30 discrete subfractions by sequential precipitation from mixtures of n-heptane and toluene. The earliest fractions precipitated were characterized by lower than average aromaticity and atomic N/C ratios and contained significant amounts of co-precipitated inorganic solids or metal atoms bound to functional groups intrinsic to the asphaltenes. The subfractions isolated in the regime where asphaltene solubility changed significantly with slight changes in the solvent were characterized by atomic H/C ratios that varied significantly with the yield of precipitated asphaltenes. Atomic N/C ratios decreased and O/C ratios increased systematically with increasing precipitated asphaltene yield in this solvent regime. The more aromatic generally formed larger aggregates in solution, suggesting that asphaltene solubility and aggregation behavior is dominated by π -bonding interactions between the aromatic moieties. After precipitation of ~ 80 % (w/w) of the asphaltenes, the remaining fractions were more “resin-like” in terms of chemical composition and aggregation behavior.

CHAPTER 3
ON DISTRIBUTION FUNCTIONS OF CHEMICAL PROPERTIES AND
AGGREGATION OF SOLUBILITY FRACTIONS IN ASPHALTENES

3.1 Introduction

The tendency of petroleum asphaltene to associate in solution and adsorb at interfaces can cause significant problems during the production, recovery, pipeline transportation, and refining of crude oil [1-11]. For example, a common method of increasing oil production involves the injection of miscible agents (e.g., carbon dioxide or natural gas) into underground reserves to displace the oil. This practice may result in the formation of asphaltene deposits that tend to plug up the reservoir wells and pipelines [1,2,12]. Similarly, asphaltene-stabilized water-in-crude oil (w/o) emulsions are formed during various stages of the production, such as by turbulent flow of fluids up a bore hole, with the addition of “wash water” during the desalting operation, and by wave agitation of crude oil spills on water [3-11]. The propensity of asphaltene to adsorb at interfaces is related to the extent of asphaltene aggregation and the solvating power of the crude oil media [13]. Asphaltene maintain a delicate balance between solvency, aggregation, and interfacial activity in solution that must ultimately be related to the chemical composition and molecular architecture of the participating components.

Asphaltene are operationally defined as the portion of crude oil insoluble in light n-alkanes (e.g., n-heptane or n-pentane), but soluble in aromatic solvents (e.g., benzene or toluene) [14]. The quantity, chemical composition, and molar mass distribution of the asphaltene “solubility class” varies significantly with the source of the crude oil and with the

method of precipitation [15-17]. Asphaltenes comprise the most polar fraction of the crude oil and consist of polyaromatic condensed rings with short aliphatic side chains and polar heteroatom-containing functional groups [18-22]. Asphaltenes are polydisperse in terms of chemical composition, with typical atomic H/C ratios varying between 1.0 to 1.3 and N, S, and O contents of a few weight percent [13,23-25]. FTIR studies have shown that sulfur is evenly distributed among the acidic, basic, and neutral fractions of asphaltenes [26-29]. X-ray absorption near-edge structure spectroscopy (XANES) reveals that sulfur exists predominantly as thiophenic heterocycles (65-85%) and sulfidic groups [30]. The thiophenic groups are only slightly polar and are not likely to contribute to intermolecular associations, such as hydrogen bonding. Unlike sulfur, oxygen and nitrogen containing moieties in asphaltenes are generally polar and capable of participating in strong intermolecular associations. For example, FTIR and XANES spectroscopy reveal several polar functional groups, such as carboxylic acids, carbonyls, phenols, pyrroles, and pyridines, that are capable of participating in proton donor-acceptor interactions [29,31,32]. Sjöblom and coworkers used diffuse reflectance FTIR to show that the interfacially active components of fractionated asphaltenes contained significant concentrations of acidic and open chain carbonyl groups that introduce a strong hydrogen bonding contribution to the mechanical film strength and prevent water droplet coalescence [33].

Various metals (e.g., Ni, V, Fe, Al, Na, Ca, and Mg) have also been shown to accumulate in the asphaltenic fraction of crude oil, typically in concentrations much less than 1 % (w/w) [13,17,34,35]. Vanadium and nickel are generally the most abundant of the trace metals, are present to some extent as chelated porphyrin complexes, and have been linked to catalyst poisoning during upgrading of heavy oils [36-38]. The concentrations of Fe, Al, Na,

Ca, and Mg have also been reported to vary in deposits as a function of well depth [39] and among asphaltene subfractions [13,35].

Several of the above-described problems encountered during petroleum production may be related to or predominantly contributed to by a particular subfraction of the total asphaltenes. Separation of the total asphaltenes into subfractions is often motivated by an attempt to probe the relationship between the chemical composition, solubility, aggregation behavior, and emulsion-stabilizing properties of discrete portions of the asphaltene fraction. Previous methods of separating asphaltenes into subfractions include gel permeation chromatography [40], sequential elution solvent chromatography [41], liquid-liquid extraction [42-44], dialysis fractionation [45], ultracentrifugation [46], and precipitation by the addition of flocculants [13,21,32,34,35,42,47-50].

Two different experimental methods are common for the separation of asphaltenes into subfractions by precipitation and will be referred to as the “coarse” and “fine” fractionation methods. The solvent/anti-solvent combination used and exact procedure for isolation of the precipitated asphaltenes generally varies between researchers; however, in both methods the total asphaltene fraction is typically dispersed in a “good” solvent (e.g., toluene) at a fixed solute concentration and a flocculating solvent (e.g., n-heptane) is added to induce partial precipitation. During a coarse fractionation, two asphaltenic fractions (i.e., insolubles and solubles) are isolated by asphaltene precipitation at a given solvent condition. Typically, the ratio of flocculant to solvent is varied so that several pairs of more and less soluble fractions are isolated. For example, Yarranton and Masliyah studied the solubility behavior and molar mass distribution from vapor pressure osmometry (v.p.o.) and interfacial tension measurements of several Athabasca n-C₇ asphaltenic coarse fractions precipitated

from mixtures of hexane and toluene [48]. Andersen et al. isolated several coarse fractions of Boscan n-C₇ asphaltenes by precipitation in mixtures of heptane and toluene [42,49]. Spiecker et al. studied the solubility and aggregation behavior by SANS of coarse asphaltenic fractions precipitated from various parent asphaltenes by a similar procedure [13]. In each of the above studies, the relative aromaticities, N/C contents, and aggregate sizes (in toluene or pyridine) of the less soluble fractions generally decreased with increasing yield of precipitated asphaltenes (i.e., at higher flocculant/solvent ratios). Sulfur and oxygen contents were typically distributed evenly throughout the fractions. Furthermore, the less soluble fractions were generally more aromatic, had a higher N/C content, and formed larger aggregates in toluene and pyridine than the more soluble fractions. The various studies offered differing results concerning the isolation of trace metal species. UV-vis and HPLC-SEC measurements on Boscan asphaltenes indicated that metalloporphyrins were preferentially extracted in the more soluble fraction and contents decreased with decreasing asphaltene yield of the insoluble fraction [42,49]. In contrast, higher concentrations of various trace metals (e.g., Fe, Ni, V, Na) were observed in the less soluble fractions compared to the more soluble fractions as determined by the inductively coupled plasma (ICP) technique [13].

Instead of generating only two fractions, one of which represents at least half of the original asphaltenes by mass, the fine fractionation procedure here separates the total asphaltenes into several discrete subfractions by a step-wise increase in the concentration of the flocculating solvent. During each precipitation step, a small amount of asphaltenic material is precipitated and isolated, the soluble filtrate is recovered, and the next fraction is precipitated after a change in solvent conditions. The major difference between the coarse

and fine fractionation methods is that the coarse fractions precipitated at higher flocculant contents likely contain the entire subset of chemical species present in fractions precipitated at lower flocculant contents; whereas each fine fraction should represent the discrete subset of asphaltenes that precipitate within the range of two solvent conditions. For example, Yang et al. isolated six asphaltenic subfractions from Athabasca bitumen by step-wise increasing the ratio of n-heptane to bitumen (H/B) [35]. The first fraction to precipitate was the most aromatic and had the highest concentration of Fe, Ca, Mg, and Al. Atomic H/C ratio was observed to increase and metalloporphyrin contents decrease systematically as the fractionation proceeded (i.e., at higher H/B ratios). Unlike the previous analyses of coarse fractions by SANS and v.p.o. [13,48], no significant variations in aggregate molar mass were observed by v.p.o. for the fractions dissolved in toluene at 50°C. Groenzin et al. isolated six subfractions of n-C₅ asphaltenes by sequential precipitation in mixtures of n-pentane and toluene [21]. Fluorescence depolarization measurements on solutions of the asphaltenic fractions in toluene indicated that the less soluble fractions emitted at higher wavelengths than more soluble fractions, possibly suggesting that the less soluble fraction contained a higher population of larger chromophores.

Buenrostro-Gonzalez et al. compared the chemical composition of subfractions isolated by step-wise increasing the amount of flocculant (i.e., acetone or n-heptane) added to a 2.3 % (w/w) solution of Mayan n-C₇ asphaltenes in toluene [32]. Ten discrete fractions were isolated for each solvent mixture, but not enough material was precipitated during the first few fractionations (i.e., the least soluble asphaltenic fractions) to perform subsequent chemical analyses. There were no apparent trends in atomic H/C, N/C, S/C, or O/C with the order of fractionation for the heptane-toluene fractions analyzed. Similarly, there were no

apparent trends in atomic H/C, N/C, or S/C for the acetone-toluene fractions; however, O/C content appeared to increase continuously for the third through sixth fraction. These results suggested that polar interactions dominated the solubility behavior at low acetone contents, while dispersion interactions dominated the solubility behavior at high acetone contents and for the heptane-toluene fractions. Similar polar fractionations performed by Fogler and coworkers were completed by sequentially increasing the amount of n-pentane flocculant to a mixture of Mobil and Venezuelan n-C₇ asphaltenes in methylene chloride [34,47]. Marked differences in physical appearance, crystallinity, and solubility behavior (in dodecylbenzene sulfonic acid) were observed between the most polar and least polar fractions. Similarly, the more polar fractions had higher metals contents (i.e., Fe, Ni, and V) than the least polar fraction.

In the current study, the fractionation of asphaltenes is expanded to the isolation of 20-30 asphaltenic fine fractions per crude oil (i.e., HO, B6, and CS), with typical fractions representing ~ 1 to 18 % of the total asphaltenes by mass. The various fine fractions were isolated by precipitation of asphaltenes from mixtures of n-heptane and toluene. Combustion elemental analyses and ICP metals analyses were performed to measure the carbon, hydrogen, nitrogen, sulfur (B6 only), oxygen (B6 only), and trace metals contents of each subfraction. SANS measurements were performed on all of the HO and B6 subfractions dissolved in mixtures of d-toluene (or d-methylnaphthalene) and d-methanol. The preparatory-scale separation of the asphaltenes into several discrete subfractions allowed the development of the first ever chemical and colloidal distribution functions for petroleum asphaltenes.

3.2 Experimental

3.2.1 Materials

Asphaltenes were isolated from three crude oils identified as B6, Hondo (HO), and Canadon Seco (CS). HO and B6 crude oils were obtained from off-shore California. CS crude oil was obtained from Argentina. The crude oils were asphaltene rich and varied in viscosity, resin/asphaltene (R/A) mass ratio, and asphaltene chemical composition. Physical and chemical properties of the crude oils and isolated asphaltenes are summarized in Table 3.1. Asphaltene isolation and fractionation experiments were performed using toluene, n-heptane, and methylene chloride (HPLC grade) obtained from Fisher Scientific. The deuterated solvents used in SANS experiments (i.e., d-toluene, d-methylnaphthalene, and d-methanol) were obtained from CDN Isotopes and had > 99.9% chemical purity and >99.5% perdeuteration.

3.2.2 Asphaltene Precipitation

Asphaltenes were precipitated from the corresponding source crude oils by the addition of excess n-heptane (40:1 v/v). The crude oil/n-heptane mixtures were subjected to 24 hours of constant, gentle shaking to ensure that all of the material was completely dispersed. After this equilibration period, the precipitated asphaltenes were removed by vacuum filtration through 15 cm diameter, 1.5 μm Whatman 934-AH glass microfiber filter paper. The filter cake was rinsed with an excess of n-heptane to remove co-precipitated maltenes. The filter cake (i.e., precipitated asphaltenes) was completely dissolved from the filter paper and recovered in a different collection flask by the addition of excess methylene chloride under partial vacuum. Most of the solvent was removed from the asphaltene

solutions by rotary evaporation under partial vacuum at 40°C. Once nearly dry, the asphaltenes were moved into a nitrogen-flushed vacuum oven at 50°C for 24 h. The dry asphaltenes were transferred to glass jars and stored under argon to prevent oxidation. The asphaltenes isolated from the crude oils by the above method will be referred to as the “whole” asphaltenes for the remainder of the text.

3.2.3 Desalting of B6 Asphaltenes

The whole B6 asphaltenes precipitated according to the above procedure were suspected to contain co-precipitated inorganic salts, because the source crude oil was sampled from the bottom of a 5-gallon drum containing a mixture of crude oil and sedimented seawater. Spiecker et al. observed a relatively high concentration of sodium in whole B6 asphaltenes (9300 ppm) and a subfraction of B6 asphaltenes that was insoluble in 60:40 n-heptane: toluene (25000 ppm) obtained from the same crude oil source used in this study [13]. The Na content in the whole B6 asphaltenes was reduced from 9300 ppm to 35 ppm by extracting a crude oil-methylene chloride mixture with deionized water prior to the asphaltene precipitation. The reduction in Na content suggested that the B6 asphaltenes contained either co-precipitated inorganic salts (e.g., NaCl) or water-soluble soaps of corresponding carboxylic acids. In this study, a similar desalting procedure was followed for the whole B6 asphaltenes prior to the fine fractionation steps. Whole B6 asphaltenes were dissolved in methylene chloride (1 g / 100 ml) and extracted with a 0.1 M solution of HCl. The organic and aqueous phases were intermingled in a 500 ml separatory funnel in a 1:1 ratio (v/v). The addition of HCl was expected to increase the surface area of contact between the organic and aqueous phases by the formation of a weak emulsion that could be broken by

gravity settling. After the acid extraction, the organic phase was extracted with deionized water (3x). The whole B6 asphaltenes were recovered from the organic phase by rotary evaporation of the methylene chloride solvent and subsequent drying in the vacuum oven according to the procedure described above.

3.2.4 Asphaltene Fine Fractionation

The whole HO, CS, and desalted B6 asphaltenes were further separated into several subfractions by sequential fractionation in mixtures of n-heptane and toluene. A schematic representation of the fine fractionation procedure is shown in Figure 3.1. During the fractionations, approximately 20 g of whole asphaltenes were dissolved in toluene solution such that the total asphaltene concentration was 1 % (w/w) after flocculant addition. Upon dissolution in toluene, enough n-heptane was added to the solution to induce partial precipitation of approximately 1-2 % of the whole asphaltenes. The asphaltene solutions were subjected to 24 hours of constant, gentle shaking to allow equilibration of the samples. The precipitated asphaltenes were isolated by vacuum filtration and recovered similar to the above-described procedure for asphaltene precipitation. The precipitated asphaltenes became the first fine fraction, P1. The soluble asphaltenes were recovered from the filtrate (S1 fraction) by rotary evaporation and dried in a nitrogen-flushed vacuum oven at 50°C for 24 h. The S1 fraction was then dispersed in a mixture of toluene and n-heptane containing a higher concentration of flocculant according to the above procedure such that another 1-2 % of the whole asphaltenes were precipitated. The fractionation procedure continued using progressively more n-heptane as a flocculant until 20-30 fine fractions were isolated. During the final fractionation step, the soluble asphaltenes from the previous fraction were dispersed

in pure n-heptane to obtain a precipitated fraction (i.e., PN in Fig. 1) and an n-heptane soluble fraction (i.e., SN).

3.2.5 Chemical Characterization

The B6 asphaltenic fractions were characterized by combustion elemental analysis (carbon, hydrogen, nitrogen, sulfur, and oxygen) at the University of Alberta (Department of Chemistry, Edmonton, Alberta, Canada) using a Carlo Erba instrument. The HO and CS asphaltenic fractions were characterized by combustion elemental analysis (carbon, hydrogen, and nitrogen) at Nalco Energy Services Division (Sugar Land, TX). Metals analyses for all of the asphaltenic fractions were performed at Nalco Energy Services Division using a Jerrel Ash 9000 by the ICP technique.

3.2.6 SANS Measurements

Solutions with mass concentration of 1 % (w/w) were prepared by dissolving various asphaltenic fine fractions in mixtures of d-toluene, d-methylnaphthalene, and d-methanol. During the sample preparation, d-toluene or d-methylnaphthalene was initially added to the dry asphaltenes and the solution was subjected to constant, gentle shaking until the asphaltenes were completely dissolved. Upon dissolution of the asphaltenes, the second solvent (i.e., d-methanol) was added to the solutions. The solutions were allowed to equilibrate for at least one week prior to performing the scattering experiments. SANS measurements were performed on all of the HO fine fractions in 90:10 d-toluene: d-methanol (v/v), all of the B6 fine fractions in 90:10 d-methylnaphthalene: d-methanol (v/v), and the most soluble 30 % (w/w) of the B6 fine fractions in d-toluene.

Most of the SANS measurements were performed on the Small-Angle Neutron Diffractometer (SAND) at the Intense Pulsed Neutron Source Division of Argonne National Laboratory (Argonne, IL); however, additional experiments were performed on the 30 m, NG3 and 8 m, NG1 small angle spectrometers at the NIST Center for Neutron Research (Gaithersburg, MD). The SAND instrument at Argonne National Laboratory is a time-of-flight diffractometer attached to an accelerator-based pulsed neutron source (30 Hz). Each pulse contains neutrons with wavelengths ranging from 1 to 14 Å. The higher energy neutrons had lower wavelengths and reached the sample ahead of the lower energy neutrons. Thus, the energy of each scattered neutron was determined by its “time-of-flight” to the detector. The available Q range for the SAND instrument extended from 0.0035 to 2 Å⁻¹. During the NG3 and NG1 (NIST) experiments, the source-to-sample distance was varied from 4 to 16 m while the sample-to-detector distance was varied from 1.2 to 15 m. Neutrons of 6 Å wavelength and 0.22 spread ($\Delta\lambda/\lambda$) were scattered from the sample and collected on a two dimensional detector (65 cm by 65 cm, 1 cm by 1 cm resolution). The available Q range extended from 0.0015 to 0.6 Å⁻¹.

The samples were measured at 25°C in cylindrical quartz sample cells (NGS Precision) with a path length of 2 mm. The absolute scattering intensity, I(Q), for each sample was obtained from the total detector counts corrected for background radiation, neutron transmission through the sample, scattering from the quartz cell, and detector sensitivity. The resulting scattering intensity versus scattering angle (I(Q) vs. Q) curves were fit to a polydisperse oblate cylinder form factor to determine the average aggregate size [51].

3.3 Results

Cumulative % asphaltenes precipitated as function of volume % toluene in n-heptane-toluene mixtures or so-called “differential solubility profiles” for the various asphaltenes are presented in Figure 3.2. Each data point in Figure 3.2 represents a different asphaltenic fine fraction. The abscissa represents the % toluene (v/v) in the heptane-toluene solvent for the fractionation. The ordinate represents the total amount of asphaltenic material precipitated after the fractionation. The amount of a given asphaltene fine fraction may be determined from Figure 3.2 as the difference between the total amount of precipitated material from sequential fractionations. As shown in Figure 3.2, less than 5 % (w/w) of the whole B6 asphaltenes were precipitated after the fractionation in 61 % toluene (v/v). In subsequent fractionations performed in solvent conditions containing 50 % to 60 % toluene (v/v), significant amounts of asphaltenic material were precipitated with small changes in the blend composition. For example, 17.84 % (w/w) of the whole B6 asphaltenes precipitated as the solvent composition was changed from 55 % to 54.5 % toluene (v/v). Similar trends were observed in the solubility curves for HO and CS asphaltenes; however, the range of heptane concentrations corresponding to the steepest slopes in Figure 3.2 varied depending on the crude oil source.

Chemical analyses of the asphaltenic fractions can provide additional information to help understand differences in the asphaltene solubility behaviors. For example, Figure 3.3 shows histograms of atomic H/C, N/C, and Na/C ratios for the HO fine fractions. Fractions with similar elemental composition were grouped into bins and plotted versus the percentage of the whole asphaltenes. As shown in Figure 3.3a, the solubility fractions isolated from whole HO asphaltenes represented a continuous monomodal distribution in H/C ratios from

1.16 to 1.33. It seems reasonable to ascribe a smooth distribution to our histogram data, given that each “bin” or fine fraction is comprised of asphaltenes with yet another distribution of chemical compositions and structures; however, the distributions of chemical and physical properties for each fine fraction are likely narrower than the whole asphaltene distributions. The bin for H/C = 1.46 represented the portion of HO asphaltenes that remained soluble after the final fractionation in n-heptane. By our working definition, this fraction is more chemically similar to resins than asphaltenes. The range of atomic N/C ratios for the HO asphaltenic fractions was also continuously distributed between 0.019 and 0.025 (Figure 3.3b). The histograms shown in Figure 3.3 were fit to a log-normal probability distribution function given by:

$$P(x) = \frac{1}{S\sqrt{2\pi}x} \exp\left[-(\ln x - M)^2 / (2S^2)\right] \quad (1)$$

where M and S are the central value of the distribution and the geometric standard deviation, respectively. A log-normal distribution was selected because it is right-skewed, positive-definite, and was generally observed to provide a better quality of fit to the histograms than a normal distribution. Because the log-normal distribution is skewed towards larger values, the M value is generally smaller than the mean value (x_{avg}) given by:

$$x_{\text{avg}} = \exp(M + S^2/2) \quad (2)$$

The variance is given by:

$$\sigma^2 = \exp(S^2 + 2M) [\exp(S^2) - 1] \quad (3)$$

Mean and variance values for the fits of a log-normal distribution to H/C, N/C, S/C, O/C, and trace metals contents for B6, CS and HO asphaltenic fractions are shown in Table 3.2. The magnitude of σ is greater than x_{avg} in some instances, particularly for alkali and alkaline earth

metals contents (i.e., Na, K, Ca, Mg), indicating that the log-normal function did not accurately model the distribution of these metals contents. For example, a fit of the log-normal distribution to Na/C ratio of HO asphaltenes is shown in Figure 3.3c. The concentration range of sodium in HO asphaltenes and other alkali and alkaline earth metals in the remaining fractions generally varied over 2 – 3 orders of magnitude, with the highest concentrations observed for the earliest precipitated fractions.

The variation in the atomic H/C ratios for the fine fractions as a function of total amount of asphaltenes precipitated is shown in Figure 3.4. The values of chemical contents and physical properties plotted in the Figures 3.4 - 3.11 represent a moving average of the properties over three consecutive data points and are weighted by the relative mass concentration of each fraction (i.e., % of whole asphaltenes). This averaging tends to smooth out random fluctuations in the curves due to uncertainty in the property measurement, allowing general trends in the properties to be more easily observed. The end-points on the plots are represented by the experimental values without averaging, as the first and final fractions did not occur in the middle of three consecutive fractionations.

B6 and HO fine fractions displayed similar variations in atomic H/C ratios with increasing yield of precipitated asphaltenes, as shown in Figure 3.4. The most aromatic fractions of the B6 asphaltenes ($H/C = 1.16$) were precipitated near 54.5 % toluene (v/v) and corresponded with the largest fraction isolated in the steepest portion of the solubility profile. The two largest fractions of HO asphaltenes were precipitated from 50 % and 48 % toluene (v/v) and were among the most aromatic ($H/C = 1.17$) and least aromatic ($H/C = 1.28$), respectively. Similarly, the most aromatic CS fractions were also observed in the steepest portion of the solubility profile, although nearly 70 % (w/w) of the CS fractions had a similar

high aromaticity ($H/C \sim 1.03$). A general decrease in the H/C ratio was observed over the first $\sim 10\%$ (w/w) of B6, CS, and HO asphaltenes precipitated. The H/C ratio generally increased over the final $\sim 20\%$ (w/w) of precipitated asphaltenes. Furthermore, the n-heptane soluble fraction was invariably the least aromatic of the fine fractions. This fraction likely consisted of adsorbed resins that were not removed during the initial asphaltene precipitation, as the observed H/C ratios were similar to those obtained for the resins by SARA fractionation of the crude oils (Table 3.1).

The variation in atomic N/C for the fine fractions as a function of total amount of asphaltenes precipitated is shown in Figure 3.5. After precipitation of $\sim 12\%$ (w/w) of the B6 asphaltenes, the nitrogen content was observed to systematically decrease with increasing flocculant concentration. The most significant decrease in N/C ratio occurred with the final $\sim 10 - 20\%$ (w/w) of precipitated material. CS asphaltenes followed a similar trend; however, a narrower distribution and lower concentration of nitrogen species was observed for these fractions. HO asphaltenes also followed a similar trend to B6 after passing through a local minimum near the fraction isolated in 48% toluene (v/v). The local minimum corresponded with a local maximum in atomic H/C ratio (Figure 3.4).

Figure 3.6 presents atomic O/C and S/C ratios for the B6 fine fractions. Sulfur contents appeared evenly distributed throughout most of the fractions; however, a significant decrease was apparent for the most soluble $\sim 10\%$ (w/w) of the whole asphaltenes. The earliest two fractions of B6 asphaltenes had relatively high O/C ratios. The O/C ratio of the remaining fractions generally increased with increasing precipitated asphaltene yield up to $\sim 93\%$ (w/w) precipitated and was followed by a significant decrease for the most soluble $\sim 7\%$ (w/w) of whole asphaltenes.

Variations in the atomic Na/C ratio of the fine fractions are shown in Figure 3.7. Even after desalting of the whole asphaltenes, the first (70 % toluene) fraction of B6 asphaltenes precipitated had a Na content of 3.7 % (w/w). As previously mentioned, the whole B6 asphaltenes were isolated from a crude oil source containing significant amounts of sea water. The Na/C ratio of the B6 fine fractions was observed to decrease significantly with increasing flocculant addition from 37000 to 30 ppm. Similar decreases in atomic Na/C ratio with increasing yield of precipitated asphaltenes were observed for the HO and CS fine fractions, although sodium contents of the earliest fractions precipitated were significantly lower than the B6 fractions. Figure 3.8 shows a similar reduction in other alkali and alkaline earth metals contents (i.e., Ca/C, K/C, and Mg/C) of the B6 fine fractions with increasing precipitated asphaltene yield.

The atomic V/C ratio of the HO fractions was observed to decrease systematically with increasing yield of precipitated asphaltenes (Figure 3.9). A similar trend was observed for the B6 fractions after the first ~ 20 % (w/w) of asphaltenes were precipitated; however, the V/C ratio increased systematically for the earliest precipitated B6 fractions. The total V content was negligible in all of the CS fine fractions. The Ni/C ratio for the B6 fractions followed a similar trend to V/C ratio (Figure 3.10). As shown in Figure 3.10, higher than average Al and Fe contents were also observed for the first two B6 fine fractions. A local maximum was observed in the Al and Fe contents of the B6 fine fraction precipitated in 53 % toluene (v/v) that corresponded with a significant increase in atomic H/C ratio from 1.16 to 1.26 (Figure 3.4) and an observable increase in atomic O/C ratio from 0.0251 to 0.0269 (Figure 3.6).

SANS measurements were performed on 1 % (w/w) solutions of B6 fine fractions dispersed in mixtures of 90:10 d-methylnaphthalene: d-methanol (v/v) and in d-toluene. The HO fine fractions were dispersed in mixtures of 90:10 d-toluene: d-methanol (v/v). In previous studies, it was observed that the addition of a small amount of d-methanol to solutions of asphaltenes in d-toluene (or d-methyl naphthalene) was sufficient to disrupt interactions between polar heteroatoms within the aggregates and reduce the aggregate size [52,53]. Since several of the earliest fractions isolated were insoluble in d-toluene and d-methylnaphthalene, a small amount of d-methanol was added to the mixtures to enable dissolution of the asphaltenes.

Aggregate average radius of gyration values, $\langle R_G^2 \rangle^{1/2}$, were obtained from non-linear least squares fits of the scattering intensity curves to a polydisperse oblate cylinder model [51]. Variation in the average aggregate size with increasing yield of precipitated asphaltenes is shown in Figure 3.11. Once isolated, the B6 fine fractions had a limited solubility in d-toluene at the given solute concentration. As shown in the figure, the fraction isolated in 49 % toluene (v/v) formed aggregates in d-toluene with an average size of $\sim 93 \text{ \AA}$, even though $\sim 65 \text{ %}$ (w/w) of the whole asphaltenes had precipitated prior to this fractionation. The average aggregate size in d-toluene generally decreased with increasing yield of precipitated material for the remaining B6 fine fractions. A small amount of d-methanol (i.e., 10 % v/v) was added to the solutions of B6 fine fractions in d-methylnaphthalene in an attempt to dissolve the less soluble fractions. The addition of d-methanol was effective at completely dissolving all of the B6 fine fractions in d-methylnaphthalene except for those isolated in 70 %, 55.5%, and 54.5% toluene (v/v).

Figure 3.11 indicates a significant increase in aggregate size of the B6 fine fractions from the earliest fractions precipitated to the fraction isolated in 54.5 % toluene (v/v). The aggregate size generally decreased with increasing precipitated asphaltene yield for the remaining fractions. Similar behavior was observed for the HO fine fractions in 90:10 d-toluene: d-methanol (v/v). The aggregate size increased significantly from the first fraction to the second fraction (i.e., the transition to higher slopes in the solubility profile) and was followed by a systematic decrease in aggregate size of the remaining HO fine fractions. Figure 3.12a indicates an apparent monomodal distribution of aggregate sizes between 20 to 65 Å for the HO fine fractions in 90:10 d-toluene: d-methanol (v/v). A similar monomodal distribution is observed for the soluble B6 fine fractions (Figure 3.12b.); however, the mean is shifted to larger values by two insoluble fractions (i.e., those isolated in 55.5 % and 54.5 % toluene). Values of the mean and variance of $\langle R_G^2 \rangle^{1/2}$ for the HO and B6 fine fractions are shown in Table 3.3.

3.4 Discussion

The combustion elemental analyses indicated three distinct trends in the chemical composition of the fine fractions that appeared to correlate with changes in the slope of the differential solubility profile. As shown in Figure 3.2, the solubility profiles (cumulative % precipitated versus % toluene in precipitating solvent) for the asphaltenes have similar shapes. The slopes of the solubility profiles are relatively low at high toluene contents. Typical fractions consisting of ~ 1 to 2 % (w/w) of the whole asphaltenes were isolated by changes in the n-heptane concentration in the precipitation solvent of ~ 1 to 3 % (v/v) in the high % toluene regime. Figure 3.4 indicates a general decrease in atomic H/C ratios over this

region of the solubility profile for each of the asphaltenes. Figure 3.5 also indicates a lower atomic N/C ratio for the B6 fine fractions in this regime. The lower aromaticity and nitrogen content of these fractions compared to fractions isolated after the transition to steeper slopes in the solubility curves was reflected in the formation of smaller aggregates in solution (Figure 3.11). This observation was consistent with previous studies that indicated the size of aggregates in solution generally increases with increasing aromaticity and N/C content of the asphaltenic fraction [13,49]. This seems reasonable if one presumes that the chief determinants of aggregate size are the number of potential intermolecular π - and H-bonds per asphaltene molecule. While the nitrogen content of the first five B6 fine fractions remained relatively constant, the atomic V/C ratio increased with increasing precipitated asphaltene yield (Figure 3.9), suggesting a lower concentration of metalloporphyrins in the earliest fractions. This result was consistent with the observation by Andersen et al. that the metalloporphyrins were preferentially extracted into the more soluble asphaltenic fractions [42,49].

Figure 3.6 indicates significantly higher oxygen content of the earliest precipitated B6 fine fraction that coincided with higher than average aluminum and iron contents (Figure 3.10). If we assume that all of the Al and Fe species in the first B6 fine fraction were present as alumina and iron oxide (i.e., Al_2O_3 and Fe_2O_3), then oxygen in the form of metal oxides would account for approximately 0.96 % (w/w) of the total chemical species. Normalized to the total carbon content in the first fraction, the atomic O/C ratio estimated for inorganic oxygen (~ 0.013) was roughly the difference between the experimentally measured O/C ratio for the first fraction (~ 0.037) and the mean O/C ratio for the B6 fractions (~ 0.025). These results suggest the elevated oxygen content in the earliest B6 fine fractions was largely

related to the presence of inorganic oxides that co-precipitated with the asphaltenes. The co-precipitated alumina and iron oxide particles were not expected to be soluble in methylene chloride during recovery of the precipitated asphaltenes and, therefore, were not expected to pass through the 1.5 μm diameter pores of the filter paper. A reasonable explanation for the presence of nearly 1 % (w/w) of inorganic material in the earliest precipitated fraction is that the alumina and iron species were intimately bound to the asphaltene particles and were small enough to pass through the filter paper when the asphaltenes were solubilized. Yang et al. observed a similar enrichment in the oxygen content of “fine solids” extracted from the earliest precipitating fraction of Athabasca asphaltenes in a 10:1 toluene: water mixture (v/v) [35]. Furthermore, the corresponding toluene soluble fraction after extraction was enriched in Fe, Ca, Mg, and Al contents compared to the remaining more soluble fractions. Similar trends in these metals contents were observed for B6 asphaltenes, as shown in Figures 3.8 and 3.10.

The earliest fractions of B6 asphaltenes possessed relatively high concentrations of alkali and alkaline earth metals, particularly Na and Ca that accounted for 3.7 % and 2.6 % (w/w) of the fraction mass, respectively. The sums of the C, H, N, S, and O contents from combustion of the first two B6 fine fractions were ~ 71 % and 82 % (w/w), respectively. The incomplete combustion of the fractions, along with the enriched Na and Ca contents, suggests that a significant portion of the fractions contained co-precipitated metal oxides and inorganic salts. The ICP metals results further suggest that inorganic salts were intimately bound within the asphaltene aggregate structures and did not completely co-precipitate with the least soluble asphaltenic fraction, rather the Na and Ca contents gradually decreased as the largest aggregate formers were precipitated from solution. The local maxima in atomic

Al/C, Fe/C, and O/C ratios for the B6 fine fraction isolated in 53 % toluene (v/v) suggests that some inorganic fine solids may remain bound within the asphaltenic aggregates even after ~ 50 % (w/w) of the whole asphaltenes have been precipitated.

Distinct changes in the chemical composition and aggregation behavior of the fine fractions become apparent above a critical n-heptane concentration that is unique for each asphaltene. This regime represents the steepest portion of the differential solubility profiles (Figure 3.2) where significant increases in the amount of precipitated material occur with very small changes in the solvent composition. Asphaltenic fractions within this solubility regime showed a significant variation in atomic H/C ratios, although N/C ratios generally decreased and O/C ratios increased systematically with increasing precipitated asphaltene yield. Furthermore, the more aromatic B6 and HO fine fractions generally formed the largest aggregates in solution (Figure 3.11). These results suggest that asphaltene solubility and aggregation behavior is dominated by π -bonding interactions between the aromatic moieties.

The slopes of the differential solubility profiles generally decreased after approximately 80 % (w/w) of the total asphaltenes precipitated (Figure 3.2). This solubility regime was generally characterized by fractions with higher than average atomic H/C ratios and lower than average N/C, S/C, and O/C ratios (Figures 3.4 – 3.6). The aggregate sizes of these fractions represented the low end of the distributions (Figure 3.12) and generally decreased with increasing precipitated asphaltene yield. By this point in the fractionations, the contents of various metals are also at their lowest values (Figures 3.7 – 3.10). The trends in the chemical composition with aggregate size suggest that most of the strongly interacting chemical species have precipitated from solution during earlier fractionations, including those species that were most strongly bound to inorganic solids. The chemical composition

of the remaining fractions deviated from typical asphaltenes and approached the composition of petroleum resins. As previously mentioned, the n-heptane soluble fractions likely consisted of petroleum resins that co-precipitated with the original whole asphaltenes.

3.5 Conclusions

Asphaltenes from three different crude sources were fractionated into 20 to 30 discrete subfractions by sequential precipitation in mixtures of heptane and toluene. Sufficient asphaltenic material was isolated during each fractionation to perform subsequent chemical analyses and SANS studies on the subfractions. Three distinct solubility regimes were indicated in which the chemical and colloidal behavior of the asphaltenic fractions varied significantly with total amount of precipitated asphaltenes. Fractions isolated in the initial, flatter portion of the solubility profile were characterized by decreasing atomic H/C ratios and increasing N/C ratios with precipitated asphaltene yield. ICP metals analyses suggested that the fractions contained significant amounts of inorganic fine solids (e.g., metal oxides and salts) that co-precipitated with the asphaltenic species. The presence of local maxima in atomic O/C, Al/C, and Fe/C ratios of a later B6 fine fraction suggested that some inorganic fine solids may remain intimately bound to the asphaltenic aggregates throughout the fractionation process.

The fine fractions isolated in the steepest region of the solubility profiles were characterized by atomic H/C and N/C ratios that varied significantly with the yield of precipitated asphaltenes. Generally, the chemical composition of the fine fractions alternated between fractions that were relatively more aromatic those with higher atomic H/C ratios. Within this solubility regime, the atomic N/C ratio of the fractions generally decreased and

the O/C ratio increased with increasing precipitated asphaltene yield. The more aromatic fine fractions generally formed larger aggregates in solution, suggesting that asphaltene solubility and aggregation behavior is dominated by π -bonding interactions between the aromatic moieties. The remaining fractions after precipitation of ~ 80 % (w/w) of the whole asphaltenes were generally less aromatic, less polar, and formed smaller aggregates in solution than the earlier precipitating fractions.

3.6 Acknowledgements

This research is supported by the Petroleum Environmental Research Forum, ExxonMobil, Shell, Equilon, ChevronTexaco, Nalco Energy Services Division, Champion Technologies, National Science Foundation Grant (CTS981727), and the NSF Graduate Research Fellowship Program. We acknowledge Darlene Mahlow at the University of Alberta for performing combustion elemental analyses on the asphaltene and resin samples. Additional combustion elemental analyses and ICP metals analyses were performed by Rebecca L. Ramsey at Nalco Energy Services in Sugar Land, TX. This work benefited from the use of facilities in the Intense Pulsed Neutron Source and the Chemistry Division, which is funded by the U. S. Department of Energy, Office of Basic Energy Sciences under contract W-31-109-ENG-38 to the University of Chicago. We would particularly like to thank Pappannan Thiyagarajan and Denis Wozniak of the Intense Pulsed Neutron Source Division at Argonne National Laboratory for their assistance with the SAND instrument. We also acknowledge the support of the National Institute of Standards and Technology, U.S. Department of Commerce, in providing the neutron research facilities used in this work and Min Lin for his assistance on the NG1 and NG3 beamlines. We would also like to thank

Matthew B. Smith, M. Lupe Marques, and Vincent Verruto for helping with the sample preparation and SANS data collection.

3.7 References

1. A. Hammami, C. H. Phelps, T. Monger-McClure, T. M. Little, "Asphaltene precipitation from live oils: An experimental investigation of onset conditions and reversibility," *Energy & Fuels*, 2000, **14**(1): p. 14-18.
2. K. Karan, A. Hammami, M. Flannery, B. A. Stankiewicz, "Evaluation of asphaltene instability and a chemical control during production of live oils," *Petroleum Science and Technology*, 2003, **21**(3-4): p. 629-645.
3. S. D. Taylor, J. Czarnecki, J. Masliyah, "Disjoining pressure isotherms of water-in-bitumen emulsion films," *Journal of Colloid and Interface Science*, 2002, **252**(1): p. 149-160.
4. H. W. Yarranton, H. Hussein, J. H. Masliyah, "Water-in-hydrocarbon emulsions stabilized by asphaltenes at low concentrations," *Journal of Colloid and Interface Science*, 2000, **228**(1): p. 52-63.
5. K. Khristov, S. D. Taylor, J. Czarnecki, J. Masliyah, "Thin liquid film technique - application to water-oil-water bitumen emulsion films," *Colloids and Surfaces a-Physicochemical and Engineering Aspects*, 2000, **174**(1-2): p. 183-196.
6. T. E. Havre, J. Sjoblom, "Emulsion stabilization by means of combined surfactant multilayer (D-phase) and asphaltene particles," *Colloids and Surfaces a-Physicochemical and Engineering Aspects*, 2003, **228**(1-3): p. 131-142.
7. N. Aske, H. Kallevik, J. Sjoblom, "Water-in-crude oil emulsion stability studied by critical electric field measurements. Correlation to physico-chemical parameters and near-infrared spectroscopy," *Journal of Petroleum Science and Engineering*, 2002, **36**(1-2): p. 1-17.
8. N. Aske, R. Orr, J. Sjoblom, H. Kallevik, G. Oye, "Interfacial properties of water-crude oil systems using the oscillating pendant drop. Correlations to asphaltene solubility by near infrared spectroscopy," *Journal of Dispersion Science and Technology*, 2004, **25**(3): p. 263-275.
9. I. H. Auflem, H. Kallevik, A. Westvik, J. Sjoblom, "Influence of pressure and solvency on the separation of water-in-crude-oil emulsions from the North Sea," *Journal of Petroleum Science and Engineering*, 2001, **31**(1): p. 1-12.

10. P. M. Spiecker, P. K. Kilpatrick, "Interfacial rheology of petroleum asphaltenes at the oil-water interface," *Langmuir*, 2004, **20**(10): p. 4022-4032.
11. P. M. Spiecker, K. L. Gawrys, C. B. Trail, P. K. Kilpatrick, "Effects of petroleum resins on asphaltene aggregation and water-in-oil emulsion formation," *Colloids and Surfaces a-Physicochemical and Engineering Aspects*, 2003, **220**(1-3): p. 9-27.
12. X. L. Yang, P. K. Kilpatrick, "Asphaltenes and Waxes Do Not Interact Synergistically and Co-Precipitate in Solid Organic Deposits," *Energy & Fuels*, submitted.
13. P. M. Spiecker, K. L. Gawrys, P. K. Kilpatrick, "Aggregation and solubility behavior of asphaltenes and their subfractions," *Journal of Colloid and Interface Science*, 2003, **267**(1): p. 178-193.
14. D. L. Mitchell, J. G. Speight, "The Solubility of Asphaltenes in Hydrocarbon Solvents," *Fuel*, 1973, **52**(4): p. 149-152.
15. G. Brons, J. M. Yu, "Solvent Deasphalting Effects on Whole Cold Lake Bitumen," *Energy & Fuels*, 1995, **9**(4): p. 641-647.
16. J. T. Miller, R. B. Fisher, P. Thiyagarajan, R. E. Winans, J. E. Hunt, "Subfractionation and characterization of Mayan asphaltene," *Energy & Fuels*, 1998, **12**(6): p. 1290-1298.
17. J. D. McLean, P. K. Kilpatrick, "Comparison of Precipitation and Extrography in the Fractionation of Crude Oil Residua," *Energy and Fuels*, 1997, **11**: p. 570-585.
18. O. P. Strausz, P. Peng, J. Murgich, "About the colloidal nature of asphaltenes and the MW of covalent monomeric units," *Energy & Fuels*, 2002, **16**(4): p. 809-822.
19. J. M. Sheremata, M. R. Gray, H. D. Dettman, W. C. McCaffrey, "Quantitative molecular representation and sequential optimization of athabasca asphaltenes," *Energy & Fuels*, 2004, **18**(5): p. 1377-1384.
20. M. R. Gray, "Consistency of asphaltene chemical structures with pyrolysis and coking behavior," *Energy & Fuels*, 2003, **17**(6): p. 1566-1569.
21. H. Groenzin, O. C. Mullins, S. Eser, J. Mathews, M. G. Yang, D. Jones, "Molecular size of asphaltene solubility fractions," *Energy & Fuels*, 2003, **17**(2): p. 498-503.
22. U. Bergmann, H. Groenzin, O. C. Mullins, P. Glatzel, J. Fetzer, S. P. Cramer, "X-ray Raman spectroscopy - A new tool to study local structure of aromatic hydrocarbons and asphaltenes," *Petroleum Science and Technology*, 2004, **22**(7-8): p. 863-875.

23. M. A. Bestougeff, "Chemical Composition and Structure of Asphaltenes . Their Importance among Natural Organic Compounds," *Bulletin De La Societe Chimique De France*, 1967, (12): p. 4773-&.
24. M. M. Boduszynski, "Characterization of "Heavy" Crude Components," *Preprints ACS Division of Petroleum Chemistry*, 1985, **30**: p. 626-640.
25. M. M. Boduszynski, "Composition of Heavy Petroleums. 2. Molecular Characterization," *Energy & Fuels*, 1988, **2**(5): p. 597-613.
26. J. F. McKay, P. M. Harnsberger, R. B. Erickson, T. E. Cogswell, D. R. Latham, "Composition of Petroleum Heavy Ends. 2. Characterization of Compound Types in Petroleum >675 C Residues," *Fuel*, 1981, **60**(1): p. 17-26.
27. J. F. McKay, P. J. Amend, P. M. Harnsberger, T. E. Cogswell, D. R. Latham, "Composition of Petroleum Heavy Ends. 1. Separation of Petroleum > 675 C Residues," *Fuel*, 1981, **60**(1): p. 14-16.
28. J. F. McKay, D. R. Latham, W. E. Haines, "Composition of Petroleum Heavy Ends. 3. Comparison of the Composition of High-Boiling Petroleum Distillates and Petroleum > 675 C Residues," *Fuel*, 1981, **60**(1): p. 27-32.
29. M. M. Boduszynski, J. F. McKay, D. R. Latham, "Asphaltenes, Where Are You?," *Proceedings of the Association of Asphalt Paving Technologists*, 1980, **49**: p. 123-143.
30. O. C. Mullins, Sulfur and Nitrogen Molecular Structures in Asphaltenes and Related Materials Quantified by XANES Spectroscopy, *in* "Asphaltenes: Fundamentals and Applications" (O. C. Mullins, Eds.), Plenum Press, New York, 1995; pp 53-96.
31. S. Mitrakirtley, O. C. Mullins, J. Vanelp, S. J. George, J. Chen, S. P. Cramer, "Determination of the Nitrogen Chemical Structures in Petroleum Asphaltenes Using Xanes Spectroscopy," *Journal of the American Chemical Society*, 1993, **115**(1): p. 252-258.
32. E. Buenrostro-Gonzalez, S. I. Andersen, J. A. Garcia-Martinez, C. Lira-Galeana, "Solubility/molecular structure relationships of asphaltenes in polar and nonpolar media," *Energy & Fuels*, 2002, **16**(3): p. 732-741.
33. L. Mingyuan, A. Christy, J. Sjoblom, Water-in-Crude Oil Emulsions from the Norwegian Continental Shelf Part VI -- Diffuse Reflectance Fourier Transform Infrared Characterization of Interfacially Active Fractions from North Sea Crude Oil, *in* "Emulsions -- A Fundamental and Practical Approach" (J. Sjoblom, Eds.), Kluwer Academic Publishers, The Netherlands, 1992; pp 157-172.

34. T. J. Kaminski, H. S. Fogler, N. Wolf, P. Wattana, A. Mairal, "Classification of asphaltenes via fractionation and the effect of heteroatom content on dissolution kinetics," *Energy & Fuels*, 2000, **14**(1): p. 25-30.
35. X. L. Yang, H. Hamza, J. Czarnecki, "Investigation of subfractions of athabasca asphaltenes and their role in emulsion stability," *Energy & Fuels*, 2004, **18**(3): p. 770-777.
36. M. F. Ali, H. Perzanowski, A. Bukhari, A. A. Al-Haji, "Nickel and Vanadyl Porphyrins in Saudi Arabian Crude Oils," *Energy & Fuels*, 1993, **7**(2): p. 179-184.
37. C. Ovalles, I. Rojas, S. Acevedo, G. Escobar, G. Jorge, L. B. Gutierrez, A. Rincon, B. Scharifker, "Upgrading of Orinoco Belt crude oil and its fractions by an electrochemical system in the presence of protonating agents," *Fuel Processing Technology*, 1996, **48**(2): p. 159-172.
38. M. E. Pena, A. Manjarrez, A. Campero, "Distribution of vanadyl porphyrins in a Mexican offshore heavy crude oil," *Fuel Processing Technology*, 1996, **46**(3): p. 171-182.
39. E. Chouparova, A. Lanzirrotti, H. Feng, K. W. Jones, N. Marinkovic, C. Whitson, P. Philp, "Characterization of petroleum deposits formed in a producing well by synchrotron radiation-based microanalyses," *Energy & Fuels*, 2004, **18**(4): p. 1199-1212.
40. N. Cyr, D. D. McIntyre, G. Toth, O. P. Strausz, "Hydrocarbon Structural Group Analysis of Athabasca Asphaltene and its G.P.C. Fractions by C-13 N.M.R.," *Fuel*, 1987, **66**: p. 1709-1714.
41. F. S. Jacobs, R. H. Filby, "Liquid Chromatographic Fractionation of Oil-Sand and Crude Oil Asphaltenes," *Fuel*, 1983, **62**(10): p. 1186-1192.
42. S. I. Andersen, A. Keul, E. Stenby, "Variation in composition of subfractions of petroleum asphaltenes," *Petroleum Science and Technology*, 1997, **15**(7-8): p. 611-645.
43. J. A. Ostlund, P. Wattana, M. Nyden, H. S. Fogler, "Characterization of fractionated asphaltenes by UV-vis and NMR self-diffusion spectroscopy," *Journal of Colloid and Interface Science*, 2004, **271**(2): p. 372-380.
44. J. A. Ostlund, M. Nyden, H. S. Fogler, K. Holmberg, "Functional groups in fractionated asphaltenes and the adsorption of amphiphilic molecules," *Colloids and Surfaces a-Physicochemical and Engineering Aspects*, 2004, **234**(1-3): p. 95-102.
45. S. Acevedo, G. Escobar, M. A. Ranaudo, J. Pinate, A. Amarin, M. Diaz, P. Silva, "Observations about the structure and dispersion of petroleum asphaltenes aggregates

- obtained from dialysis fractionation and characterization," *Energy & Fuels*, 1997, **11**(4): p. 774-778.
46. D. Fenistein, L. Barre, "Experimental measurement of the mass distribution of petroleum asphaltene aggregates using ultracentrifugation and small-angle X-ray scattering," *Fuel*, 2001, **80**(2): p. 283-287.
 47. V. Nalwaya, V. Tangtayakom, P. Piumsomboon, S. Fogler, "Studies on asphaltenes through analysis of polar fractions," *Industrial & Engineering Chemistry Research*, 1999, **38**(3): p. 964-972.
 48. H. W. Yarranton, J. H. Masliyah, "Molar Mass Distribution and Solubility Modeling of Asphaltenes," *AIChE Journal*, 1996, **42**(12): p. 3533-3543.
 49. S. I. Andersen, "Dissolution of Solid Boscan Asphaltenes in Mixed-Solvents," *Fuel Science & Technology International*, 1994, **12**(11-12): p. 1551-1577.
 50. S. I. Andersen, "Effect of Precipitation Temperature on the Composition of N-Heptane Asphaltenes .2," *Fuel Science & Technology International*, 1995, **13**(5): p. 579-604.
 51. K. L. Gawrys, P. K. Kilpatrick, "Asphaltenic aggregates are polydisperse oblate cylinders," *Journal of Colloid and Interface Science*, submitted.
 52. K. L. Gawrys, P. K. Kilpatrick, "Second virial coefficients of asphaltenic aggregates in varying solvents probed by small angle neutron scattering," *Energy & Fuels*, submitted.
 53. K. L. Gawrys, P. K. Kilpatrick, "Solvent entrainment in and flocculation of asphaltenic aggregates probed by small-angle neutron scattering," *Langmuir*, submitted.

Table 3.1 Crude oil and whole asphaltene properties

Crude	Wt % Asph	R/A Ratio	Viscosity (cP) 100°F	H/C Asph	N/C Asph	H/C Resin
B6	13.1	0.92	2030	1.22	0.0201	1.51
CS	7.5	1.19	70	1.11	0.0190	1.39
HO	14.8	1.39	363	1.24	0.0236	1.51

Table 3.2 Log-normal distribution of chemical compositions (atomic) for asphaltenic fine fractions.

	B6 asphaltenes	CS asphaltenes	HO asphaltenes
Element	$x_{avg} \pm \sigma$	$x_{avg} \pm \sigma$	$x_{avg} \pm \sigma$
H/C	1.20 ± 0.05	1.03 ± 0.03	1.23 ± 0.04
N/C	0.021 ± 0.001	0.018 ± 0.001	0.024 ± 0.001
S/C	0.032 ± 0.001	n.a.	n.a.
O/C	0.025 ± 0.002	n.a.	n.a.
Al/C (10 ⁶)	108 ± 71	57 ± 45	58 ± 21
Ca/C (10 ⁶)	367 ± 410	37 ± 56	82 ± 27
Fe/C (10 ⁶)	21.0 ± 17	14 ± 6	25 ± 13
Mg/C (10 ⁶)	137 ± 246	20 ± 9	18 ± 5
Ni/C (10 ⁶)	119 ± 10	7 ± 8	92 ± 20
K/C (10 ⁶)	45 ± 69	40 ± 17	11 ± 4
Na/C (10 ⁶)	145 ± 359	47 ± 19	88 ± 218
V/C (10 ⁶)	342 ± 34	2 ± 1	221 ± 51

Table 3.3 Log-normal distribution of aggregate sizes.

Asphaltene	Solvent	x_{avg} (Å) ± σ (Å)
Hondo	90:10 Tol:MeOD	50 ± 10
B6	90:10 MN:MeOD	60 ± 20

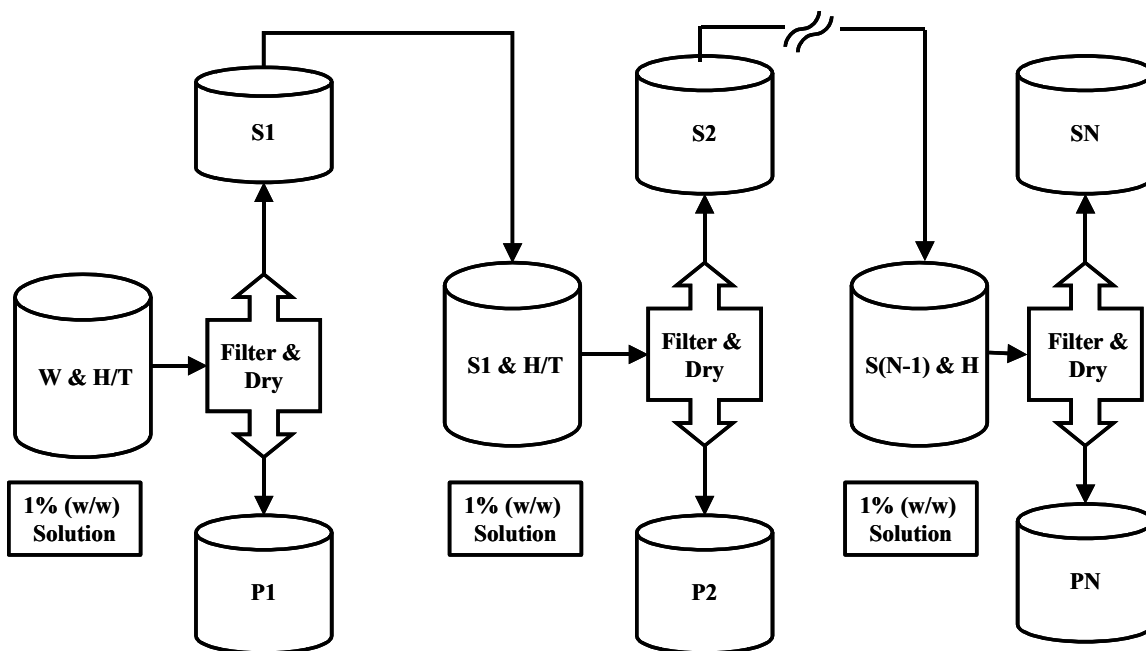


Figure 3.1 Schematic representation of the fine fractionation procedure for the preparation of N fractions. Whole asphaltenes (W) are dispersed in mixtures of heptane and toluene (H/T) at fixed solute concentration. After filtration of the equilibrated solution, the filter cake (P1) and filtrate (S1) are recovered and dried. The S1 fraction is dispersed in a H/T mixture with a higher heptane volume fraction to recover a second precipitated fraction (P2). The sequential fractionation of the soluble fraction (S2) continues until N fractions are isolated. The final precipitated fraction (PN) and soluble fraction (SN) are isolated from pure heptane.

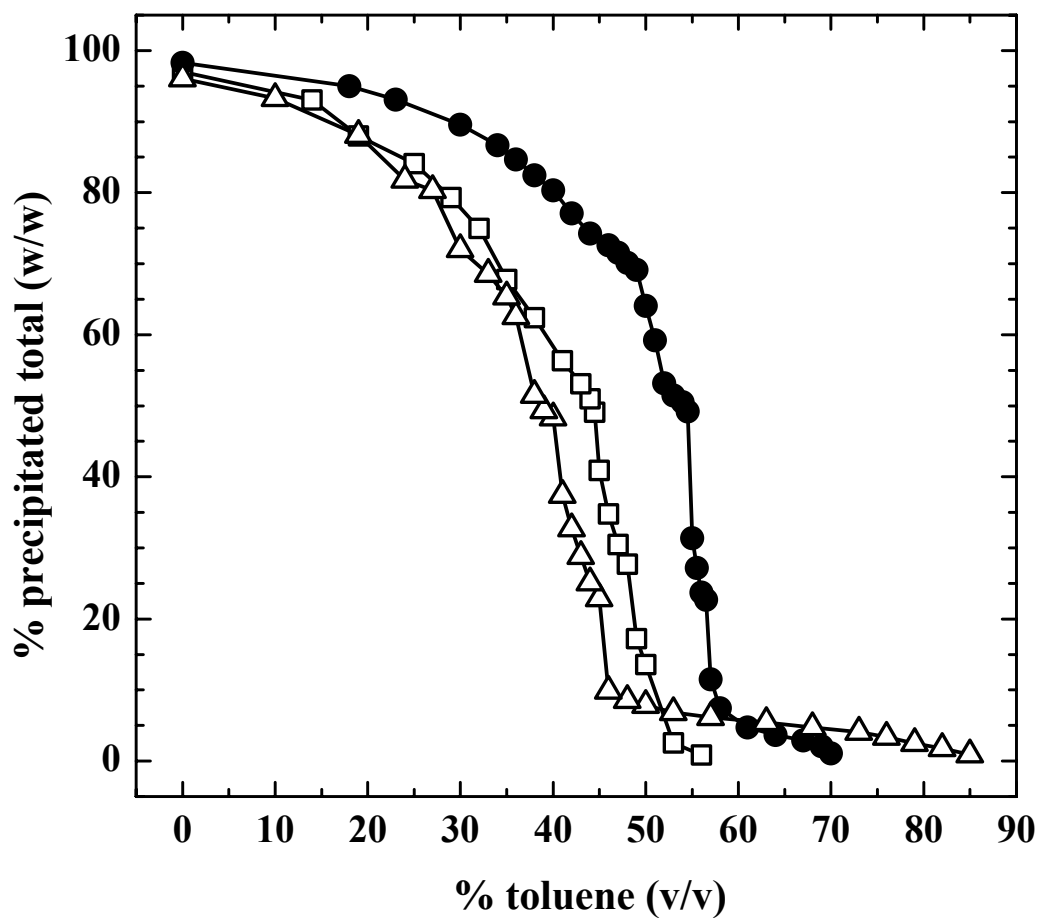


Figure 3.2 Cumulative % asphaltene precipitated as function of volume % toluene in n-heptane-toluene mixtures, so-called differential solubility profiles, for (△) CS, (□) HO, and (●) B6 asphaltene in mixtures of heptane and toluene.

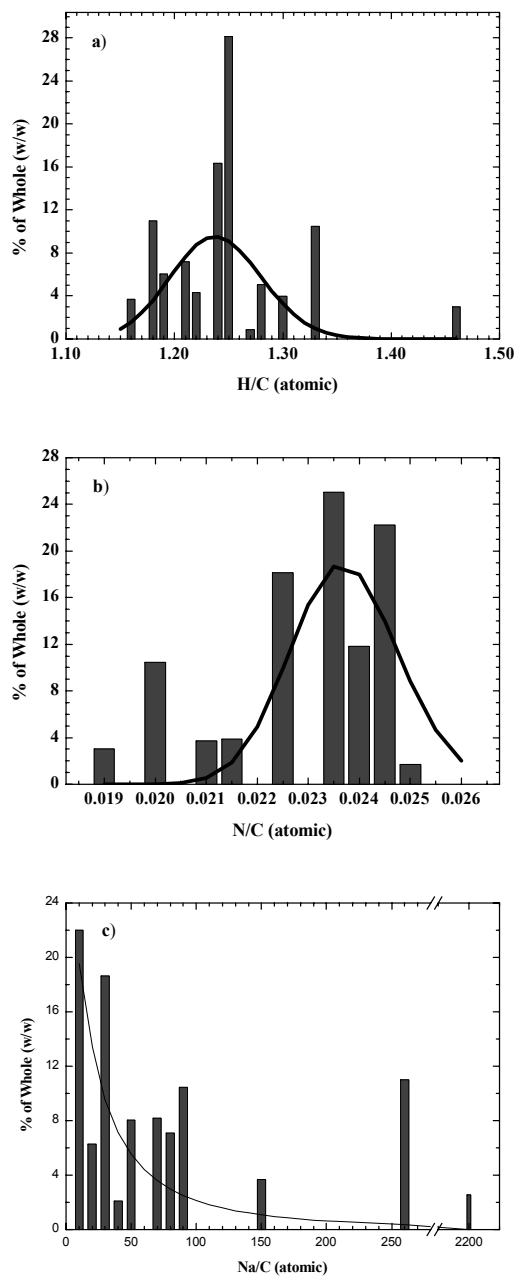


Figure 3.3a-c Histograms of atomic (a) hydrogen, (b) nitrogen, and (c) sodium contents for Hondo asphaltene solubility fractions. The solid lines represent fits of the data to log-normal distributions.

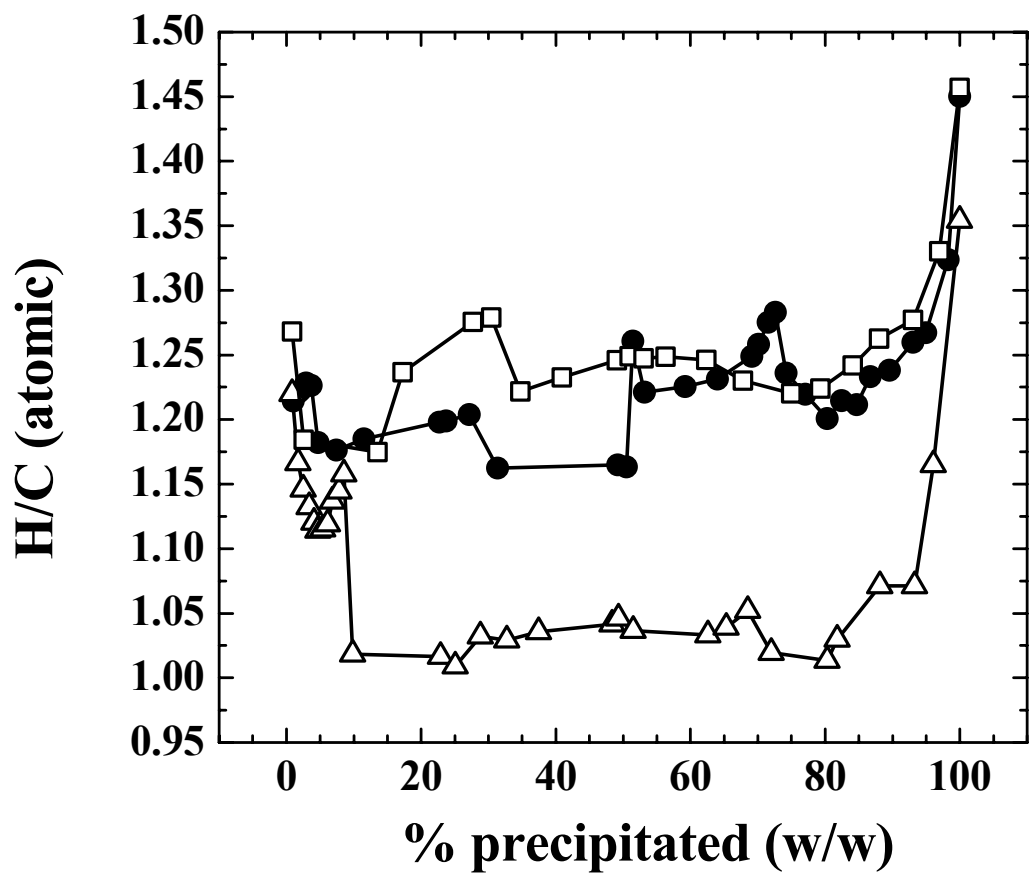


Figure 3.4 Variation in atomic hydrogen: carbon ratio for (Δ) CS, (\square) HO, and (\bullet) B6 asphaltic fractions.

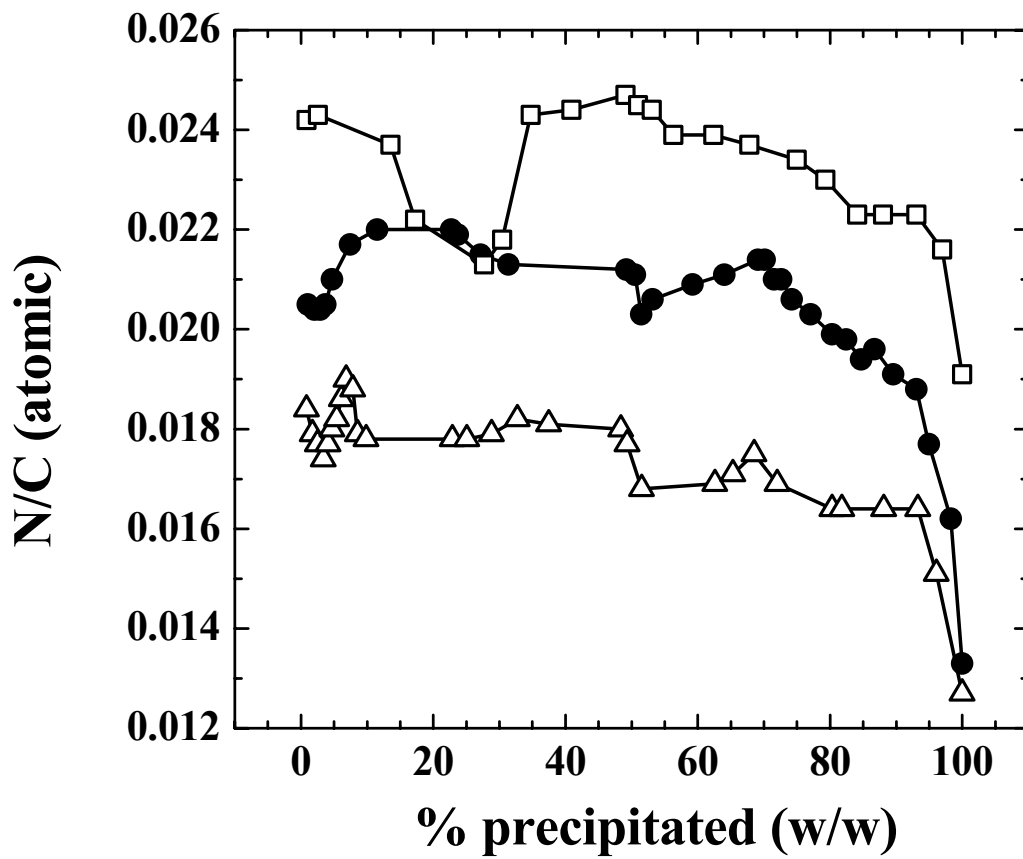


Figure 3.5 Variation in atomic nitrogen: carbon ratio for (△) CS, (□) HO, and (●) B6 asphaltenic fractions.

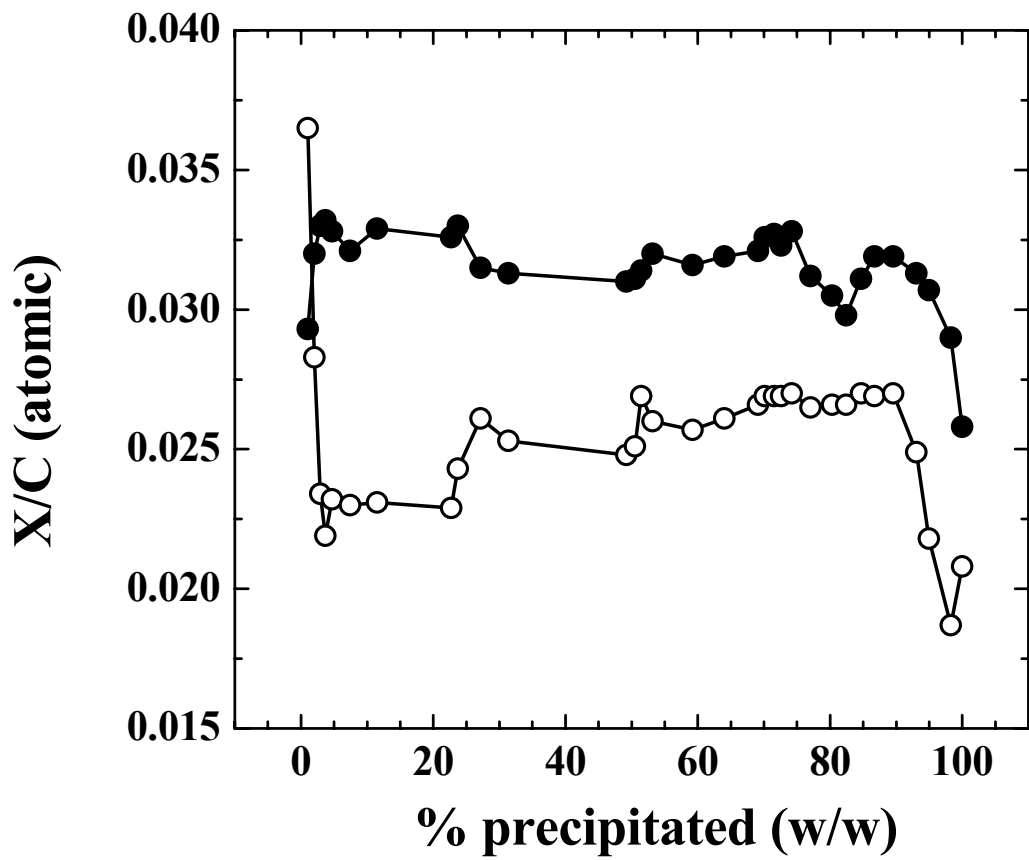


Figure 3.6 Variation in atomic (○) oxygen: carbon and (●) sulfur: carbon ratios for B6 asphaltenic fractions.

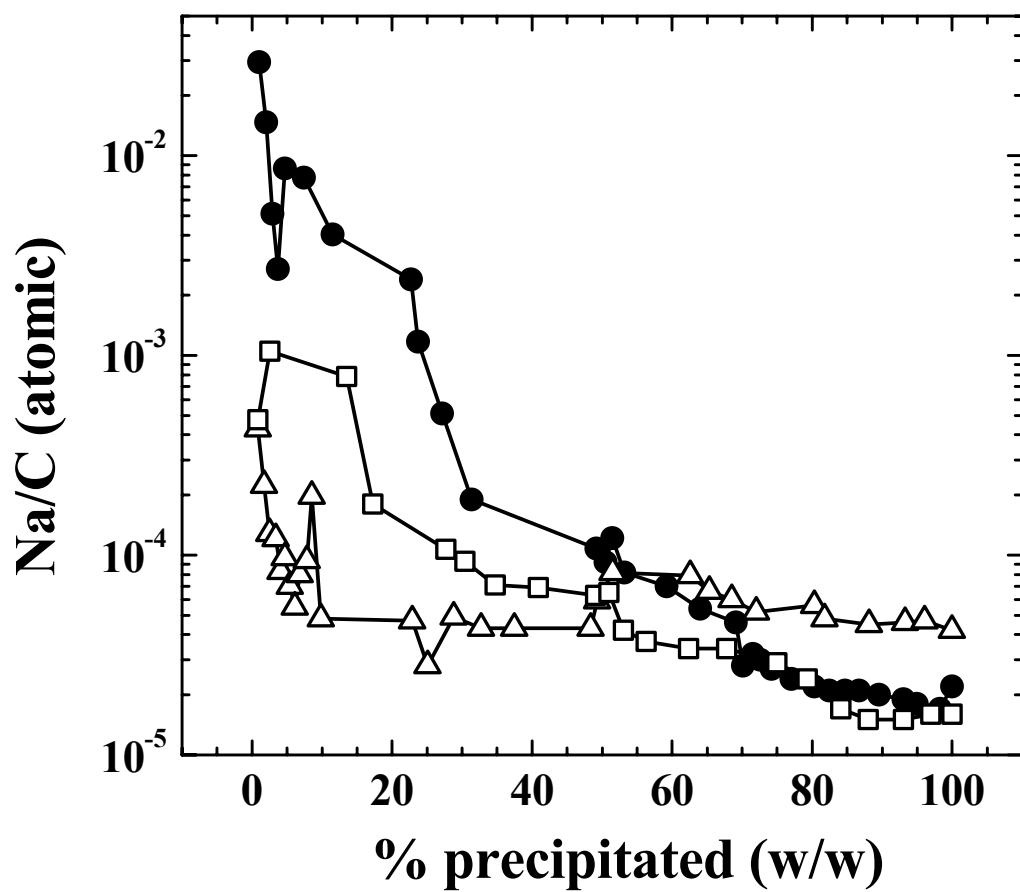


Figure 3.7 Variation in atomic sodium: carbon ratio for (△) CS, (□) HO, and (●) B6 asphaltenic fractions.

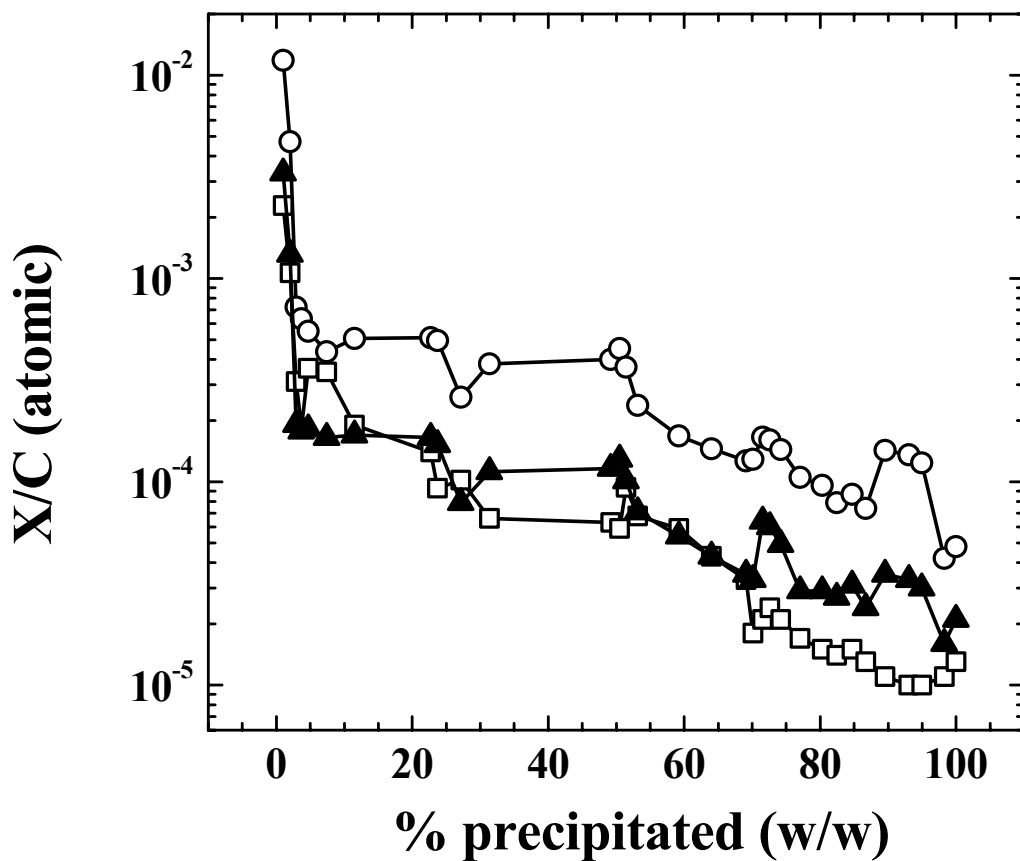


Figure 3.8 Variation in atomic (○) calcium: carbon, (□) potassium: carbon, and (▲) magnesium: carbon ratios for B6 asphaltenic fractions.

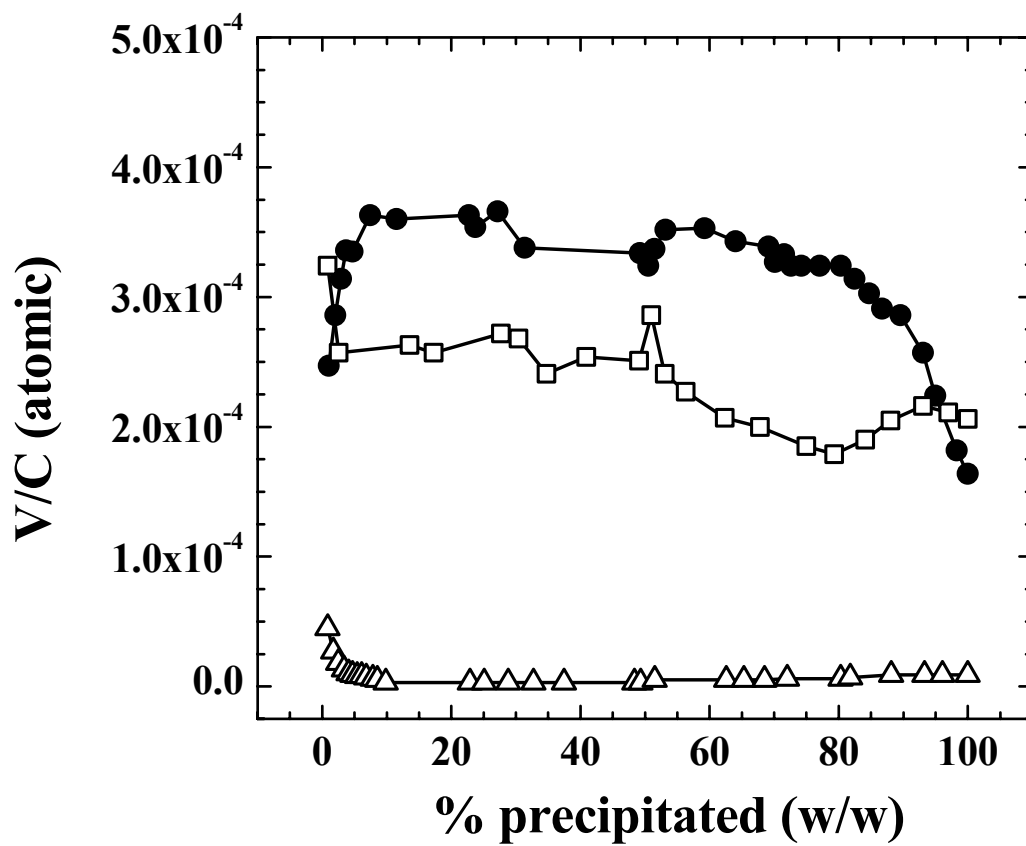


Figure 3.9 Variation in atomic vanadium: carbon ratio for (△) CS, (□) HO, and (●) B6 asphaltenic fractions.

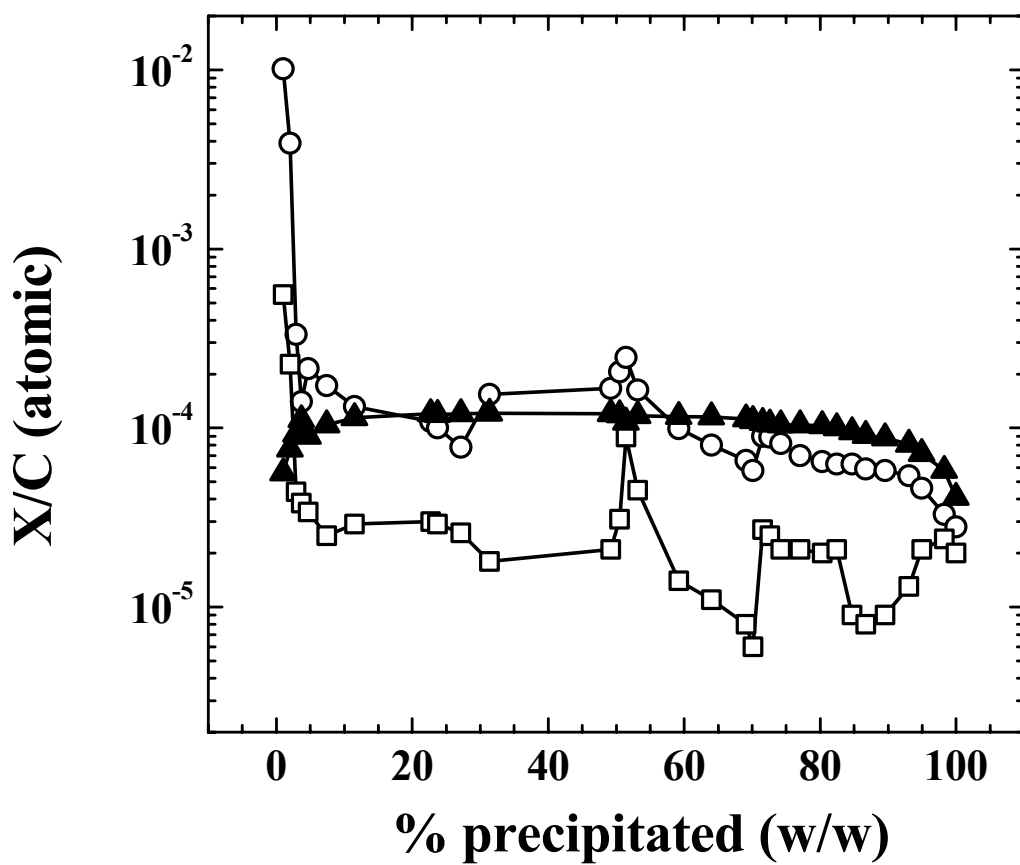


Figure 3.10 Variation in atomic (○) aluminum: carbon, (□) iron: carbon, and (▲) nickel: carbon ratios for B6 asphaltenic fractions.

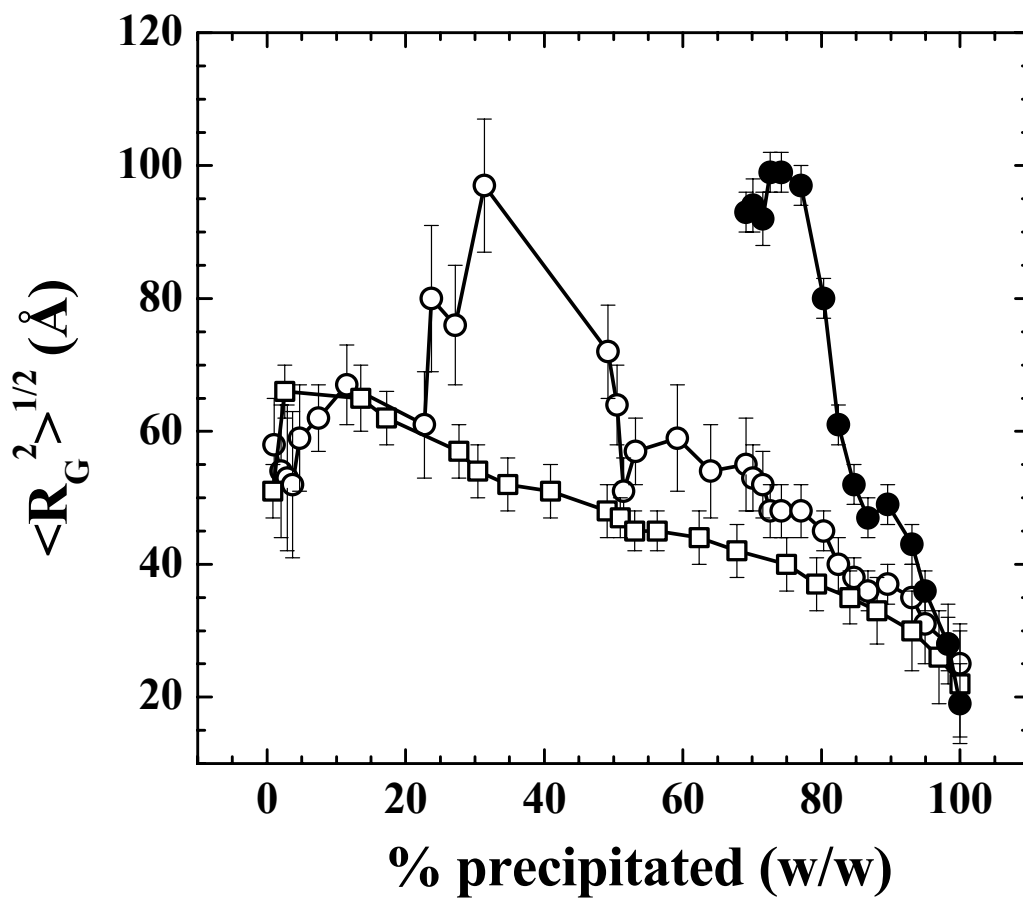


Figure 3.11 Variation in atomic aggregate size for (○) B6 asphaltene fractions in 90:10 d-methylnaphthalene: d-methanol, (●) B6 asphaltene fractions in toluene, and (□) HO asphaltene fractions in 90:10 d-toluene: d-methanol.

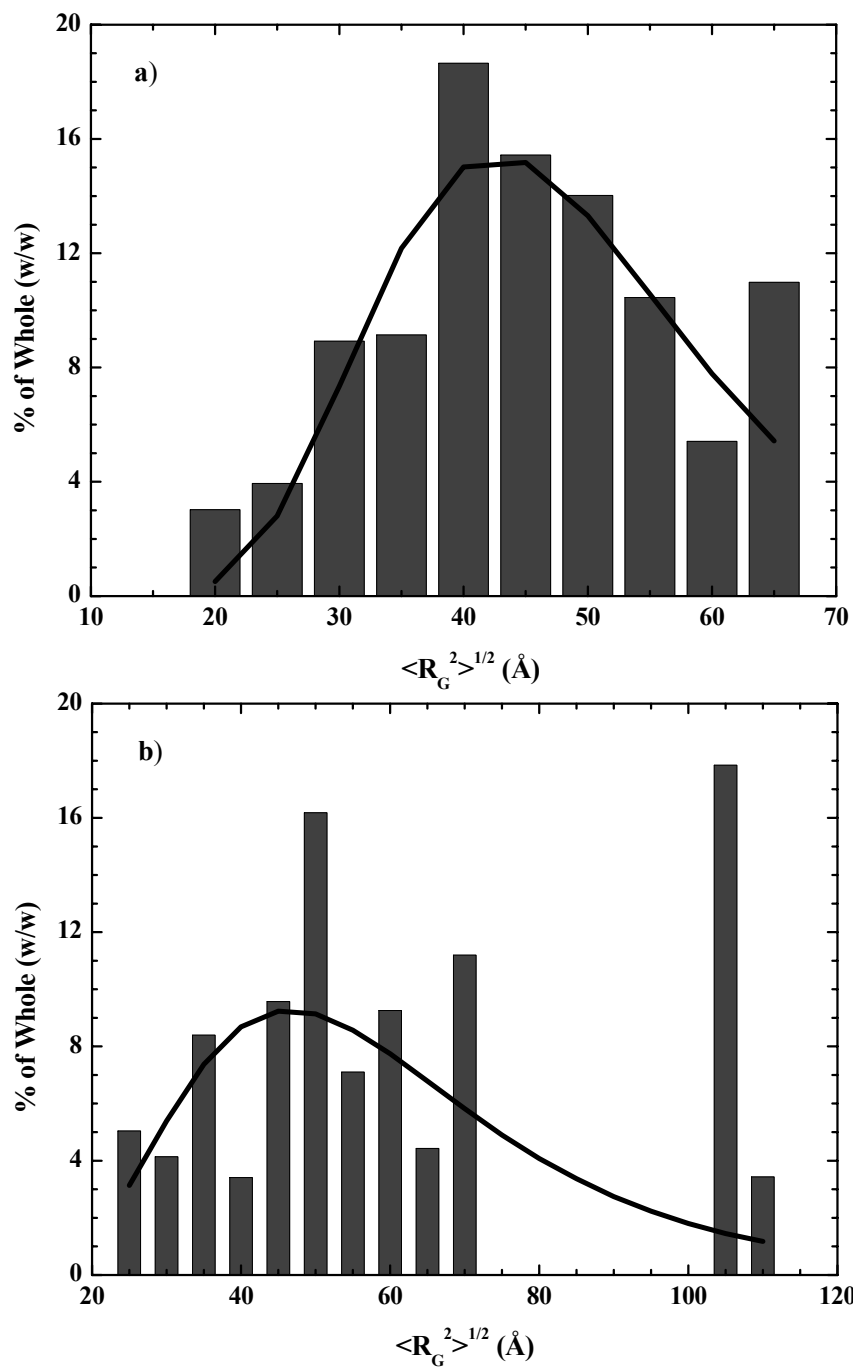


Figure 3.12a-b Histograms of aggregate size values for 1% (w/w) solutions of (a) Hondo asphaltene fractions in 90:10 d-toluene: d-methanol and (b) B6 asphaltene fractions in 90:10 d-methylnaphthalene: d-methanol. The solid lines represent fits of the data to log-normal distributions.

Solvent Entrainment in and Flocculation of Asphaltenic Aggregates Probed by Small-Angle Neutron Scattering

Keith L. Gawrys, George A. Blankenship, and Peter K. Kilpatrick

ABSTRACT

While small-angle neutron scattering (SANS) has proven to be very useful for deducing the sizes and masses of asphaltenic aggregates in solution, care must be taken to account for solvation effects within the aggregates so as to not err in the characterization of these important systems. SANS measurements were performed on solutions of asphaltenes dispersed in deuterated solvents in which a broad spectrum of solute and solvent chemical compositions was represented. Fits to the scattering intensity curves were performed using the Guinier approximation, a mass-fractal model, and a polydisperse cylinder model. The mass-fractal model provided apparent fractal dimensions (2.2 to 3) for the aggregates that generally decreased with increasing aggregate size, indicating increased surface roughness for larger aggregates. The polydisperse cylinder model provided typical values of the particle thicknesses from 5 to 32 Å, the average particle radius from 25 to 125 Å, and ~ 30 % radius polydispersity. Subsequent calculation of average aggregate molar masses suggested a range of solvent entrainment from 30 to 50 % (v/v) within the aggregates that were consistent with previous viscosity measurements. Additional calculations were performed to estimate the proportion of micro-particle to nano-particle aggregates in the solutions. The results indicate that the inclusion of solvation effects is essential for the accurate determination of aggregate molecular weights and fractal dimensions.

CHAPTER 4

SOLVENT ENTRAINMENT IN AND FLOCCULATION OF ASPHALTENIC AGGREGATES PROBED BY SMALL-ANGLE NEUTRON SCATTERING

4.1 Introduction

Petroleum asphaltenes are well known for their tendency to associate in solution and adsorb at interfaces, implicating them in petroleum production problems such as organic deposition [1,2] and water-in-crude oil emulsion formation [3-11]. Fundamental research has focused on establishing a link between asphaltene chemical composition, molecular structure, and colloidal properties. These efforts are complicated by the fact that asphaltenes, the portion of crude oil insoluble in *n*-heptane (or *n*-pentane) [12], are comprised of a polydisperse mixture of chemically heterogeneous species [13] that can vary significantly from one crude oil to another. In general, the asphaltene molecular structure is characterized by the presence of fused ring aromatic moieties, small aliphatic side chains, and polar heteroatom-containing functional groups [14-18]. The chemical composition of asphaltenes is also polydisperse; with typical atomic H/C ratios vary between 1.0 to 1.3 and N, S, and O contents of a few weight percent [19-22]. FTIR and XANES spectroscopy reveal several polar functional groups, such as carboxylic acids, carbonyls, phenols, pyrroles, and pyridines, that are capable of participating in proton donor-acceptor interactions [23-25].

The aggregation mechanism for asphaltenes is primarily governed by van der Waals dispersion interactions, electrostatic interactions between molecular charges, hydrogen bonding of polar moieties, and orientation dependent repulsive steric interactions with lesser contributions stemming from intermolecular charge transfer and weak inductive interactions

[26]. A recent proposal based on a review of the current literature suggests that strong specific forces, such as interactions between polar heteroatoms or π -bonding between aromatic moieties, drive asphaltene aggregation while weaker non-specific dispersion forces dominate asphaltene precipitation [27]. Although the intermolecular interactions that drive asphaltene aggregation are generally accepted, debate still exists over the orientation of heteroatom, alkyl, and aromatic moieties within the molecular framework. For example, two different models have been adopted in the literature to account for the degree of aromatic condensation within the fused ring backbone of asphaltenes, but both models are consistent with monomer masses between 500 to 1000 amu. One is the so-called “continental” model of asphaltenes [28], which posits a monomer molecular structure consisting of a large, highly condensed aromatic core surrounded by an aliphatic periphery, as inferred from X-ray diffraction and fluorescence depolarization experiments [18,29-33]. Interactions of “continental” monomers would likely form dense-packed aggregates through stacking interactions of the aromatic cores [32,33]. Alternatively, the so-called “archipelago” model [28] was proposed in which individual asphaltene monomers are comprised of clusters of polycondensed groups consisting of 5 to 7 aromatic rings connected by short aliphatic side chains, possibly containing polar heteroatom bridges [15,16,32,34,35]. The “archipelago” model is supported by chemical and thermal degradation studies which concluded that the extent of aromatic condensation in asphaltenes is significantly lower than generally believed [35]. Furthermore, molecular simulation studies on a proposed Athabasca asphaltene structure suggested that the presence of long aliphatic bridges gives asphaltenes the capacity to fold themselves into a complex three-dimensional globular structure with self-similar internal structure [32]. If the archipelago-like structure is valid, it seems probable that

asphaltenic aggregates possess a porous, reticulated microstructure susceptible of entraining significant amounts of surrounding solvent.

The notion that asphaltenes entrain solvent or are “swelled” by interactions with the surrounding solvent media is not novel. Swelling of “dry” Cold Lake asphaltenes was evident from the SAXS scattering spectra as a shift in apparent peak location to lower wavevectors (larger length scales) with increasing dilution by 1-methylnaphthalene [36]. Volumetric swelling studies on petroleum asphaltenes showed a solvent dependent expansion of the packed asphaltene volume (10 to 70 %) with the addition of ~ 1.5 mL solvent to 300 mg dry asphaltenes [37]. Other studies suggest that solvation of asphaltenes by the surrounding solvent modifies the aggregate geometry. Viscosity measurements on Khafji asphaltenes in benzene described four alternative means of modeling the hydrodynamic shape of solvated and unsolvated asphaltenic aggregates depending on assumptions made concerning the thickness of the solvation layer [38]. The extent of solvation for Ratawi and Hassi Messaoud asphaltenes in toluene was quantified by measuring the relative viscosity as a function of solute concentration [39,40]. Similar calculations of solvent entrainment were obtained from viscosity measurements performed on natural and synthetic Ratawi vacuum residue [41]. The results from these studies suggested that the solvated volume of the asphaltenic aggregates was 1.7 to 2.7 times the unsolvated or “dry” asphaltene volume, implying a volumetric entrainment of about 40-60%. Similar attempts to quantify the extent of solvation of Safaniya asphaltenes in mixtures of heptane and toluene were performed by a combination of SANS and viscosity measurements [42]; however, poor agreement of the effective asphaltene volume fraction within the aggregates calculated from the two methods suggested the need to include polydispersity or to modify the assumed aggregate shape.

In this regard, small-angle neutron scattering (SANS) provides the opportunity to quantify the extent of solvent entrainment within asphaltenic aggregates, assuming that the model used to describe the scattering behavior accurately reflects the particle structure. Various monodisperse and polydisperse geometric form factors have previously been applied to SANS and SAXS scattering spectra of asphaltene solutions, including spheres, ellipsoids (prolate or oblate), and cylinders (prolate or oblate) [43-53]. A recent SANS study comparing the quality of fits for various monodisperse and polydisperse structural models suggested that asphaltenic aggregates are best described by polydisperse oblate cylinders (or ellipsoids) with a Schultz-like distribution of radii [53]. One objective of this study is to show that the polydisperse oblate cylinder model is consistent with the structure of asphaltenic aggregates, regardless of the asphaltene chemical composition of solvent conditions. Applying a structural model that accurately describes the asphaltene shape allows additional information to be obtained from scattering data, such as the average aggregate molecular weight. Two methods are provided for calculating the aggregate molecular weight from the SANS fitting parameters. Another objective is to show that self-consistent values of the aggregate molecular weight are obtained from SANS measurements only after properly accounting for solvation effects.

Once the amount of solvent entrainment is known for a given sample, a method is suggested for determining the proportion of micro-particle to nano-particle aggregates in solution. The amount of asphaltene flocculation (or precipitation) is generally measured by gravimetric methods (see for example, refs. [10,22]). Mason and Lin proposed a method of quantifying the extent of micro-particle flocculation from SANS spectra of incompatible crude oil blends using a structure factor based on the Percus-Yevick (PY) closure [54]. The

nano-particle contribution to overall scattering intensity was represented using a geometry independent model (i.e., the Zimm method); however, the PY closure inherently assumes the asphaltene nano-particles behave as hard spheres. Both the PY method and the method introduced in this study account for changes in the apparent volume fraction of nano-particle scatterers after effectively removing the contribution of micro-scale aggregates from the scattering intensity distribution. In this study, the apparent reduction in the nano-particle volume fraction is calculated after assuming a fixed value for the solvent entrainment within the aggregates containing a mixture of nano-particle and micro-particle aggregates. Comparison of the nano-particle volume fraction to the total volume fraction of scatterers provides an estimate of the flocculated material. Flocculation results based on the proposed method will be compared to previous gravimetric solubility measurements for the asphaltenic fractions at the same solvent conditions.

4.2 Experimental

4.2.1 Asphaltene Precipitation

Asphaltenes were isolated from four crude oils in a 40:1 (v/v) excess of n-heptane. The source crude oils included: B6, Hondo (HO), Arab Heavy (AH), Gulf Coast (GC), and Canadon Seco (CS). These crude oils were asphaltene rich and varied in viscosity, native resin content, and asphaltene chemical composition. Asphaltenes isolated from the crude oils were separated into more (S) and less soluble (P) fractions by dissolving the whole asphaltenes in toluene and inducing partial precipitation through heptane addition according to the procedure of Spiecker et al. [10]. A shorthand notation was used to identify the fractions generated by this method. For example, the less soluble fraction of asphaltenes that

consisted of 30 % (w/w) of the whole asphaltenes was identified as the P30 fraction. The more soluble fraction that consisted of 70 % (w/w) of the whole asphaltenes was identified as the S70 fraction.

B6 and Hondo asphaltenes were also separated into several fine fractions by sequential fractionation in mixtures of heptane and toluene according to the procedure of Gawrys et al. [55]. During the fine fractionations, approximately 20 g of whole asphaltenes were dissolved in toluene solution such that the total asphaltene concentration was 1 % (w/w) after flocculant addition. Enough heptane was added to the solution to induce partial precipitation of approximately 1-2 % (w/w) of the whole asphaltenes. The precipitated asphaltenes were isolated by filtration, becoming the first “fine fraction”. The soluble asphaltenes were recovered from the filtrate and dispersed in a mixture of toluene and heptane according to the above procedure such that another 1-2 % (w/w) of the whole asphaltenes were precipitated. The fractionation procedure continued using progressively more heptane as a flocculant until 20-30 fine fractions were generated.

4.2.2 Chemical Characterization

All of the asphaltene fractions were characterized by combustion elemental analysis at the University of Alberta (Department of Chemistry, Edmonton, Alberta, Canada) using a Carlo Erba instrument. A detailed summary of the chemical composition of the asphaltene fractions is described elsewhere [22,55]. The ranges of chemical compositions for the asphaltene fractions analyzed in this study are shown in Table 4.1.

4.2.3 SANS Sample Preparation

Solutions with mass concentration of 1 % (w/w) were prepared by dissolving the various asphaltene fractions in mixtures of d-toluene, d-heptane, d-methylnaphthalene, and d-methanol. Several combinations of the above solvents were used (e.g., pure d-toluene, 40:60 (v/v) d-heptane: d-toluene, 90:10 (v/v) d-methylnaphthalene: d-methanol) for the fractions to represent a broad range of asphaltene solubility behaviors. Solvents were obtained from CDN Isotopes and had > 99.9% chemical purity and >99.5% perdeuteration. During the sample preparation, d-toluene or d-methylnaphthalene was initially added to the dry asphaltenes and the solution was subjected to constant, gentle shaking until the asphaltenes were completely dissolved. Upon dissolution of the asphaltenes, the second solvent (i.e., d-methanol or d-heptane) was added to the solutions. The solutions were allowed to equilibrate for at least one week prior to performing the scattering experiments.

4.2.4 SANS Measurements

SANS measurements were performed on the small-angle neutron diffractometer (SAND) at the Intense Pulsed Neutron Source (IPNS) Division of Argonne National Laboratory (Argonne, IL). The instrument geometry and neutron wavelength values bound the operating Q range according to:

$$Q = \frac{4\pi}{\lambda} \sin \theta \quad (1)$$

where θ is half the scattering angle and λ is the neutron wavelength. The available Q range extended from 0.0035 to 2 \AA^{-1} and was adequate for the modeling of asphaltene aggregation. The samples were measured at 25°C in cylindrical quartz sample cells (NGS Precision) with a path length of 2 mm. A typical scattering experiment consisted of 15 minutes of detecting

neutron transmission through the samples followed by 60 minutes of scattering. The absolute scattering intensity, $I(Q)$, for each sample was obtained from the total detector counts corrected for background radiation, neutron transmission through the sample, scattering from the quartz cell, and detector sensitivity.

4.2.5 SANS Model Fitting

Scattering intensity versus scattering angle ($I(Q)$ vs. Q) curves were fit to the Guinier approximation [56], a mass-fractal model, and a polydisperse radius oblate cylinder model. The fitting function for the mass-fractal model was authored by Kenneth Littrell and provided by Argonne National Laboratory for use with IgorPro software. The fitting function for polydisperse radius oblate cylinders was written by the authors [53]. The Q range over which both fits were applied was fixed between 0.006 and 0.5 \AA^{-1} . A constant background term was included in the model fits to account for incoherent scattering from all nuclei with non-zero spin in the solvent and solute. The small-particle mass-fractal model is given by [57]:

$$I(Q) = I_0 \frac{\sin[(D-1) \tan^{-1}(Q\xi)]}{(D-1)Q\xi(1+Q^2\xi^2)^{(D-1)/2}} \quad (2)$$

where I_0 , D and ξ are the scattering intensity extrapolated to $Q = 0$, the fractal dimension, and the exponential cut-off length for fractal aggregation, respectively. Equation (2) is a simplification of the mass-fractal model introduced by Chen and Teixeira [58] that describes the aggregates as a three-dimensional agglomeration consisting of elementary spherical particles with radius, R , and having a fractal-like nature. The small-particle mass-fractal

assumes that scattering from the elementary spherical particles is negligible (i.e., $\xi \gg R$ and $Q_{\max}R \ll 1$). The radius of gyration was determined from the above fitting parameters by:

$$R_G^2 = D(D+1)\xi^2/2 \quad (3)$$

The scattering intensity distribution for a polydisperse system is proportional to the ensemble average of the intra-particle structure factor, $P(Q)$, as given by:

$$I(\mathbf{Q}) = \int_0^\infty I_0 P(Q, x) f(x) dx \quad (4)$$

where $f(x)$ is a normalized distribution function for size parameter, x . The intra-particle structure factor used in this study to model polydisperse oblate cylinders is given by:

$$\begin{aligned} \langle P(Q) \rangle &= \frac{\int_0^\infty V^2 P_{ob,1}(Q, R) f_s(R) dR}{\int_0^\infty V^2 f(R) dR} \quad \{QR < 3 \\ \langle P(Q) \rangle &= \frac{\int_0^\infty V^2 P_{ob,2}(Q, R) f_s(R) dR}{\int_0^\infty V^2 f(R) dR} \quad \{QR > 3 \end{aligned} \quad (5)$$

where f_s is the Schultz distribution function. The polydisperse cylinder model utilizes two approximations of the intraparticle structure factor for an oblate cylinder. In the low Q region (i.e., $QR < 3$), the intra-particle structure factor for a monodisperse oblate cylinder of radius, R , and thickness, L , may be written as [59]:

$$P_{ob,1}(Q) = 2 \left[\frac{\sin(QL/2)}{QL/2} \right]^2 \left[\frac{1 - J_1(2QR)/QR}{(QR)^2} \right] \quad (6)$$

where $J_1(x)$ is the first order Bessel function of the first kind. In the high Q region (i.e., $QR > 3$), the intraparticle structure factor was described by an exponential approximation given by [56]:

$$P_{ob,2}(Q) = \frac{2}{(QR)^2} \exp\left(-\frac{(QL)^2}{12}\right) \quad (7)$$

Additional details of the model development are located elsewhere [53]. The average radius of gyration for polydisperse cylinders with a Schulz distribution of radii is given by [50]:

$$\langle R_g \rangle^2 = \frac{L^2}{3} + \frac{\langle R^6 \rangle}{2\langle R^4 \rangle} \quad (8)$$

where R_{avg} is the mean particle radius and z is the Schultz polydispersity parameter. The Schultz polydispersity parameter is related to the standard deviation in the radius (σ_R) by:

$$z = \left(\frac{R_{avg}}{\sigma_R}\right)^2 - 1 \quad (9)$$

4.3 Results and Discussion

4.3.1 Model Fit Parameters

The scattering intensity versus scattering angle ($I(Q)$ vs. Q) curve for a 1 % (w/w) solution of Hondo asphaltenes in 40:60 d-heptane: d-toluene (v/v) is shown in Figure 4.1. The sharp rise in the scattering intensity at low Q values for the raw data (Δ) indicated the presence of asphaltenic flocs of roughly micron size dispersed in solution [22,54,60]. Since the Porod-like upturns did not exhibit a plateau at the lowest scattering angles, it was not possible to determine the size of the flocs from these scattering experiments. Therefore, the contribution of these agglomerates to the scattering intensity distributions were effectively removed by fitting a power law function with an exponent of -4 (i.e., $I(Q) \sim Q^{-4}$) through the three lowest Q data points for this solution, extrapolating the power law function to higher Q values, and subtracting it from the original scattering data over the entire available Q range.

The corresponding power law fit appears as the dashed line in Figure 4.1. As seen in the figure, the resulting power law subtracted scattering curve (\circ) reveals the scattering behavior from nano-scale aggregates in this solution. The above power law correction was only applied to the scattering intensity curves in which the Guinier plateau did not extend to $Q = 0.006 \text{ \AA}^{-1}$.

Non-linear least squares regression of the small-particle mass-fractal (black line) and polydisperse radius oblate cylinder (grey line) models to the scattering intensity curve is also shown in Figure 4.1. There was good agreement of the I_0 parameters between the two model fits to Hondo asphaltenes in 40:60 d-heptane: d-toluene (v/v), as shown in Table 4.2; however, the value of R_G obtained from the mass-fractal fit over-predicted the corresponding value from the polydisperse cylinder fit by 11 %. In general, near parity of I_0 values was observed for the model fits to all of the scattering data (i.e., 108 total samples), but the aggregate sizes obtained from the mass-fractal fits consistently over-predicted those obtained from the polydisperse cylinder fits by 10 – 38 %. Near parity was observed between the I_0 and $\langle R_G \rangle$ parameters obtained from the polydisperse cylinder and Guinier fits (Figure 4.2), suggesting that the polydisperse cylinder model accurately describes the shape of asphaltenic aggregates. The mass-fractal model generally provided higher fit qualities to the scattering data than the polydisperse cylinder model, but the observed disparities in the aggregate size parameters suggest that the molecular structure of asphaltenic aggregates is not consistent with a mass-fractal geometry.

A major assumption of the mass-fractal model is that aggregates consist of elementary spherical particles [58]. For example, Rassamdana and Sahimi [61] estimated that the mass-to-particle size scaling relationship for diffusion limited cluster-cluster

aggregates with a nano-particle fractal dimension of 2.5 is consistent with a primary particle size of ~ 5.8 Å. This prediction is supported by small-angle X-ray scattering [44] and gel permeation chromatography [62] data that modeled the molecular structure of asphaltenes as thin disks with approximate thickness of 4 Å. X-ray diffraction experiments on Ratawi and Kuwaiti asphaltenes [63] suggested an average layer diameter of aromatic sheets between 7 to 10 Å and an average distance between aromatic sheets between 3.5 to 3.7 Å. Considering these observations, the elementary particles constituting an asphaltene mass-fractal aggregate might consist of stacks of one to two aromatic sheets, possibly connected to similar aromatic moieties by short, aliphatic linkages. With this in mind, one should be cautious in drawing conclusions concerning the fractal-nature of asphaltenic aggregates based on calculation of an apparent fractal dimension. Figure 4.3 correlates the apparent fractal dimension (D) with aggregate size parameters (R_G) obtained from the small-particle mass-fractal model for all of the samples analyzed. Filled triangles represented fractions dissolved in mixtures of d-heptane and d-toluene, while open circles represented fractions dissolved in mixtures of d-toluene (or d-methylnaphthalene) and d-methanol. The apparent fractal dimension values for the samples dissolved in mixtures of d-heptane and d-toluene appeared to decrease with increasing R_G . One possible explanation for this trend is that smaller aggregates are more globular with little surface roughness (i.e., consistent with $D \sim 3$). The amount of surface roughness increases with increasing aggregate size, corresponding to a decrease in the apparent fractal dimension. The samples dissolved in mixtures containing d-methanol appeared to follow a similar trend; however, there was increased dispersion in the data at these solvent conditions. The major implication of Figure 4.3 that stands in contrast to several previous determinations of the fractal dimension of asphaltene aggregates is that the

apparent fractal dimension is not a “fixed” quantity. The fractal dimension varies (i.e., from 2.2 to 3) with asphaltene chemical composition and solvent conditions in a manner that generally trends with the aggregate size.

Several previous studies cite apparently “fixed” values of aggregate fractal dimension for asphaltene aggregates in d-toluene that appear independent of solute composition, concentration, and/or solvent conditions; however the range of reported values varies from 1.9 to 3 depending on the analysis method [42,45,60,61,64,65]. The method of analysis most similar to that shown in Figure 4.3 involved a polydisperse mass-fractal model in which D was a fitted parameter [64]. The observed fractal dimension of Ratawi asphaltenes in d-toluene ($D \sim 3$) was independent of solute concentration at < 40 % w/w and consistent with the smallest aggregate formers observed in this study. However, an increase in the number of clusters at higher concentrations (i.e., 40 to 60 % w/w) corresponded to a decrease in the fractal dimension to $D \sim 2$. These results qualitatively agreed with the trend in fractal dimension with aggregate size observed in Figure 4.3. Since the polydisperse mass-fractal model was only applied to a single asphaltene at a single solvent condition, it is not possible to generalize the result that all asphaltenes at low concentration have a fractal dimension of $D \sim 3$.

Other studies have estimated the apparent fractal dimension either from the exponent of scaling relationship between the scattering intensity with the wave vector Q or from the scaling relationship between the aggregate molecular weight and aggregate size. Both of these methods can be problematic in the estimation of apparent fractal dimensions for asphaltenes. For example, the $I(Q) \sim Q^{-D}$ scattering relationship breaks down for small values of Q in which the scattering intensity transitions to the so-called Guinier regime and

for large values of Q where the scattering intensity is sensitive either to individual scatterers or to the aggregate surface (i.e., Porod regime) [66]. Therefore, the Q -range that describes the “fractal regime” is not easily defined and the common procedure of extracting the slope from a log-log plot of $I(Q)$ vs. Q invariably leads to a value of D that is inconsistent with one obtained from a fit to a mass-fractal structure factor [58].

The value of the apparent fractal dimension obtained from the $M \sim R_G^D$ scaling relationship is dependent on the form factor model used to fit the scattering data. For example, the mass-size scaling relationship for the entrained polydisperse cylindrical aggregates modeled in this study provided a value of the apparent fractal dimension ($D \sim 2.77 \pm 0.05$) that was consistent with the average fractal dimension value obtained from the mass-fractal fits, although the range of experimentally determined D values from the mass-fractal fits varied from 2.2 to 3 (Figure 4.3). In this case, the mass-size scaling relationship cannot be accurately modeled using a simple power law. Several studies that used the Zimm model to fit asphaltene scattering data consistently reported apparent fractal dimension values of $D \sim 2$ that were independent of the parameters that typically influence aggregate size (e.g., solvent conditions, temperature, concentration, and fractionation) [42,60,65]. The Zimm model explicitly provides that the absolute scattering intensity is proportional to Q^{-2} . The inverse Fourier transform of the scattering relationship $I \sim Q^{-2}$ provides the density distribution and the corresponding mass distribution [66], which may be biased to values of $D \sim 2$. The apparent trend in fractal dimension with aggregate size (Figure 4.3) suggests that it is inappropriate to assume that all asphaltenic aggregates will have the same fractal dimension. Furthermore, with no objective measure of the quality of fit, such as reduced χ^2 , it is not possible to judge the reliability of fractal dimensions from either of the above scaling

relationships. Mass-fractal structure factor models that incorporate the fractal dimension as a fitted parameter, such as in this study and in ref. [64], provide the least biased means to determine accurate estimates of the aggregate apparent fractal dimension; however, the observed fractal dimension values likely describe roughness of the aggregate surfaces rather than the internal structure of the asphaltenic aggregates.

As previously described, the scattering behavior of asphaltenic aggregates is more accurately described by a polydisperse radius oblate cylinder model. Figure 4.4 shows the aspect ratio (R_{avg}/L) obtained from fits of the polydisperse cylinder model for the samples dissolved in mixtures of d-heptane and d-toluene. The aspect ratio generally appeared to increase with increasing $\langle R_G^2 \rangle$. Typical particle thicknesses from the model fits ranged from 5 to 32 Å with an average value of 21 ± 6 Å. Typical values of the average particle radius ranged from 25 to 125 Å. If one assumes an asphaltene monomer consists of groups of condensed aromatic rings containing polar moieties that are interconnected by aliphatic chains, then each aromatic ring system in a given monomer has the potential to interact with aromatic rings from other molecules through dispersion and π -bonding interactions. The aggregation mechanism might then proceed through a series of stacking interactions that expands the aggregate dimension in the radial direction. As the aggregates grow in radius, more opportunities are created for growth in thickness due to the multiple connected nature of each asphaltene monomer.

The dependence of aspect ratios to $\langle R_G^2 \rangle$ in Figure 4.4 was more dispersed for samples prepared in mixtures of d-toluene (or d-methylnaphthalene) and d-methanol as opposed to those prepared in mixtures of d-heptane and d-toluene. The largest outliers from the apparent trend in aspect ratio with $\langle R_G^2 \rangle$ had particle thicknesses less than 12 Å, whereas

the particle thickness for the samples in mixtures of d-heptane and d-toluene ranged from 16 to 32 Å. The presence of d-methylnaphthalene in many of these solutions likely disrupted π -bonding interactions between aromatic sheets. The resulting aggregates tended to have higher aspect ratios (R_{avg}/L), as the aggregation was driven by edge-to-edge interactions of polar moieties, likely through H-bonding, rather than face-to-face interactions of aromatic groups. Figure 4.5 indicates that the polydispersity (σ_R/R_{avg}) in the aggregate radii is relatively independent of the particle size with typical values ranging from 30 to 32 %. This narrow range of polydispersity values for the samples suggests a similar shape to the aggregate size distributions for asphaltene solutions that is relatively independent of asphaltene chemical composition and solvent conditions.

4.3.2 Solvent Entrainment

Additional information concerning the morphology and composition of asphaltenic aggregates, including the extent of solvent entrainment, was obtained through the calculation of apparent aggregate molecular weight values. The zero-Q scattering intensity is related to the first and second moments of the particle volume (V) as given by:

$$I_0 = \frac{\phi \langle V^2 \rangle (\Delta\rho)^2}{\langle V \rangle} \quad (12)$$

where ϕ and $\Delta\rho$ are the volume fraction of scatterers and the difference between the scattering length density of the solvent and scatterers, respectively. For a given phase, j , the scattering length density is a product of the mass density, d_j , and the summation of contributions from individual atomic species, i , as given by:

$$\rho_j = d_j \sum_i \frac{b_i x_i}{m_i} \quad (13)$$

where b_i , x_i , and m_i are the bound coherent scattering length, mass fraction, and atomic mass of species i , respectively. The mass densities of asphaltene solutions in toluene were measured using a 2 mL pycnometer. An average asphaltene dry mass density of 1.1 g/cm³ was calculated by extrapolating the solution data to pure solute. Mass densities of solvent mixtures and asphaltenes containing entrained solvent were calculated assuming no volume change on mixing.

The weight-averaged molecular weight of the aggregate, M_w , is related to the zero-Q scattering intensity, I_0 , according to:

$$M_w = \frac{I_0 N_A d_m}{\phi (\Delta\rho)^2} \quad (14)$$

where N_A and d_m are Avogadro's number and the scatterer mass density, respectively. Alternatively, M_w is related to the first and second moments of the particle volume as given by:

$$M_w = \frac{N_A d_m \langle V^2 \rangle}{\langle V \rangle} \quad (15)$$

Equations (14) and (15) provide independent means of calculating the apparent aggregate weight-averaged molecular weight from the fit parameters for the polydisperse oblate cylinder model. Figure 4.6 compares the values of the apparent molecular weight obtained from these equations assuming either that scatterers consist of dry asphaltenes with no entrained solvent (○) or assuming that the aggregates are solvated and therefore contain some amount of entrained solvent (□). With the assumption of no solvent entrainment, the average mass density (i.e., 1.1 g/cm³) and chemical composition of dry asphaltenes were

used for the calculation of the solute scattering length density. As shown in Figure 4.6, the values of the molecular weight obtained from equation (14) consistently over-predicted the values obtained from equation (15) by a factor of ~ 2.6 . This inconsistency in the calculated values suggests that asphaltenes are solvated to some extent by the solvent and that the entrained solvent contributes to the coherent scattering of neutrons within the aggregates. The weight-averaged molecular weight values were recalculated for the assumption of solvent entrainment, as shown in Figure 4.6. The assumption of solvent entrainment affected the values of the solute mass density (d_m) and the mass fractions of atomic species used in equation (13), thus reducing the scattering contrast between the solute and solvent. Similarly, changes in the solute mass density affected the values of the solute mass fraction (ϕ) used in equation (14). The amount of entrained solvent was determined for all samples individually by forcing the parity of equations (14) and (15).

Values of solvent entrainment within the aggregates are presented on a volume percent basis as a function of aggregate size, as shown in Figure 4.7. As indicated in the figure, a relatively narrow range of solvent entrainment values between ~ 20 to 50 % (v/v) was observed for the asphaltenic fractions dispersed in mixtures of d-toluene and d-heptane. The data point in the figure with a solvent entrainment value of 60 % (v/v) represented the B6 P40 fraction dispersed in 70:30 d-toluene: d-heptane (v/v). Precipitation of significant amounts of asphaltenes was visually observed in this sample, suggesting an incorrect value of the scatterer volume fraction was used in the solvent entrainment calculation. Additional discussion concerning this sample is presented in the next section. An apparent decrease in the extent of solvent entrainment was observed for the smallest aggregate formers (Figure 4.7). Samples in which the calculated value of the % solvent entrainment was ≤ 22 % (v/v)

invariably had values of the particle thickness $< 10 \text{ \AA}$ and values of the particle aspect ratio (R_{avg}/L) that did not follow the general trend shown in Figure 4.4. One possible explanation for these deviations is that polydisperse radius oblate cylinders approximate the shape of asphaltenic aggregates, particularly for those with aggregate sizes $> 40 \text{ \AA}$. Perturbations from the oblate cylindrical shape are more significant at smaller aggregate sizes and are reflected by incorrect calculations of the particle volume that also affect the entrainment calculations. It is likely that the polydisperse oblate cylinder model inaccurately describes the scattering behavior of aggregates with particle thicknesses $< 10 \text{ \AA}$.

Additional evidence supporting the extent of solvent entrainment from asphaltene scattering curves is shown in Table 4.3. SANS experiments were performed on solutions of HO and GC asphaltenes (1 % w/w) in mixtures of deuterated and hydrogenated toluene. These experiments allowed variation in the scattering length density of the solvent while maintaining the same solvating power for asphaltenes. As shown in the table, the experimental I_0 values decreased with increasing hydrogenation of the solvent; however, there were no significant changes in either the average size ($\langle R_G^2 \rangle$) or the shape (R , L , and σ_R) of the aggregates. There were also no significant changes in the amount of solvent entrainment in the aggregates, as calculated by the method described above, indicating that the analysis methods are internally consistent and further supporting the fact of solvent entrainment in asphaltenic aggregates.

With regards to the molecular packing of asphaltenes within the aggregates determined from molecular recognition studies [28,32,67], the range of observed solvent entrainment values appears more consistent with the archipelago rather than the continental-type molecular structure. Aggregation of continental-type asphaltenes is dominated by

stacking interactions of the aromatic regions, but is limited by steric interference from saturated rings and alkyl groups that are deformed out of plane with the aromatic moieties [28]. Solvent entrainment within the continental-type aggregates would likely be limited to the ~ 3.8 Å spacing between interacting aromatic moieties [67] and the saturated regions at the periphery of the aggregate where the enthalpy of adsorption for a solvent-asphaltene interaction is significantly lower [32]. On the other hand, increased flexibility of aromatic and saturated hydrocarbon moieties in archipelago-type molecules enables the existence of grooves, channels, or internal cavities in the aggregate structure [32] which would facilitate solvent entrainment to the extent observed in Figure 4.7.

The range of observed solvent entrainment values in Figure 4.7 is also consistent with similar values obtained from viscosity measurements performed on Ratawi vacuum residue asphaltenes in toluene [39], Hassi Messaoud deposit asphaltenes in toluene [40], and natural and synthetic Ratawi vacuum residue [41]. In each of these studies, the degree of solvation ($S = \phi_{m,dry}/\phi_{m,solvated}$) was determined by application of Eilers equation to the relative viscosity (η_r) data. Eilers equation has the form:

$$\frac{\eta_r^{1/2} - 1}{\phi} = \frac{[\eta]}{2} + \frac{\eta_r^{1/2} - 1}{\phi_m} \quad (16)$$

where $[\eta]$ and ϕ_m are the intrinsic viscosity and maximum particle packing fraction, respectively. The authors assumed a monodisperse hard-sphere geometry; therefore, ideal packing of a face-centered cubic was assumed for the “dry” asphaltene maximum packing fraction ($\phi_{m,dry} = 0.74$). Experimental values of $\phi_{m,solvated}$ were determined using equation (16). Typical values of the degree of solvation (S) ranged from 1.7 to 2.7 and corresponded to solvent entrainment values of 42 to 63 % (v/v). The values obtained from viscosity

measurements overlapped with the range of values observed from our SANS experiments, even though different assumptions were made concerning the aggregate geometries. Fenistein et al. approximated 97 – 98 % (v/v) solvent entrainment from SANS measurements and 80 – 85 % (v/v) entrainment from viscosity measurement performed on Safaniya vacuum residue asphaltenes ($\phi = 3$) in mixtures of d-heptane and d-toluene [42]. The SANS and viscosity calculations were both performed assuming a monodisperse hard-sphere geometry for the aggregates. The lack of agreement between the calculated entrainment values from the SANS and viscosity methods suggests that the SANS method is more sensitive to the assumed aggregate geometry. A previous SANS study has shown that asphaltene aggregation is better described by a polydisperse oblate cylinder model than a monodisperse sphere model [53].

The average aggregate molecular weight values presented in Figure 4.6 may be assumed to consist of a linear combination of molecular weight contributions from both dry asphaltene (M_{dry}) and entrained solvent components (M_{ent}), as given by:

$$M_w = \phi_{ent} M_{ent} + (1 - \phi_{ent}) M_{dry} \quad (17)$$

where ϕ_{ent} is the volume fraction of entrained solvent within the aggregates. A direct comparison of the dry aggregate molecular weight values (M_{dry}) obtained from equations (14) and (17) with and without the assumption of solvent entrainment is shown in Figure 4.8. As shown in the figure, different values of the apparent dry aggregate molecular weight were observed for the two assumptions. In fact, the value of M_{dry} for the assumption of solvent entrainment consistently over-predicted the corresponding value for the assumption of no solvent entrainment by a factor of ~ 1.6 . The lack of parity between aggregate molecular weight values obtained from equations (14) and (15) for the assumption of no solvent

entrainment (Figure 4.6), as well as the lack of parity between dry aggregate molecular weight values (Figure 4.8), indicates that the inclusion of solvation effects is essential for the accurate calculation of the average aggregate molecular weight.

4.3.3 Asphaltene Flocculation

Using the calculated solvent entrainment values, attempts were made to estimate the relative amounts of asphaltenic material present in micron-scale flocs versus nanoparticle aggregates. Since the spread of solvent entrainment values for asphaltenes in mixtures of d-toluene and d-heptane (Figure 4.7) was relatively narrow for aggregates dispersed in mixtures of d-toluene and d-heptane, an average solvent entrainment value of 40 % (v/v) was assumed for all samples with $R_G > 50 \text{ \AA}$. The total volume fraction of scatterers (ϕ_{total}) was calculated based on this assumed value of solvent entrainment. As previously discussed, the effective contribution of micro-particle scatterers was modeled as a power-law function and subtracted from the composite scattering curves for those spectra containing significant low-Q upturns. Thus the polydisperse cylinder fits applied to power-law corrected scattering curves revealed information concerning the scattering behavior of nano-particles only. The volume fraction of nano-particle scatterers (ϕ_{nano}) was calculated from equation (12), using the I_0 , $\langle V \rangle$, and $\langle V^2 \rangle$ parameters obtained from the polydisperse cylinder fits and the scattering contrast calculated for the assumption of 40 % (v/v) solvent entrainment. The volume fraction of micro-particle scatterers (ϕ_{flocs}) was thus given by:

$$\phi_{flocs} = \frac{\phi_{total} - \phi_{nano}}{\phi_{total}} \quad (18)$$

A comparison of individual micro-particle volume fractions obtained from SANS experiments to volume fractions of precipitated material observed from gravimetric experiments [22] is presented in Table 4.4. As indicated in the table, the volume fraction of precipitated material observed from the gravimetric experiments was generally less than 0.06 for the samples shown with a few exceptions. Unfortunately, the accuracy of the micro-particle volume fraction from the SANS experiments was poor, particularly for asphaltene samples in the soluble solvent regime as uncertainty in the results was propagated from the power-law corrections, polydisperse cylinder model fitting, and subsequent solvent entrainment calculations. The SANS micro-particle volume fractions presented in Table 4.4 provided estimates that roughly trended with the gravimetric results. One interesting observation was that the amount of flocculated material from the SANS measurements generally increased with increasing amounts of heptane flocculant. Furthermore, the largest amounts of flocculated material were observed for the three samples in the insoluble solvent regime (i.e., B6 P40 in 60 % toluene, CS Whole in 45 % toluene, and CS P40 in 50 % toluene). For the case of CS Whole asphaltenes in 45 % toluene the amount of precipitated/flocculated material from the two measurement methods agreed within 5 %. More accurate estimates of micro-particle flocculation would likely be obtained by probing larger length scales of aggregation by USANS (or USAXS) measurements.

4.4 Conclusions

Small-angle scattering measurements were performed on 108 solutions of asphaltenes dispersed in deuterated solvents. The samples measured possessed wide diversity in the chemical composition of the asphaltenes (e.g., H/C from 1.09 to 1.45 and heteroatom

contents of 2.5 to 6 % wt.), as well as variation in the quality of the solvent for dispersing asphaltenes. In many cases, aggregates of HO and B6 asphaltenes were further dispersed with the addition of d-methanol. Scattering intensity curves were fit to the Guinier approximation, a mass-fractal model, and a polydisperse radius oblate cylinder model. While similar values of I_0 were obtained from the three models, the R_G parameter obtained from the mass-fractal fits generally over-predicted the aggregate sizes from the Guinier and polydisperse cylinder fits by 10 – 38 %, suggesting that the molecular structure of asphaltenic aggregates are probably not consistent with that of a mass-fractal. Values of the apparent fractal dimension from the mass-fractal fits appeared to decrease with increasing aggregate size, suggesting that the smallest aggregate formers were more globular with little surface roughness (i.e., $D \sim 3$) while the largest aggregate formers were more dendritic with higher surface roughness ($D \sim 2.2$ to 2.4).

Regardless of the asphaltene and solvent chemical compositions, parameters obtained from fitting the scattering data to a polydisperse oblate cylinder model were consistent with those obtained from the Guinier approximation. Typical values of the aggregate thickness from the polydisperse cylinder fits ranged from 5 to 32 Å, while the average particle radius ranged from 25 to 125 Å. The polydispersity in the particle radius appeared independent of the particle size (~ 30 %). Assuming an asphaltene monomer consists of groups of condensed aromatic rings containing polar moieties that are interconnected by aliphatic chains; the asphaltene aggregation mechanism might proceed through a series of localized stacking interactions of aromatic rings. The physical linkage of one ring system to another in a monomer somewhat increases the particle thickness, but significantly expands the aggregate in the radial dimension, where polydispersity in the aggregate size is most evident.

Discrepancies between average aggregate molecular weight values obtained from two independent methods suggested the need to include the solvation effects in the calculations. Solvent entrainment within the aggregates roughly varied from 30 to 50 % (v/v) and was consistent with solvation values previously obtained from viscosity measurements. Estimates of the % solvent entrainment were likely incorrect for smaller aggregate formers with particle thicknesses $< 10 \text{ \AA}$, as perturbations of the aggregate volume from that of a polydisperse oblate cylinder become more significant.

Attempts to use the observed solvent entrainment values to estimate the relative proportions of micro-scale and nano-scale aggregates in solution were limited in accuracy; however, the volume fraction of micro-scale flocs generally increased with decreasing solvent quality. Furthermore, flocculation was only observed to be greater than 20 % for those samples that were dispersed in an insoluble solvent regime. Beyond the calculation of aggregate sizes, the inclusion of solvent entrainment is crucial for the calculation of additional parameters from the scattering data, including the aggregate molecular weight and the estimation of flocculated material.

4.5 Acknowledgements

This research is supported by the Petroleum Environmental Research Forum, ExxonMobil, Shell, Equilon, ChevronTexaco, Nalco Energy Services Division, Champion Technologies, National Science Foundation Grants (CTS981727), and the NSF Graduate Research Fellowship Program. We acknowledge Darlene Mahlow at the University of Alberta for performing combustion elemental analyses on the asphaltene and resin samples. This work benefited from the use of facilities in the Intense Pulsed Neutron Source and the

Chemistry Division, which is funded by the U. S. Department of Energy, Office of Basic Energy Sciences under contract W-31-109-ENG-38 to the University of Chicago. We would particularly like to thank Pappannan Thiyagarajan and Denis Wozniak of the Intense Pulsed Neutron Source Division at Argonne National Laboratory for their assistance with the SAND instrument. We also acknowledge the support of the National Institute of Standards and Technology, U.S. Department of Commerce, in providing the neutron research facilities used in this work and Min Lin for his assistance on the NG1 and NG3 beamlines. We would also like to thank Matthew B. Smith, M. Lupe Marques, and Vincent Verruto for helping with the sample preparation and SANS data collection.

4.6 References

1. A. Hammami, C. H. Phelps, T. Monger-McClure, T. M. Little, "Asphaltene precipitation from live oils: An experimental investigation of onset conditions and reversibility," *Energy & Fuels*, 2000, **14**(1): p. 14-18.
2. K. Karan, A. Hammami, M. Flannery, B. A. Stankiewicz, "Evaluation of asphaltene instability and a chemical control during production of live oils," *Petroleum Science and Technology*, 2003, **21**(3-4): p. 629-645.
3. S. D. Taylor, J. Czarnecki, J. Masliyah, "Disjoining pressure isotherms of water-in-bitumen emulsion films," *Journal of Colloid and Interface Science*, 2002, **252**(1): p. 149-160.
4. H. W. Yarranton, H. Hussein, J. H. Masliyah, "Water-in-hydrocarbon emulsions stabilized by asphaltenes at low concentrations," *Journal of Colloid and Interface Science*, 2000, **228**(1): p. 52-63.
5. K. Khristov, S. D. Taylor, J. Czarnecki, J. Masliyah, "Thin liquid film technique - application to water-oil-water bitumen emulsion films," *Colloids and Surfaces a-Physicochemical and Engineering Aspects*, 2000, **174**(1-2): p. 183-196.
6. T. E. Havre, J. Sjoblom, "Emulsion stabilization by means of combined surfactant multilayer (D-phase) and asphaltene particles," *Colloids and Surfaces a-Physicochemical and Engineering Aspects*, 2003, **228**(1-3): p. 131-142.
7. N. Aske, R. Orr, J. Sjoblom, H. Kallevik, G. Oye, "Interfacial properties of water-crude oil systems using the oscillating pendant drop. Correlations to asphaltene solubility by near infrared spectroscopy," *Journal of Dispersion Science and Technology*, 2004, **25**(3): p. 263-275.

8. I. H. Auflem, H. Kallevik, A. Westvik, J. Sjoblom, "Influence of pressure and solvency on the separation of water-in-crude-oil emulsions from the North Sea," *Journal of Petroleum Science and Engineering*, 2001, **31**(1): p. 1-12.
9. N. Aske, H. Kallevik, J. Sjoblom, "Water-in-crude oil emulsion stability studied by critical electric field measurements. Correlation to physico-chemical parameters and near-infrared spectroscopy," *Journal of Petroleum Science and Engineering*, 2002, **36**(1-2): p. 1-17.
10. P. M. Spiecker, K. L. Gawrys, C. B. Trail, P. K. Kilpatrick, "Effects of petroleum resins on asphaltene aggregation and water-in-oil emulsion formation," *Colloids and Surfaces a-Physicochemical and Engineering Aspects*, 2003, **220**(1-3): p. 9-27.
11. P. M. Spiecker, P. K. Kilpatrick, "Interfacial rheology of petroleum asphaltenes at the oil-water interface," *Langmuir*, 2004, **20**(10): p. 4022-4032.
12. J. G. Speight, ed. *Fuel Science and Technology Handbook*. 1990, Marcel Dekker: New York.
13. X. L. Yang, H. Hamza, J. Czarnecki, "Investigation of subfractions of athabasca asphaltenes and their role in emulsion stability," *Energy & Fuels*, 2004, **18**(3): p. 770-777.
14. O. P. Strausz, P. Peng, J. Murgich, "About the colloidal nature of asphaltenes and the MW of covalent monomeric units," *Energy & Fuels*, 2002, **16**(4): p. 809-822.
15. J. M. Sheremata, M. R. Gray, H. D. Dettman, W. C. McCaffrey, "Quantitative molecular representation and sequential optimization of athabasca asphaltenes," *Energy & Fuels*, 2004, **18**(5): p. 1377-1384.
16. M. R. Gray, "Consistency of asphaltene chemical structures with pyrolysis and coking behavior," *Energy & Fuels*, 2003, **17**(6): p. 1566-1569.
17. U. Bergmann, H. Groenzin, O. C. Mullins, P. Glatzel, J. Fetzer, S. P. Cramer, "X-ray Raman spectroscopy - A new tool to study local structure of aromatic hydrocarbons and asphaltenes," *Petroleum Science and Technology*, 2004, **22**(7-8): p. 863-875.
18. H. Groenzin, O. C. Mullins, S. Eser, J. Mathews, M. G. Yang, D. Jones, "Molecular size of asphaltene solubility fractions," *Energy & Fuels*, 2003, **17**(2): p. 498-503.
19. M. M. Boduszynski, "Composition of Heavy Petroleums. 2. Molecular Characterization," *Energy & Fuels*, 1988, **2**(5): p. 597-613.
20. M. M. Boduszynski, "Characterization of "Heavy" Crude Components," *Preprints ACS Division of Petroleum Chemistry*, 1985, **30**: p. 626-640.
21. M. A. Bestougeff, "Chemical Composition and Structure of Asphaltenes . Their Importance among Natural Organic Compounds," *Bulletin De La Societe Chimique De France*, 1967, (12): p. 4773-&.
22. P. M. Spiecker, K. L. Gawrys, P. K. Kilpatrick, "Aggregation and solubility behavior of asphaltenes and their subfractions," *Journal of Colloid and Interface Science*, 2003, **267**(1): p. 178-193.
23. M. M. Boduszynski, J. F. McKay, D. R. Latham, "Asphaltenes, Where Are You?," *Proceedings of the Association of Asphalt Paving Technologists*, 1980, **49**: p. 123-143.
24. E. Buenrostro-Gonzalez, S. I. Andersen, J. A. Garcia-Martinez, C. Lira-Galeana, "Solubility/molecular structure relationships of asphaltenes in polar and nonpolar media," *Energy & Fuels*, 2002, **16**(3): p. 732-741.

25. S. Mitrakirtley, O. C. Mullins, J. Vanelp, S. J. George, J. Chen, S. P. Cramer, "Determination of the Nitrogen Chemical Structures in Petroleum Asphaltenes Using Xanes Spectroscopy," *Journal of the American Chemical Society*, 1993, **115**(1): p. 252-258.
26. J. Murgich, "Intermolecular forces in aggregates of asphaltenes and resins," *Petroleum Science and Technology*, 2002, **20**(9-10): p. 983-997.
27. G. Porte, H. G. Zhou, V. Lazzeri, "Reversible description of asphaltene colloidal association and precipitation," *Langmuir*, 2003, **19**(1): p. 40-47.
28. J. Murgich, "Molecular simulation and the aggregation of the heavy fractions in crude oils," *Molecular Simulation*, 2003, **29**(6-7): p. 451-461.
29. T. F. Yen, J. G. Erdman, S. S. Pollack, "Investigation of Structure of Petroleum Asphaltenes By X-Ray Diffraction," *Analytical Chemistry*, 1961, **33**(11): p. 1587-&.
30. H. Groenzin, O. C. Mullins, "Asphaltene molecular size and structure," *Journal of Physical Chemistry A*, 1999, **103**(50): p. 11237-11245.
31. H. Groenzin, O. C. Mullins, "Molecular size and structure of asphaltenes from various sources," *Energy & Fuels*, 2000, **14**(3): p. 677-684.
32. J. Murgich, J. A. Abanero, O. P. Strausz, "Molecular recognition in aggregates formed by asphaltene and resin molecules from the Athabasca oil sand," *Energy & Fuels*, 1999, **13**(2): p. 278-286.
33. A. Sharma, H. Groenzin, A. Tomita, O. C. Mullins, "Probing order in asphaltenes and aromatic ring systems by HRTEM," *Energy & Fuels*, 2002, **16**(2): p. 490-496.
34. V. Calemma, P. Iwanski, M. Nali, R. Scotti, L. Montanari, "Structural Characterization of Asphaltenes of Different Origins," *Energy & Fuels*, 1995, **9**(2): p. 225-230.
35. O. P. Strausz, T. W. Mojelsky, E. M. Lown, "The Molecular-Structure of Asphaltene - an Unfolding Story," *Fuel*, 1992, **71**(12): p. 1355-1363.
36. E. B. Sirota, "Swelling of asphaltenes," *Petroleum Science and Technology*, 1998, **16**(3-4): p. 415-431.
37. L. Carbognani, E. Rogel, "Solvent swelling of petroleum asphaltenes," *Energy & Fuels*, 2002, **16**(6): p. 1348-1358.
38. W. Takeshige, "Hydrodynamic shape and size of Khafji asphaltene in benzene," *Journal of Colloid and Interface Science*, 2001, **234**(2): p. 261-268.
39. E. Y. Sheu, M. M. Detar, D. A. Storm, "Rheological Properties of Vacuum Residue Fractions in Organic-Solvents," *Fuel*, 1991, **70**(10): p. 1151-1156.
40. Y. Bouhadda, D. Bendedouch, E. Sheu, A. Krallafa, "Some preliminary results on a physico-chemical characterization of a Hassi Messaoud petroleum asphaltene," *Energy & Fuels*, 2000, **14**(4): p. 845-853.
41. D. A. Storm, E. Y. Sheu, "Rheological Studies of Ratawi Vacuum Residue at 366-K," *Fuel*, 1993, **72**(2): p. 233-237.
42. D. Fenistein, L. Barre, D. Broseta, D. Espinat, A. Livet, J. N. Roux, M. Scarsella, "Viscosimetric and neutron scattering study of asphaltene aggregates in mixed toluene/heptane solvents," *Langmuir*, 1998, **14**(5): p. 1013-1020.
43. J. C. Ravey, G. Ducouret, D. Espinat, "Asphaltene Macrostructure by Small-Angle Neutron-Scattering," *Fuel*, 1988, **67**(11): p. 1560-1567.
44. P. Herzog, D. Tchoubar, D. Espinat, "Macrostructure of Asphaltene Dispersions by Small-Angle X-Ray-Scattering," *Fuel*, 1988, **67**(2): p. 245-250.

45. E. Y. Sheu, K. S. Liang, S. K. Sinha, R. E. Overfield, "Polydispersity Analysis of Asphaltene Solutions in Toluene," *Journal of Colloid and Interface Science*, 1992, **153**(2): p. 399-410.
46. D. Espinat, J. C. Ravey, V. Guille, J. Lambard, T. Zemb, J. P. Cotton, "Colloidal Macrostructure of Crude-Oil Studied by Neutron and X-Ray Small-Angle Scattering Techniques," *Journal De Physique IV*, 1993, **3**(C8): p. 181-184.
47. Y. N. Xu, Y. Koga, O. P. Strausz, "Characterization of Athabasca Asphaltenes by Small-Angle X-Ray-Scattering," *Fuel*, 1995, **74**(7): p. 960-964.
48. P. Thiagarajan, J. E. Hunt, R. E. Winans, K. B. Anderson, J. T. Miller, "Temperature-Dependent Structural-Changes of Asphaltenes in 1-Methylnaphthalene," *Energy & Fuels*, 1995, **9**(5): p. 829-833.
49. C. Bardon, L. Barre, D. Espinat, V. Guille, M. H. Li, J. Lambard, J. C. Ravey, E. Rosenberg, T. Zemb, "The colloidal structure of crude oils and suspensions of asphaltenes and resins," *Fuel Science & Technology International*, 1996, **14**(1-2): p. 203-242.
50. M. Y. Lin, E. B. Sirota, H. Gang, "Neutron scattering characterization of asphaltene particles," *Abstracts of Papers of the American Chemical Society*, 1997, **213**: p. 66-70.
51. L. Barre, D. Espinat, E. Rosenberg, M. Scarsella, "Colloidal structure of heavy crudes and asphaltene solutions," *Revue de l'Institut Francais du Petrole*, 1997, **52**(2): p. 161-175.
52. R. Tanaka, J. E. Hunt, R. E. Winans, P. Thiagarajan, S. Sato, T. Takanohashi, "Aggregates structure analysis of petroleum asphaltenes with small-angle neutron scattering," *Energy & Fuels*, 2003, **17**(1): p. 127-134.
53. K. L. Gawrys, P. K. Kilpatrick, "Asphaltenic aggregates are polydisperse oblate cylinders," *Journal of Colloid and Interface Science*, submitted.
54. T. G. Mason, M. Y. Lin, "Asphaltene nanoparticle aggregation in mixtures of incompatible crude oils," *Physical Review E*, 2003, **67**(5): p.
55. K. L. Gawrys, P. M. Spiecker, P. K. Kilpatrick, "On distribution functions of chemical properties and aggregation of solubility fractions in asphaltenes," *Energy & Fuels*, submitted.
56. A. Guinier, G. Fournet, *Small Angle Scattering of X-rays*; John Wiley & Sons: New York, 1955.
57. X. J. Hu, K. Littrel, S. Ji, D. G. Pickles, W. M. Risen, "Characterization of silica-polymer aerogel composites by small-angle neutron scattering and transmission electron microscopy," *Journal of Non-Crystalline Solids*, 2001, **288**(1-3): p. 184-190.
58. S. H. Chen, J. Teixeira, "Structure and Fractal Dimension of Protein-Detergent Complexes," *Physical Review Letters*, 1986, **57**(20): p. 2583-2586.
59. J. S. Pedersen, "Form factors of block copolymer micelles with spherical, ellipsoidal and cylindrical cores," *Journal of Applied Crystallography*, 2000, **33**(1): p. 637-640.
60. J. N. Roux, D. Broseta, B. Deme, "SANS study of asphaltene aggregation: Concentration and solvent quality effects," *Langmuir*, 2001, **17**(16): p. 5085-5092.
61. H. Rassamdana, M. Sahimi, "Asphalt flocculation and deposition .2. Formation and growth of fractal aggregates," *AIChE Journal*, 1996, **42**(12): p. 3318-3332.
62. S. Acevedo, G. Escobar, M. A. Ranaudo, L. B. Gutierrez, "Discotic Shape of Asphaltenes Obtained from Gpc Data," *Fuel*, 1994, **73**(11): p. 1807-1809.

63. M. N. Siddiqui, M. F. Ali, J. Shirokoff, "Use of X-ray diffraction in assessing the aging pattern of asphalt fractions," *Fuel*, 2002, **81**(1): p. 51-58.
64. Y. C. Liu, E. Y. Sheu, S. H. Chen, D. A. Storm, "Fractal Structure of Asphaltenes in Toluene," *Fuel*, 1995, **74**(9): p. 1352-1356.
65. D. Fenistein, L. Barre, "Experimental measurement of the mass distribution of petroleum asphaltene aggregates using ultracentrifugation and small-angle X-ray scattering," *Fuel*, 2001, **80**(2): p. 283-287.
66. J. Teixeira, "Small-Angle Scattering by Fractal Systems," *Journal of Applied Crystallography*, 1988, **21**: p. 781-785.
67. J. Murgich, J. Rodriguez, Y. Aray, "Molecular recognition and molecular mechanics of micelles of some model asphaltenes and resins," *Energy & Fuels*, 1996, **10**(1): p. 68-76.

Table 4.1 Ranges of chemical compositions (molar ratios) for asphaltene fractions.

H/C	N/C	S/C	O/C
1.09 - 1.45	0.010 - 0.025	0.002 - 0.047	0.012 - 0.036

Table 4.2 Model fitting parameters for Hondo asphaltenes in 40:60 d-heptane: d-toluene (v/v).

Small-Particle Mass-Fractal Model					
I_0 (cm ⁻¹)	D	ξ (Å)	χ^2	R_G (Å)	
4.11 ± 0.05	2.53 ± 0.02	38.4 ± 0.5	1.4585	81 ± 2	
Polydisperse Oblate Cylinder Model					
I_0 (cm ⁻¹)	R_{avg} (Å)	σ_R (Å)	L (Å)	χ^2	$\langle R_G^2 \rangle^{1/2}$ (Å)
4.14 ± 0.04	69.4 ± 0.7	22.3 ± 0.1	20.5 ± 0.3	5.7508	73 ± 2

Table 4.3 Estimation of solvent entrainment for HO and GC asphaltenes in mixtures of deuterated toluene and hydrogenated toluene.

Asphaltene	vol% d-tol	I_0 (cm ⁻¹)	R_{avg} (Å)	L (Å)	σ_R (Å)	χ^2	$\langle R_G^2 \rangle^{1/2}$ (Å)	% ent
HO	100	2.11 ± 0.02	57.2 ± 0.9	24.3 ± 0.4	18.1 ± 0.2	3.7053	47 ± 5	47 ± 8
HO	80	1.27 ± 0.02	56 ± 1	18.7 ± 0.9	17.5 ± 0.3	1.7258	41 ± 6	40 ± 10
HO	60	0.65 ± 0.02	52 ± 3	26 ± 4	17.0 ± 0.2	0.9968	50 ± 7	50 ± 10
GC	100	1.90 ± 0.02	53.6 ± 0.8	24.2 ± 0.4	16.5 ± 0.2	4.1881	43 ± 5	43 ± 8
GC	80	1.09 ± 0.02	54 ± 2	26 ± 1	17.2 ± 0.5	1.4130	48 ± 7	50 ± 10
GC	60	0.59 ± 0.02	61 ± 6	18 ± 3	19 ± 2	0.7566	40 ± 10	40 ± 10

Table 4.4 Volume fraction of micro-particles from SANS for various asphaltene fractions in mixtures of d-heptane and d-toluene with comparison to precipitated volume fraction from gravimetric experiments.

Solute		Solvent		SANS		Gravimetric
Asphaltene	Fraction	vol % T	vol % H	$\langle R_G^2 \rangle^{1/2}$ (Å)	ϕ_{flocs}	ϕ_{ppt}
AH	P30	100	0	58 ± 3	0.00	0.01
AH	P30	50	50	60 ± 3	0.00	0.02
B6	Whole	100	0	62 ± 4	0.00	0.00
B6	Whole	60	40	72 ± 3	0.00	0.02
B6	Whole	55	45	72 ± 3	0.00	0.01
B6	P40	100	0	131 ± 5	0.05	0.05
B6	P40	90	10	118 ± 5	0.09	0.03
B6	P40	80	20	107 ± 5	0.19	0.06
B6	P40	70	30	73 ± 9	0.57	0.36
CS	Whole	100	0	63 ± 3	0.01	0.00
CS	Whole	80	20	79 ± 7	0.03	0.01
CS	Whole	70	30	78 ± 3	0.04	0.01
CS	Whole	60	40	90 ± 4	0.06	0.01
CS	Whole	55	45	113 ± 5	0.06	0.02
CS	Whole	45	55	92 ± 5	0.26	0.27
CS	P40	100	0	98 ± 5	0.25	0.00
CS	P40	90	10	106 ± 6	0.17	0.01
CS	P40	80	20	97 ± 6	0.24	0.03
CS	P40	50	50	84 ± 5	0.28	> 0.51
HO	Whole	100	0	51 ± 3	0.00	0.00
HO	Whole	60	40	73 ± 2	0.01	0.01
HO	P39	100	0	107 ± 4	0.03	0.00
HO	P39	90	10	118 ± 5	0.00	0.01
HO	P39	80	20	106 ± 5	0.09	0.01

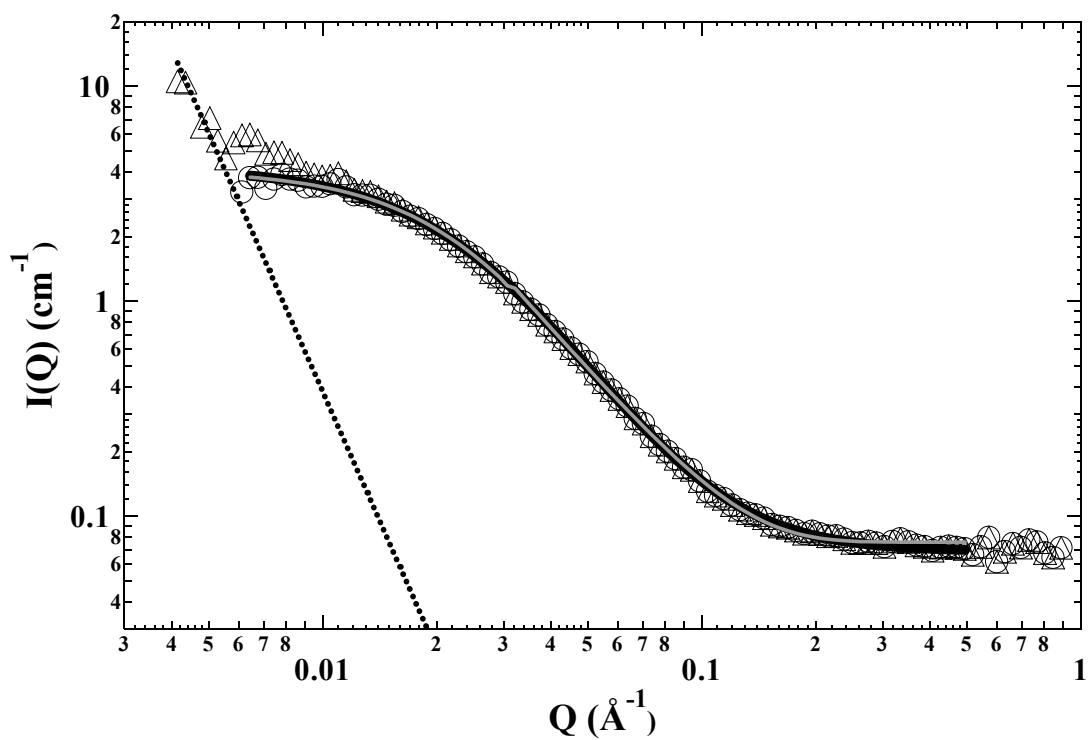


Figure 4.1 Example model fits to scattering curve for Hondo asphaltenes (1% wt) in 40:60 d-heptane: d-toluene (v/v). Legend: (Δ) raw data, (dashed line) power law fit, (\circ) power law corrected data, (black line) mass fractal fit, (grey line) polydisperse cylinder fit.

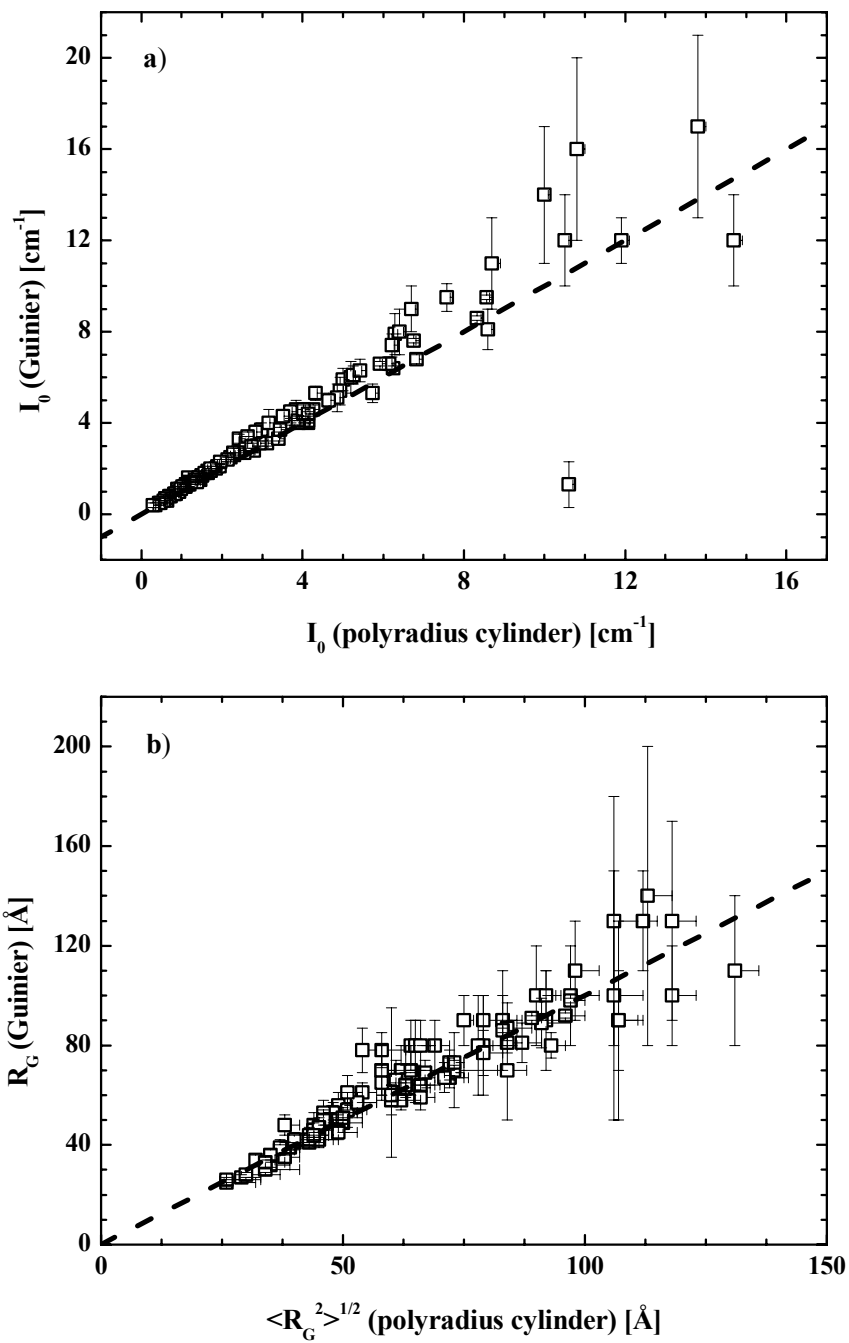


Figure 4.2 Comparison of (a) I_0 and (b) $\langle R_G \rangle$ parameters obtained from polydisperse oblate cylinder and Guinier fits. Dashed lines represent parity lines.

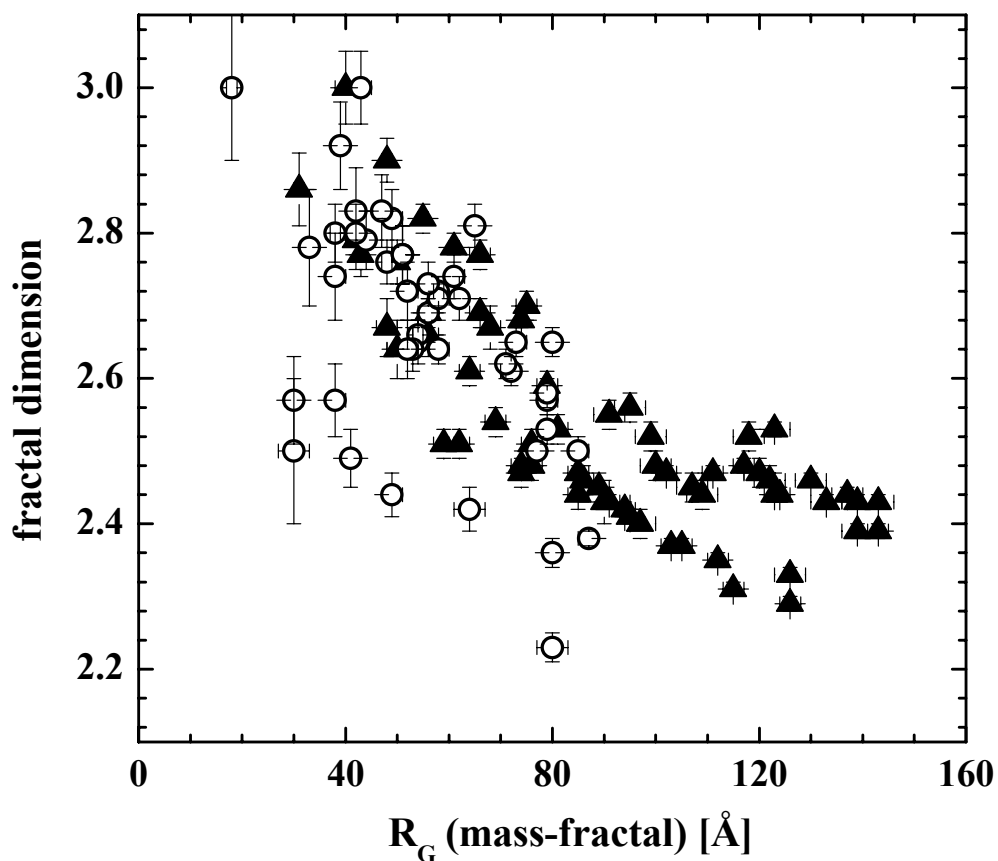


Figure 4.3 Correlation of apparent fractal dimension with aggregate size parameters obtained from the mass-fractal model. Filled triangles represent fractions dissolved in mixtures of d-heptane and d-toluene. Open circles represent fractions dissolved in mixtures of d-toluene (or d-methylnaphthalene) and d-methanol.

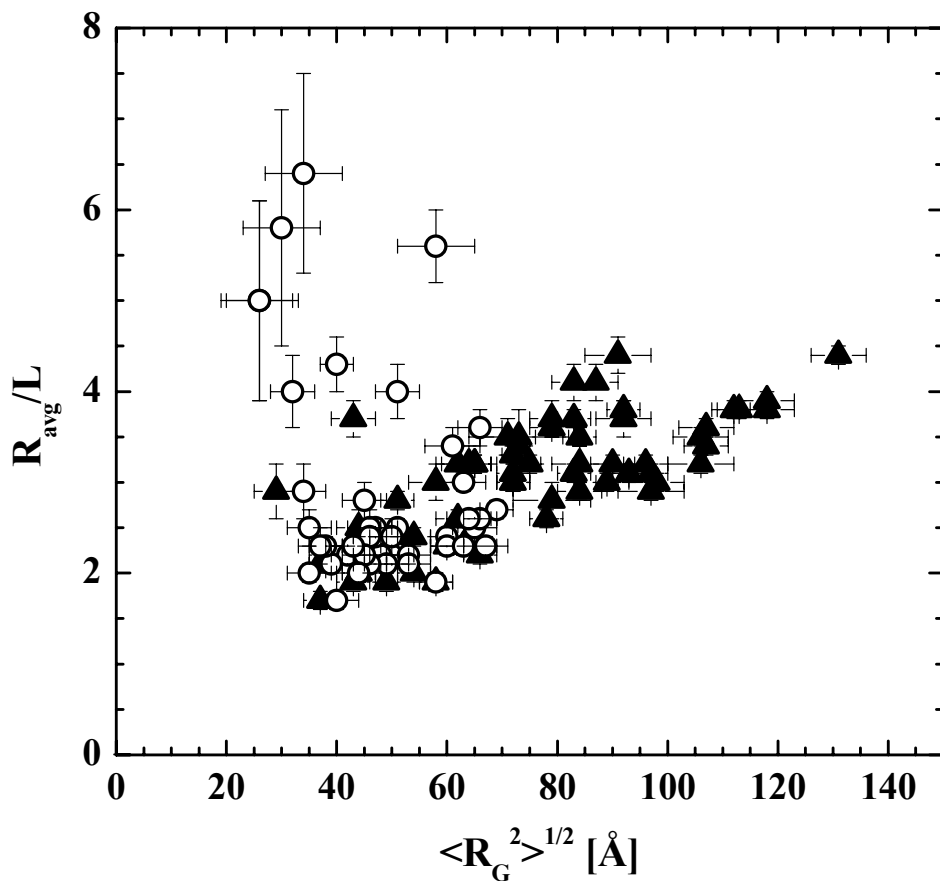


Figure 4.4 Correlation of particle aspect ratio with average aggregate size parameters obtained from the polydisperse cylinder model. Filled triangles represent fractions dissolved in mixtures of d-heptane and d-toluene. Open circles represent fractions dissolved in mixtures of d-toluene (or d-methylnaphthalene) and d-methanol.

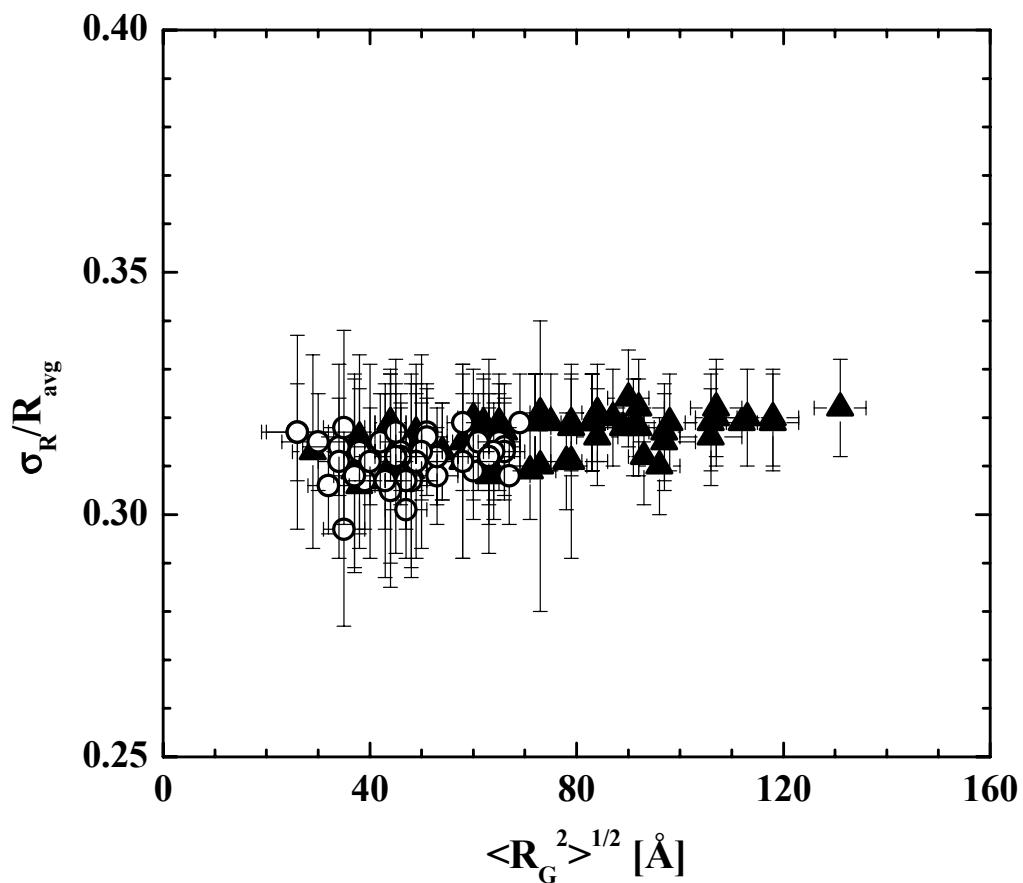


Figure 4.5 Correlation of radius polydispersity with aggregate size parameters obtained from the polydisperse cylinder model. Filled triangles represent fractions dissolved in mixtures of d-heptane and d-toluene. Open circles represent fractions dissolved in mixtures of d-toluene (or d-methylnaphthalene) and d-methanol.

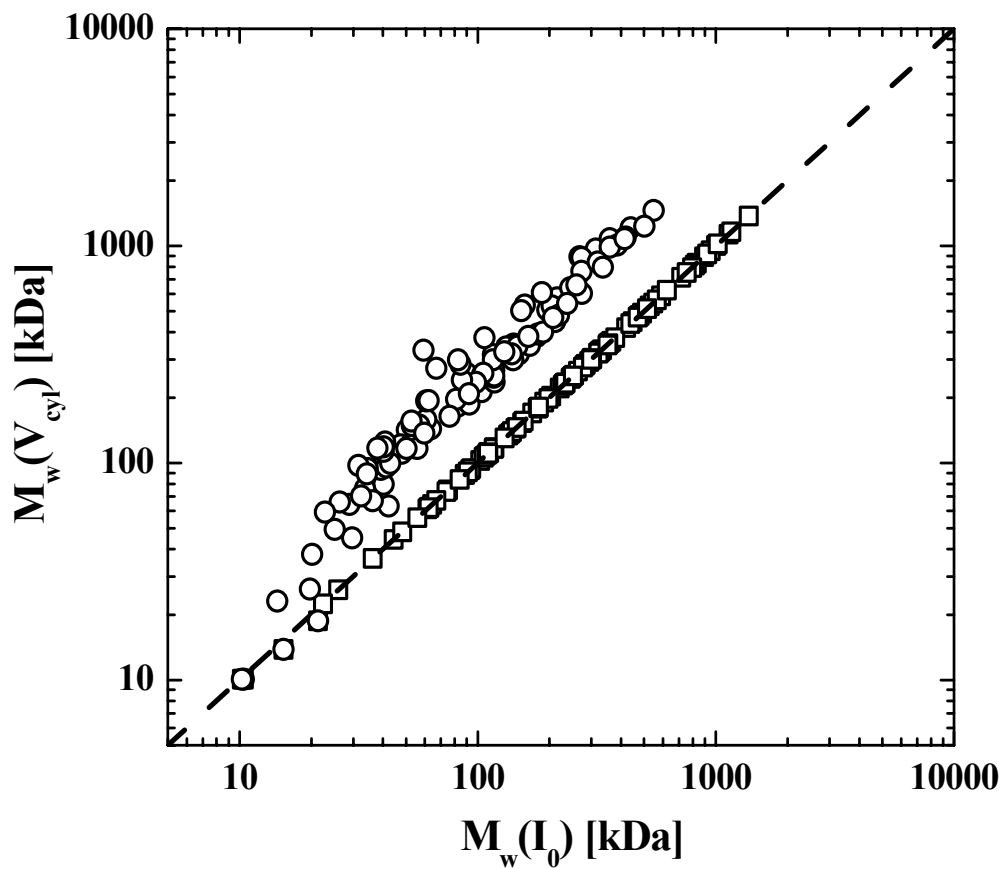


Figure 4.6 Parity plot comparing apparent molecular weight calculated from the moments of the particle volume (equation 15) and from I_0 measurements (equation 14) assuming (○) no solvent entrapment and (□) solvent entrapment. The dashed line represents the parity line.

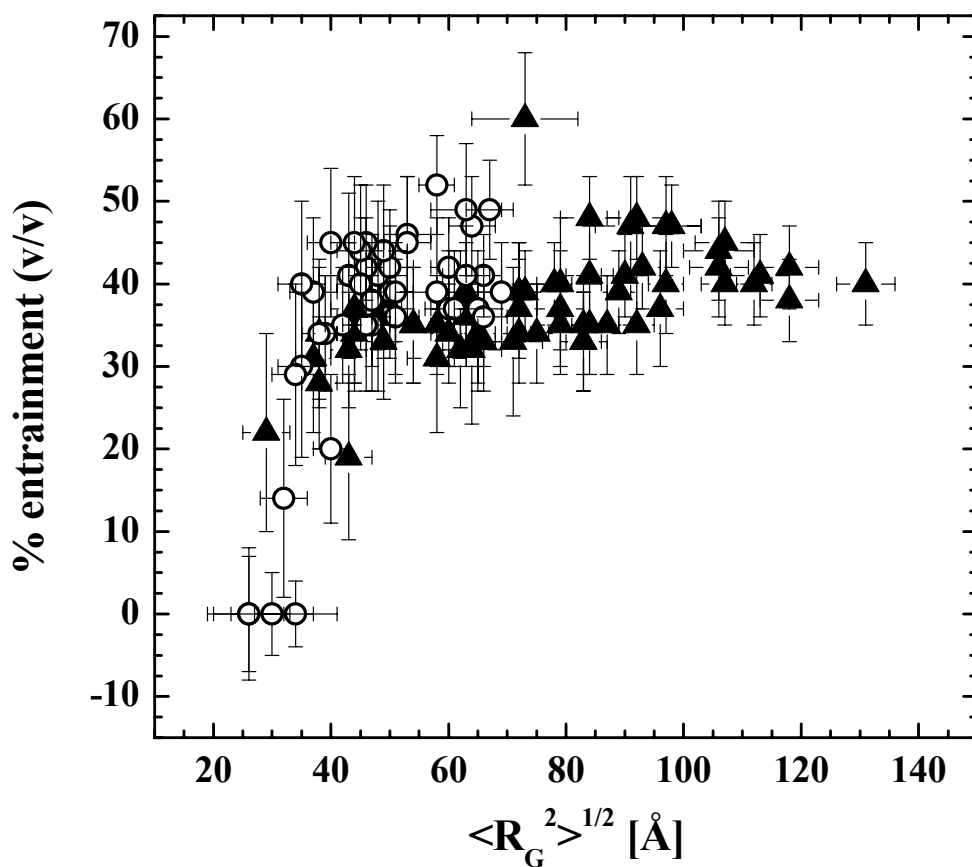


Figure 4.7 Variation in percentage solvent entrapment with aggregate size. Filled triangles represent fractions dissolved in mixtures of d-heptane and d-toluene. Open circles represent fractions dissolved in mixtures of d-toluene (or d-methylnaphthalene) and d-methanol.

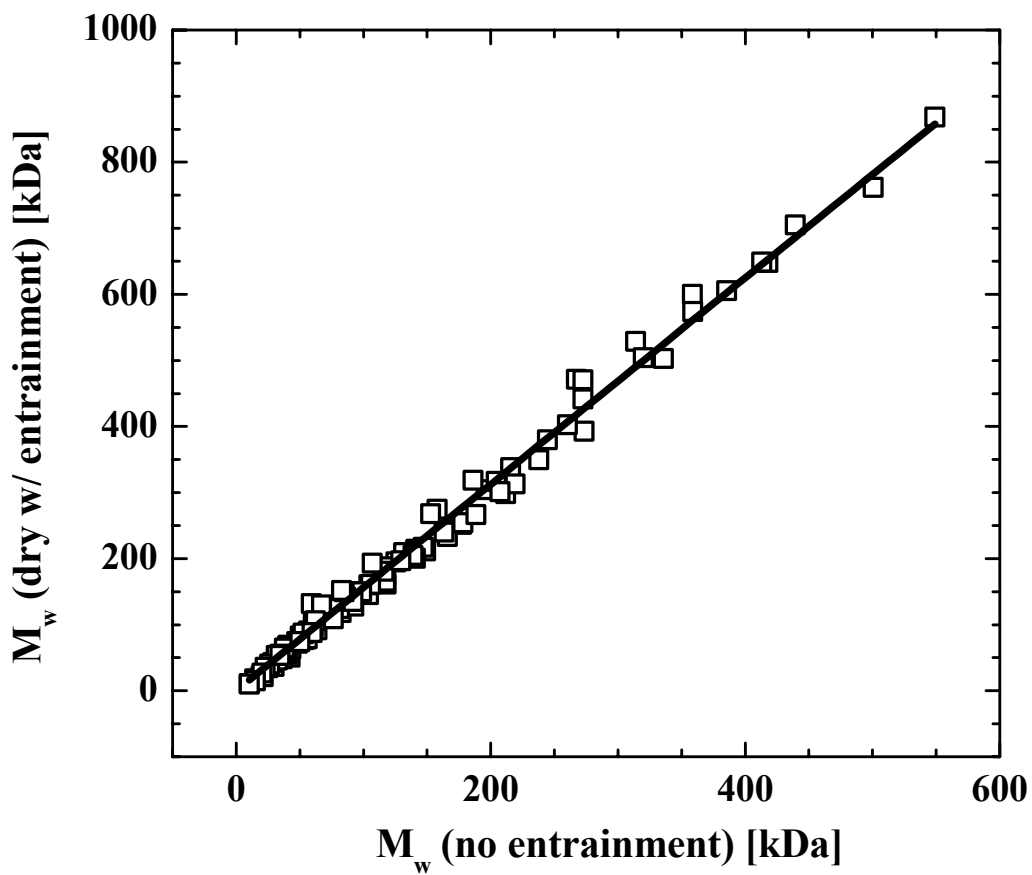


Figure 4.8 Average aggregate molecular weight (dry) for the assumption of solvent entrainment compared to the average aggregate molecular weight for the assumption of no solvent entrainment. Solid line represents best-fit line through the data.

Second virial coefficients of asphaltenic aggregates in varying solvents probed by small angle neutron scattering

Keith L. Gawrys and Peter K. Kilpatrick

ABSTRACT

While previous studies have reported values of second virial coefficients (A_2) for proteins, polymers, and other macromolecules and their corresponding solubility behavior in various solvents, little work has been performed to calculate the A_2 values for petroleum asphaltenes. In this study, small-angle neutron scattering (SANS) experiments were performed on various mixtures of asphaltenes and resins dispersed in perdeuterated solvents at different solute concentrations. The resulting SANS scattering curves were analyzed using a polydisperse oblate cylinder model and apparent aggregate masses were calculated after accounting for solvent entrainment within the aggregates. Changes in the apparent aggregate mass with concentration were interpreted as deviations from ideal dilute solution behavior (non-interacting aggregates plus solvent), which were quantified through the determination of aggregate A_2 values. This study investigates the roles of source crude, chemical composition, solvent conditions, and the influence of selective solvating agents on asphaltene A_2 values.

CHAPTER 5

SECOND VIRIAL COEFFICIENTS OF ASPHALTENIC AGGREGATES IN VARYING SOLVENTS PROBED BY SMALL ANGLE NEUTRON SCATTERING

5.1 Introduction

Small-angle neutron scattering (SANS) is frequently used to deduce sizes and infer morphologies of colloidal aggregates in solution. Proper analyses of SANS scattering intensity curves can provide values for the aggregate radius of gyration (R_G), molar mass (M), polydispersity, and apparent “fractal” dimension. Scattering theory shows that the concentration dependence of the absolute scattering intensity (I) is related to the radius of gyration and molar mass of the aggregates by an equation analogous to the virial expansion of the osmotic pressure [1]:

$$\frac{KC}{I(Q)} = \frac{1}{M} \left(1 + Q^2 \langle R_G^2 \rangle / 3 \right) + 2A_2C \quad (1)$$

where Q is the scattering wavevector, K is an instrumental constant, and A_2 is the second virial coefficient. In the small- Q limit, i.e. when the Q^2 term in equation (1) can be neglected, we recover:

$$\frac{KC}{I_0} = \frac{1}{M} + 2A_2C \quad (2)$$

where I_0 is the absolute scattering intensity extrapolated to zero- Q . Second virial coefficients and higher virial terms are phenomenological quantities, rather than those derived rigorously from molecular thermodynamics, that account for deviations from ideal solution behavior [1]. The second virial coefficient describes binary interactions in solution, such as solute-solute or aggregate-aggregate interactions, with the sign of A_2 reflecting the nature of these

interactions. For example, a positive A_2 value corresponds to a net repulsion between interacting species. A negative A_2 value corresponds to net attraction between interacting species.

Previous determinations of second virial coefficients from scattering experiments have allowed predictions of appropriate solvent conditions for the crystallization of proteins and other biological macromolecules [2-9] and for polymerization reactions [10-14]. SANS experiments on solutions of octyl- β -glucoside in water indicated changes in the sign and magnitude of A_2 at the critical micelle concentration as surfactant concentration is increased [15]. Second virial coefficient measurements have also provided direct evidence of a solvation layer around C_{60} in CS_2 solvent [16]. One would also expect that A_2 values for asphaltenic aggregates are related to the solubility behavior of asphaltenes in solution. Nevertheless, there is a remarkable absence of second virial coefficient values reported in the literature for asphaltenic aggregates. In fact, the second virial term in equation (2) is often neglected during the calculation of asphaltene aggregate masses by assuming that the aggregates are non-interacting in solution [17]. The value of M obtained by neglecting the second virial term in equation (2) are commonly referred to as “apparent” molar mass, as it has been shown to vary significantly with asphaltene concentration in solution [18]. Concentration dependent apparent aggregate molar masses were also observed during measurements of asphaltene solutions by vapor pressure osmometry [19,20]. Such variation in the apparent aggregate molar mass with concentration suggests that A_2 and possible higher order virial terms are significant in asphaltenic interactions and are necessary for the calculation of a “true” aggregate molar mass.

In one notable exception, Espinat et al. calculated A_2 values for Safaniya vacuum residue asphaltenes in d-toluene from SANS scattering curves using the Zimm method and observed two concentration domains for asphaltene aggregation [21]. The value of A_2 was nearly zero at higher concentrations (2.5 – 4.7 % w/w), suggesting that asphaltene aggregates were non-interacting. A negative A_2 value on the order of 10^{-4} cm³mol/g² was observed in the lower concentration domain (0.025 – 1% w/w) that was suggestive of attractive interactions between the asphaltene aggregates. Although widely used, the Zimm approximation [22] only models the region of the scattering spectra where the quantity $Q_{\max}R_G \leq 1$ and does not assume any particular morphology for the particles. The A_2 values for Safaniya asphaltenes were calculated by assuming no significant entrainment of solvent within the aggregates [21]; however, previous SANS and viscosity measurements on asphaltene solutions indicated a range of solvent entrainment within the aggregates from 50 to 70 % (v/v) [23-26]. Furthermore, the values of the dry average aggregate mass for the assumption of solvent entrainment were approximately a factor of 2.5 larger than the corresponding values for the assumption of no solvent entrainment [23], suggesting the need to include solvent entrainment effects in the calculation of aggregate masses. Evidence of solvent entrainment within the aggregates indicates the significance of solute-solvent interactions in the solutions of asphaltenes and further justifies the need to quantify the magnitudes of these interactions through the calculation of A_2 values.

To this point, the roles of source crude, chemical composition, solvent conditions, and the influence of selective solvating agents on asphaltene A_2 values have been largely unexplored. The intent of this study is to show that A_2 values for asphaltenes vary with solvent conditions and may be used to indicate the onset of asphaltene precipitation.

Furthermore, the magnitude of the observed A_2 value is dependent on the chemical composition of the solute (e.g., atomic H/C). The addition of selective solvating agents, such as petroleum resins, has previously been shown to modify the size of asphaltenic aggregates, likely through disruption of π -bonding interactions between aromatic sheets or through selective binding to and disruption of H-bonding sites and interactions in the asphaltenes [27,28]. Similar changes are expected in the A_2 values of asphaltenic aggregates that are modified by selective solvating agents. Correlating changes in A_2 values for modified asphaltene solutions with concentration and chemical composition of the selective solvating agent may enable the selection of more efficient dispersants or demulsifiers for a given petroleum mixture. This study will show that accounting for inter-aggregate interactions and issues such as solvent entrainment within aggregates are necessary for the calculation of aggregate molar masses.

5.2 Experimental

5.2.1 Asphaltene and Resin Isolation

Hondo (HO) and Gulf Coast (GC) asphaltenes were precipitated from their corresponding source crude oil or blend by the addition of excess n-heptane (40:1 v/v). All solvents were obtained from Fisher Scientific and were HPLC grade. The crude oil/n-heptane mixtures were allowed to equilibrate for 24 h. During this period, the mixtures were subjected to constant, gentle shaking to ensure all of the material was completely dispersed and/or dissolved. After this equilibration period, the precipitated asphaltenes were removed by gravimetric filtration through 18.5 cm diameter, Whatman 542 hardened ashless filter paper. The filter cake was washed with additional n-heptane via Soxhlet extraction to

remove any co-precipitated maltenes. A second Soxhlet extraction was performed using toluene as the wash solvent to dissolve the asphaltenes from the filter paper, leaving behind any inorganic insolubles. Both extraction procedures continued until the overflow from the extractions became colorless. Most of the solvent was removed from the asphaltene solutions by rotary evaporation under partial vacuum at 60°C. Once nearly dry, the asphaltenes were moved into a nitrogen-flushed vacuum oven at 50°C for 24-36 h. The dry asphaltenes were transferred to glass jars and stored under argon to prevent oxidation.

Two batches of Hondo asphaltenes (i.e., HO1 and HO2) were prepared and used in the subsequent experiments that varied slightly in chemical composition. HO2 asphaltenes were prepared according to the procedure described above while HO1 asphaltenes were prepared according to the procedure of Spiecker et al [29]. The major difference in the isolation procedures was that the latter procedure omitted the Soxhlet extraction steps. The HO1 asphaltenes likely contained a small amount of co-precipitated resins, as reflected by the higher H/C mass ratio observed for this batch compared to HO2 (See Table 5.1). Asphaltenes were also isolated from Arab Heavy (AH) and B6 crude oils by the procedure that omitted the Soxhlet extraction steps. The asphaltenes isolated from B6 crude oil were separated into several fine fractions by sequential fractionation in mixtures of heptane and toluene according to the procedure of Gawrys et al [30]. A specific fine fraction of B6 asphaltenes (i.e., B6f46) was characterized in this study. The B6f46 fraction represented the portion of all B6 asphaltenes that was soluble in a mixture of 47 % toluene: 53 % n-heptane (v/v) at a concentration of 1 % (w/w), but was insoluble in a mixture of 46 % toluene: 54 % n-heptane (v/v) at the same concentration.

Hondo, B6, and Africa resins were isolated from the deasphalted crude oil fractions (i.e., maltenes) of their source crudes according to the procedure described by Spiecker et al. [27].

5.2.2 Chemical Characterization

The isolated asphaltene and resin fractions were characterized by combustion elemental analysis at the University of Alberta (Department of Chemistry, Edmonton, Alberta, Canada) using a Carlo Erba instrument. Elemental analysis results for the various petroleum fractions are shown in Table 5.1. Also shown in the table is the elemental composition of 5 β -cholanic acid (CA), a commercially available compound (Sigma-Aldrich, 99 % purity) that is used to model naturally occurring petroleum naphthenates.

5.2.3 SANS Sample Preparation

In order to calculate the second virial coefficients for asphaltenic aggregates, a series of solutions were prepared in perdeuterated solvents with concentrations ranging from 0.025 – 4 % w/w. Similarly, solutions of resins were prepared over a concentration range between 0.5 – 10 % w/w and asphaltene-resin mixtures were prepared at fixed resin: asphaltene mass ratio. The perdeuterated solvents included mixtures of toluene, heptane, and methanol. Solvents were obtained from CDN Isotopes and had >99.9% chemical purity and >99.5% perdeuteration. During the sample preparation, d-toluene was initially added to the dry asphaltenes and the solution was subjected to constant, gentle shaking until the asphaltenes were completely dissolved. Upon dissolution of the asphaltenes, the second solvent (i.e., d-methanol or d-heptane) was added to the solutions. Each concentration series was prepared

by dilution with the corresponding solvent blend of the highest concentrated solution that had no evidence of precipitation.

5.2.4 SANS Measurements

SANS measurements were performed on the small-angle neutron diffractometer (SAND) at the Intense Pulsed Neutron Source (IPNS) Division of Argonne National Laboratory (Argonne, IL). The available Q range for the SAND instrument extended from 0.0035 to 2 \AA^{-1} and was adequate for obtaining detailed scattering spectra to characterize asphaltene aggregation. The samples were measured at 25°C in cylindrical quartz sample cells (NGS Precision) with a path length of 2 mm. A typical scattering experiment consisted of 15 minutes of detecting neutron transmission through the samples followed by 60 minutes of scattering. The absolute scattering intensity, $I(Q)$, for each sample was obtained from the total detector counts corrected for background radiation, neutron transmission through the sample, scattering from the quartz cell, and detector sensitivity. Scattering intensity versus scattering angle ($I(Q)$ vs. Q) curves were fit to a polydisperse radius oblate cylinder model that was previously shown to describe the SANS scattering behavior of asphaltenes with a wide range of chemical compositions in a variety of solvents [23,31]. The model fits were applied to the data over the Q range between 0.01 and 0.35 \AA^{-1} . A constant background term was included in the model fits to account for incoherent scattering from all nuclei with non-zero spin in the solvent and solute.

5.2.5 SANS Model Fitting

The scattering intensity distribution for a system with radius polydispersity is proportional to the ensemble average of the intra-particle structure factor, $P(Q,R)$, as given by:

$$I(\mathbf{Q}) = \int_0^{\infty} I_0 P(Q,R) f(R) dR \quad (3)$$

where I_0 is the absolute scattering intensity extrapolated to $Q = 0$ and $f(R)$ is a normalized distribution function for the aggregate radius, R . An example is the Schultz distribution function given by:

$$f(R) = \frac{R^z}{\Gamma(z+1)} \left[\frac{R_{avg}}{z+1} \right]^{z+1} \exp\left(-\frac{(z+1)R}{R_{avg}}\right) \quad (4)$$

In the above equation, $\Gamma(n)$ is the gamma function, R_{avg} is the average particle radius, and z is the polydispersity parameter defined by:

$$z = \left(\frac{R_{avg}}{\sigma_R} \right)^2 - 1 \quad (5)$$

where σ_R is the standard deviation of the average size parameter. The intra-particle structure factor for a monodisperse cylinder with radius R and length L is given by:

$$P_{cyl}(Q) = \int_{\beta=0}^{\pi/2} \left[\frac{2J_1(QR \sin \beta)}{QR \sin \beta} \frac{\sin((QL \cos \beta)/2)}{(QL \cos \beta)/2} \right]^2 \sin \beta d\beta \quad (6)$$

where $J_1(x)$ represents a first order Bessel function of the first kind and β is the orientational averaging angle. One simplification of equation (6) for a monodisperse flat disk (i.e., oblate cylinder) may be written as [32]:

$$P_{ob,1}(Q) = 2 \left[\frac{\sin(QL/2)}{QL/2} \right]^2 \left[\frac{1 - J_1(2QR)/QR}{(QR)^2} \right] \quad (7)$$

Alternatively, the high Q region of a monodisperse flat disk may also be described by an exponential approximation given by [33]:

$$P_{ob,2}(Q) = \frac{2}{(QR)^2} \exp\left(-\frac{(QL)^2}{12}\right) \quad (8)$$

A direct analytical solution for the case of polydisperse oblate cylinders with a Schultz distribution of radii is obtained by taking advantage of the flat disk approximations given above. Specifically, the intra-particle structure factor used in this study to model polydisperse radius oblate cylinders takes the form:

$$\begin{aligned} \langle P(Q) \rangle &= \frac{\int_0^\infty V^2 P_{ob,1}(Q, R) f(R) dR}{\int_0^\infty V^2 f(R) dR} \quad \{QR < 3 \\ \langle P(Q) \rangle &= \frac{\int_0^\infty V^2 P_{ob,2}(Q, R) f(R) dR}{\int_0^\infty V^2 f(R) dR} \quad \{QR > 3 \end{aligned} \quad (9)$$

where the simplifications in equations (7) and (8) are applied over the limited Q-range in which the model assumptions are valid. Additional information concerning the model development is located elsewhere [31].

The zero-Q scattering intensity, I_0 , is related to the first and second moments of the particle volume (i.e., $\langle V \rangle$ and $\langle V^2 \rangle$, respectively) as given by [34]:

$$I_0 = \frac{\phi \langle V^2 \rangle (\Delta\rho)^2}{\langle V \rangle} \quad (10)$$

where ϕ is the volume fraction of scatterers and $\Delta\rho$ is the scattering contrast. The scattering contrast is defined as the difference between the scattering length density of the solvent (s) and scatterer (m) as given by:

$$\Delta\rho = \rho_s - \rho_m \quad (11)$$

For a given phase, j, the scattering length density is a product of the mass density, d_j , and the summation of contributions from individual atomic species, i, as given by:

$$\rho_j = d_j \sum_i \frac{b_i x_i}{m_i} \quad (12)$$

where b_i , x_i , and m_i are the bound coherent scattering length, mass fraction, and atomic mass of species i, respectively. Mass densities of asphaltene and resin solutions in toluene were measured using a 2 mL pycnometer. Average asphaltene and resin dry mass densities of 1.1 and 1.0 g/cm³, respectively, were calculated by extrapolating the solution data to pure solute. Mass densities of asphaltene, resin, and solvent mixtures were calculated assuming no change in the molar volume on mixing.

5.3 Results and Discussion

The scattering intensity versus scattering angle ($I(Q)$ vs. Q) curves of HO1 asphaltenes (0.25 to 4.38 % w/w) in d-toluene are shown in Figure 5.1. Non-linear least squares fits to the polydisperse radius oblate cylinder model are represented in the figure as the solid black lines. As shown in the figure, the polydisperse cylinder model accurately predicted the scattering intensity over the entire Q range studied, regardless of solute concentration. The aggregate size parameters obtained from the model fits for HO1 asphaltenes in d-toluene were relatively independent of the solute volume fraction (Table

5.2). Average values of the average aggregate radius (R_{avg}), radius spread (σ_R), and particle thickness (L) were 49 ± 3 , 15 ± 1 , and 19 ± 2 Å, respectively. The average radius of gyration for polydisperse cylinders with a Schulz distribution of radii is given by:

$$\langle R_G \rangle^2 = \frac{L^2}{3} + \frac{R_{\text{avg}}^2}{2} \frac{(z+6)(z+5)}{(z+1)^2} \quad (13)$$

where z is the Schulz polydispersity parameter defined in equation (5). The average $\langle R_G^2 \rangle^{1/2}$ value (52 ± 3 Å) for HO1 asphaltenes in d-toluene also appeared independent of solute concentration. Similar trends in the aggregate size parameters with solute concentration were observed as solute and solvent composition were varied. A decrease in the model fit quality (i.e., increase in χ^2) was observed with increasing solute concentration, particularly at the highest concentration in Table 5.2. This was likely attributed to contributions from a small amount of flocculated asphaltenic aggregates to the scattering intensity distribution at low Q values. Average $\langle R_G^2 \rangle^{1/2}$ values for mixtures of asphaltenes and resins in various solvents are presented in Table 5.3. As shown in the table, Hondo asphaltenes formed significantly larger aggregates in 40:60 d-heptane: d-toluene (v/v) than in d-toluene or 90:10 d-toluene: d-methanol. This observation was expected as it has been previously reported that asphaltenic aggregates grow to their largest size very near the solubility limit [29]. Also interesting is the observation that the average aggregate size decreased with the addition of a small amount of d-methanol to the d-toluene solution. This indicates the importance of hydrogen bonding interactions in the aggregation mechanism for Hondo asphaltenes. The addition of 10 % (v/v) d-methanol was sufficient to disrupt interactions between polar heteroatoms within the aggregates and further reduce the aggregate size. Table 5.3 indicates that petroleum resins were also effective at reducing the aggregate size of Hondo asphaltenes

in d-toluene, likely through the disruption of aromatic π -bonding interactions within the aggregates. This result was also previously observed in other SANS studies of asphaltene-resin mixtures [27,28]. Petroleum resins were observed to self-interact in d-toluene and 40:60 d-heptane: d-toluene; however, the aggregates formed were significantly smaller than those of asphaltenes. SANS scattering intensity distributions for 5 β -cholanolic acid (CA) in d-toluene suggested that the model compound did not significantly self-interact and was likely present in solution as either monomers or dimers. The addition of CA to HO1 asphaltenes in d-toluene did not significantly affect the average aggregate radius of gyration.

Additional information concerning the morphology of asphaltenic aggregates was obtained through the calculation of apparent aggregate molar mass values. The apparent weight-averaged molar mass of the aggregate, $\langle M_{app} \rangle$, is related to the zero-Q scattering intensity, I_0 , according to:

$$\langle M_{app} \rangle = \frac{I_0 N_A d_m}{\phi (\Delta\rho)^2} \quad (14)$$

where N_A and d_m are Avogadro's number and the scatterer mass density, respectively. Alternatively, $\langle M_{app} \rangle$ is related to the first and second moments of the particle volume as obtained by combination of equations (10) and (14) given by:

$$\langle M_{app} \rangle = \frac{N_A d_m \langle V^2 \rangle}{\langle V \rangle} \quad (15)$$

Equations (14) and (15) provide independent means of calculating the apparent aggregate molar mass from the fit parameters for the polydisperse oblate cylinder model, as well as a means of estimating the percentage of entrained solvent within the aggregates [23]. For example, Figure 5.2 compares the values of I_0 calculated from equation (10) for the

concentration series of HO1 asphaltenes in d-toluene to those obtained directly from polydisperse cylinder fits to the experimental data. As shown in the figure, the values of I_0 calculated from equation (10) generally over-predicted the experimental values by a factor of 2.75 when no solvent entrainment is assumed. For the assumption of no solvent entrainment, the average mass density (i.e., 1.1 g/cm^3) and chemical composition of dry asphaltenes were used for the calculation of the solute scattering length density (equation 12). This inconsistency in the I_0 values suggests that asphaltenes are solvated to some extent by the solvent and that the entrained solvent contributes to the coherent scattering of neutrons within the aggregates.

The I_0 values were recalculated for various values of solvent entrainment, as shown in Figure 5.2. The assumption of solvent entrainment affected the values of the solute mass density (d_m) and the mass fractions of atomic species used in equation (12), thus reducing the scattering contrast between the solute and solvent. Similarly, changes in the solute mass density affected the values of the solute volume fraction (ϕ) used in equation (10). Figure 5.2 indicates that parity is obtained for the calculated and experimental values of I_0 when the aggregate is assumed to consist of 41 % (v/v) entrained solvent. Similar calculations of the extent of solvent entrainment were performed for the remaining concentration series containing mixtures of asphaltenes and resins in various solvents (Table 5.3). A relatively narrow range of solvent entrainment values between ~ 36 to 43 % (v/v) was observed for all of the solutions containing asphaltenes only. Pure resin solutions and asphaltene-resin mixtures were observed to entrain solvent to a slightly lesser extent. These values are consistent with the extent of solvent entrainment observed from previous SANS measurements [23]. Assuming the values of solvent entrainment shown in Table 5.3, the

values of the apparent weight-averaged molar mass of the aggregates obtained from equations (14) and (15) are also self-consistent.

The apparent molar mass in equation (14) was observed to decrease with increasing solute concentration for mixtures of HO1 asphaltenes and B6 resins in d-toluene (Figure 5.3), suggesting deviations from ideal solution behavior or, equivalently, interactions between the aggregates in solution. The sign (i.e., attractive or repulsive) and magnitude of the inter-aggregate interactions were quantified by the calculation of aggregate second virial coefficients (A_2). Second virial coefficient values were determined from a virial expansion of the absolute scattering intensity extrapolated to the limit $Q = 0$, as given by [1]:

$$\frac{\phi(\Delta\rho)^2}{I_0 N_A d_m} = \frac{1}{\langle M \rangle} + 2A_2 d_m \phi \quad (16)$$

The term on the left side of equation (16) represents the inverse of the apparent aggregate molar mass. Figure 5.4 shows a plot of this term as a function of solute volume fraction for mixtures of HO1 asphaltenes and B6 resins with resin: asphaltene mass ratio (R/A) of 4.94 in d-toluene. The slope of a least squares linear fit through the data provides the value of the aggregate second virial coefficient. The intercept provides the value of the average aggregate molar mass. For this case, values of $\langle M \rangle$ and A_2 were 30 ± 20 kDa and $6 \times 10^{-4} \pm 1 \times 10^{-4}$ mol cm^3/g^2 , respectively. The positive sign of A_2 indicates that the resin-modified asphaltenic aggregates experienced net repulsive interactions at this solvent condition. The magnitude of these repulsive interactions is not apparent until the $\langle M \rangle$ and A_2 values are compared to the remaining samples (Table 5.3).

For example, the A_2 value for HO1 asphaltenes in d-toluene (no resins) was ~ 20 times smaller than the corresponding mixture of HO1 asphaltenes and B6 resins (R/A =

4.94). In fact, the A_2 value for the mixture at the highest R/A ratio was on the same order of magnitude as the pure resin solutions. HO1 asphaltenes in d-toluene (no resins) formed larger, less repulsive aggregates than the corresponding asphaltene solutions with added resins. The addition of resins to HO1 asphaltenes effectively reduced the average aggregate mass and increased the nature of the repulsive interactions between the aggregates. A similar reduction in the aggregate mass and increase in repulsive interactions were observed with the addition of CA to HO1 asphaltenes; however, the average radius of gyration did not change significantly. This suggests that CA did interact with the HO1 asphaltenes, but, unlike resins, was not effective at disrupting aromatic π -bonding within the aggregates. The carbon structure of CA is completely saturated; therefore, the most likely interaction mechanism between CA and asphaltenes would occur through the proton donating and/or accepting capability of the carboxylic acid moiety.

The effect of solvent on the A_2 values of Hondo asphaltenes is also shown in Table 5.3. Hondo asphaltenes formed aggregates that were net repulsive in nature ($A_2 \sim 2 \times 10^{-5} \text{ mol cm}^3/\text{g}^2$) in good solvents (i.e., d-toluene and 90:10 d-toluene: d-methanol). The sign of A_2 changed to a negative value in 40:60 d-heptane: d-toluene, suggesting the aggregates were net attractive at this solvent condition. As previously mentioned, HO2 asphaltenes were near the solubility limit in 40:60 d-heptane: d-toluene (v/v). These results indicate that A_2 values have the potential to predict the onset of asphaltene precipitation. For example, one would expect the A_2 value of HO2 asphaltenes in d-toluene to be slightly repulsive ($\sim 10^{-5} \text{ mol cm}^3/\text{g}^2$). The addition of a small amount of d-heptane (e.g., 10 % v/v) should increase the attractive interactions of the asphaltene aggregates, as observed by a slight increase in $\langle R_G^2 \rangle^{1/2}$ and $\langle M \rangle$ and a slight decrease in A_2 . With continued addition of d-heptane, the A_2

value is expected to pass through zero and become slightly negative (i.e., attractive). The above experiments involving Hondo asphaltenes were performed in the concentration range between 0.25 and 4 % (w/w).

In the high dilution limit (i.e., 0.025 to 0.1 % w/w), HO2 asphaltenes formed aggregates in d-toluene with a similar size and mass as HO1 asphaltenes (0.25 to 4 % w/w) in the same solvent. Because of increased percent uncertainty in the absolute scattering intensity of more dilute solutions, there was large uncertainty in the A_2 value of dilute HO2 aggregates in d-toluene (Table 5.3). It is not conclusive whether or not dilution affects the magnitude of A_2 for this sample. The A_2 value obtained from measurements of similar dilute solutions of B6f46 asphaltenes in d-toluene was near unity, but the aggregate interactions were not conclusively attractive or repulsive. Espinat et al. observed a negative A_2 value in the low concentration regime for Safaniya asphaltenes in d-toluene (0.025 – 1% w/w) that was suggestive of attractive interactions between the asphaltene aggregates [21]. A second aggregation process, namely, the interaction of asphaltene monomers or small oligomers to form larger aggregates, could explain attractive A_2 values in the dilute concentration regime.

Attractive values of A_2 in the dilute concentration regime were also observed from vapor pressure osmometry (VPO) experiments. Peramanu et al. calculated the aggregate mass of Athabasca and Cold Lake asphaltenes in 1,2-dichlorobenzene at 120°C from VPO in the concentration range from 1.7 to 3.1 g/L [19]. In a VPO experiment, the aggregate molar mass is related to the voltage difference (ΔE) and solute concentration (C) by:

$$\frac{\Delta E}{C} = K \left(\frac{1}{M} + A_2 C \right) \quad (17)$$

where K is a proportionality constant determined from a standard of known molar mass (e.g., benzil). We estimated the value of K using the asphaltene masses shown for Athabasca and Cold Lake asphaltenes (Table 3 of ref. [19]) and, subsequently, estimated the A_2 values for the asphaltenes using equation (17) and Figure 1 of ref. [19]. The resulting A_2 values of Athabasca and Cold Lake asphaltenes were approximately -5×10^{-5} and -6×10^{-5} $\text{cm}^3 \text{mol/g}^2$, respectively, and were on the same order of magnitude as HO2 asphaltenes in d-toluene (0.025 to 0.1 % w/w) from SANS. The above VPO results further support the hypothesis that aggregates are dispersed into small oligomers and monomers at high dilution (i.e., < 1 % w/w). Asphaltene monomers have a natural tendency to associate in the most dispersive of solvent conditions (e.g., 1,2-dichlorobenzene at 130°C) [20]; hence, the observed A_2 values indicated attractive interactions.

We also used equation (17) to estimate the A_2 value for Athabasca asphaltenes in toluene from VPO data at 50°C in the concentration range from 5 to 40 g/L [20]. The VPO response and aggregate mass used in the calculation were obtained from Figure 5 and Table 4 of ref. [20], respectively. The resulting A_2 value for Athabasca asphaltenes ($\sim -1 \times 10^{-6}$ $\text{cm}^3 \text{mol/g}^2$) was consistent with the magnitude of A_2 values observed for other asphaltene samples in the same concentration range (Table 5.3). Differences in the sign of A_2 values for HO1, AH, and GC asphaltenes in d-toluene (Table 5.3) suggest that asphaltene chemical composition does influence the type of interactions between the aggregates. For example, the A_2 value for HO1 asphaltenes indicated the aggregates were slightly repulsive in d-toluene. The sign and uncertainty in the magnitude of the A_2 value for AH and GC asphaltenes suggested the aggregates were attractive in d-toluene. AH asphaltenes were more aromatic and contained lower polar heteroatom contents (Table 5.1) than the

corresponding HO2 asphaltenes. GC asphaltenes were more aromatic and contained more polar heteroatom contents than both AH and HO1 asphaltenes. These results suggest differences in asphaltene chemical composition affect the nature of aggregate interactions in a given solvent. Figure 5.5 correlates the A_2 values to atomic H/C for all of the samples dispersed in d-toluene, including resins and mixtures of asphaltenes and resins. As indicated in the figure, the observed A_2 values appear to approximate a first order exponential growth function with decreasing solute aromaticity. This suggests that the interactions between asphaltenes, resins, and the d-toluene solvent are strongly dominated by dispersion and π -bonding interactions.

Additional information concerning the nature of the aggregate interactions is obtained from calculations of the second virial coefficient based on the concept of the excluded volume of the solute particles. The excluded volume is the volume surrounding and including a given particle that is physically excluded to another particle due to its spatial extension. The calculated A_2 values based on excluded volume analyses consider changes in the entropy upon mixing of solute and solvent molecules, but assume a negligible enthalpy of mixing [1]. In effect, the model implies that interactions between solute-solute, solvent-solvent, and solute-solvent pairs are energetically equivalent. The second virial coefficient for a heterogeneous collection of rigid (i.e., excluded) particles is given by [35]:

$$A_{2,excluded} = \frac{4N_A \langle V \rangle \langle f \rangle}{\langle M \rangle^2} \quad (18)$$

where f is a numerical factor that describes deviations from a spherical shape. Ishihara derived an expression for f for the case of homogeneous rigid ovaloids:

$$f = \frac{1}{4} + \frac{HF}{16\pi V} \quad (19)$$

where H and F are the mean radius of curvature and surface area, respectively. For the case of polydisperse cylinders with a Schultz distribution of radii, the average value of f is given by:

$$\langle f \rangle = \frac{1}{4} \left\{ 1 + \frac{(z+1)}{(z+2)} + \frac{R_{avg}}{L} \right\} \quad (20)$$

Table 5.3 provides estimates of the $A_{2,excluded}$ calculated for the mixtures of asphaltenes and resins by combination of equations (18) and (20). In all of the experiments, the magnitude of $A_{2,excluded}$ was greater than or agreed with the experimentally measured A_2 value within statistical uncertainty. These results suggest that aggregate interactions are not completely steric-repulsive in nature; rather interactions of the asphaltenes with the solvent media (e.g., solvent entrainment) are significant.

5.4 Conclusions

SANS experiments were performed solutions of asphaltenes and resins in mixtures of d-toluene, d-heptane, and d-methanol at various solute concentrations. The resulting scattering curves were analyzed using a polydisperse radius cylinder model and apparent aggregate masses were calculated assuming significant entrainment of solvent (i.e., 21 – 43 % v/v) within the aggregates. Changes in the apparent aggregate mass with concentration indicated deviations from ideal solution behavior, which were quantified through the determination of aggregate A_2 values. A_2 values were previously reported or inferred from SANS and VPO experiments studying asphaltenes in toluene and 1,2-dichlorobenzene;

however, this study was the first to investigate the roles of source crude, chemical composition, solvent conditions, and the influence of selective solvating agents on asphaltene A_2 values.

Results of the second virial determination for Hondo asphaltenes (0.25 – 4 % w/w) in d-toluene and 90:10 d-toluene: d-methanol (v/v) indicated that the aggregates experienced net repulsive interactions at these solvent conditions with A_2 values on the order of 10^{-5} mol cm^3/g^2 . A negative A_2 value was observed for HO2 asphaltenes in 40:60 d-heptane: d-toluene at the same concentration range, indicating flocculation (i.e., attractive interactions) of the aggregates. We could not conclude from these SANS experiments if dilution affects the sign and magnitude of the A_2 values; however, negative A_2 values were previously observed from dilute solutions of asphaltenes measured by v.p.o., suggesting that asphaltene monomers or small oligomers were interacting to form larger aggregates. B6 resins effectively reduced the aggregate mass of HO1 asphaltenes in d-toluene and increased the magnitude of the observed A_2 values, likely through the disruption of aromatic π -bonding interactions within the aggregates. A_2 values for HO1 asphaltenes and B6 resins were on the same order of magnitude as pure resin solutions (i.e., 10^{-4} mol cm^3/g^2). A_2 values appeared to vary significantly with chemical composition, specifically atomic H/C of the solute mixture, suggesting that the interactions between asphaltenes, resins, and the d-toluene solvent are strongly dominated by dispersion and π -bonding interactions. The magnitude of the experimentally measured A_2 values generally under-predicted or agreed with the values of A_2 calculated from an excluded volume model, suggesting that the types of interactions between the solute and solvent are not completely steric repulsive. The structure of

asphaltenic aggregates is more diffuse than that of a rigid body; thus, energetic interactions of the solute and solvent are significant.

5.5 Acknowledgements

This research is supported by the Petroleum Environmental Research Forum, ExxonMobil, Shell, Equilon, ChevronTexaco, Nalco Energy Services Division, Champion Technologies, National Science Foundation Grant (CTS981727), and the NSF Graduate Research Fellowship Program. We acknowledge Darlene Mahlow at the University of Alberta for performing combustion elemental analyses on the asphaltene and resin samples. This work benefited from the use of facilities in the Intense Pulsed Neutron Source and the Chemistry Division, which is funded by the U. S. Department of Energy, Office of Basic Energy Sciences under contract W-31-109-ENG-38 to the University of Chicago. We would particularly like to thank Pappannan Thiyagarajan and Denis Wozniak of the Intense Pulsed Neutron Source Division at Argonne National Laboratory for their assistance with the SAND instrument. We would also like to thank Matthew B. Smith, M. Lupe Marques, and Vincent Verruto for helping with the sample preparation and SANS data collection.

5.6 References

1. P. C. Hiemenz, *Principles of Colloid and Surface Chemistry*; Marcel Dekker: New York, 1977.
2. M. Casselyn, J. Perez, A. Tardieu, P. Vachette, J. Witz, H. Delacroix, "Spherical plant viruses: interactions in solution, phase diagrams and crystallization of brome mosaic virus," *Acta Crystallographica Section D-Biological Crystallography*, 2001, **57**: p. 1799-1812.

3. A. Tardieu, F. Bonnete, D. S. Finet, D. Vivares, "Understanding salt or PEG induced attractive interactions to crystallize biological macromolecules," *Acta Crystallographica Section D-Biological Crystallography*, 2002, **58**: p. 1549-1553.
4. A. George, W. W. Wilson, "Predicting Protein Crystallization from a Dilute-Solution Property," *Acta Crystallographica Section D-Biological Crystallography*, 1994, **50**: p. 361-365.
5. A. George, Y. Chiang, B. Guo, A. Arabshahi, Z. Cai, W. W. Wilson, Second virial coefficient as predictor in protein crystal growth, *in* "Macromolecular Crystallography, Pt A" Eds.), 1997; pp 100-110.
6. B. L. Neal, D. Asthagiri, O. D. Velev, A. M. Lenhoff, E. W. Kaler, "Why is the osmotic second virial coefficient related to protein crystallization?," *Journal of Crystal Growth*, 1999, **196**(2-4): p. 377-387.
7. O. D. Velev, E. W. Kaler, A. M. Lenhoff, "Protein interactions in solution characterized by light and neutron scattering: Comparison of lysozyme and chymotrypsinogen," *Biophysical Journal*, 1998, **75**(6): p. 2682-2697.
8. D. Vivares, F. Bonnete, "X-ray scattering studies of *Aspergillus flavus* urate oxidase: towards a better understanding of PEG effects on the crystallization of large proteins," *Acta Crystallographica Section D-Biological Crystallography*, 2002, **58**: p. 472-479.
9. F. Bonnete, D. Vivares, "Interest of the normalized second virial coefficient and interaction potentials for crystallizing large macromolecules," *Acta Crystallographica Section D-Biological Crystallography*, 2002, **58**: p. 1571-1575.
10. D. Chillura-Martino, R. Triolo, J. B. McClain, J. R. Combes, D. E. Betts, D. A. Canelas, J. M. DeSimone, E. T. Samulski, H. D. Cochran, J. D. Londono, "Neutron scattering characterization of homopolymers and graft-copolymer micelles in supercritical carbon dioxide," *Journal of Molecular Structure*, 1996, **383**(1-3): p. 3-10.
11. E. De Luca, R. W. Richards, I. Grillo, S. M. King, "Molecular characterization of a hyperbranched polyester. II. Small-angle neutron scattering," *Journal of Polymer Science Part B-Polymer Physics*, 2003, **41**(12): p. 1352-1361.
12. D. Li, B. X. Han, Q. Huo, J. Wang, B. Z. Dong, "Small-angle X-ray scattering by dilute solution of bisphenol A polycarbonate during adding antisolvent CO₂," *Macromolecules*, 2001, **34**(14): p. 4874-4878.
13. D. Li, B. X. Han, Z. M. Liu, J. Liu, X. G. Zhang, S. G. Wang, X. F. Zhang, J. Wang, B. Z. Dong, "Effect of gas antisolvent on conformation of polystyrene in toluene:

- Viscosity and small-angle X-ray scattering study," *Macromolecules*, 2001, **34**(7): p. 2195-2201.
14. D. Li, Z. M. Liu, B. X. Han, G. Y. Yang, Z. H. Wu, Y. Liu, B. Z. Dong, "Small-angle X-ray scattering study on the conformation of polystyrene in compressed CO₂-tetrahydrofuran mixtures," *Macromolecules*, 2000, **33**(21): p. 7990-7993.
 15. R. Giordano, G. Maisano, J. Teixeira, "SANS studies of octyl-beta-glucoside and glycine micellar solutions," *Journal of Applied Crystallography*, 1997, **30**(2): p. 761-764.
 16. S. J. Henderson, "Measurement of the second virial coefficient of C-60 in CS₂ solution from small-angle neutron scattering," *Langmuir*, 1997, **13**(23): p. 6139-6145.
 17. R. E. Overfield, E. Y. Sheu, S. K. Sinha, K. S. Liang, "SANS Study of Asphaltene Aggregation," *Fuel Science & Technology International*, 1989, **7**(5-6): p. 611-624.
 18. J. N. Roux, D. Broseta, B. Deme, "SANS study of asphaltene aggregation: Concentration and solvent quality effects," *Langmuir*, 2001, **17**(16): p. 5085-5092.
 19. S. Peramanu, B. B. Pruden, P. Rahimi, "Molecular weight and specific gravity distributions for athabasca and cold lake bitumens and their saturate, aromatic, resin, and asphaltene fractions," *Ind. Eng. Chem. Res.*, 1999, **38**(8): p. 3121-3130.
 20. H. W. Yarranton, H. Alboudwarej, R. Jakher, "Investigation of asphaltene association with vapor pressure osmometry and interfacial tension measurements," *Ind. Eng. Chem. Res.*, 2000, **39**(8): p. 2916-2924.
 21. D. Espinat, E. Rosenberg, M. Scarsella, L. Barre, D. Fenistein, D. Broseta, Colloidal Structural Evolution from Stable to Flocculated State of Asphaltene Solutions and Heavy Crudes, in "Structures and Dynamics of Asphaltenes" (O. C. Mullins and E. Y. Sheu, Eds.), Plenum Press, New York, 1998; pp 145-201.
 22. B. H. Zimm, "The Scattering of Light and the Radial Distribution Function of High Polymer Solutions," *Journal of Chemical Physics*, 1948, **16**(12): p. 1093-1099.
 23. K. L. Gawrys, G. A. Blankenship, P. K. Kilpatrick, "Solvent entrainment in and flocculation of asphaltenic aggregates probed by small-angle neutron scattering," *Langmuir*, submitted.
 24. Y. Bouhadda, D. Bendedouch, E. Sheu, A. Krallafa, "Some preliminary results on a physico-chemical characterization of a Hassi Messaoud petroleum asphaltene," *Energy & Fuels*, 2000, **14**(4): p. 845-853.
 25. D. A. Storm, E. Y. Sheu, "Rheological Studies of Ratawi Vacuum Residue at 366-K," *Fuel*, 1993, **72**(2): p. 233-237.

26. E. Y. Sheu, M. M. Detar, D. A. Storm, "Rheological Properties of Vacuum Residue Fractions in Organic-Solvents," *Fuel*, 1991, **70**(10): p. 1151-1156.
27. P. M. Spiecker, K. L. Gawrys, C. B. Trail, P. K. Kilpatrick, "Effects of petroleum resins on asphaltene aggregation and water-in-oil emulsion formation," *Colloids and Surfaces A: Physicochem. Eng. Aspects*, 2003, **220**(1-3): p. 9-27.
28. C. Bardon, L. Barre, D. Espinat, V. Guille, M. H. Li, J. Lambard, J. C. Ravey, E. Rosenberg, T. Zemb, "The colloidal structure of crude oils and suspensions of asphaltenes and resins," *Fuel Science & Technology International*, 1996, **14**(1-2): p. 203-242.
29. P. M. Spiecker, K. L. Gawrys, P. K. Kilpatrick, "Aggregation and solubility behavior of asphaltenes and their subfractions," *J. Colloid Interf. Sci.*, 2003, **267**(1): p. 178-193.
30. K. L. Gawrys, G. A. Blankenship, P. K. Kilpatrick, "On Distribution Functions of Chemical Properties and Aggregation of Solubility Fractions in Asphaltenes," *Energy & Fuels*, submitted.
31. K. L. Gawrys, P. K. Kilpatrick, "Asphaltenic aggregates are polydisperse oblate cylinders," *Journal of Colloid and Interface Science*, submitted.
32. J. S. Pedersen, "Form factors of block copolymer micelles with spherical, ellipsoidal and cylindrical cores," *Journal of Applied Crystallography*, 2000, **33**(1): p. 637-640.
33. A. Guinier, G. Fournet, *Small Angle Scattering of X-rays*; John Wiley & Sons: New York, 1955.
34. E. Y. Sheu, "Polydispersity Analysis of Scattering Data from Self-Assembled Systems," *Physical Review A*, 1992, **45**(4): p. 2428-2438.
35. A. Isihara, "Determination of Molecular Shape by Osmotic Measurement," *Journal of Chemical Physics*, 1950, **18**(11): p. 1446-1449.

Table 5.1 Elemental composition (atomic) of asphaltenes and resins.

Solute	H/C	N/C	S/C	O/C
HO1 asph	1.29	0.0216	0.0405	0.0200
HO2 asph	1.22	0.0208	0.0319	0.0203
GC asph	1.09	0.0129	0.0292	0.0380
AH asph	1.18	0.0106	0.0377	0.0149
B6f46 asph	1.29	0.0210	0.0329	0.0277
B6 resin	1.51	0.0160	0.0325	0.0187
HO2 resin	1.48	0.0168	0.0349	0.0199
AFR resin	1.50	0.0055	0.0028	0.0013
β -cholanolic acid (CA)	1.67	--	--	0.0833

Table 5.2 Summary of aggregate size parameters for HO1 asphaltenes in toluene as a function of concentration.

$\phi_{\text{asphaltene}}$	I_0 (cm ⁻¹)	R_{avg} (Å)	σ_R (Å)	L (Å)	I_{incoh} (cm ⁻¹)	χ^2	R_G (Å)
0.0385 ± 0.0003	5.85 ± 0.02	45.6 ± 0.3	14.3 ± 0.1	20.9 ± 0.1	0.069 ± 0.001	18.72	48 ± 1
0.0178 ± 0.0005	3.18 ± 0.02	49.4 ± 0.5	15.5 ± 0.2	19.9 ± 0.2	0.053 ± 0.001	9.91	52 ± 1
0.0134 ± 0.0004	2.69 ± 0.02	51.8 ± 0.5	16.4 ± 0.1	18.4 ± 0.2	0.050 ± 0.001	7.35	54 ± 1
0.0092 ± 0.0004	1.77 ± 0.01	50.3 ± 0.6	15.7 ± 0.2	17.0 ± 0.3	0.046 ± 0.001	4.74	52 ± 2
0.0046 ± 0.0004	0.96 ± 0.01	51.8 ± 0.9	16.2 ± 0.4	19 ± 1	0.045 ± 0.001	4.71	54 ± 4
0.0023 ± 0.0004	0.51 ± 0.01	52 ± 1	16.7 ± 0.2	19 ± 1	0.046 ± 0.001	2.83	55 ± 4

Table 5.3 Summary of aggregate molar masses, second virial coefficients, and percent solvent entrainment values for mixtures of asphaltenes and resins in various solvents.

Solute	Solute Conc. (% wt.)	Dopant	Solvent	entrainment (% vol.)	$\langle R_G^2 \rangle^{1/2}$ (Å)	$\langle M \rangle$ (kDa)	A_2 (measured) (mol cm ³ /g ²)	A_2 (excluded) (mol cm ³ /g ²)
HO2 asph	0.5-4	--	40:60 H:T	39	69 ± 2	297 ± 7	-5x10 ⁻⁶ ± 2x10 ⁻⁶	1.1x10 ⁻⁵ ± 1x10 ⁻⁶
HO1 asph	0.25-4	--	Toluene	41	52 ± 3	183 ± 5	3.3x10 ⁻⁵ ± 8x10 ⁻⁶	2.2x10 ⁻⁵ ± 5x10 ⁻⁶
HO2 asph	0.5-4	--	90:10 T:MeOD	43	44 ± 2	101 ± 2	1.5x10 ⁻⁵ ± 5x10 ⁻⁶	3.2x10 ⁻⁵ ± 5x10 ⁻⁶
HO1 asph	0.4-4	B6 resin (R/A=1)	Toluene	27	40 ± 2	43 ± 3	1.0x10 ⁻⁴ ± 2x10 ⁻⁵	1.6x10 ⁻⁴ ± 2x10 ⁻⁵
HO1 asph	0.5-4	B6 resin (R/A=5)	Toluene	30	22 ± 4	30 ± 20	6x10 ⁻⁴ ± 1x10 ⁻⁴	6x10 ⁻⁴ ± 4x10 ⁻⁴
HO1 asph	0.4-1	CA (R/A=2)	Toluene	10	50 ± 4	46 ± 3	2.6x10 ⁻⁴ ± 7x10 ⁻⁵	2.3x10 ⁻⁴ ± 4x10 ⁻⁵
B6 resin	0.5-10	--	40:60 HT	21	17 ± 2	4.9 ± 0.1	2.1x10 ⁻⁴ ± 5x10 ⁻⁵	1.0x10 ⁻³ ± 2x10 ⁻⁴
HO2 resin	1-10	--	Toluene	24	18 ± 2	6.6 ± 0.8	9x10 ⁻⁴ ± 2x10 ⁻⁴	9x10 ⁻⁴ ± 2x10 ⁻⁴
AFR resin	0.5-10	--	Toluene	26	16 ± 2	5.3 ± 0.1	6.7x10 ⁻⁴ ± 5x10 ⁻⁵	1.0x10 ⁻³ ± 3x10 ⁻⁴
AH asph	0.5-3	--	Toluene	36	48 ± 2	104 ± 7	-3x10 ⁻⁵ ± 2x10 ⁻⁵	2.6x10 ⁻⁵ ± 3x10 ⁻⁶
GC asph	0.5-2	--	Toluene	36	57 ± 3	150 ± 10	-4x10 ⁻⁵ ± 2x10 ⁻⁵	2x10 ⁻⁵ ± 1x10 ⁻⁵
HO2 asph	0.025-1	--	Toluene	39	56 ± 3	190 ± 10	4x10 ⁻⁵ ± 4x10 ⁻⁵	1.2x10 ⁻⁵ ± 8x10 ⁻⁶
B6f46 asph	0.05-1	--	Toluene	40	88 ± 2	630 ± 10	1x10 ⁻⁶ ± 3x10 ⁻⁶	5.8x10 ⁻⁶ ± 5x10 ⁻⁷

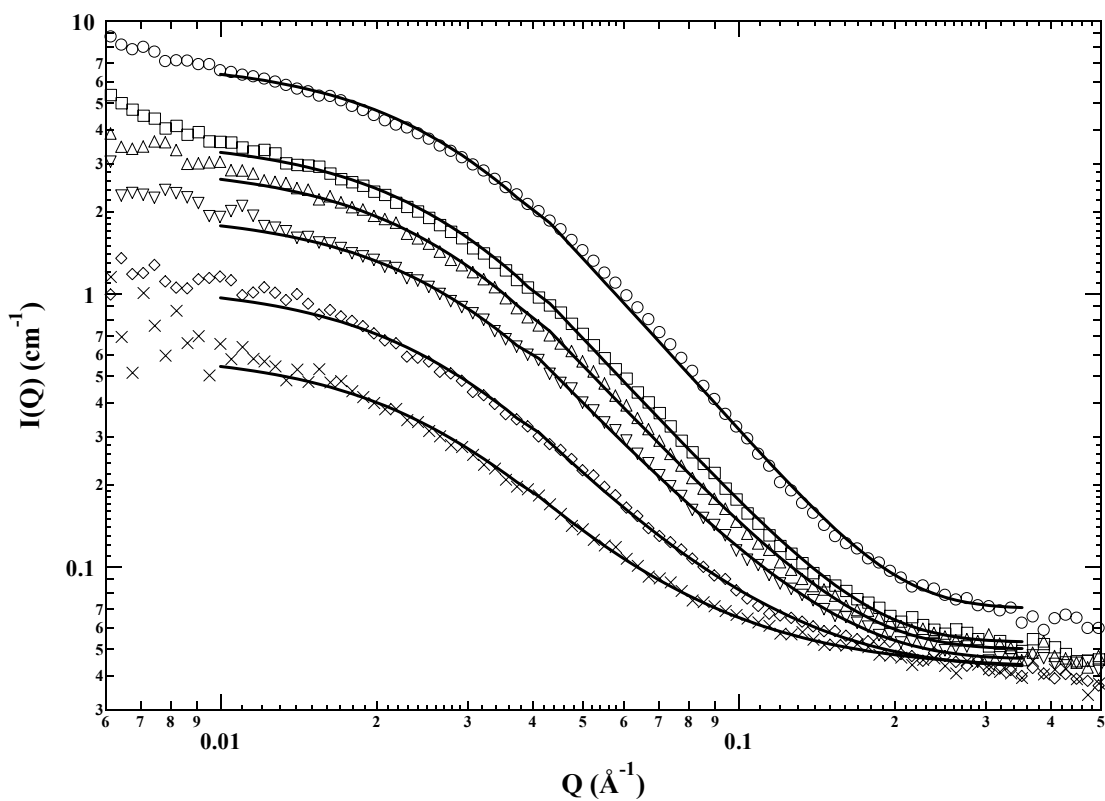


Figure 5.1 SANS scattering curves for HO1 asphaltenes in d-toluene as a function of concentration: (○) 4.38 % w/w, (□) 1.98 % w/w, (△) 1.49 % w/w, (▽) 1.02 % w/w, (◇) 0.51 % w/w, and (x) 0.25 % w/w. Solid lines represent fits to polydisperse radius cylinder model.

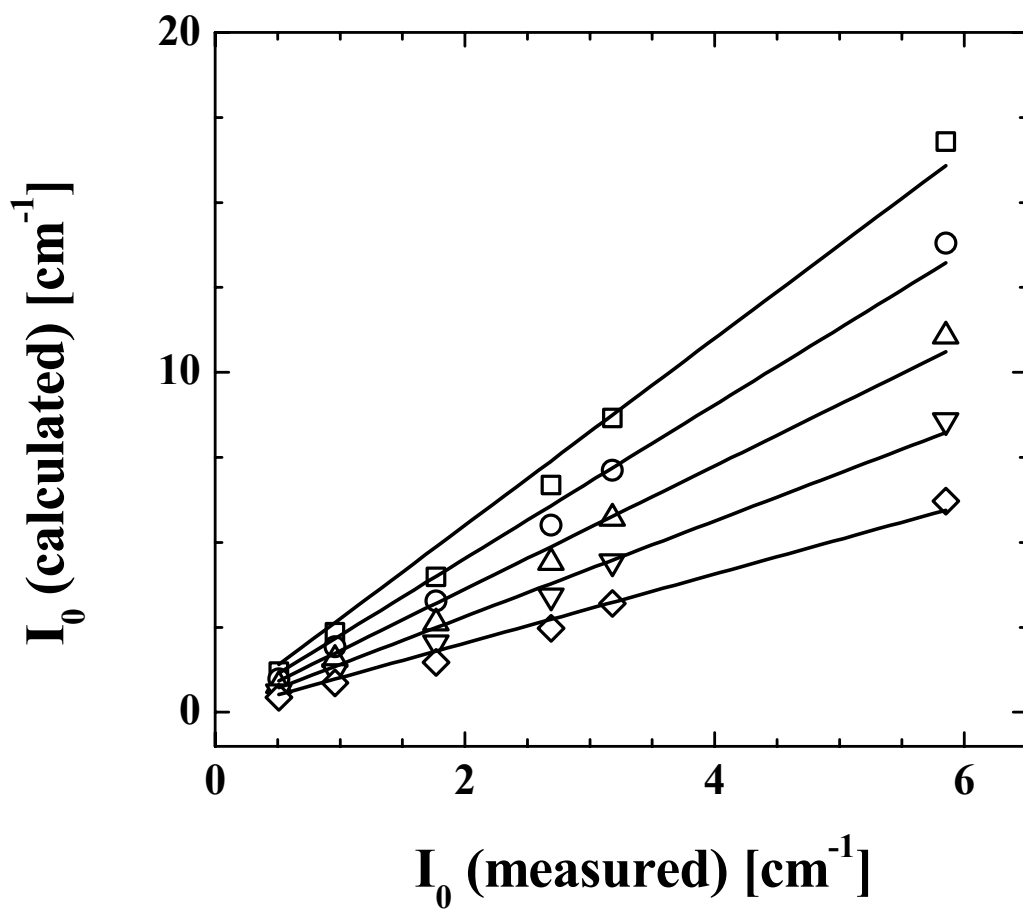


Figure 5.2 Comparison of calculated I_0 values (Equation 10) with those obtained from polydisperse cylinder fits for a concentration series of HO1 asphaltenes in d-toluene assuming various values of solvent entrainment. Legend: (□) no entrainment, slope = 2.75; (○) 10 % (v/v), slope = 2.26; (△) 20 % (v/v), slope = 1.81; (▽) 30 % (v/v), slope = 1.41; and (◇) 41 % (v/v), slope = 1.02.

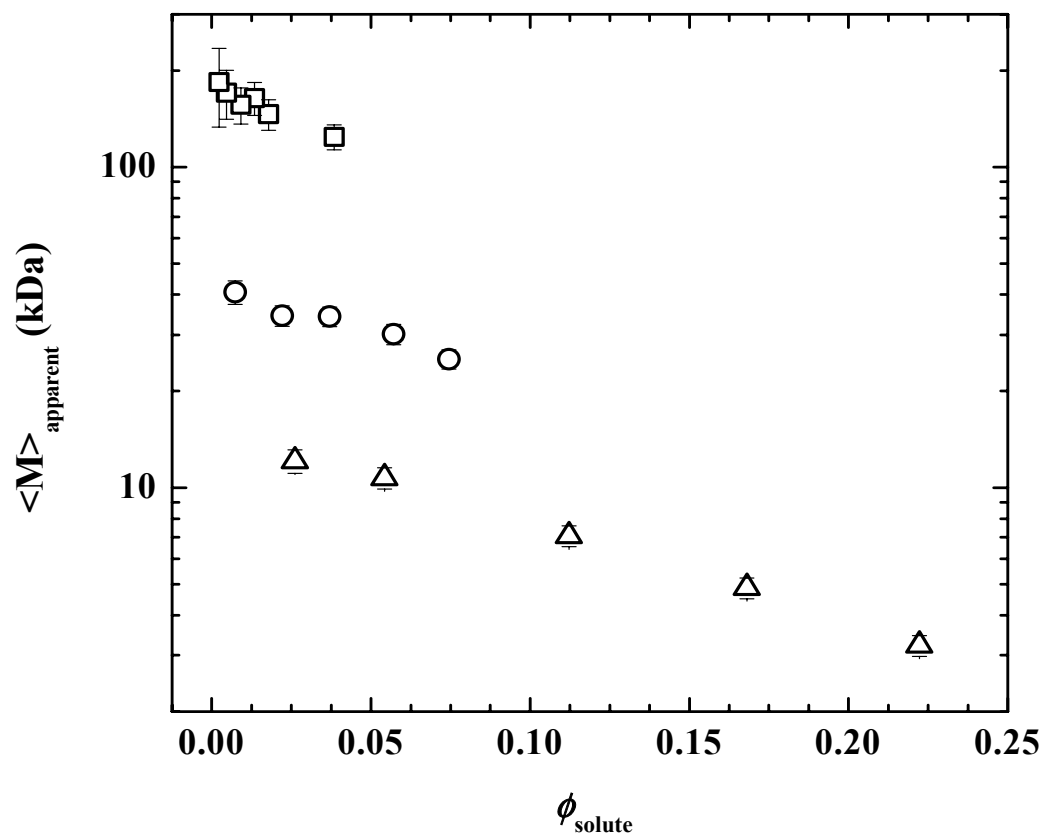


Figure 5.3 Concentration dependence of apparent molar mass (Equation 14) for mixtures of HO1 asphaltenes and B6 resins in d-toluene at various resin: asphaltene mass ratios (R/A). Legend: (\square) no resins; (\circ) R/A = 1.02; (\triangle) R/A = 4.94.

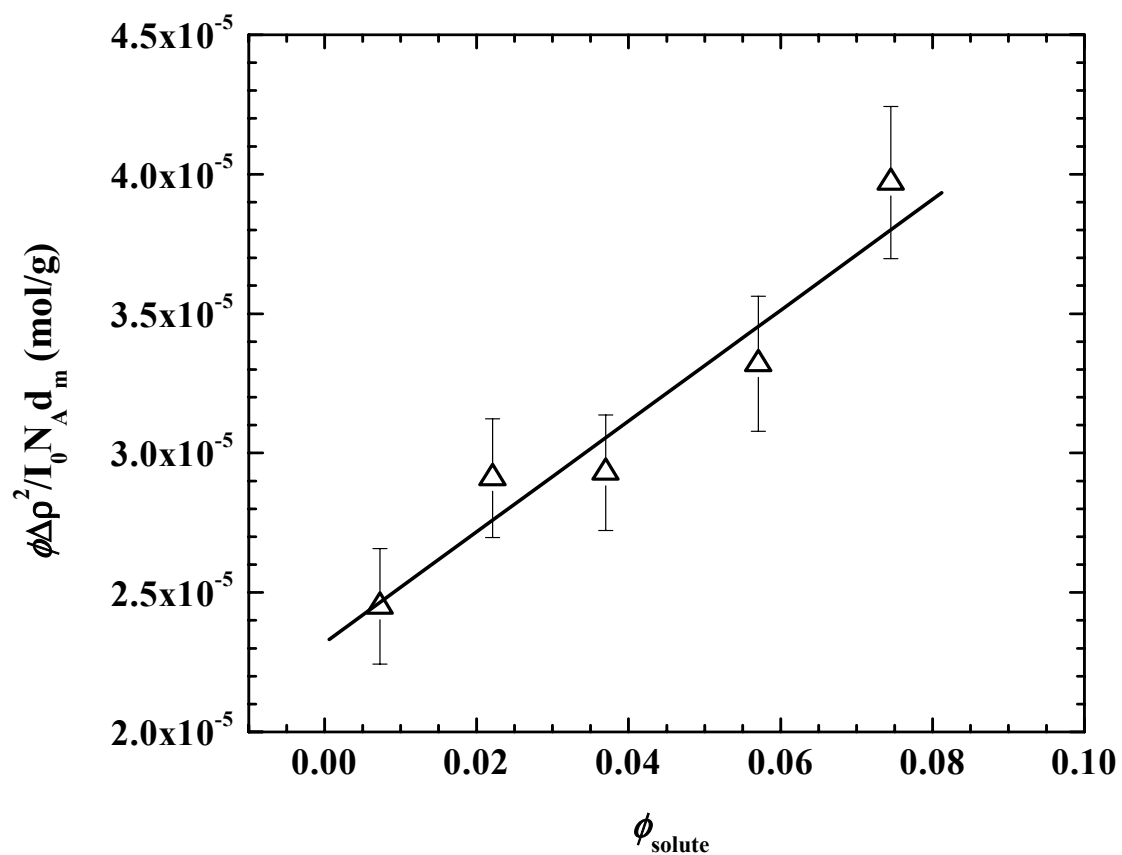


Figure 5.4 Second virial determination for mixtures of HO1 asphaltenes and B6 resins in d-toluene ($R/A = 4.94$). Parameters for best linear fit (solid line) through the data: slope = $2.0 \times 10^{-4} \pm 4 \times 10^{-5}$, intercept = $2.3 \times 10^{-5} \pm 2 \times 10^{-6}$, $R^2 = 0.9632$.

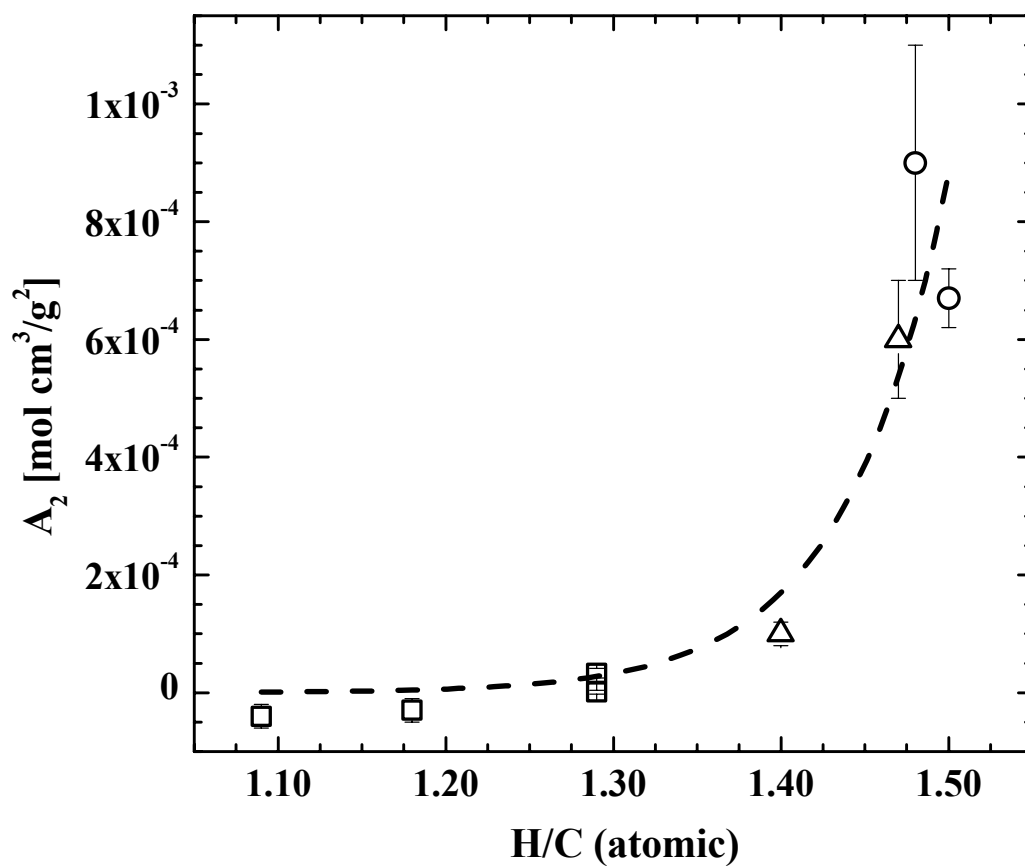


Figure 5.5 Correlation of A_2 values to atomic H/C ratio for (\square) asphaltenes, (\circ) resins, and (\triangle) mixtures of asphaltenes and resins in d-toluene. The dashed line represents the best fit of the data to an exponential function.

**Estimation of the Three-Dimensional Solubility Parameters for Polyaromatic
Compounds by UV-Vis Spectroscopy**

Keith L. Gawrys, George Blankenship, and Peter K. Kilpatrick

ABSTRACT

The ability to predict solute solubility in a binary solvent system has a wide range of practical applications (e.g., solvent selection for paints and coatings, refrigerants, polymers, etc.). In this work, the solubility of 9-anthracenecarboxylic acid (ACA) and phenanthridine (PHD) in various binary solvent mixtures was determined by UV-vis absorption spectroscopy. The solubility results were fit to a thermodynamic model based on regular solution theory with a Flory-Huggins correction for excess entropy of mixing. The three-dimensional solubility parameter concept of Hansen was incorporated to account for contributions from dispersion, polar, and hydrogen bond interactions. The solubility parameter model provided accurate predictions of ACA and PHD solubility in many binary solvent mixtures with less than 30 % error, but the predictive capability of the model decreased significantly when the polar and/or hydrogen-bonding contributions to the solvent solubility parameter deviated significantly from that of the solute. There was lower overall error in the solubility predictions for PHD compared to ACA because, on average, the Hansen partial solubility parameters for PHD more closely matched the range of partial solubility parameters found in the binary solvent mixtures (i.e., the solubility of PHD was generally higher than ACA in the selected solvents). Additional experiments measured the solubility behavior of a multi-component solvent mixture of ACA and PHD in 2-butanol. The results suggested the need to modify the existing model to account for solute-solute complexation effects.

CHAPTER 6

ESTIMATION OF THE THREE-DIMENSIONAL SOLUBILITY PARAMETERS FOR POLYAROMATIC COMPOUNDS BY UV-VIS SPECTROSCOPY

6.1 Introduction

The use of multi-component solubility parameters to predict the solubility behavior of polyaromatic compounds has wide practical application in several key industries. For example, solubility parameters are used in the paintings and coatings industry to select solvents, predict environmental stress cracking in paint plasticizers, and for predicting compatibility of polymers and pigments in coating formulations [1,2]. Multicomponent solubility parameters are also used in the petroleum industry to predict solvent conditions for asphaltene deposition in pipelines [3-5]. Applications of multi-component solubility parameters in the pharmaceutical industry include the modeling of drug delivery and adsorption in the digestive tract and the adhesion of film coatings to the active drug ingredient in pill tablets [6,7].

In this paper, the solubility behaviors of two polyaromatic compounds, 9-anthracenecarboxylic acid (ACA) and phenanthridine (PHD), are studied that may serve as simple model molecules for petroleum asphaltenes or for organic dyes and pigments in the textile industry. Asphaltenes comprise the most polar fraction of crude oil and consist of polyaromatic condensed rings with short aliphatic side chains and polar heteroatom-containing functional groups [8-12]. Asphaltenes are polydisperse in terms of chemical composition, functionality, and distribution of chemical functional groups. While debate exists over the molecular size of asphaltene monomers, typical molecular weights values

obtained from vapor pressure osmometry are on the order of 4000 amu [12] and fluorescence depolarization measurements range from 500 to 1000 amu [13]. Molecular structures of ACA, PHD, and a representative asphaltene molecule with molecular weight of 1093 amu are shown in Figure 6.1. While the molecular weight of ACA and PHD are much smaller than that of typical asphaltenes, there are some similarities in terms of aromaticity and polar functionality. For example, FTIR and XANES spectroscopy reveal that asphaltenes contain polar functional groups, such as carboxylic acids, carbonyls, phenols, pyrroles, and pyridines, that are capable of participating in proton donor-acceptor interactions [14-16]. Sjöblom and coworkers used diffuse reflectance FTIR to show that the interfacially active components of fractionated asphaltenes contained significant concentrations of acidic and open chain carbonyl groups that introduce a strong hydrogen-bonding contribution to the mechanical film strength and prevent water droplet coalescence [17].

The objective of this study is to develop an experimental method and apply an existing thermodynamic model to accurately predict the solubility of pure solutes in binary mixtures, with the intention of extending these analyses to multi-component solute mixtures, such as petroleum asphaltenes. Here, a UV-vis spectroscopic technique was developed to measure the solubility of ACA and PHD in several binary solvent mixtures. The solubility of ACA and PHD in the solvent mixtures was then fit to a thermodynamic model based on regular solution theory with corrections for excess entropy of mixing to calculate partial solubility parameters describing various intermolecular forces (i.e., dispersion, polar, and hydrogen-bonding interactions). Knowledge of the partial solubility parameters should allow the prediction of the pure solute solubility in a large number of multi-component solvents.

6.2 Theory

6.2.1 Solubility Parameter Theory

Hildebrand and Scott first introduced the solubility parameter (δ) concept in 1964, although the previous work of Scatchard et al. was contributory to the development [18,19]. Scatchard derived a quantitative relationship to predict the energy of mixing (ΔU^m) for nonelectrolytes in nonpolar solutions:

$$\Delta U^m = (x_1 V_1 + x_2 V_2) \left[\left(\frac{\Delta U^v}{V_1} \right)^{1/2} - \left(\frac{\Delta U^v}{V_2} \right)^{1/2} \right]^2 \phi_1 \phi_2 \quad (1)$$

where ΔU^v is the internal energy of vaporization, x_i is the mole fraction, V_i is the molar volume, ϕ_i is the volume fraction, and the subscripts refer to the two components of the binary mixture [19]. Hildebrand et al. later rederived the above equation in a more rigorous manner and defined δ_i as $(\Delta U^v/V_i)^{1/2}$ or the work that must be done to overcome the interactions between molecules of a pure substance [18]. Equation 1 assumes no excess volume or entropy of mixing and forms the basis of "regular solution" theory. However, these assumptions are only valid for non-polar components in which dispersion forces dominate the intermolecular interactions. In a regular solution, the activity coefficients of the components are given by [20]:

$$\gamma_1 = \frac{V_1 \phi_2^2}{RT} \exp(\delta_1 - \delta_2)^2; \quad \gamma_2 = \frac{V_2 \phi_1^2}{RT} \exp(\delta_1 - \delta_2)^2 \quad (2)$$

where R is the universal gas constant and T is temperature.

The original form of the regular solution theory cannot be applied to ACA, PHD, and more complex polynuclear aromatic compounds-- such as petroleum asphaltene—due to the polar nature of these solutes. Moreover, the large discrepancy in size between the solute and

solvent molecules violates the assumption of no excess entropy of mixing. Because of chemical similarities between polymers and asphaltenes (i.e., large size and polydispersity of functional groups), variations of Flory-Huggins theory of polymer solutions have been used to predict asphaltene solubility [21-26]. According to Flory-Huggins theory, the chemical potential (μ_a) of a polymer in a solvent is given by:

$$\mu_a - \mu_0 = RT \left[\ln \phi_a + \left(1 - \frac{V_a \phi_s}{V_s} \right) \right] + V_a (\delta_a - \delta_s)^2 \phi_s^2 \quad (3)$$

where μ_0 is a reference chemical potential and the subscripts (a) and (s) represent the polymer and solvent, respectively. In its original application, the theory assumes that polymer precipitation is a reversible process and that pure solute separates from the solution at the flocculation point. The latter assumption has been modified in petroleum applications to assume that a pure asphaltenic phase separates from solution at the onset of precipitation.

Hirschberg et al. were among the first to apply Flory-Huggins theory to asphaltenic systems [21]. To reduce the complexity of the model, they assumed the crude oil was a homogeneous binary mixture of asphaltene and solvent with the precipitated phase consisting of a homogeneous solid. Since asphaltenes are chemically heterodisperse, other studies have used Flory-Huggins theory along with an equation of state to predict fluid properties such as asphaltene molar volume and enthalpy of vaporization [22,24]. Yarranton et al. applied a solubility model based on regular solution theory that included the Flory-Huggins excess entropy of mixing term [25]. In the modified regular solution model, the activity coefficient of the solute (a) is given by:

$$\gamma_a = \exp \left\{ 1 - \frac{V_a \phi_s}{V_s} + \ln \left(\frac{V_a}{V_s} \right) + \frac{V_a \phi_s^2}{RT} (\delta_a - \delta_s)^2 \right\} \quad (4)$$

Using equation (4) they correlated asphaltene solubility parameters and asphaltene molar volumes to molar mass distributions obtained from interfacial tension measurements and vapor pressure osmometry. Masliyah et al. later applied an extended solubility parameter model containing three-components to predict asphaltene solubility in highly polar solvents [26].

The regular solution theory implies that components with similar solubility parameters will be mutually soluble, but this is not always the case. There are several types of interactions that occur between organic molecules, including London dispersion forces, permanent dipole interactions, dipole-induced-dipole interactions, and Lewis acid/base interactions (e.g., hydrogen-bonding). Since all of these forces contribute to δ to different extents, a similarity of solubility parameters does not assure miscibility. There have been numerous attempts to extend solubility parameter theory to more practical applications, (e.g., solvent selection for paints and coatings, refrigerants, polymers, nutraceuticals, drugs, fullerenes, etc.) by incorporating contributions from polar and/or hydrogen-bonding interactions [2-7,27-36].

Burrell [29] and Beerbower [30] used the overall solubility parameter along with correlations for a hydrogen-bonding parameter. Blanks and Prausnitz [31] split the energy of vaporization of polar fluids into polar and nonpolar contributions. The nonpolar parameter was estimated from experimental measurements of the energy of vaporization of a homomorph (i.e., a saturated hydrocarbon that closely resembles it in size and shape). The polar parameter was calculated from the difference in the squares of the overall solubility parameter and the nonpolar parameter. The model was limited to polymer systems without the ability to hydrogen bond. Crowley et al. [32] introduced a three-dimensional system for

polymer phase diagrams, but used arbitrary axes (i.e., δ , the dipole moment, and a spectroscopic parameter for hydrogen-bonding). Hansen introduced the perhaps most popular convention for three-dimensional solubility parameters by assuming that the total energy of vaporization is the sum of the energies of vaporization arising from dispersion, polar, and hydrogen-bonding forces [2,33]:

$$\Delta E^v = \Delta E_d^v + \Delta E_p^v + \Delta E_h^v \quad (5)$$

This allowed the overall solubility parameter to be written as the vector sum of the various contributions:

$$\delta^2 = \delta_d^2 + \delta_p^2 + \delta_h^2 \quad (6)$$

where the subscripts (d), (p), and (h) represent contributions from dispersion, polar, and hydrogen-bonding, respectively. Several methods have been used to calculate Hansen's solubility parameters for a given solvent [37-39]. For example, the δ_d parameter may be calculated from the energy of vaporization of a homomorph [31]. The remaining contribution to ΔE^v is attributed to polar and hydrogen-bonding forces, whose individual contributions are isolated by fitting solubility results to a large number of solvents. Since nonpolar interactions are dependent on the polarizability of a substance, Koenhen et al. [39] developed a simple correlation relating δ_d to refractive index for several solvents. Polar contributions have been estimated through correlations with the dipole moment [37] and through group contribution methods [40]. Similarly, the effect of hydrogen-bonding is often obtained by subtraction of the polar and dispersion contributions from the total energy of vaporization or through group contribution methods.

6.2.2 Three-Dimensional Solubility Parameters

Here, the three-dimensional solubility parameters for the solutes will be calculated by a method called the extended Hansen solubility approach as described in the work by Martin et al. [41]. An extension of regular solution theory to describe polar and hydrogen-bonding interactions, the method relates the mole fraction solubility of the solute (x_a) to the Hansen partial solubility parameters by:

$$\frac{x_a^{\text{ideal}}}{x_a} = \exp \left\{ \frac{V_a \phi_s^2}{RT} \left[(\delta_{da} - \delta_{ds})^2 + (\delta_{pa} - \delta_{ps})^2 + (\delta_{ha} - \delta_{hs})^2 \right] \right\} \quad (7)$$

where x_a^{ideal} is the mole fraction ideal solubility and the subscripts (a) and (s) represent the solute and solvent, respectively. The mole fraction ideal solubility (x_a^{ideal}) for a solute is calculated from knowledge of the enthalpy of fusion (ΔH^{fus}) and triple point temperature (T_t) by [20]:

$$-\ln(x_a^{\text{ideal}}) = \frac{\Delta H^{\text{fus}}}{RT_t} \left(\frac{T_t}{T} - 1 \right) - \frac{\Delta C_p}{R} \left(\frac{T_t}{T} - 1 \right) + \frac{\Delta C_p}{R} \ln \left(\frac{T_t}{T} \right) \quad (8)$$

where ΔC_p is the change in the heat capacity from the solid to liquid phase. Since there is usually little difference between the triple point temperature and normal melting point temperature (T_m) of solids and between the enthalpies of fusion at these temperatures, it is reasonable to substitute T_m for T_t . Furthermore, the second and third terms on the right side of equation (5) are often neglected in the estimation of x_a^{ideal} due to lack of physical property data for ΔC_p and the tendency of these terms to cancel one another, especially when T approaches T_t . Equation (8) may then be simplified to:

$$-\ln(x_a^{\text{ideal}}) = \frac{\Delta H_m^{\text{fus}}}{RT_m} \left(\frac{T_m}{T} - 1 \right) \quad (9)$$

As previously described, regular solution theory is valid for mixtures in which the excess entropy of mixing is equal to zero. For the case of polynuclear aromatic compounds similar to ACA and PHD, the molecular size difference between the solvent and solute may be significant. The non-zero excess entropy of mixing is thus accounted for with the inclusion of a Flory-Huggins term in equation (7) [26]:

$$\frac{x_a^{\text{ideal}}}{x_a} = \exp \left\{ 1 - \frac{V_a \phi_s}{V_s} + \ln \left(\frac{V_a}{V_s} \right) + \frac{V_a \phi_s^2}{RT} \left[c_1 (\delta_{da} - \delta_{ds})^2 + c_2 (\delta_{pa} - \delta_{ps})^2 + c_3 (\delta_{ha} - \delta_{hs})^2 \right] \right\} \quad (10)$$

The coefficients c_1 , c_2 , and c_3 are also included in equation (10) as experimentally determined values, unique to the given solute, that effectively weight the intermolecular interactions. For example, the coefficient c_1 describes the fraction of nearest neighbor molecules upon which the dispersion forces act. Since dispersion interactions are omnidirectional and experienced by all parts of the molecules, the value of c_1 is assumed unity. Not all nearest neighbor molecules experience polar and hydrogen-bonding interactions; therefore, the coefficients c_2 and c_3 are allowed to vary between 0 and 1. After assuming $c_1 = 1$ and expanding the polynomials in equation (10), the multiple linear regression equation for determining solute solubility is given by:

$$\frac{RT}{V_a \phi_s^2} \left[\ln \left(x_a^{\text{ideal}} / x_a \right) - 1 + \frac{V_a \phi_s}{V_s} + \ln \left(\frac{V_a}{V_s} \right) \right] - \delta_{ds}^2 = c_2 \delta_{ps}^2 + c_3 \delta_{hs}^2 + A \delta_{ds} + B \delta_{ps} + C \delta_{hs} + D \quad (11)$$

where

$$A = -2\delta_{da}; B = -2c_2 \delta_{pa}; C = -2c_3 \delta_{ha}; D = c_0 + \delta_{da}^2 + c_2 \delta_{pa}^2 + c_3 \delta_{ha}^2 \quad (12)$$

and c_0 is a constant term from the regression equation that should approach zero [41]. The inputs of the regression equation include the values of the Hansen partial solubility parameters of the binary solvent and their squares, as well as the experimental solubility data

shown as the left side of equation (11). The output of the multiple regression provides the parameters c_2 , c_3 , A, B, C, and D from which the Hansen partial solubility parameters of the solute (i.e., δ_{da} , δ_{pa} , δ_{ha}) are obtained.

6.3 Experimental

6.3.1 Materials

Prior to performing the solubility experiments, 9-anthracenecarboxylic acid (ACA, 98 %, Aldrich) was recrystallized from ethanol (HPLC, Fisher Scientific) and dried at 70°C in a vacuum oven. Phenanthridine (PHD, 98 %) was used as obtained from Aldrich. The solvents butyl benzoate (BBZ, 99 %), n-butyl butyrate (NBB, 98 %), 2-butanol (IBA, 99+ %), dipropyl ketone (DPK, 98 %), 1-methyl naphthalene (MN, 95 %), and propylene carbonate (PC, 99 %) were obtained from Aldrich. HPLC grade toluene (T), heptane (H), and 2-propanol (IPA) were obtained from Fisher Scientific. Methylbenzoate (MB, 99 %) was obtained from Lancaster. Anisole (AN, 99 %) was obtained from Acros.

6.3.2 Physical Property Data

The Hansen partial solubility parameters for the solvents used in the solubility measurements are shown in Table 6.1 [40]. Values of V_s for the binary solvent mixture were calculated from the mole fraction weighted values of the pure solvent. Similarly, the values of the Hansen partial solubility parameters of the solvents were assumed volume fraction additive. The partial molar volume of PHD in the subcooled liquid ($V_a = 156 \text{ cm}^3/\text{mol}$) at 298 K was estimated from density values of the saturated liquid between 380 and 500 K [42]. A comparable value for PHD ($V_a = 151 \pm 3 \text{ cm}^3/\text{mol}$) was estimated using a macroscopic

property calculation algorithm provided as part of the ACD/Chemsketch software package [43]. Since the estimates of V_a obtained for PHD by the two methods agreed within 5 %, the software was also used to estimate the partial molar volume of ACA in the subcooled liquid ($V_a = 178 \text{ cm}^3/\text{mol}$). The values of ΔH_m^{fus} , T_m , and x_a^{ideal} at 25°C used for the calculation of the mole fraction solubility ideal solution (equation 9) are shown for PHD and anthracene in Table 6.2 [44,45]. The value of x_a^{ideal} for ACA was not determined because of a lack of phase change data for the solute, but was approximated by the anthracene value.

6.3.3 Solubility Experiments

The UV-vis absorption spectra for ACA and PHD dissolved in 2-butanol were measured on a Shimadzu UV-2101PC UV-vis scanning spectrophotometer (Figure 6.2). Several solutions of varying concentration were prepared for each solute so that the absorption peak at λ_{max} has an absorbance between 0.1 and 1.2. Samples were measured in 1 cm pathlength Suprasil quartz cells. The molar absorptivity of ACA at $\lambda_{\text{max}} = 383.0 \text{ nm}$ was calculated from a Beer-Lambert calibration curve of absorbance versus standard solution concentration (Figure 6.3). Beer-Lambert law describes the relationship between UV spectral response and concentration in dilute solutions:

$$A_{i,\lambda} = \epsilon_{i,\lambda} c_i l \quad (13)$$

where $A_{i,\lambda}$ is the absorbance at wavelength λ , $\epsilon_{i,\lambda}$ is the wavelength dependent molar absorptivity (or molar extinction coefficient), c_i is the solute concentration, and l is the path length of the measurement cell. Beer's law fails in concentrated solutions where $\epsilon_{i,\lambda}$ is no longer constant, but depends on the refractive index of the solution [46]. Molar extinction coefficient values for ACA and PHD at selected wavelengths are shown in Table 6.3.

The solubilities of ACA and PHD were determined in various binary solvent mixtures at 25°C. Saturated solutions were prepared by introducing an excess amount of individual solutes into screw-capped vials containing 2 mL of solvent. To aid in the dissolution and break up the largest solid aggregates, the sealed samples were placed in a sonicator for 5 minutes followed by submersion in a 60°C water bath for 1 hr. The samples were then shaken for an additional 24 hours at 25°C to assure saturation. Each saturated solution was loaded into a 3 mL syringe and plunged through a Whatman glass microfiber filter disk with polypropylene housing (GF/A, 13 mm diameter, 1.6 µm pore size). The filtrate was collected and diluted with a known amount of 2-butanol into the Beer-Lambert regime. UV-vis absorption spectra for the diluted solutions were measured the solute concentration at saturation was determined using the Beer-Lambert calibration curves.

In additional experiments, excess ACA was added to 2-butanol solutions of varying initial PHD concentration ranging from 0 to 5 % (w/w). The above procedure was repeated to determine the ACA concentration at saturation.

6.4 Results and Discussion

6.4.1 Estimation of Solubility Parameters for ACA and PHD

The mole fraction solubility of ACA in various binary solvent mixtures are shown in Figure 6.4a-d. The binary solvent mixtures included: methylnaphthalene (MN) in 2-butanol (IBA), MN in methyl benzoate (MB), dipropyl ketone (DPK) in IBA, butyl benzoate (BBZ) in n-butyl butyrate (NBB), 2-propanol (IPA) in anisole (AN), heptane (H) in toluene (T), and ethyl alcohol (EA) in propylene carbonate (PC). As shown in the figures, a 2- to 4-fold increase in solubility was observed for ACA in solvent blends containing roughly a 50 %

(v/v) mixture of MN:IBA, DPK:IBA, IPA:AN, and EC:PC compared to the single solvent solubilities. Each of these solvent pairs consisted of an alcohol or protic solvent (i.e., EA, IPA, IBA) and a relatively non-protic solvent (i.e., MN, DPK, AN, PC). Thus the major variation in the Hansen partial solubility parameters for these solvent blends occurred in the δ_{hs} parameter (Table 6.1). In particular, the occurrence of the solubility maximum in mixtures of IBA and DPK (Figure 6.4b) indicates the relative importance of hydrogen-bonding interactions in the solubility of ACA. As shown in Table 6.1, the Hansen partial solubility parameters of IBA and DPK only vary in terms of δ_{hs} . Since the solubility maximum in this binary solvent pair was observed in the mixture containing 60 % IBA (v/v), the value of δ_{ha} was estimated as $10.7 \text{ (MPa)}^{1/2}$.

Another solubility maximum was observed in the binary solvent mixture containing NBB and BBZ (Figure 6.4b), which only varied significantly in terms of the δ_{ds} parameter. The value of δ_{da} for ACA was estimated as $17.2 \text{ (MPa)}^{1/2}$, corresponding with the solubility maximum in 60 % BBZ (v/v). The mole fraction solubility of ACA in 60:40 BBZ:NBB (v/v) was ~ 1.2 times the solubility in pure BBZ. In comparison, the mole fraction solubility of ACA in 60:40 IBA:DPK was approximately 2.8 times the solubility in pure DPK. Considering that the value of δ_{ds} ranges between 15.6 to 18.3 $\text{(MPa)}^{1/2}$ in the NBB:BBZ mixtures and approximately 14 to 20 $\text{(MPa)}^{1/2}$ in most normal organic solvents [40], the difference between the dispersion parameters of the solute and solvent is generally no more than 2 to 3 $\text{(MPa)}^{1/2}$. On the other hand, the values of δ_{ps} and δ_{hs} for the solvents used in this study range between 0 to 19 $\text{(MPa)}^{1/2}$. Therefore, the difference between the solute and solvent parameters for these interactions may be much larger, as observed for the binary mixtures of IBA and DPK. This suggests that solvent selection should be dictated more by a

need to match the polar and hydrogen-bonding parameters of the solute, as the difference in the dispersive properties is relatively small in most normal organic solvents. The sensitivity of solute solubility to the polar and hydrogen-bonding parameters of the solvent is most obvious for solutions of ACA in blends of heptane and toluene (Figure 6.4c), where the δ_{ps} and δ_{hs} values range between 0 to 2 (MPa)^{1/2}. The very low solubility of ACA in these solvent blends, as well as the similarly low solubility in MN, suggests that polar and hydrogen-bonding interactions are important to ACA solubility.

Similar analyses may be performed on the solubility curves for PHD in the same binary solvent mixtures (Figure 6.5a-d.). The solubility maximum observed for PHD in mixtures of IBA and DPK (Figure 6.5a.) corresponded with a value of $\delta_{hs} = 8.7$ (MPa)^{1/2}. The solubility of PHD in solvent blends containing NBB and BBZ was maximized in pure BBZ, suggesting that the solvent blend did not bracket the value of δ_{da} for PHD. From this we can infer, that δ_{da} was at least 18.3 (MPa)^{1/2}.

6.4.2 Pure Solute Solubility Modeling

As we have just shown, if a combination of solvents is selected such that each binary solvent mixture only probes one Hansen partial solubility parameter at a time, then it is possible to estimate the Hansen partial solubility parameters of the solute based on a limited amount of experimental data. However, the predictive model described in equation (11) contains regression coefficients (i.e., c_1 , c_2 , and c_3) that effectively weight the contributions of each type of intermolecular interaction. These coefficients are not easy to estimate from the shape of the solubility curves, but rather are calculated after regression of the entire set of solubility data. The mole fraction solubility of ACA in mixtures of heptane and toluene were

so low that they approached the detection limits of the experimental method. Therefore, all solubility data in this binary mixture except pure toluene were excluded from the regression analyses for ACA. The regression analyses for PHD included the solubility data for all of the binary solvent mixtures.

The values of the Hansen partial solubility parameters and the corresponding weighting coefficients for ACA and PHD are provided in Table 6.4. As shown in the table, the estimates of δ_{da} and δ_{ha} obtained for ACA based on the shapes of the solubility curves in IBA:DPK and NBB:BBZ were accurate within 2 %. The estimate of δ_{ha} for PHD was accurate within 5 %, and the assumption of $\delta_{da} > 18.3 \text{ (MPa)}^{1/2}$ was also correct. The values of the weighting coefficients in Table 6.4 suggest that ACA molecules interact with approximately 17 % and 61 % of nearest neighbor solvent molecules through polar and hydrogen-bonding interactions, respectively. Similarly, PHD molecules interact with approximately 32 % and 21 % of nearest neighbor solvent molecules through polar and hydrogen-bonding interactions, respectively. The higher importance of hydrogen-bonding interactions in ACA is expected due to the protic nature of the carboxylic acid group, which is able to both donate and accept protons intermolecularly. On the other hand, the pyridinic nitrogen of PHD is only a proton acceptor. The higher value of δ_{pa} for ACA compared to PHD was likely attributed to the presence of two oxygen atoms in the carboxylic acid group, each with a higher electronegativity than the lone pyridinic nitrogen. As shown in Table 6.4, values of $c_0 = -2.03$ and -13.47 were obtained for ACA and PHD as the constant term from the regression analyses, respectively. Since this parameter does not have a thermodynamic interpretation derived in regular solution theory, it is expected to approach zero [41]. A non-

zero value of the c_0 parameter might suggest that the estimation of the mole fraction ideal solubility was in error.

The values of the mole fraction solubility for ACA in the solvent blends calculated using equation (11) are shown as the solid lines in Figures 6.4a-d. Similar curves showing the calculated mole fraction solubility of PHD are provided in Figures 6.5a-d. As shown in the figures, the model provided relatively accurate predictions solute solubility in some solvent blends, but had large uncertainty in others. The experimental and calculated mole fraction solubilities of ACA in selected solvents with % error values are shown in Table 6.5. The data in Table 6.5 suggests that the % error in the calculated mole fractions increases as one or more of the Hansen partial solubility parameters of the solvent deviate significantly from the solute values. For example, the solvent blend consisting of IBA and DPK only varies in the value of δ_{hs} and has a minimum % error in the solvent blend containing 60 % IBA (v/v). As previously discussed, the hydrogen-bonding parameter for this solvent mixture ($\delta_{hs} = 10.7 \text{ (MPa)}^{1/2}$) was very close to the value calculated in Table 6.4. The absolute error appeared to increase linearly with the square of the difference in the hydrogen-bonding parameter ($\delta_{ha}-\delta_{hs}^2$), as shown in Figure 6.6. In other solvents where more than one solubility parameter varies with the blend composition, the error in the calculated mole fraction appears to trend with the weighted sum of the squared difference in the solubility parameters (i.e., $c_1(\delta_{da}-\delta_{ds})^2 + c_2(\delta_{pa}-\delta_{ps})^2 + c_3(\delta_{ha}-\delta_{hs})^2$). For example, Figure 6.7 correlates the % error in mole fraction solubility to the above solubility contrast term for ACA in mixtures of (●) EA:PC and (□) MN:IBA. These trends in the % error with the solubility contrast suggest that the uncertainty in the model predictions increases in solvents where there is a

significant mismatch in one or more of the solute and solvent Hansen partial solubility parameters.

The same trends in % error with the solubility contrast term were apparent for PHD in Table 6.6, although the overall error in the solubility predictions for PHD is significantly less than the errors for ACA. One reason for the reduced error in PHD is that the Hansen partial solubility parameters of PHD were better bracketed in the selected solvents than ACA, particularly in terms of the polar parameter. For example, the only solvent combination with $\delta_{ps} > \delta_{pa}$ was EA and PC. The polar parameters of all other solvents were significantly lower than δ_{pa} , thus the multiple regression data set was likely biased with these lower parameter values. Additional solubility measurements in more polar solvents are needed to improve the quality of the model fits. The ACA solubility data was also regressed using ten fewer data points than the PHD data. Furthermore, more reliable phase change (Table 6.2) and physical property data were available for PHD to estimate the mole fraction ideal solubility and partial molar volume. These results suggest that a larger number of solvents that probe all ranges above and below the solute solubility parameters are needed to improve the fit qualities.

6.4.3 Solubility of Mixed Solutes

In addition to the pure component solubility data, an attempt was made to predict the solubility of ACA in mixtures containing 2-butanol and varying initial concentrations of PHD ranging from 0 to 5 % (w/w). The mole fraction solubility of ACA was calculated using the previously described UV-visible technique assuming that PHD did not significantly contribute to the absorption spectra in the wavelength range near 381 nm. Figure 6.8 shows the mole fraction solubility plotted versus the initial mole fraction of PHD in 2-butanol. As

shown in the figure, the solubility of ACA increased approximately 10 % as the initial PHD mole fraction increased up to ~ 0.007 . This initial increase in solubility was followed by a significant decrease below the starting value with increasing PHD concentration.

If we assume that the addition of PHD to 2-butanol only affects the composite solubility parameters of the solvent, then the ability of the solvent to dissolve ACA should increase with increasing PHD concentration as all of Hansen partial solubility parameters of the PHD-IBA are changed to values that closer resemble ACA. The solid line in Figure 6.8 represents the model prediction for the solubility of ACA in the mixtures of IBA and PHD. As shown in Table 6.5, the fitting model over-predicted the solubility of ACA in pure 2-butanol by ~ 58 %. The solid line in Figure 6.8 has been shifted vertical to better visualize the expected solubility trend. The observation of a dramatic decrease in ACA solubility at PHD concentrations above $x_{\text{PHD}(\text{initial})} = 0.007$ is inconsistent with the model prediction and suggests that ACA and PHD are interacting in solution to form an associated complex with an independent set of Hansen partial solubility parameters. In order to accurately model the solubility of ACA these mixtures, the extended Hansen solubility approach must be modified to account for solute aggregation. Furthermore, additional single component solute data is needed for ACA in order to improve the solubility prediction in pure 2-butanol.

As previously mentioned, the mole fraction solubility of ACA was determined spectroscopically by assuming that PHD does not absorb near 381 nm. If this assumption is invalid, then the actual mole fraction solubility of ACA will be slightly less than the value determined from the absorbance at 381 nm. Since the values of the ACA mole fractions shown in Figure 6.8 would decrease rather than increase, PHD absorption cannot explain the deviations from the expected solubility behavior.

6.5 Conclusions

A UV-visible spectroscopic method has been developed to determine the mole fraction solubilities of polynuclear aromatic compounds (i.e., ACA and PHD) in various multi-component mixtures. Binary solvent mixtures were selected with a wide range of Hansen partial solubility parameters to probe specific intermolecular interactions between the solvent and solute. For example, one solvent combination was selected to probe dispersion interactions, another to probe hydrogen-bonding interactions, etc. The solubility results were analyzed using the extended Hansen solubility approach, a thermodynamic model based on regular solution theory that includes three solubility parameters representing the work required to overcome specific interactions between the solute and solvent (i.e., dispersion, polar, and hydrogen-bonding interactions). The model also included a Flory-Huggins term to correct for non-zero entropy of mixing.

The solubility parameter model provided accurate fits of PHD solubility in most binary solvent mixtures with less than 30 % error. The model fits were less accurate for ACA, likely due to a fewer number of data points in the regression and a selection of solvents that did not adequately probe the range of polar parameters with values above the polar parameter for ACA. The predictive capability of the model was also observed to decrease when one or more of the Hansen partial solubility parameters of the solvent deviated significantly from that of the solute.

Additional experiments measured the solubility behavior of ACA in a multi-component solvent mixture containing various initial concentrations of PHD in 2-butanol. Assuming that the PHD addition modified the Hansen solubility parameters of the solvent

only, the mole fraction solubility of ACA was expected to increase monotonically with increasing PHD concentration. Instead, the solubility of ACA was observed to initially increase by 10 %, and then decrease dramatically below the starting value. These results suggested the need to modify the existing model to account for solute-solute complexation effects, particularly if it is desirable to apply the model to large aggregate formers, such as petroleum asphaltenes. Furthermore, additional solubility measurements in more polar solvents are needed to improve the accuracy of the model parameters describing ACA solubility.

6.6 Acknowledgements

This research is supported by the Petroleum Environmental Research Forum, ExxonMobil, Shell, Equilon, ChevronTexaco, Nalco Energy Services Division, Champion Technologies, National Science Foundation Grant (CTS981727), the National Science Foundation Graduate Research Fellowship Program, and the National Science Foundation Research Experience for Undergraduates Program. We would also like to thank Amisha Shah and George Blankenship for assistance with the solubility measurements.

6.7 References

1. C. M. Hansen, L. Just, "Prediction of Environmental Stress Cracking in Plastics with Hansen Solubility Parameters," *Ind. Eng. Chem. Res.*, 2001, **40**: p. 21-25.
2. C. M. Hansen, "The Three Dimensional Solubility Parameter - Key to Paint Component Affinities: I. Solvents Plasticizers, Polymers, and Resins," *Journal of Paint Technology*, 1967, **39**(505): p. 104-117.
3. P. Redelius, "Bitumen solubility model using Hansen solubility parameter," *Energy & Fuels*, 2004, **18**(4): p. 1087-1092.

4. R. Karlsson, U. Isacson, "Bitumen structural stability characterization using turbidimetric titration," *Energy & Fuels*, 2003, **17**(6): p. 1407-1415.
5. P. G. Redelius, "Solubility parameters and bitumen," *Fuel*, 2000, **79**(1): p. 27-35.
6. P. Bustamante, M. A. Pena, J. Barra, "The modified extended Hansen method to determine partial solubility parameters of drugs containing a single hydrogen bonding group and their sodium derivatives: benzoic acid/ Na and ibuprofen/Na," *International Journal of Pharmaceutics*, 2000, **194**: p. 117-124.
7. M. Genty, G. Gonzalez, C. Clere, V. Desangle-Gouty, J.-Y. Legendre, "Determination of the passive absorption through the rat intestine using chromatographic indices and molar volume," *European Journal of Pharmaceutical Sciences*, 2001, **12**: p. 223-229.
8. U. Bergmann, H. Groenzin, O. C. Mullins, P. Glatzel, J. Fetzer, S. P. Cramer, "X-ray Raman spectroscopy - A new tool to study local structure of aromatic hydrocarbons and asphaltenes," *Petroleum Science and Technology*, 2004, **22**(7-8): p. 863-875.
9. M. R. Gray, "Consistency of asphaltene chemical structures with pyrolysis and coking behavior," *Energy & Fuels*, 2003, **17**(6): p. 1566-1569.
10. H. Groenzin, O. C. Mullins, S. Eser, J. Mathews, M. G. Yang, D. Jones, "Molecular size of asphaltene solubility fractions," *Energy & Fuels*, 2003, **17**(2): p. 498-503.
11. J. M. Sheremata, M. R. Gray, H. D. Dettman, W. C. McCaffrey, "Quantitative molecular representation and sequential optimization of athabasca asphaltenes," *Energy & Fuels*, 2004, **18**(5): p. 1377-1384.
12. O. P. Strausz, P. Peng, J. Murgich, "About the colloidal nature of asphaltenes and the MW of covalent monomeric units," *Energy & Fuels*, 2002, **16**(4): p. 809-822.
13. H. Groenzin, O. C. Mullins, "Molecular size and structure of asphaltenes from various sources," *Energy & Fuels*, 2000, **14**(3): p. 677-684.
14. M. M. Boduszynski, J. F. McKay, D. R. Latham, "Asphaltenes, Where Are You?," *Proceedings of the Association of Asphalt Paving Technologists*, 1980, **49**: p. 123-143.
15. E. Buenrostro-Gonzalez, S. I. Andersen, J. A. Garcia-Martinez, C. Lira-Galeana, "Solubility/molecular structure relationships of asphaltenes in polar and nonpolar media," *Energy & Fuels*, 2002, **16**(3): p. 732-741.
16. S. Mitrakirtley, O. C. Mullins, J. Vanelp, S. J. George, J. Chen, S. P. Cramer, "Determination of the Nitrogen Chemical Structures in Petroleum Asphaltenes Using

- Xanes Spectroscopy," *Journal of the American Chemical Society*, 1993, **115**(1): p. 252-258.
17. L. Mingyuan, A. Christy, J. Sjoblom, Water-in-Crude Oil Emulsions from the Norwegian Continental Shelf Part VI -- Diffuse Reflectance Fourier Transform Infrared Characterization of Interfacially Active Fractions from North Sea Crude Oil, in "Emulsions -- A Fundamental and Practical Approach" (J. Sjoblom, Eds.), Kluwer Academic Publishers, The Netherlands, 1992; pp 157-172.
 18. J. H. Hildebrand, R. L. Scott, *Solubility of Nonelectrolytes*; Dover: New York, 1964.
 19. G. Scatchard, "Equilibria in Non-Electrolyte Solutions in Relation to the Vapor Pressures and Densities of the Components," *Chemical Reviews*, 1931, **8**(2): p. 321-333.
 20. J. M. Prausnitz, R. N. Lichtenthaler, E. G. Azevedo, *Molecular Thermodynamics of Fluid-Phase Equilibria*; Prentice-Hall PTR: Upper Saddle River, N.J., 1999.
 21. A. Hirschberg, L. N. J. deJong, B. A. Schipper, J. G. Meijer, "Influence of Temperature and Pressure on Asphaltene Flocculation," *Society of Petroleum Engineers Journal*, 1984, (June): p. 283-293.
 22. N. E. Burke, R. E. Hobbs, S. F. Kashou, "Measurement and Modeling of Asphaltene Precipitation," *Journal of Petroleum Technology*, 1990, **Nov**: p. 1440-1456.
 23. H. Laux, I. Rahimian, T. Butz, "Thermodynamics and mechanism of stabilization and precipitation of petroleum colloids," *Fuel Processing Technology*, 1997, **53**(1-2): p. 69-79.
 24. H. Rassamdana, B. Dabir, M. Nematy, M. Farhani, M. Sahimi, "Asphalt Flocculation and Deposition: I. The Onset of Precipitation," *AIChE Journal*, 1996, **42**(1): p. 10-22.
 25. H. W. Yarranton, J. H. Masliyah, "Molar Mass Distribution and Solubility Modeling of Asphaltenes," *AIChE Journal*, 1996, **42**(12): p. 3533-3543.
 26. K. D. Mannistu, H. W. Yarranton, J. H. Masliyah, "Solubility modeling of asphaltenes in organic solvents," *Energy & Fuels*, 1997, **11**(3): p. 615-622.
 27. M. A. Pena, Y. Daali, J. Barra, P. Bustamante, "Partial solubility parameters of lactose, mannitol and saccharose using the modified extended Hansen method and evaporation light scattering detection," *Chemical & Pharmaceutical Bulletin*, 2000, **48**(2): p. 179-183.

28. C. M. Hansen, A. L. Smith, "Using Hansen solubility parameters to correlate solubility of C-60 fullerene in organic solvents and in polymers," *Carbon*, 2004, **42**(8-9): p. 1591-1597.
29. H. Burrell, B. Immergut, Solubility Parameter Values, in "Polymer Handbook" (E. H. Immergut, Eds.), Wiley, New York, 1966; pp
30. A. Beerbower, "Picking the Right Elastomer to Fit Your Fluids," *Chemical Engineering*, 1967, **74**: p. 118-128.
31. R. F. Blanks, J. M. Prausnitz, "Thermodynamics of Polymer Solubility in Polar and Nonpolar Systems," *Industrial and Engineering Chemistry Fundamentals*, 1964, **3**(1): p. 1-8.
32. J. D. Crowley, G. S. T. Jr., J. W. L. Jr., "A Three-Dimensional Approach to Solubility Part I," *Journal of Paint Technology*, 1966, **38**: p. 269-280.
33. C. Hansen, A. Beerbower, Solubility Parameters, in "Encyclopedia of Chemical Technology" Eds.), Wiley, New York, 1971; pp 889-909.
34. A. Grubenmann, "The Solvent Dependence of the Solubility of Organic-Solids and Solubility Parameter Theory - Investigation by Means of an Organic Pigment," *Dyes and Pigments*, 1993, **21**(4): p. 273-292.
35. J.-C. Remigy, E. Nakache, P. D. Brechot, "Computer-Aided Method for the Determination of Hansen Solubility Parameters. Application to the Miscibility of Refrigerating Lubricant and New Refrigerant," *Ind. Eng. Chem. Res.*, 1999, **38**: p. 4470-4476.
36. C. M. Hansen, "Cohesion Parameters for Surfaces, Pigments, and Fillers," *JOCCA - Surface Coatings International*, 1997, **80**(8): p. 386-392.
37. A. Beerbower, J. R. Dickey, "Advanced Methods for Predicting Elastomer/Fluids Interactions," *ASLE Interactions*, 1969, **12**: p. 1-20.
38. E. B. Bagley, T. P. Nelson, J. M. Scigliano, "Three-Dimensional Solubility Parameters and Their Relationship To Internal Pressure Measurements In Polar and Hydrogen Bonding Solvents," *Journal of Paint Technology*, 1971, **43**(555): p. 35-42.
39. D. M. Koenhen, C. A. Smolders, "Determination of Solubility Parameters of Solvents and Polymers By Means of Correlations With Other Physical Quantities," *Journal of Applied Polymer Science*, 1975, **19**(4): p. 1163-1179.
40. C. M. Hansen, *Hansen Solubility Parameters: A User's Handbook*; CRC Press: Boca Raton, 1999.

41. P. L. Wu, A. Beerbower, A. Martin, "Extended Hansen Approach - Calculating Partial Solubility Parameters of Solid Solutes," *Journal of Pharmaceutical Sciences*, 1982, **71**(11): p. 1285-1287.
42. A. Das, N. A. M. Gadalla, S. Kudchadker, K. N. Marsh, A. S. Rodgers, R. C. Wilhoit, "Thermodynamic and Thermophysical Properties of Organic Nitrogen-Compounds .2. 1-Butanamine and 2-Butanamine, 2-Methyl-1-Propanamine, 2-Methyl-2-Propanamine, Pyrrole, 1-Methylpyrrole, 2-Methylpyrrole, and 3-Methylpyrrole, Pyridine, 2-Methylpyridine, 3-Methylpyridine, and 4-Methylpyridine, Pyrrolidine, Piperidine, Indole, Quinoline, Isoquinoline, Acridine, Carbazole, Phenanthridine, 1-Naphthalenamine and 2-Naphthalenamine, and 9-Methylcarbazole," *Journal of Physical and Chemical Reference Data*, 1993, **22**(3): p. 659-782.
43. ACD/Chemsketch v. 5.06. Advanced Chemistry Development: Toronto, Canada, 2001.
44. *CRC Handbook of Chemistry and Physics*; CRC Press: Boca Raton, FL, 1982.
45. E. S. Domalski, E. D. Hearing, "Heat capacities and entropies of organic compounds in the condensed phase, vol 3 (vol 25, pg 1, 1996)," *Journal of Physical and Chemical Reference Data*, 1997, **26**(6): p. 1501-1505.
46. H.-H. Perkampus, *UV-Vis Spectroscopy and Its Applications*; Springer-Verlag: Berlin, 1992.

Table 6.1 Hansen partial solubility parameter values of various solvents [40].

Solvent	Symbol	v_s (cm ³ /mol)	δ_{ds} (MPa) ^{1/2}	δ_{ps} (MPa) ^{1/2}	δ_{hs} (MPa) ^{1/2}
heptane	H	147.4	15.3	0.0	0.0
1-methyl naphthalene	MN	138.8	20.6	0.8	4.7
toluene	T	106.8	18.0	1.4	2.0
butyl benzoate	BBZ	178.0	18.3	2.9	5.5
n-butyl butyrate	NBB	166.7	15.6	2.9	5.6
anisole	AN	119.1	17.8	4.1	6.7
dipropyl ketone	DPK	140.8	15.8	5.7	4.9
2-butanol	IBA	92.0	15.8	5.7	14.5
2-propanol	IPA	106.0	15.8	6.1	16.4
methyl benzoate	MB	124.9	17.0	8.2	4.7
ethanol	EA	58.5	15.8	8.8	19.4
propylene carbonate	PC	85.0	20.0	18.0	4.1

Table 6.2 Phase change data and ideal mole fraction solubility for anthracene [44] and PHD [45].

Solute	ΔH^{fus} (KJ/mol)	T_m (K)	x_a^{ideal} (298 K)
anthracene	28.86	489.6	0.0105
phenanthridine	22.83	379.4	0.1385

Table 6.3 Molar extinction coefficients for ACA and PHD in 2-butanol at selected wavelengths.

Solute	λ (nm)	$\epsilon_{i\lambda}$ (mM ⁻¹ cm ⁻¹)	R ²
ACA	381.0	714.75	0.9998
PHD	345.9	37.40	0.9992

Table 6.4 Hansen partial solubility parameters of ACA and PHD and corresponding weighting coefficients from regression analyses.

Parameter	ACA	PHD
δ_{da} (MPa) ^{1/2}	17.45	20.60
δ_{pa} (MPa) ^{1/2}	9.51	6.66
δ_{ha} (MPa) ^{1/2}	10.62	8.31
c_0	-2.03	-13.47
c_1	1.000	1.000
c_2	0.181	0.317
c_3	0.658	0.214
R^2	0.9702	0.9951

Table 6.5 Mole fraction solubility of ACA in binary solvent mixtures.

Solvent 1 = MN; Solvent 2 = IBA				Solvent 1 = MN; Solvent 2 = MB				Solvent 1 = DPK; Solvent 2 = IBA			
ϕ_1	x_a	x_a (calc)	% error	ϕ_1	x_a	x_a (calc)	% error	ϕ_1	x_a	x_a (calc)	% error
0.0	0.0119	0.0252	-52.8	0.0	0.0122	0.0117	4.8	0.0	0.0119	0.0252	-52.8
0.1	0.0256	0.0337	-24.0	0.1	0.0132	0.0114	15.9	0.1	0.0225	0.0322	-30.1
0.2	0.0345	0.0398	-13.4	0.2	0.0130	0.0108	20.3	0.2	0.0309	0.0379	-18.4
0.3	0.0400	0.0423	-5.4	0.3	0.0103	0.0099	4.5	0.3	0.0381	0.0414	-7.9
0.4	0.0474	0.0405	16.9	0.4	0.0093	0.0088	6.4	0.4	0.0409	0.0422	-3.0
0.5	0.0498	0.0348	43.0	0.5	0.0079	0.0075	4.9	0.5	0.0426	0.0402	6.0
0.6	0.0462	0.0264	75.2	0.6	0.0067	0.0062	8.0	0.6	0.0435	0.0355	22.8
0.7	0.0436	0.0173	151.8	0.7	0.0054	0.0050	7.6	0.7	0.0412	0.0288	42.8
0.8	0.0365	0.0099	270.9	0.8	0.0036	0.0039	-6.8	0.8	0.0363	0.0214	69.7
0.9	0.0215	0.0049	340.9	0.9	0.0023	0.0029	-21.8	0.9	0.0296	0.0144	105.7
1.0	0.0009	0.0021	-57.8	1.0	0.0009	0.0021	-57.8	1.0	0.0182	0.0084	116.2
Solvent 1 = BBZ; Solvent 2 = NBB				Solvent 1 = IPA; Solvent 2 = AN				Solvent 1 = EA; Solvent 2 = PC			
ϕ_1	x_a	x_a (calc)	% error	ϕ_1	x_a	x_a (calc)	% error	ϕ_1	x_a	x_a (calc)	% error
0.0	0.0078	0.0079	-1.3	0.0	0.0033	0.0210	-84.1	0.0	0.0065	0.0028	133.2
0.1	0.0083	0.0085	-1.6	0.1	0.0217	0.0297	-26.3	0.1	0.0146	0.0095	52.6
0.2	0.0091	0.0089	2.4	0.2	0.0360	0.0379	-4.8	0.2	0.0227	0.0238	-4.6
0.3	0.0093	0.0093	0.0	0.3	0.0412	0.0440	-5.9	0.3	0.0284	0.0416	-31.8
0.4	0.0091	0.0095	-5.2	0.4	0.0470	0.0471	-0.3	0.4	0.0321	0.0548	-41.5
0.5	0.0098	0.0097	1.1	0.5	0.0435	0.0470	-7.0	0.5	0.0319	0.0595	-46.3
0.6	0.0104	0.0098	5.9	0.6	0.0401	0.0438	-7.7	0.6	0.0308	0.0552	-44.2
0.7	n.a.	n.a.	n.a.	0.7	0.0393	0.0378	3.6	0.7	0.0276	0.0429	-35.6
0.8	0.0100	0.0097	3.6	0.8	0.0298	0.0301	-0.7	0.8	0.0228	0.0258	-11.6
0.9	n.a.	n.a.	n.a.	0.9	0.0172	0.0217	-19.9	0.9	0.0166	0.0109	52.8
1.0	0.0095	0.0092	3.9	1.0	0.0124	0.0140	-11.0	1.0	0.0105	0.0032	223.6

Table 6.6 Mole fraction solubility of PHD in binary solvent mixtures.

Solvent 1 = MN; Solvent 2 = IBA				Solvent 1 = MN; Solvent 2 = MB				Solvent 1 = DPK; Solvent 2 = IBA			
ϕ_1	x_a	x_a (calc)	% error	ϕ_1	x_a	x_a (calc)	% error	ϕ_1	x_a	x_a (calc)	% error
0.0	0.0342	0.0545	-37.3	0.0	0.1130	0.1046	8.0	0.0	0.0342	0.0545	-37.3
0.1	0.0572	0.0743	-23.0	0.1	0.1214	0.1185	2.4	0.1	0.0453	0.0606	-25.2
0.2	0.0842	0.0934	-9.9	0.2	0.1194	0.1301	-8.2	0.2	0.0560	0.0659	-15.0
0.3	0.1054	0.1103	-4.4	0.3	0.1197	0.1390	-13.9	0.3	0.0685	0.0703	-2.5
0.4	0.1194	0.1240	-3.7	0.4	0.1272	0.1451	-12.3	0.4	0.0694	0.0735	-5.6
0.5	0.1192	0.1341	-11.1	0.5	0.1269	0.1482	-14.4	0.5	0.0833	0.0756	10.3
0.6	0.1321	0.1403	-5.8	0.6	0.1308	0.1484	-11.9	0.6	0.0877	0.0763	15.0
0.7	0.1409	0.1422	-1.0	0.7	0.1340	0.1456	-8.0	0.7	0.0874	0.0756	15.5
0.8	0.1605	0.1396	15.0	0.8	0.1322	0.1397	-5.4	0.8	0.0932	0.0735	26.8
0.9	0.1486	0.1318	12.7	0.9	0.1388	0.1307	6.2	0.9	0.0922	0.0700	31.7
1.0	0.1461	0.1187	23.1	1.0	0.1461	0.1187	23.1	1.0	0.0851	0.0653	30.4
Solvent 1 = BBZ; Solvent 2 = NBB				Solvent 1 = H; Solvent 2 = T				Solvent 1 = IPA; Solvent 2 = AN			
ϕ_1	x_a	x_a (calc)	% error	ϕ_1	x_a	x_a (calc)	% error	ϕ_1	x_a	x_a (calc)	% error
0.0	0.0682	0.0478	42.6	0.0	0.0675	0.0753	-10.3	0.0	0.1126	0.1320	-14.7
0.1	0.0700	0.0561	24.9	0.1	0.0645	0.0657	-1.8	0.1	0.1395	0.1297	7.6
0.2	0.0742	0.0649	14.3	0.2	0.0554	0.0563	-1.5	0.2	0.1456	0.1255	16.0
0.3	0.0771	0.0742	4.0	0.3	0.0443	0.0473	-6.4	0.3	0.1453	0.1197	21.5
0.4	0.0846	0.0837	1.1	0.4	0.0360	0.0390	-7.7	0.4	0.1390	0.1122	23.8
0.5	0.0909	0.0934	-2.7	0.5	0.0410	0.0316	29.7	0.5	0.1263	0.1034	22.1
0.6	0.0981	0.1030	-4.7	0.6	0.0232	0.0253	-8.4	0.6	0.1111	0.0933	19.1
0.7	0.1002	0.1123	-10.8	0.7	0.0192	0.0199	-3.5	0.7	0.0929	0.0822	13.1
0.8	0.1091	0.1213	-10.1	0.8	0.0137	0.0155	-11.9	0.8	0.0675	0.0703	-3.9
0.9	0.1141	0.1297	-12.0	0.9	0.0098	0.0119	-18.4	0.9	0.0449	0.0581	-22.7
1.0	0.1172	0.1376	-14.8	1.0	0.0079	0.0091	-12.8	1.0	0.0265	0.0461	-42.4
Solvent 1 = EA; Solvent 2 = PC											
ϕ_1	x_a	x_a (calc)	% error								
0.0	0.0354	0.0262	35.4								
0.1	0.0459	0.0442	3.7								
0.2	0.0534	0.0633	-15.6								
0.3	0.0693	0.0785	-11.8								
0.4	0.0774	0.0879	-12.0								
0.5	0.0804	0.0910	-11.7								
0.6	0.0819	0.0880	-7.0								
0.7	0.0837	0.0795	5.3								
0.8	0.0780	0.0658	18.6								
0.9	0.0668	0.0483	38.3								
1.0	0.0519	0.0300	72.9								

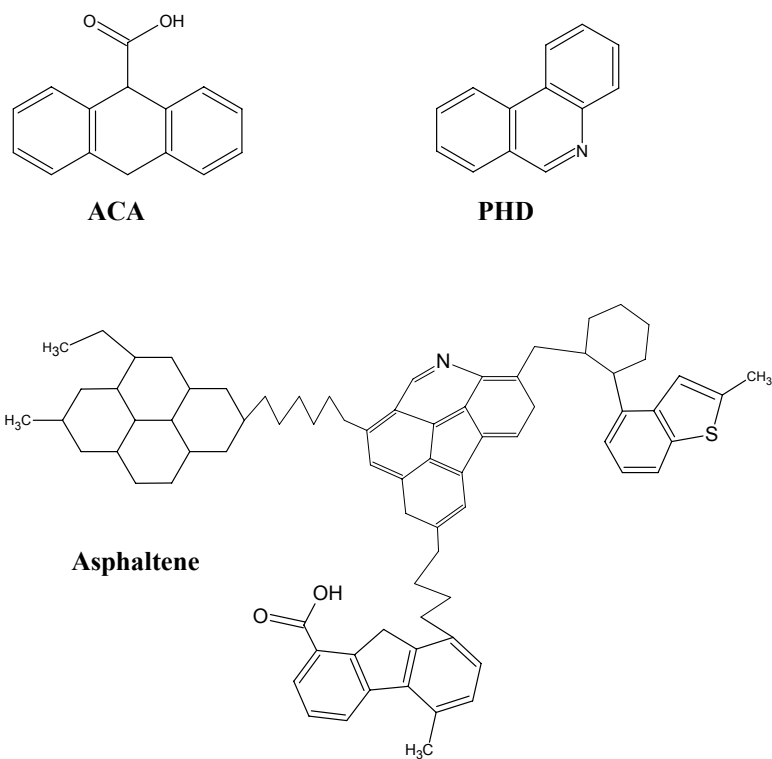


Figure 6.1 Molecular structures of 9-anthracenecarboxylic acid (ACA), phenanthridine (PHD), and a representative asphaltene molecule with molecular formula $C_{77}H_{89}NO_2S$ and molecular weight of 1093 amu.

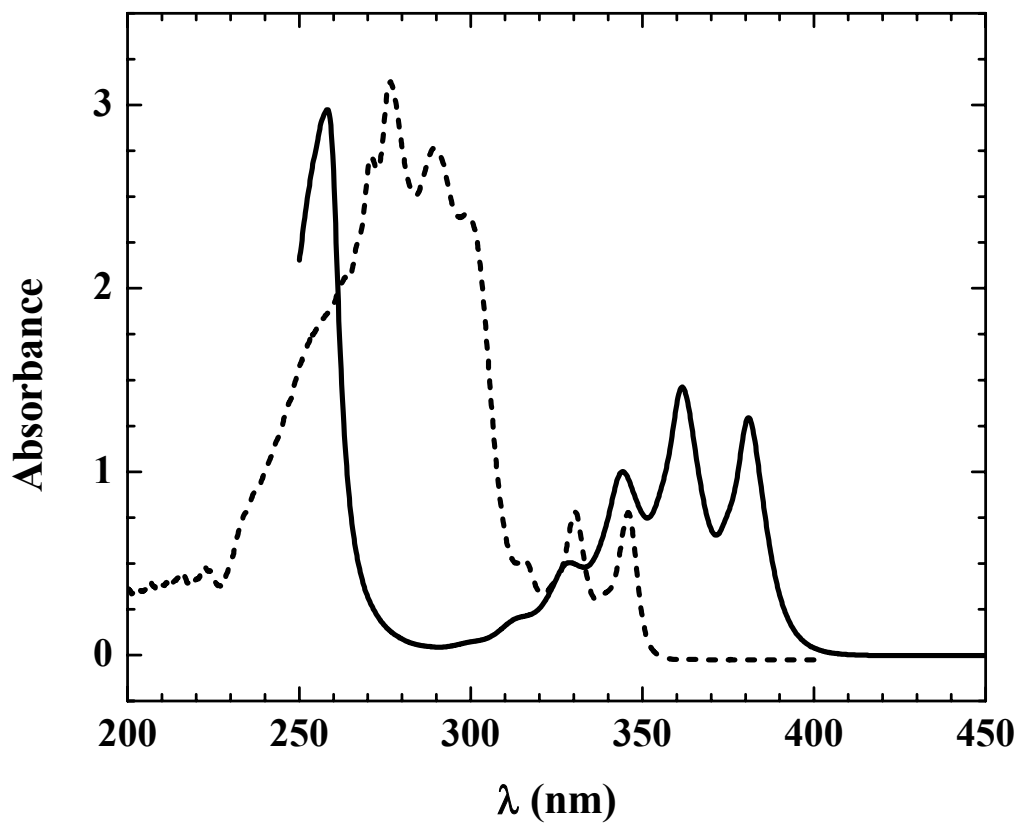


Figure 6.2 UV-vis absorption spectra for (—) ACA and (---) PHD in 2-butanol.

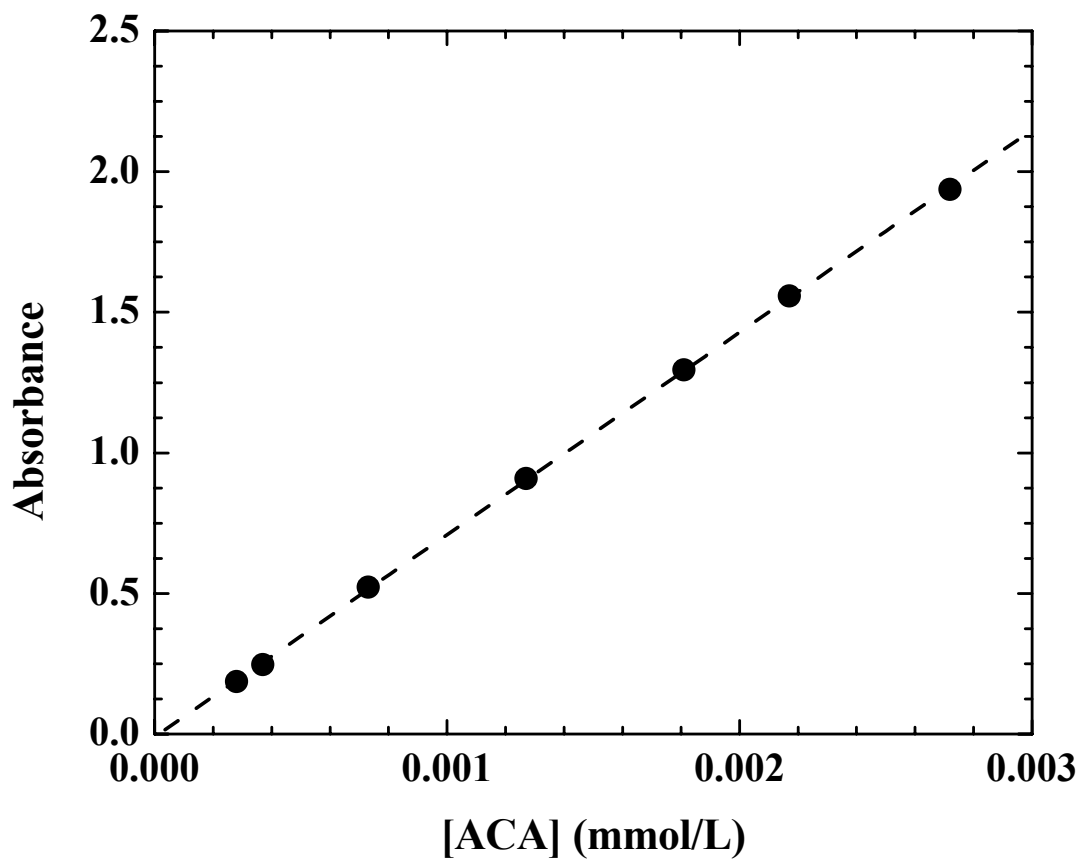


Figure 6.3 Beer-Lambert calibration curve for ACA in 2-butanol at $\lambda_{\text{max}} = 381.0$ nm. The dashed line represents the best linear fit through the data.

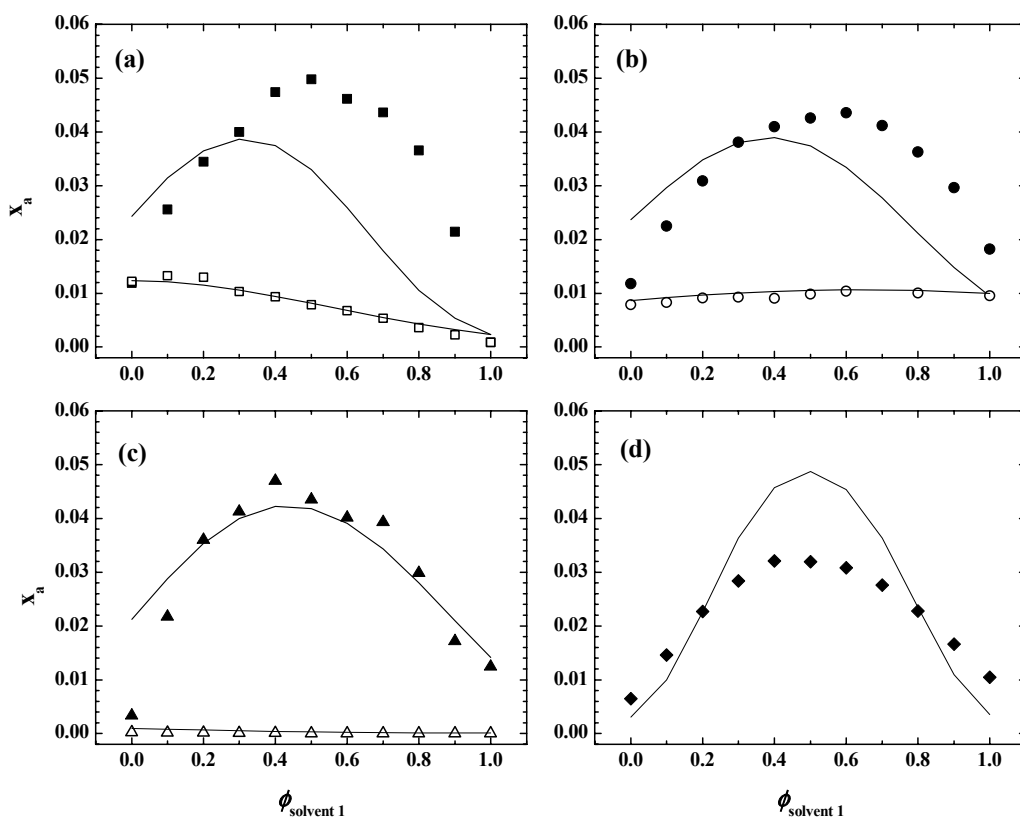


Figure 6.4a-d Solubility of ACA in mixed solvents. Solid lines represent solubility calculated from three-dimensional solubility parameter model. Legend: (■) Solvent 1: MN, Solvent 2: IBA; (□) Solvent 1: MN, Solvent 2: MB; (●) Solvent 1: DPK, Solvent 2: IBA; (○) Solvent 1: BBZ, Solvent 2: NBB; (▲) Solvent 1: IPA, Solvent 2: AN; (△) Solvent 1: H, Solvent 2: T; (◆) Solvent 1: EA, Solvent 2: PC.

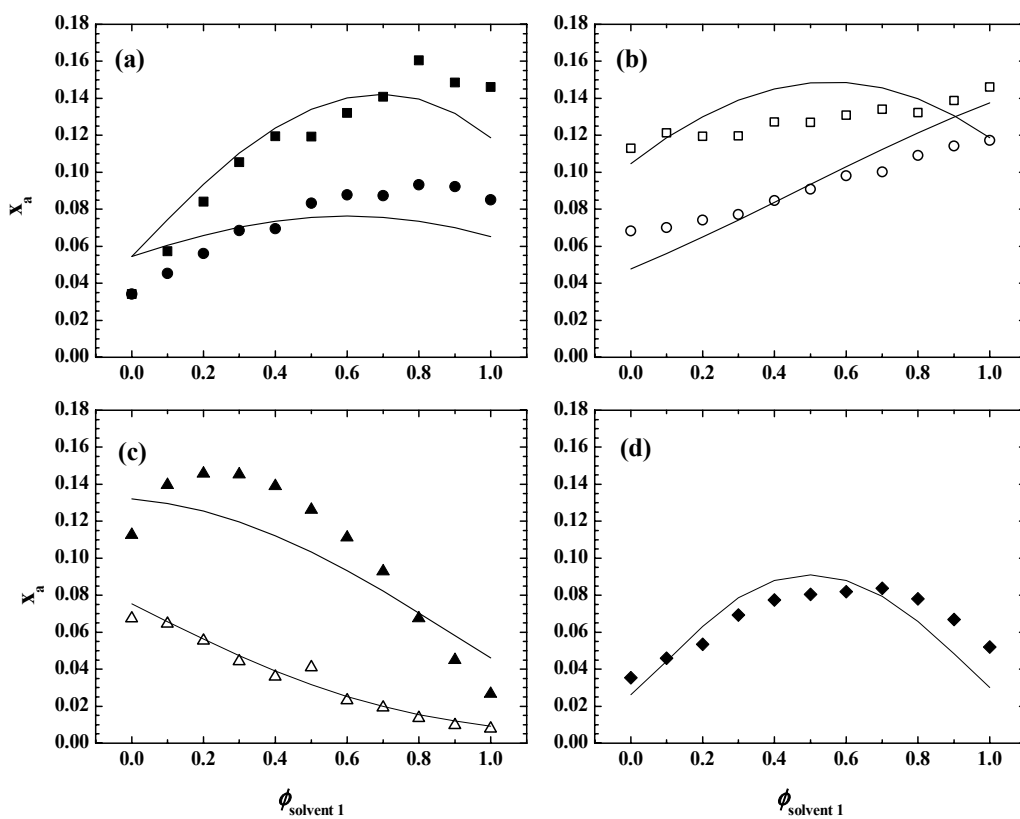


Figure 6.5a-d Solubility of PHD in mixed solvents. Solid lines represent solubility calculated from three-dimensional solubility parameter model. Legend: (■) Solvent 1: MN, Solvent 2: IBA; (□) Solvent 1: MN, Solvent 2: MB; (●) Solvent 1: DPK, Solvent 2: IBA; (○) Solvent 1: BBZ, Solvent 2: NBB; (▲) Solvent 1: IPA, Solvent 2: AN; (△) Solvent 1: H, Solvent 2: T; (◆) Solvent 1: EA, Solvent 2: PC.

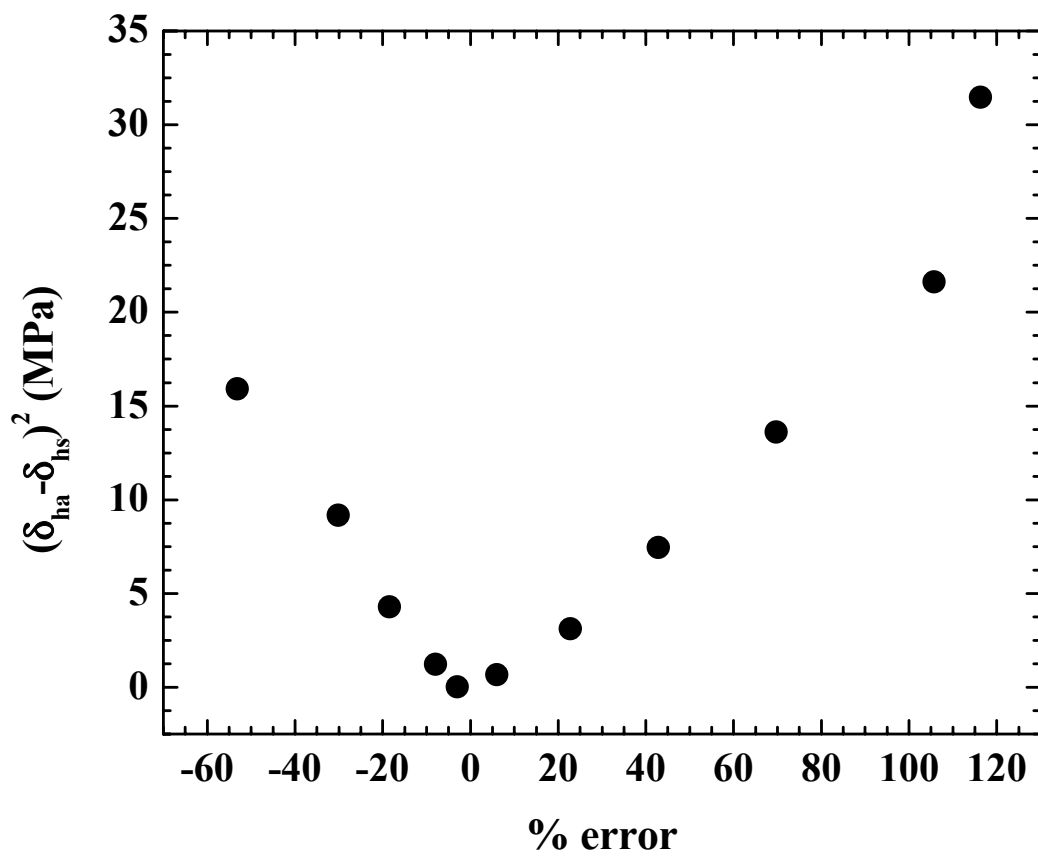


Figure 6.6 Correlation of % error in calculated mole fraction solubility to square of difference in hydrogen bonding parameters of ACA and IBA:DPK solvent blends.

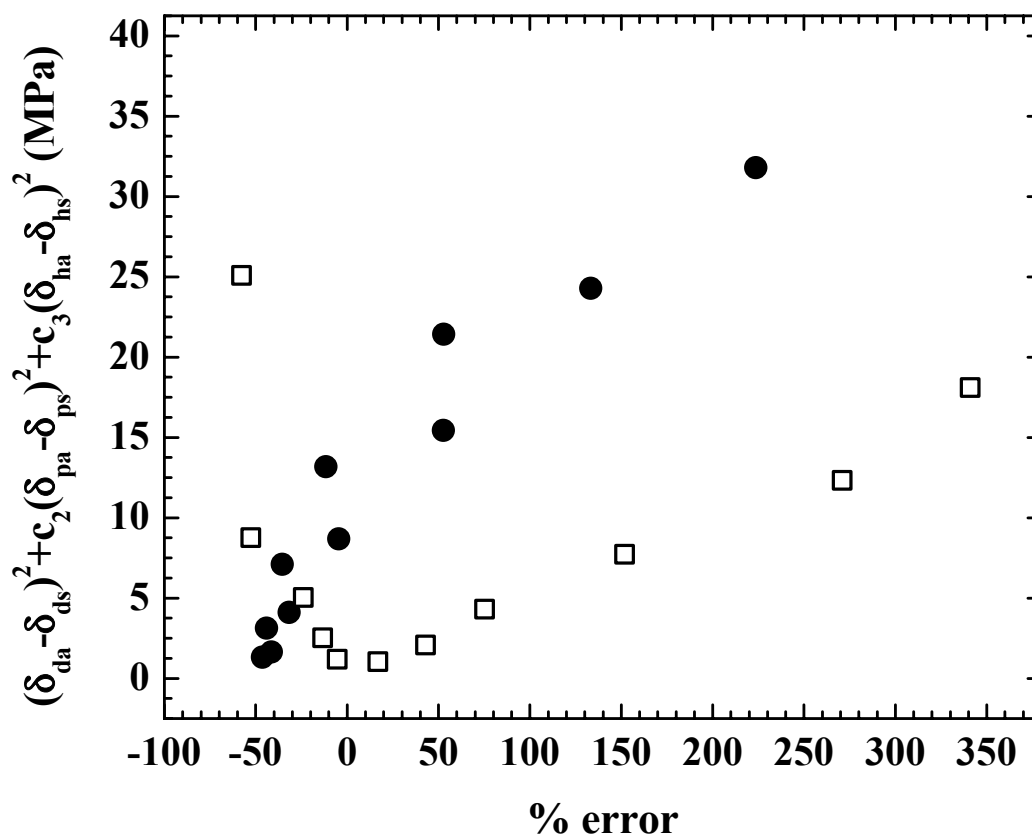


Figure 6.7 Correlation of % error in calculated mole fraction solubility to weighted sum of squared differences in solubility parameters of ACA and (●) EA:PC and (□) MN:IBA solvent blends.

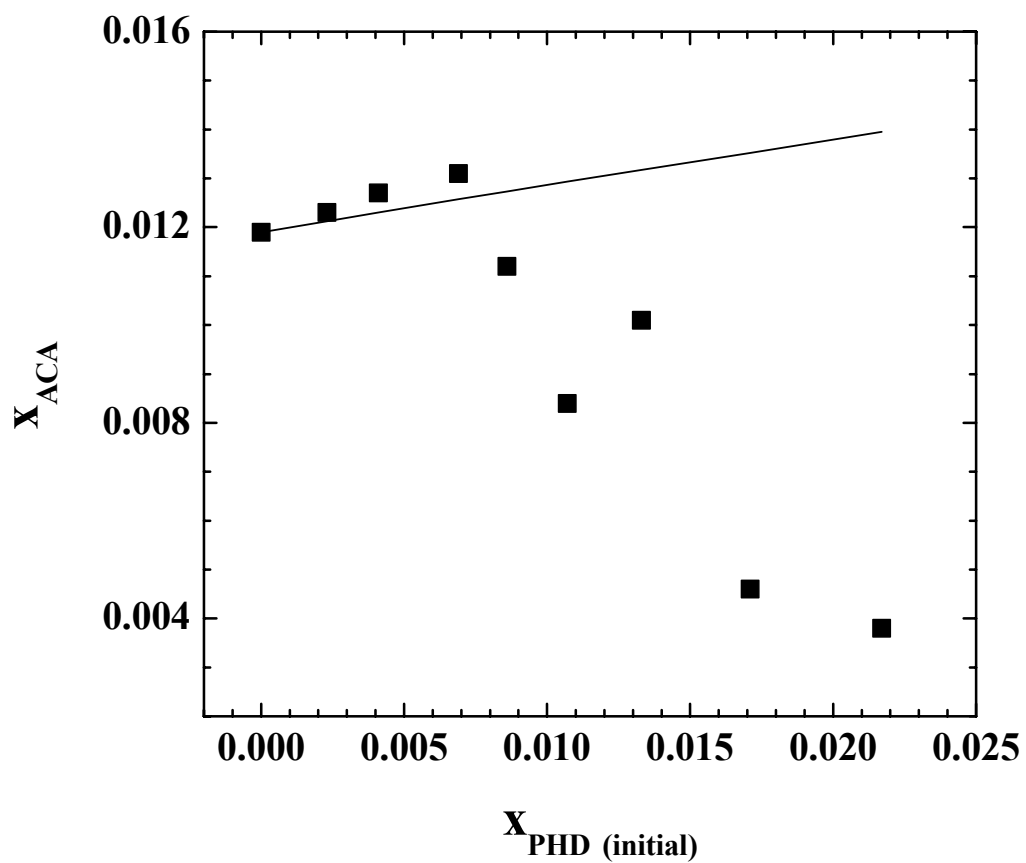


Figure 6.8 Solubility of ACA in solutions of 2-butanol with varying initial concentrations of PHD. The solid line represents ACA solubility calculated from the three-dimensional solubility parameter model assuming PHD modifies the solvent solubility parameters.

CHAPTER 11

CONCLUSIONS AND FUTURE WORK

11.1 Conclusions

We have studied the roles of chemical composition and solvency on the aggregation and solubility behavior of asphaltenes. Asphaltenes from three different crude sources were separated on a preparatory-scale into 20 to 30 discrete subfractions by sequential precipitation in mixtures of heptane and toluene. Three distinct solubility regimes were indicated in which the chemical and colloidal behavior of the asphaltenic fractions varied significantly with total amount of precipitated asphaltenes. The earliest subfractions isolated were characterized by decreasing atomic H/C ratios and increasing N/C ratios with precipitated asphaltene yield. ICP metals analyses suggested that the fractions contained significant amounts of co-precipitated inorganic solids or metal atoms bound to functional groups intrinsic to the asphaltenes. The subfractions isolated in the regime where asphaltene solubility changed significantly with slight changes in the solvent were characterized by atomic H/C ratios that varied significantly with the yield of precipitated asphaltenes. Atomic N/C ratios decreased and O/C ratios increased systematically with increasing precipitated asphaltene yield in this solvent regime. The most aromatic subfractions generally formed the largest aggregates in solution, suggesting that asphaltene solubility and aggregation behavior is dominated by π -bonding interactions between the aromatic moieties. After precipitation of > 80 % (w/w) of the asphaltenes, the remaining fractions were more “resin-like” in chemical composition and aggregation behavior.

Small-angle neutron scattering (SANS) has proven useful for deducing the sizes and morphologies of asphaltenic aggregates in solution. Various intra-particle structure factor models have been applied in the past to determine aggregate size parameters from scattering intensity curves of asphaltene solutions, but not all of these models accurately reflected the morphology of the asphaltenic aggregates in solution. In this work, we showed that an oblate cylinder model with radius polydispersity best described the shape of asphaltenic aggregates, as the corresponding form factor model consistently provided the lowest reduced χ^2 values of the various geometric models and values of the I_0 and R_G parameters that were consistent with Guinier analyses.

The polydisperse radius oblate cylinder model and a small-particle mass-fractal model were used to analyze the SANS scattering curves obtained for 108 asphaltene samples possessing a wide variation in the chemical composition of the asphaltenes and solvent quality. Values of the apparent fractal dimension from the mass-fractal fits appeared to decrease with increasing aggregate size, suggesting that the smallest aggregate formers were more globular with little surface roughness (i.e., $D \sim 3$) while the largest aggregate formers were more dendritic with higher surface roughness ($D \sim 2.2$ to 2.4). Typical values of the aggregate thickness from the polydisperse cylinder fits ranged from 5 to 32 Å, while the average particle radius ranged from 25 to 125 Å. The polydispersity in the particle radius appeared independent of the particle size and was approximately 30 %.

Assuming an asphaltene monomer consists of groups of condensed aromatic rings containing polar moieties that are interconnected by aliphatic chains (i.e., the “archipelago” model of asphaltene structure), the asphaltene aggregation mechanism might proceed through a series of localized stacking interactions of aromatic rings. The physical linkage of one ring

system to another in a monomer somewhat increases the particle thickness, but significantly expands the aggregate in the radial dimension, where polydispersity in the aggregate size is most evident. Discrepancies between average aggregate molecular weight values obtained from two independent methods suggested the need to include the solvation effects in the calculations. Solvent entrainment within the aggregates roughly varied from 30 to 50 % (v/v) and was consistent with previous viscosity measurements.

Attempts to use the observed solvent entrainment values to estimate the relative proportions of micro-scale and nano-scale aggregates in solution were limited in accuracy; however, the volume fraction of micro-scale flocs generally increased with decreasing solvent quality. Furthermore, flocculation was only observed to be greater than 20 % for those samples that were dispersed in an insoluble solvent regime.

Changes in the apparent aggregate mass with concentration indicated deviations from ideal solution behavior (i.e., non-interacting asphaltenes plus solvent), which were quantified through the determination of aggregate second virial coefficients (A_2). A_2 values were previously reported or inferred from SANS and VPO experiments studying asphaltenes in toluene and 1,2-dichlorobenzene; however, this study was the first to investigate the roles of source crude, chemical composition, solvent conditions, and the influence of selective solvating agents on asphaltene A_2 values.

Results of the second virial determination for Hondo asphaltenes (0.25 – 4 % w/w) in d-toluene and 90:10 d-toluene: d-methanol (v/v) indicated that the aggregates experienced net repulsive interactions at these solvent conditions with A_2 values on the order of 10^{-5} mol cm^3/g^2 . A negative A_2 value was observed for HO2 asphaltenes in 40:60 d-heptane: d-toluene at the same concentration range, indicating flocculation (i.e., attractive interactions)

of the aggregates. It was not conclusive from our SANS data whether or not the A_2 values were affected by increasing solute dilution; however, A_2 values estimated from previous SANS and vapor pressure osmometry data suggested that asphaltene monomers or small oligomers interact in dilute solutions to form larger aggregates. B6 resins effectively reduced the aggregate mass of HO1 asphaltenes in d-toluene and increased the magnitude of the observed A_2 values, likely through the disruption of aromatic π -bonding interactions within the aggregates. A_2 values for HO1 asphaltenes and B6 resins were on the same order of magnitude as pure resin solutions (i.e., 10^{-4} mol cm³/g²). A_2 values appeared to vary significantly with chemical composition, specifically atomic H/C of the solute mixture, suggesting that the interactions between asphaltenes, resins, and the d-toluene solvent are strongly dominated by dispersion and π -bonding interactions.

The magnitude of the experimentally measured A_2 values generally under-predicted or agreed with the values of A_2 calculated from an excluded volume model, suggesting that the types of interactions between the solute and solvent are not completely steric repulsive. The structure of asphaltenic aggregates is more diffuse than that of a rigid body; thus, energetic interactions of the solute and entrained solvent are significant.

A UV-visible spectroscopic method has been developed to determine the mole fraction solubilities of polynuclear aromatic compound in various binary solvent mixtures with the intention of extending the method to petroleum mixtures. The solubility results were analyzed using the extended Hansen solubility approach, a thermodynamic model based on regular solution theory that includes three solubility parameters representing the work required to overcome specific interactions between the solute and solvent (i.e., dispersion,

polar, and hydrogen-bonding interactions). The model also included a Flory-Huggins term to correct for non-zero entropy of mixing.

The solubility parameter model provided accurate fits of phenanthridine (PHD) solubility in most binary solvent mixtures with less than 30 % error. The model fits were less accurate for 9-anthracenecarboxylic acid (ACA), likely due to a fewer number of data points in the regression and a selection of solvents that did not adequately probe the range of polar parameters with values above the polar parameter for ACA. The predictive capability of the model was also observed to decrease when one or more of the Hansen partial solubility parameters of the solvent deviated significantly from that of the solute.

Additional experiments measured the solubility behavior of ACA in a multi-component solvent mixture containing various initial concentrations of PHD in 2-butanol. Assuming that the PHD addition modified the Hansen solubility parameters of the solvent only, the mole fraction solubility of ACA was expected to increase monotonically with increasing PHD concentration. Instead, the solubility of ACA was observed to initially increase by 10 %, and then decrease dramatically below the starting value. These results suggested the need to modify the existing model to account for solute-solute complexation effects, particularly if it is desirable to apply the model to large aggregate formers, such as petroleum asphaltene.

11.2 Future Work

Asphaltenes maintain a delicate balance between solvency, aggregation, and interfacial activity in solution that must ultimately be related to the chemical composition of the participating components. With this in mind, there is still incredible debate over the

definition of asphaltenes, the molecular structure (i.e., “continental” versus “archipelago” models), and typical molar mass of asphaltene monomers. A collaborative effort is needed to standardize the means by which asphaltenes and resins are isolated from petroleum fluids and analyzed, so that results obtained by various researchers are more easily compared. Discussions to this effect were started at the 4th and 5th International Conferences on “Petroleum Phase Behaviour and Fouling” in 2003 and 2004, respectively, with similar debates anticipated at future conferences.

Several aspects of this research may be extended to further probe the influence of asphaltene and solvent chemical compositions on aggregation behavior. For example, the fine fractionation of asphaltenes from mixtures of heptane and toluene provided detailed distributions of asphaltene chemical composition; however, additional experiments are needed to relate the chemical composition to the aggregation and emulsion-stabilizing behaviors of the asphaltenic fractions. One motivation for performing the fine fractionation work was to determine if there is a problematic asphaltenic fraction that, once isolated from the whole asphaltenes, decreases the tendency of the remaining asphaltenes to strongly aggregate and/or form stable emulsions. If such a fraction exists, we have shown that it cannot be isolated by precipitation from heptane and toluene.

Precipitation of asphaltenes from mixtures of heptane ($\delta_{ds} = 15.3$, $\delta_{ps} = 0.0$, $\delta_{hs} = 0.0$) and toluene ($\delta_{ds} = 18.0$, $\delta_{ps} = 1.4$, $\delta_{hs} = 2.0$) are driven mainly by differences in the dispersion interactions between the solvent and asphaltenes. Researchers have previously obtained a wider distribution of asphaltene chemical compositions by fractionation in acetone and toluene compared to heptane and toluene. The replacement of heptane with acetone ($\delta_{ds} = 15.5$, $\delta_{ps} = 10.4$, $\delta_{hs} = 7.0$) introduces significant polar and hydrogen-bonding contributions to

the solvent character. If heptane is replaced with a more protic solvent, such as methanol ($\delta_{ds} = 15.1$, $\delta_{ps} = 12.3$, $\delta_{hs} = 22.3$), precipitation should be driven to an even larger extent by differences in the hydrogen-bonding contributions to the overall solubility parameters.

Many of the SANS calculations were performed using a polydisperse radius oblate cylinder form factor to describe the shape of the asphaltenic aggregates. Although the polydisperse oblate cylinder model provides a reasonable approximation for the shape of asphaltenic aggregates, a polydisperse oblate ellipsoid model is probably more appropriate. Development of a polydisperse oblate ellipsoid model would require more complex numerical integration techniques that the polydisperse oblate cylinder model avoided by making several simplifying assumptions. The change to the polydisperse ellipsoid shape should increase the accuracy of the aggregate volume calculations, thus reducing the uncertainty in the % solvent entrapment. It is also possible to modify the fitting algorithm for the polydisperse oblate cylinder model to include both radius and length polydispersity without the need to solve the integrals numerically. The inclusion of length polydispersity should improve the quality of fits for the larger aggregate formers that tended to have significantly higher reduced χ^2 values. Subsequently, the uncertainty in calculations based on the % solvent entrapment should also be reduced, such as the percentage micro-particle versus nano-particle material and the second virial coefficients.

The virial coefficient studies should be extended to additional asphaltenic fractions with chemical compositions that are significantly different from Hondo asphaltenes. A similar range of solvents and solute concentrations to those performed on Hondo asphaltenes should also be investigated for the various asphaltene fractions. Since there is sufficient neutron scattering contrast between asphaltenic aggregates and petroleum maltenes, the virial

coefficient analyses may also be extended to diluted crude oil solutions. Furthermore, the virial coefficient analyses have the potential to help assess the effectiveness of various dispersants and other selective solvating agents. For example, the method may be used to identify which dispersant (A, B, or C) is more effective at reducing the size of asphaltenic aggregates in a given crude oil at a fixed dispersant: asphaltene mass ratio. The method may also be used to determine the optimum dispersant: asphaltene mass ratio needed to disperse aggregates to a particular size. When the experiments are performed using a more cost-efficient vapor pressure osmometer instead of a SANS instrument, the technique then has practical applications for crude oil production.

Throughout the course of the asphaltene aggregation studies, several selective solvating agents (e.g., resins, tetrahydrocarbazole, phenanthridine, ethylbenzoic acid, β -cholanic acid) have been added to solutions of asphaltenes to study the effect on aggregate size with concentration. Additional experiments are needed to correlate the aggregation behavior of these modified asphaltenic aggregates with the corresponding film-forming and emulsion-stabilizing properties.

Petroleum resins are particularly interesting as selective solvating agents because they are naturally occurring in the crude oil. Furthermore, resins have been shown to self-aggregate in solution, although the resin aggregates are typically significantly smaller than asphaltenic aggregates. One can argue that the apparent reduction in aggregate size observed with increasing resin content in mixed asphaltene-resin solutions is completely caused by an increase in the number of smaller resin aggregates in solution with no mixed-solute interactions between the asphaltenes and resins.

We propose to use SANS scattering curves for solutions in a fixed solvent containing (1) pure asphaltenes, (2) pure resins, and (3) mixed asphaltenes and resins at various resin: asphaltene mass ratios to estimate the percentage of resin partitioning between the bulk phase (i.e., self-interaction) and co-adsorption to asphaltenic aggregates. In concept, we can show that a subtraction of the “pure resin” contribution (2) from a composite scattering curve describing interactions of asphaltenes and resins (3) does not result in the “pure asphaltene” scattering curve (1). In fact, the resin-subtracted curve invariably under-predicts the “pure asphaltene” scattering curve, suggesting that the resins effectively disperse the asphaltenic aggregates by adsorption on the asphaltene aggregate surface and subsequent disruption of aromatic π -bonding interactions. Using the polydisperse oblate cylinder model, we should be able to accurately calculate the aggregate volumes. In theory, the volume of the composite asphaltene-resin aggregate should equal the sum of volume contributions (weighted by the volume fraction) from bulk resins and from resin-modified asphaltenic aggregates. Thus, the estimation of resin partitioning might proceed as follows:

Assume a value for the % partitioning of resins between the bulk solution and adsorption to asphaltenes. Subtract the effective bulk resin contribution from the composite SANS scattering curve. Fit the polydisperse oblate cylinder model to the composite, bulk resin, and residual scattering curves to determine the particle volumes. Perform the volume summation using the proper weighting based on the assumed resin partitioning. The volume balance should close when the correct value of resin partitioning is assumed. If the method works, it would likely be the first attempt to quantitatively distinguish between the subset of resins that interact with asphaltenes and those that remain relatively inactive in solution.

Additional work has been proposed to use SANS to directly study asphaltenic emulsions. Analyses of asphaltenic emulsions is more complicated than that of asphaltene solutions, because the scattering intensity profile consists of contributions of nanoparticle asphaltenic aggregates in the oil continuous phase and the adsorbed asphaltenic film on the surface of the water droplets. The contribution from the adsorbed asphaltenic film is shifted to lower Q values than the nano-particle scatterers, because typical emulsion droplet sizes are on the order of 1 μm . Therefore, it may be necessary to combine ultra-small-angle (USANS) and SANS scattering methods. Subsequent modeling of the asphaltenic emulsion films to a polydisperse core-shell model should provide estimates of the thickness and scattering length density of the film. The film scattering length density may be further used to estimate the amount of solvent entrainment (i.e., water or oleic solvent) in the asphaltenic film.

APPENDIX A
AGGREGATION AND SOLUBILITY BEHAVIOR OF ASPHALTENES
AND THEIR SUBFRACTIONS

P. Matthew Spiecker, Keith L. Gawrys, and Peter K. Kilpatrick

[Reprinted from *Journal of Colloid and Interface Science* 267 (2003) 178-193]

A.1 Abstract

Asphaltenes from four different crude oils (Arab Heavy, B6, Canadon Seco, and Hondo) were fractionated in mixtures of heptane and toluene and analyzed chemically, by vapor pressure osmometry (VPO), and by small angle neutron scattering (SANS). Solubility profiles of the asphaltenes and their sub-fractions indicated strong cooperative asphaltene interactions of a particular sub-fraction that is polar and hydrogen bonding. This sub-fraction had lower H/C ratios and modestly higher N, V, Ni, and Fe contents than the less polar and more soluble sub-fraction of asphaltenes. VPO and SANS studies indicated that the less soluble sub-fractions formed aggregates that were considerably larger than the more soluble sub-fractions. In general, asphaltene aggregate size increased with decreasing solvent aromaticity up to the solubility limit, beyond which the aggregate size decreased with heptane addition. The presence of a low wavevector Q feature in the scattering curves at 25°C indicated that the individual aggregates were flocculating; however, the intensity of the feature was diminished upon heating of the samples to 80°C. The solubility mechanism for Canadon Seco asphaltenes, the largest aggregate formers, appears to be dominated by aromatic π -bonding interactions due to their low H/C ratio and low nitrogen content. B6 and Hondo asphaltenes formed similar sized aggregates in heptol and the solubility mechanism is most likely driven by polar interactions due to their relatively high H/C ratios and high nitrogen contents. Arab Heavy, the least polar asphaltene, had a H/C ratio similar to Canadon Seco but formed the smallest aggregates in heptol. The enhancement in polar and π -bonding interactions for the less soluble sub-fraction indicated by elemental analysis is reflected by the aggregate size from SANS. The less soluble asphaltenes contribute the majority of species responsible for aggregation and likely cause many petroleum production problems such as pipeline deposition and water-in-oil emulsion stabilization.

A.2 Introduction

The study of asphaltene colloidal properties has been motivated by their propensity to aggregate, flocculate, precipitate, and to adsorb onto interfaces. The tendencies of asphaltenes to participate in colloidal and interfacial phenomena have posed great challenges for the petroleum industry. Problems associated with well production, pipeline transfer, land and sea-based transportation and, ultimately, oil refining have all been linked to the presence of asphaltenic colloids [1-13]. During visbreaking and catalytic hydrocracking large amounts of sludge and sediment can form [14] ostensibly due to the flocculation of asphaltenes during processing [15]. Coke generation and asphaltene adsorption within catalytic cracking beds can reduce the effective catalyst surface area as well as the efficiency of coal hydrolysis [16]. Asphaltene deposition within reservoir rocks has been blamed for pronounced reductions in well productivity [17]. Asphaltenes have also been found to facilitate the formation of extremely stable water-in-crude oil emulsions [5,18-26]. Understanding asphaltene chemistry and the fundamental mechanisms of colloid formation has been the driving force behind much petroleum research for the last half-century.

Asphaltenes are defined as the portion of crude oil insoluble in *n*-alkanes such as *n*-heptane or *n*-pentane yet soluble in benzene or toluene [27,28]. The “solubility class” definition of asphaltenes generates a broad distribution of molecular structures that can vary greatly from one crude oil to another. In general, asphaltenes are characterized by fused ring aromaticity, small aliphatic side chains, and polar heteroatom-containing functional groups. It is common to characterize asphaltenes by their average properties (see Table A.1). The most common techniques for determining the chemical composition of asphaltenes include combustion elemental analysis (H/C, N, S) [29-33] inductively coupled plasma (V, Ni, Fe) [34-38], and Fourier transform infrared spectroscopy (polar functional group concentrations) [39-44]. A wealth of information can be drawn from these chemical analyses. H/C ratios between 1.0 and 1.2 and N, S, and O content of a few weight percent suggest that much of the asphaltene backbone consists of fused aromatic carbon interspersed with polar functional groups containing five to seven heteroatoms per molecule. FTIR analysis reveals many groups capable of forming hydrogen bonds, including carboxylic acids, carbonyls, phenols, and pyrrolic and pyridinic nitrogen [45-49]. These groups are capable of donating or accepting protons inter- and intra-molecularly. The most plausible mechanisms of asphaltene

aggregation involve π - π overlap between aromatic sheets, hydrogen bonding between functional groups and other charge transfer interactions. The degree to which aggregate sizes vary is controlled by the polydispersity and chemistry of asphaltene monomers. While these chemical analyses provide valuable information concerning asphaltene chemistry and offer possible mechanisms of interaction, they do not directly probe the colloidal properties of asphaltenes.

The notion of asphaltenes forming colloidal aggregates in crude oil was originally proposed by Nellensteyn [1] and later by Pfeiffer and Saal [2]. They proposed that “dispersions” of asphaltenic aggregates in heavy crudes are solvated by resins and other aromatic compounds. X-ray diffraction measurements by Yen et al. suggested that asphaltene molecules contain a core or several cores of fused aromatic rings with an aliphatic periphery [28]. The flat aromatic core permits cofacial stacking of approximately four to five parallel sheets mediated by π - π bonding [4]. These early structural examinations were followed by more detailed and revealing investigations of the mechanisms of asphaltene aggregation and colloid formation [8,50-52].

The degree of asphaltene aggregation can be obtained from molar mass and neutron or x-ray scattering measurements. Asphaltene molecular weights have been probed by numerous techniques to yield values from one to several thousands of Daltons. The most common technique for measuring number average molecular weights is vapor pressure osmometry in an aromatic and/or polar solvent (e.g., toluene, benzene, pyridine, or *o*-dichlorobenzene) at elevated temperature (50-130°C) [29,53-59]. Typical molar masses range from ca. 800 to 3,000 g/mol in the best solvents. The dissociating power of each solvent varies and the smallest molar mass value observed is not necessarily indicative of the molar mass of an asphaltene monomer. Molar mass variations with solvent and temperature suggest changes in aggregate size rather than conformational changes in asphaltene structure. Inter-aggregate π -bonding and hydrogen bonding is far weaker than covalent bonding between carbon atoms and can be broken down in the presence of a good solvent or at higher temperatures. Toluene, a weaker solvent, often results in MW of 3,000-6,000 g/mol. This size suggests that, under these solvent conditions, the asphaltenes are not large monomers, but rather small oligomers of three to six monomers.

Small-angle neutron scattering (SANS) and small-angle x-ray scattering (SAXS) are powerful tools to deduce sizes and morphologies of colloidal aggregates in solution. Numerous studies have been performed over the past decade to probe the effects of solvent, temperature and crude oil source on asphaltene aggregate size and polydispersity [8,11,13,51,52,60-74]. While both x-ray and neutron scattering can provide colloid structure information, SANS offers the advantage of solvent-solute contrast via deuteration to decrease data collection times and probe the entire asphaltene aggregate. SAXS, on the other hand, can only discern the aromatic asphaltene core.

Proper analysis of the scattering intensity curves can provide aggregate size (R_g or ξ), shape, molecular weight, and fractal aggregate dimension. However, careful consideration of the molecular picture presented earlier can help guide the analysis. The most logical shape to consider might be a flat disk with a large diameter to thickness ratio. In addition, asphaltene polydispersity should be accounted for. Mono- and polydisperse spheres [51,75], flat disks [12,60,62], prolate cylinders [64], and spherical vesicles [76], have all been suggested as possible asphaltene structures. Sheu et al. suggested a polydisperse spheres model with a Schultz distribution best fit their scattering data [75]. Porte et al. suggested that asphaltenes aggregate through 2-D stacking interactions in which the highly flexible monomolecular sheets spontaneously bend out of the aromatic plane, forming hollow spherical vesicles [76]. This vesicle model was quantitatively consistent with both scattering and viscosity data. Overfield et al. measured R_g of vacuum resid asphaltenes in deuterated toluene at several temperatures [51]. R_g decreased from 116 Å at 25°C to 55 Å at 100°C and was explained by aggregate dissociation rather than an asphaltene conformational change. Aggregate size changes caused by temperature variation were, however, reversible. Lin et al. fit $Q > 0.01 \text{ \AA}^{-1}$ data to a disk-like model with average R_g around 40 Å [69]. At smaller Q values (i.e. larger length scales) the data suggest the presence of larger aggregates or particles too sizeable to probe by Guinier analysis. They suggested that these large particles had diameters of approximately 1,000 Å and often formed at high concentrations and/or low temperatures. Espinat et al. measured the scattered intensity from asphaltenes in several solvents and at low and high temperature [62]. In toluene, 2 wt % Boscan asphaltene solutions formed larger aggregates at room temperature (234 Å diameter) than at 76°C (175 Å). At room temperature, aggregate sizes were two to four times smaller in high polarity solvents such as

pyridine and tetrahydrofuran than benzene. However, at elevated temperatures (up to 80°C), the solvent effect was less significant and aggregate size approached a minimum. Increased heptane fraction in mixtures of heptane and toluene tend to enhance asphaltene aggregation and lead to higher R_g values [13]. Fenistein and Barré fractionated asphaltenes by ultracentrifugation and found that R_g and molecular weight increased with fraction density/weight [72]. Roux et al. used SANS to study temperature and concentration effects on the structure of Safaniya asphaltenes in toluene [74]. At asphaltene volume fractions less than 3-4%, aggregates were well solvated with molecular weights on the order of 10^5 g/mol and R_g values from 30 to 90 Å.

Molecular weights determined from neutron scattering of polydisperse asphaltene systems are weight averaged and may be biased by the presence of a small number of high mass aggregates. As the aforementioned aggregate size data suggests, asphaltene solubility can vary appreciably in solvents containing different polarities and aromatic carbon content. Solvents that more closely resemble and interact with asphaltene microstructure can affect a greater state of dissolution than low polarity, aliphatic solvents. The application of heat can further disrupt the aggregation process and reduce the equilibrium aggregate size. Through asphaltene solubility and aggregate size measurements in different solvents and temperature regimes, we will begin to unravel the complex mechanisms of aggregation. By fractionating and concentrating the more polar and aromatic material, we should be able to enhance the degree of asphaltenic aggregation. Several recent studies have probed the effects of asphaltene fractionation by differential solubility in terms of chemical composition. Nalwaya et al. [35] and Kaminski et al. [77] have fractionated asphaltenes in mixtures of pentane and methylene chloride to analyze their chemistry and dissolution kinetics. Higher polarity fractions had lower rates of dissolution compared to lower polarity fractions. These authors linked the high polarity to heteroatom and metals content, particularly iron, nickel, and vanadium.

Yarranton and Masliyah employed solubility and precipitation methods to study the solution behavior of heptane precipitated Athabasca asphaltenes [58]. Asphaltenes were added to premixed hexane-toluene solutions and then filtered in the solubility method. The precipitation method involved complete dissolution in toluene followed by hexane addition and filtration. Both methods yielded identical mass fractions of insoluble asphaltenes except

at low solute concentrations. At a toluene volume fraction equal to 0.5, less than 10 % (w/w) of the asphaltenes were insoluble. Presumably, the insolubles mass fraction was negligible in solvents that were more aromatic. Of greater significance, molar masses were inversely proportional to the extent of precipitation. In solvents very close to the solubility limit (slightly below 50 % (v/v) toluene), where only a small fraction precipitated, asphaltene insolubles had the highest molar mass. As the solvent blends became less aromatic, the fraction precipitated increased and molar mass decreased. These results suggest that the asphaltenes most prone to precipitation have the largest monomer or unit sheets and/or aggregate to the greatest extent.

Andersen et al. studied the precipitation of asphaltenes in mixtures of heptane and toluene from undiluted Boscan crude oil and from the heptane insoluble portion of Boscan crude [57]. They found that asphaltenes were more soluble in crude oil (presumably due to resins and other aromatics) than in heptane-toluene blends that mimicked the crude composition. Enhanced solubility reduced the yield of insolubles and concentrated the more polar and aromatic structures as evidenced from fluorescence measurements. Of greatest consequence was the large difference between soluble and insoluble asphaltene molar masses by VPO. The soluble asphaltenes formed aggregates nearly five times smaller than corresponding insolubles.

In this work, we have determined the solubility profiles of four asphaltenes in mixtures of heptane and toluene, or so-called “heptol” mixtures, at fixed concentration. At solvent conditions where asphaltenes precipitate (high ratios of heptane to toluene), we have isolated the soluble and insoluble material for further study. Additional solubility profiles were prepared for the more and less soluble fractions in heptol. Detailed chemical analyses were performed to measure the degree of polarity and aromaticity in the insoluble fraction. Intermolecular interactions were probed with SANS in various heptol mixtures at 25°C and 80°C. Comparison of asphaltene fraction chemical composition to solubility and aggregate size data can help elucidate the mechanism of asphaltene aggregation and its dependence on chemistry and solvency. Heuristics and fundamental understanding, gleaned from careful scattering and nanostructural studies, can enable mitigating the deleterious effects of asphaltene aggregation.

A.3 Experimental

A.3.1 Asphaltene Source

Asphaltenes were precipitated from four crude oils: B6 and Hondo (off-shore California), Arab Heavy (Safaniya), and Canadon Seco (Argentina). For brevity the following abbreviations will be used to describe the asphaltenes generated from Hondo, Arab Heavy, and Canadon Seco crude oils, respectively: HO, AH, and CS. These crude oils are asphaltene rich and vary in viscosity, resin to asphaltene (R/A) ratio, and asphaltene H/C ratio and heteroatom content. Basic crude oil and asphaltene properties are summarized in Table A.2.

A.3.2 Asphaltene Precipitation

All crude oils were stored near 0°C in sealed containers under an argon blanket to minimize possible oxidation. The crude oil was warmed to room temperature and shaken vigorously to ensure homogeneity before sampling. Several (typically 6-8) 15-20 g aliquots of crude oil were diluted with *n*-heptane 40:1 by volume and gently shaken for 24 hrs. Since the crude oils were viscous and only partially soluble in heptane, the flasks were initially hand shaken to completely disperse all material. After the continuous shaking, the precipitated asphaltenes were removed by vacuum filtration through 15 cm diameter, 1.5 µm Whatman 934-AH glass microfiber filter paper. The filter cake was rinsed with 10 mL aliquots of *n*-heptane to remove any maltenes that may have reported to the “soluble” fraction. All solvents used were HPLC grade and obtained from Fisher Scientific. Additional aliquots of heptane were added to the filter cake until the washings eluted through the filter paper were clear in color. The filtrate was isolated and methylene chloride was used to redissolve the asphaltenes under partial vacuum. The methylene chloride-asphaltene solution was rotary evaporated under partial vacuum at 40°C. After evaporating a substantial volume of solvent, the remaining solution was transferred to glass jars and placed under an argon stream for further drying. Once nearly dry, the samples were moved into a nitrogen flushed vacuum oven at 50°C for 24-36 hours. Throughout the remainder of this manuscript, the asphaltenes isolated from the original crude source will be referred to as the “Whole” asphaltenes.

A.3.3 Asphaltene Solubility Determination

The solubility of all asphaltenes was determined gravimetrically in mixtures of heptane and toluene. Asphaltene solutions with a concentration of 0.75% (mass solute/volume solvent) or ~ 1% wt. were prepared by dissolving the asphaltenes (~0.1125 g) in 15 mL of a heptol. Asphaltenes were completely dissolved in toluene prior to the addition of heptane, which served as a nonsolvent, and the solutions were allowed to equilibrate for 12 hrs. The solutions were then vacuum filtered through 5.5 cm diameter, 1.5 μm Whatman 934-AH glass microfiber filter paper and a rinse solvent (7.5 mL) of equivalent heptol composition was poured immediately onto the filter cake to remove any remaining soluble material. The filtrate was isolated and the precipitate was redissolved using warm methylene chloride. Two solutions were generated during the fractionation process: one solution containing the more soluble or so-called “Soluble” asphaltenes in heptol and the other containing the less soluble or so-called “Precipitate” asphaltenes in methylene chloride. Each solution was rotary evaporated and dried in a nitrogen flushed, 50°C vacuum oven for 24 hours. The solubility of asphaltenes in heptol was subsequently gauged by the mass percentage of material that precipitated in a particular solvent mixture. A solubility profile for the “Whole” asphaltene was generated by performing the above gravimetric experiments under a range of solvent compositions. To probe the chemical differences between the asphaltenes that precipitated and those that remained soluble, each asphaltene was separated into Precipitate and Soluble fractions at the preparative scale. The corresponding heptol mixture needed to generate the Precipitate and Soluble fractions was asphaltene specific and was chosen to generate an approximate 1:2 mass ratio of Precipitate to Soluble. The Precipitate and Soluble fractions had markedly different chemical compositions and physical properties and sufficient material was generated per batch for the subsequent analyses.

A.3.4 Chemical Characterization

Elemental analysis (C, H, N, S, and O) and vapor pressure osmometry were performed by Darlene Mahlow at the University of Alberta (Dept. of Chemistry, Edmonton, Alberta, Canada). Number average molecular weights of selected asphaltenes were determined in toluene at 53°C with a Corona Wescan Vapor Pressure Osmometer. In the VPO device, vapor pressure is measured indirectly using two thermistors to measure voltage

changes (ΔV) caused by changes in temperature. The measuring chamber contains a solvent reservoir and two wicks that provide a saturated solvent atmosphere around the thermistors. At one thermistor, the pure solvent is replaced by solution. Subsequent condensation of the solvent from the saturated atmosphere into solution releases heat and increases the thermistor temperature. Condensation and thermistor temperature will increase until the vapor pressure of the solution matches that of the pure solvent at the given chamber temperature. Solutions were prepared at concentrations ranging from 1 to 20 mg/mL. The values of $\Delta V/C$ at each concentration were converted to an apparent molar mass using the calibration factor determined for a standard solute (Benzil). Metal analyses (Fe, Ni, V, and Na) were performed at Ondeo-Nalco Energy Systems (Sugar Land, TX). Metals content was determined by inductively coupled plasma (ICP) method with a Jerrel Ash 9000 after ashing the samples at 600°C and dissolving in HCl and deionized water.

A.3.5 Small Angle Neutron Scattering: 25°C

Neutron scattering is an important technique for determining solute aggregate sizes on a submicron scale. A broad wave vector (Q) range, high neutron flux and large number of scatterers are the ideal conditions to probe the scattering behavior of aggregates. Most of the SANS measurements reported were performed on the 30 m, NG7 and 8 m, NG1 small angle spectrometers at the NIST Center for Neutron Research (Gaithersburg, MD)-- with the exception of the SANS data presented in Figure A.9, which was collected on the SAND instrument at the Intense Pulsed Neutron Source at Argonne National Laboratory (Argonne, IL).

During the SANS (NIST) experiments, the source-to-sample distance was varied from 4 to 16 m while the sample-to-detector distance was varied from 1.2 and 15 m. Neutrons of 6 Å and 0.22 spread ($\Delta\lambda/\lambda$) were scattered from the sample and collected on a two dimensional detector (65 cm by 65 cm, 1 cm by 1 cm resolution). The instrument geometry and neutron wavelength values bound the operating Q range following the equation:

$$Q = 4\pi\lambda^{-1} \sin \theta \quad (1)$$

where θ is half of the scattering angle and λ is the neutron wavelength. The available Q range extended from 0.0015 to 0.6 \AA^{-1} but an intermediate range of 0.0022 to 0.3 \AA^{-1} was adequate for most asphaltene solutions.

Asphaltene solutions of 1 % (w/w) were prepared in perdeuterated solvents -- toluene and heptane or 1-methylnaphthalene -- to enhance scattering contrast. Solvents were obtained from CDN Isotopes and had >99.9 % chemical purity and >99.5 % perdeuteration. Dissolution was performed first in perdeuterated toluene followed by heptane addition and equilibration over several days. All solutions were transferred from glass vials to the quartz cells without filtration, even in the cases where some precipitation was evident (a low temperature phenomenon).

Samples were measured at 25°C in cylindrical quartz sample cells (NSG Precision Cells) with a path length of 5 mm. During beam operation, samples were run at high Q with the detector positioned 1.2 m from the sample (large θ). After each sample had been run, the detector was repositioned to 15 m to allow for low Q scanning (small θ). The scattering intensity, $I(Q)$, was obtained from the total detector counts corrected for neutron transmission through the sample, background radiation, scattering through an empty cell, and detector sensitivity. For the data collected, it was necessary to splice the low Q and high Q data obtained from different detector positions.

The Small Angle Neutron Diffractometer (SAND) instrument at Argonne National Laboratory is a time-of-flight diffractometer attached to an accelerator-based pulsed neutron source (30 Hz). Each pulse contained neutrons with wavelengths ranging from 1 to 14 \AA . The higher energy neutrons had lower wavelengths and reached the sample ahead of the lower energy neutrons. Thus, the energy of each scattered neutron was determined by its "time-of-flight" to the detector. The sample-to-detector distance was fixed at 2 m. Neutrons were collected on an area detector (40 cm by 40 cm, 4 to 6 mm FWHM resolution). The available Q range extended from 0.0035 to 2 \AA^{-1} . The data presented in Figure A.9 were collected at 25°C in cylindrical quartz sample cells (NSG Precision Cells) with a path length of 2 mm.

A.3.6 Small Angle Neutron Scattering: 80°C

High temperature neutron scattering of the asphaltene samples was performed on both NG1 (8 m) and NG7 (30 m) beamlines. Both instruments had multisample holders, with attached circulating water-glycol baths, capable of maintaining 80°C. All samples were initially dissolved in toluene and underwent a temperature cycle (80°C, 1 hour) prior to heptane addition to ensure complete dissolution. Immediately prior to measurement, the asphaltene solutions were transferred to 5 mm path length quartz cells and placed in an 80°C bath for 1 hour. This time allowed the solutions to reach thermodynamic equilibrium.

A.4 Data Handling

Scattering intensity versus scattering angle ($I(Q)$ vs. Q) curves were fit to Lorentzian lineshapes using non-linear least squares regression to determine the aggregate size and morphology. Following the Ornstein-Zernike formalism the scattering intensity, I , can be related to the scattering vector, Q , by:

$$I(Q) = \frac{I_0}{1 + (Q\xi)^2} \quad (2)$$

where I_0 is the zero- Q scattering intensity and ξ is the correlation length [71,78]. In some systems, a Porod upturn was observed at low Q where the scattering intensity increased monotonically with decreasing Q . Roux et al. observed a similar low Q feature for Safaniya asphaltenes in toluene, particularly at low temperature (i.e., 8°C and 20°C), that diminished in intensity with heating [74]. A low Q upturn indicates the presence of large agglomerates in solution. Incoherent scattering of all nuclei in the solvent and solute with non-zero spin was also manifested in the scattering curves at large Q values (typically $Q > 0.1$) as an isotropic background signal. The Q values that marked the transition between the various length scales of aggregation were determined from inflection points in the scattering curves. The Lorentzian lineshape described in Equation 2 was applied to all samples over the intermediate range of Q values between the inflection points.

The zero- Q scattering intensity, I_0 , provides additional information concerning the particle geometry and is related to the weight-average molecular weight (M) of the aggregates by the expression:

$$I_0 = \frac{\Delta\rho^2 CM}{N_A d^2} \quad (3)$$

where N_A is Avogadro's number, C is the concentration of scatterers, d is the scatterer density, and $\Delta\rho^2$ is the coherent scattering contrast between the solvent and solute. Given that elemental compositions of the asphaltenes are available, it is possible to calculate the scattering contrast terms, and subsequently, the weight-average molecular weight of the aggregates; however, this calculation and subsequent comparison to asphaltene aggregate sizes will be addressed in a future paper.

A.5 Results and Discussion

Solubility profiles for the Whole asphaltenes isolated from AH, B6, CS, and HO crude oils were determined by the previously described gravimetric method (Figure A.1). The asphaltenes were completely soluble in pure toluene and in heptol mixtures of high aromaticity ($> 52\%$ (v/v) toluene). The observed amount of precipitated material increased with heptane addition in the insoluble regime. The critical heptol concentration for the initial formation of precipitates ranged from 45-52% (v/v) toluene depending on the asphaltene. The addition of heptane to toluene reduced the three dimensional solubility parameters of the solvent [79,80], resulting in flocculation and precipitation of the asphaltene aggregates.

The results in Figure A.1 compared well with those obtained by Andersen et al. [57], who performed a series of precipitation and re-dissolution experiments on Boscan asphaltenes in heptol. The direct addition of heptol to the crude oil precipitated less material than observed in Figure A.1, likely due to the solubilizing effects of resins and other aromatic components present in the crude oil; however, better agreement was obtained after precipitating the asphaltenes in heptane and redissolving in heptol. For example, Andersen observed that 13%, 46%, and 60% (w/w) of the asphaltenes precipitated in solvent compositions of 50%, 40%, and 30% (v/v) toluene, respectively. The Boscan asphaltenes were slightly less soluble than CS, the least soluble asphaltene presented in Figure A.1.

The process of precipitation was likely controlled by dispersion and π - π bonding interactions between the asphaltenes and the solvent mixture, as suggested by the refractive index measurements performed by Buckley [81,82]. Buckley performed heptane titration experiments on an Alaskan crude oil dissolved in toluene and various solvents and observed

a nearly constant value of the index of refraction for the solution at the solubility limit [81]. Buckley also showed that asphaltene precipitation was reversible by adding toluene to a precipitated mixture of crude oil in heptane and observing that the asphaltenes completely redissolved in solutions with the same refractive index value at which they initially precipitated [82]. Porte et al proposed that while precipitation was controlled by weak dispersion forces, asphaltene aggregation was driven by strong specific polar and hydrogen bonding forces [76]. As previously mentioned, asphaltenes are characterized by their high aromaticity, the presence of polar heteroatoms, and their ability to participate in hydrogen bonding interactions. If asphaltenes containing a higher percentage of fused aromatic rings and polar heteroatoms tend to form the largest aggregates in solution, then it seems reasonable that these species would be the first to precipitate from solution as the solvent quality decreases below the solubility limit.

A.5.1 Asphaltene Fractionation

To test the hypothesis that fractionation concentrated the more aromatic and polar asphaltenes in the less soluble fractions, so-called “Soluble” and “Precipitate” fractions were prepared for the various asphaltenes on a preparatory scale. The fractionation conditions and amounts of each fraction generated are shown in Table A.3. Due to its high solubility, AH was precipitated at the highest ratio of heptane to toluene. The other three asphaltenes underwent fractionation at heptol ratios close or equal to 40 % toluene. Throughout the course of the study, AH and B6 were fractionated three times each, with reasonable reproducibility (see Table A.3).

There were several differences observed between the Precipitate and Whole asphaltenes. After the initial filtration and heptol rinse steps, the Precipitate fraction remaining on the filter paper was significantly less soluble in methylene chloride than the Whole. B6, CS, and HO were the least soluble and required submerging in warm to hot solvent for several minutes to completely redissolve. This behavior indicates the Precipitate fraction had an enhanced degree of inter-aggregate bonding compared to the Whole and Soluble fractions. The Soluble fraction appears to cooperatively solvate the Precipitate fraction through disruption of the strong polar and hydrogen-bonding interactions that drive self-association in the Precipitate fraction.

Solubility curves of the Soluble and Precipitate asphaltenes are shown in Figures A.2a-d. The Precipitate solubility curves provided the most convincing support for cooperative aggregate interaction. For example, one would expect that if the B6 Precipitate fraction were non-interacting, it would begin to precipitate at the same heptol ratio as B6 Whole (~ 52% toluene) and become completely insoluble at the original fractionation condition of 40% toluene. However, removal of the Soluble fraction from the Whole asphaltenes caused the Precipitate fraction to become insoluble at a higher toluene volume fraction than expected, particularly with B6 and HO. In fact, the B6 Precipitate fraction was observed to be slightly insoluble in pure toluene.

Also noteworthy was the solubility behavior of the Soluble asphaltenes at the same heptol ratios used for their preparation. One would expect AH Soluble to be completely soluble in 30% toluene, however, ~15% of the asphaltenes precipitated at this condition. Both B6 and HO Soluble demonstrated this “early” precipitation behavior to a lesser degree while CS Soluble behaved “ideally”. In these cases, it is likely that the Solubles may benefit from some portion of the Precipitate to help them retain solubility. In all cases, the Soluble fraction was far more soluble than either the Whole or Precipitate fractions. Removing the Soluble fraction from the Precipitate fraction dramatically decreased the kinetics of dissolution and the ultimate solubility of the Precipitate fraction. In this sense, the Soluble fraction acted cooperatively to keep the more aromatic and polar material in solution.

Strictly speaking, solubility profiles for the Soluble and Precipitate fractions would have been best compared to the Whole asphaltenes when dissolved at heptol concentrations that mimicked the fractionation condition-- 0.25% (w/v) for the Precipitate fraction and 0.5% (w/v) for the Soluble fraction. However, solubility studies by Cimino et al. [17] and Porte et al. [76] indicated that the onset of precipitation is nearly independent of dilution at low concentrations (< 2% wt.). Cimino et al. dissolved pentane precipitated asphaltenes from a light crude oil in several different solvents at ambient conditions and titrated with an anti-solvent until the precipitation threshold was observed [17]. The authors plotted the mass ratio of nonsolvent:asphaltene vs. the mass ratio solvent:asphaltene and observed a linear dependence of the two variables, suggesting that asphaltene concentration did not affect the solubility limit over the range of concentrations studied. Porte et al. obtained similar results for Lagrave crude oil dissolved in toluene (solvent) and pentane (nonsolvent) [76]. The

solubility limit corresponded to a pentane volume fraction of 0.5, regardless of concentration. The authors explained this observation by a small value of the entropy of mixing of the aggregates in the solvent. It seems reasonable to extend this assumption to the Whole, Soluble, and Precipitate fractions in this study, which only vary in terms of aromaticity and heteroatom content.

A.5.2 Asphaltene Fraction Chemistry

Combustion elemental analysis was performed to determine H/C ratio and polar heteroatom content in each fraction generated (i.e., Whole, Soluble, and Precipitate), as shown in Table A.4. H/C ratio correlates well with aromaticity (i.e., a lower H/C ratio implies a greater number of fused aromatic rings). In all cases, the Precipitate fraction was enriched in aromatic carbon while the Soluble aromaticity was diminished. As shown in the table, nitrogen content decreased modestly with increasing asphaltene solubility. Nitrogen can be found in several functional forms including amines, amides (carbonyl amides), pyrroles, and pyridines. Some nitrogen-containing functional groups, such as pyridine, are basic and can participate in strong hydrogen bonding interactions that are much greater than dispersion forces between aromatic asphaltenic cores. Sulfur is typically found in thiophenic rings, sulfides, and, to a smaller extent, in sulfoxide groups. Sulfoxides may be present because of asphaltene oxidation during handling. As stated previously, asphaltenes were handled under argon atmosphere to minimize oxidation. AH, B6, and HO asphaltenes contained modestly higher concentrations of sulfur than CS asphaltenes; however, there did not appear to be a correlation between asphaltene fraction or solubility behavior and sulfur content. Again, the variations from Soluble to Precipitate are subtle, but both increased polarity and aromaticity contribute to the macroscopic solubility behavior.

This phenomenon was first observed by Szewczyk et al., who fractionated C₇-asphaltenes obtained from Rospomare crude oil in mixtures of σ -xylene and n-heptane [83]. Four complementary fractions of “Soluble” and “Insoluble” asphaltenes were isolated with the Insoluble fractions (FI1 to FI4) consisting of 37, 56, 64, and 74% (w/w) of the unfractionated asphaltenes, respectively. Combustion chemical analyses showed that the Insoluble fractions were typically higher in aromaticity and heteroatom content (i.e., N and O) than the corresponding Soluble fractions. For the most part, sulfur content remained

evenly distributed throughout the fractions. Chemical analysis of pyrolysis products suggested that oxygen was located near the periphery of the aggregates, causing them to be more accessible to aggregation through polar and hydrogen bonding interactions. Many of the above observations (e.g., increase in nitrogen content and aromaticity with decreasing asphaltene yield and even distribution of sulfur species) were also verified by Andersen et al. in the chemical analyses of Boscan asphaltene fractions [57].

The results of metals analyses for the various asphaltene fractions are shown in Table A.5. Ni and V are often bound within porphyrin rings in asphaltenes and have been associated with difficulties during hydrocatalytic upgrading of crude oils [84]. In general, the Precipitate fractions were enriched with Fe, Ni, V and Na. B6 and HO fractions contained significantly more Ni and V than the AH and CS fractions. Kaminski et al. fractionated asphaltenes in mixtures of methylene chloride and pentane and found that the most polar fraction contained the highest concentrations of Fe, Ni, and V and typically had the lowest dissolution rates in dodecyl benzene sulfonic acid-heptane mixtures [77].

The relatively high concentration of Na in the B6 fractions may be due in part to its offshore source (see Table A.5). Water containing dissolved salts may have been dispersed in the crude oil during the asphaltene precipitation and subsequently partitioned into the Precipitate fraction during the fractionation process. In order to test for the presence of water-soluble salts, B6 crude oil was dissolved in methylene chloride and extracted with deionized water in a separatory funnel. The Na content of the Whole asphaltenes precipitated from the water-extracted crude oil was reduced to from 9300 ppm to 35 ppm. Total Ca and K contents were also reduced while Ni, V and Fe contents remained unchanged. This suggests that the high alkali and alkaline earth metals contents in B6 were attributable to either water-soluble inorganic salts or water-soluble soaps of corresponding carboxylic acids.

Based on the relative aromaticity and nitrogen content of the four Whole asphaltenes, some plausible explanations of precipitation can be offered. AH and CS Whole contained less nitrogen and had a relatively low H/C ratio compared to B6 and HO Whole asphaltenes. The aggregation mechanism for AH and CS asphaltenes was likely dominated by dispersion forces or differences between asphaltene and solvent aromaticity (π - π bonding interactions). B6 and HO Whole asphaltenes had relatively low aromaticities but were relatively nitrogen rich, suggesting polar and hydrogen bonding interactions may play a significant role in the

asphaltene association mechanism. As we will demonstrate in the next section, variations in the chemical composition of the asphaltene fractions are linked to the size of aggregates formed in solution. In a subsequent paper, we will demonstrate the impact of aggregate formation on the stability of asphaltene stabilized water-in-oil emulsions [85].

A.5.3 Vapor pressure osmometry of asphaltenes and their fractions

VPO apparent molar masses of B6 Soluble, Whole and Precipitate fractions in toluene are shown in Figure A.3. B6 Soluble had the lowest molar mass of all the fractions with a maximum value of $\sim 3,000$ g/mol. The limited number of data points does not allow an accurate prediction of the zero concentration molar mass; however, extrapolation of the two lowest concentration data points predicts a value of ~ 2000 g/mol. B6 Whole was slightly more aromatic, polar and less soluble than the Soluble fraction, and the molar mass values for B6 Whole were roughly 500 g/mol higher than the Soluble fraction over the concentration range studied. B6 Precipitate molar mass values were higher than the Whole and Soluble asphaltenes by almost an order of magnitude. Even at high dilution, the apparent molar mass of B6 Precipitate asphaltenes exceeded 10,000 g/mol, suggesting strong intermolecular interactions within the aggregate. B6 Precipitate asphaltenes were also more difficult to dissolve than the Whole and Soluble fractions. Nevertheless, the molar mass values observed for B6 Whole, Soluble, and Precipitate fractions were consistent with those obtained by Yarranton [59]. For example, Yarranton found that the molar mass values of heptane precipitated Athabasca asphaltenes increased with bulk concentration from ~ 2000 g/mol at low concentration to a limiting value of ~ 10000 g/mol at 20 g/L (~ 2 wt %). Low concentration extrapolation revealed apparent monomer molar masses of approximately 1,000-2,000 g/mol.

In contrast to B6 asphaltenes, CS Whole and Precipitate fractions had nearly identical molar masses at each concentration examined (Figure A.4). Zero concentration extrapolation indicated minimum sized aggregate molar masses of approximately 3,000 g/mol. The relatively low molar mass of CS Precipitate asphaltenes compared to B6 Precipitate suggests that heating of the samples to 53°C might significantly disrupt the dispersion and π - π bonding forces that dominate asphaltene aggregation in CS asphaltenes, but is ineffective at disrupting the polar and hydrogen bonding forces that dominate aggregation in B6 Precipitate

asphaltenes. A similar response to heating was observed for the fractions when studied by SANS at 25°C and 80°C, as seen in the next sections.

The VPO results presented in Figures A.3 and A.4 show definite qualitative differences in the aggregation behavior of B6 and CS asphaltene fractions; however, the effect of precipitated solids within the samples on VPO measurements are not easily quantified. For example, the occurrence of 25000 ppm of sodium in the B6 Precipitate fraction suggested that this fraction may have contained as much as 6% (w/w) inorganic solids, assuming that sodium occurred in the form of NaCl. The presence of NaCl in the fraction is not expected to interact appreciably with the solvent and affect the vapor pressure; however, uncertainty is introduced in the effective asphaltene concentration. Inorganic solids may have been present in other asphaltene fractions and affected the VPO measurements to a lesser extent (e.g., B6 Whole contained 9300 ppm sodium). Furthermore, voltage measurements collected at low concentrations (<1 g/L) were subject to greater uncertainty than those collected at higher concentrations due to low instrument sensitivity. The total uncertainty in any of the molar masses presented was estimated to be less than 20%. Within this estimated uncertainty, general qualitative differences in molar mass between the Whole, Soluble, and Precipitate fractions are readily apparent. The SANS measurements discussed in the next section will provide a more sensitive measurement of how asphaltene aggregate size varies within the fractions as a function of temperature and solvent conditions.

A.5.4 Small Angle Neutron Scattering: 25°C

Neutron scattering curves of intensity (I) versus scattering vector (Q) of B6 Whole asphaltenes in several mixtures of deuterated heptol are shown in Figure A.5. Based on the shape of the neutron scattering curve alone, one can readily distinguish solutions of small aggregates from flocculated systems. For example, the low Q plateau behavior for B6 Whole asphaltenes in pure toluene indicated that the solution contained soluble, non-interacting nanoparticle aggregates. The remaining B6 Whole scattering curves exhibited an intense low Q feature superimposed on a Guinier plateau. The presence of a low Q feature indicated that reduced solvent aromaticity was driving a small fraction of the nanoparticle aggregates to flocculate into microscale aggregates or “flocs” that retained their solubility in solution. The absence of a second plateau region in the lowest Q range suggested that the largest flocs had

a size greater than the order of $1/Q_{\min}$ (or $\geq 1000 \text{ \AA}$). The floc size must have been smaller than $1.5 \text{ }\mu\text{m}$, however, because all solutions above 55% toluene were soluble to filtration. As shown in the next section, the intensity of the low Q upturn was observed to diminish with heating to 80°C ; however, a feature of similar scattering intensity reappeared with subsequent cooling of the sample to 25°C , suggesting an equilibrium condition between the nanoparticle aggregates and microscale aggregates at this temperature. The relative ordering of the intensities at intermediate Q from Figure A.5 suggests that the nanoparticle aggregates were the largest in 55% toluene with aggregate size decreasing as the solvent quality became more aromatic.

Prior to measurement, partial precipitation was observed in the B6 Whole sample dispersed in 40% toluene. For this sample, the scattering intensity in the intermediate Q range decreased relative to 55% toluene, suggesting that solvent conditions have driven the largest aggregates to precipitate, thus leaving the smaller, soluble aggregates behind in solution. In fact, the remaining soluble aggregates were half the size of those in 55 % toluene, as shown in the following section. It can also be deduced from the figure that the size of the large agglomerates (i.e., precipitated material) in the 40% toluene sample was likely greater than those observed for the remaining soluble samples, as indicated by the steeper power law slope in the low Q regime.

$I(Q)$ versus Q scattering curves were fit using the Ornstein-Zernicke formalism to determine solute correlation lengths. Two examples of the Lorentzian fits are shown in Figure A.6. AH Soluble asphaltenes are well dissolved in 50% toluene (Figure A.6a) as shown by the Guinier plateau at low Q values ($\xi = 29.9 \text{ \AA}$). An example of an asphaltene exhibiting significant low Q scattering is shown in Figure A.6b. Here, the low Q upturn is truncated at the inflection point and the intermediate Q portion of the scattering curve for B6 Whole in 60% toluene was fit to obtain a correlation length of 79 \AA . In both cases, the data was truncated in the high Q range to remove the effects of incoherent background scattering.

Correlation lengths deduced from SANS scattering curves of the Whole asphaltenes dissolved in solutions of varying heptol ratio appear in Figure A.7. For each of the asphaltenes the correlation length increased with decreasing toluene content within the soluble regime. This increase suggested that inter-aggregate associations increased as the solvating power of heptol decreased. The maximum in correlation length was near the

solubility limit of the Whole asphaltenes. Crossing the solubility limit caused agglomeration and precipitation of the largest aggregates. The resulting correlation length in the precipitated regime is only a measure of the material remaining in solution and is hence lower than the correlation lengths of the asphaltenes at the solubility limit. Aggregate ξ tended to plateau above 70 % toluene where additional solvent aromaticity was insufficient to further disrupt inter-aggregate bonds. Similar behavior was seen using Cold Lake asphaltenes in mixtures of 1-methylnaphthalene and dodecane [71]. At low to moderate asphaltene concentrations correlation lengths increased to a maximum as the aliphatic solvent volume fraction increased. Upon reaching a critical dodecane volume fraction, the correlation length decreased due to phase separation.

Differences in the solubility behavior of the Soluble and Precipitate fractions suggested that less soluble material would be more prone to aggregation. A comparison of aggregate sizes for Soluble, Whole, and Precipitate fractions (Figures A.7-A.8) indicated the Soluble fraction indeed formed the smallest aggregates while the Precipitate fraction formed the largest aggregates. Similar behavior was observed when comparing the SAXS scattering intensity curves for the Soluble and Insoluble fractions generated by Szewczyk et al. and dissolved in σ -xylene (9 % wt.) [83]. The scattering intensity in the Guinier regime decreased systematically with increasing solubility. Subsequent fitting of the data to a polydisperse disk model indicated that the least soluble aggregates possessed significantly higher values for the average gyration radius, weight-average molecular weight, polydispersity, and Flory self-association constant than the more soluble fractions. Furthermore, these values were observed to decrease with decreasing fraction aromaticity and nitrogen content.

Similar to the Whole asphaltenes, the aggregate size of the Soluble asphaltenes increased with decreasing solvent aromaticity, with the maximum correlation length corresponding to the limit of solubility in solution (Figure A.8a). The scattering curves for the Precipitate asphaltenes showed substantial overlap in scattering intensity between large agglomerates (Porod scattering) and smaller aggregates, and suggested a higher degree of intermolecular association than the Whole and Soluble fractions. The Precipitate fractions for B6, CS, and HO were particularly difficult to dissolve in pure toluene and, once in solution, formed large aggregates with correlation lengths ranging from $\sim 100 \text{ \AA}$ (HO) to \sim

800 Å (CS) as shown in Figure A.8b. The CS and B6 Precipitate fractions were partially insoluble in pure toluene and aggregate size did not appear to vary with solvent conditions. As indicated in Figure A.8b, AH Precipitate remained soluble over a broad range of solution conditions with a solubility limit of ~ 65% toluene that matched closely to the value observed in Figure A.2a. Similarly, Figure A.2d suggested that the solubility limit of HO Precipitate was near 80% toluene and the maximum correlation length observed occurred at 85% toluene. One would expect that if additional SANS experiments were performed in which solvent aromaticity decreased below 80% toluene, the maximum correlation length for HO Precipitate asphaltenes would occur near the observed solubility limit.

An interesting observation concerning the aggregation behavior of the HO Precipitate fraction is the slight, yet reproducible, decrease in aggregate size for solutions in 95 % toluene compared to pure toluene. The correlation length increased upon further heptane addition as the flocculation threshold was approached. Similar behavior was observed by Fenistein et al. for two chemically different asphaltenes dissolved in toluene with a small amount of heptane (< 15% vol.) added as a flocculant [13]. The reduction in aggregate size was attributed to a decrease in the intrinsic viscosity of the solution, indicating a contraction of the aggregates. The intrinsic viscosity of the solutions tended to increase at heptane concentrations above 15% vol. and a corresponding increase in aggregate size was observed.

A comparison of scattering intensity curves for HO Whole asphaltenes in toluene and the weight-averaged summation of scattering intensities from HO Soluble and Precipitate fractions in toluene provided additional evidence that the Soluble fraction interacted with the Precipitate fraction to disrupt intra-aggregate forces (Figure A.9). The total asphaltene concentration in each solution was 1% wt. The summation intensity, I_{sum} , was weight-averaged to model the fractionation conditions according to the equation:

$$I_{\text{sum}} = 0.33I_{\text{ppt}} + 0.67I_{\text{sol}} \quad (4)$$

where I_{ppt} and I_{sol} are the scattering intensities of the Precipitate and Soluble fractions, respectively. As shown in the figure, the good agreement of the incoherent scattering intensities ($Q > 0.2 \text{ \AA}^{-1}$) for the Whole and summation curves suggested that this weight-averaging of the Precipitate and Soluble scattering curves was probably appropriate. Fits of the scattering curves to Lorentzian lineshapes provided correlation lengths for HO Whole and for the hypothetical recombined Whole asphaltenes of 41 Å and 74 Å, respectively. The

observation that the Whole fraction had a lower correlation length than predicted by the hypothetical recombination of the fractions suggested that the Soluble fraction was indeed disrupting polar and H-bonding interactions that influenced self-association of the Precipitate fraction.

A.5.5 Small Angle Neutron Scattering: 80°C

Comparing the scattering curves and correlation lengths of the asphaltenes at 25 and 80°C revealed dramatic but predictable temperature effects. A series of comparative scattering plots for B6 Soluble, Whole and Precipitate at low and high temperatures is shown in Figures A.10a-c. B6 Soluble did not show intense low Q scattering at 25°C and the effect of heating was minimal; correlation lengths were reduced modestly from 51 Å to 39 Å. B6 Whole and Precipitate fractions displayed a significant low Q upturn at 25°C that decreased in intensity with heating to 80°C. In these two cases, scattering intensities in the range $Q < 0.01 \text{ \AA}^{-1}$ were reduced significantly and correlation lengths decreased from 79 Å (Whole) and 240 Å (Precipitate) to 57 Å and 69 Å, respectively. The dramatic reduction of the low Q upturn indicated that heating was effective at disrupting the largest flocs.

Table A.6 presents correlation lengths of asphaltene fractions at similar heptol ratios at 25°C and at 80°C. In general, heating the samples reduced the aggregate sizes of the fractions while maintaining the same relative ordering of aggregate sizes between fractions and crude sources that was observed at 25°C (i.e., $\xi_{\text{Soluble}} < \xi_{\text{Whole}} < \xi_{\text{Precipitate}}$ and $\xi_{\text{AH}} < \xi_{\text{HO}} < \xi_{\text{B6}} < \xi_{\text{CS}}$). In addition, reduction of low Q upturn extended the Guinier plateau to a lower Q range and reduced the uncertainty in aggregate sizes. The Precipitate fraction was generally the most responsive to heating with greater than two-fold reductions in aggregate size. The positive temperature response of the Precipitate fractions relative to the Soluble fractions indicated a high degree of intra-aggregate bonding in the Precipitate fractions. The process of fractionation typically enriched the least soluble asphaltenes with polar and aromatic moieties, species that were likely responsible for aggregation and flocculation. .

The relative polarity and aromaticity of B6 asphaltenic fractions compared to CS asphaltenic fractions also appeared to affect the responses of the aggregates to heating. On a percentage change in correlation length basis, CS Precipitate aggregates that are primarily

stabilized through π -bonding interactions were more receptive to heating than B6 Precipitate aggregates, which are mainly stabilized through polar and hydrogen bonding interactions. The disruption of dispersion and π - π bonding interactions in CS Precipitate at 53°C might explain the similarities between the molar masses of CS Precipitate and CS Whole determined from VPO. Similarly, heating of B6 Precipitate to 53°C was apparently not effective at disrupting the stronger polar and hydrogen bonding forces that dominated self-aggregation in this fraction. Hence, significant differences were observed between the molar masses of the B6 Whole and Precipitate fractions.

An attempt was made to find the aggregate size corresponding to an asphaltene monomer or irreducible oligomer by dissolving each of the asphaltene fractions in deuterated 1-methylnaphthalene. This solvent was more aromatic with a larger molecular dimension than toluene, suggesting that it may interact more effectively with asphaltene aggregates through dispersion forces. A comparison of correlation lengths obtained for the various asphaltene fractions in toluene and 1-methyl naphthalene at 80°C is shown in Table A.7. In all cases, 1-methylnaphthalene was a better solvent for asphaltenes than toluene, with the largest reduction in aggregate sizes occurring in the Precipitate fractions. As expected, CS Precipitate, with its aggregation behavior dominated by dispersion forces and π - π bonding interactions, showed the largest reduction in aggregate size (~ 41%). Most other fractions showed a reduction in correlation length of 10-25% when dissolved in 1-methyl naphthalene instead of toluene. It would be difficult to further reduce aggregate sizes except by dissolution in a more polar solvent (e.g., a 1-methyl naphthalene/methanol mixture) or by addition of a solvating agent (such as resins).

In all cases, Soluble asphaltenes were affected the least and Precipitates were affected the most by the temperature increase. This evidence suggests the Precipitate fraction was enriched with temperature-sensitive intermolecular bonds—most likely hydrogen bonds. Another possibility for the occurrence and disappearance of low Q scattering features with temperature fluctuations that must be discarded is the that waxes were co-precipitated with the asphaltenes during their preparation and subsequent fractionation. Most waxes have melting points above 60-70°C, which could explain the disappearance of a low Q upturn at 80°C; however, Bragg scattering peaks that are indicative of crystallinity were not evident in the scattering curves at 25°C. To rule out the possibility of wax contamination, high

temperature simulated distillation (HTSimDist) was performed on B6 and CS Whole [86]. Neither B6 nor CS asphaltenes contained any discernable wax peaks. These findings ruled out the possibility of neutron scattering from non-asphaltenic structures that may be present in crude oil. Each of the aggregation phenomena seen resulted from the propensity of asphaltenes to form aggregates mediated by intermolecular bonding.

A.6 Conclusions

The solubility behaviors, chemical properties and aggregation extents of four asphaltenes and their soluble and insoluble fractions were examined. Whole, unfractionated asphaltenes were soluble to filtration in heptol containing greater than 52 % (v/v) toluene. The more and less soluble fractions had solubility limits approximately 10 % (v/v) lower and 30% (v/v) higher in toluene, respectively, than the corresponding Whole asphaltenes. The mechanism of precipitation was controlled by dispersion interactions between the asphaltenes and solvent; however, the “early” precipitation behavior of the less soluble fractions in relatively aromatic solvents suggested that the Soluble fraction served to disrupt the strong polar and hydrogen-bonding interactions that drive self-association in the Precipitate fraction. Further evidence of a cooperative interaction between the Soluble and Precipitate fractions was observed from the SANS studies. The observation that HO Whole asphaltenes had a lower correlation length than predicted by the hypothetical recombination of the Soluble and Precipitate fractions suggested interaction of the more and less soluble fractions.

In general, several key trends were demonstrated by the neutron scattering behavior of asphaltene-heptol systems. For example, aggregate correlation length increased with decreasing solvent aromaticity up to the solubility limit, beyond which the aggregate size decreased with heptane addition. The maximum in soluble aggregate size, as calculated from the Lorentzian portion of the scattering curve in the accessible Q range, always appeared at the limit of asphaltene solubility. Crossing the solubility limit caused significant agglomeration and precipitation of the largest aggregates that, consequently, consisted of the most polar and aromatic asphaltenes. After precipitation, the remaining soluble material tended to form smaller, more labile aggregates with dispersion forces as the dominant contribution to aggregation behavior.

Number average molar masses determined by VPO in toluene at 53°C indicated that B6 Precipitate asphaltenes were more highly aggregated than the corresponding B6 Whole and Soluble fractions. The CS Precipitate and Whole fractions had similar molar mass values that were slightly higher than those observed for B6 Whole asphaltenes. The relatively low molar mass of the CS Precipitate fraction relative to the B6 Precipitate fraction suggested a distinct difference in the aggregation mechanisms of the two fractions.

By comparing the elemental analysis, VPO, and SANS results, we can deduce the mechanisms that influence the solubility and aggregation of asphaltenes in solution. Of the four crude asphaltenes, CS asphaltenes formed the largest aggregates in heptol. The solubility mechanism for CS asphaltenes appeared to be dominated by aromatic π - π bonding interactions due to their relatively low H/C ratio (~ 1.1) and nitrogen content (~ 1.3 % w/w). B6 and HO asphaltenes formed similar sized aggregates in heptol that were smaller than the corresponding CS sub-fractions. With B6 and HO asphaltenes, the solubility mechanism was likely driven by polar interactions due to their high H/C ratios (> 1.2) and relatively high nitrogen contents (1.8 % to 2.1 % w/w). AH asphaltenes, possessing the lowest nitrogen contents (0.9 % to 1.1 % w/w) and relatively low H/C ratios, formed the smallest aggregates in heptol. The ability to participate in polar and H-bonding interactions was the major difference in the aggregation behaviors of CS and AH asphaltenes, the largest and smallest aggregate formers, respectively.

The presence of a Porod feature in the neutron scattering curves indicated the asphaltene solutions contained both individual aggregates and a portion of highly aggregated or precipitated material larger than 1000 Å in size. Heating the samples to 80°C aided the dissolution of the agglomerates and was effective at reducing the intensity of the low Q scattering. The observation that heating was most effective at reducing the correlation lengths of the less soluble asphaltenes suggested that temperature sensitive inter-aggregate bonds, most likely hydrogen bonds, were being broken. Similarities in correlation length between samples prepared at 25°C and samples that were heated to 80°C then allowed to cool back to 25°C suggested that heating the samples to aid dissolution did not appear to adversely affect the scattering measurements. Aggregate sizes were further reduced when measurements were performed in 1-methyl naphthalene (a more dispersive solvent) rather than toluene. Methyl naphthalene was most effective at reducing the aggregate sizes of CS

Precipitate asphaltenes, an observation consistent with the notion that aggregation in CS asphaltenes is dominated by dispersion and π - π bonding forces rather than polar interactions. It was suggested that aggregate sizes could be further reduced by dissolution in a more polar solvent, such as a mixture of 1-methyl naphthalene/methanol, or by the addition of solvating resins.

Fractionation appears to concentrate the more polar species into the least soluble sub-fraction as indicated by elemental analysis. SANS data indicates the less soluble (more polar) asphaltenes contribute the majority of the species responsible for asphaltene aggregation in solution. This more polar, less soluble fraction is likely the major cause for many petroleum production problems such as pipeline deposition and water-in-oil emulsion stabilization.

A.7 Acknowledgements

This research has been supported by PERF 97-07, Industrial Emulsion Consortium, ExxonMobil, Shell, ChevronTexaco, Ondeo-Nalco, and the National Science Foundation (CTS9817127). We would like to thank Eric Sirota of ExxonMobil Corporate Research and Min Lin of NIST for their assistance on the NG-7 and NG-1 beamlines. We acknowledge the support of the National Institute of Standards and Technology, U.S. Department of Commerce, in providing the neutron research facilities used in this work. This work utilized facilities supported in part by the National Science Foundation under Agreement No. DMR-9986442. Additional neutron scattering experiments were performed at the Intense Pulsed Neutron Source at Argonne National Laboratory supported by the U.S. Department of Energy under contract no. W-31-109-ENG-38. We particularly want to thank to Pappannan Thiagarajan and Denis Wozniak for their assistance on the SAND instrument. We also want to thank Marit-Helen Ese, Jihong Tong, and George Blankenship for helping with the sample preparation and SANS data collection. We appreciate Paul Lindemuth of Ondeo Nalco Energy Services for facilitating the ICP metals analyses and Darlene Mahlow at the University of Alberta for performing the elemental analyses (C, H, N, S, O) and vapor pressure osmometry experiments.

A.8 References

1. F. J. Nellensteyn, "The Constitution of Asphalt," *J. I. Petrol. Technol.*, 1924, **10**: p. 311-325.
2. J. P. Pfeiffer, R. N. J. Saal, "Asphaltic Bitumen as Colloid System," *J. Phys. Chem.*, 1940, **44**: p. 139-149.
3. H. Neumann, "Investigations Regarding the Separation of Crude Oil Emulsions," *Petrochemie*, 1965, **18**: p. 776-779.
4. J. P. Dickie, T. F. Yen, "Macrostructures of the Asphaltic Fractions by Various Instrumental Methods," *Anal. Chem.*, 1967, **39**(14): p. 1847-1852.
5. S. A. Berridge, M. T. Thew, A. G. Loriston-Clarke, "The Formation and Stability of Emulsions of Water in Crude Petroleum and Similar Stocks," *J. I. Petrol.*, 1968, **54**(539): p. 333-357.
6. J. G. Speight, "Structural Analysis of Athabasca Asphaltenes by Proton Magnetic Resonance Spectroscopy," *Fuel*, 1971, **50**: p. 102-112.
7. J. G. Speight, S. E. Moschopedis, "Some Observations on the Molecular "Nature" of Petroleum Asphaltenes," *Preprints ACS Division of Petroleum Chemistry*, 1979, **24**(4): p. 910-923.
8. J. C. Ravey, G. Ducouret, D. Espinat, "Asphaltene Macrostructure by Small Angle Neutron Scattering," *Fuel*, 1988, **67**(11): p. 1560-1567.
9. E. Y. Sheu, M. M. D. Tar, D. A. Storm, "Solution Properties of Colloids Formed by Petroleum Vacuum Residues," *Macromolecular Reports*, 1991, **A28**: p. 159-175.
10. B. Siffert, C. Bourgeois, E. Papirer, "Structure and Water-Oil Emulsifying Properties of Asphaltenes," *Fuel*, 1984, **63**(6): p. 834-837.
11. P. Herzog, D. Tchoubar, D. Espinat, "Macrostructure of Asphaltene Dispersions by Small-angle X-ray Scattering," *Fuel*, 1988, **67**: p. 245-250.
12. C. Bardon, L. Barre, D. Espinat, V. Guille, M. H. Li, J. Lambard, J. C. Ravey, E. Rosenberg, T. Zemb, "The colloidal structure of crude oils and suspensions of asphaltenes and resins," *Fuel Sci. Technol. Int.*, 1996, **14**(1-2): p. 203-242.
13. D. Fenistein, L. Barre, D. Broseta, D. Espinat, A. Livet, J. N. Roux, M. Scarsella, "Viscosimetric and neutron scattering study of asphaltene aggregates in mixed toluene/heptane solvents," *Langmuir*, 1998, **14**(5): p. 1013-1020.

14. G. W. Mushrush, J. G. Speight, *Petroleum Products: Instability and Incompatibility*; Taylor and Francis: Bristol, PA, 1995.
15. D. A. Storm, S. J. DeCanio, E. Y. Sheu, Sludge Formation During Heavy Oil Conversion, in "Asphaltene Particles in Fossil Fuel Exploration, Recovery, Refining, and Production Processes" (M. K. Sharma and T. F. Yen, Eds.), Plenum Press, New York, 1994; pp 81-90.
16. J.-R. Lin, J.-K. Park, T. F. Yen, Upgrading From Petroleum and Coal-Derived Asphaltenes, in "Asphaltene Particles in Fossil Fuel Exploration, Recovery, Refining, and Production Processes" (M. K. Sharma and T. F. Yen, Eds.), Plenum Press, New York, 1994; pp 91-100.
17. R. Cimino, S. Correria, A. D. Bianco, T. P. Lockhart, Solubility and Phase Behavior of Asphaltenes in Hydrocarbon Media, in "Asphaltenes: Fundamentals and Applications" (E. Y. Sheu and O. C. Mullins, Eds.), Plenum Press, New York, 1995; pp 97-130.
18. H. Fordedal, Y. Schildberg, J. Sjöblom, J.-L. Volle, "Crude Oil Emulsions in High Electric Fields as Studied by Dielectric Spectroscopy. Influence of Interaction Between Commercial and Indigenous Surfactants," *Colloid. Surface. A*, 1996, **106**: p. 33-47.
19. J. E. Strassner, "Effect of pH on Interfacial Films and Stability of Crude Oil-Water Emulsions," *J. Petrol. Technol.*, 1968, **20**: p. 303-312.
20. J. Sjöblom, O. Urdahl, K. G. N. Borge, L. Mingyuan, J. O. Saeten, A. A. Christy, T. Gu, "Stabilization and Destabilization of Water-in-Crude Oil Emulsions from the Norwegian Continental Shelf. Correlation with Model Systems," *Adv. Colloid Interfac. Sci.*, 1992, **41**: p. 241-271.
21. S. E. Taylor, "Resolving Crude Oil Emulsions," *Chemistry and Industry*, 1992, **20**: p. 770-773.
22. M. vanderWaarden, "Stability of Emulsions of Water in Mineral Oils Containing Asphaltenes," *Kolloid Z. Z. Polymer*, 1958, **156**(2): p. 116-122.
23. H. J. Neumann, B. Paczynska-Lahme, "Petroleum Emulsions--Properties, Stability and Demulsification," *Chem. Eng. Technol.*, 1981, **53**: p. 911-916.
24. E. Y. Sheu, M. B. Shields, "Asphaltene Surface Activity at Oil-Water Interfaces," *SPE International Symposium on Oilfield Chemistry*, 1995, **SPE 28995**: p. 523-532.
25. J. D. McLean, P. K. Kilpatrick, "Effects of Asphaltene Solvency on Stability of Water-in-Crude Oil Emulsions," *J. Colloid Interf. Sci.*, 1997, **189**: p. 242-253.

26. J. D. McLean, P. M. Spiecker, A. P. Sullivan, P. K. Kilpatrick, The Role of Petroleum Asphaltenes in the Stabilization of Water-in-Oil Emulsions, *in* "Structures and Dynamics of Asphaltenes" (O. C. Mullins and E. Y. Sheu, Eds.), Plenum Press, New York, 1998; pp 377-422.
27. D. L. Mitchell, J. G. Speight, "The Solubility of Asphaltenes in Hydrocarbon Solvents," *Fuel*, 1973, **52**(4): p. 149-152.
28. T. F. Yen, J. G. Erdman, S. S. Pollack, "Investigation of Structure of Petroleum Asphaltenes By X-Ray Diffraction," *Anal. Chem.*, 1961, **33**(11): p. 1587-&.
29. M. M. Boduszynski, "Composition of Heavy Petroleums. 2. Molecular Characterization," *Energy & Fuels*, 1988, **2**(5): p. 597-613.
30. M. A. Bestougeff, P. Gendrel, "Study on the Structure of Asphaltenic Constituents by Combined Physical and Chemical Methods," *Preprints ACS Division of Petroleum Chemistry*, 1964, **9**(2): p. B51-B68.
31. J. F. McKay, D. R. Latham, W. E. Haines, "Composition of Petroleum Heavy Ends. 3. Comparison of the Composition of High-Boiling Petroleum Distillates and Petroleum > 675 C Residues," *Fuel*, 1981, **60**(1): p. 27-32.
32. M. M. Boduszynski, "Characterization of "Heavy" Crude Components," *Preprints ACS Division of Petroleum Chemistry*, 1985, **30**: p. 626-640.
33. J. G. Speight, "A Structural Investigation of the Constituents of Athabasca Bitumen by Proton Magnetic Resonance Spectroscopy," *Fuel*, 1970, **49**: p. 76-90.
34. W. R. Biggs, R. J. Brown, J. C. Fetzer, "Elemental Profiles of Hydrocarbon Materials by Size-Exclusion Chromatography/Inductively Coupled Plasma Atomic Emission Spectrometry," *Energy & Fuels*, 1987, **1**(3): p. 257-262.
35. V. Nalwaya, V. Tangtayakom, P. Piumsomboon, S. Fogler, "Studies on asphaltenes through analysis of polar fractions," *Ind. Eng. Chem. Res.*, 1999, **38**(3): p. 964-972.
36. J. G. Reynolds, W. R. Biggs, "Effects of Asphaltene Precipitation and a Modified D 2007 Separation on the Molecular Size of Vanadium- and Nickel-Containing Compounds in Heavy Residua," *Fuel Sci. Techn. Int.*, 1986, **4**(6): p. 749-777.
37. J. G. Reynolds, W. R. Biggs, "Application of Size Exclusion Chromatography Coupled with Element-Specific Detection to the Study of Heavy Crude Oil and Residua Processing," *Accounts Chem. Res.*, 1988, **21**(9): p. 319-326.
38. J. G. Reynolds, E. L. Jones, J. A. Bennett, W. R. Biggs, "Characterization of Nickel and Vanadium Compounds in Tar Sand Bitumen by Petroporphyrin Quantitation and

- Size Exclusion Chromatography Coupled with Element Specific Detection," *Preprints ACS Division of Petroleum Chemistry*, 1988, **33**(2): p. 239-246.
39. H. H. Hasiba, F. W. Jessen, "Film-Forming Compounds From Crude Oils, Interfacial Films and Paraffin Deposition," *J. Can. Petrol. Techn.*, 1968, **7**(1): p. 1-12.
 40. J. C. Petersen, "Quantitative Method Using Differential Infrared Spectrometry for the Determination of Compound Types Absorbing in the Carbonyl Region in Asphalts," *Anal. Chem.*, 1975, **47**(1): p. 112-117.
 41. S. I. Andersen, "Effect of Precipitation Temperature on the Composition of n-Heptane Asphaltenes," *Fuel Sci. Techn. Int.*, 1994, **12**(1): p. 51-74.
 42. C. L. Chang, H. S. Fogler, "Stabilization of Asphaltenes in Aliphatic Solvents Using Alkylbenzene-Derived Amphiphiles .1. Effect of the Chemical- Structure of Amphiphiles On Asphaltene Stabilization," *Langmuir*, 1994, **10**(6): p. 1749-1757.
 43. M. U. Hasan, M. N. Siddiqui, M. Arab, "Separation and Characterization of Asphaltenes from Saudi Arabian Crudes," *Fuel*, 1988, **67**(8): p. 1131-1134.
 44. J. M. Jacobson, M. R. Gray, "Use of IR Spectroscopy and Nitrogen Titration Data in Structural Group Analysis of Bitumen," *Fuel*, 1987, **66**(6): p. 749-752.
 45. R. V. Barbour, J. C. Petersen, "Molecular Interactions of Asphalt: An Infrared Study of the Hydrogen-Bonding Basicity of Asphalt," *Anal. Chem.*, 1974, **46**(2): p. 273-277.
 46. M. M. Boduszynski, J. F. McKay, D. R. Latham, "Asphaltenes, Where Are You?," *Proceedings of the Association of Asphalt Paving Technologists*, 1980, **49**: p. 123-143.
 47. T. Ignasiak, O. P. Strausz, D. S. Montgomery, "Oxygen Distribution and Hydrogen Bonding in Athabasca Asphaltene," *Fuel*, 1977, **56**: p. 359-365.
 48. S. E. Moschopedis, J. G. Speight, "Investigation of Hydrogen Bonding by Oxygen Functions in Athabasca Bitumen," *Fuel*, 1976, **55**: p. 187-192.
 49. J. C. Petersen, "An Infra-red Study of Hydrogen Bonding in Asphalt," *Fuel*, 1967, **46**(4-5): p. 295-305.
 50. H. P. Maruska, M. L. Rao, "The Role of Polar Species in the Aggregation of Asphaltenes," *Fuel Sci. Techn. Int.*, 1987, **5**(2): p. 119-168.
 51. R. E. Overfield, E. Y. Sheu, S. K. Sinha, K. S. Liang, "SANS Study of Asphaltene Aggregation," *Fuel Sci. Techn. Int.*, 1989, **7**(5-6): p. 611-624.

52. E. Y. Sheu, D. A. Storm, M. M. D. Tar, "Asphaltenes in Polar Solvents," *J. Non-Cryst. Solids*, 1991, **131-133**: p. 341-347.
53. M. M. H. Al-Jarrah, A. H. Al-Dujaili, "Characterization of Some Iraqi Asphalts II. New Findings on the Physical Nature of Asphaltenes," *Fuel Sci. Techn. Int.*, 1989, **7(1)**: p. 69-88.
54. S. Acevedo, B. Mendez, A. Rojas, I. Layrisse, H. Rivas, "Asphaltenes and Resins From the Orinoco Basin," *Fuel*, 1985, **64**: p. 1741-1747.
55. I. A. Wiehe, K. S. Liang, "Asphaltenes, Resins, and other petroleum macromolecules," *Fluid Phase Equilibr.*, 1996, **117(1-2)**: p. 201-210.
56. J. F. McKay, P. J. Amend, T. E. Cogswell, P. M. Harnsberger, R. B. Erickson, D. R. Latham, Petroleum Asphaltenes: Chemistry and Composition, in "Analytical Chemistry of Liquid Fuel Sources: Tar Sands, Oil Shale, Coal, and Petroleum" (P. C. Uden and S. Siggia, Eds.), p. 128-142. ACS Advances in Chemistry Series v. 170, Washington, 1978.
57. S. I. Andersen, A. Keul, E. Stenby, "Variation in composition of subfractions of petroleum asphaltenes," *Pet. Sci. Technol.*, 1997, **15(7-8)**: p. 611-645.
58. H. W. Yarranton, J. H. Masliyah, "Molar Mass Distribution and Solubility Modeling of Asphaltenes," *AICHE J.*, 1996, **42(12)**: p. 3533-3543.
59. H. W. Yarranton, H. Alboudwarej, R. Jakher, "Investigation of asphaltene association with vapor pressure osmometry and interfacial tension measurements," *Ind. Eng. Chem. Res.*, 2000, **39(8)**: p. 2916-2924.
60. J. C. Ravey, D. Espinat, "Macrostructure of Petroleum Asphaltenes by Small Angle Neutron Scattering," *Prog. Coll. Pol. Sci.*, 1990, **81**: p. 127-130.
61. E. Y. Sheu, M. M. D. Tar, D. A. Storm, "Colloidal Structure of Vacuum Residue in Solvents," *Preprints ACS Division of Fuel Chemistry*, 1992, **37(2)**: p. 844-848.
62. D. Espinat, J. C. Ravey, V. Guille, J. Lambard, T. Zemb, J. P. Cotton, "Colloidal Macrostructure of Crude-Oil Studied By Neutron and X- Ray Small-Angle Scattering Techniques," *J. Phys. IV*, 1993, **3(C8)**: p. 181-184.
63. D. A. Storm, E. Y. Sheu, M. M. Detar, "Macrostructure of Asphaltenes in Vacuum Residue By Small-Angle X-Ray-Scattering," *Fuel*, 1993, **72(7)**: p. 977-981.
64. P. Thiagarajan, J. E. Hunt, R. E. Winans, K. B. Anderson, J. T. Miller, "Temperature-Dependent Structural-Changes of Asphaltenes in 1-Methylnaphthalene," *Energy & Fuels*, 1995, **9(5)**: p. 829-833.

65. Y. N. Xu, Y. Koga, O. P. Strausz, "Characterization of Athabasca Asphaltenes By Small-Angle X-Ray- Scattering," *Fuel*, 1995, **74**(7): p. 960-964.
66. Y. C. Liu, E. Y. Sheu, S. H. Chen, D. A. Storm, "Fractal Structure of Asphaltenes in Toluene," *Fuel*, 1995, **74**(9): p. 1352-1356.
67. H. Rassamdana, M. Sahimi, "Asphalt Flocculation and Deposition: II. Formation and Growth of Fractal Aggregates," *AICHE J.*, 1996, **42**(12): p. 3318-3332.
68. L. Barre, D. Espinat, E. Rosenberg, M. Scarsella, "Colloidal structure of heavy crudes and asphaltene solutions," *Rev. Inst. Fr. Pet.*, 1997, **52**(2): p. 161-175.
69. M. Y. Lin, E. B. Sirota, H. Gang, "Neutron scattering characterization of asphaltene particles," *Abstr. Pap. Am. Chem. Soc.*, 1997, **213**: p. 66-FUEL.
70. J. T. Miller, R. B. Fisher, P. Thiyagarajan, R. E. Winans, J. E. Hunt, "Subfractionation and characterization of Mayan asphaltene," *Energy & Fuels*, 1998, **12**(6): p. 1290-1298.
71. E. B. Sirota, "Swelling of asphaltenes," *Pet. Sci. Technol.*, 1998, **16**(3-4): p. 415-431.
72. D. Fenistein, L. Barre, "Experimental measurement of the mass distribution of petroleum asphaltene aggregates using ultracentrifugation and small-angle X-ray scattering," *Fuel*, 2001, **80**(2): p. 283-287.
73. T. G. Savvidis, D. Fenistein, L. Barre, E. Behar, "Aggregated structure of flocculated asphaltenes," *AICHE J.*, 2001, **47**(1): p. 206-211.
74. J. N. Roux, D. Broseta, B. Deme, "SANS study of asphaltene aggregation: Concentration and solvent quality effects," *Langmuir*, 2001, **17**(16): p. 5085-5092.
75. E. Y. Sheu, K. S. Liang, S. K. Sinha, R. E. Overfield, "Polydispersity Analysis of Asphaltene Solutions in Toluene," *J. Colloid Interf. Sci.*, 1992, **153**(2): p. 399-410.
76. G. Porte, H. G. Zhou, V. Lazzeri, "Reversible description of asphaltene colloidal association and precipitation," *Langmuir*, 2003, **19**(1): p. 40-47.
77. T. J. Kaminski, H. S. Fogler, N. Wolf, P. Wattana, A. Mairal, "Classification of asphaltenes via fractionation and the effect of heteroatom content on dissolution kinetics," *Energy & Fuels*, 2000, **14**(1): p. 25-30.
78. P.-G. de Gennes, *Scaling Concepts in Polymer Physics*; Cornell University Press: Ithaca, NY, 1979.
79. C. M. Hansen, "Universality of Solubility Parameter," *Ind. Eng. Chem. Prod. R. D.*, 1969, **8**(1): p. 2-&.

80. A. F. M. Barton, *CRC Handbook of Solubility Parameters and other Cohesion Parameters*; CRC Press: Boca Raton, FL, 1983.
81. J. S. Buckley, "Microscopic investigation of the onset of asphaltene precipitation," *Fuel Sci. Technol. Int.*, 1996, **14**(1-2): p. 55-74.
82. J. S. Buckley, "Predicting the onset of asphaltene precipitation from refractive index measurements," *Energy & Fuels*, 1999, **13**(2): p. 328-332.
83. V. Szewczyk, F. Behar, E. Behar, M. Scarsella, "Evidence of the physicochemical polydispersity of asphaltenes," *Rev. Inst. Fr. Pet.*, 1996, **51**(4): p. 575-590.
84. M. F. Ali, H. Perzanowski, A. Bukhari, A. A. Al-Haji, "Nickel and Vanadyl Porphyrins in Saudi Arabian Crude Oils," *Energy & Fuels*, 1993, **7**(2): p. 179-184.
85. P. M. Spiecker, K. L. Gawrys, C. B. Trail, P. K. Kilpatrick, "Effects of petroleum resins on asphaltene aggregation and water-in-oil emulsion formation," *Colloids and Surfaces A*, 2003, **220**: p. 9-27.
86. P. M. Spiecker. Ph.D. Thesis. North Carolina State University, 2001.

Table A.1 Typical Values of Elemental Compositions in Asphaltenes

Element (wt%)	
H/C	1.0-1.2
Nitrogen	1.0-1.2
Sulfur	2.0-6.0
Oxygen	0.8-2.0
Vanadium (ppm)	100-300

Table A.2 Crude oil properties

Crude	Wt % Asph	R/A Ratio	H/C Asph	Viscosity (cP) 100°F
AH	6.7	1.12	1.14	33.8
B6	13.1	0.92	1.22	2030
CS	7.5	1.19	1.11	70
HO	14.8	1.39	1.29	363

Table A.3 Asphaltene fractionation results (wt%)

Asphaltene	<i>n</i> -Heptane-Toluene Ratio	Precipitate	Soluble
AH	70:30	38.4	61.6
		34.4	65.6
		32.2	67.8
	Average	35±3	65±3
B6	60:40	33.2	66.8
		31.6	68.4
		32.4	67.6
	Average	32.4±0.8	67.6±0.8
CS	60:40	35.7	64.3
HO	61:39	28.2	71.8
		33.1	66.9
	Average	30.7	69.3

Table A.4 Asphaltene fraction composition in wt.%, except H/C ratio (atomic)

Asphaltene	H/C			Nitrogen		
	Soluble	Whole	Precipitate	Soluble	Whole	Precipitate
AH	1.17	1.14	1.13	0.92	1.02	1.08
B6	1.30	1.24	1.22	1.81	1.87	1.93
CS	1.12	1.11	1.09	1.32	1.32	1.39
HO	1.30	1.29	1.24	1.95	1.99	2.11

Asphaltene	Sulfur			Oxygen		
	Soluble	Whole	Precipitate	Soluble	Whole	Precipitate
AH	8.06	8.32	7.66	1.92	1.64	2.52
B6	7.25	6.68	6.33	2.67	2.9	2.81
CS	0.52	0.52	0.48	2.11	1.73	2.27
HO	8.42	8.53	8.48	2.51	2.1	2.66

Table A.5 Metals analysis (ppm)

Asphaltene	Iron			Nickel			Vanadium			Sodium		
	Sol	W	Ppt	Sol	W	Ppt	Sol	W	Ppt	Sol	W	Ppt
AH	14	26	50	84	160	160	350	490	540	31	31	31
B6	7.9	35	47	350	330	410	1000	1000	1200	27	9300	25000
CS	51	77	150	19	21	28	42	48	48	43	130	180
HO	6.3	16	12	340	360	410	930	950	1100	11.9	550	1800

Table A.6 Correlation length (Å) of Whole, Soluble and Precipitate asphaltenes in heptol at 25 and 80°C: 1 wt %.

Asphaltene Fraction			ξ (Å)	
Asph.	Fraction	% Toluene	25 °C	80 °C
AH	Soluble	40	38 ± 1	30 ± 1
AH	Whole	50	61 ± 1	36 ± 1
B6	Soluble	50	51 ± 1	39 ± 1
B6	Whole	55	99 ± 2	65 ± 1
B6	Whole	60	79 ± 1	57 ± 1
B6	Whole	80	59 ± 1	44 ± 1
B6	Precipitate	85	230 ± 10	89 ± 1
B6	Precipitate	90	250 ± 10	82 ± 1
B6	Precipitate	100	240 ± 40	69 ± 1
CS	Soluble	60	75 ± 1	51 ± 1
CS	Soluble	100	68 ± 2	42 ± 1
CS	Whole	60	202 ± 7	74 ± 1
CS	Whole	80	143 ± 5	57 ± 1
CS	Precipitate	90	700 ± 200	104 ± 2
HO	Soluble	50	43 ± 1	39 ± 1
HO	Whole	100	45 ± 1	32 ± 1
HO	Precipitate	90	146 ± 2	62 ± 1
HO	Precipitate	100	150 ± 2	55 ± 1

Table A.7 Correlation length (Å) of asphaltenes in 1-methylnaphthalene and toluene (80°C)

Asphaltene	Soluble		Whole		Precipitate	
	MN	Tol	MN	Tol	MN	Tol
AH	18.5±0.2		23.9±0.2	28.1±0.6	30.2±0.3	39.2±0.6
B6	23.7±0.5	28.1±0.6	35.6±0.8	40.0±0.7	51.0±0.8	69±1
CS	33.8±0.8	41.7±0.7	39.6±0.8	48±1	47.0±0.8	80±2
HO	23.0±0.2		29.5±0.6	31.5±0.7	45.4±0.9	55±1

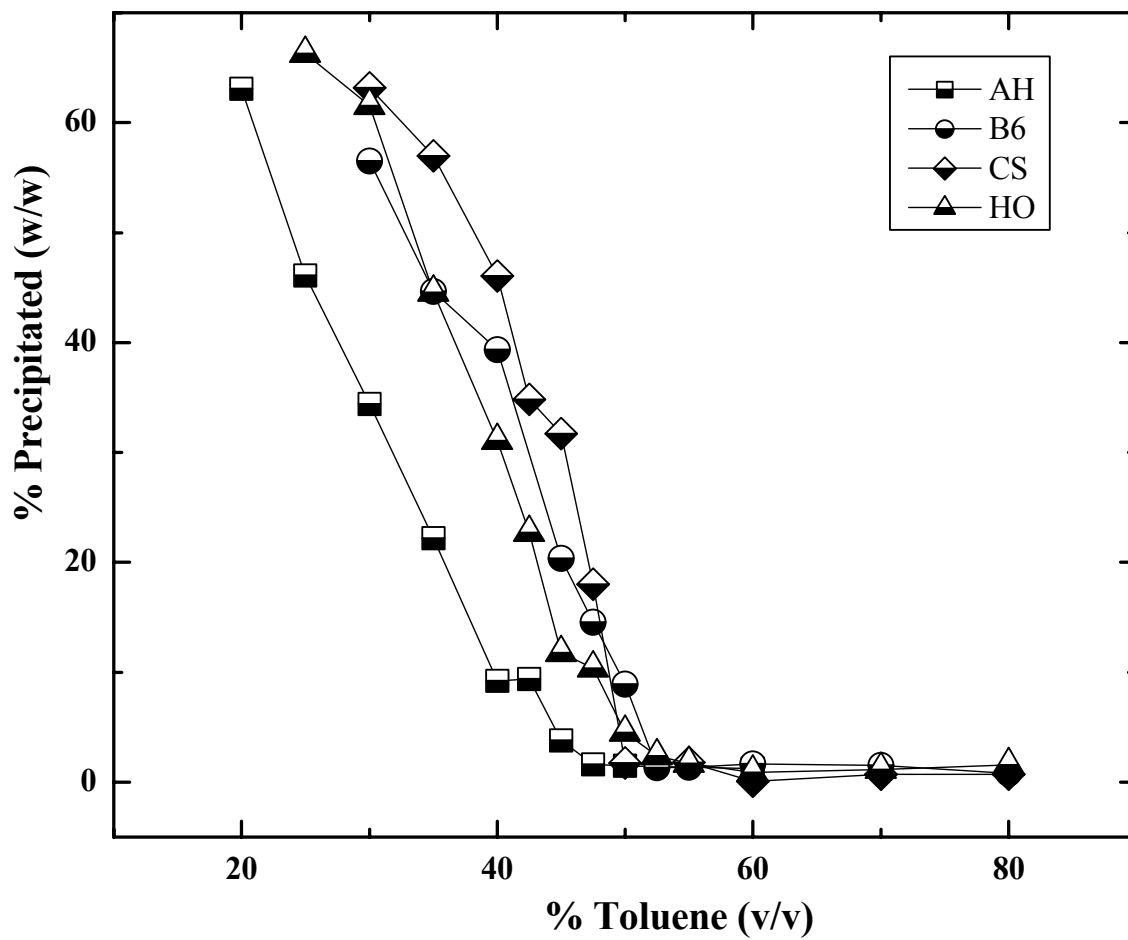


Figure A.1 Solubility profiles of Whole asphaltenes in heptol.

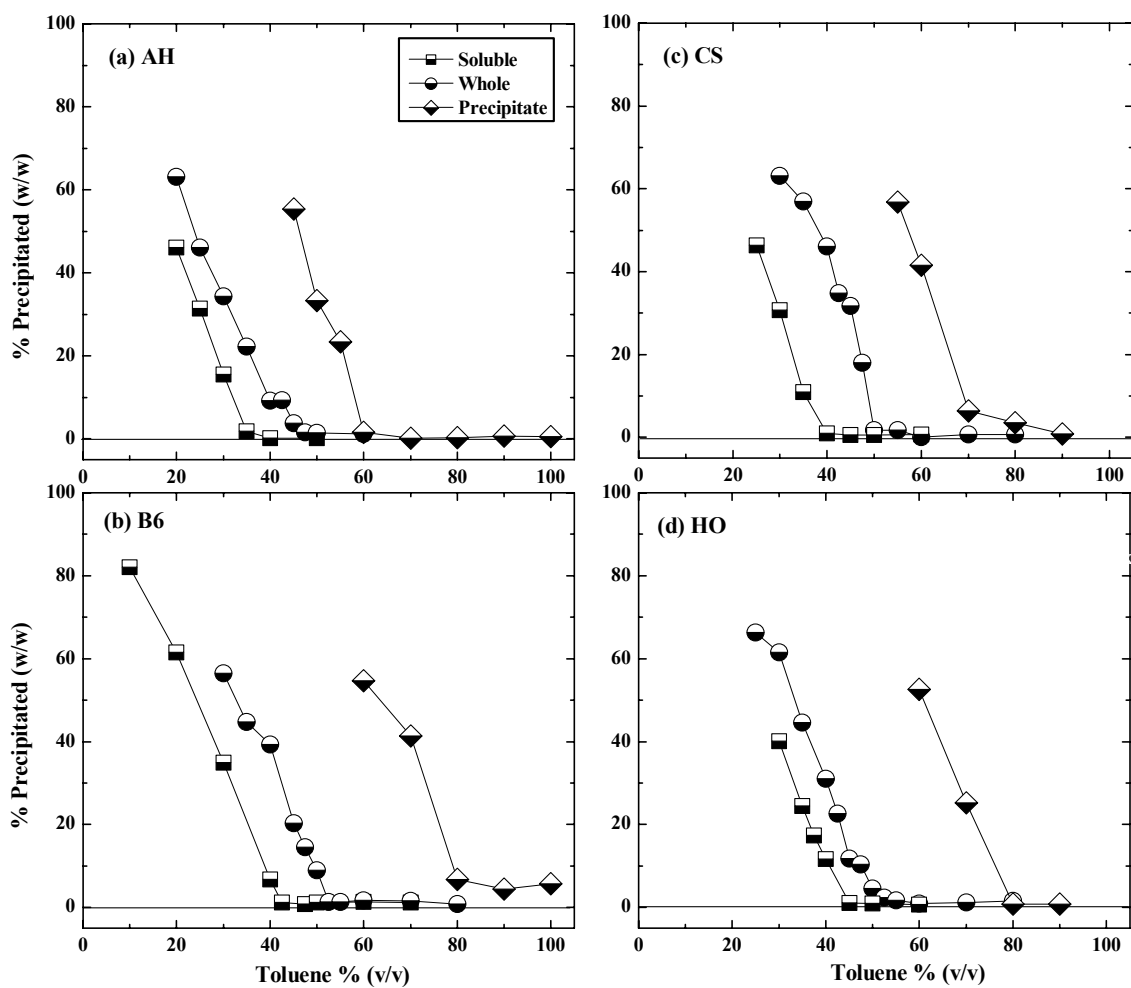


Figure A.2 Solubility profiles of Whole, Soluble and Precipitate asphaltenes in heptol.

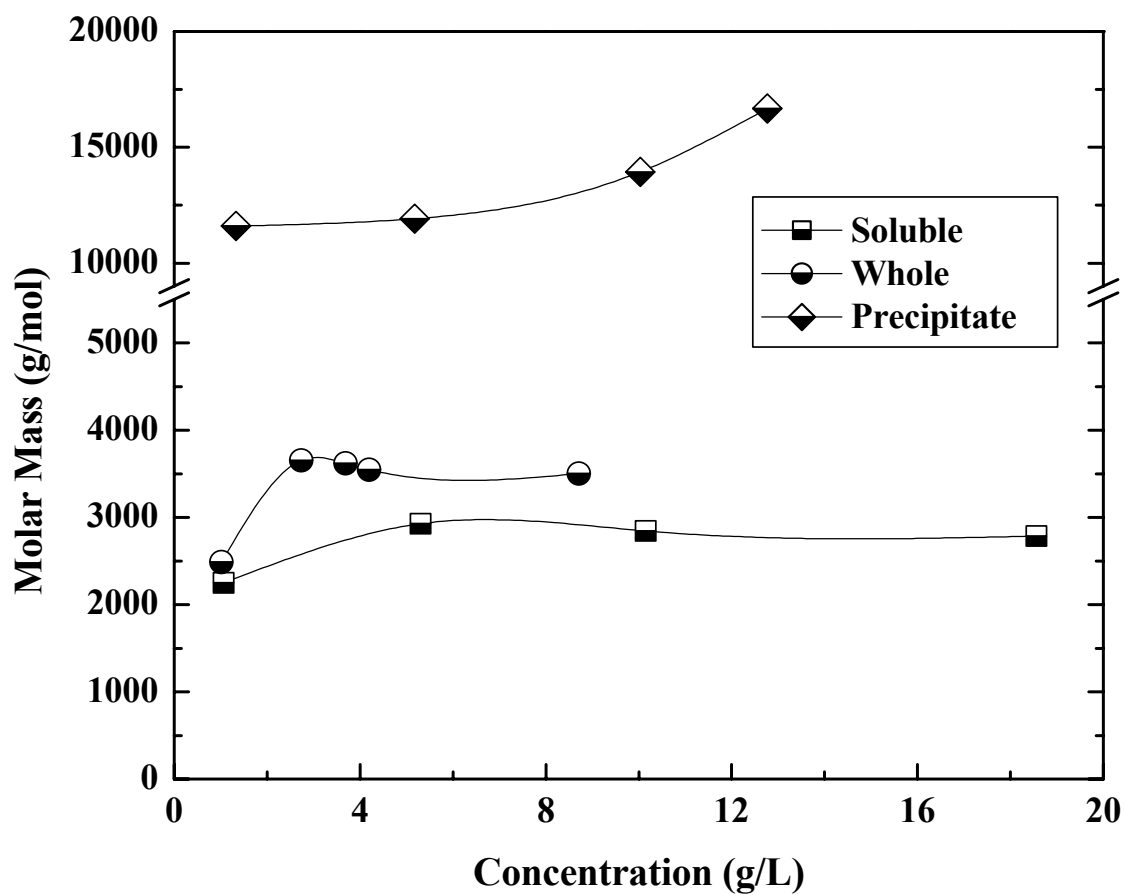


Figure A.3 VPO molar masses of B6 asphaltenes (Soluble, Whole and Precipitate) in toluene at 53°C

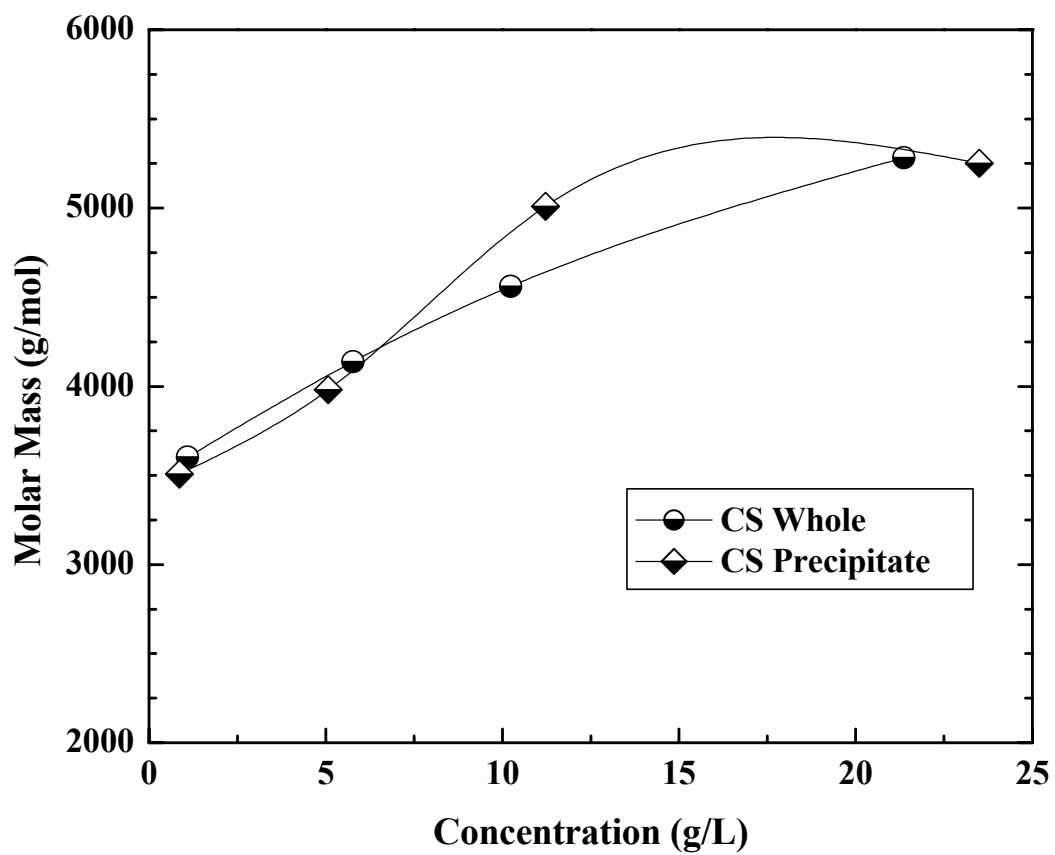


Figure A.4 VPO molar masses of CS (Whole and Precipitate) asphaltenes in toluene at 53°C

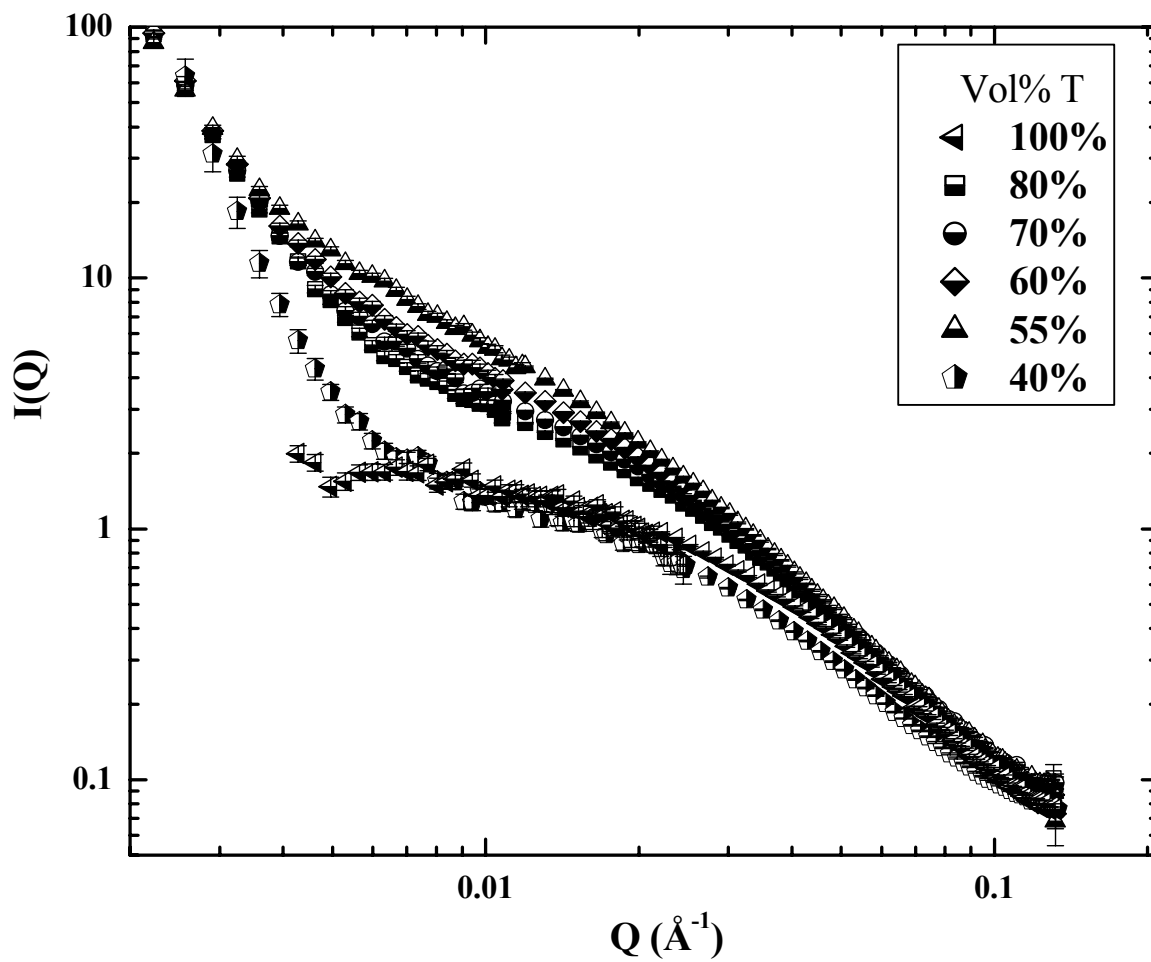


Figure A.5 SANS curves of B6 Whole asphaltenes in mixtures of d-heptane and d-toluene at 1 wt%, 25°C.

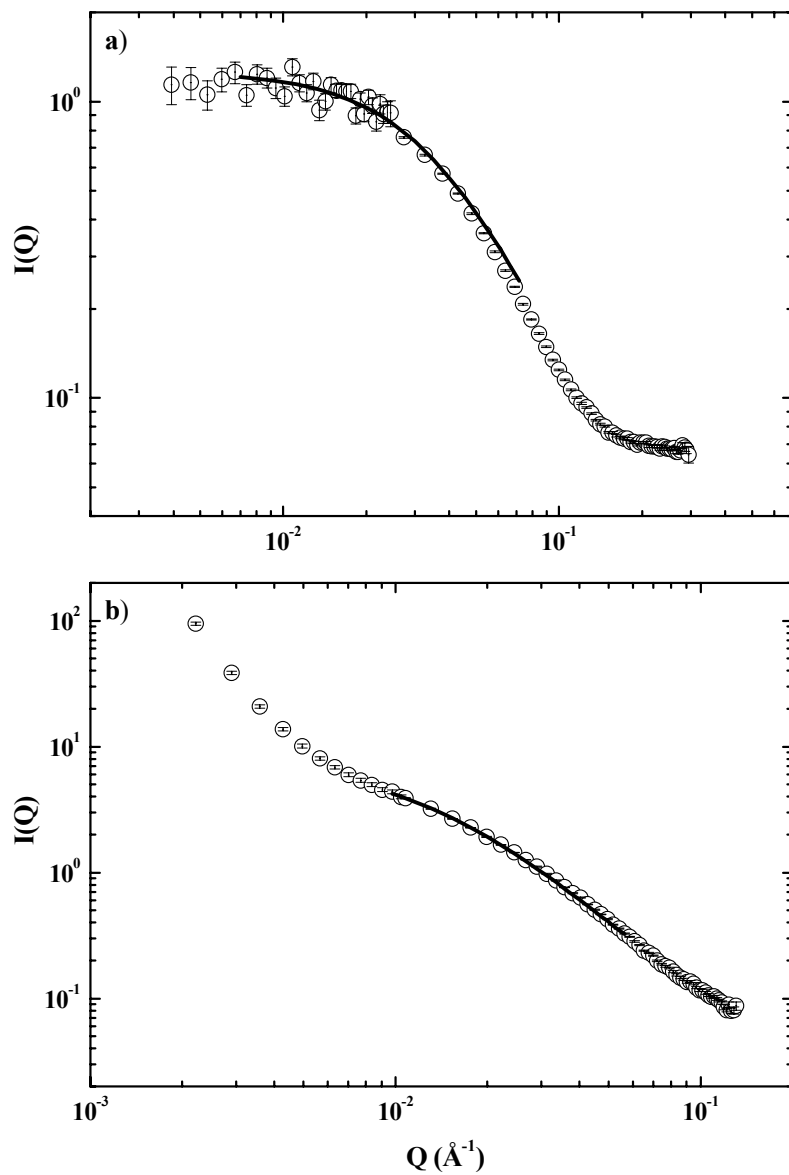


Figure A.6 SANS fits using Lorentzian line shapes. a.) AH Soluble asphaltenes: 1 wt %, 50 % (v/v) toluene in heptane, 25°C; $I_0 = 1.27 \pm 0.02$, $\xi = 29.9 \pm 0.3$, $R^2 = 0.9987$; b.) B6 Whole asphaltenes: 1 wt %, 60 % (v/v) toluene in heptane, 25°C; $I_0 = 6.7 \pm 0.1$, $\xi = 79 \pm 1$, $R^2 = 0.9974$. Note: Every other point displayed.

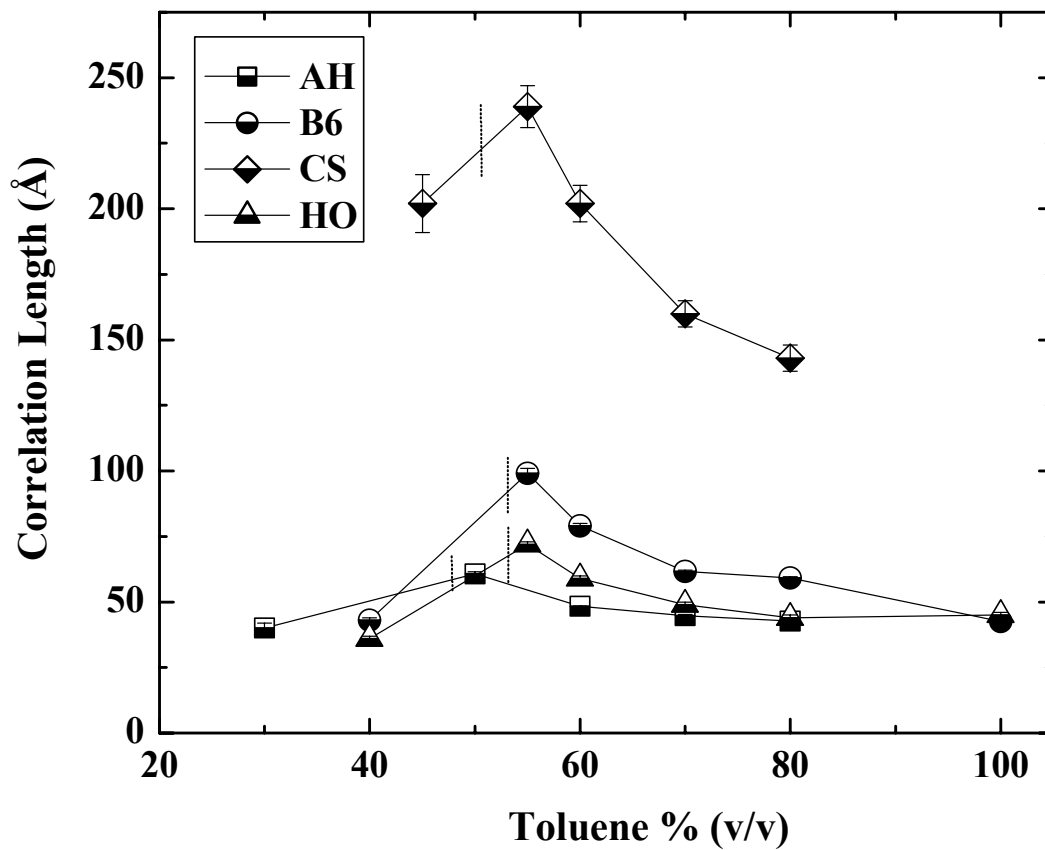


Figure A.7 Correlation lengths of Whole asphaltenes in heptol determined by SANS: 1 wt %, 25°C. The vertical dashed lines represent the solubility limit for a 1 wt% asphaltene solution in heptol.

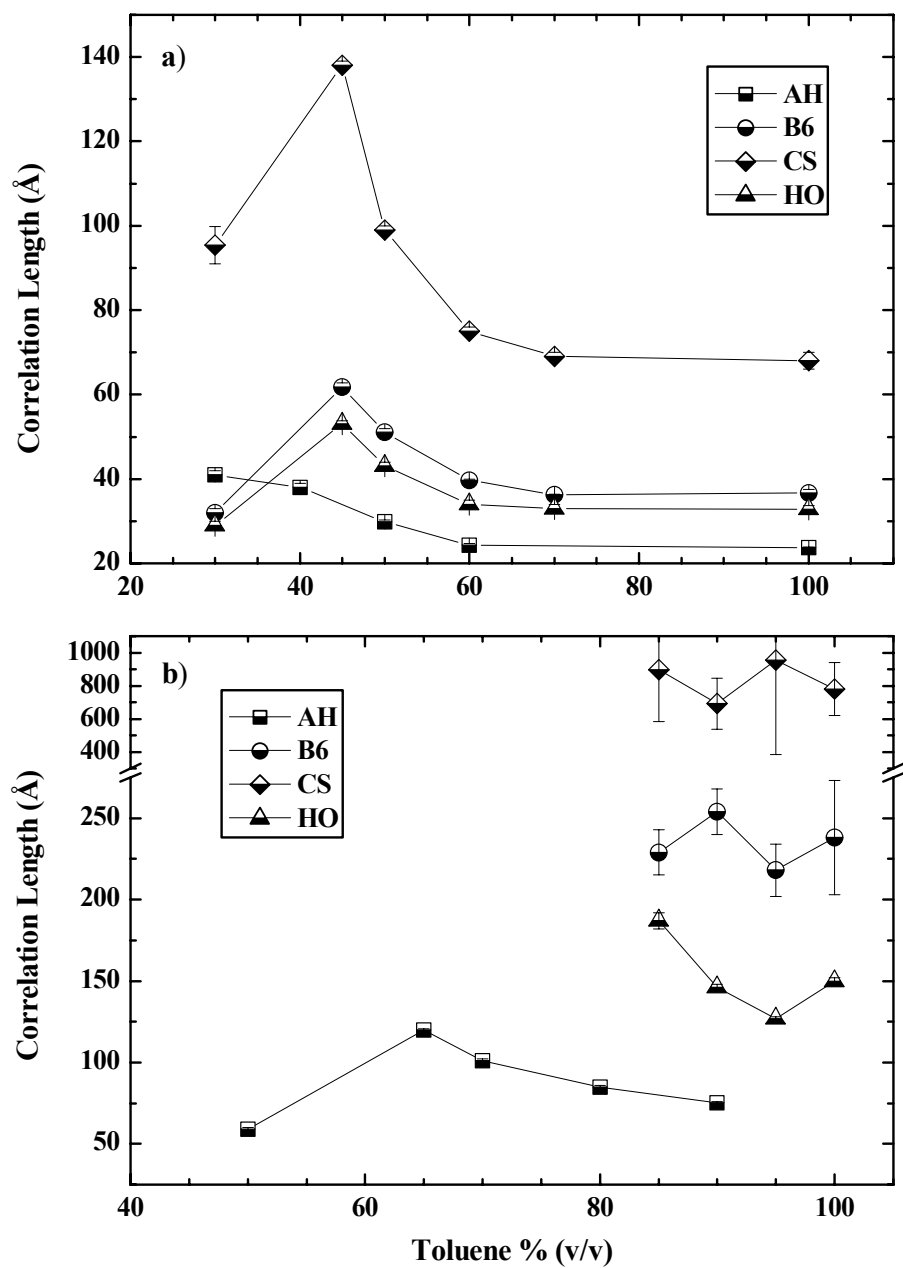


Figure A.8a-b Correlation lengths of (a) Soluble and (b) Precipitate asphaltenes in heptol by SANS: 1 wt %, 25°C.

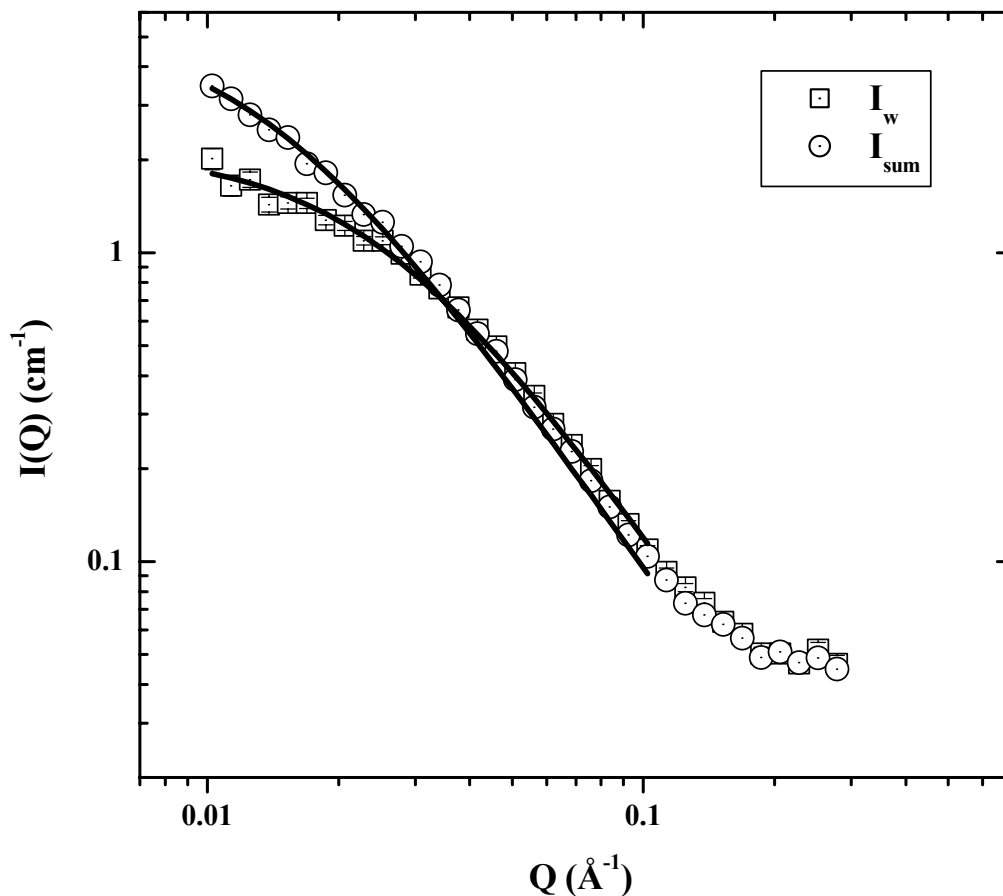


Figure A.9 Comparison of scattering intensities for HO Whole asphaltenes in toluene (I_w) and the weight-averaged summation of scattering intensities from HO Soluble and Precipitate fractions in toluene (I_{sum}). Fits of the scattering curves to Lorentzian lineshapes appear as solid lines with parameters for I_w given as $I_0: 2.12 \pm 0.05$, $\xi: 41 \pm 2$, $R^2: 0.9573$ and parameters for I_{sum} given as $I_0: 5.4 \pm 0.1$, $\xi: 74 \pm 2$, $R^2: 0.9964$. Note: Every other point displayed.

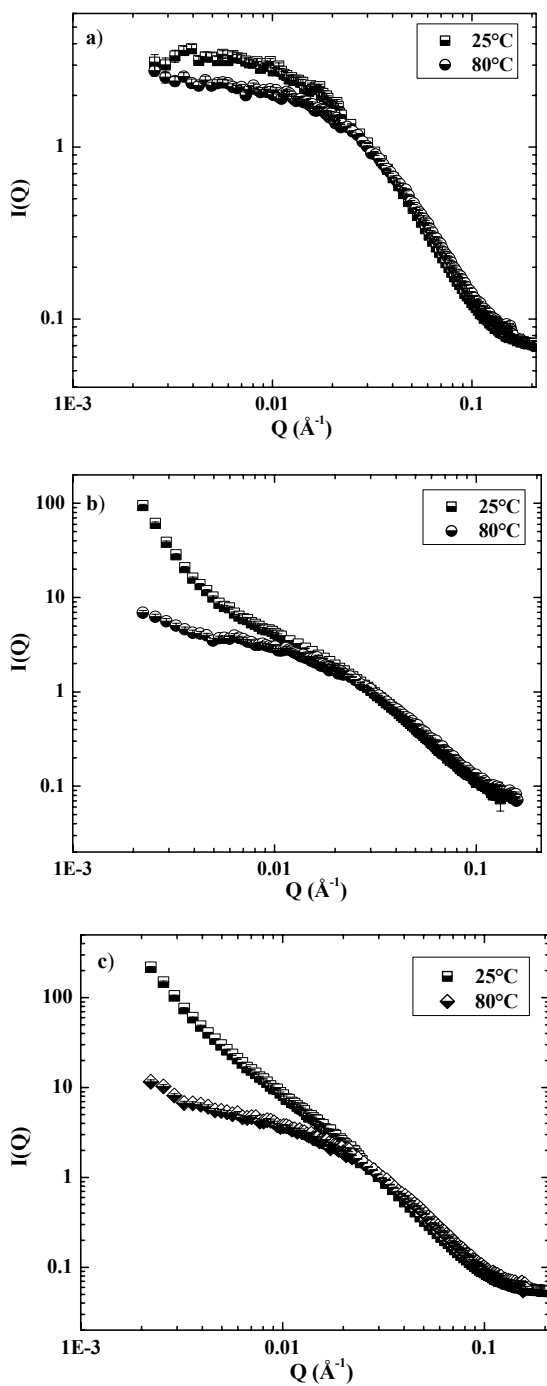


Figure A.10a-c SANS curves of asphaltenes (1% wt.) in heptol: a.) B6 Soluble in 50 % toluene; b.) B6 Whole in 60 % toluene; c.) B6 Precipitate in 100 % toluene

APPENDIX B
EFFECTS OF PETROLEUM RESINS ON ASPHALTENE AGGREGATION AND
WATER-IN-OIL EMULSION FORMATION

P. Matthew Spiecker, Keith L. Gawrys, Chad B. Trail, and Peter K. Kilpatrick

[Reprinted from *Colloids and Surfaces A: Physicochem. Eng. Aspects* 220 (2003) 9-27]

B.1 Abstract

Asphaltenes from four crude oils were fractionated by precipitation in mixtures of heptane and toluene. Solubility profiles generated in the presence of resins (1:1 mass ratio) indicated the onset of asphaltene precipitation occurred at lower toluene volume fractions (0.1-0.2) than without resins. Small-angle neutron scattering (SANS) was performed on solutions of asphaltene fractions in mixtures of heptane and toluene with added resins to determine aggregate sizes. Water-in-oil emulsions of asphaltene-resin solutions were prepared and separated by a centrifuge method to determine the vol % water resolved. In general, the addition of resins to asphaltenes reduced the aggregate size by disrupting the π - π and polar bonding interactions between asphaltene monomers. Interaction of resins with asphaltenic aggregates rendered the aggregates less interfacially active and thus reduced emulsion stability. The smallest aggregate sizes observed and the weakest emulsion stability at high resin to asphaltene (R/A) ratios presumably corresponded to asphaltenic monomers or small oligomers strongly interacting with resin molecules. It was often observed that, in the absence of resins, the more polar or higher molecular weight asphaltenes were insoluble in solutions of heptane and toluene. The addition of resins re-dissolved these asphaltenes and aggregate size by SANS increased until the solubility limit was reached. This corresponded approximately to the point of maximum emulsion stability. Asphaltene chemistry plays a vital role in dictating emulsion stability. The most polar species typically required significantly higher resin concentrations to disrupt asphaltene interactions and completely destabilize emulsions. Aggregation and film formation are likely driven by polar heteroatom interactions, such as hydrogen bonding, which allow asphaltenes to absorb, consolidate, and form cohesive films at the oil-water interface.

B.2 Introduction

Emulsion challenges during petroleum recovery have been attributed to colloidal aggregation of asphaltenes and waxes [1-6]. Many early studies were performed on the film forming and emulsifying behavior of crude oil-water systems [1,7-15]. These and later studies often pointed to the asphaltenic constituents in crude oil as being responsible for film formation and stabilization [10,11,16,17].

Asphaltenes, or *n*-heptane insolubles and toluene solubles, are the most refractory compounds present in crude oil and are generally distinguished by a fused aromatic core with polar heteroatom functionality [18,19]. Studies indicate the presence of carboxylic acids, carbonyls, phenols, pyrroles and pyridinic functional groups capable of accepting or donating protons [20-24]. Vapor pressure osmometry measurements suggest number average molecular weights range from ca. 800 to 3000 Daltons [25-32]. Even lower asphaltene molecular weights are observed in hot, polar solvents suggesting that aggregates formed through stacking interactions between asphaltene monomers. The most plausible mechanisms of asphaltene aggregation involve π - π overlap between aromatic sheets, hydrogen bonding between functional groups and other charge transfer interactions.

Small angle neutron scattering (SANS) has been applied to probe solvent and temperature effects on asphaltene aggregation [33-44]. Proper analysis of the scattering intensity curves can provide aggregate size, shape, molecular weight, and fractal dimension. Asphaltenic aggregates are comprised of cofacial stacks of planar, fused aromatic ring moieties connected by aliphatic chains and rings. Recent structural and molecular modeling seem to confirm the so-called “archipelago” model of asphaltenes, as opposed to the more widely implied and invoked “island” model [45]. In the “archipelago” model, individual asphaltene monomers are comprised of aromatic and fused aromatic ring moieties, some with polar functional groups, connected to each other by aliphatic polymethylene chains and rings that likely contain some sulfide and carbonyl functional groups (see Figure B.1). Asphaltenic aggregates have been modeled as mono- and polydisperse spheres [35,46], flat disks [37,47,48], and prolate cylinders [38]. Asphaltene polydispersity, however, makes the precise shape difficult to discriminate. With the archipelago-like structure of Figure B.1, it seems probable that asphaltenic aggregates possess a porous reticulated microstructure.

While the effects of temperature, solvent aromaticity, and polarity have received much attention, the solvation of asphaltene aggregates by resins has not been fully explored. What we mean here by the expression “solvation” is the strong local interaction of asphaltenic aggregates by resin molecules, a phenomenon referred to in previous studies by the curious term “peptized;” we do not mean by solvation the “swelling” of asphaltenic aggregates, although as we show in a subsequent publication, resins definitely fill in solvent voids in asphaltenic aggregates created by the reticulated structure of asphaltenes. Espinat et al. measured neutron and X-ray scattering intensities from asphaltenic aggregates in several solvents, at low and high temperatures and with added resins [37]. The scattering curves were fit using a thin disc form factor model. In toluene, 2 wt % Boscan asphaltene solutions formed larger aggregates at room temperature (234 Å diameter) than at 76°C (175 Å). At room temperature, aggregate sizes were 2-4 times smaller in high polarity solvents such as pyridine and tetrahydrofuran than in benzene. They also found that resin-asphaltene ratios of 2:1 by mass reduced the scattering intensity at low Q suggesting the formation of smaller aggregates. However, the effect of resin solvation on asphaltene aggregate size was not explicitly reported. Bardon et al. observed resin solvation of Safaniya asphaltenes using SANS and SAXS [47]. Weight average molecular weights of 2 wt % asphaltene solutions in toluene with R/A ratios of 2, 4, and 8:1 were reduced by factors of 2.6, 4.6, and 7.5 respectively.

In two submitted publications [44,49] we examined the aggregation and emulsion stabilizing behavior of asphaltenes and their more and less soluble fractions in mixtures of heptane and toluene (so-called “heptol”). Gravimetric solubility measurements indicated that asphaltenes start to precipitate at concentrations between 45 and 52 % (v/v) toluene in heptol. Precipitation concentrated the most polar and aromatic constituents as measured by H/C ratio and nitrogen content. In addition, SANS indicated that the less soluble fraction formed the largest aggregates in heptol while the more soluble fraction formed considerably smaller aggregates. Asphaltenes and their various sub-fractions are well known to stabilize water-in-oil emulsions near the point of incipient flocculation [50]. The degree of aggregation and proximity to the solubility limit governs the stability of emulsions prepared in heptol.

In this study, we have taken another step towards understanding the mechanisms of asphaltene aggregation and emulsion formation in petroleum and petroleum-derived systems

through the addition of solvating molecules. Crude oils are usually characterized by SARA fractionation where asphaltenes are removed by precipitation with a paraffinic solvent and the deasphalted oil (DAO or maltenes) is separated into saturates, aromatics and resins by chromatographic separation [51-55]. Resins are the most polar and aromatic species present in deasphalted oil and, it has been suggested, contribute to the enhanced solubility of asphaltenes in crude oil by solvating the polar and aromatic portions of the asphaltenic molecules and aggregates [25,56,57]. The solubility of asphaltenes in crude oil is mediated largely by resin solvation and thus resins play a critical role in precipitation, and emulsion stabilization phenomena [37,40,58-60]. Resins, although quite surface-active, have not been found to stabilize significantly water-in-oil emulsions by themselves in model systems, a fact that mitigates somewhat against the notion that resins and asphaltenes form a simple continuum of molecular structures and functions [61,62]. However, the presence of resins in solution can destabilize emulsions via asphaltene solvation and/or replacement at the oil-water interface [62-66].

Here we probe the effects of resins on asphaltene aggregation and emulsion formation. Aggregation is likely controlled by the ability of asphaltene monomers to stack through aromatic and polar interactions. By fractionating asphaltenes into solubility classes, the most polar and aromatic species can be concentrated. The effectiveness of solvating resins on these more and less soluble asphaltenes will aid in elucidating the mechanisms of colloid formation and emulsion stabilization in petroleum derived fluids.

B.3 Experimental

B.3.1 Asphaltene Precipitation and Fractionation

Asphaltenes were precipitated from four crude oils in a 40:1 excess of *n*-heptane. The crude oils were obtained from several locations around the world: B6 and Hondo (off-shore California), Arab Heavy (Safaniya), and Canadon Seco (Argentina). For brevity the following abbreviations will be used to describe the asphaltenes generated from Hondo, Arab Heavy, and Canadon Seco crude oils, respectively: HO, AH, and CS. These crude oils are asphaltene rich and vary in viscosity, resin content and asphaltene H/C ratio. Basic crude oil and asphaltene properties can be found in Table B.1. Resin content was determined by sequential elution chromatography (discussed in the next section), H/C ratios were calculated

from combustion elemental analysis (Perkin Elmer Series II CHNSO), and viscosity measurements were performed on a Rheometrics Dynamic Stress Rheometer with concentric cylinder geometry. Asphaltenes precipitated from the crude oils were separated into more and less soluble fractions by dissolving in toluene and inducing partial precipitation through heptane addition. Enough heptane was added during fractionation to generate approximately 33 % (w/w) insoluble asphaltenes from a 0.75 % (w/v) asphaltene solution in toluene. All solvents were HPLC grade and obtained from Fisher Scientific. Details of the precipitation and fractionation procedures can be found in another publication [44]. A summary of the elemental composition of the asphaltene fractions is provided in Table B.2.

B.3.2 SARA Fractionation

Petroleum resins were isolated via the SARA technique where DAO is charged to silica gel and extracted with solvents of increasing polarity [51-53,67]. After a two stage filtration to ensure complete removal of the asphaltenes, the heptane-diluted crude oil was rotary evaporated until dry. The DAO was dissolved in methylene chloride (Fisher-HPLC grade) and adsorbed to activated silica gel (Chromatographic silica gel, 35-60 mesh, Fisher). Silica gel activation proceeded under vacuum at 120°C for 48 hours. The silica gel-DAO slurry was shaken for 24 hours then rotary evaporated until dry and placed in a nitrogen flushed vacuum oven at 50°C for 24 hours.

Chromatography columns (2 cm x 100 cm with 250 mL solvent reservoir) were initially filled with a mixture of 68:32 heptane-toluene (v/v). Clean activated silica gel was added until the depth reached ~20 cm. Finally, silica gel with adsorbed DAO was transferred to the column until full. A solvent mixture containing 68 % (v/v) heptane and 32 % (v/v) toluene eluted saturates, mono-, di-, and triaromatics from the silica gel. Once the saturates and aromatics were extracted a more polar solvent (40:30:30 acetone:toluene:methylene chloride) was eluted to obtain the resins. The resin-solvent mixture was filtered to remove any silica gel fines and rotary evaporated until dry. The resins were transferred to jars and placed in a nitrogen flushed vacuum oven at 60°C for 48 hours or until completely dry. Combustion elemental analyses of the resins appear in Table B.3.

B.3.3 Asphaltene and Resin Solubility

The solubility of asphaltenes and their sub-fractions were determined in heptol with added resins. Resins from the crude oil were only added to their complementary asphaltenes. Solubility profiles of the asphaltenes without resins were obtained in another study [44] and will be used for comparison. Resin-asphaltene solutions were prepared in various mixtures of heptane and toluene. The asphaltene concentration was 0.75 % w/v (~1 wt %) in 15 mL solvent and the resin-asphaltene ratio was 1:1 by mass. Resins and asphaltenes were dissolved together in toluene and allowed to shake for 12 hours prior to heptane addition. After an additional 12 hours, the solutions were vacuum filtered through 1.5 μm Whatman 934 AH filter paper to collect precipitates and rinsed with 7.5 mL of heptol at the same toluene volume fraction. To ensure all of the resins were removed, the precipitate was rinsed with neat heptane prior to dissolution in methylene chloride. The % precipitated was determined from the mass ratio of precipitated asphaltenes to the original asphaltene mass.

B.3.4 Small-Angle Neutron Scattering

Neutron scattering of asphaltenic aggregates solvated by resins and other dopants was performed on the NG7 and NG1 small angle spectrometers at the NIST Center for Neutron Research (Gaithersburg, MD) or on the Small Angle Neutron Diffractometer (SAND) at Argonne National Laboratory (IPNS, Argonne, IL). Samples were measured in cylindrical quartz cells (NSG Precision Cells) with a path length of 5 mm (all NG7 samples) or 2 mm (all SAND samples).

Mixtures of asphaltenes and resins were prepared at resin:asphaltene (R/A) ratios between 0.25:1 and 10:1. Asphaltene solutions (1 wt %) were prepared in perdeuterated heptane and toluene solutions (CDN Isotopes, Canada) and studied at 25 and 80°C. Scattering intensity versus scattering angle ($I(Q)$ vs. Q) data were fit to Lorentzian line shapes using a non-linear least squares regression to determine the aggregate correlation lengths. Following Ornstein-Zernike formalism the scattering intensity, I , can be related to the scattering vector, Q , by:

$$I(Q) = \frac{I_0}{1 + (Q\xi)^2} \quad (1)$$

where ξ is the correlation length, I_0 is the scattering intensity at $Q = 0$ [42,68]. In some asphaltene systems, a Porod upturn was observed at low Q where the scattering intensity increased monotonically with decreasing Q . Furthermore, incoherent scattering of all nuclei in the solvent and solute with non-zero spin was manifested in the scattering curves at large Q values (typically $Q > 0.1$) as an isotropic background signal. The Q values that marked the transition from the Guinier regime to the Porod or incoherent scattering regimes were determined from inflection points in the scattering curves. The Lorentzian line shape described in Equation 1 was applied over the intermediate range of Q values between the inflection points.

In the absence of a significant low Q upturn, Guinier analysis was also performed to calculate the radius of gyration, R_g , which is defined as the mean squared distance from the center of gravity of the scatterer. The Guinier approximation applies to aggregates in dilute solution and is strictly valid in the low Q range where QR_g is less than 1. The Guinier approximation has the form:

$$I(Q) = I_0 e^{(-Q^2 R_g^2 / 3)} \quad (2)$$

where

$$I_0 = N_p V_p (\Delta\rho)^2 \quad (3)$$

and N_p is the number of scatterers, V_p is the scatterer volume, and $\Delta\rho^2$ is the coherent scattering contrast between the solvent and solute. Given that elemental compositions of the asphaltenes and resins are available, it is possible to calculate the scattering contrast terms and subsequently, the weight-average molecular weight of the aggregates in the Guinier regime. These analyses will be addressed in a future paper.

Comparing the analytical form of the Guinier approximation and Lorentzian lineshapes predicts that R_g should be proportional to ξ by a scale factor of $\sqrt{3}$ (or ~ 1.73). A comparison of the R_g and ξ values obtained from experiments on asphaltene and resin mixtures in heptol provides the relation $R_g = 1.71\xi$. This suggests that Guinier analysis and Lorentzian fits are equally suitable for extracting relevant aggregation behavior from scattering curves. Further details concerning the SANS instruments, experimental conditions, and data analysis methods are provided in another paper [44].

B.3.5 Resin-Asphaltene Emulsions

Water-in-oil emulsions were prepared by homogenizing water and model oil solutions containing asphaltenes and resins. Asphaltenes and resins were dissolved together in toluene for approximately 12 hours followed by heptane addition. A 4 mL aliquot of this solution with an asphaltene concentration of 0.37 % w/v (~0.5 % w/w) was homogenized with a 6 mL aliquot of deionized water. A Virtis Virtishear Cyclone I.Q. homogenizer with a 6 mm rotor-stator emulsion generator assembly was lowered into the oil-water system and run at 15,000 rpm for 3 minutes.

After aging 24 hours, the emulsions were centrifuged for 1 hour at 15,000 rpm. The stability of the emulsions was calculated from the volume of water resolved:

$$\% \text{ Water resolved} = \frac{\text{Volume resolved}}{\text{Initial volume}} \times 100 \quad (4)$$

Complete details on solution preparation and homogenization can be found elsewhere [49].

B.4 Results and Discussion

B.4.1 Asphaltene-Resin Solubility:

The effect of adding resins (1:1 mass ratio) on asphaltene solubility is shown in Figures B.2 a-d. The half filled markers represent solubility data determined for asphaltenes in neat heptol while the filled markers represent asphaltene solubility with resins. As mentioned before, the solubility limits of the whole asphaltene fractions were approximately 50 % toluene. The more soluble fraction or “Soluble” asphaltenes precipitated at toluene volume fractions between 0.3-0.4 while the less soluble or “Precipitate” asphaltenes precipitated at considerably higher aromaticity (0.6-0.8). This indicates that the Soluble fraction cooperatively solvates the Precipitate fraction in solution.

The process of fractionation generated unique asphaltene classes distinguished by their solubility behavior. The “Precipitate” fractions were characterized by higher aromaticity, polarity, molecular weight, and aggregate size than the Whole or Soluble asphaltene fractions. Their behavior in the presence of resins should help elucidate the molecular mechanisms of solvation and aggregation.

The asphaltene solubility limit, after resin addition, was reduced as much as 10 % (v/v) toluene. In the precipitated regime, resins were capable of enhancing asphaltene

solubility (reducing the percentage of precipitates) between 10 and 50 %. Resins appear to enhance the solubility of the Precipitate asphaltenes more so than the Soluble. The solvating interactions between the polar, aromatic resins and highly polar aromatic Precipitate asphaltenes are quite strong. Soluble asphaltenes are less polar and aromatic and do not respond as favorably to resin addition in highly aliphatic solvents. Of note is the considerable solvating effect of CS resins on CS Whole and Precipitate fractions. These interactions suggest that CS resins play a significant role in asphaltene solvation in the crude oil.

Asphaltenes form aggregates in solution through intermolecular π - and hydrogen bonds between asphaltene monomers. Resins reduce the tendency for asphaltenes to aggregate by disrupting these intermolecular interactions. From Table B.3 we see that resins contain polar heteroatoms within a mixed aromatic-aliphatic carbon matrix. Similar to asphaltenes, resins are polydisperse and only mean chemical properties can be measured. Polar functional groups give resins the capacity to disrupt the electron donor-acceptor interactions partly responsible for asphaltene aggregation. Resins, however, are less aromatic than asphaltenes as gauged by H/C ratios between 1.31 and 1.51. Due to decreased aromaticity, their solubility in more aliphatic solvents is considerably higher than asphaltenes. Aromatic moieties in resins likely solvate the fused ring portion of the asphaltenes, producing a solvated, stabilized, resin-asphaltene aggregate. The ability of resins to dissociate intermolecular asphaltene bonds facilitates aggregate size reduction.

B.4.2 SANS: Asphaltenes and Resins in Heptol

Small angle neutron scattering (SANS) allows us to probe the effects of resins on asphaltene aggregation. In another SANS study, we found that asphaltene Precipitate fractions formed larger aggregates than the unfractionated or more soluble fractions [44]. Scattering curves were fit with Lorentzian lineshapes to determine the solute correlation lengths. Figure B.3 shows typical $I(Q)$ versus Q neutron scattering curves for CS Whole asphaltenes with added B6 resins in 60 % toluene at 25°C. The solid lines represent the non-linear least squares fit of the Lorentzian lineshape to the data. Based on the shape of the neutron scattering curve alone, one can readily distinguish two length scales of aggregate sizes in typical asphaltene solutions. For example, the scattering curve for CS Whole

asphaltenes with no added resins in 60% toluene (Figure B.3a.) is a superposition of a Guinier plateau at intermediate Q and an intense power law feature at low Q . The Guinier plateau region indicated scattering from soluble, non-flocculating aggregates on the order of approximately 20 to 100 Å. The presence of a low Q feature indicated flocculation of a portion of the soluble aggregates. The absence of a second plateau region in the lowest Q range suggests that the largest flocs had a size greater than the order of $1/Q_{\min}$ (or ≥ 200 Å). The decrease in intensity of the low Q feature with increasing resin content indicated that resins were effective at dissolving the larger flocs into non-interacting aggregates. A reduction in the correlation length from 101 Å (no resins) to 23 Å (10 % resin) indicated that resins were also effective at solubilizing the individual asphaltene aggregates.

One trivial explanation for the decrease in SANS scattering intensity with increasing resin content is the notion that resins themselves form small aggregates similar to asphaltenes. Upon mixing the asphaltene aggregates with an increasing number of smaller resin aggregates the average particle size is expected to decrease. While resin aggregation is certainly a plausible explanation for reduced correlation lengths, asphaltene-resin interaction in solution cannot be fully discounted. The solubility studies discussed previously have shown that resins play a role in enhancing asphaltene solubility in solution. We will also show that resins are capable of modifying the surface-activity of asphaltenes, thus affecting their ability to stabilize emulsions. The resins used in this study were incapable of forming stable emulsions under at any concentration or solvent condition.

Results from both the solubility and emulsion studies suggest that some interactions with resins modify the asphaltene aggregates to some extent. Bardon et al. compared the scattering curve of an asphaltene-resin mixture to the sum of the scattering intensities from pure asphaltenes and pure resins [47]. Since the sum of the individual scatterers was larger than the scattering by the mixture, they concluded that asphaltenes were solvated by asphaltenes. Furthermore, they assumed the pure asphaltene scattering intensity was the difference between the mixed asphaltene-resin and pure resin (same concentration) scattering patterns. The correlation lengths reported in this study were calculated using scattering curves from the mixed asphaltene-resin solutions.

The effect of resins from different crude oils on asphaltene aggregation is shown in Figure B.4. B6 Whole asphaltenes in pure toluene and 60 % (v/v) toluene in heptol were

combined with AH and B6 resins at 80°C. As shown in the figure, B6 Whole correlation lengths in pure toluene were identical with either AH or B6 resin addition. In the mixed solvent, AH resins appear to solubilize B6 asphaltenes slightly more effectively than B6 resins. Above a 4:1 R/A ratio, the correlation lengths obtained for the asphaltene-resin systems were within 10 %, regardless of the resin type. This suggests that resins from different sources are approximately equal in effectiveness at solvating asphaltenic aggregates. Modest differences in resin aromaticity and polarity (see Table B.3) are secondary to differences in asphaltene chemistry and solvent conditions for dictating aggregate size in crude oil systems.

The aggregation behavior of B6 Whole asphaltene-resin solutions shown in Figure B.4 is typical of the other Whole asphaltenes as well. In the absence of resins, Whole asphaltene correlation lengths followed the trend: CS > B6 > HO > AH. Resin addition was effective at disrupting the intermolecular bonding and aggregation of each asphaltene to a similar extent. The greatest decrease in aggregate size occurred between 0.5 and 2:1 R/A suggesting resins strongly solvate asphaltenes at ratios close to those found in crude oil (Table B.1). As the R/A ratio approached 10:1 the Whole asphaltene correlation lengths neared a common value of approximately 11-14 Å, suggesting this may be close to a solvated monomer or irreducible oligomer.

In less aromatic solvents, asphaltenes form larger aggregates due to solvent-solute incompatibility. Heptane-toluene mixtures of increasingly aliphatic solvent possess a lower degree of π -bond solvating capability and polarity than a pure toluene solvent. As a result, asphaltenes without resins in 60 % (v/v) toluene have larger correlation lengths than in pure toluene. For example, B6 Whole asphaltenic aggregates have correlation lengths of 79.0 Å at a toluene volume fraction of 0.6 as compared to 42.6 Å in pure toluene. However, at a R/A ratio of 10:1 the B6 Whole correlation length appears to plateau at similar values (~ 14-18 Å) regardless of the solvent aromaticity. This indicates that high resin concentrations are apparently more effective at reducing aggregate size than solvent alone. This comes as no surprise since resins are more chemically similar to asphaltenes and have been linked to asphaltene solubility in a variety of systems including crude oil.

B.4.3 Asphaltene-Resin Emulsion Stability: Effect of varied R/A ratio

Asphaltene emulsions were prepared in the presence of resins at R/A ratios from 0.5 to 10 and their stabilities were gauged by measuring % water resolved after centrifugation. These emulsion stabilities were compared to aggregate correlation lengths determined by SANS (Figures B.5-B.7). As shown in Figure B.5, resin addition decreased both the aggregate correlation length and stability of emulsions formed by CS Whole asphaltenes in 60% toluene. This trend was also observed for B6 and HO Whole asphaltenes, although CS Whole asphaltenes formed much weaker emulsions than both B6 and HO Whole at similar solvent conditions. CS asphaltenic aggregates were the most aromatic and least polar of the Whole asphaltenes studied. The lack of polarity and possible inability to form a network of hydrogen bonds likely reduced interfacial film strength. Resin addition up to R/A ratios of 2:1 effectively solvated the aggregates and further reduced their emulsion stabilizing ability.

Conversely, B6 Whole aggregates in 60% toluene were sufficiently surface-active enough (due to high polarity) even at R/A ratios approaching 5:1 to adsorb at oil-water interfaces and form emulsion-stabilizing films with 72% water resolved. Correlation lengths observed for B6 Whole asphaltenes in 60% toluene at 80°C decreased with resin addition from 47 Å (0.5:1 R/A ratio) to 18 Å (10:1 R/A ratio). Correlation lengths observed for HO Whole asphaltenes in 60% toluene at 80°C decreased were slightly lower and varied with resin addition from 38 Å (0.5:1 R/A ratio) to 14 Å (10:1 R/A ratio). Both B6 and HO Whole asphaltenes were high in polarity but HO Whole lacked the surface activity to maintain a cohesive oil-water interfacial film at R/A ratios greater than 2:1 (92 % water resolved). However, emulsions formed by HO Wholes asphaltenes were still more stable than those formed by CS Whole asphaltenes under similar conditions. Based on the emulsion stability results of the Whole asphaltenes, it is apparent that higher resin concentrations are needed to destabilize emulsions when asphaltenes are more polar.

B6 Precipitate emulsions prepared in pure toluene remained very stable in systems containing up to 2:1 resins (Figure B.6). This was due primarily to the high proportion of film forming species in B6 Precipitate. The fractionation process concentrated the most aromatic and polar asphaltenes in the Precipitate fraction and, as a result, they tended to aggregate, adsorb and consolidate into elastic films at oil-water interfaces. As the R/A ratio approached 2:1, the film forming portion of Precipitate asphaltenes were in sufficient supply

to maintain nearly complete emulsion stability. The slight increase in stability from 0 to 0.25:1 R/A was likely due to enhanced asphaltene solubility and lability of the aggregates. In the absence of resins, the aggregate size may have been too large for asphaltenes to effectively cover water droplet interfaces and for w/o emulsions to achieve high stability. As the large aggregates were solvated by resins, they became more interfacially active and formed a cohesive film. Beyond 2:1 R/A the asphaltenic aggregates became increasingly soluble, less surface-active, and consequently formed weaker emulsions. The most dramatic decrease in asphaltene correlation length occurred below a R/A ratio of 2:1, beyond which a minimum aggregate size was approached. It appears that above this ratio of 2:1, the asphaltenes were sufficiently solvated that they lost their interfacial activity.

B6 Precipitate asphaltenes were beyond the limit of solubility in 30% toluene and the emulsions prepared without resins were not particularly stable (Figure B.7). The increase in correlation length with addition of resins to a R/A ratio of 10:1 indicated that resins facilitated the dissolution of the insoluble asphaltenes. As more interfacially active material was dissolved, the emulsion stability increased. The maximum in correlation length did not coincide with the maximum in emulsion stability, perhaps because different initial amounts of asphaltenes were used. The emulsions were tested at an asphaltene concentration of 0.5 wt % and SANS experiments were performed at 1 wt %. Fewer resins were needed to dissolve asphaltenes at the lower concentration, thus the maximum in emulsion stability was shifted to a R/A ratio of 5:1. At R/A of 20:1, the additional resins simply solvated the asphaltenic aggregates and tended to reduce the emulsion stability.

Similar trends in aggregate size and emulsion stability were observed for CS Precipitate asphaltenes in pure toluene and in 50 % toluene. In pure toluene, correlation length increased from 101 Å (no resins) to 128 Å (0.5:1 R/A ratio) as resin addition dissolved the insoluble species followed by a monotonic decrease with further resin addition to 26 Å (10:1 R/A ratio). CS Precipitate asphaltenes did not form particularly stable emulsions in pure toluene and the addition of resins had a modest effect on emulsion stability. As expected, CS Precipitate asphaltenes were also partially insoluble in 50 % toluene and the addition of resins up to a R/A ratio of 2:1 aided the dissolution of the insoluble species. Correlation lengths observed for CS Precipitate in 50% toluene increased from 98 Å (0.5:1 R/A ratio) to 108 Å (2:1 R/A ratio) followed by a decrease to 31 Å (10:1 R/A ratio). As

more interfacially active material was dissolved, the emulsion stability increased markedly from 52% water resolved (no resins) to 25% water resolved (5:1 R/A ratio).

B.4.4 Asphaltene (Soluble, Whole, Precipitate)-Resin Emulsion Stability:

The stability of emulsions prepared with AH Whole and its fractions at several heptol ratios are shown in Figure B.8. As with the previous experiments, the asphaltene concentration was 0.37 % (w/v), or equivalently 0.5 % (w/w), and the resin-asphaltene ratio was varied. The volume fractions of toluene were chosen such that the asphaltenes were either above or below their solubility limits. AH Soluble asphaltenes in 60 % toluene formed weak emulsions that became increasingly unstable as resin concentration increased (Figure B.8a). The asphaltenes were very soluble at these conditions and could not form interfacial films capable of withstanding rupture. AH Soluble asphaltenes in 30 % toluene were partially precipitated. Resin addition initially solvated the flocculated aggregates at R/A ratios of 0.25 and 0.5 resulting in enhanced emulsion stability. Further solvation by resins completely destabilized the emulsions at a R/A ratio of 2. AH Whole asphaltenes formed emulsions in 55 % toluene with close to 50 % water resolved (Figure B.8b). In the insoluble regime, (30 % toluene) the emulsions were considerably weaker due to non-surface-active, flocculated asphaltenic aggregates; however, resin addition reversed this behavior. At higher R/A ratios, the 30 % toluene system became highly solvated and emulsions were destabilized. Much the same effect was seen with AH Precipitate asphaltenes (Figure B.8c) where the emulsions containing the most soluble asphaltenes became unstable while partially insoluble systems actually formed stronger emulsions.

The emulsions formed by CS Whole asphaltenes and asphaltene fractions were typically unstable. In the soluble regime, the ability of each asphaltene to form stable emulsions decreased with resin addition (Figure B.9). The emulsion stability of CS Soluble at 40 % toluene appeared to increase slightly up to an R/A of 0.5:1 followed by a decrease. CS Whole asphaltenes formed unstable emulsions beyond an R/A of 1:1 due to resin solvation. The behavior of partially insoluble CS Precipitate at 50 % toluene suggests that resins were capable of a modest enhancement of emulsion stability. Even when the systems were rendered more soluble with resins, emulsion stability did not increase appreciably. High aromaticity, as suggested by low H/C ratios, likely caused large aggregate formation

through π - π interactions between asphaltene monomers and reduced aggregate lability. These properties suggest that CS asphaltenes are inherently weak emulsifiers due possibly to large aggregate formation, low polarity and an inability to form hydrogen bonds.

Unlike the weak emulsions formed by AH and CS asphaltenes over a wide range of solvent conditions, B6 and HO asphaltene-stabilized emulsions were considerably stronger. The effects of resins on emulsion stability in the soluble and insoluble regimes are quite apparent. In Figure B.10a, resins are shown to destabilize emulsions in the soluble regime of B6 Soluble. In the insoluble regime (30 % toluene), emulsion stability is reduced only after reaching a 5:1 R/A ratio. Resins initially dissolved precipitated asphaltenes and rendered them interfacially active until the system became too soluble and the driving force for film formation disappeared. In a highly aliphatic solvent (10 % toluene: 90 % heptane) B6 Soluble asphaltenes did not form stable emulsions even with an R/A of 5:1.

B6 Whole asphaltenes were studied at three solvent conditions in the presence of resins (Figure B.10b). B6 Whole asphaltenes were completely soluble at both 60 % and 100 % toluene. B6 Whole asphaltenes were very soluble in pure toluene but still formed stable emulsions up to a R/A of 0.25:1. Beyond this point the emulsion stability rapidly decreased as a result of enhanced solubility. At 60 % toluene, B6 Whole asphaltenes approached their limit of solubility in solution and, consequently, formed larger aggregates in solution and were stronger emulsion formers than in pure toluene. As discussed in another paper [44], we observed an increase in aggregate size with decreasing solvent aromaticity up to the asphaltene solubility limit as the soluble asphaltenes attempted to minimize interactions with the increasingly aliphatic solvent. As shown in Figure B.10b, the proximity to the solubility limit also corresponds to a maximum in emulsion stability. Emulsions of B6 Whole asphaltenes in 60% toluene eventually became unstable at a 10:1 R/A ratio, while a R/A ratio of 5:1 was needed to completely destabilize emulsions in pure toluene. Solutions containing a fraction of insoluble asphaltenes (40 % toluene) were also able to form very stable emulsions up to a R/A ratio of 5:1. The dissolution of these insoluble asphaltenes facilitated strong interfacial film formation up to $R/A > 10$, at which point the asphaltenes were so strongly solvated by resins that they ceased to be effectively surface-active.

B6 Precipitate asphaltenes were appreciably insoluble at both 30 % and 60 % toluene but soluble in pure toluene. B6 Precipitate formed stable emulsions in 60 % and 100 %

toluene; however, at 30 % toluene, B6 Precipitate asphaltenes were not sufficiently soluble to stabilize emulsions (Figure B.10c). The effect of adding resins at 30 % toluene was to effectively dissolve the insoluble asphaltenes and form strongly stable emulsions above a R/A of 5:1. Even at 20:1 R/A, there still existed a sufficient supply of film forming material to form relatively stable emulsions, a remarkable observation. This level of solubility is quite high and suggests that B6 Precipitate asphaltenes have unique molecular structures that allow them to stabilize emulsions in the presence of large concentrations of strongly solvating resins. In particular, a balance between aromaticity and hydrogen bonding capacity must exist to allow stability in both pure toluene with no resins (high aromaticity, low polarity) and in highly aliphatic solvents with substantial resin content (low aromaticity, high polarity).

The effectiveness of resins at solubilizing asphaltenes surely depends on asphaltene and resin chemistry and on the supporting aliphatic and aromatic solvent. B6 Whole asphaltenes formed stable emulsions at 40% toluene without resins but were only 60 % soluble (Figure B.2). The amount of precipitated material decreased below 10 % at an R/A of 1:1. Above this resin content, the asphaltenes were soluble and formed stable emulsions up to R/A of 5:1. Further solvation by addition of resins eventually destabilized the emulsions. At 30 % toluene, B6 Precipitate asphaltenes did not form stable emulsions. Apparently, either the amount of soluble material was insufficient and/or the soluble material was in aggregates of too large a size to effectively cover water droplet surfaces. Emulsion stability increased slightly by adding resins of equal mass ratio to asphaltenes. Solubility measurements indicated that the asphaltenes were nearly insoluble at these conditions. However, at an R/A of 5:1, B6 Precipitate solubility increased from essentially insoluble to 55% soluble and emulsion stability reached a maximum. Further solvation with resins did not enhance gravimetric solubility, but emulsion stability decreased substantially.

HO Whole and its more and less soluble fractions behaved in a very similar fashion to B6 asphaltenes; however, HO Precipitate asphaltenes were observed to form even stronger emulsions than B6 Precipitate fractions (Figure B.10d). HO Precipitate asphaltenes were solubilized with resins at 30 % toluene and formed stable emulsions up to R/A ratios of 20:1. Again, in the regime in which HO Precipitate asphaltenes were soluble, the addition of resins led to emulsion destabilization.

The power of resins to solvate asphaltenes of all chemistries is evident from SANS, solubility, and emulsion stability measurements. In addition, the ability to dissolve insoluble asphaltenes and render them capable of emulsion stabilization is remarkable. However, this resin-asphaltene interaction appears to act primarily with HO and B6 Precipitate, and CS to a lesser degree, and must be linked significantly to the molecular structure of these asphaltenes. HO and B6 Precipitate fractions have the highest polarity of any of the fractions previously prepared (see Table B.2). The H/C ratio of these fractions is also lower than B6 or HO Whole but not as low as AH or CS asphaltenes, indicating a moderate level of aromaticity. These chemical properties suggest that aggregation and film formation may be driven more so by polar heteroatom interactions such as hydrogen bonding than by π - π bonding between asphaltenic aromatic moieties. AH and CS asphaltenes contain low concentrations of polar nitrogen and likely aggregate via aromatic stacking. Without sufficient proton donor-acceptor sites, the asphaltenes cannot adsorb and form a cohesive film at the oil-water interface.

B.5 Conclusions

In this study, resins isolated by SARA fractionation had a strong solvating effect on asphaltenes and their more and less soluble subfractions – so-called “Soluble” and “Precipitate” asphaltenes. At an R/A ratio of 1:1, the toluene concentration at which asphaltenes began to precipitate in heptol was reduced by as much as 10 %. The sizes of asphaltenic aggregates, as gauged by correlation lengths from neutron scattering, were observed to decrease significantly upon addition of resins. At room temperature, the correlation lengths of Whole asphaltenes approached a value of approximately 14-18 Å at high resin concentrations (R/A of 10:1) regardless of asphaltene, resin type, or % toluene (in the soluble regime). Furthermore, the greatest decreases in aggregate size occurred at conditions found in typical crude oils (i.e., R/A ratios between 0.5 and 2:1). It is not known to what extent the aggregates can be dissociated by resin addition. The presumed minimum would be a single asphaltene monomer solvated completely by resins. In the portion of the phase diagram in which asphaltenes were insoluble, aggregate sizes increased with resin addition up to the solubility limit as the more polar, insoluble asphaltenes were dissolved into

solution. Once the insolubles were dissolved, additional resins solvated the largest of the soluble aggregates as observed by a decrease in the correlation length.

Asphaltene stabilized emulsions were susceptible to the effects of resin solvation. Soluble asphaltenes typically formed the weakest emulsions because the aggregates were small, well solvated, less aromatic, and less polar than the Whole and Precipitate fractions, and consequently, less interfacially active. Soluble and Whole asphaltenes at toluene concentrations in the insoluble regime could be solvated by resin addition to produce slightly more stable emulsions. Resins completely destabilized emulsions of Whole and Soluble asphaltenes in the portion of phase space at which these asphaltenes were soluble at a R/A of 2:1, except in the case of B6 Whole, which formed stable emulsions up to a R/A of 10:1.

AH and CS Precipitate asphaltenes were poor emulsion formers without resins and their emulsions were only modestly more stable with resins. Their lack of polarity, even when solvated to become more labile, prevented them from interacting strongly at oil-water interfaces. B6 and HO Precipitate, however, formed very stable emulsions in their soluble regime that were resistant to the solvating effects of resins. Both approached complete instability near a R/A of 10:1. At 60 % toluene B6 and HO Precipitate asphaltenes were partially insoluble but formed very stable emulsions due to their highly polar and H-bonding nature. Resins added to these systems dissolved the insoluble asphaltenic flocs, rendering them interfacially active. Once B6 Precipitate asphaltenes were solubilized, emulsions remained stable even at a R/A of 20:1. In highly aliphatic solvents (30 % toluene), B6 and HO Precipitate asphaltenes were largely insoluble and did not form stable emulsions. Resins were able to solvate these systems to a considerable extent and led to stable emulsions at R/A ratios of 20:1.

Comparisons between aggregate sizes and the stability of oil-in-water emulsions formed at various R/A ratios suggested that the most stable emulsions formed from soluble aggregates of maximum size and greatest interfacial activity. These aggregates invariably formed at the limit of asphaltene solubility. Modest differences in resin aromaticity and polarity are secondary to asphaltene chemistry and solvent conditions for dictating aggregate size and emulsion stability in asphaltene solutions.

The remarkable ability of resins to solvate asphaltenes can be attributed to the polar and dispersive nature of the resin molecules. In highly aromatic solvents, where π - π

interactions between asphaltenic aggregates are largely mitigated, resins serve to further disrupt polar and hydrogen-bonding interactions within asphaltene aggregates. At low solvent aromaticity, resin solvation aids to break flocs by disruption of dispersion and hydrogen bonding interactions between aggregates. For systems containing asphaltenes with high polarity and surface activity (e.g., B6 and HO Whole and Precipitate), resin solvation is sometimes insufficient to induce complete emulsion destabilization. Weak emulsion formers and Soluble asphaltenes possessing a lower polarity and aromaticity are easily destabilized in the presence of resins. Aggregation and film formation in petroleum fluids are likely driven by polar heteroatom interactions, such as hydrogen bonding. The most polar asphaltenes, typically concentrated in the least soluble fraction, require the largest concentration of resins to completely destabilize asphaltene emulsions and likely cause many petroleum production problems such as pipeline deposition and water-in-crude oil emulsion stabilization.

B.6 Acknowledgements

This work was supported by grants from the National Science Foundation (CTS-981727), PERF (97-07), and shared consortium funding from ExxonMobil, Ondeo-Nalco Energy Systems, Shell Oil Company and Texaco. Special thanks go to George Blankenship and Semaj McIver who assisted with the experimental work. We would like to thank Eric Sirota of ExxonMobil Corporate Research for acquiring the SANS beam time at NIST and Min Lin for his assistance on the NG-7 and NG-1 beamlines. We are grateful to the Department of Energy, Argonne National Laboratory, and particularly to Pappannan Thiyagarajan and Denis Wozniak for their assistance on the SAND instrument. We also want to thank Marit-Helen Ese and Jihong Tong for helping with the SANS data collection.

B.7 References

1. S. A. Berridge, M. T. Thew, A. G. Loriston-Clarke, "The Formation and Stability of Emulsions of Water in Crude Petroleum and Similar Stocks," *Journal of the Institute of Petroleum*, 1968, **54**(539): p. 333-357.
2. C. M. Blair, "Interfacial Films Affecting the Stability of Petroleum Emulsions," *Chemistry and Industry*, 1960: p. 538-544.

3. F. J. Nellensteyn, "The Constitution of Asphalt," *Journal of the Institute of Petroleum Technologists*, 1924, **10**: p. 311-325.
4. J. P. Pfeiffer, R. N. J. Saal, "Asphaltic Bitumen as Colloid System," *Journal of Physical Chemistry*, 1940, **44**: p. 139-149.
5. A. S. C. Lawrence, W. Killner, "Emulsions of Seawater in Admiralty Fuel Oil with Special Reference to their Demulsification," *Journal of the Institute of Petroleum*, 1948, **34**: p. 281.
6. M. O. Denekas, F. T. Carlson, J. W. Moore, C. G. Dodd, "Material Adsorbed at Crude Petroleum-Water Interfaces," *Ind. and Eng. Chem.*, 1951, **43**(5): p. 1165-1169.
7. C. G. Dodd, "The Rheological Properties of Films at Crude Petroleum-Water Interfaces," *Journal of Physical Chemistry*, 1960, **64**(5): p. 544-550.
8. H. Neumann, "Investigations Regarding the Separation of Crude Oil Emulsions," *Petrochemie*, 1965, **18**: p. 776-779.
9. O. K. Kimbler, R. L. Reed, I. H. Silberberg, "Physical Characteristics of Natural Films Formed at Crude Oil-Water Interfaces," *Society of Petroleum Engineers Journal*, 1966, (6): p. 153-165.
10. J. E. Strassner, "Effect of pH on Interfacial Films and Stability of Crude Oil-Water Emulsions," *Journal of Petroleum Technology*, 1968, **20**: p. 303-312.
11. G. D. M. Mackay, A. Y. McLean, O. J. Betancourt, B. D. Johnson, "The Formation of Water-in-Oil Emulsions Subsequent to an Oil Spill," *Journal of the Institute of Petroleum*, 1973, **59**(568): p. 164-172.
12. R. J. R. Cairns, D. M. Grist, E. L. Neustadter. *The Effect of Crude Oil-Water Interfacial Properties on Water-Crude Oil Emulsion Stability*. in *Theory and Practice of Emulsion Technology*. 1974. Brunel University: Academic Press.
13. J. J. Oren, G. D. M. MacKay, "Electrolyte and pH Effect on Emulsion Stability of Water-in-Petroleum Oils," *Fuel*, 1977, **56**(10): p. 382-384.
14. T. J. Jones, E. L. Neustadter, K. P. Whittingham, "Water-in-Crude Oil Emulsion Stability and Emulsion Destabilization by Chemical Demulsifiers," *Journal of Canadian Petroleum Technology*, 1978, **17**(2): p. 100-108.
15. A. L. Bridie, T. T. Wanders, W. Zegveld, H. B. v. d. Heijde, "Formation, Prevention and Breaking of Sea Water in Crude Oil Emulsions 'Chocolate Mousses'," *Mar. Pollut. Bull.*, 1980, **11**: p. 343-348.

16. S. E. Taylor, "Resolving Crude Oil Emulsions," *Chemistry and Industry*, 1992, **20**: p. 770-773.
17. C. S. Shetty, A. D. Nikolov, D. T. Wasan, "Demulsification of Water in Oil Emulsions Using Water Soluble Demulsifiers," *Journal of Dispersion Science and Technology*, 1992, **13**(2): p. 121-133.
18. D. L. Mitchell, J. G. Speight, "The Solubility of Asphaltenes in Hydrocarbon Solvents," *Fuel*, 1973, **52**(4): p. 149-152.
19. T. F. Yen, J. G. Erdman, S. S. Pollack, "Investigation of Structure of Petroleum Asphaltenes By X-Ray Diffraction," *Analytical Chemistry*, 1961, **33**(11): p. 1587-&.
20. R. V. Barbour, J. C. Petersen, "Molecular Interactions of Asphalt: An Infrared Study of the Hydrogen-Bonding Basicity of Asphalt," *Analytical Chemistry*, 1974, **46**(2): p. 273-277.
21. M. M. Boduszynski, J. F. McKay, D. R. Latham, "Asphaltenes, Where Are You?," *Proceedings of the Association of Asphalt Paving Technologists*, 1980, **49**: p. 123-143.
22. T. Ignasiak, O. P. Strausz, D. S. Montgomery, "Oxygen Distribution and Hydrogen Bonding in Athabasca Asphaltene," *Fuel*, 1977, **56**: p. 359-365.
23. S. E. Moschopedis, J. G. Speight, "Investigation of Hydrogen Bonding by Oxygen Functions in Athabasca Bitumen," *Fuel*, 1976, **55**: p. 187-192.
24. J. C. Petersen, "An Infra-red Study of Hydrogen Bonding in Asphalt," *Fuel*, 1967, **46**(4-5): p. 295-305.
25. M. M. H. Al-Jarrah, A. H. Al-Dujaili, "Characterization of Some Iraqi Asphalts II. New Findings on the Physical Nature of Asphaltenes," *Fuel Science and Technology International*, 1989, **7**(1): p. 69-88.
26. S. Acevedo, B. Mendez, A. Rojas, I. Layrisse, H. Rivas, "Asphaltenes and Resins From the Orinoco Basin," *Fuel*, 1985, **64**: p. 1741-1747.
27. M. M. Boduszynski, "Composition of Heavy Petroleums. 2. Molecular Characterization," *Energy & Fuels*, 1988, **2**(5): p. 597-613.
28. I. A. Wiehe, K. S. Liang, "Asphaltenes, Resins, and other petroleum macromolecules," *Fluid Phase Equilibria*, 1996, **117**(1-2): p. 201-210.
29. J. F. McKay, P. J. Amend, T. E. Cogswell, P. M. Harnsberger, R. B. Erickson, D. R. Latham, "Petroleum Asphaltenes: Chemistry and Composition," *Analytical*

- Chemistry of Liquid Fuel Sources, Advances in Chemistry Series*, 1978, **170**: p. 128-142.
30. S. I. Andersen, A. Keul, E. Stenby, "Variation in composition of subfractions of petroleum asphaltenes," *Petroleum Science and Technology*, 1997, **15**(7-8): p. 611-645.
 31. H. W. Yarranton, J. H. Masliyah, "Molar Mass Distribution and Solubility Modeling of Asphaltenes," *AIChE Journal*, 1996, **42**(12): p. 3533-3543.
 32. H. W. Yarranton, H. Alboudwarej, R. Jakher, "Investigation of asphaltene association with vapor pressure osmometry and interfacial tension measurements," *Industrial & Engineering Chemistry Research*, 2000, **39**(8): p. 2916-2924.
 33. P. Herzog, D. Tchoubar, D. Espinat, "Macrostructure of Asphaltene Dispersions by Small-angle X-ray Scattering," *Fuel*, 1988, **67**: p. 245-250.
 34. J. C. Ravey, G. Ducouret, D. Espinat, "Asphaltene Macrostructure by Small Angle Neutron Scattering," *Fuel*, 1988, **67**(11): p. 1560-1567.
 35. R. E. Overfield, E. Y. Sheu, S. K. Sinha, K. S. Liang, "SANS Study of Asphaltene Aggregation," *Fuel Science & Technology International*, 1989, **7**(5-6): p. 611-624.
 36. E. Y. Sheu, D. A. Storm, M. M. D. Tar, "Asphaltenes in Polar Solvents," *Journal of Non-Crystalline Solids*, 1991, **131-133**: p. 341-347.
 37. D. Espinat, J. C. Ravey, V. Guille, J. Lambard, T. Zemb, J. P. Cotton, "Colloidal Macrostructure of Crude-Oil Studied By Neutron and X-Ray Small-Angle Scattering Techniques," *Journal De Physique Iv*, 1993, **3**(C8): p. 181-184.
 38. P. Thiyagarajan, J. E. Hunt, R. E. Winans, K. B. Anderson, J. T. Miller, "Temperature-Dependent Structural-Changes of Asphaltenes in 1-Methylnaphthalene," *Energy & Fuels*, 1995, **9**(5): p. 829-833.
 39. H. Rassamdana, M. Sahimi, "Asphalt Flocculation and Deposition: II. Formation and Growth of Fractal Aggregates," *AIChE Journal*, 1996, **42**(12): p. 3318-3332.
 40. L. Barre, D. Espinat, E. Rosenberg, M. Scarsella, "Colloidal structure of heavy crudes and asphaltene solutions," *Revue De L Institut Francais Du Petrole*, 1997, **52**(2): p. 161-175.
 41. M. Y. Lin, E. B. Sirota, H. Gang, "Neutron scattering characterization of asphaltene particles," *Abstracts of Papers of the American Chemical Society*, 1997, **213**: p. 66-70.

42. E. B. Sirota, "Swelling of asphaltenes," *Petroleum Science and Technology*, 1998, **16**(3-4): p. 415-431.
43. D. Fenistein, L. Barre, "Experimental measurement of the mass distribution of petroleum asphaltene aggregates using ultracentrifugation and small-angle X-ray scattering," *Fuel*, 2001, **80**(2): p. 283-287.
44. P. M. Spiecker, K. L. Gawrys, P. K. Kilpatrick, "Aggregation and solubility behavior of petroleum asphaltenes and their subfractions," *Journal of Colloid and Interface Science*, submitted, 2002: p.
45. O. P. Strausz, P. Peng, J. Murgich, "About the colloidal nature of asphaltenes and the MW of covalent monomeric units," *Energy & Fuels*, 2002, **16**(4): p. 809-822.
46. E. Y. Sheu, K. S. Liang, S. K. Sinha, R. E. Overfield, "Polydispersity Analysis of Asphaltene Solutions in Toluene," *Journal of Colloid and Interface Science*, 1992, **153**(2): p. 399-410.
47. C. Bardon, L. Barre, D. Espinat, V. Guille, M. H. Li, J. Lambard, J. C. Ravey, E. Rosenberg, T. Zemb, "The colloidal structure of crude oils and suspensions of asphaltenes and resins," *Fuel Science & Technology International*, 1996, **14**(1-2): p. 203-242.
48. J. C. Ravey, D. Espinat, "Macrostructure of Petroleum Asphaltenes by Small Angle Neutron Scattering," *Progress in Colloid and Polymer Science*, 1990, **81**: p. 127-130.
49. P. M. Spiecker, P. K. Kilpatrick, "The Role of Asphaltene Solubility and Chemistry on the Stability of Water-in-Oil Emulsions," *Journal of Colloid and Interface Science*, 2003, **267**: p. 178-193.
50. M. vanderWaarden, "Stability of Emulsions of Water in Mineral Oils Containing Asphaltenes," *Kolloid Z. Z. Polymer*, 1958, **156**(2): p. 116-122.
51. R. Miller, "Hydrocarbon Class Fractionation with Bonded-Phase Liquid Chromatography," *Analytical Chemistry*, 1982, **54**(11): p. 1742-1746.
52. J. G. Reynolds, "Characterization of Heavy Residua by Application of a Modified D 2007 and Asphaltene Separation: Effect of Solvents on Physical and Chemical Properties of Fractions Derived From Hondo 850°F Residuum," *Fuel Science and Technology International*, 1987, **5**(5): p. 593-620.
53. M. F. Ali, A. Bukhari, M. U. Hasan, "Structural Characterization of Arabian Heavy Crude Oil Residue," *Fuel Science and Technology International*, 1989, **7**(8): p. 1179-1208.

54. M. Alula, M. Diack, R. Gruber, G. Kirsch, J. C. Wilhelm, D. Cagniant, "Efficiency of Sequential Elution Solvent Chromatography-Extrography Technique for the Characterization of Hydroliquefaction and Pyrolysis Products," *Fuel*, 1989, **68**(10): p. 1330-1335.
55. W. R. Middleton, "Gradient Elution Chromatography Using Ultraviolet Monitors in the Analytical Fractionation of Heavy Petroleum," *Analytical Chemistry*, 1967, **39**(14): p. 1839-1846.
56. J. G. Reynolds, W. R. Biggs, "Effects of Asphaltene Precipitation and a Modified D 2007 Separation on the Molecular Size of Vanadium- and Nickel-Containing Compounds in Heavy Residua," *Fuel Science and Technology International*, 1986, **4**(6): p. 749-777.
57. L. X. Nghiem, M. S. Hassam, R. Nutakki, A. E. D. George, "Efficient Modelling of Asphaltene Precipitation," *Society of Petroleum Engineers*, 1993, **5**: p. 375-384.
58. S. I. Andersen, K. S. Birdi, "Aggregation of Asphaltenes as Determined by Calorimetry," *Journal of Colloid and Interface Science*, 1991, **142**(2): p. 497-502.
59. J. Murgich, J. A. Abanero, O. P. Strausz, "Molecular recognition in aggregates formed by asphaltene and resin molecules from the Athabasca oil sand," *Energy & Fuels*, 1999, **13**(2): p. 278-286.
60. J. Murgich, O. P. Strausz, "Molecular mechanics of aggregates of asphaltenes and resins of the Athabasca oil," *Petroleum Science and Technology*, 2001, **19**(1-2): p. 231-243.
61. J. D. McLean, P. K. Kilpatrick, "Effects of asphaltene aggregation in model heptane-toluene mixtures on stability of water-in-oil emulsions," *Journal of Colloid and Interface Science*, 1997, **196**(1): p. 23-34.
62. H. Fordedal, Y. Schildberg, J. Sjoblom, J.-L. Volle, "Crude Oil Emulsions in High Electric Fields as Studied by Dielectric Spectroscopy. Influence of Interaction Between Commercial and Indigenous Surfactants," *Colloids and Surfaces A: Physicochemical and Engineering Aspects*, 1996, **106**: p. 33-47.
63. R. A. Mohammed, A. I. Bailey, P. F. Luckham, S. E. Taylor, "Dewatering of Crude Oil Emulsions 2. Interfacial Properties of the Asphaltic Constituents of Crude Oil," *Colloids and Surfaces A: Physicochemical and Engineering Aspects*, 1993, **80**: p. 237-242.
64. H. Fordedal, Ø. Midttun, J. Sjöblom, O. K. Kvalheim, Y. Schildberg, J.-L. Volle, "A Multivariate Screening Analysis of W/O Emulsions in High External Electric Fields as Studied by Means of Dielectric Time Domain Spectroscopy, II," *Journal of Colloid and Interface Science*, 1996, **182**: p. 117-125.

65. J. D. McLean, P. K. Kilpatrick, "Effects of Asphaltene Solvency on Stability of Water-in-Crude Oil Emulsions," *Journal of Colloid and Interface Science*, 1997, **189**: p. 242-253.
66. O. V. Gafonova, H. W. Yarranton, "The stabilization of water-in-hydrocarbon emulsions by asphaltenes and resins," *Journal of Colloid and Interface Science*, 2001, **241**(2): p. 469-478.
67. J. D. McLean, P. K. Kilpatrick, "Comparison of Precipitation and Extrography in the Fractionation of Crude Oil Residua," *Energy and Fuels*, 1997, **11**: p. 570-585.
68. P.-G. de Gennes, *Scaling Concepts in Polymer Physics*; Cornell University Press: Ithaca, NY, 1979.

Table B.1 Crude oil properties

Crude	Wt % Asph	R/A Ratio	H/C Asph	Viscosity (cP)
				100°F
AH	6.7	1.12	1.14	33.8
B6	13.1	0.92	1.24	2030
CS	7.5	1.19	1.11	70
HO	14.8	1.39	1.29	363

Table B.2 Asphaltene fraction composition in wt %, except H/C

	H/C			Nitrogen			Sulfur		
	Sol	Whole	Ppt	Sol	Whole	Ppt	Sol	Whole	Ppt
Asphaltene									
AH	1.17	1.14	1.13	0.92	1.02	1.08	8.06	8.32	7.66
B6	1.30	1.24	1.22	1.81	1.87	1.93	7.25	6.68	6.33
CS	1.12	1.11	1.09	1.32	1.32	1.39	0.52	0.52	0.48
HO	1.30	1.29	1.24	1.95	1.99	2.11	8.42	8.53	8.48

Table B.3 Resin composition in wt %, except H/C (O by difference)

Resin source	H/C	N	S	O
AH	1.31	0.81	6.49	1.53
B6	1.51	1.48	6.91	1.98
CS	1.39	1.52	0.88	2.77
HO	1.51			

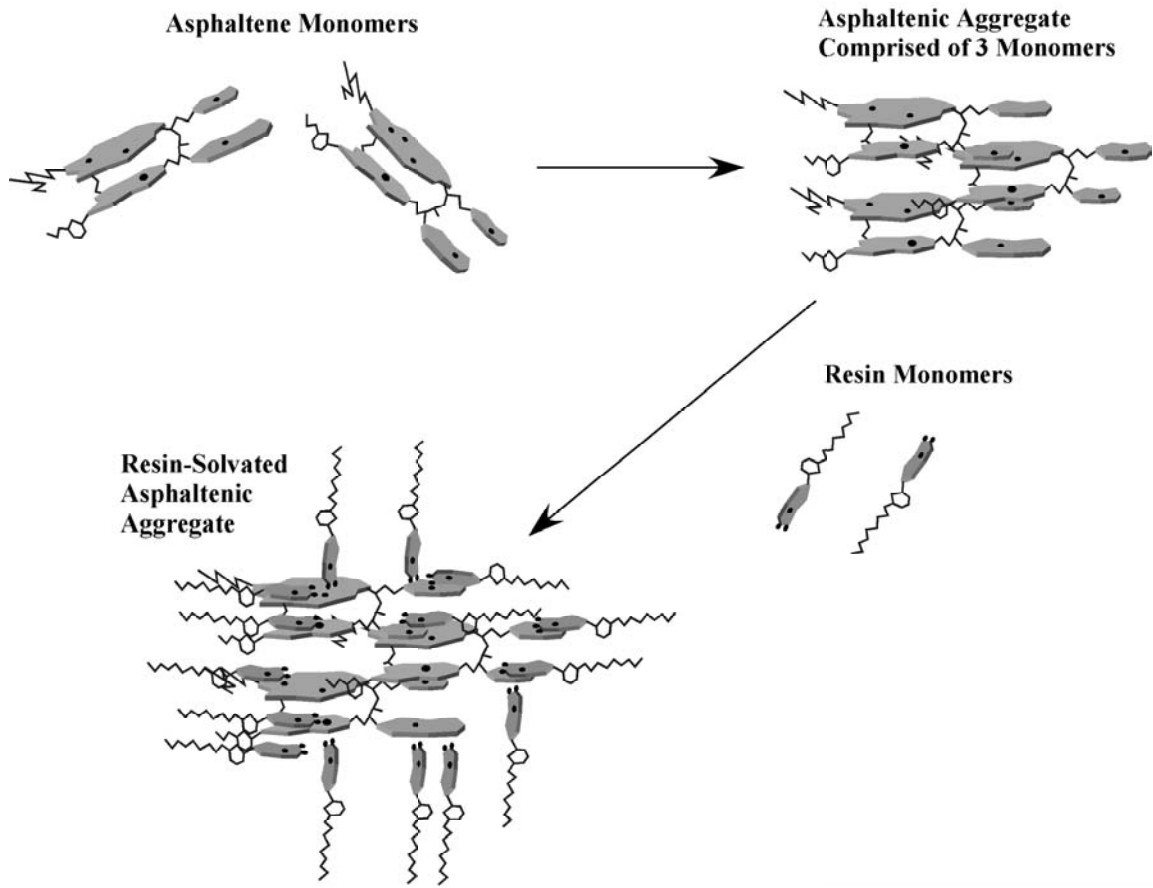


Figure B.1 Schematic illustration of archipelago model of asphaltene monomers, asphaltenic aggregate in absence of resins, and asphaltenic aggregate in presence of resins.

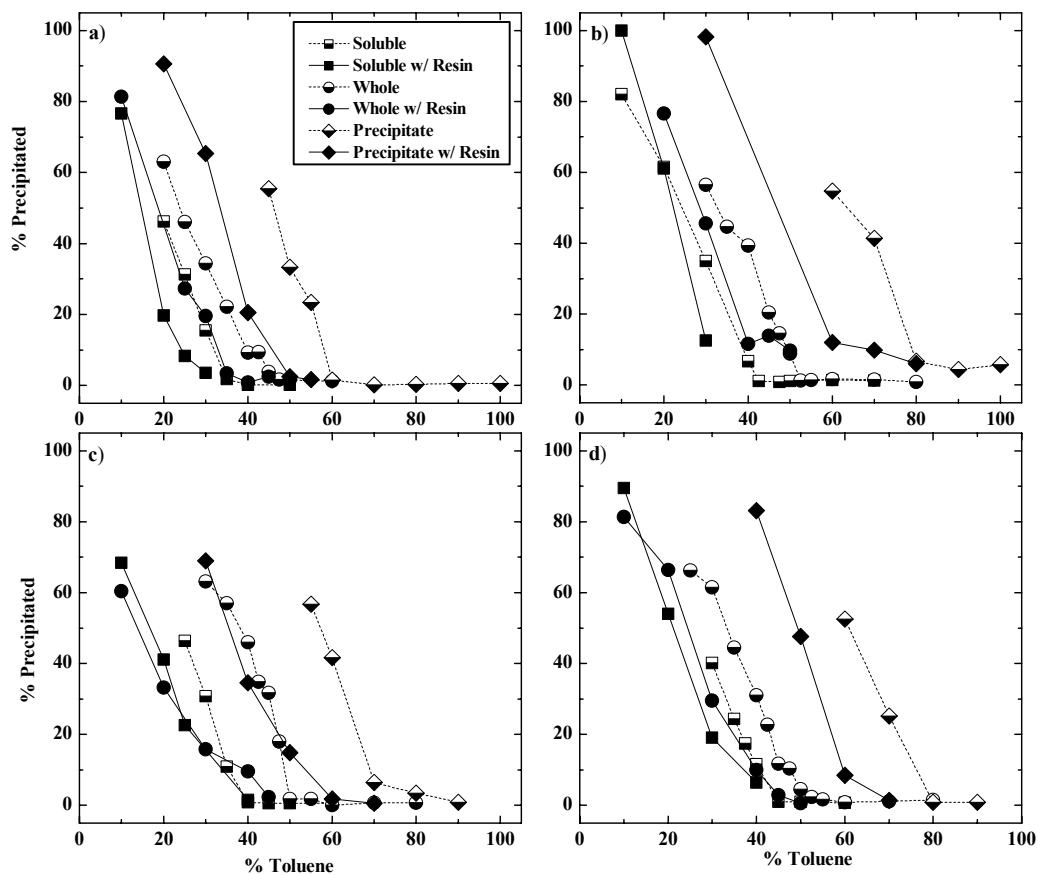


Figure B.2 Solubility of 0.75 % (w/v) Whole asphaltenes and their more and less soluble subfractions in heptol with and without resins. Half filled markers denote systems without resins. R/A ratio was fixed at 1:1 by mass. (a) AH; (b) B6; (c) CS; (d) HO

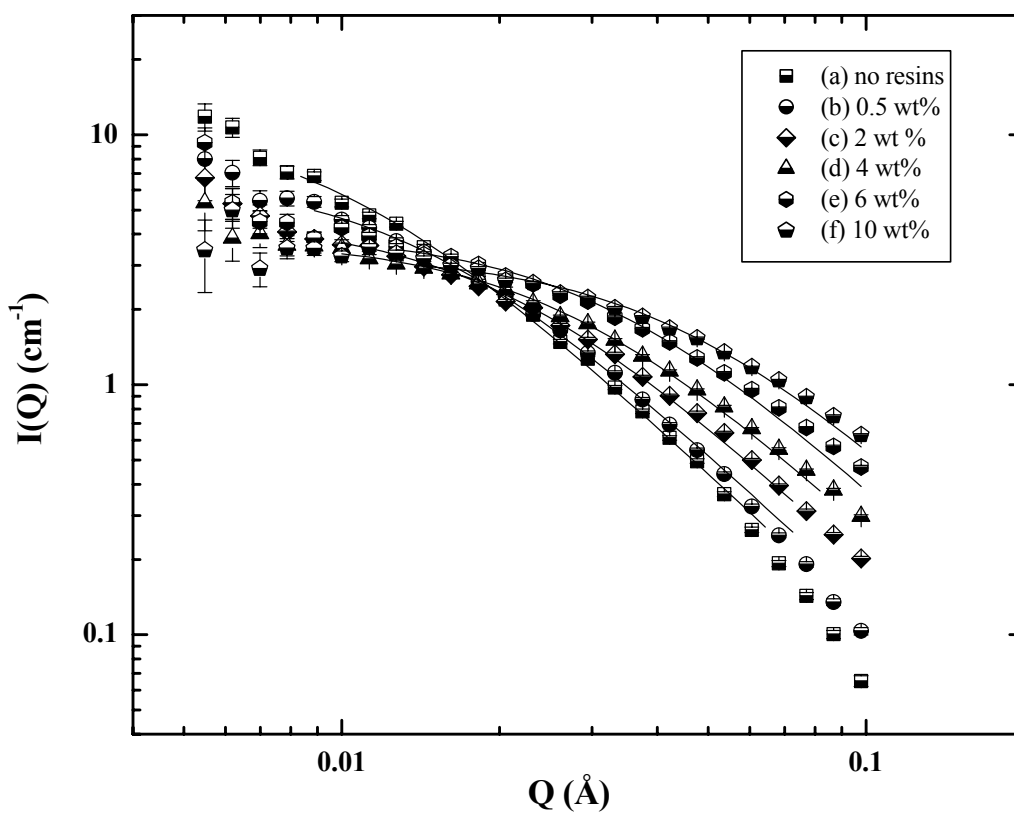


Figure B.3 SANS fits (2 mm path length) using Lorentzian lineshapes. Canadon Seco Whole asphaltenes at 25°C in 60 % toluene with: a) No Resins: $I_0: 11.7 \pm 0.4$, $\xi: 101 \pm 3$, $R^2: 0.9958$; b) 0.5 wt% B6 Resins: $I_0: 6.9 \pm 0.1$, $\xi: 70 \pm 1$, $R^2: 0.9962$; c) 2 wt% B6 Resins: $I_0: 4.56 \pm 0.06$, $\xi: 48.5 \pm 0.8$, $R^2: 0.9967$; d) 4 wt% B6 Resins: $I_0: 3.80 \pm 0.03$, $\xi: 36.9 \pm 0.5$, $R^2: 0.9970$; e) 6 wt% B6 Resins: $I_0: 4.02 \pm 0.05$, $\xi: 31.1 \pm 0.6$, $R^2: 0.9940$; f) 10 wt% B6 Resins: $I_0: 3.30 \pm 0.04$, $\xi: 22.5 \pm 0.4$, $R^2: 0.9922$
 Note: Every 2nd data point plotted above $Q = 0.006$.

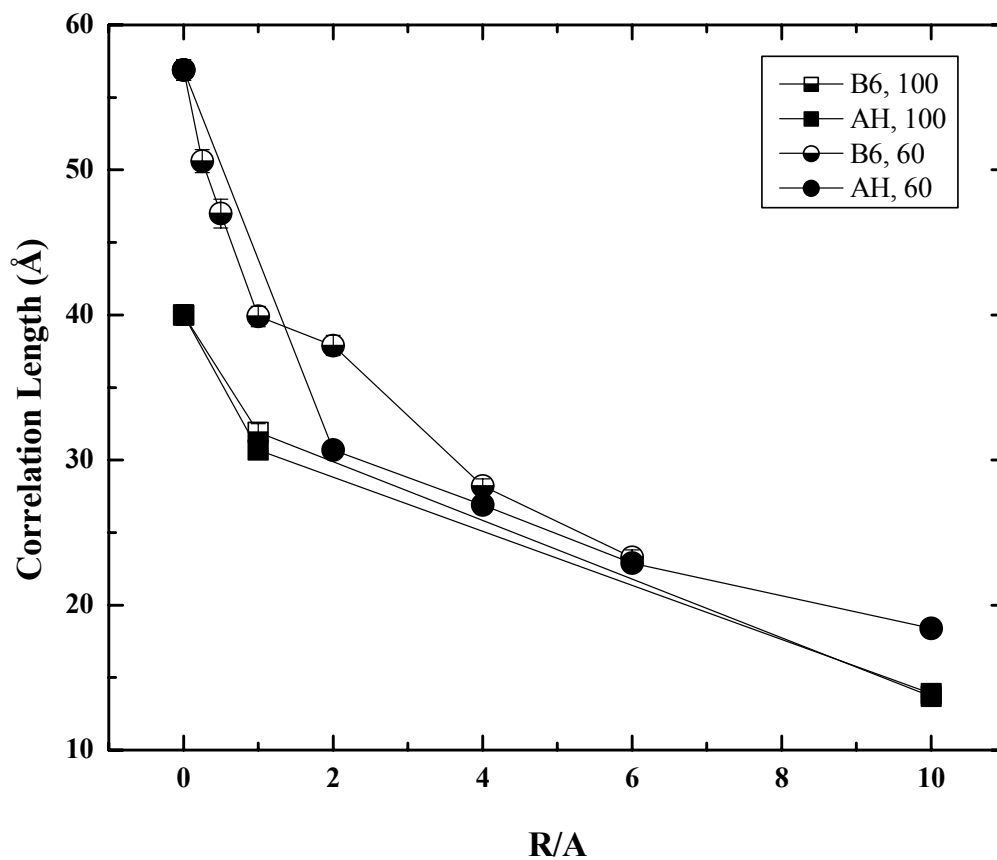


Figure B.4 Correlation length (ξ) of 1 wt % B6 Whole asphaltenic aggregates with AH and B6 Resins in pure toluene and 60 % toluene at 80°C determined from SANS (5 mm path length). Legend displayed as (resin type, % toluene).

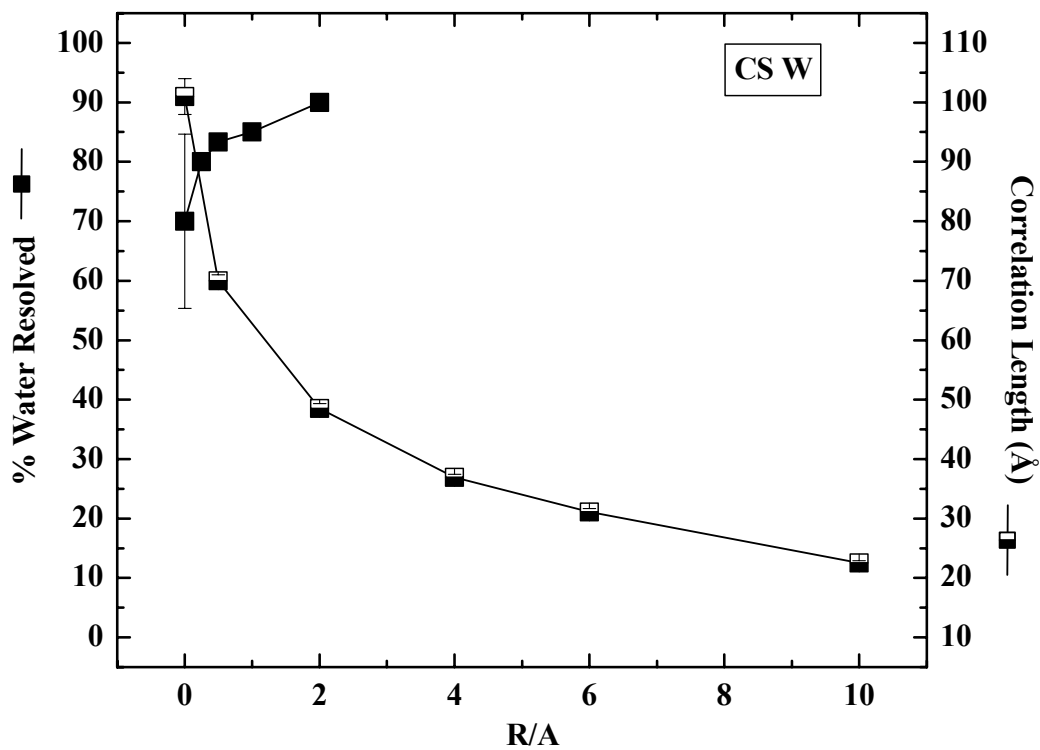


Figure B.5 Emulsion stability (% water resolved) and aggregate ξ of CS Whole asphaltenes in 60 % toluene with added resins. R/A represents mass ratio of resins to asphaltenes. Emulsions tested using CS resins, 0.5 wt % asphaltenes. SANS ξ measured at 25°C using B6 resins, 1 wt % asphaltenes, 2 mm path length.

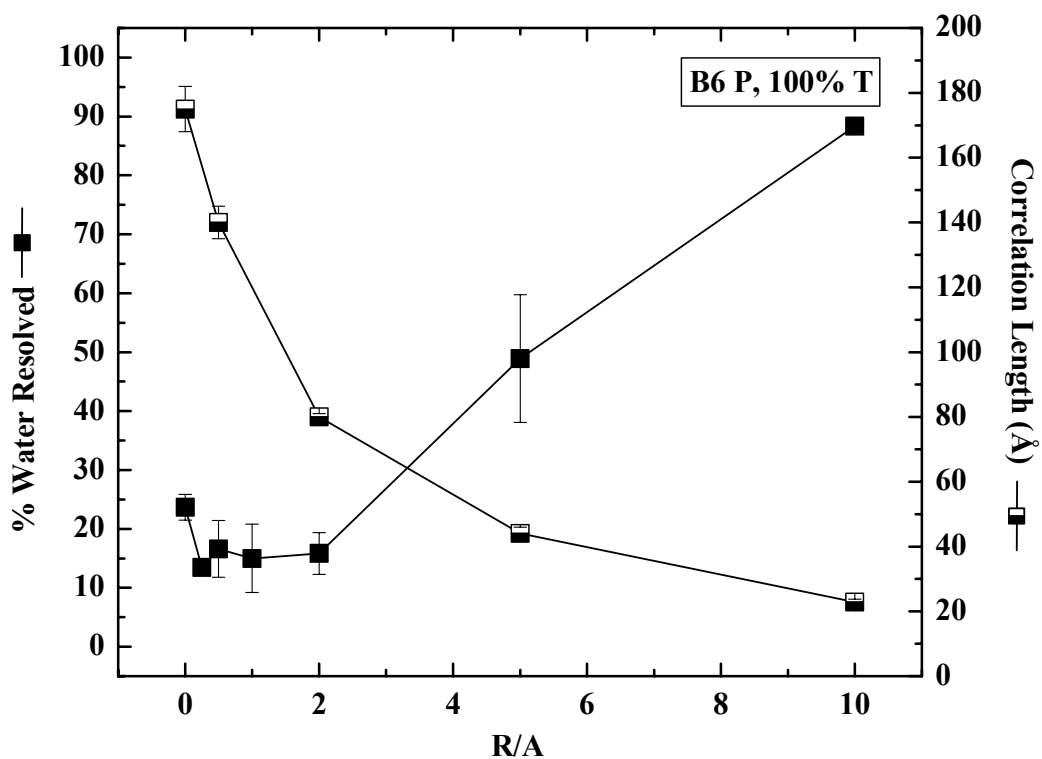


Figure B.6 Emulsion stability (% water resolved) and aggregate ξ of B6 Precipitate asphaltenes in toluene with B6 resins. Emulsions tested at 0.5 wt % and ξ determined by SANS at 25°C, 1 wt % asphaltenes, and 2 mm path length.

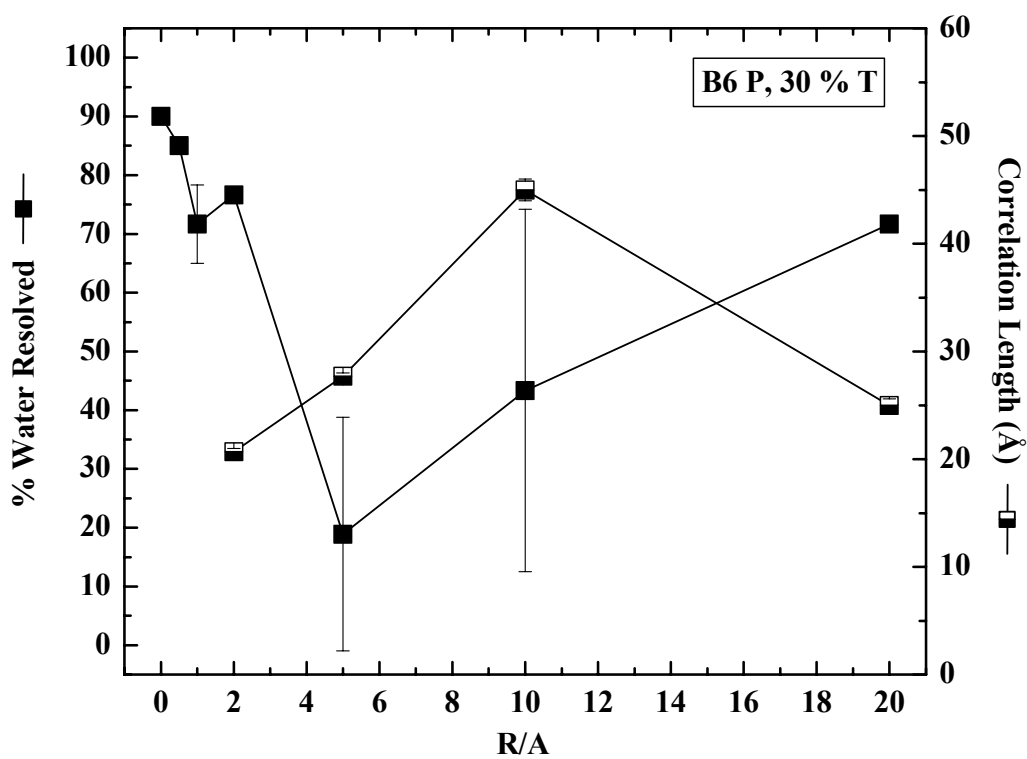


Figure B.7 Emulsion stability (% water resolved) and aggregate ξ of B6 Precipitate asphaltenes in 30 % toluene with B6 resins. Emulsions tested at 0.5 wt % and ξ determined by SANS at 25°C, 1 wt % asphaltenes, and 2 mm path length.

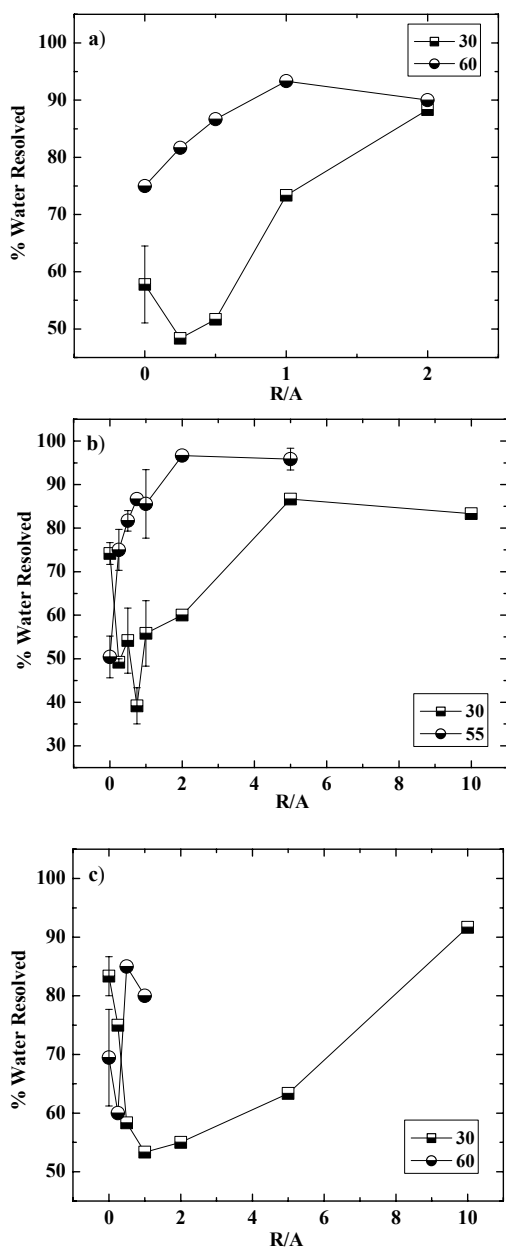


Figure B.8 Emulsion stability (% water resolved) of AH asphaltenes in heptol with AH resins. Emulsions tested at 0.5 wt %, 25°C.

- a) Soluble: 30, 60 % toluene
- b) Whole: 30, 55 % toluene
- c) Precipitate: 30, 60 % toluene

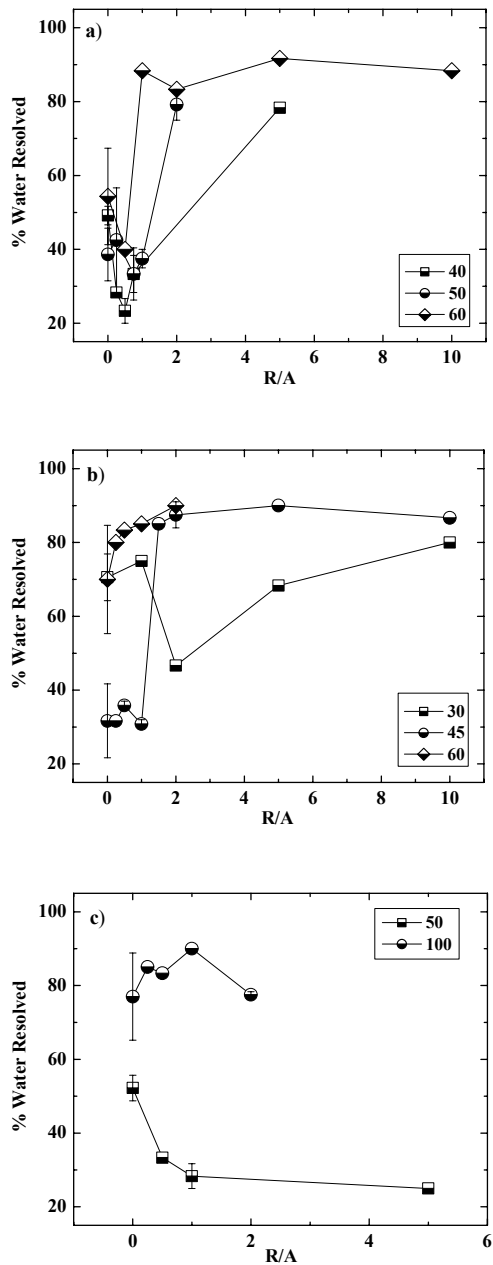


Figure B.9 Emulsion stability (% water resolved) of CS asphaltenes in heptol with CS resins. Emulsions tested at 0.5 wt %, 25°C.

- a) Soluble: 40, 50, 60 % toluene
- b) Whole: 30, 45, 60 % toluene
- c) Precipitate: 50, 100 % toluene

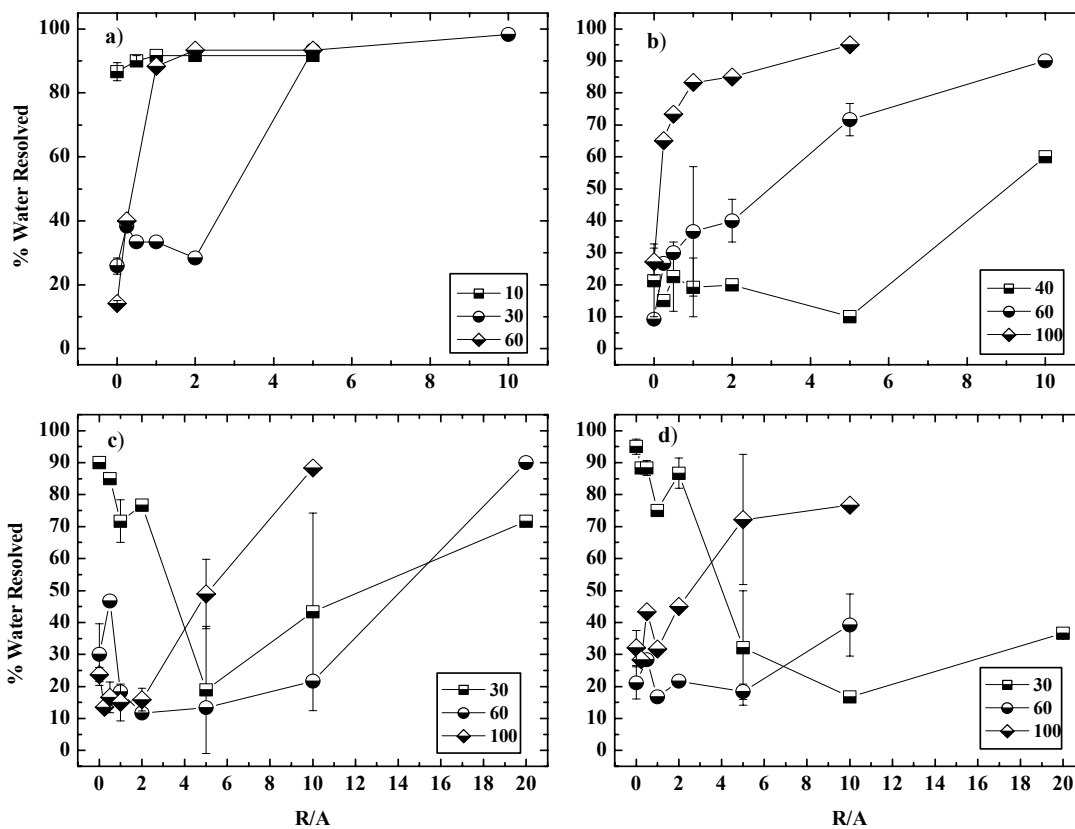


Figure B.10 Emulsion stability (vol % water resolved) and solubility (wt % precipitated) of B6 asphaltenes in heptol with B6 resins. Emulsions tested at 0.5 wt %, 25°C.

- a) B6 Soluble: 10, 30, 60 % toluene
- b) B6 Whole: 40, 60, 100 % toluene
- c) B6 Precipitate: 30, 60, 100 % toluene
- d) HO Precipitate: 30, 60, 100 % toluene

APPENDIX C
THE ROLE OF ASPHALTENE SOLUBILITY AND CHEMISTRY ON
ASPHALTENE AGGREGATION

Keith L. Gawrys, P. Matthew Spiecker, and Peter K. Kilpatrick

[Reprinted from *Petroleum Science and Technology* 21 (2003) 461-489]

C.1 Abstract

Asphaltenes from four different crude oils (Arab Heavy, B6, Canadon Seco, and Hondo) were fractionated in mixtures of heptane and toluene and analyzed by small angle neutron scattering (SANS). Fractionation appeared to concentrate the most polar species into the least soluble sub-fraction as indicated by elemental analysis. SANS results indicated a wide spectrum of asphaltene aggregate sizes and molecular weights; however, the less soluble (more polar) fraction contributed the majority of the species responsible for asphaltene aggregation in solution. This more polar, less soluble fraction is likely the major cause for many petroleum production problems such as deposition and water-in-oil emulsion stabilization. A comparison of molecular weight and aggregate size indicated that asphaltenes formed fractal aggregates in solution by with dimensions between 1.7 and 2.1. This was consistent with the “archipelago” model of asphaltene structure. Resins were shown to effectively solvate asphaltene aggregates as observed by an increase in asphaltene solubility, reduction in aggregate size and molecular weight, and an increase in the fractal dimension to ~ 3 .

C.2 Introduction

The study of asphaltene colloidal properties has been motivated by their propensity to aggregate, flocculate, precipitate, and to adsorb onto interfaces. The tendencies of asphaltenes to participate in colloidal and interfacial phenomena have posed great challenges for the petroleum industry. Problems associated with well production, pipeline transfer, land and sea-based transportation and, ultimately, oil refining have all been linked to the presence of asphaltenic colloids [1-5]. During visbreaking and catalytic hydrocracking large amounts of sludge and sediment can form [6] ostensibly due to the flocculation of asphaltenes during processing [7]. Coke generation and asphaltene adsorption within catalytic cracking beds

can reduce the effective catalyst surface area as well as the efficiency of coal hydrolysis [8]. Asphaltene deposition within reservoir rocks has been blamed for pronounced reductions in well productivity [9]. Asphaltenes have also been found to facilitate the formation of extremely stable water-in-crude oil emulsions [10-13]. Understanding asphaltene chemistry and the fundamental mechanisms of colloid formation has been the driving force behind much petroleum research for the last half-century.

Asphaltenes are defined as the portion of crude oil insoluble in *n*-alkanes such as *n*-heptane or *n*-pentane yet soluble in benzene or toluene. The “solubility class” definition of asphaltenes generates a broad distribution of molecular structures that can vary greatly from one crude oil to another. In general, asphaltenes are characterized by fused ring aromaticity, small aliphatic side chains, and polar heteroatom-containing functional groups. H/C ratios between 1.0 and 1.2 and N, S, and O content of a few weight percent suggest that much of the asphaltene backbone contains fused aromatic carbon interspersed with a handful of polar functional groups. Depending on the solvent chosen, number average molecular weights by vapor pressure osmometry can range from ca. 800 to 3000 g/mol [14-21]. Many studies have indicated the presence of carboxylic acids, carbonyl, phenol, pyrroles, and pyridine functionality [22-26]. These groups are capable of donating or accepting protons inter- and intra-molecularly. The most plausible mechanisms of asphaltene aggregation involve π - π overlap between aromatic sheets, hydrogen bonding between functional groups and other charge transfer interactions. The degree of aggregation is controlled by the polydispersity and chemistry of asphaltene monomers.

While the study of asphaltenes has been a fruitful area of research lately, there are just a handful of investigations on asphaltene subfractions. It is now well recognized that asphaltenes from different crude oil sources can have vastly different properties. At the same time, asphaltenes are comprised of a polydisperse collection of molecular chemistries that determine their overall chemical and physical properties. Certainly, this polydispersity will reveal fractions highly prone to aggregation and interfacial adsorption and others that are quite soluble. To help improve the conversion of crude oil into useful product by reducing losses to insoluble colloids, it is necessary to better understand the factors that affect the aggregation and precipitation of asphaltenes. In this study, we investigate the aggregation

and solubility behavior of asphaltenes and their subfractions, with and without the solvating effects of aromaticity and resins.

In this regard, small angle neutron scattering (SANS) is already established as a powerful tool for probing the effects of solvent and temperature on asphaltene aggregation [5,27-36]. Proper analysis of the scattering intensity curves can provide aggregate size, shape, molecular weight, and fractal dimension. To date, mono- and polydisperse spheres [27,28], flat disks [5,29,30], and prolate cylinders [31] have all been suggested as possible asphaltene structures. Sheu et al. suggested a polydisperse spheres model with a Schultz distribution best fit their scattering data [28]. Lin et al. fit $Q > 0.01 \text{ \AA}^{-1}$ data to a disk-like model with average R_g around 40 \AA [37]. At smaller Q values (i.e. larger length scales) the data suggest the presence of larger aggregates or particles too sizeable to probe by Guinier analysis. They suggested that these large particles had diameters of approximately $1,000 \text{ \AA}$ and often formed at high concentrations and/or low temperatures. Asphaltene polydispersity makes the precise shape of asphaltenic aggregates difficult to discriminate.

While the effects of temperature, solvent aromaticity, and polarity have received much attention, the solvation of asphaltene aggregates by resins has not been fully explored. Espinat et al. measured neutron and X-ray scattering intensities from asphaltenic aggregates in several solvents, at low and high temperatures and with added resins [29]. The scattering curves were fit using a thin disc form factor model to calculate the aggregate diameter and thickness. In toluene, 2 wt % Boscan asphaltene solutions formed larger aggregates at room temperature (234 \AA diameter) than at 76°C (175 \AA). At room temperature, aggregate sizes were 2-4 times smaller in high polarity solvents such as pyridine and tetrahydrofuran than in benzene. They also found that resin-asphaltene ratios of 2:1 by mass reduced the scattering intensity at low Q suggesting the formation of smaller aggregates. However, the effect of resin solvation on asphaltene aggregate size was not explicitly reported. Bardon et al. observed resin solvation of Safaniya asphaltenes using SANS and SAXS [5]. Weight average molecular weights of 2 wt % asphaltene solutions in toluene with R/A ratios of 2, 4, and 8:1 were reduced by factors of 2.6, 4.6, and 7.5 respectively.

Molecular weights determined from neutron scattering of polydisperse systems are weight averaged and may be biased by the presence of a small number of high mass aggregates. Fenistein and Barré fractionated asphaltenes in toluene by ultracentrifugation

and found that R_g and molecular weight increased with fraction density/weight [38]. At large Q they found that the internal structure of the aggregates was not dependent on aggregate size. However, at small Q the power law dependence of R_g on molecular weight gave a fractal dimension of 1.99. Roux et al. used SANS to study temperature and concentration effects on the structure of Safaniya asphaltenes in toluene [39]. At asphaltene volume fractions less than 3-4%, aggregates were well solvated with molecular weights on the order of 10^5 g/mol and R_g values from 30 to 90 Å. They also concluded that asphaltenes form tenuous fractal structures with dimension ≈ 2 over the asphaltene concentration range constituting non-flocculating aggregates [39-44].

Several additional studies have used SANS and SAXS to obtain the fractal dimensions of asphaltenic aggregates as a function of solvent, temperature, and concentration in hopes of elucidating the mechanism of colloidal aggregation [40-44]. Fenistein et al. found that asphaltenes isolated from Safaniya crude and vacuum residue formed open aggregates ($D_f = 2.0$ and 2.2 , respectively) in heptol mixtures ranging from 0 % to 45 % heptane [40]. Liu et al. applied a fractal structure factor model to Ratawi vacuum residue asphaltenes in toluene at concentrations from 10 to 80 % wt. [41]. Below 40 % wt. there were no large flocs in solution and the dispersed aggregates had a fractal dimension of ~ 3 . With the onset of flocculation between 40 and 60 % wt the fractal dimension decreased from ~ 3 to ~ 1.8 as inter-aggregate interactions overcame the entropic energy. Above the solubility limit of 60 % wt the fractal dimension increased again to ~ 3 indicating the onset of precipitation or a phase inversion. Dabir et al. observed that asphaltene aggregates have different self-similar structures depending on the length scale probed by SANS [44]. They obtained a fractal dimension of $D_f \sim 1.8$ at larger length scales (small Q) and another dimension $d_f \sim 2.5$ at smaller length scales (large Q). All of these studies suggest that asphaltene aggregates possess fractal-like character, probably due to the presence of interstitial voids or pores within the aggregates. As far as we know, little effort has been made to probe the effects of resin solvation on aggregate internal structure. Furthermore, little effort has been made to study in detail the role of asphaltene chemistry (i.e., polarity and aromaticity) on the internal structure of aggregates formed. A systematic SANS study of asphaltene solubility fractions as a function of solvent conditions and resin concentration can provide additional insight into the mechanism driving asphaltene aggregation.

Here, we review our work on the aggregation of asphaltenes, their solubility fractions, and each of these fractions with added resins. We have determined the solubility profiles of four asphaltenes in mixtures of heptane and toluene at fixed concentration. At solvent conditions where asphaltenes precipitate (high ratios of heptane to toluene), we have isolated the soluble and insoluble material for further study. Additional solubility profiles were prepared for the soluble and insoluble fractions in mixtures of heptane and toluene and for each of the fractions with added resins. Detailed chemical analyses were performed to measure the polarity and aromaticity of each fraction. By fractionating and concentrating the more polar and aromatic material, we should be able to enhance the degree of asphaltenic aggregation. Since aggregation is likely controlled by the ability of asphaltene monomers to stack through aromatic and polar interactions, the addition of polar resins to asphaltene solutions is expected to affect the nature of the asphaltenic aggregates. Here SANS is used to monitor changes in aggregate size, molecular weight, and fractal dimension of asphaltene-resin solutions in heptane-toluene as a function of asphaltene chemistry, solvent aromaticity, and resin concentration. The effectiveness of solvating resins on the more and less soluble fractions of asphaltenes will aid in elucidating the mechanisms of colloid formation in petroleum systems.

C.3 Experimental

C.3.1 Asphaltene Precipitation and Fractionation

Asphaltenes were precipitated from four crude oils in a 40:1 excess of *n*-heptane. The crude oils were obtained from several locations around the world: B6 and Hondo (off-shore California), Arab Heavy (Safaniya), and Canadon Seco (Argentina). These crude oils are asphaltene rich and vary in viscosity, resin content and asphaltene H/C ratio. Basic crude oil and asphaltene properties can be found in Table C.1. Resin content was determined by sequential elution chromatography (discussed in the next section), H/C ratios were calculated from combustion elemental analysis (Perkin Elmer Series II CHNSO), and viscosity measurements were performed on a Rheometrics Dynamic Stress Rheometer with concentric cylinder geometry. Asphaltenes precipitated from the crude oils were separated into more and less soluble fractions by dissolving in toluene and inducing partial precipitation through heptane addition. Enough heptane was added during fractionation to generate approximately

33 % (w/w) insoluble asphaltenes from a 0.75 % (w/v) asphaltene solution in toluene. All solvents were HPLC grade and obtained from Fisher Scientific. Details of the precipitation and fractionation procedures can be found in a previous publication [32]. A summary of the elemental composition of the asphaltene fractions is provided in Table C.2.

C.3.2 SARA Fractionation

Petroleum resins were isolated via the SARA technique where DAO is charged to silica gel and extracted with solvents of increasing polarity [34-36,45]. A detailed description of the extrography procedure is provided in a previous publication [46]. Combustion elemental analyses of the isolated resins appear in Table C.3.

C.3.3 Asphaltene and Resin Solubility

The solubility of asphaltenes and their subfractions was determined gravimetrically in mixtures of heptane and toluene. Similarly, the solubility of the fractions with added resins was determined. Asphaltene solutions had a concentration of 0.75 % (w/v) (mass solute/volume solvent) corresponding to a mass concentration of approximately 1 % (w/w). For the resin-asphaltene system, resins were initially dissolved with asphaltenes at a 1:1 mass ratio in toluene. Dissolution in toluene was followed by heptane addition and equilibration over night. The solutions were vacuum filtered through 5.5 cm diameter, 1.5 μm Whatman 934-AH glass microfiber filter paper. A rinse solvent (7.5 mL) equivalent in heptol composition to the asphaltene solution was poured immediately onto the filter paper to remove any remaining soluble material. The filtrate was isolated and the precipitate was redissolved using warm methylene chloride. The per cent precipitated material was determined from the mass ratio of precipitated asphaltenes to the original asphaltene mass.

C.3.4 Small Angle Neutron Scattering

Neutron scattering of asphaltenic aggregates with and without the addition of resins was performed on the NG7 and NG1 small angle spectrometers at the National Institute of Standards and Technology (NCNR, Gaithersburg, MD) or on the Small Angle Neutron Diffractometer (SAND) at Argonne National Laboratory (IPNS, Argonne, IL). Samples

were measured in cylindrical quartz cells (NSG Precision Cells) with a path length of 5 mm (all NG7 samples) or 2 mm (all SAND samples).

Solutions of the asphaltene fractions (1 wt %) were prepared in perdeuterated heptane and toluene (CDN Isotopes, Canada) and studied at 25 and 80°C. Mixtures of asphaltenes and resins were prepared at resin:asphaltene (R/A) ratios between 0.25:1 and 10:1. Scattering intensity versus scattering angle ($I(Q)$ vs. Q) data were fit to Lorentzian line shapes using a non-linear least squares regression to determine the aggregate correlation lengths. Following Ornstein-Zernike formalism the scattering intensity, I , can be related to the scattering vector, Q , by:

$$I(Q) = \frac{I_0}{1 + (Q\xi)^2} + A \quad (1)$$

where ξ is the correlation length and A is a background correction factor [47,48]. This Lorentzian line shape form was applied to systems with characteristic scattering curves that plateaued at low Q . In the other systems scattering intensity increased monotonically with decreasing Q . A power law term was necessary to account for these large agglomerates in solution. The scattering curves collected on the NG7 instrument includes data collected at two different detector distances (i.e., 1.2 and 15 m). For the cases where it was necessary to splice two data sets into a single curve, the natural logarithm of the scattering intensity expression was taken to reduce the bias towards the Q regions containing a high density of data points. The functional form of this equation is:

$$\ln[I(Q)] = \ln \left[\frac{I_1}{Q^4} + \frac{I_0}{1 + (Q\xi)^2} + A \right] \quad (2)$$

In the absence of a significant low Q upturn, Guinier analysis was also performed to calculate the radius of gyration, R_g , which is defined as the mean squared distance from the center of gravity of the scatterer. The Guinier approximation has the form:

$$I(Q) = I(0)e^{(-Q^2 R_g^2 / 3)} \quad (3)$$

where

$$I(0) = N_p V_p (\Delta\rho)^2 \quad (4)$$

The zero-Q intensity is related to the weight-average molecular weight (M) of the aggregates through the relation:

$$I(0) = \frac{MC\Delta\rho^2}{d_a^2 N_{Av}} \quad (5)$$

where C is the concentration of the solution (w/v), $\Delta\rho^2$ is the scattering contrast, d_a is the mass density of dry solute, and N_{Av} is the Avogadro number. Mass densities of asphaltene and resin solutions in toluene were measured using a 2 mL pycnometer. Dry mass densities of 1.15 g/cm³ and 1.0 g/cm³ were calculated for the asphaltene fractions and resins, respectively, by extrapolating the solution data to pure solute. Average structural formulas were calculated for the resins and asphaltenes using the elemental analysis results from Tables C.2 and C.3. Scattering length densities of the solvent and solute were calculated by inputting the compound formula and mass density into the Scattering Length Density Calculator provided on the Internet by the Materials Science and Engineering Laboratory at the NIST Center for Neutron Research (<http://www.ncnr.nist.gov/resources/sldcalc.html>). Further details concerning the SANS instruments, experimental conditions, and data analysis methods are provided in a previous paper [32].

C.4 Results and Discussion

C.4.1 Asphaltene-Resin Solubility

The trends observed in the solubility profiles of Canadon Seco (CS) asphaltene fractions both with and without resins (Figure C.1) were representative of the remaining crude asphaltenes. The half filled markers represent solubility data determined for asphaltenes in neat heptol while the filled markers represent asphaltene solubility in heptol with added resins. Solubility profiles for the remaining asphaltenes are presented in a previous paper [46]. CS Whole asphaltenes were found to be completely soluble in pure toluene and in heptol mixtures of high aromaticity (>52 % (v/v) toluene). The critical heptol concentration, below which precipitation was observed to increase significantly with heptane addition, ranged from 45-52 % (v/v) toluene for the Whole asphaltenes. Above the critical heptol concentration the entropic contribution of the dispersed asphaltenes dominated the free energy of the system (i.e., the aggregates were sufficiently well solvated to remain in

solution). As the solvent became more aliphatic inter-aggregate enthalpic forces become unfavorable and dominate the free energy of the system, leading to a decrease in solubility.

The solubility curves of the more and less soluble fractions in Figure C.1 indicated that the Soluble fraction cooperatively solvated the Precipitate fraction when they interacted in solution. The Precipitate solubility curves provided the most convincing support for cooperative aggregate interaction because the Precipitate asphaltenes became insoluble at a much higher toluene fraction than the Whole asphaltenes. If the Precipitate fraction asphaltenes were appreciably non-interacting, they would begin to precipitate at the same heptol ratio as the Whole and then proceed at a much steeper slope. In all cases, the Soluble fraction was far more soluble than either the Whole or Precipitate.

As mentioned before, asphaltenes are characterized by their high aromaticity, the presence of polar heteroatoms and their ability to form hydrogen bonds. H/C ratio (a measure of aromaticity) and nitrogen contents of all asphaltenes and their fractions are shown in Table C.2. In all cases, the Precipitate fraction was enriched in aromatic carbon while the Soluble aromaticity was diminished. The opposite trend was observed for nitrogen content of the fractions. Nitrogen can be found in several functional forms including amines, amides (carbonyl amides), pyrroles, and pyridines that are relatively polar and basic (i.e., hydrogen bond accepting). Fractionation appears to concentrate the most polar and aromatic material in the Precipitate fraction (i.e., the first asphaltenes to precipitate from solution). The Precipitate fraction likely contributes the majority of species responsible for asphaltene aggregation due to an enhancement of aromatic π - π bonding, polar, and hydrogen bonding interactions.

After resin addition, 1:1 w/w relative to asphaltenes (Figure C.1), the asphaltene solubility limit was reduced by 10 to 20 % (v/v) toluene. In the precipitated regime, resins were capable of enhancing asphaltene solubility (reducing the percentage of precipitates) between 10 and 50 %. The less polar and less aromatic Soluble fraction did not respond as markedly to resin addition. The ability of resins to solvate asphaltene fractions was related to the solvent conditions and intermolecular interactions driving precipitation near the solubility limits. The mechanism inducing precipitation of the Soluble fraction was likely driven by dispersion interactions, while the corresponding mechanism for the Precipitate fraction was likely driven by polar and hydrogen bonding interactions. From Table C.3 we see that resins

contain polar heteroatoms but are less aromatic than asphaltenes as gauged by H/C ratios between 1.31 and 1.51. These polar functional groups give resins the capacity to disrupt the electron donor-acceptor interactions partly responsible for asphaltene aggregation, thus facilitating a reduction in asphaltene aggregate size. The reduced aromaticity of resins compared to asphaltenes enables resins to remain soluble in more aliphatic solvents while still sufficiently solvating the fused ring portion of the asphaltenes. The combination of polar functionality and intermediate aromaticity in the resins increased asphaltene solubility through the formation of well solvated, resin-stabilized aggregates. We have sketched a plausible asphaltene monomer, aggregate, and resin-solvated aggregate in Figure C.2 to illustrate the principles discussed here as well as the observations from SANS described below.

C.4.2 SANS: Aggregate Size Analysis

Neutron scattering curves of intensity (I) versus scattering vector (Q) of Hondo (HO) Whole asphaltenes in several mixtures of deuterated heptol are shown in Figure C.3 as an illustration of the type and quality of scattering curves we obtained. HO Whole asphaltenes were in the soluble regime at all solvent conditions except 40% toluene. Based on the shape of the neutron scattering curve alone, one can readily distinguish two length scales of aggregates dissolved in solution. For example, the plateau behavior at intermediate Q for HO Whole asphaltenes in pure toluene indicated that the solution contained soluble dispersed aggregates of approximately 100 Å size. The presence of a low Q feature superimposed on the plateau indicated that a small portion of dissolved asphaltenes were flocculated. The absence of a second plateau region in the lowest Q range suggested that the largest flocs had a size greater than the order of $1/Q_{\min}$ (or ≥ 500 Å).

An increase in the scattering intensity at intermediate Q with decreasing solvent aromaticity suggested that the asphaltene aggregate size increased. Beyond the solubility limit, the scattering intensity decreased, suggesting that the largest aggregates flocculated or precipitated, thus leaving the smaller, soluble aggregates behind in solution. The remaining soluble aggregates were less than half the size of those in 55 % toluene, as shown in the following section.

$I(Q)$ versus Q scattering curves were fit with Lorentzian line shapes to determine solute correlation lengths. Figure C.4 shows typical $I(Q)$ versus Q neutron scattering curves for CS Precipitate asphaltenes with added B6 resins in pure toluene at 25°C. The solid lines represent the non-linear least squares fit of the Lorentzian lineshape to the data. The decrease in intensity of the low Q feature with increasing resin content indicated that resins were effective at dissolving the larger flocs into smaller aggregates. A reduction in the correlation length from 110 Å (no resins) to 38 Å (10 % resin) indicated that resins were also effective at solubilizing the smaller non-flocculated aggregates.

Correlation lengths deduced from SANS scattering curves of the solubility fractions dissolved in solutions of varying heptol ratio appear in Figure C.5. While the solubility curves for these asphaltenes appeared to be fairly similar, the neutron scattering data indicated significant differences in the aggregate sizes of the Whole asphaltenes that reflected the differences in asphaltene chemistry. Moreover, a comparison of the elemental analysis and SANS results for the solubility fractions provided information about the mechanisms of solubility and colloid formation in each asphaltene [32].

In general, several key trends were demonstrated by the neutron scattering behavior of asphaltene-heptol systems. For example, aggregate correlation length increased with decreasing solvent aromaticity up to the solubility limit, beyond which the aggregate size decreased with heptane addition. The maximum in soluble aggregate size, as calculated from the Lorentzian portion of the scattering curve in the accessible Q range, always appeared at the limit of asphaltene solubility. Crossing the solubility limit caused significant agglomeration and precipitation of the largest aggregates that, consequently, consisted of the most polar and interfacially-active asphaltenes. After precipitation, the remaining soluble material consisted of less polar and less aromatic asphaltenes, which tended to form smaller, more labile aggregates with dispersion forces as the dominant contribution to aggregation behavior.

From Figure C.5, it is apparent that the most soluble asphaltenes were least prone to aggregation. The Soluble fractions formed smaller aggregates than the Whole, which formed smaller aggregates than the Precipitate fractions. The scattering curves of Precipitated asphaltenes were nearly featureless and thus had considerable overlap between large agglomerate scattering and the smaller aggregate Guinier plateau. Once in solution, the

Precipitate asphaltenes formed very large aggregates with correlation lengths from 100 Å (AH) to nearly 500 Å (CS). It was clear that enhanced aromatic and polar inter-aggregate forces created very large and sparingly soluble aggregates in even the most aromatic solvents. The wide variation in aggregate size between the Soluble and Precipitate fractions indicated the cooperative interaction of the more and less soluble material present in the Whole asphaltenes. The more soluble asphaltenes must aid the dissolution of the more highly aromatic and polar material.

Resin addition was effective at reducing the aggregate size of asphaltenes in solution. The effect of resins on the aggregation behavior of B6 Whole asphaltenes (Figure C.6) at 80°C is typical of all other soluble asphaltenes. In general, resin addition in the soluble regime decreased the aggregate size of the asphaltenes with the greatest reduction occurring at resin-to-asphaltene (R/A) ratios between 0.5 and 2:1 R/A. This suggested that resins strongly solvated asphaltenes at ratios close to those found in crude oil (see Table C.1). Asphaltenes formed larger aggregates in less aromatic solvents due to solvent-solute incompatibility. Heptane-toluene mixtures of increasingly aliphatic solvent possess a lower degree of π -bond solvating capability and polarity than a pure toluene solvent. As a result, asphaltenes in 60 % (v/v) toluene had larger correlation lengths than in pure toluene. However, as the R/A ratio approached 10:1 the Whole asphaltene correlation lengths, even in 60% (v/v) toluene, commonly approached 20 Å, which was probably close to the size of a solvated monomer or irreducible oligomer (see Figure C.2). This indicated that high resin concentrations were apparently more effective at reducing aggregate size than aromatic solvent alone.

Resin solvation of asphaltenes was perhaps the most dramatic for the addition of B6 resins to CS Precipitate (Figure C.7) and B6 Precipitate (Figure C.8) asphaltenes in pure toluene. In both cases, asphaltene correlation lengths were reduced by approximately 45 to 55% with the addition of 2 % wt resins. Here, the initial role of the resins was to disrupt the polar and hydrogen-bonding interactions binding the flocculated aggregates. Above R/A ratios of 2:1, most of the largest agglomerates were dispersed and the increasingly soluble asphaltenes approached a plateau in aggregate size. Consequently, at high R/A ratios the aggregates became less surface-active and formed weaker water-in-oil emulsions, as discussed in a previous paper [46].

CS Precipitate asphaltenes were beyond the limit of solubility in 50 % toluene (Figure C.7) and, similarly B6 Precipitate asphaltenes were insoluble in 30% toluene (Figure C.8). The increase in correlation length with resin addition up to an R/A ratio of 2:1 for CS Precipitate (10:1 for B6 Precipitate) indicated that resins aided the redissolution of the insoluble asphaltene. Redissolution brought the most polar, aromatic, and surface-active asphaltenes back into solution, thus increasing the extent of polar and hydrogen bonding between the aggregates. The maximum in correlation length observed in Figures C.7 and C.8 corresponded to the solubility limit of asphaltene fractions. At higher R/A ratios, the insolubles were completely redissolved and additional resins assisted in breaking flocs by disruption of dispersion and hydrogen bonding interactions between aggregates. In this case, the correlation length once again decreased with resin content similar to B6 Whole.

C.4.3 SANS: Molecular Weight and Fractal Dimension Analysis

The aggregate weight-average molecular weight (MW) determined for the asphaltene solubility fractions trended similar to the correlation length. For example, the solvent compositions corresponding to the maxima in molecular weight for B6 Soluble and Whole asphaltenes (Figure C.9) exactly matched the maxima in correlation length (Figure C.5b.). Molecular weights of the aggregates varied significantly among the fractions of the different crudes. Typical values of MW for the Whole asphaltenes ranged in magnitude from 40,000 to 400,000 g/mol for AH, B6, and HO samples and $\sim 10^6$ g/mol for CS. MW values for the Soluble fractions were on the order of 20,000 to 130,000 g/mol for AH, B6, and HO samples and 2 to 9×10^5 g/mol for CS. The Precipitate fractions showed the widest variation in MW range (10^5 to 10^6 g/mol for AH, 10^6 to 2×10^6 g/mol for B6 and HO, and $\sim 10^7$ g/mol for CS. Additional information concerning the role on asphaltene chemistry on observed molecular weights is presented in a previous paper [49]. All of the values listed above applied to samples measured in 5 mm quartz cells.

The apparent MW decreased dramatically when the path length of neutrons through the samples was decreased. This was especially true for the largest aggregate formers. The largest discrepancy in measured apparent MW vs. path length occurred with CS Precipitate, which showed values that differed by an order of magnitude (Figure C.10). Differences in

the apparent correlation length and molecular weight with changes in sample cell size were most likely attributed to multiple scattering effects. As the path length increased, the probability of a neutron interacting with more than one scatterer increased. The data collected in 5 mm cells were biased towards the presence of the larger aggregates in the population, thus the weight-average molecular weight appeared to increase. However, similar trends in aggregate growth with decreasing aromaticity were observed regardless of the neutron path length, as shown in Figure C.10. Previous studies have shown that multiple scattering affects only the magnitude of the scattering intensity (i.e., apparent ξ and MW), but not the estimated fractal dimension [50,51].

The effect of resin addition on the apparent MW of CS Precipitate asphaltenes in pure toluene and 50 % toluene is shown in Figure C.11. Apparent MW decreased with increasing resin content in pure toluene by approximately 2 orders of magnitude from $\sim 10^6$ g/mol (no added resins) to $\sim 10^4$ g/mol (10 % (w/w) added resins). This dramatic reduction further indicated the significant role that resins played in disrupting inter-aggregate interactions between flocs. As previously stated, CS Precipitate was in the insoluble regime in 50 % toluene up to an R/A ratio of 2:1. In this concentration range, the role of resins was to redissolve the insoluble material. As indicated in the figure, the molecular weight of the CS Precipitate aggregates was not affected by the addition of resins in the insoluble regime, but decreased with additional resins in the soluble regime. Although MW remained constant, the correlation length increased from 60 Å with no added resins to 106 Å at R/A of 2:1 (Figure C.7). One possible explanation for this observation is that the internal structure of the asphaltene aggregates differed at these conditions. The aggregates formed near the solubility limit (R/A of 2:1) likely possessed a higher porosity than those formed prior to resin addition.

Figure C.12 presents the variation of molecular weight with correlation length for each of the Whole asphaltenes and their subfractions in heptol. The estimated fractal dimension (D) of the asphaltene aggregates was obtained from the relationship:

$$M \propto \xi^D \quad (6)$$

As shown in the figure, the fractal dimension of the aggregates varied from ~ 1.7 (AH) to 2.1 (HO). This result was consistent with previous studies [39-44] and suggested that the asphaltenes formed fractal-like aggregates of high porosity in heptol mixtures. The modest

differences in fractal dimension for the individual asphaltenes also suggested that the internal structure of asphaltenes from different crude sources are fundamentally different.

This fractal-like behavior supports the so-called “archipelago” model of asphaltenes in which the monomer molecular structure is comprised of fused ring aromatic moieties connected by aliphatic and heteroatomic groups (see Figure C.2). The notion that asphaltenes are composed of aromatic “islands” connected by alkyl moieties was originally proposed by Dickie and Yen based on X-ray diffraction measurements [2]. The “archipelago” model is further supported by chemical and thermal degradation studies which concluded that the extent of aromatic condensation in asphaltenes is significantly lower than generally believed [52]. Furthermore, molecular simulation studies on a proposed Athabasca asphaltene structure suggested that the presence of long aliphatic bridges gives asphaltenes the capacity to fold themselves into a complex three-dimensional globular structure with self-similar internal structure [53].

In the SANS experiments, the asphaltene scatterers contained some percentage of entrained solvent in interstitial space which did not give rise to scattering contrast (being deuterated). This results in the “self-similar” appearance of fractals as the aggregates grew to larger and larger dimensions. Interestingly, the addition of resins apparently solvated much of this interstitial space and also diminished the size of the aggregates. The resulting fractal dimension as measured by SANS increased to ~ 2.7 , which is consistent with a dense packed aggregate of low porosity (see Figure C.2). Analysis of the most soluble resin-asphaltene samples (i.e., those with scattering curves that plateau in the Guinier region) provided a fractal dimension ~ 3 , as discussed in a previous paper [49]. These results are fully consistent with the “archipelago” model of asphaltene structure.

C.5 Conclusions

In this study, small angle neutron scattering (SANS) was used to investigate the effects of chemistry, solvent conditions, and resin content on the aggregation behavior of four asphaltenes and their more and less soluble sub-fractions. The solubility behavior of the fractions indicated that the least soluble, most polar sub-fractions are highly interactive and aggregate to form large sparingly soluble agglomerates with a highly porous internal structure. The forces which drive this aggregation are apparently a combination of hydrogen

bonding, π - π aromatic ring bonding, and electron donor-acceptor interactions among the polar and aromatic moieties of the individual asphaltene monomers. The largest aggregate sizes, as gauged by SANS, are always observed at the limit of solubility. When unsolvated by resin molecules in simple solvents, such as heptane and toluene, the asphaltenic aggregates have fractal dimensions which vary between 1.7 – 2.1 depending on the chemistry of the asphaltenes. When solvated by resins, the intercalation of resins into the interstitial space of the asphaltenes produces solvated aggregates with dimensions much closer to 3, suggesting dense compact aggregates. The size, dimension, and compactness of asphaltenic aggregates all have strong influences on the surface activity and tendency of asphaltenes to form colloidal aggregates and to stabilize emulsions and foams. Our work is strongly supportive of the so-called “archipelago” model of asphaltene molecular structure.

C.6 Acknowledgements

We are grateful to the National Science Foundation (grant CTS-981727), the Petroleum Environmental Research Forum (contract 97-07), and shared consortium funding from ExxonMobil, Texaco, Ondeo-Nalco Energy Systems, and Shell Oil Company for partial support of this research. Special thanks go to George Blankenship, Marit-Helen Ese, Jihong Tong, Chad Trail, and Semaj McIver who assisted with the experimental work. We are also grateful to Eric Sirota and Min Lin of ExxonMobil Research and Engineering for arranging beamtime at the NIST NG-7 and NG-1 beamlines for the SANS experiments, and to Thiyaga Pappannan and Dennis Wozniak at Argonne National Laboratories (SAND beamline) for arranging and assisting with beamtime there.

C.7 References

1. Pfeiffer, J.P. and R.N.J. Saal, *Asphaltic Bitumen as Colloid System*. Journal of Physical Chemistry, 1940. **44**: p. 139-149.
2. Dickie, J.P. and T.F. Yen, *Macrostructures of the Asphaltic Fractions by Various Instrumental Methods*. Analytical Chemistry, 1967. **39**(14): p. 1847-1852.
3. Speight, J.G. and S.E. Moschopedis, *Some Observations on the Molecular "Nature" of Petroleum Asphaltenes*. Preprints -- ACS Division of Petroleum Chemistry, 1979. **24**(4): p. 910-923.

4. Sheu, E.Y., M.M.D. Tar, and D.A. Storm, *Solution Properties of Colloids Formed by Petroleum Vacuum Residues*. Macromolecular Reports, 1991. **A28**: p. 159-175.
5. Bardon, C., et al., *The colloidal structure of crude oils and suspensions of asphaltenes and resins*. Fuel Science & Technology International, 1996. **14**(1-2): p. 203-242.
6. Mushrush, G.W. and J.G. Speight, *Petroleum Products: Instability and Incompatibility*. Applied Energy Technology Series. 1995, Bristol, PA: Taylor and Francis.
7. Storm, D.A., S.J. DeCanio, and E.Y. Sheu, *Sludge Formation During Heavy Oil Conversion*, in *Asphaltene Particles in Fossil Fuel Exploration, Recovery, Refining, and Production Processes*, M.K. Sharma and T.F. Yen, Editors. 1994, Plenum Press: New York. p. 81-90.
8. Lin, J.-R., J.-K. Park, and T.F. Yen, *Upgrading From Petroleum and Coal-Derived Asphaltenes*, in *Asphaltene Particles in Fossil Fuel Exploration, Recovery, Refining, and Production Processes*, M.K. Sharma and T.F. Yen, Editors. 1994, Plenum Press: New York. p. 91-100.
9. Cimino, R., et al., *Solubility and Phase Behavior of Asphaltenes in Hydrocarbon Media*, in *Asphaltenes: Fundamentals and Applications*, E.Y. Sheu and O.C. Mullins, Editors. 1995, Plenum Press: New York. p. 97-130.
10. Berridge, S.A., M.T. Thew, and A.G. Loriston-Clarke, *The Formation and Stability of Emulsions of Water in Crude Petroleum and Similar Stocks*. Journal of the Institute of Petroleum, 1968. **54**(539): p. 333-357.
11. Sjöblom, J., et al., *Stabilization and Destabilization of Water-in-Crude Oil Emulsions from the Norwegian Continental Shelf. Correlation with Model Systems*. Advances in Colloid and Interface Science, 1992. **41**: p. 241-271.
12. McLean, J.D. and P.K. Kilpatrick, *Effects of Asphaltene Solvency on Stability of Water-in-Crude Oil Emulsions*. Journal of Colloid and Interface Science, 1997. **189**: p. 242-253.
13. McLean, J.D., et al., *The Role of Petroleum Asphaltenes in the Stabilization of Water-in-Oil Emulsions*, in *Structures and Dynamics of Asphaltenes*, O.C. Mullins and E.Y. Sheu, Editors. 1998, Plenum Press: New York. p. 377-422.
14. Al-Jarrah, M.M.H. and A.H. Al-Dujaili, *Characterization of Some Iraqi Asphalts II. New Findings on the Physical Nature of Asphaltenes*. Fuel Science and Technology International, 1989. **7**(1): p. 69-88.
15. Acevedo, S., et al., *Asphaltenes and Resins From the Orinoco Basin*. Fuel, 1985. **64**: p. 1741-1747.

16. Boduszynski, M.M., *Composition of Heavy Petroleums. 2. Molecular Characterization*. Energy & Fuels, 1988. **2**(5): p. 597-613.
17. Wiehe, I.A. and K.S. Liang, *Asphaltenes, Resins, and other petroleum macromolecules*. Fluid Phase Equilibria, 1996. **117**(1-2): p. 201-210.
18. McKay, J.F., et al., *Petroleum Asphaltenes: Chemistry and Composition*. Analytical Chemistry of Liquid Fuel Sources, Advances in Chemistry Series, 1978. **170**: p. 128-142.
19. Andersen, S.I., A. Keul, and E. Stenby, *Variation in composition of subfractions of petroleum asphaltenes*. Petroleum Science and Technology, 1997. **15**(7-8): p. 611-645.
20. Yarranton, H.W. and J.H. Masliyah, *Molar Mass Distribution and Solubility Modeling of Asphaltenes*. AIChE Journal, 1996. **42**(12): p. 3533-3543.
21. Yarranton, H.W., H. Alboudwarej, and R. Jakher, *Investigation of asphaltene association with vapor pressure osmometry and interfacial tension measurements*. Industrial & Engineering Chemistry Research, 2000. **39**(8): p. 2916-2924.
22. Barbour, R.V. and J.C. Petersen, *Molecular Interactions of Asphalt: An Infrared Study of the Hydrogen-Bonding Basicity of Asphalt*. Analytical Chemistry, 1974. **46**(2): p. 273-277.
23. Boduszynski, M.M., J.F. McKay, and D.R. Latham, *Asphaltenes, Where Are You?* Proceedings of the Association of Asphalt Paving Technologists, 1980. **49**: p. 123-143.
24. Ignasiak, T., O.P. Strausz, and D.S. Montgomery, *Oxygen Distribution and Hydrogen Bonding in Athabasca Asphaltene*. Fuel, 1977. **56**: p. 359-365.
25. Moschopedis, S.E. and J.G. Speight, *Investigation of Hydrogen Bonding by Oxygen Functions in Athabasca Bitumen*. Fuel, 1976. **55**: p. 187-192.
26. Petersen, J.C., *An Infra-red Study of Hydrogen Bonding in Asphalt*. 1967: p. 295-305.
27. Overfield, R.E., et al., *SANS Study of Asphaltene Aggregation*. Fuel Science & Technology International, 1989. **7**(5-6): p. 611-624.
28. Sheu, E.Y., et al., *Polydispersity Analysis of Asphaltene Solutions in Toluene*. Journal of Colloid and Interface Science, 1992. **153**(2): p. 399-410.

29. Espinat, D., et al., *Colloidal Macrostructure of Crude-Oil Studied By Neutron and X-Ray Small-Angle Scattering Techniques*. Journal De Physique Iv, 1993. **3**(C8): p. 181-184.
30. Ravey, J.C. and D. Espinat, *Macrostructure of Petroleum Asphaltenes by Small Angle Neutron Scattering*. Progress in Colloid and Polymer Science, 1990. **81**: p. 127-130.
31. Thiyagarajan, P., et al., *Temperature-Dependent Structural-Changes of Asphaltenes in 1- Methyl-naphthalene*. Energy & Fuels, 1995. **9**(5): p. 829-833.
32. Spiecker, P.M., K.L. Gawrys, and P.K. Kilpatrick, *Aggregation and solubility behavior of petroleum asphaltenes and their subfractions*. Journal of Colloid and Interface Science, 2003. **267**: p. 178-193.
33. Spiecker, P.M. and P.K. Kilpatrick, *The Role of Asphaltene Solubility and Chemistry on the Stability of Water-in-Oil Emulsions*. Journal of Colloid and Interface Science, to be submitted, 2001.
34. Miller, R., *Hydrocarbon Class Fractionation with Bonded-Phase Liquid Chromatography*. Analytical Chemistry, 1982. **54**(11): p. 1742-1746.
35. Reynolds, J.G., *Characterization of Heavy Residua by Application of a Modified D 2007 and Asphaltene Separation: Effect of Solvents on Physical and Chemical Properties of Fractions Derived From Hondo 850°F Residuum*. Fuel Science and Technology International, 1987. **5**(5): p. 593-620.
36. Ali, M.F., A. Bukhari, and M.U. Hasan, *Structural Characterization of Arabian Heavy Crude Oil Residue*. Fuel Science and Technology International, 1989. **7**(8): p. 1179-1208.
37. Lin, M.Y., E.B. Sirota, and H. Gang, *Neutron scattering characterization of asphaltene particles*. Abstracts of Papers of the American Chemical Society, 1997. **213**: p. 66-FUEL.
38. Fenistein, D. and L. Barre, *Experimental measurement of the mass distribution of petroleum asphaltene aggregates using ultracentrifugation and small-angle X-ray scattering*. Fuel, 2001. **80**(2): p. 283-287.
39. Roux, J.N., D. Broseta, and B. Deme, *SANS study of asphaltene aggregation: Concentration and solvent quality effects*. Langmuir, 2001. **17**(16): p. 5085-5092.
40. Fenistein, D., et al., *Viscosimetric and neutron scattering study of asphaltene aggregates in mixed toluene/heptane solvents*. Langmuir, 1998. **14**(5): p. 1013-1020.
41. Liu, Y.C., et al., *Fractal Structure of Asphaltenes in Toluene*. Fuel, 1995. **74**(9): p. 1352-1356.

42. Savvidis, T.G., et al., *Aggregated structure of flocculated asphaltenes*. Aiche Journal, 2001. **47**(1): p. 206-211.
43. Rassamdana, H. and M. Sahimi, *Asphalt Flocculation and Deposition: II. Formation and Growth of Fractal Aggregates*. AICHE Journal, 1996. **42**(12): p. 3318-3332.
44. Dabir, B., et al., *Asphalt flocculation and deposition .3. The molecular weight distribution*. Fuel, 1996. **75**(14): p. 1633-1645.
45. McLean, J.D. and P.K. Kilpatrick, *Comparison of Precipitation and Extrography in the Fractionation of Crude Oil Residua*. Energy and Fuels, 1997. **11**: p. 570-585.
46. Spiecker, P.M., C.B. Trail, and P.K. Kilpatrick, *Effects of petroleum resins on asphaltene aggregation and water-in-oil emulsion formation*. Colloids and Surfaces A: Physicochem. Eng. Aspects, 2003. **220**: p. 9-27.
47. de Gennes, P.-G., *Scaling Concepts in Polymer Physics*. 1979, Ithaca, NY: Cornell University Press.
48. Sirota, E.B., *Swelling of asphaltenes*. Petroleum Science and Technology, 1998. **16**(3-4): p. 415-431.
49. Gawrys, K.L., P.M. Spiecker, and P.K. Kilpatrick, *Internal structure of asphaltene solubility fractions by SANS: Effects of solvent, temperature, and resins*. Langmuir, to be submitted, 2002.
50. Chen, Z., et al., *Optical-Properties of Aggregate Clusters*. Physical Review B, 1988. **37**(10): p. 5232-5235.
51. Lattuada, M., H. Wu, and M. Morbidelli, *Estimation of fractal dimension of colloidal gels in the presence of multiple scattering*. Physical Review E, 2001. **6406**(6): p. art. no.-061404.
52. Strausz, O.P., T.W. Mojelsky, and E.M. Lown, *The Molecular-Structure of Asphaltene - an Unfolding Story*. Fuel, 1992. **71**(12): p. 1355-1363.
53. Murgich, J., J.A. Abanero, and O.P. Strausz, *Molecular recognition in aggregates formed by asphaltene and resin molecules from the Athabasca oil sand*. Energy & Fuels, 1999. **13**(2): p. 278-286.

Table C.1 Crude oil properties

Crude	Wt % Asph	Wt % Resin	H/C Asph	Viscosity (cP) 100°F
AH	6.7	7.5	1.14	33.8
B6	13.1	12.05	1.22	2030
CS	7.5	8.93	1.11	70
HO	14.8	20.6	1.29	363

Table C.2 Asphaltene fraction composition in wt %, except H/C

Asphaltene	H/C			Nitrogen			Sulfur		
	Sol	Whole	Ppt	Sol	Whole	Ppt	Sol	Whole	Ppt
AH	1.17	1.14	1.13	0.92	1.02	1.08	8.06	8.32	7.66
B6	1.30	1.24	1.22	1.81	1.87	1.93	7.25	6.68	6.33
CS	1.12	1.11	1.09	1.32	1.32	1.39	0.52	0.52	0.48
HO	1.30	1.29	1.24	1.95	1.99	2.11	8.42	8.53	8.48

Table C.3 Resin composition in wt %, except H/C (O by difference)

Resin source	H/C	N	S	O
AH	1.31	0.81	6.49	1.53
B6	1.51	1.48	6.91	1.98
CS	1.39	1.52	0.88	2.77
HO	1.51	---	---	---

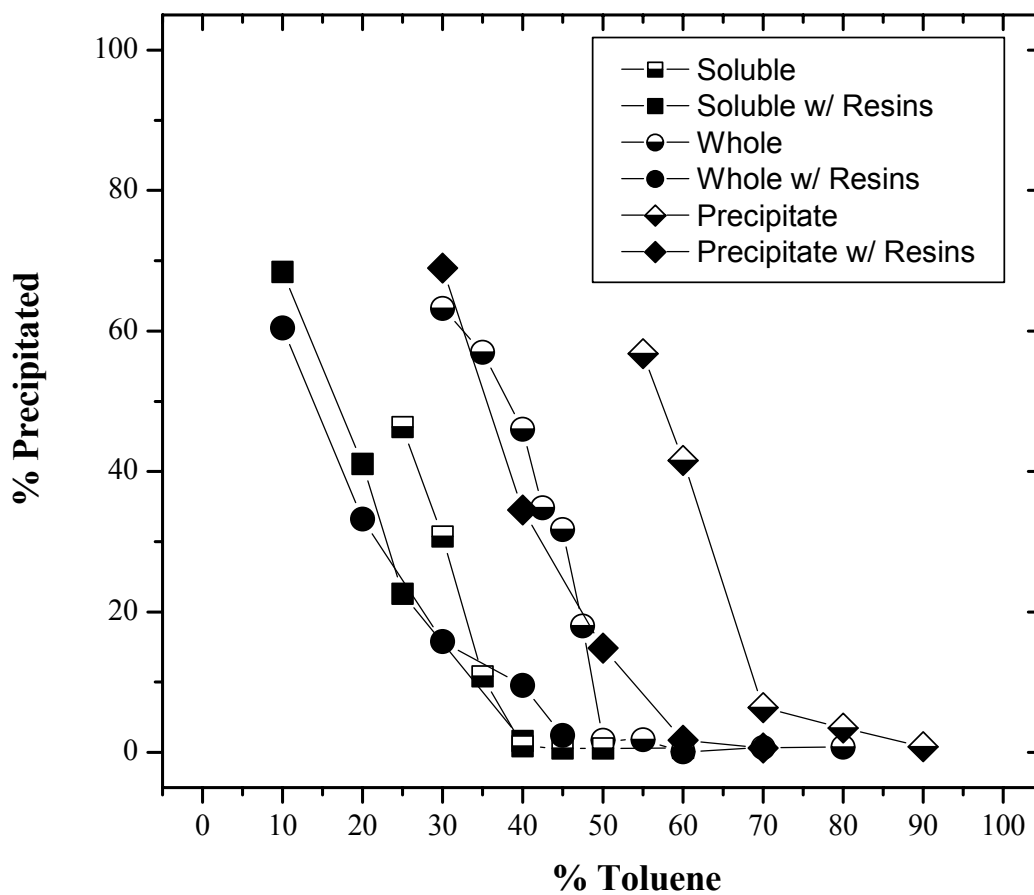


Figure C.1 Solubility of 0.75 % (w/v) CS Whole asphaltenes and their more and less soluble subfractions in heptol with and without resins. Half filled markers denote systems without resins. R/A ratio was fixed at 1:1 by mass.

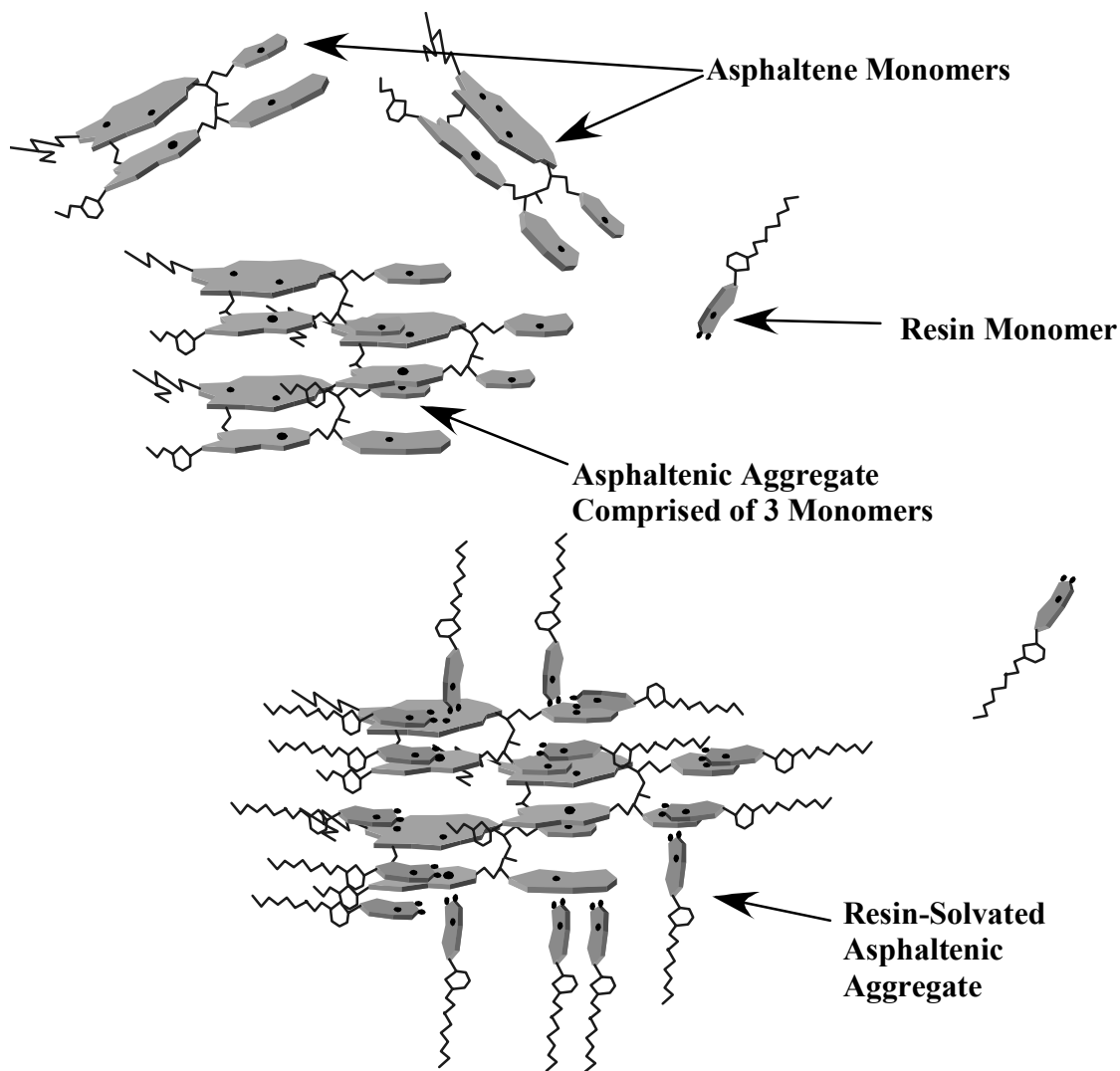


Figure C.2 Schematic illustrating the likeliest molecular structure of asphaltene and resin monomers, asphaltenic aggregates in the absence of solvating resins, and asphaltenic aggregates in the presence of solvating resins. The jagged lines represented aliphatic hydrocarbon moieties, the grey shaded regions represent aromatic or fused aromatic rings, and the black dots represent polar functional groups.

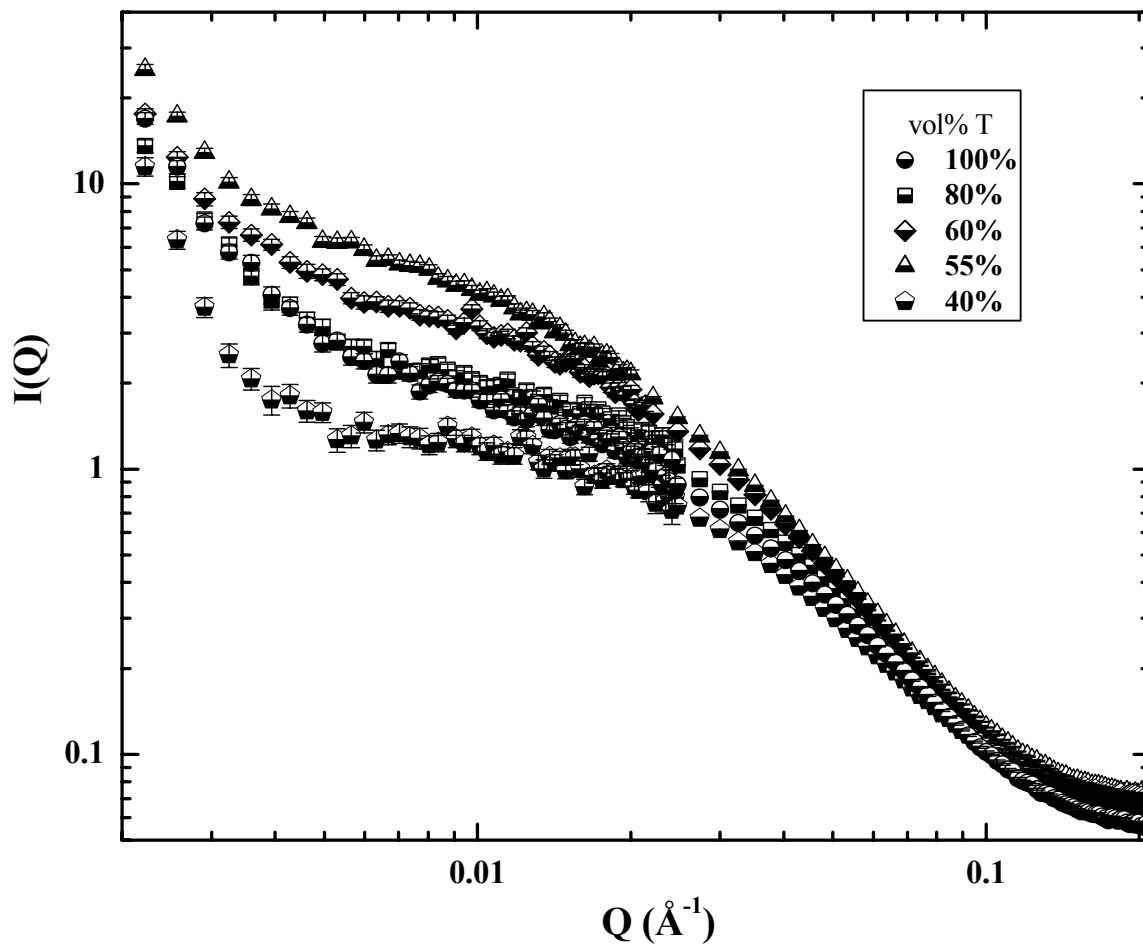


Figure C.3 SANS curves of HO Whole asphaltenes in mixtures of d-heptane and d-toluene at 1 wt%, 25°C, 5 mm path length

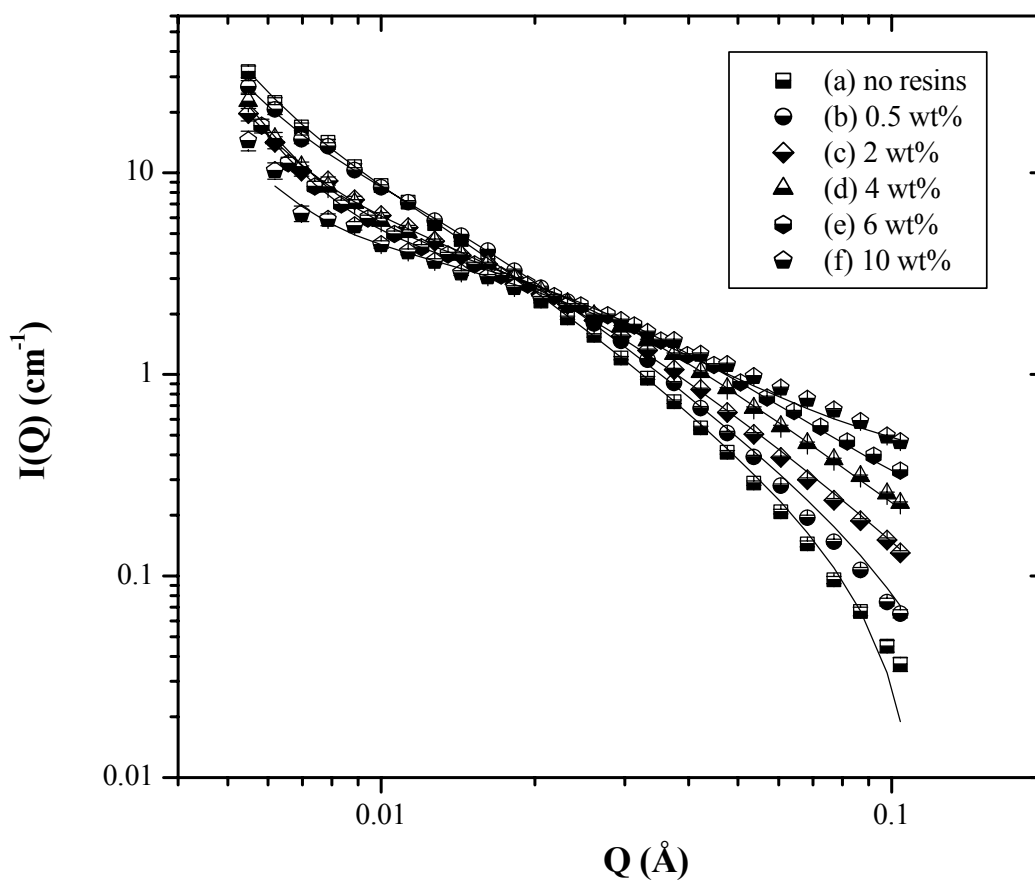


Figure C.4 SANS fits (2 mm path length) using Lorentzian lineshapes. CS Precipitate asphaltenes at 25°C in pure toluene with: a) No Resins: Background: -0.12 ± 0.07 , I_0 : 15 ± 1 , I_1 : $1.94\text{E-}8 \pm 8.\text{E-}10$, ξ : 110 ± 8 ; b) 0.5 wt% B6 Resins: Background: -0.06 ± 0.06 , I_0 : 14.8 ± 0.9 , I_1 : $1.39\text{E-}8 \pm 5.\text{E-}10$, ξ : 103 ± 6 ; c) 2 wt% B6 Resins: Background: -0.02 ± 0.03 , I_0 : 6.9 ± 0.2 , I_1 : $1.22\text{E-}8 \pm 2.\text{E-}10$, ξ : 63 ± 2 ; d) 4 wt% B6 Resins: Background: 0.01 ± 0.06 , I_0 : 5.0 ± 0.2 , I_1 : $1.53\text{E-}8 \pm 3.\text{E-}10$, ξ : 47 ± 3 ; e) 6 wt% B6 Resins: Background: 0.09 ± 0.05 , I_0 : 4.3 ± 0.1 , I_1 : $1.44\text{E-}8 \pm 2.\text{E-}10$, ξ : 41 ± 2 ; f) 10 wt% B6 Resins: Background: 0.2 ± 0.1 , I_0 : 3.6 ± 0.2 , I_1 : $8.4\text{E-}9 \pm 4.\text{E-}10$, ξ : 38 ± 5 . Note: Every 2nd data point plotted above $Q = 0.006$

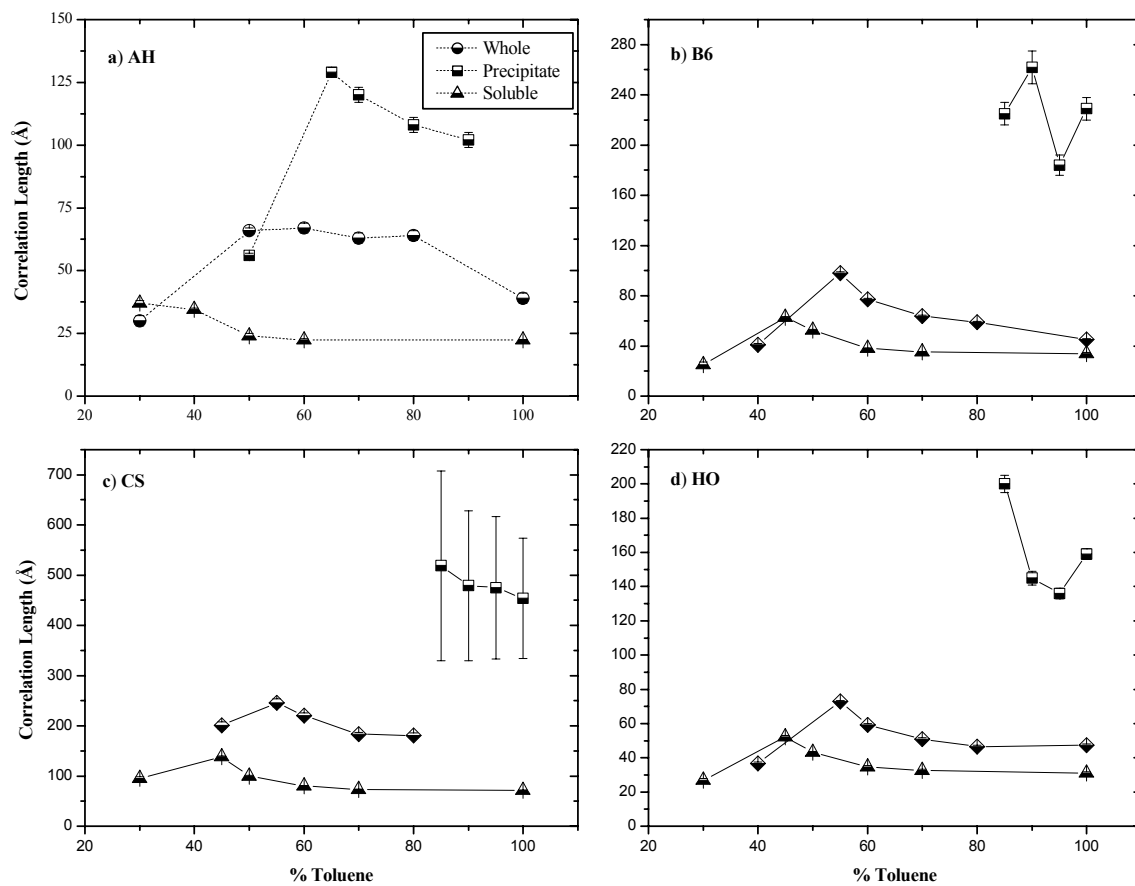


Figure C.5 Correlation lengths of B6 solubility fractions in heptol determined by SANS: 1 wt %, 25°C, 5 mm path length.

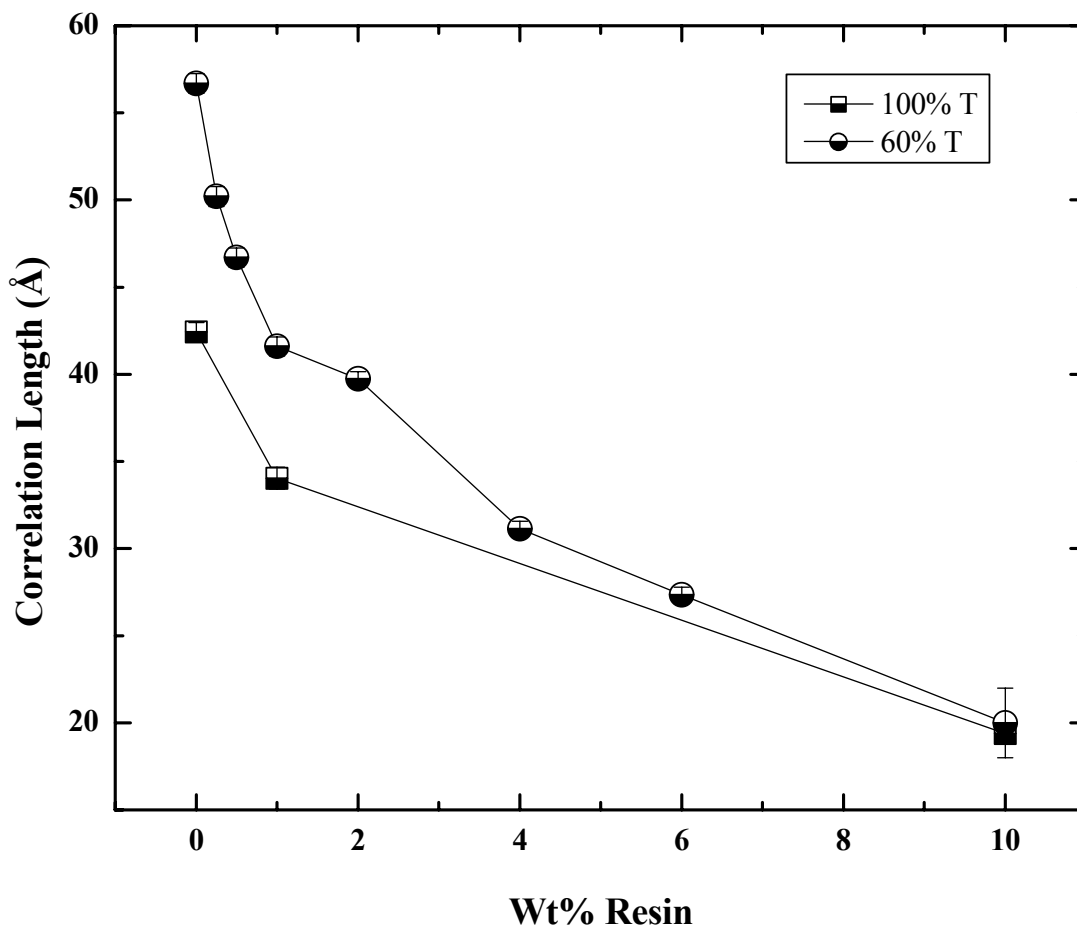


Figure C.6 Correlation length ξ of B6 Whole asphaltene aggregates with B6 resins in pure toluene and 60 % toluene determined from SANS: 1 wt % asphaltenes, 80°C, 5 mm path length.

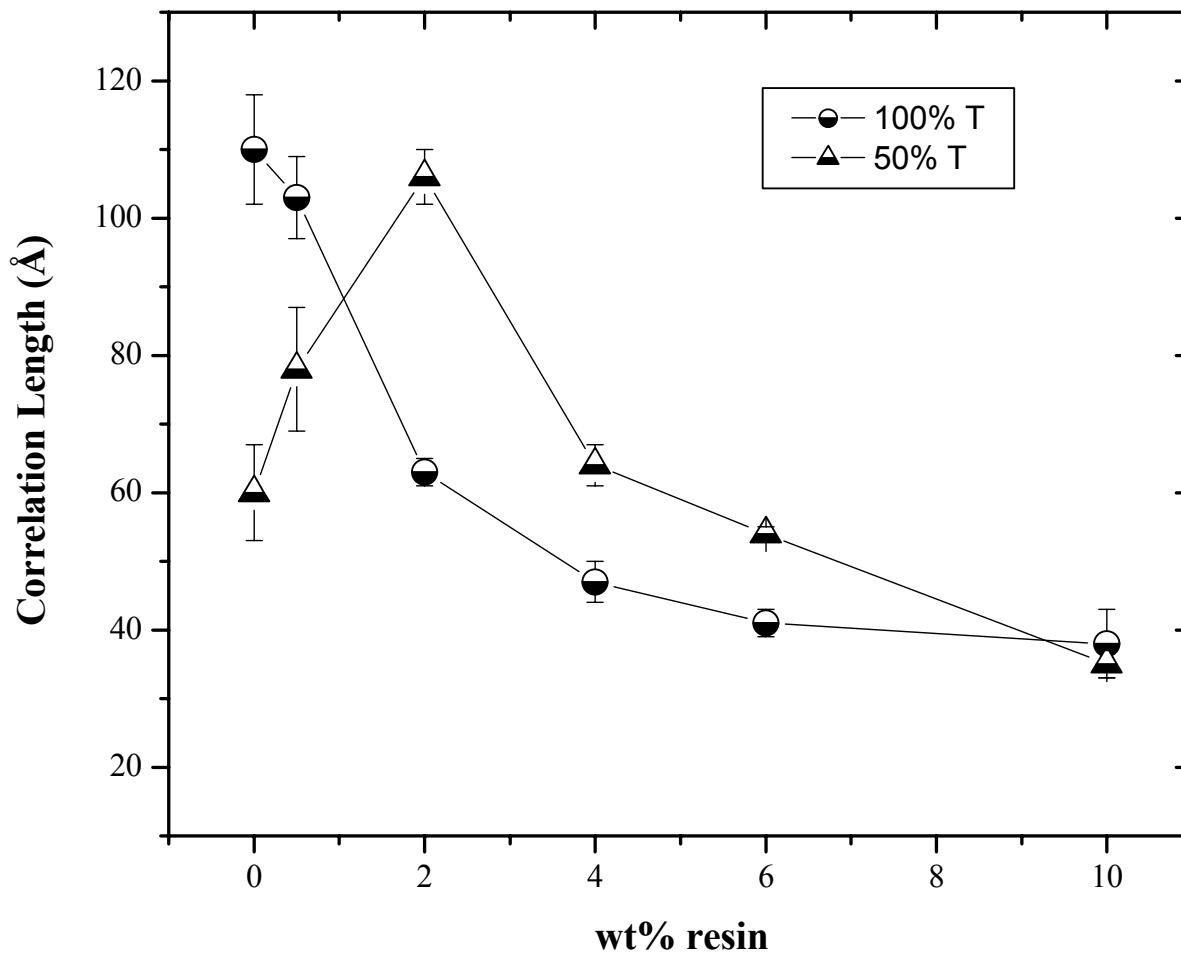


Figure C.7 Correlation length ξ of CS Precipitate asphaltene aggregates with B6 resins in pure toluene and 50 % toluene determined from SANS: 1 wt % asphaltenes, 25°C, 2 mm path length.

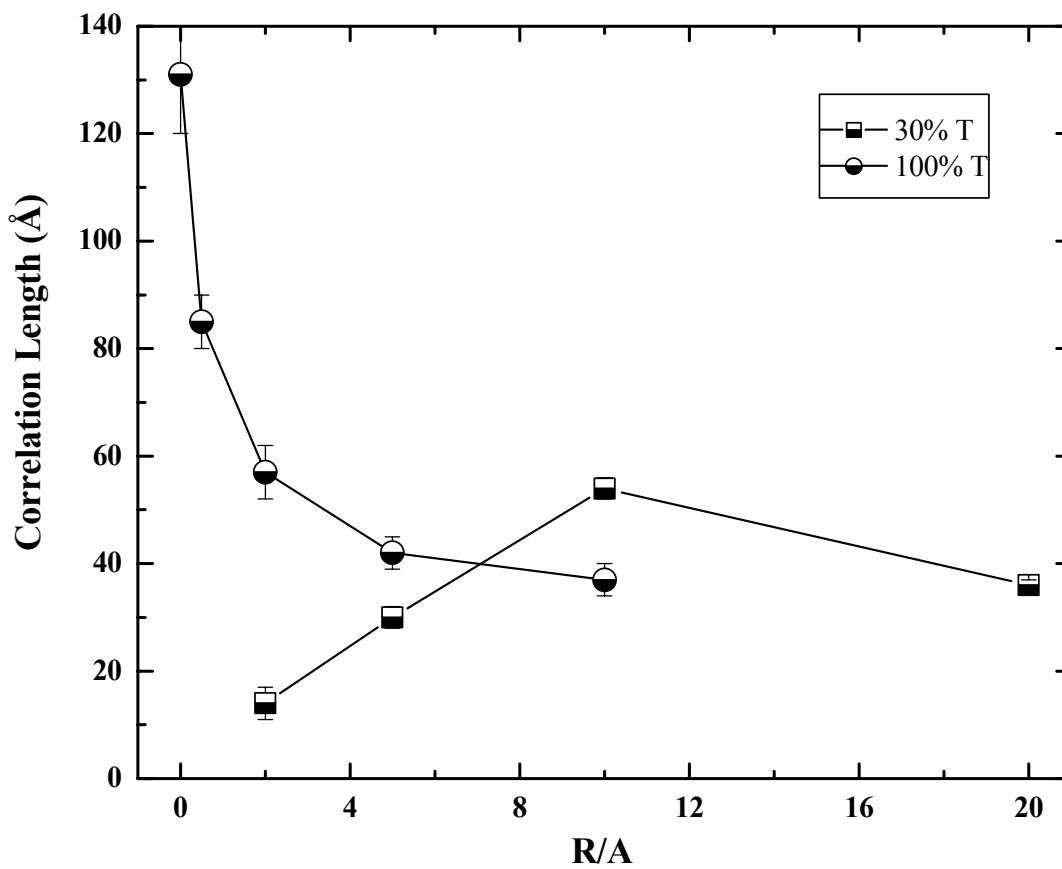


Figure C.8 Correlation length ξ of B6 Precipitate asphaltene aggregates with B6 resins in pure toluene and 30 % toluene determined from SANS: 1 wt % asphaltenes, 25°C, 2 mm path length.

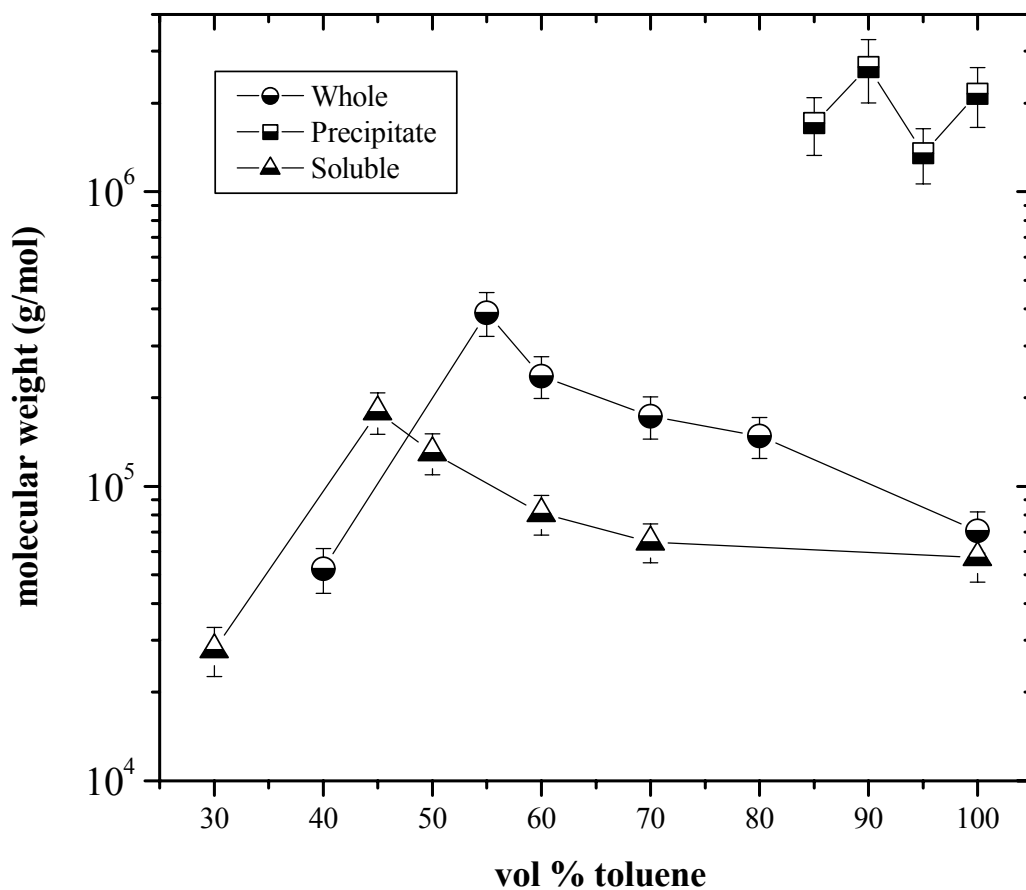


Figure C.9 Weight average molecular weight of B6 asphaltene solubility fractions in heptol determined by SANS: 1 wt %, 25°C, 5 mm path length.

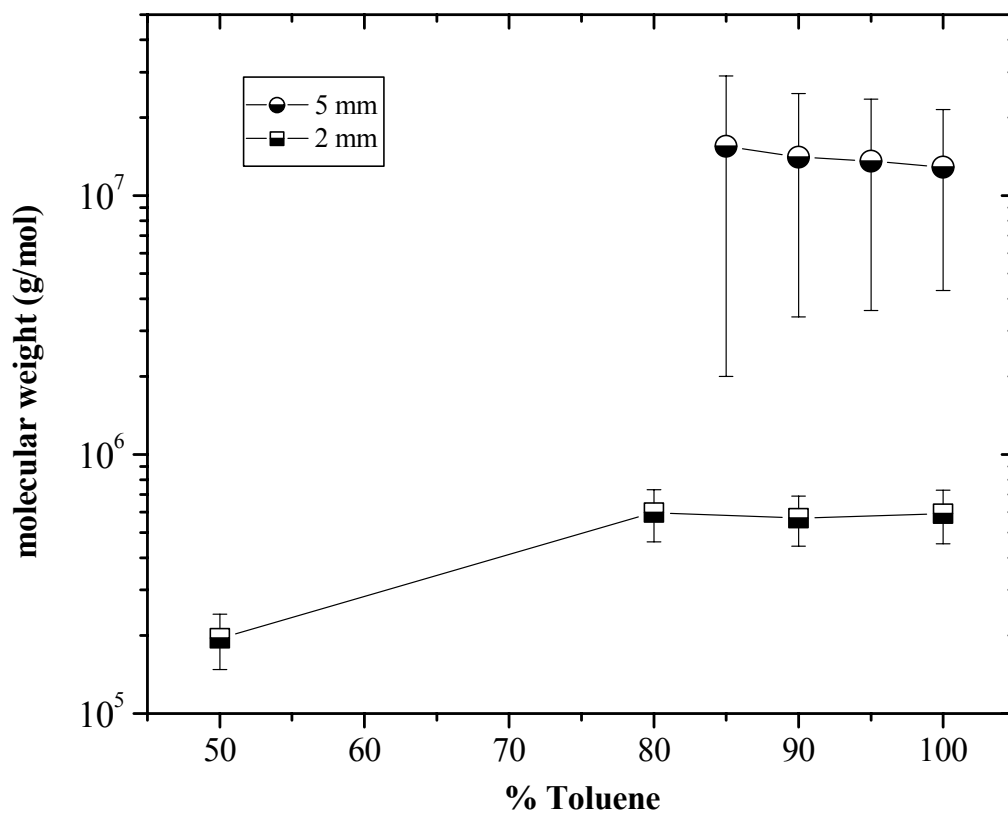


Figure C.10 Weight average molecular weight of CS Precipitate asphaltenes in heptol determined by SANS at various neutron path lengths: 1 wt %, 25°C .

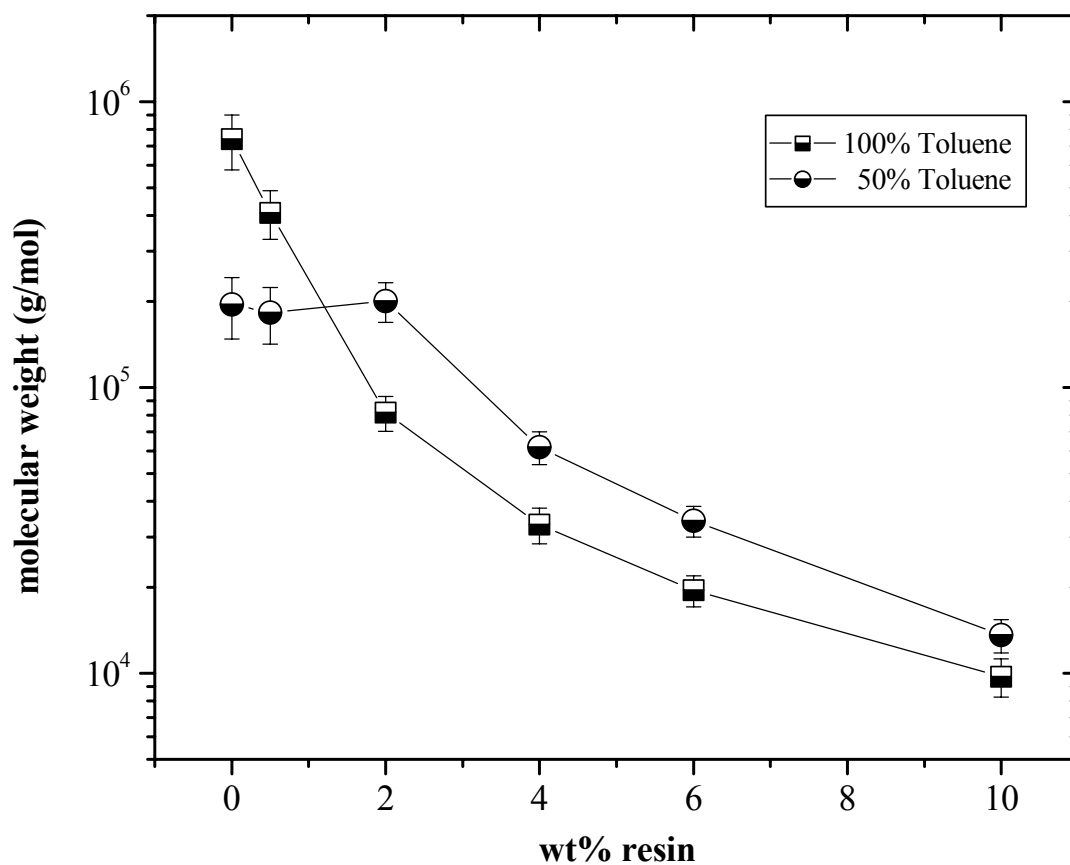


Figure C.11 Weight average molecular weight of CS Precipitate asphaltenes in pure toluene and 50 % toluene with added resins determined by SANS: 1 wt % asphaltenes, 25°C, 2 mm path length.

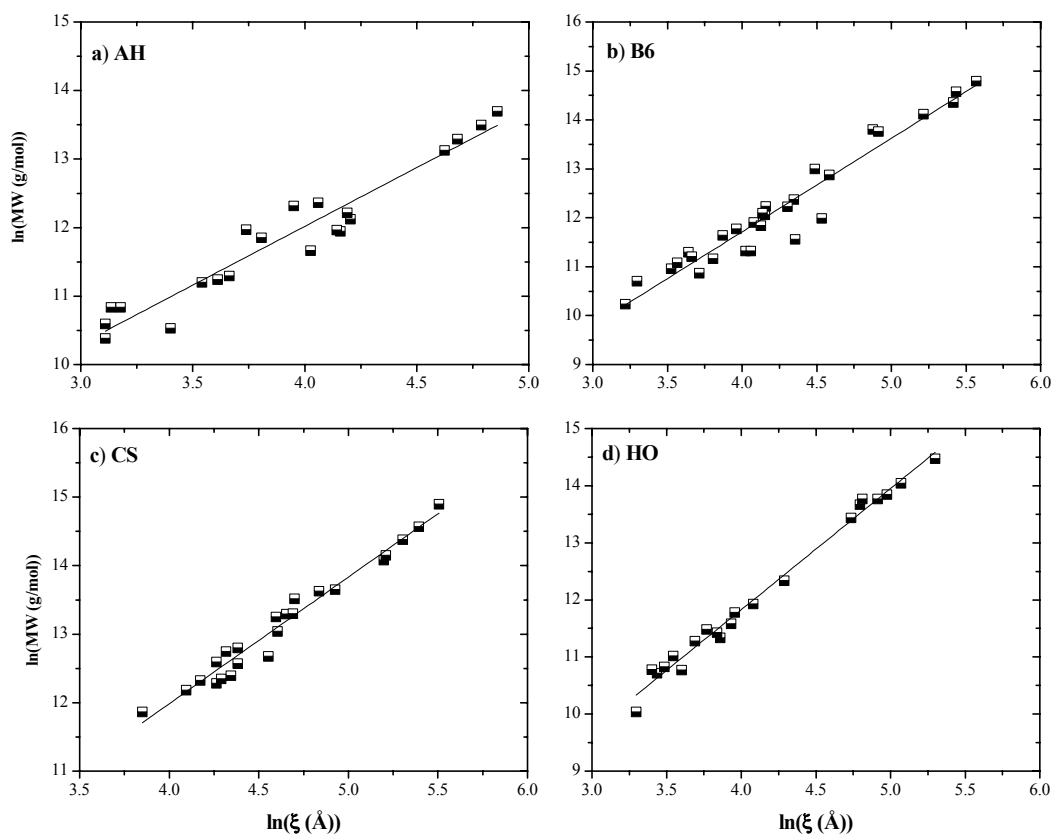


Figure C.12 Variation of aggregate molecular weight with ξ in all Whole asphaltenes and their sub-fractions dissolved in heptol:

- a) AH: slope of best fit line = 1.7 ± 0.1 , intercept = 5.2 ± 0.4 , $R^2 = 0.931$
- b) B6: slope of best fit line = 1.91 ± 0.09 , intercept = 4.1 ± 0.4 , $R^2 = 0.938$
- c) CS: slope of best fit line = 1.85 ± 0.07 , intercept = 4.6 ± 0.3 , $R^2 = 0.970$
- d) HO: slope of best fit line = 2.12 ± 0.05 , intercept = 3.3 ± 0.2 , $R^2 = 0.989$

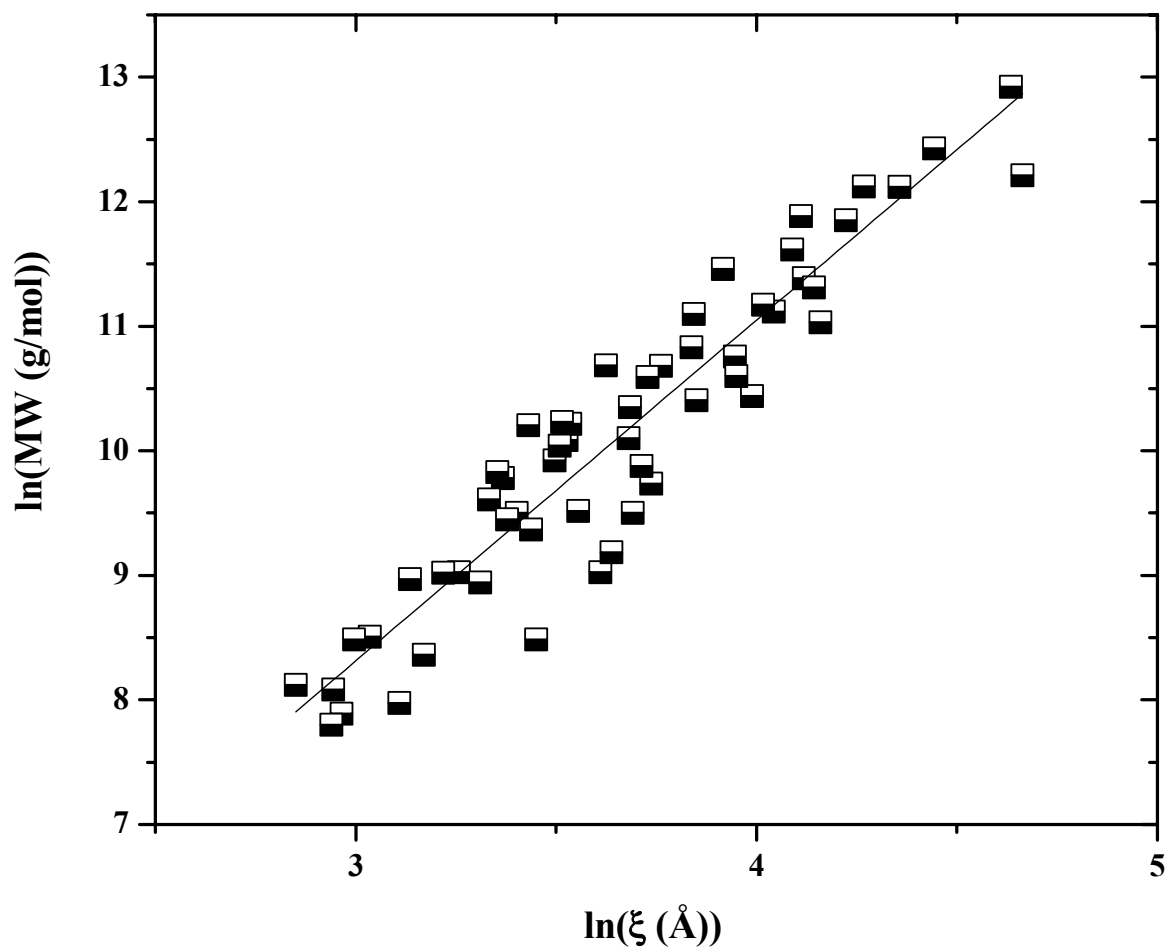


Figure C.13 Variation of aggregate molecular weight with ξ in all asphaltenes solvated with resins: slope of best fit line = 2.7 ± 0.1 , intercept = 0.1 ± 0.5 , $R^2 = 0.888$.

APPENDIX D

ASPHALTENE AGGREGATION: TECHNIQUES FOR ANALYSIS

Keith L. Gawrys and Peter K. Kilpatrick

[Reprinted from *Instrumentation Sci. Techn.* 32(3) (2004) 247-253]

D.1 Introduction

The study of asphaltene colloidal properties is motivated by their propensity to aggregate, flocculate, precipitate, adsorb onto interfaces, and hence pose considerable challenges for the petroleum industry. Asphaltenes are defined toluene (or benzene) soluble, yet *n*-heptane (or *n*-pentane) insoluble, portion of crude oil. The “solubility class” definition of asphaltenes generates a broad distribution of molecular structures that vary greatly among crude sources. Asphaltenes are generally characterized by fused ring aromaticity, small aliphatic side chains, and polar heteroatom-containing functional groups (e.g., carboxylic acids, carbonyl, phenol, pyrroles, and pyridines) capable of donating or accepting protons inter- and intra-molecularly. H/C ratios between 1.0-1.2 and N, S, and O content of a few weight percent suggest that the asphaltene backbone mostly contains fused aromatic carbon interspersed with occasional polar functional groups. The most plausible mechanisms of asphaltene aggregation involve π - π overlap between aromatic rings, hydrogen bonding between functional groups and other charge transfer interactions, with the degree of aggregation controlled by the polydispersity, chemical composition, and steric arrangement or inter-connectivity of functional groups in the asphaltene monomers. Understanding asphaltene chemistry and the fundamental mechanisms of colloid formation has been the driving force behind much petroleum research of the last half-century.

This article discusses four instrumental techniques used to study asphaltene aggregation: near-infrared (NIR) spectroscopy, pulsed-field gradient spin echo nuclear magnetic resonance (PFG-SE NMR), vapor pressure osmometry (VPO), and small-angle neutron scattering (SANS). A brief introduction to each technique is provided, with particular emphasis on applications and recent findings.

D.2 Instrumental Techniques

D.2.1 Near-Infrared (NIR) Spectroscopy

The near-infrared (NIR) spectroscopic region of the electromagnetic spectrum spans the wavelength range from 780-2500 nm-- the most prominent absorption bands associated with the overtones or combinations of stretching vibrations from carbon-hydrogen bonds. Such vibrational modes are described theoretically using an anharmonic oscillator model. NIR spectra also possess a background elevation due to light scattering by particles and aggregates. NIR experiments are relatively simple, time efficient, and non-invasive. The NIR technique can be quickly and accurately exploited to generate a large amount of information; however, it is still unclear whether or not it can quantitatively predict aggregate sizes [1-2]. For example, Auflem et al. performed NIR experiments to study the disintegration of North Sea asphaltenes (0.125% wt) dissolved in 70/30 n-heptane/toluene by adding various amphiphiles and naphthenic acids as a function of concentration [1]. Changes in asphaltene aggregate size were observed as a decrease in the optical density at 1600 nm. Aske et al. pressurized North Sea crude oil (~0.8% wt asphaltenes) to 300 bar and then depressurized in incremental steps with NIR spectra recorded at each pressure [2]. The aggregation onset pressure, as well as changes in the fluid compressibility and aggregate size, were determined from multivariate analysis of the NIR spectra. Furthermore, re-pressurization showed reversibility of the crude oil aggregates to their original aggregate size after 72 hours at 300 bar.

D.2.2 Pulsed-Field Gradient Spin Echo Nuclear Magnetic Resonance (PFG-SE NMR)

Pulsed-field gradient spin echo nuclear magnetic resonance (PFG-SE NMR) is a non-invasive, relatively fast instrumental technique to probe molecular self-diffusion coefficients using magnetic field gradients of varying strength to effect large signal attenuation. Asphaltene polydispersity can be accounted for in the data analysis by assuming a log-normal distribution of diffusion coefficients. A log-normal distribution is reasonable because diffusion coefficients are positive-definite and may vary over several orders of magnitude. Deuterated solvents are typically used to prevent signal attenuation from proton spin-spin relaxation. Östlund et al. studied the self-diffusion of Venezuelan asphaltenes (0.044 to 5% wt) in d-toluene [3]. Fitting the signal attenuation in the range from 0.7 to 1.9 ppm provided a

polydispersity ($\sigma \sim 0.6$) that was concentration independent. A median diffusion coefficient, D_m , on the order of 1×10^{-10} to 2×10^{-10} m²/s monotonically decreased with increasing concentration, indicating an increase in the average aggregate size. Model fitting of the diffusion coefficients based on particle geometry and concentration suggested that asphaltene aggregates could not be spherical in shape, because of large obstruction effects. Instead, a disc-like structure was proposed. In another study, deuterated n-pentane and n-heptane ($\leq 30\%$ wt) were added to Venezuelan asphaltenes (3.7% wt) in d-toluene and d-ethylbenzene [4]. Non-linear increases in D_m with flocculant concentration were observed that could not be attributed to changes in the solvent viscosity alone. For example, D_m of asphaltenes in toluene increased from ca. 1.15×10^{-10} m²/s with no flocculant added to 1.35×10^{-10} m²/s at 30% pentane. The polydispersity of the solute increased from $\sigma = 0.6$ to 0.7 at the highest flocculant concentration, further suggesting that n-alkane addition was inducing flocculation. Sjöblom et al. showed that PFG-SE NMR is applicable to study the interactions of asphaltenes with various additives, such as naphthenic acids, which serve to solvate asphaltenes and decrease aggregate sizes [5].

D.2.3 Vapor Pressure Osmometry (VPO)

Vapor pressure osmometry (VPO) takes advantage of the change in vapor pressure when a small amount of solute is added to a pure solvent. The VPO measuring chamber consists of a solvent reservoir with two wicks providing a saturated solvent atmosphere around two thermistors. Condensation of solvent from the atmosphere into an asphaltene solution placed at one thermistor releases heat and increases the thermistor temperature until the solution vapor pressure matches the pure solvent. Subsequent small voltage changes induced at the thermistor are related to the number-averaged molar mass of the solute. Due to differences in vapor pressure, VPO measurements are limited to single solvent solutions and are impractical for the study of whole crudes. Yarranton et al. observed the molar masses of Athabasca and Cold Lake bitumen asphaltenes in toluene and 1,2-dichlorobenzene increased with concentration to a limiting value of 10-20 g/L ($\sim 1-2$ wt %) [6]. Figure D.1 shows the VPO molar mass of Athabasca C7-asphaltenes in 1,2-dichlorobenzene at two different temperatures. Linear extrapolation (75°C) at concentrations below 3 g/L suggested monomer molar masses of ca. 1000 g/mol. The molar mass at high concentration approached 6000

g/mol, a value indicative of an aggregate with approximately six monomers. The degree of asphaltene association varied with solvent polarity and temperature with no clear indication that asphaltenes were completely dissociated in the low concentration limit. Spiecker et al. performed VPO measurements on whole asphaltenes and their more and less soluble subfractions in toluene at 53°C [7]. So-called “soluble” and “precipitate” fractions were generated by asphaltene precipitation in heptane-toluene, with the “precipitate” fraction accounting for the least soluble 30-40% of the whole asphaltenes by mass. The apparent molar masses of the “precipitate” fraction (12,000-17,000 g/mole) from B6 crude oil were substantially higher than the corresponding “whole” and “soluble” asphaltenes (2500-3500 g/mole) due to significant polar and H-bonding interactions among the asphaltene monomers in the absence of the solvating character of the complementary more soluble fraction.

D.2.4 Small-Angle Neutron Scattering (SANS)

Small-angle neutron scattering (SANS) is used to deduce sizes and morphologies of colloidal aggregates in solution. Proper analysis of SANS scattering intensity curves provides values for aggregate radius of gyration (R_g), molar mass, and apparent “fractal” dimension. Molar masses are weight-averaged and may be biased toward the presence of a small number of high mass aggregates in solution. SANS studies typically employ selective solvent deuteration to maximize the coherent scattering contrast between the solvent and solute. Perhaps the major drawback of SANS is the monetary cost of deuterated solvents and the limited availability of beamtime at national laboratories. Nevertheless, numerous studies have been performed over the past decade to probe the effects of concentration, solvent, temperature, and various additives on asphaltene aggregation behavior. For example, Roux et al. used SANS to study temperature and concentration effects on the structure of Safaniya asphaltenes in toluene [8]. Aggregate R_g values were nearly constant (~ 70 Å) at asphaltene volume fractions less than 3-4%, indicating that asphaltenes did not dissociate with dilution to $\sim 0.3\%$ v/v. Aggregate R_g and molar mass decreased with increasing concentration ($> 3-4\%$ v/v) due to aggregate interpenetration. Fenistein performed SANS analysis on dilute solutions ($\sim 3\%$ v/v) of Safaniya asphaltenes dissolved in d-toluene with varying d-heptane concentration (0 to 45% v/v) [9]. R_g values increased with heptane content from 69 to 144 Å and molecular weights increased from 90 to 570 kDa. Apparent “fractal” dimensions of ~ 2

obtained from the scaling behavior of the scattering intensity at intermediate wavevectors suggested that asphaltenes form highly porous aggregates consistent with the so-called “archipelago” model of asphaltenes in which the monomer molecular structure is comprised of fused-ring aromatic moieties connected by aliphatic and heteroatomic groups. The aggregate depicted in Figure D.2(c) is consistent with the observed fractal-like dimensions as the “scatterers” in a SANS experiment contain some percentage of entrained deuterated solvent in the interstitial space that does not give rise to scattering contrast.

Spiecker performed SANS analysis on dilute solutions (~1% wt) of “whole”, “soluble”, and “precipitate” asphaltene fractions in deuterated heptane/toluene solutions [7]. Enhancement of polar and π -bonding interactions for the less soluble subfractions indicated by elemental analysis results was reflected by the large aggregate sizes for B6 “precipitate” asphaltenes compared to the “whole” and “soluble” fractions in Figure D.3. The less soluble (i.e., “precipitate”) subfractions contributed the majority of species responsible for asphaltene aggregation. In another study, SANS measurements were performed on 1% wt asphaltene solutions in mixtures of heptane-toluene at various resin-to-asphaltene ratios [10]. Correlation length of soluble aggregates decreased with increasing resin content to a minimum value of ca. 20 Å, presumably corresponding to asphaltene monomers or dimers solvated by resins. Aggregate size increased with resin content in the presence of insoluble asphaltenes, as more polar material was dissolved into solution. Upon dissolution of the insolubles, additional resins served to decrease the correlation length.

D.3 Conclusions

This article has provided an introduction to four different, yet complementary, experimental methods used to study asphaltene aggregation: near-infrared (NIR) spectroscopy, pulsed-field gradient spin echo nuclear magnetic resonance (PFG-SE NMR), vapor pressure osmometry (VPO), and small-angle neutron scattering (SANS). These methods represent a small subset of those currently employed by researchers in petroleum science and engineering. While each technique has its own advantages and disadvantages, all provide valuable insight into the fundamental mechanisms driving asphaltene colloidal behavior.

D.4 References

1. Auflem, I.H.; Havre, T.E.; Sjöblom, J. Near-IR study on the dispersive effects of amphiphiles and naphthenic acids on asphaltenes in model heptane-toluene mixtures. *Colloid Polym. Sci.* **2002**, 280, 695-700.
2. Aske, N.; Kallevik, H.; Johnsen, E.E.; Sjöblom, J. Asphaltene aggregation from crude oils and model systems studied by high-pressure NIR spectroscopy. *Energy & Fuels* **2002**, 16, 1287-1295.
3. Östlund, J.-A.; Andersson, S.-I., Nyden, M. Studies of asphaltenes by the use of pulsed-field gradient spin echo NMR. *Fuel* **2001**, 80, 1529-1533.
4. Östlund, J.-A.; Löfroth, J.-E.; Holmberg, K.; Nyden, M. Flocculation behavior of asphaltenes in solvent/nonsolvent systems. *J. Colloid Interf. Sci.* **2002**, 253, 150-158.
5. Sjöblom, J.; Aske, N.; Auflem, I.H.; Brandal, Ø.; Havre, T.E.; Sæther, Ø.; Westvik, A.; Johnsen, E.E.; Kallevik, H. Our current understanding of water-in-crude oil emulsions: recent characterization techniques and high pressure performance. *Adv. Colloid Interf. Sci.* **2003**, 100, 399-473.
6. Yarranton, H.W.; Alboudwarej, H.; Jakher, R. Investigation of asphaltene association with vapor pressure osmometry and interfacial tension measurements. *Ind. Eng. Chem. Res.* **2000**, 39, 2916-2924.
7. Spiecker, P.M.; Gawrys, K.L.; Kilpatrick, P.K. Aggregation and solubility behavior of asphaltenes and their subfractions. *J. Colloid Interf. Sci.* **2003**, 267(1), 178-193.
8. Roux, J.-N. SANS study of asphaltene aggregation: concentration and solvent quality effects. *Langmuir* **2001**, 17, 5085-5092.
9. Fenistein, D.; Barré, L.; Broseta, D.; Espinat, D.; Livet, A.; Roux, J.-N.; Scarsella, M. Viscometric and neutron scattering study of asphaltene aggregates in mixed toluene/heptane solvents. *Langmuir* **1998**, 14, 1013-1020.
10. Spiecker, P.M.; Gawrys, K.L.; Trail, C.B.; Kilpatrick, P.K. Effects of petroleum resins on asphaltene aggregation and water-in-oil emulsion formation. *Colloids and Surfaces A* **2003**, 220(1-3), 9-27.

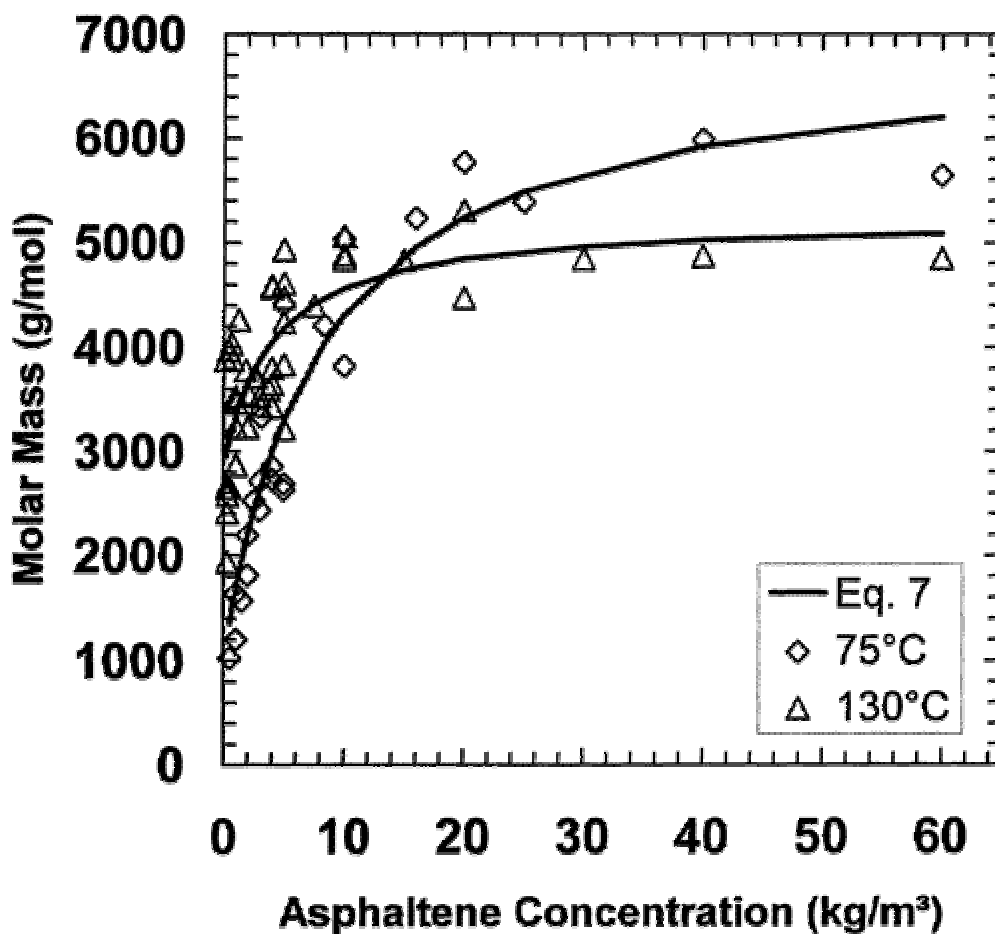


Figure D.1 VPO molar masses of Athabasca C7-asphaltenes in 1,2-dichlorobenzene.
 [Reproduced with permission from *Ind. Eng. Chem. Res.* **2000**, 39(8), 2916-2924. Copyright 2000 Am. Chem. Soc.]

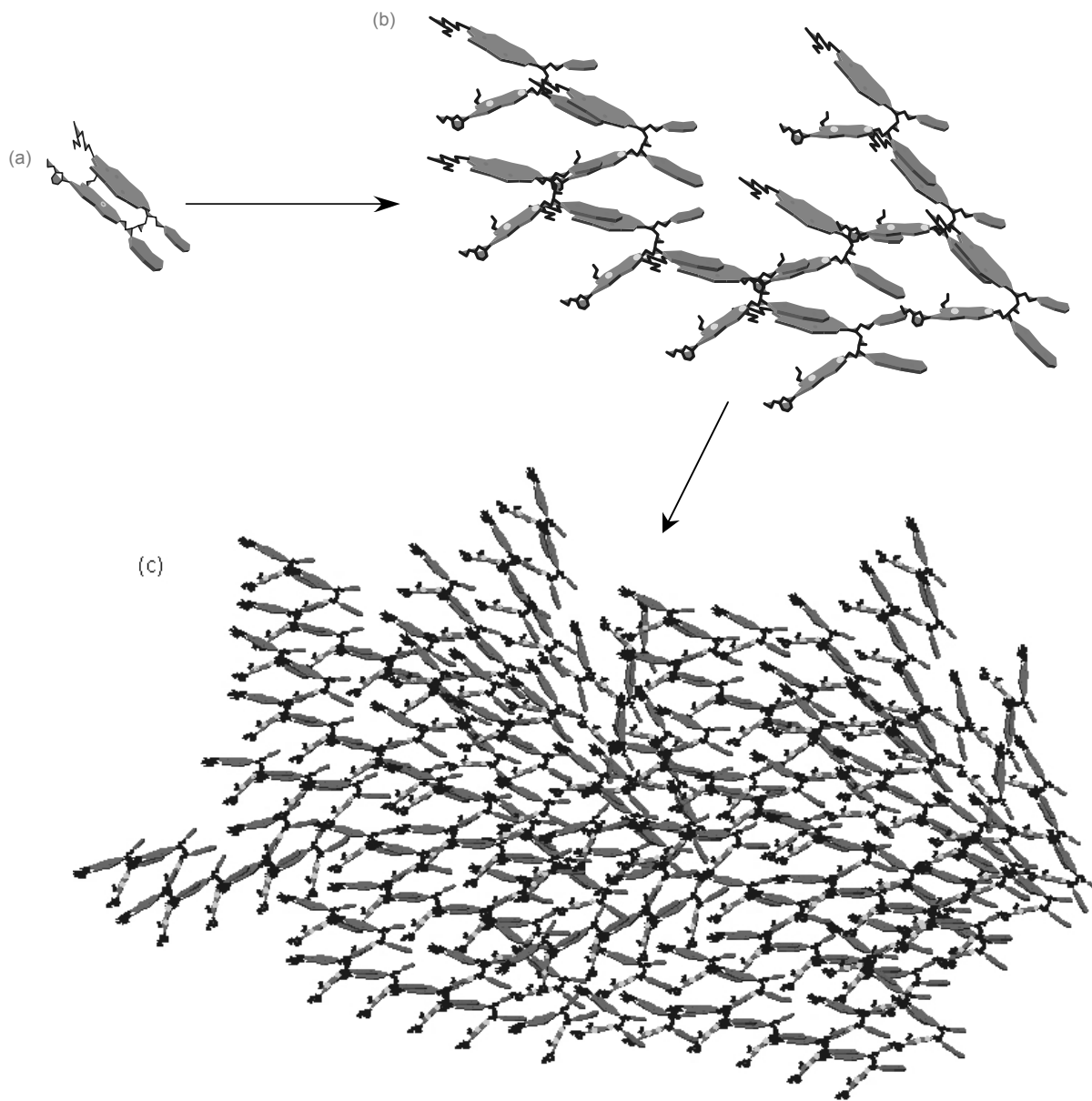


Figure D.2 Schematic illustration depicting (a) an asphaltene monomer; (b) an asphaltene aggregate with size ca. 3-4 nm, molecular weight ca. 20-25 kDa, and apparent “fractal” dimension between 1-2; and (c) an asphaltene aggregate with size ca. 12-15 nm, molecular weight ca. 200-400 kDa, and apparent “fractal” dimension between 2-2.5.

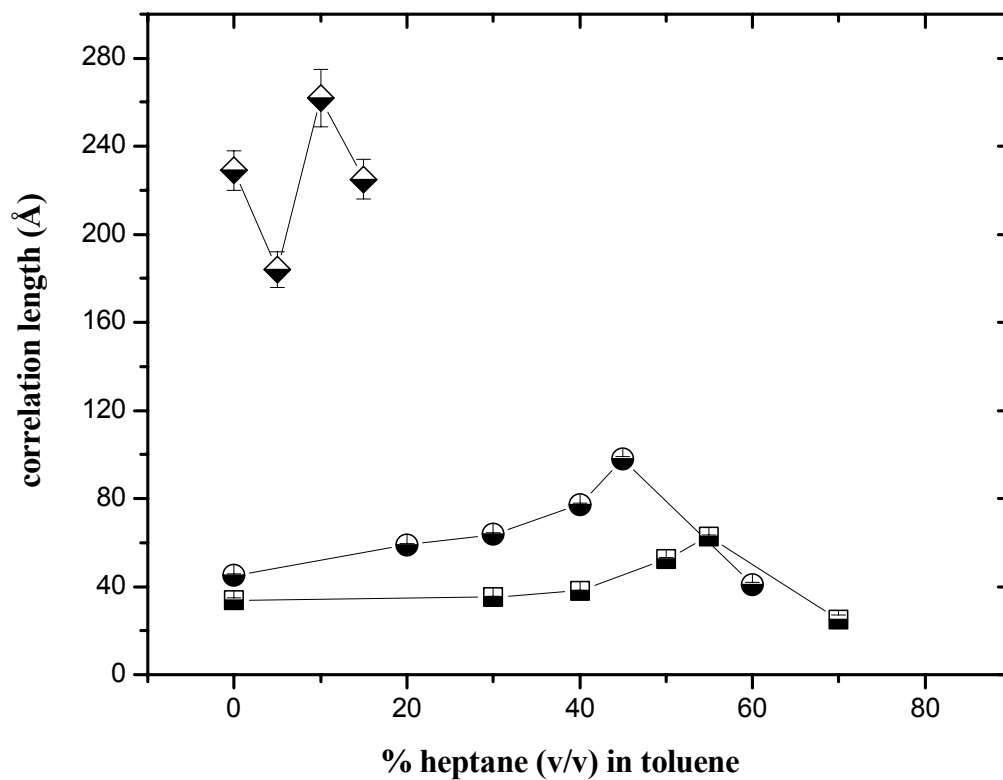


Figure D.3 Aggregate sizes B6 Soluble (□), Whole (●), and Precipitate (◆) asphaltene fractions (1% wt) as a function of d-heptane content in d-toluene. Correlation length (ξ) scales with radius of gyration (R_g) according to the relation: $\xi = R_g / \sqrt{3}$.

APPENDIX E
SYNTHESIS AND CHARACTERIZATION OF SUBSTITUTED TRIPHENYLENES
TO MIMIC THE SOLUBILITY BEHAVIOR AND INTERFACIAL ACTIVITY OF
ASPHALTENES

Keith L. Gawrys and Peter K. Kilpatrick

E.1 Introduction

Several major problems associated with oil recovery are related to the aggregation, precipitation, and interfacial adsorption of petroleum asphaltenes. Forming the heaviest fraction of crude oil, asphaltenes are defined by their solubility in toluene and insolubility in n-heptane or n-pentane. Asphaltenes are flat or planar molecules with polyaromatic cores containing 4-10 fused rings and polar functional groups. Attached to the polar core are hydrophobic naphthenic rings and short aliphatic side-chains. As a solubility class, asphaltenes are remarkably polydisperse in carbon backbone structure, polar heteroatom functionality, and molecular weight. As a result, the exact chemical nature of asphaltenes has not yet been characterized. Even accurate measurements of asphaltene molecular weights are often confounded by the tendency of asphaltenes to form aggregates in most common aromatic solvents (e.g., benzene, toluene, or pyridine). Figure E.1 shows a “typical” asphaltene molecular structure assembled from elemental analysis and spectroscopic characterization of functional groups [1].

The propensity of asphaltenes to adsorb at interfaces, and subsequently, form stable water-in-crude oil (w/o) emulsions is strongly related to the extent of asphaltene aggregation and the solvating power of the crude oil media. In solution, asphaltenes aggregate in stacks to minimize interactions of the polar core with non-polar solvents. The core of the asphaltenic aggregate is hydrophilic, while the periphery is hydrophobic. Asphaltenic aggregates adsorb and orient parallel to oil-water interfaces in order to maximize interactions of the polar core with the water phase, while the aliphatic periphery remains solvated in the non-polar oil phase. Asphaltenes maintain a delicate balance between solvency, aggregation, and interfacial activity in solution that must ultimately be related to the molecular chemistry of the participating components.

The current research attempts to determine the extent to which asphaltene physical properties are attributable to shape, size, aromaticity, or polar functionality of the asphaltene molecules. In this study we plan to synthesize several model compounds that mimic the chemical functionality and physical interactions of asphaltenes when aggregated in solution, adsorbed at model oil-water interfaces, and stabilized in model w/o emulsions. Unlike asphaltenes, the model compounds studied will be monodisperse in molecular weight, chemical structure, and functionality. Moreover, the reaction chemistry for the synthesis of the model compounds is sufficiently tunable to begin a detailed study of how specific chemical structure (e.g., aromatic ring size, hydrophobicity of aliphatic periphery, polar functionality, discotic nature) relates to asphaltene behavior.

E.2 Proposed Synthesis Reactions

In the search for model compounds that mimic the physical properties of asphaltenes, it is logical to begin with those that have an aromatic core and an aliphatic periphery. Substituted triphenylenes of the type 2,3,6,7,10,11-hexa-*n*-alkoxytriphenylene (HAT_n, where *n* represents the alkyl chain length) are suggested because they consist of a four-ring condensed aromatic core with aliphatic pendant groups. The earliest attempts at model compound synthesis focused on the production of HAT₆, since several synthesis methods for this compound are found in the literature [2-5]. In particular, the reaction scheme proposed by Boden et al. [6] worked well and most of the syntheses are performed using modifications of this method (Scheme E.1). The scheme consists of reacting catechol with a bromoalkane in a S_N2 type reaction to form the di-alkyloxybenzene precursor. The triphenylene product is obtained after oxidative trimerization of the precursor over a Lewis acid catalyst (e.g., FeCl₃, MoCl₅, FeCl₃/AlCl₃). The available side chains for the precursor may be chosen independently from among hydrogen, halogen, alkyl, alkoxy, hydroxy, acyloxy, and aryloxy groups [7].

HAT₆ and similar symmetrical alkoxy-substituted triphenylene derivatives are of particular interest in this study because they have molecular weights, H/C ratios, and discotic shapes that fall near the range of typical asphaltenes. However, these molecules differ from asphaltenes in several aspects. For example, the side chains are connected to the aromatic core by ether linkages. Significant concentrations of ether linkages are not expected in

asphaltene structure and greatly inflate the total oxygen content. Moreover, symmetric alkoxy-substituted triphenylenes lack: (1) variation in pendant side chain length and/or branching, (2) donatable protons for H-bonding, (3) fused ring systems larger than 4 aromatic rings, and (4) carboxylic acid functional groups. However, the synthesis reactions for substituted triphenylenes may be modified to introduce a more “asphaltene-like” character into the product.

The synthesis of HAT4-iso is proposed to obtain a model asphaltene compound with significant branching in the aliphatic periphery (Scheme E.2). The ability of the branched side chains to lie out of plane with the aromatic core is expected to hinder the stacking ability of the aromatic cores, thus modifying the solubility and aggregation behavior of the compound. While some branching in the aliphatic periphery is probably consistent with asphaltene structure, typical asphaltene molecules have more variation in the alkyl chain length and less symmetry of structure than HAT6 or HAT4-iso. The symmetry of HATn may be broken in several ways, e.g. by changing the length of the aliphatic side chains, by changing the chemical nature of one or more side chain, or by changing the degree of substitution of the aromatic core. A hodgepodge of mixed alkoxy-substituted triphenylene products with lower symmetry can be obtained by slowly reacting mixtures of σ -dialkyloxybenzene precursors under the oxidative trimerization conditions. For example, the reaction of veratrole and 1,2-diisobutyloxybenzene over the Lewis acid catalyst should result in a distribution of products (Scheme E.3a). Similarly, asymmetric triphenylenes of mixed chain lengths may be formed by direct trimerization of 1-methoxy-2-alkoxybenzene (Scheme E.3b).

Whereas alkoxy-substituted triphenylenes are potential candidates to model the most soluble asphaltene fraction, products capable of participating in electron donor/acceptor interactions such as hydrogen bonding are potential mimics for the most polar asphaltene subfraction. For this reason, substituted triphenylenes containing carboxylic acid and hydroxyl moieties are of particular interest. We have already had some success with the synthesis of mono-hydroxytriphenylenes. For example, 2-hydroxy-3,6,7,10,11-penta-isobutyloxytriphenylene (HAT4-OH) was formed and isolated as a side product of the HAT4-iso synthesis reaction. Additional polar functional groups will be incorporated by the

use of phenolic and alcoholic precursors during the oxidative trimerization reaction (Scheme E.4). The alcoholic triphenylene may be further oxidized to form the carboxylic acid.

E.3 Preliminary Results

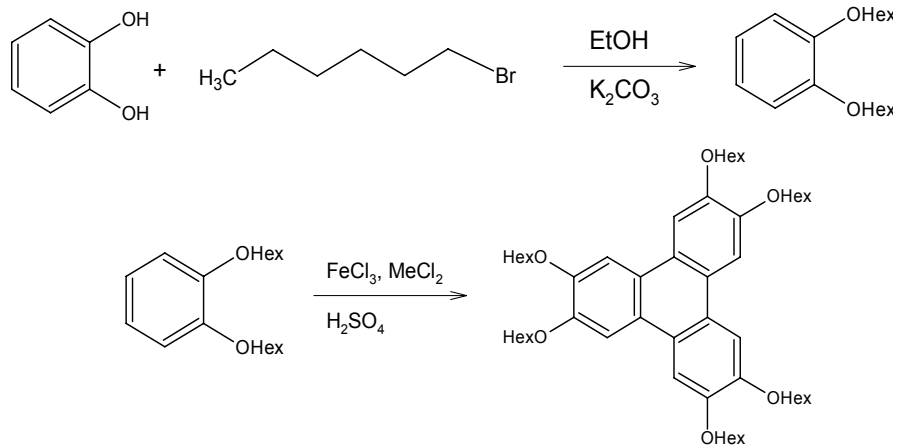
Early attempts to synthesize symmetric hexaalkoxytriphenylenes have proven successful, although the product yields obtained were significantly lower than expected from the literature [2]. HAT6 was obtained via oxidative trimerization of 1,2-dihexyloxybenzene as an off-white solid (18% yield). The product work-up consisted of column chromatography (silica gel, 1:1 dichloromethane:petroleum ether) followed by recrystallization from hot ethanol. Chemical shifts and integrated peak intensities from ¹H-NMR compared closely to values expected from the literature (Figure E.2). Similarly, elemental analysis for total carbon and hydrogen content were within 0.3% of the expected values. The synthesis of the branched triphenylene HAT4-iso has proven equally successful. In addition, HAT4-OH was isolated as a fortuitous side-product. Current efforts are focusing on the synthesis of polar functionalized triphenylenes, which are expected to behave most like asphaltenes in terms of solubility, aggregation behavior, and film forming properties. Although substituted triphenylenes are widely studied for their potential applications as “molecular wires” in molecular device applications [8], this research is the first attempt to systematically synthesize model compounds that adequately mimic the physical properties of crude oil fractions.

E.4 References

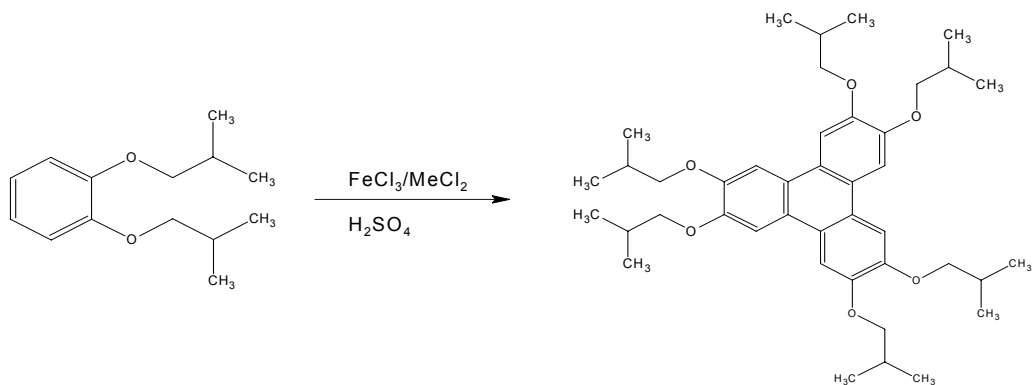
1. Kilpatrick, P.K., *Asphaltene Emulsions*, in *Encyclopedic Handbook of Emulsion Technology*, J. Sjoblom, Editor. 2000, Dekker: New York.
2. Cooke, G., V. Sage, and T. Richomme, *Synthesis of Hexa-Alkyloxytriphenylenes Using FeCl₃ Supported on Alumina*. *Synthetic Communications*, 1999. 29(10): p. 1767-1771.
3. Kumar, S. and M. Manickam, *Oxidative Trimerization of O-Dialkoxybenzenes to Hexaalkoxytriphenylenes: Molybdenum (V) Chloride as a Novel Reagent*. *Chem. Commun.*, 1997: p. 1615-1616.
4. Naarmann, H., M. Hanack, and R. Mattmer, *A High Yield Easy Method for the Preparation of Alkoxy-Substituted Triphenylenes*. *Synthesis*, 1994: p. 477-478.

5. Borner, R.C. and R.F. Jackson, *A Flexible and Rational Synthesis of Substituted Triphenylenes by Palladium-Catalysed Cross-Coupling of Arylzinc Halides*. J. Chem. Soc., Chem. Commun., 1994: p. 845-846.
6. Boden, N., *et al.*, *The Synthesis of Triphenylene-Based Discotic Mesogens: New and Improved Routes*. Liquid Crystals, 1993. 15(6): p. 851-858.
7. Bushby, R.J., *et al.*, *Synthesis of Substituted Triphenylenes, Useful as Discotic Liquid Crystals*, 1994. International Patent Application PCT/GB94/01263, World Intellectual Property Organization Pub. No. WO 94/29243.
8. Boden, N., R.J. Bushby, and J. Clements, *Mechanism of Quasi-One-Dimensional Electronic Conductivity in Discotic Liquid Crystals*. Journal of Chemical Physics, 1993. 98(7): p. 5920-5931.

Scheme E.1 Synthesis of 2,3,6,7,10,11-hexahexyloxytriphenylene (HAT6)

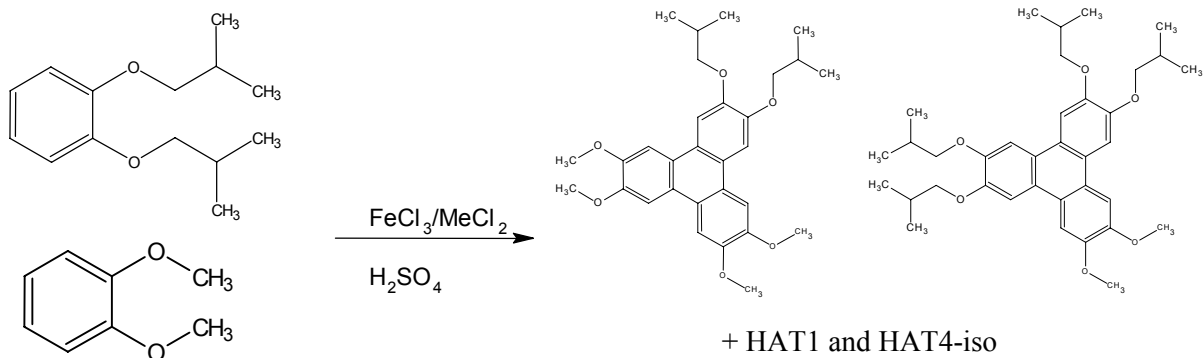


Scheme E.2 Synthesis of branched alkoxytriphenylenes via oxidative trimerization

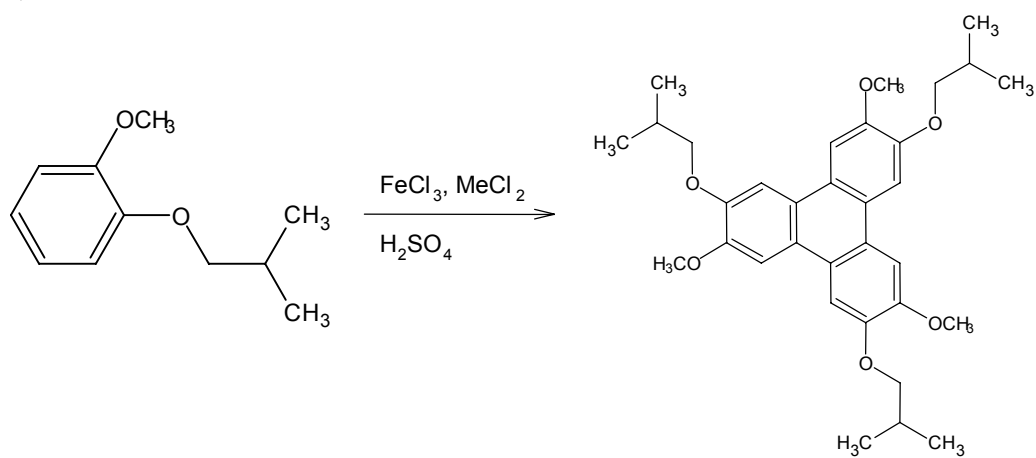


Scheme E.3 Variation of alkyl-chain length and extent of branching via (a) Mixed trimerization of 2 or more precursors and (b) Direct trimerization of asymmetric dialkoxybenzenes

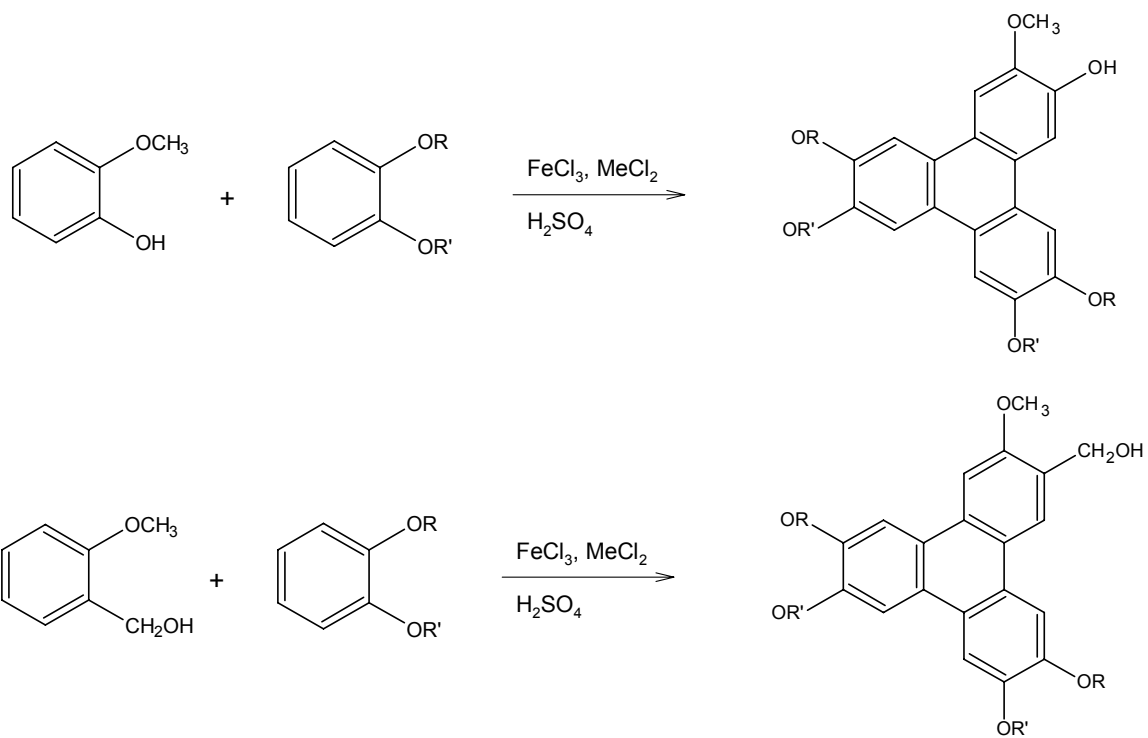
a.)



b.)



Scheme E.4 Synthesis of polar functionalized triphenylenes



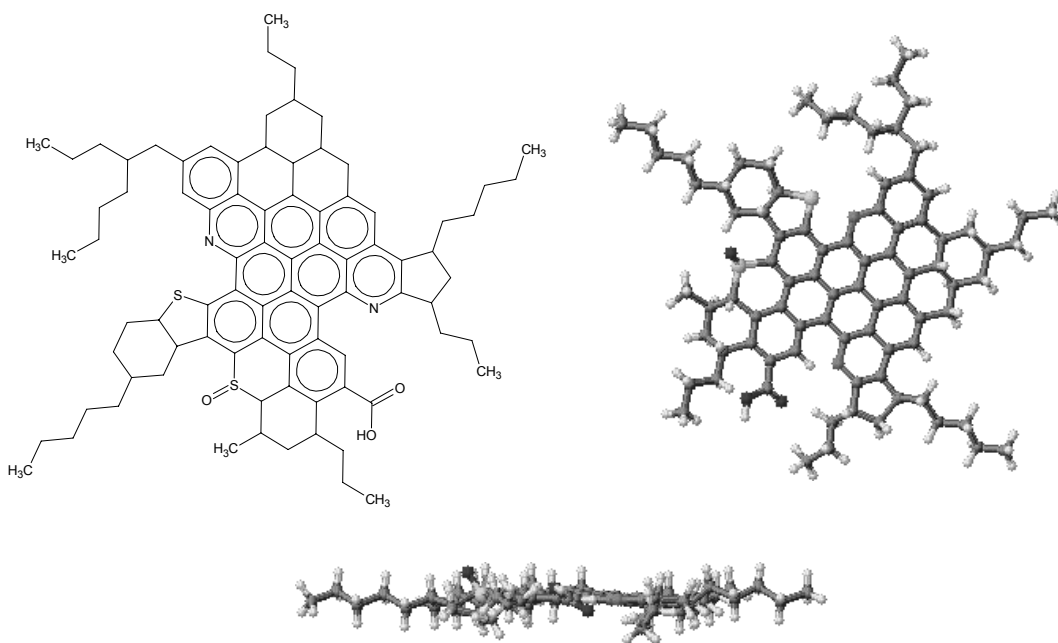


Figure E.1 Representative 2D and 3D structures of a plausible asphaltene molecule with a structural formula of $C_{84}H_{98}N_2S_2O_3$, a molecular weight of 1248 amu, and an H/C ratio of 1.18. The 3D side view shows the flat, planar shape of the aromatic core.

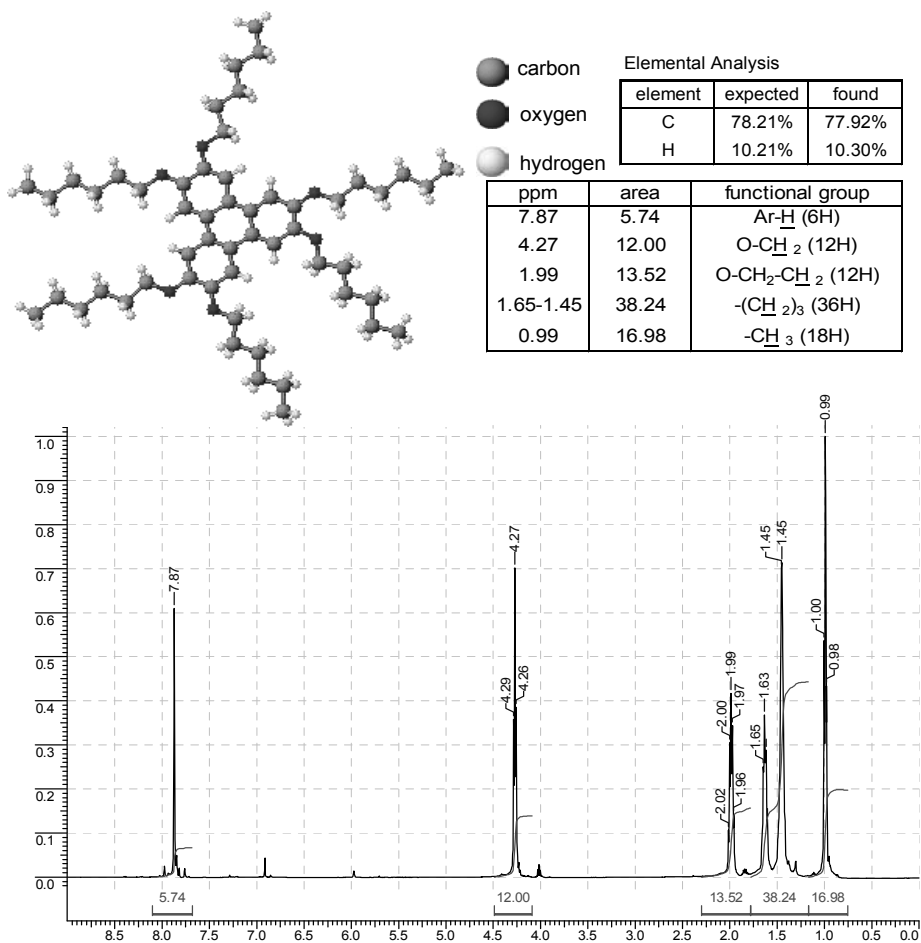


Figure E.2 ^1H -NMR spectra and elemental analysis results for HAT6

ppm	integral	assignment	# protons
7.98	1.09	Ar-H	1
7.83-7.81	3.89	Ar-H	4
7.77	1.04	Ar-H	1
5.91	0.83	-OH	1
4.10-4.08	2.27	-OCH ₂	2
4.02-3.97	8.06	-OCH ₂	8
2.29-2.23	5.00	-CH	5
1.57	0.80	?	1
1.18-1.14	30.00	-CH ₃	30

MS (FAB): m/z = 604

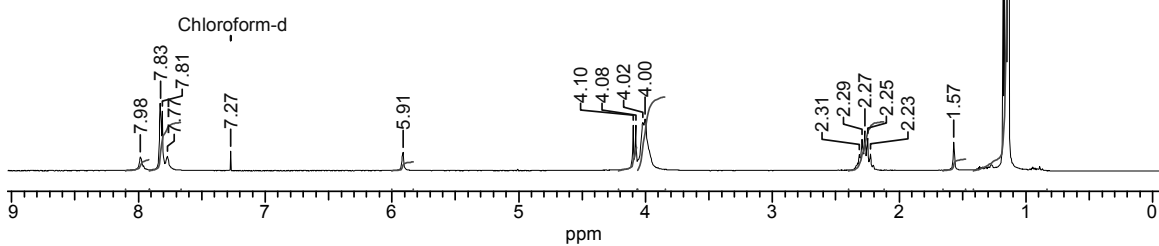
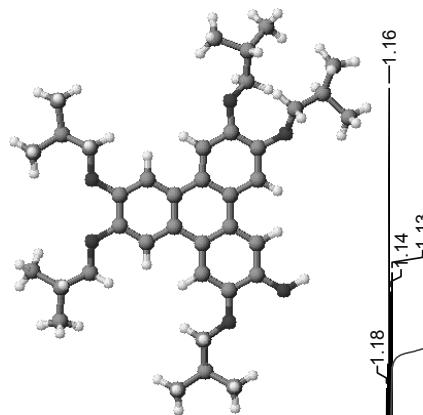


Figure E.3 ^1H -NMR spectra and mass spectroscopy results for HAT4-OH

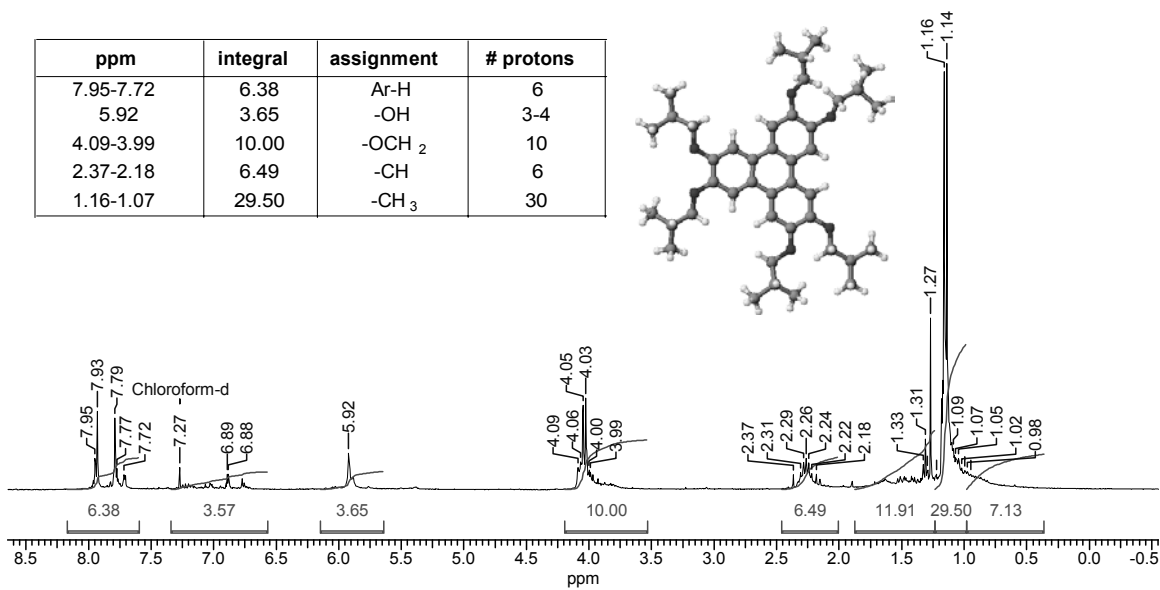


Figure E.4 H^1 -NMR spectra for HAT4-iso

APPENDIX F SANS DOPANT DATA

This section compiles the scattering intensity curves for various mixtures of asphaltenes and selective solvating agents, such as petroleum resins (R), phenanthridine (PHD), β -cholanic acid (CA), ethoxybenzoic acid (EBA), tetrahydrocarbazole (THC), and d-methanol (MeOD). The raw scattering data in IgorPro files may be located along the file path *F:/Thesis/Data files/Sans dopant data*. Scattering intensity profiles were collected at either Argonne National Laboratory (ANL) or NIST. The neutron pathlength through the samples (2 mm or 5 mm) and sample temperature (25°C or 80°C) are also specified.

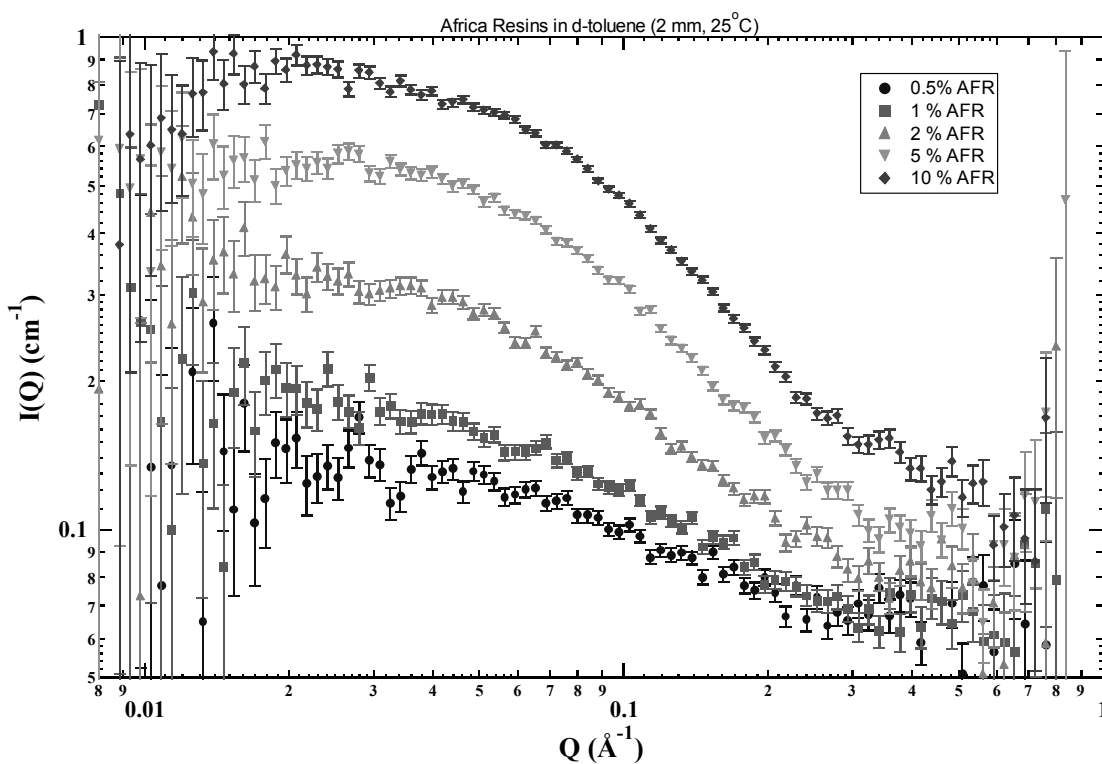


Figure F.1 Africa resins in d-toluene (ANL, 2 mm, 25°C).

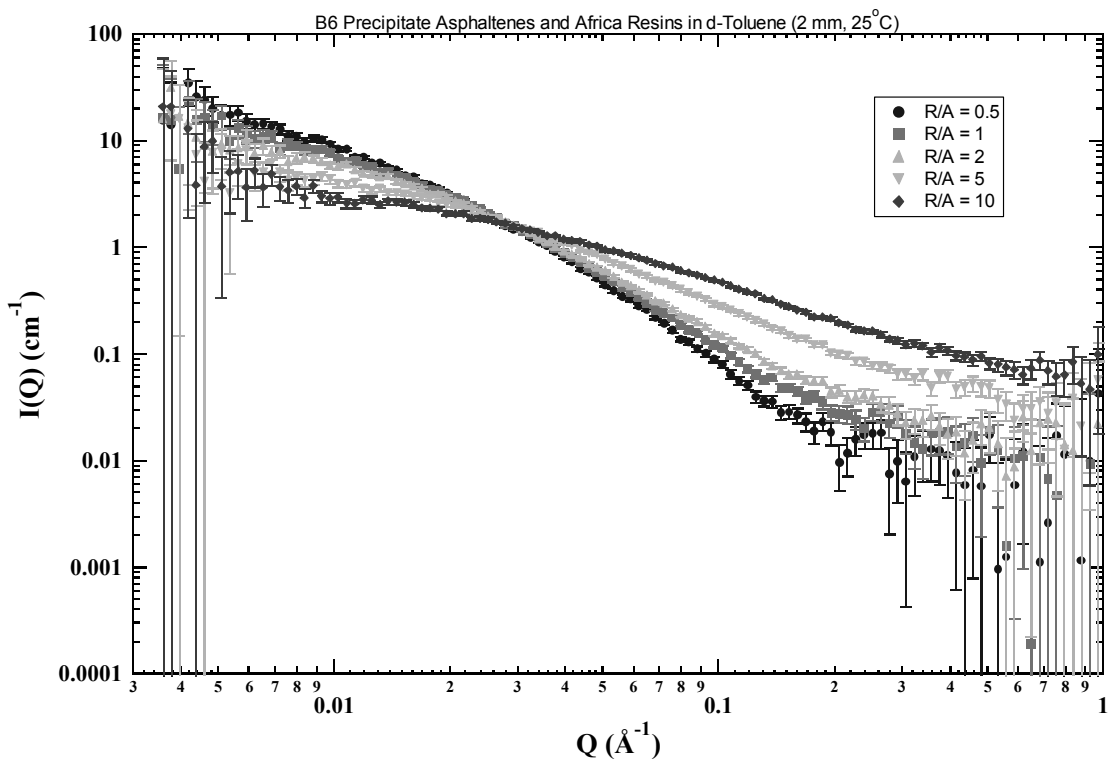


Figure F.2 B6 P asphaltenes (1% wt.) and Africa resins in d-toluene (ANL, 2 mm, 25°C).

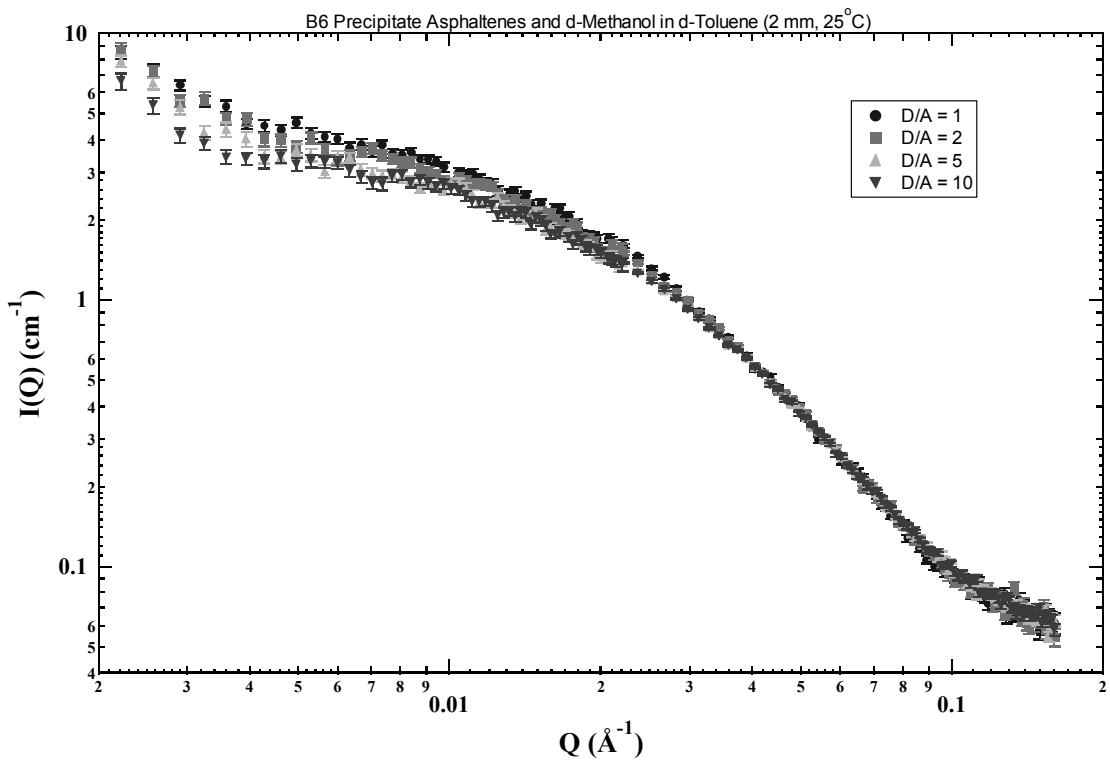


Figure F.3 B6 P asphaltenes (1% wt.) and d-methanol in d-toluene (ANL, 2 mm, 25°C).

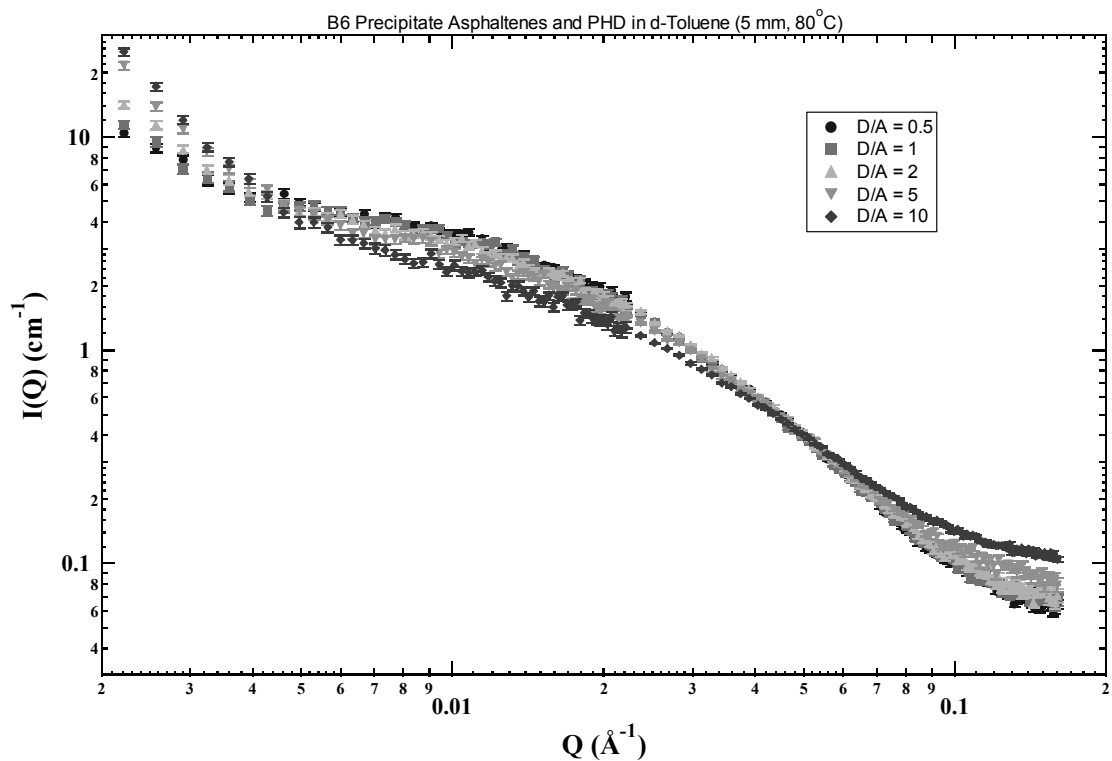


Figure F.4 B6 P asphaltenes (1% wt.) and PHD in d-toluene (NIST, 5 mm, 80°C).

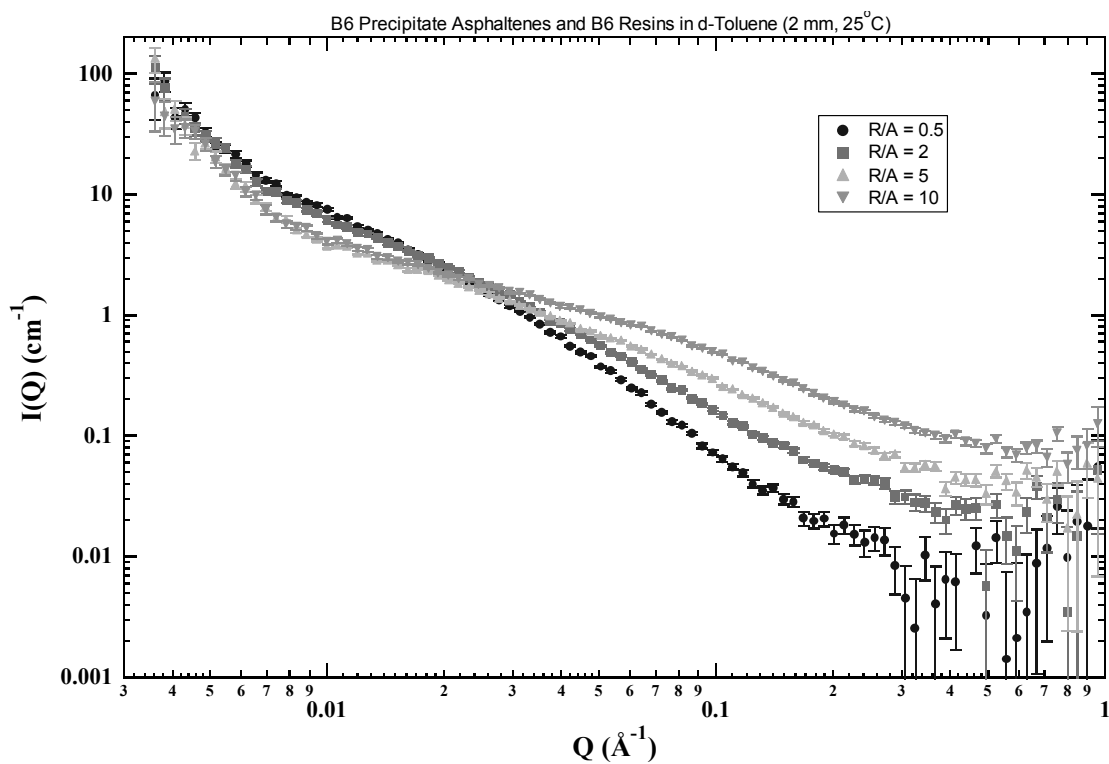


Figure F.5 B6 P asphaltenes (1% wt.) and B6 resins in d-toluene (ANL, 2 mm, 25°C).

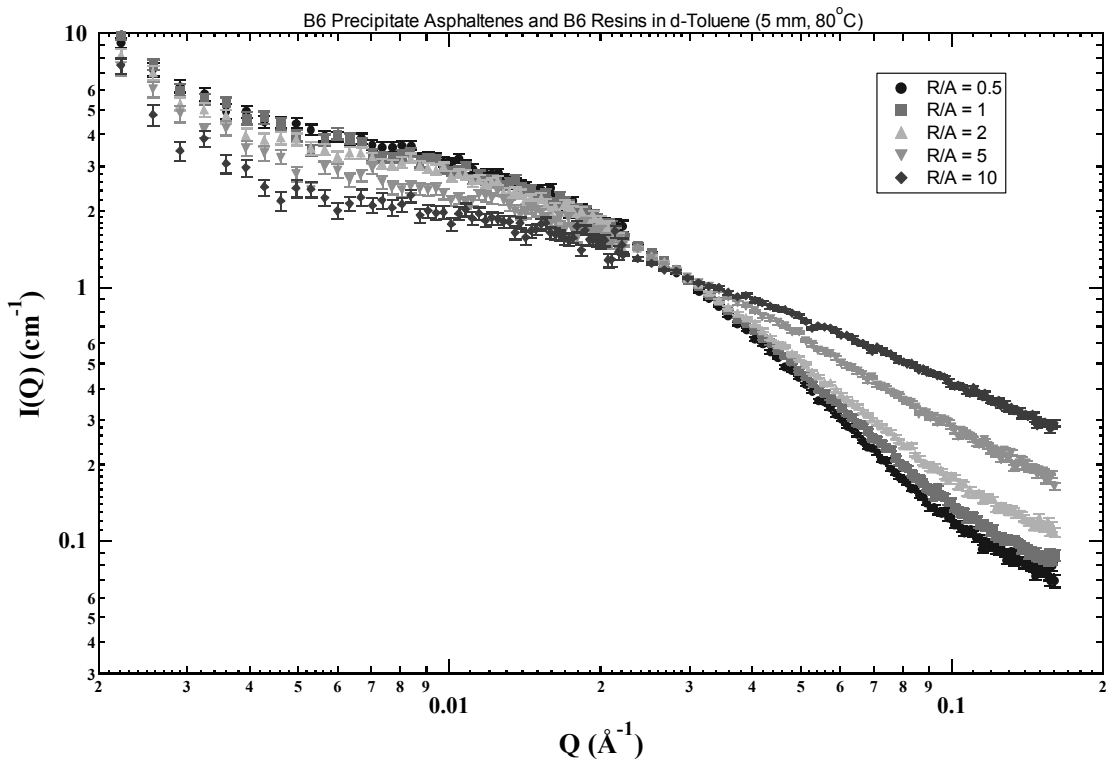


Figure F.6 B6 P asphaltenes (1% wt.) and B6 resins in d-toluene (NIST, 5 mm, 80°C).

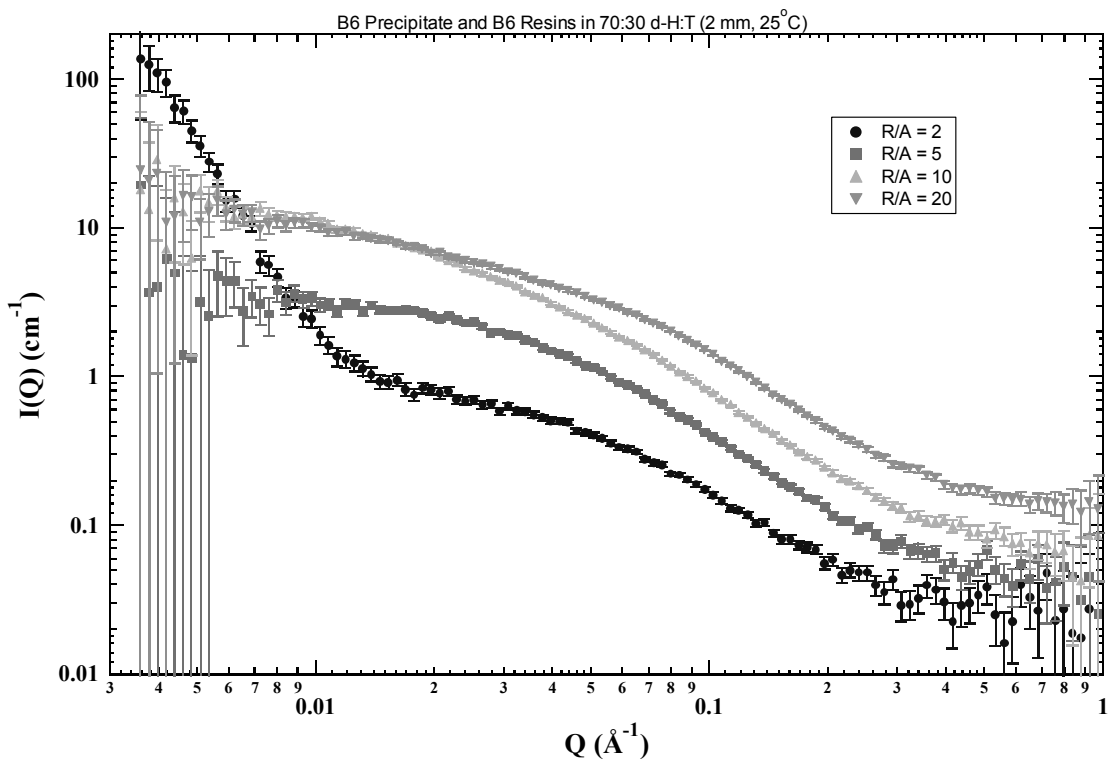


Figure F.7 B6 P asphaltenes (1% wt.) and B6 resins in 70:30 d-H:T (ANL, 2 mm, 25°C).

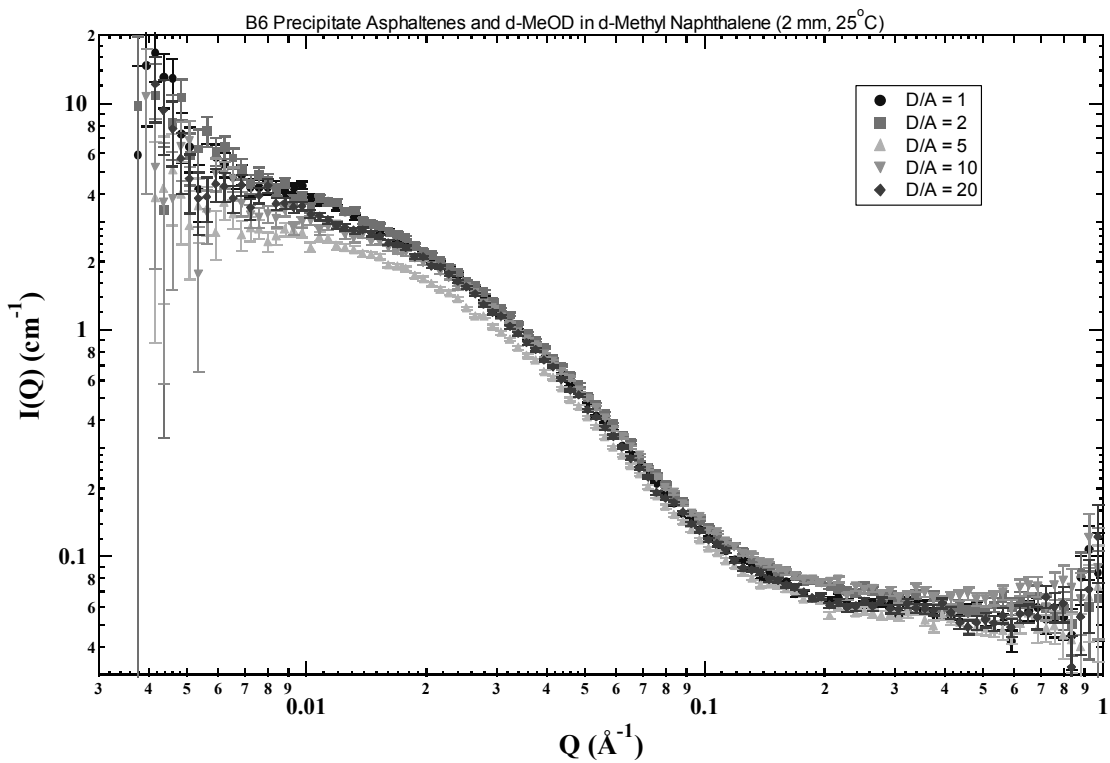


Figure F.8 B6 P asphaltenes (1% wt.) and B6 resins in d-MN (ANL, 2 mm, 25°C).

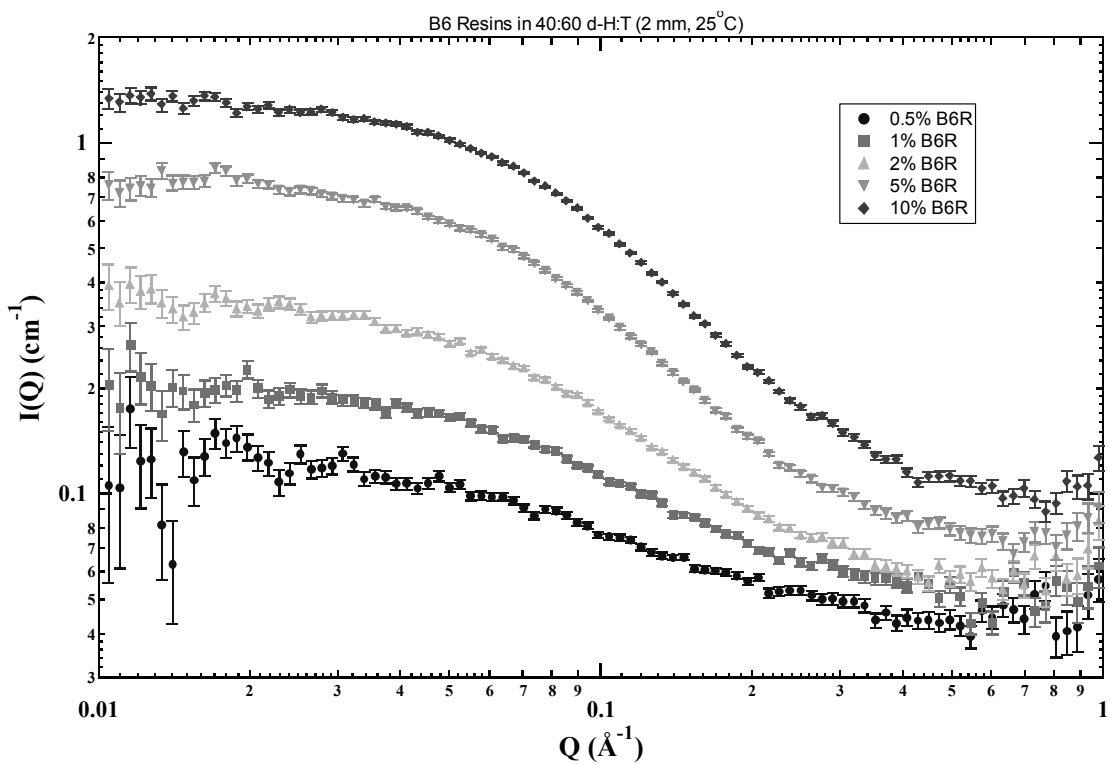


Figure F.9 B6 resins in 40:60 d-H:T (ANL, 2 mm, 25°C).

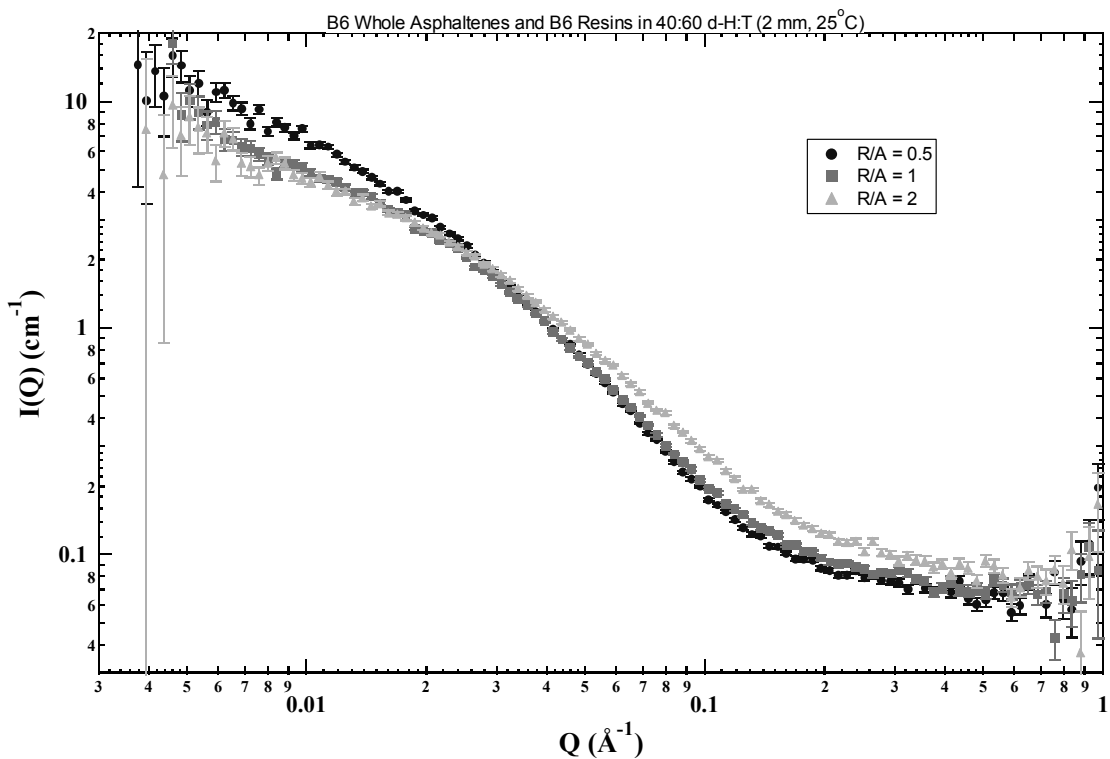


Figure F.10 B6 W asphaltenes (1% wt.) and B6 resins in 40:60 d-H:T (ANL, 2 mm, 25°C).

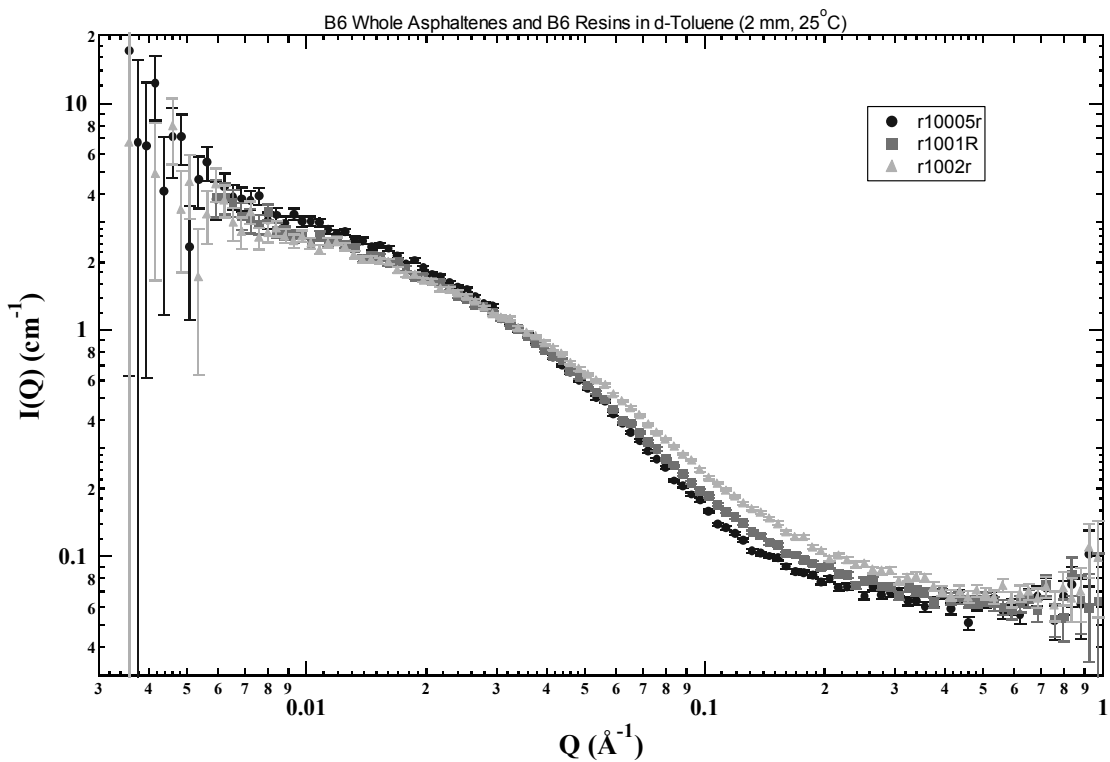


Figure F.11 B6 W asphaltenes (1% wt.) and B6 resins in d-toluene (ANL, 2 mm, 25°C).

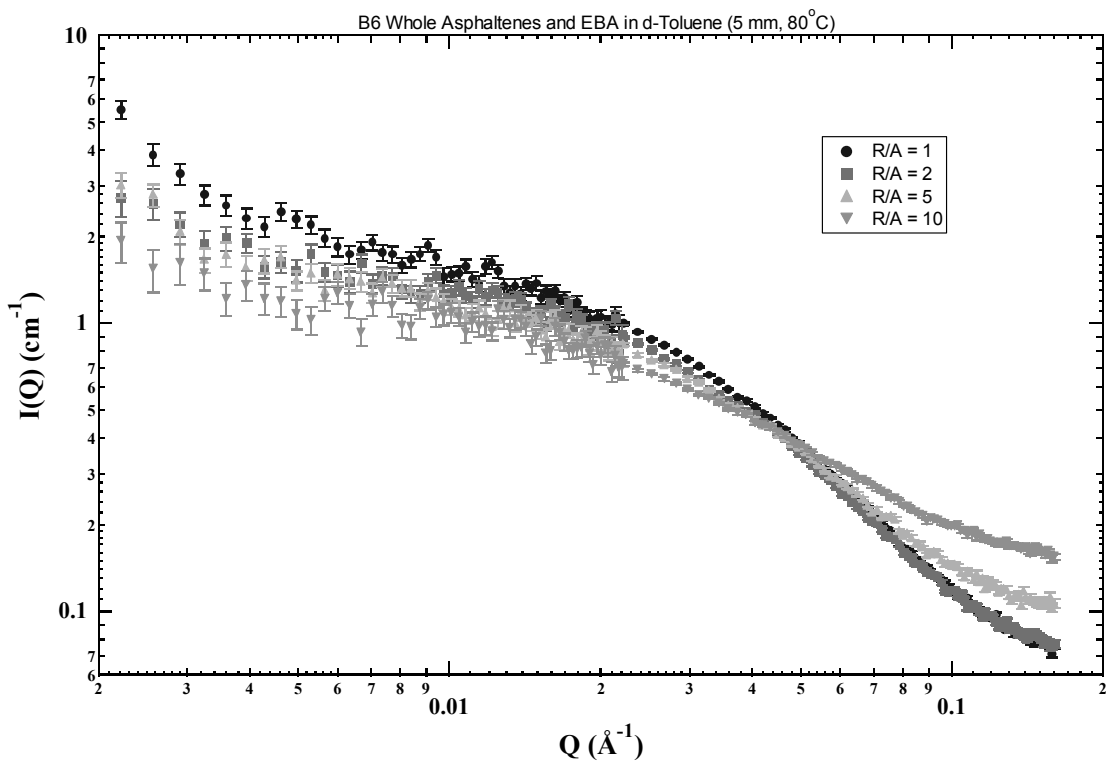


Figure F.12 B6 W asphaltenes (1% wt.) and EBA in d-toluene (NIST, 5 mm, 80°C).

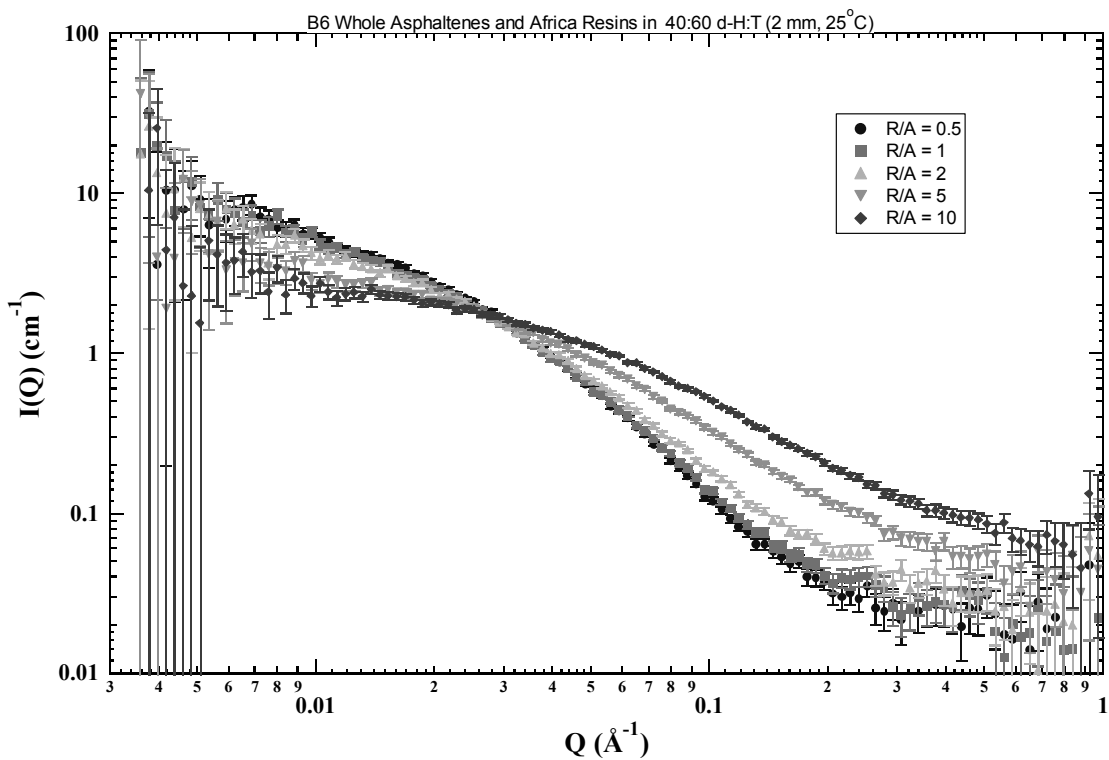


Figure F.13 B6 W asphaltenes (1% wt.) and Africa resins in 40:60 d-H:T (ANL, 2 mm, 25°C).

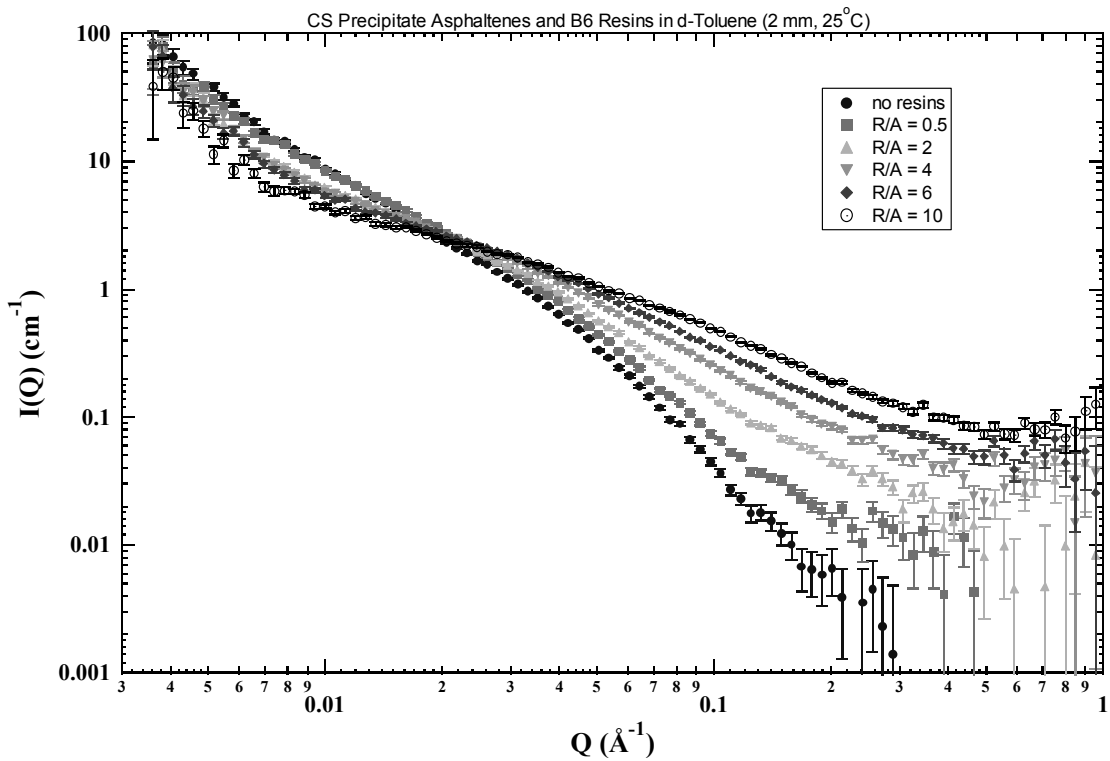


Figure F.14 CS P asphaltenes (1% wt.) and B6 resins in d-toluene (ANL, 2 mm, 25°C).

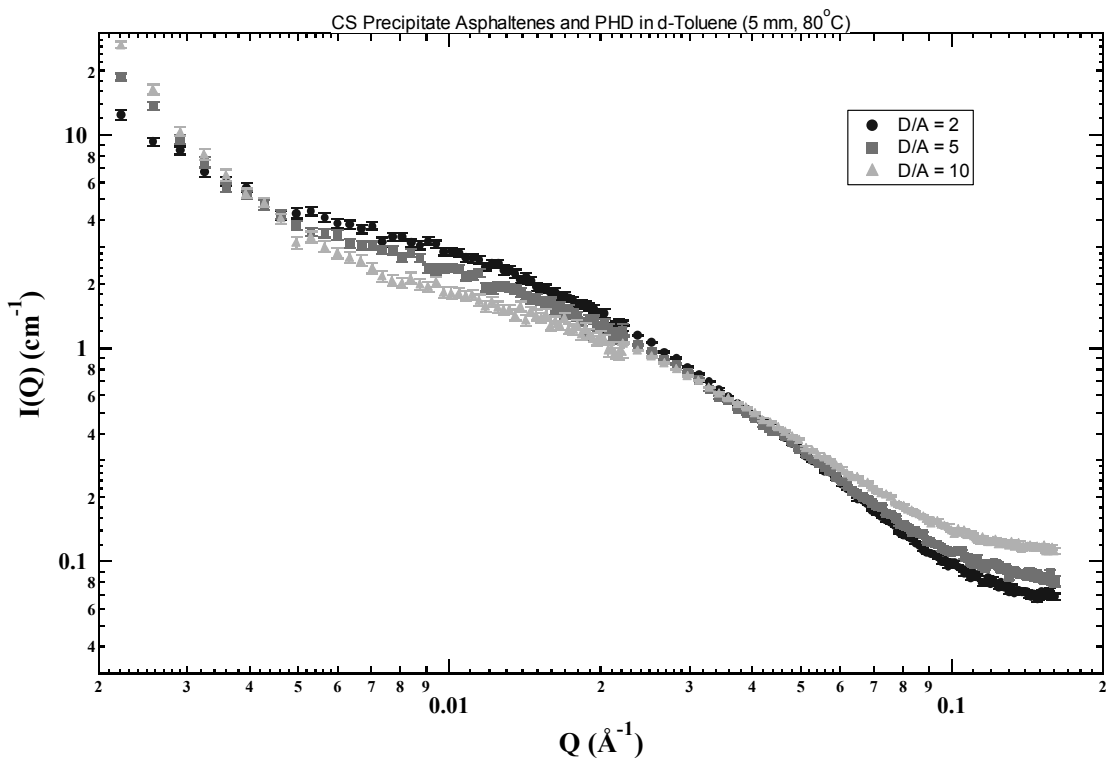


Figure F.15 CS P asphaltenes (1% wt.) and PHD in d-toluene (NIST, 5 mm, 80°C).

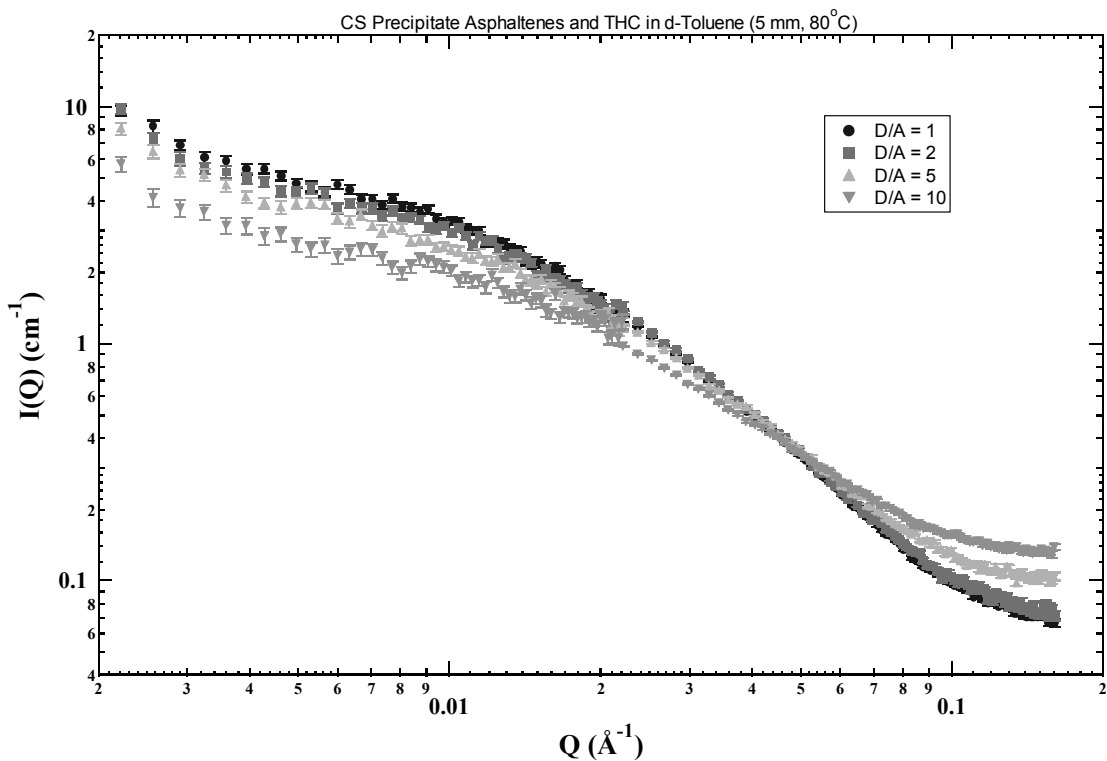


Figure F.16 CS P asphaltenes (1% wt.) and THC in d-toluene (NIST, 5 mm, 80°C).

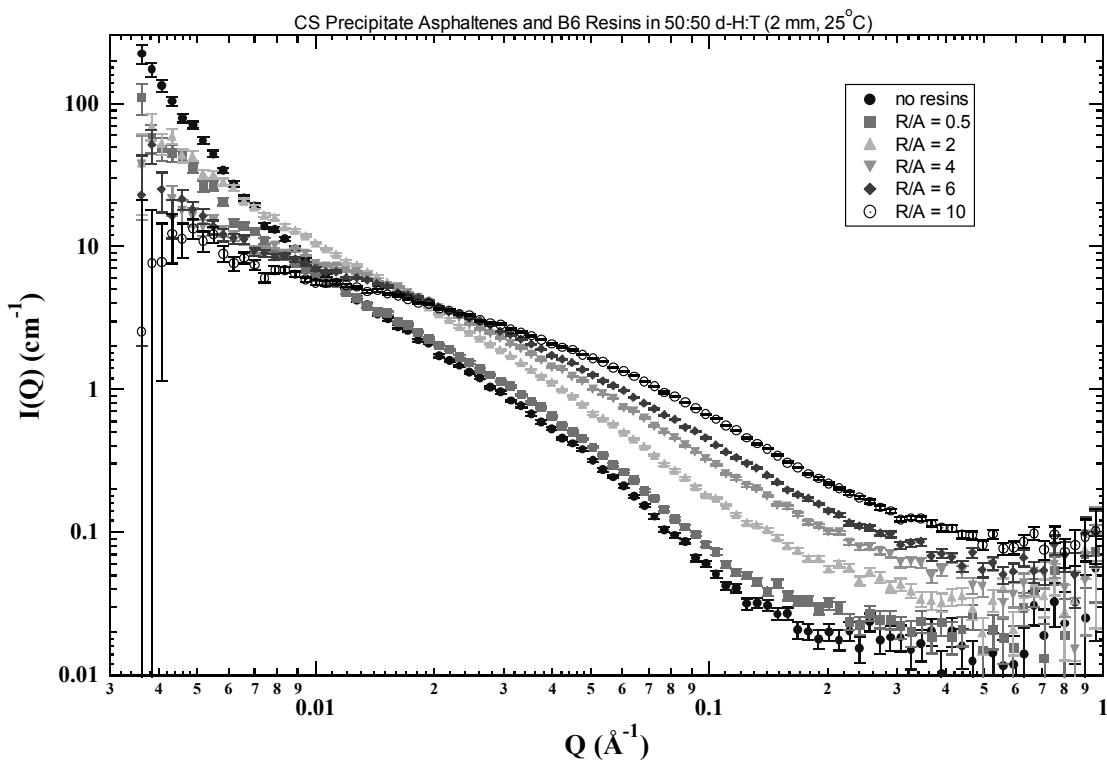


Figure F.17 CS P asphaltenes (1% wt.) and B6 resins in 50:50 d-H:T (ANL, 2 mm, 25°C).

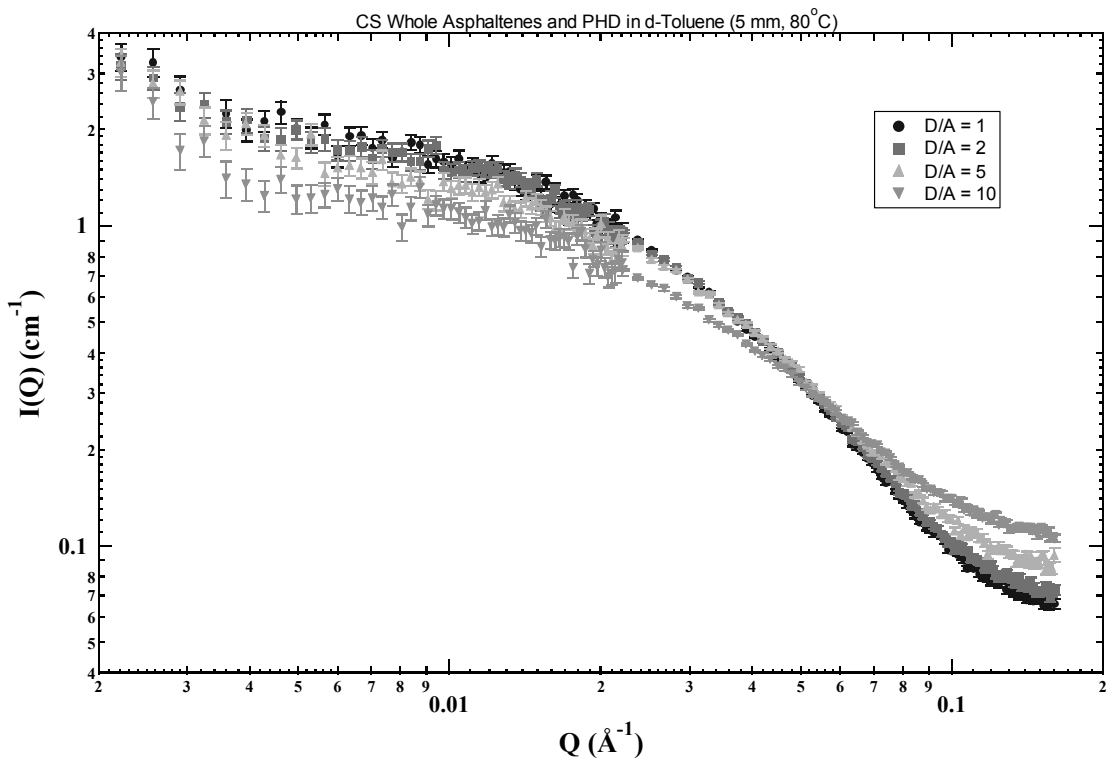


Figure F.18 CS W asphaltenes (1% wt.) and PHD in d-toluene (NIST, 5 mm, 80°C).

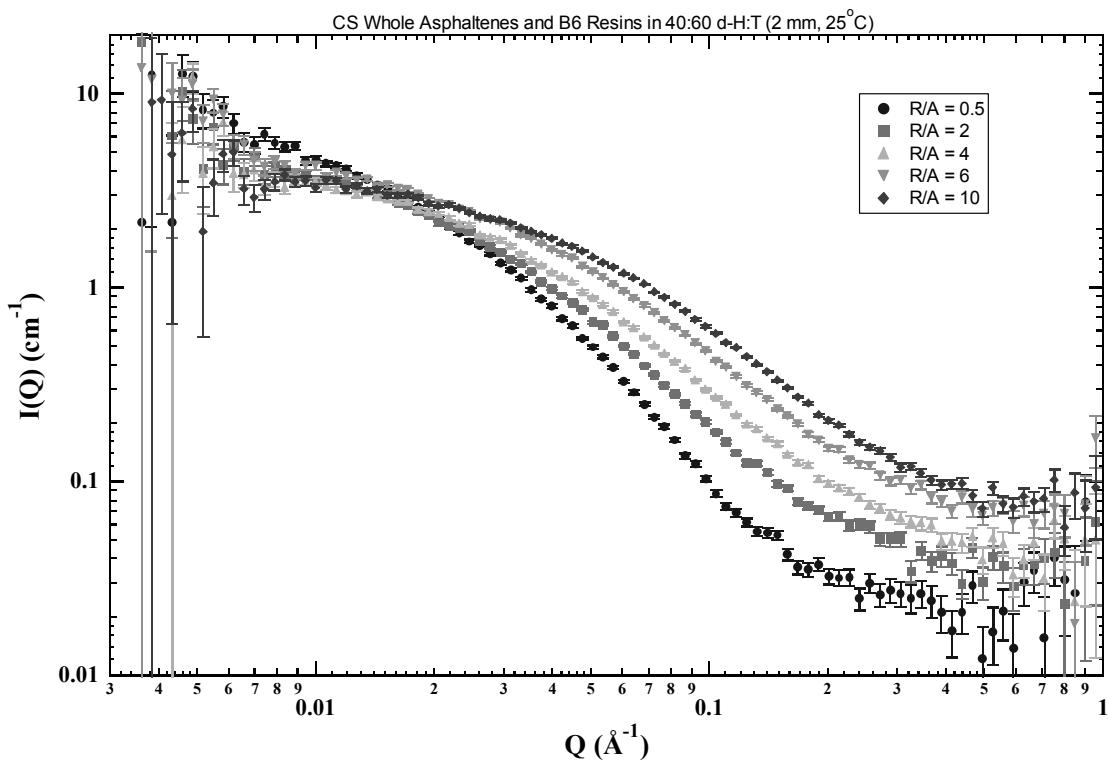


Figure F.19 CS W asphaltenes (1% wt.) and B6 resins in 40:60 d-H:T (ANL, 2 mm, 25°C).

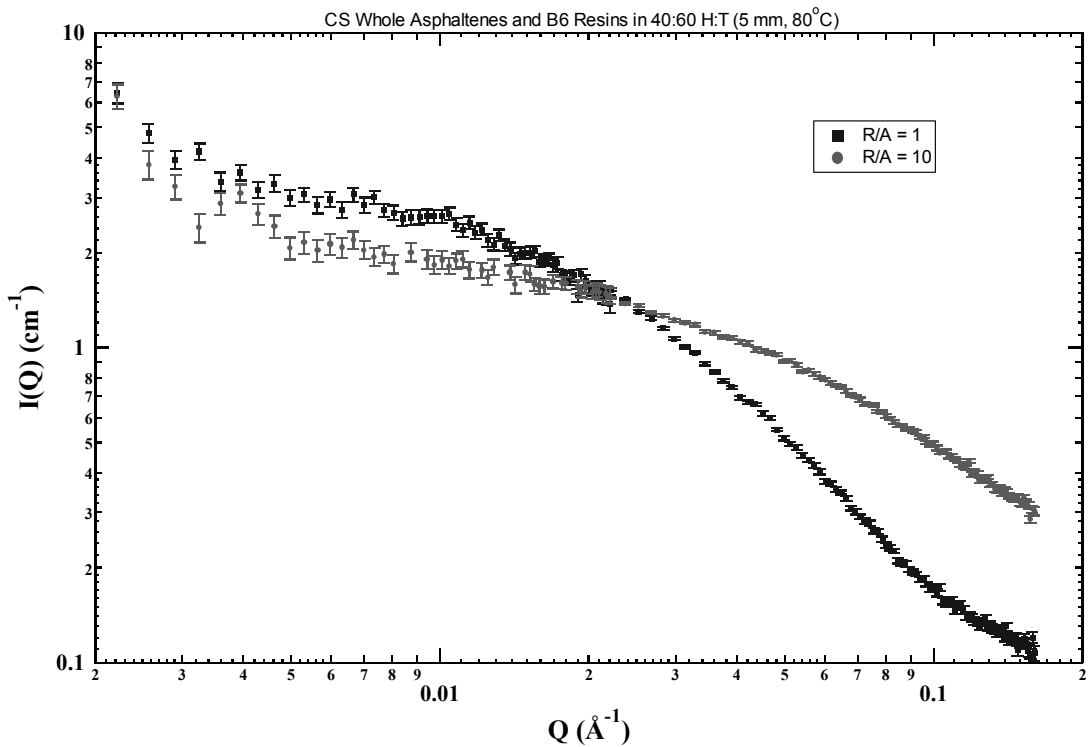


Figure F.20 CS W asphaltenes (1% wt.) and B6 resins in 40:60 d-H:T (NIST, 5 mm, 80°C).

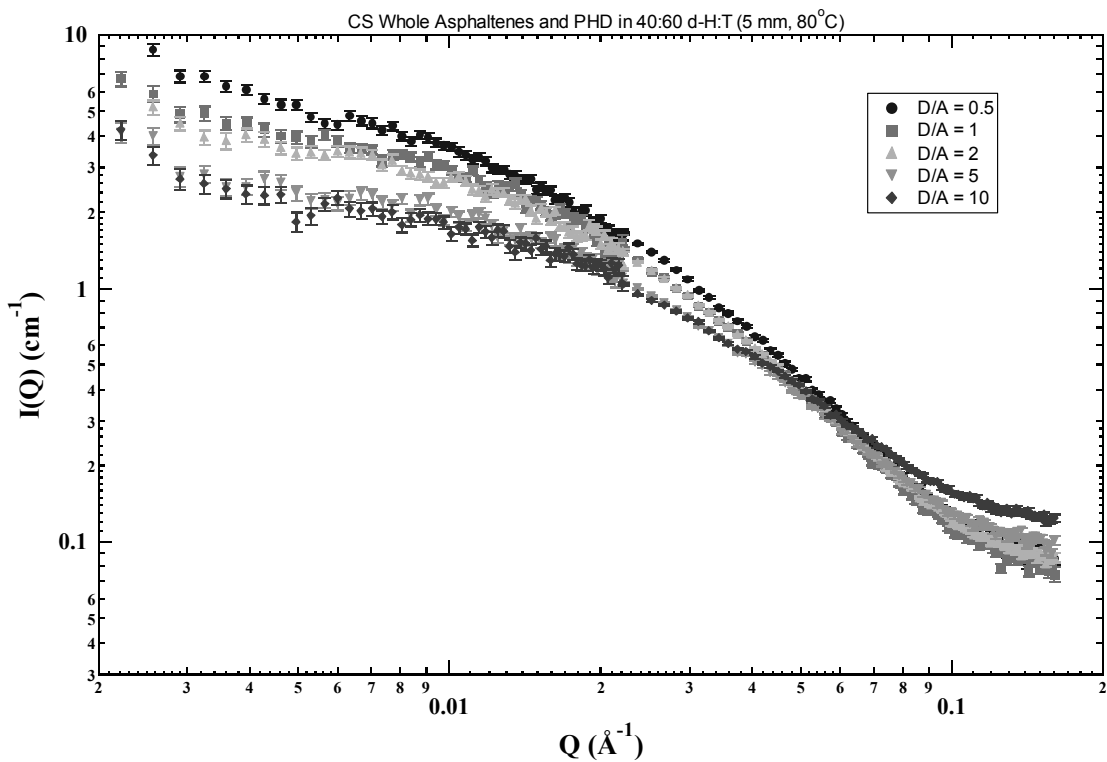


Figure F.21 CS W asphaltenes (1% wt.) and PHD in 40:60 d-H:T (NIST, 5 mm, 80°C).

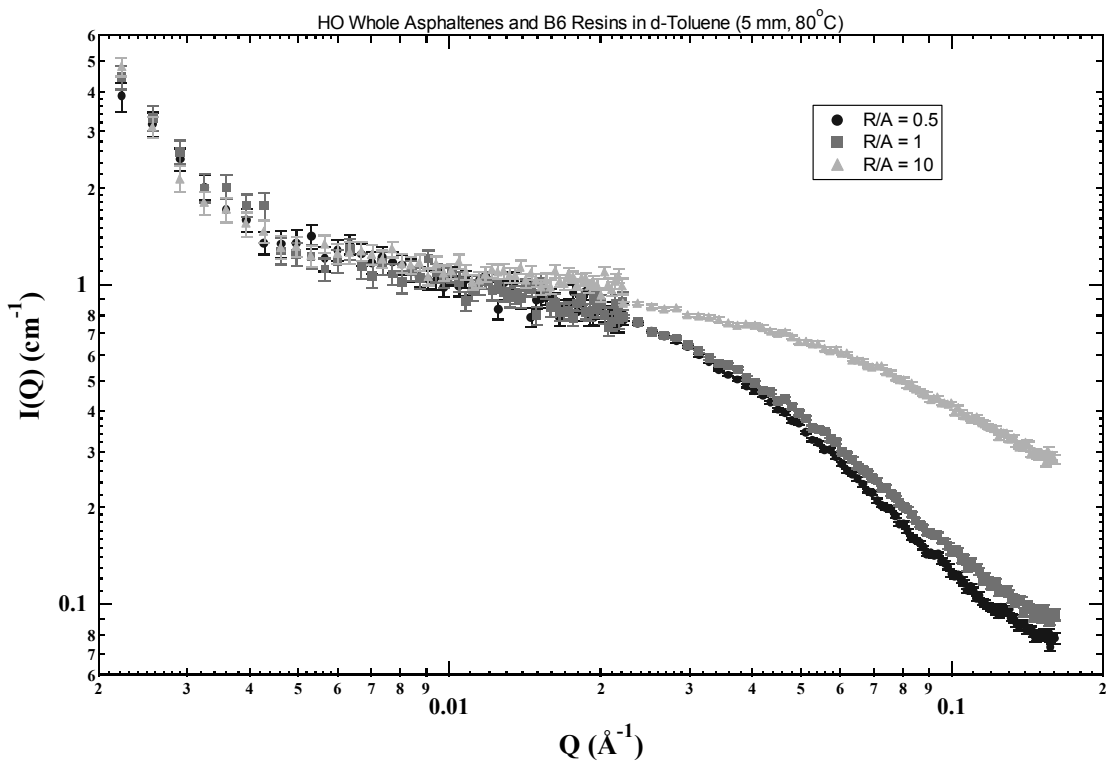


Figure F.22 HO W asphaltenes (1% wt.) and B6 resins in d-toluene (NIST, 5 mm, 80°C).

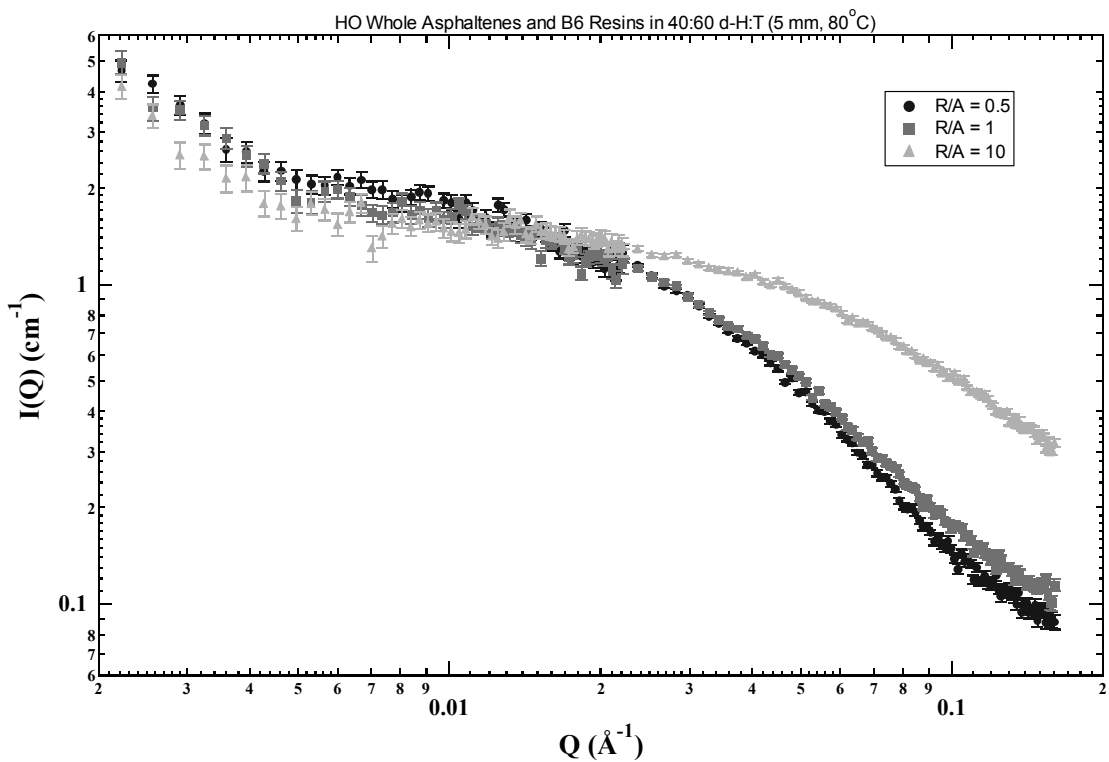


Figure F.23 HO W asphaltenes (1% wt.) and B6 resins in 40:60 d-H:T (NIST, 5 mm, 80°C).

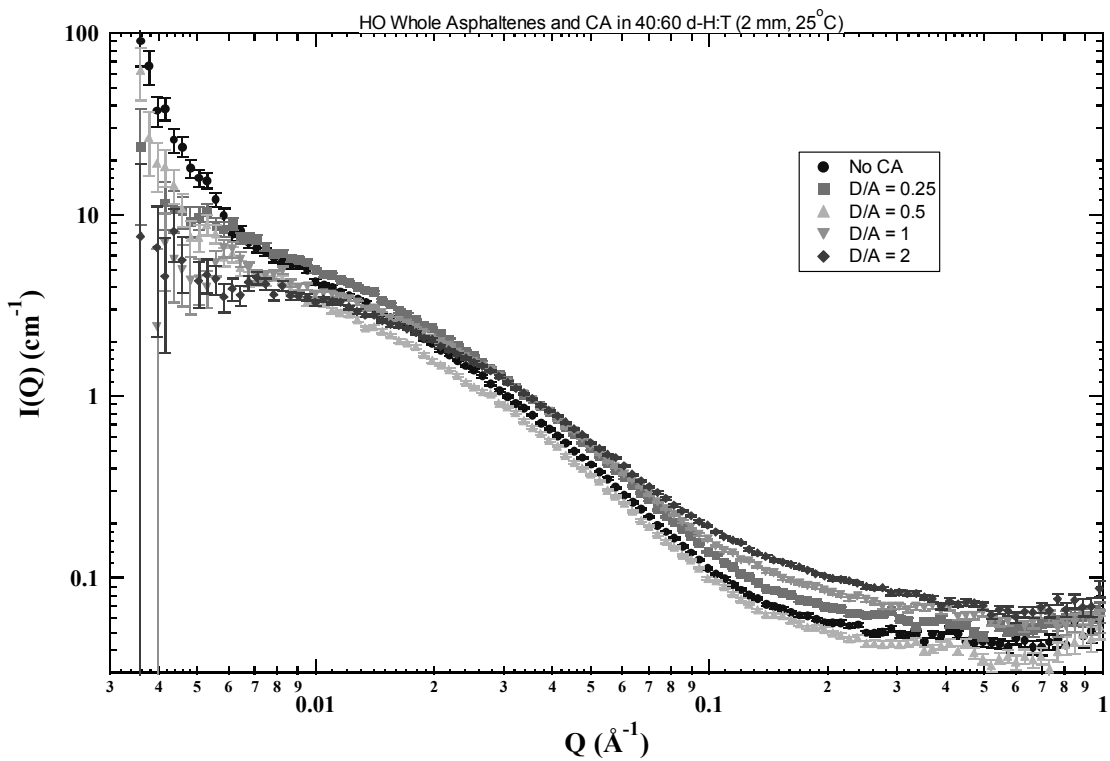


Figure F.24 HO W asphaltenes (1% wt.) and CA in 40:60 d-H:T (ANL, 2 mm, 25°C).

APPENDIX G

PREDICTION OF RESIN PARTITIONING INTO ASPHALTENIC AGGREGATES

Keith L. Gawrys and Peter K. Kilpatrick

G.1 Abstract

In this study, SANS scattering intensity curves were collected for three different asphaltene fractions as a function of resin concentration. The contribution of resins to the coherent scattering in mixed asphaltene-resin aggregates was effectively removed by subtracting the appropriate lineshape (at the given resin concentration and solvent condition) from the scattering intensity curves for the mixed asphaltene and resin solution. Both the unmodified and residual scattering curves after resin subtraction were fit to a Teixeira mass fractal structure factor in order to determine aggregate size, molecular weight, and fractal dimension. Comparison of the molecular weight values for the mixed asphaltene-resin aggregates to the weight-averaged summation of molecular weights from the individual scattering components provided a semi-quantitative estimate of the amount of resin partitioning between asphaltene aggregates and the surrounding medium. Additional studies in which asphaltenes were doped with model compounds that do not contribute to the neutron scattering intensity provided further evidence that interactions with dopant molecules modify the internal structure of the asphaltene aggregates.

G.2 Introduction

Asphaltenes are well known for their tendency to associate in solution and adsorb at interfaces, linking the class of compounds to petroleum production problems such as pipeline deposition and water-in-crude oil emulsion formation. Understanding the composition, molecular structure, and colloidal properties of asphaltenes has been the primary focus of petroleum research over the past several decades. Asphaltenes, the portion of crude oil insoluble in *n*-alkanes (such as *n*-heptane or *n*-pentane), are comprised of a polydisperse mixture of chemically heterogeneous species that can vary greatly from one crude oil to another. Asphaltene molecular structure is generally characterized by the presence of fused ring aromatic moieties, small aliphatic side chains, and polar heteroatom-containing functional groups, as indicated by H/C ratios between 1.0 and 1.2 and N, S, and O contents of

a few weight percent. FTIR analysis reveals several polar functional groups, such as carboxylic acids, carbonyls, phenols, pyrroles, and pyridines, that are capable of participating in proton donor-acceptor interactions [1-5]. Asphaltene aggregates formed in solution vary in size depending on the polydispersity and chemistry of the asphaltene monomers. Previous small angle neutron scattering (SANS) studies on asphaltene solubility fractions suggested that asphaltene aggregation is dominated by the least soluble fraction that is, consequently, the most polar and least aromatic [6,7].

The aggregation mechanism for asphaltenes, similar to that of other well characterized organic compounds of similar structure, is primarily governed by van der Waals dispersion interactions, electrostatic interactions between molecular charges, and orientation dependent repulsive exchange (steric) interactions with lesser contributions stemming from intermolecular charge transfer and weak inductive interactions [8]. Terms describing site-specific interactions, (e.g., hydrogen bonding, acid-base interactions, and aromatic stacking interactions) have also been applied to describe asphaltene aggregation; however, these interactions include contributions from each of the intermolecular forces listed above. A recent proposal based on a review of the current literature suggests that strong specific forces, such as interactions between polar heteroatoms or aromatic moieties, drive asphaltene aggregation while weaker non-specific dispersion forces dominate asphaltene precipitation [9].

Crude oils are typically characterized by SARA fractionation in which the asphaltene fraction is removed by precipitation in a paraffinic solvent and the remaining deasphalted oil is separated into saturates, aromatics, and resins by chromatographic separation [10-14]. Resins constitute the most polar and aromatic fraction of the deasphalted oil and have been shown to co-precipitate with the more aromatic asphaltene fraction after n-heptane addition to crude oils [15]. Resins have also been reported to increase the solubility of asphaltenes in various solvents [16-20]. Although resins are surface-active, they generally do not stabilize water-in-oil emulsions by themselves in model solutions; however, the addition of resins has been shown to reduce the stability asphaltene-stabilized emulsions [20-25]. Among the earliest models for asphaltene stabilization in crude oil was the proposal that asphaltenes form the cores of micelles (or aggregates) peptized (or stabilized) by resin and maltene molecules [26]. Later modifications to the model suggested that the resin adsorption layers

form a gradual and continuous transition from highly aromatic, polar, and high molecular weight core to the less aromatic, non-polar, and lower molecular weight oil phase [16,27]. As proposed by the above models, flocculation of asphaltenes occurred when the solvent conditions reduced the amount of resin material available for adsorption to the asphaltene surface, leading to asphaltene self-interaction.

Further evidence for resin stabilization of asphaltene aggregates is provided by macro-scale dissolution studies that showed asphaltenes from various Alberta crude oils did not redissolve in their corresponding oil fraction after removal of the resin fractions [28]. Redissolution typically occurred with resin addition at resin-to-asphaltene mass ratios similar to the conditions found in the natural crudes. Electrodeposition studies [29], infrared absorption measurements [4], molecular mechanics simulations [30-33], and small-angle X-ray and neutron scattering studies [20, 34] on mixtures of asphaltenes and resins suggest that charge transfer, van der Waals, electrostatic, and repulsive exchange interactions all contribute to the asphaltene-resin aggregation mechanism; however, the extent that individual intermolecular forces participate in these interactions has yet to be determined.

Along with the debate over the asphaltene-stabilization mechanism, various studies suggest that the asphaltene-resin interaction is accompanied by a change in the structure of the asphaltene aggregates. For example, measurements of a hypothetical asphaltene critical micelle concentration (CMC) using a calorimetric titration procedure were performed on toluene solutions of asphaltenes precipitated from different n-alkane solvents at different temperatures [35]. The definition of asphaltenes was considered any material that precipitated from n-heptane at 25°C; therefore, additional material generated from other precipitation methods was assumed to report to the resin fraction. CMC values reduced by the amount of precipitated material were observed to decrease with resin addition, suggesting that asphaltene-resin interactions modify the structure of the asphaltene micelles. Vapor pressure osmometry (VPO) studies on n-pentane (C5) and n-heptane (C7) precipitated Athabasca asphaltenes indicated that the limiting aggregate number-averaged molar mass was higher in the C7-asphaltenes, regardless of solvent, suggesting that the addition of resins reduces the size of asphaltene aggregates [36]. The procedure for n-pentane precipitation of asphaltenes from crude oil invariably generates a higher asphaltene yield than the n-heptane fractionation method with the difference consisting of some portion of native resins. Small-

angle X-ray scattering (SAXS) experiments on toluene solutions of asphaltenes and resins isolated from Safaniya vacuum residue indicated that resins self-interact to form aggregates in solution that are smaller than asphaltenes [34]. After subsequent subtraction of resin contribution to the SAXS scattering intensity of mixed asphaltene-resin solutions, the weight-averaged molecular weight of the residual asphaltene aggregates were observed to decrease significantly with increasing resin content. Volumetric swelling measurements indicated expansion of asphaltenes immersed in solutions of *n*-heptane and native resins compared to solutions of the same asphaltenes in *n*-heptane [37]. Adsorption isotherms for resins on asphaltene particles as determined by UV-vis absorption spectroscopy (400 nm) showed continuous increase in the amount of adsorbed resins with no indication of plateau behavior at high concentrations, suggesting possible resin penetration of asphaltene micropores [37,38].

Based upon this previous experimental evidence, a rough model for resin destabilization of asphaltene aggregates in solution was proposed which entails resin adsorption onto the surface of asphaltene aggregates, surface diffusion into the asphaltene micropores, partial disruption of asphaltene intra-aggregate interactions, and subsequent diffusion of the smaller resin-stabilized asphaltene particle into the bulk solution [37]. A schematic illustration depicting asphaltene aggregates in the absence and presence of stabilizing resins is shown in Figure G.1. Robust thermodynamic models for asphaltene solubility have accounted for resin adsorption onto asphaltene surfaces and suggest resin partitioning between the surface and bulk phases; however, a large number of parameters (and experiments) are required to fit the models [39-42]. More recently, a polymer-like model for asphaltene association has been applied to fit molar mass data obtained from vapor pressure osmometry [43]. The model neglects resin adsorption onto asphaltene surfaces by implicitly assuming that the two species exist in solution as mixed oligomers (aggregates).

The purpose of this paper is to use small-angle neutron scattering (SANS) as a tool for predicting the amount of resin partitioning between asphaltene aggregates and the bulk solution in model crude oil mixtures (i.e., mixtures of *n*-heptane and toluene). Similar studies of resin partitioning have been performed by UV-vis spectroscopic methods, as previously described; however, the solvent was limited to *n*-heptane to prevent dissolution of

the asphaltene solids [37,38]. Knowledge of resin partitioning coefficients in model mixtures may be directly applied to various models for predicting asphaltene solubility.

G.3 Experimental

G.3.1 Sample Preparation and Characterization

Asphaltenes were extracted from B6 (off-shore California) and Canadon Seco (Argentina) crude oil sources by n-heptane precipitation following the standard ASTM D2007-80 method. The total asphaltene yields from B6 and Canadon Seco crude oils were 13.1 and 7.5 % by mass, respectively. B6 crude oil, with a resin-to-asphaltene mass ratio of 0.92, also served as the source for the petroleum resins used in the experiments. Petroleum resins were isolated via the SARA technique by which deasphalted oil was charged to silica gel and extracted with solvents of increasing polarity [11-13,44]. The B6 asphaltenes were further separated into more and less soluble asphaltenic fractions (i.e., so-called “Soluble” and “Precipitate” fractions, respectively) by precipitation of the original “Whole” asphaltenes (1 % wt.) in a 60:40 (v/v) mixture of heptane in toluene. The fractionation of B6 Whole asphaltenes generated an approximate 1:2 mass fraction split of Precipitate:Soluble asphaltenes. Furthermore, the two fractions differed significantly in terms of chemical composition and physical properties [7]. Additional procedural details for the precipitation and fractionation of asphaltenes and the isolation of petroleum resins can be found in previous works [7,20]. Combustion elemental analysis (Carlo Erba EA 1108) was performed on the asphaltene and resin fractions at the University of Alberta (Department of Chemistry, Edmonton, Alberta, Canada). A summary of the chemical composition of the asphaltene and resin samples is provided in Table G.1.

G.3.2 Small-Angle Neutron Scattering

Small-angle neutron scattering (SANS) experiments were performed at two locations. The SANS measurements for the solutions of B6 resins in mixtures of d-heptane and d-toluene were performed on the 8 m, NG1 small-angle scattering instrument at the National Institute of Standards and Technology Center for Neutron Research (Gaithersburg, MD). The neutron wavelength was 8.4 Å with a wavelength spread (fwhm) $\Delta\lambda/\lambda$ of 0.25. The sample-to-detector distance was 3.84 m with the detector offset by 3.5° from the incident beam to obtain

larger scattering angles. The available Q-range for the measurements was 0.007 to 0.126 Å⁻¹. The remaining SANS experiments were performed on the Small-Angle Neutron Diffractometer (SAND) instrument at the Intense Pulsed Neutron Source at Argonne National Laboratory (Argonne, IL). SAND is a time-of-flight diffractometer attached to an accelerator-based pulsed neutron source (30 Hz). Each pulse contained neutrons with wavelengths ranging from 1 to 14 Å. The higher energy neutrons had lower wavelengths and reached the sample ahead of the lower energy neutrons. Thus, the energy of each scattered neutron was determined by its “time-of-flight” to the detector. The sample-to-detector distance was fixed at 2 m. Neutrons were collected on an area detector (40 cm by 40 cm, 4 to 6 mm FWHM resolution). The available Q range extended from 0.0035 to 2 Å⁻¹. Mixtures of asphaltenes and resins were prepared in 40:60 d-heptane:d-toluene (v/v) or in d-toluene at a fixed asphaltene concentration (1 % wt.) with resin:asphaltene (R/A) mass ratios varying from 0 to 10:1. Similar solutions of B6 resins in the absence of asphaltenes were prepared in 60 % and 100 % toluene at the following concentrations: 0.5, 1, 2, 4, 5, 6, and 10 % wt. Per-deuterated toluene and heptane (CDN Isotopes, 99.9 % purity, 99.5 % perdeuteration) solvents were used to obtain a maximum scattering contrast between the solvent and solutes. Asphaltenes and resins were initially dissolved in d-toluene, followed by d-heptane addition and equilibration over several days. Prior to measurement, the solutions were transferred from glass vials into quartz cells (NGS Precision) of 2 mm path length. All samples were measured at ambient conditions. The scattering intensity, I(Q), was obtained from the total detector counts corrected for neutron transmission through the sample, background radiation, scattering through an empty cell, and detector sensitivity. All data were converted to an absolute scale with reference to standard polymer samples.

G.3.3 Data Analysis

In order to effectively remove the contribution of resins to the coherent scattering of asphaltene-resin mixtures, an attempt was made to model the scattering intensity of the pure resin solutions over the entire Q range studied. The scattering intensity curves for the B6 resins were similar to those previously observed for asphaltene solutions [7] and it was reasonable to fit the pure resin scattering data to a lineshape containing the following

scattering contributions: 1) an incoherent scattering term; 2) a Lorentzian term; and 3) a Porod-like power law. This modified Lorentzian lineshape has the form [45]:

$$I(Q) = \frac{I_1}{Q^n} + \frac{I_0}{1+Q^2\xi^2} + I_{incoh} \quad (1)$$

The incoherent scattering term (I_{incoh}) is independent of Q and reflects isotropic background scattering from all nuclei with non-zero spins, particularly hydrogen, which is most abundant in the samples. The Lorentzian term describes coherent scattering from the resin aggregates and is has previously been applied to scattering intensity curves for asphaltenes in good solvents containing a low Q Guinier plateau [7,20,45-50]. The Lorentian lineshape (or Zimm formula) has the form:

$$I(Q) = \frac{I_0}{1+Q^2\xi^2} \quad (2)$$

where I_0 is the coherent scattering intensity extrapolated to zero- Q and ξ is the aggregate correlation length. The correlation length is related to the z-average radius of gyration of a particle, R_{GZ} , by the expression:

$$\xi = \sqrt{\frac{1}{3}}R_{GZ} \quad (3)$$

The Porod-like power law term [$I_{surf} (Q_1/Q)^n$] describes surface scattering from the aggregates in samples exhibiting a low Q upturn where I_{surf} is the intensity of surface scattering at the lowest available wave vector Q_1 and n is the power law exponent [45]. The quantity, $I_{surf} Q_1^n$, is combined into a single parameter, I_1 , in Equation 1.

During the subsequent analyses, the scattering intensity curves for the pure components, asphaltene-resin mixtures, and the residual aggregates (i.e., after subtraction of the resin contribution) were fit to the Teixeira mass fractal structure factor [51-54] given by:

$$I(Q) = \frac{I_0 \sin[(D-1) \tan^{-1}(Q\xi)]}{(D-1)Q\xi(1+Q^2\xi^2)^{(D-1)/2}} \quad (4)$$

where D is the fractal dimension, a value describing the scaling behavior of aggregate size with molecular weight ($M \sim \xi^D$). In the limit that $D = 2$, the Teixeira model reduces to the more commonly used Zimm formula.

In order to apply the Teixeira model, the available Q range for the samples was truncated to remove contributions from incoherent scattering and low Q Porod-like scattering. For most of the scattering intensity curves, the transition from coherent to incoherent scattering approximately occurred in the Q range between 0.10 and 0.17 Å⁻¹. In the low Q range, the transition from Porod-like scattering to nanoparticle aggregate scattering approximately occurred between 0.01 and 0.03 Å⁻¹. The upper and lower bounds of the Teixeira model fits were initially fixed between 0.01 ≤ Q ≤ 0.10 Å⁻¹. The upper bound remained fixed while the value of Q at the lower bound was increased point-by-point until the apparent aggregate fractal dimension no longer varied significantly with Q, implying that contributions from Porod-like scattering have been eliminated. The fractal dimension was less sensitive to changes in the value of Q at the upper bound. Therefore, once the value of Q at the lower bound was determined, the upper bound was increased point-by-point until the value of χ^2 was minimized (i.e., with minimal changes in the apparent fractal dimension). The Teixeira model was applied to all samples over the range of Q values between the upper and lower bounds as determined by the above methods to obtain values for the aggregate I_0 , ξ , and D .

The zero-Q scattering intensity (I_0) values were subsequently used to determine the weight-average molecular weight (M) of the aggregates through the relation:

$$I_0 = \frac{\phi MC (\rho_{solute} - \rho_{solvent})^2}{d_a^2 N_{Av}} \quad (5)$$

where ϕ is the solute volume fraction, C is the concentration of scatters in solution (w/w), ρ_{solute} is the scattering length density of the solute, $\rho_{solvent}$ is the scattering length density of the solvent, d_a is the mass density of the scatterers, and N_{Av} is the Avogadro number. Mass densities of asphaltene and resin solutions in toluene were measured using a 2 mL pycnometer and were used to approximate d_a . Asphaltene and resin dry mass density (d_m) values of 1.15 g/cm³ and 1.0 g/cm³, respectively, were calculated by extrapolating the solution data to pure solute. Average structural formulas were calculated for the resins and asphaltenes using the elemental analysis results from Table G.1. Coherent scattering length densities of the solvent and solute were calculated from the average structural formulas according to the relationship:

$$\rho = d_m \sum_i b_i \frac{x_i}{m_i} \quad (6)$$

where b_i , x_i , and m_i are the scattering length, mass fraction, and atomic mass of species i , respectively. The coherent scattering length density for mixed asphaltene-resin solutes were determined by volume averaging of the medium density and average structural formulas based on the solution concentrations of asphaltenes and resins.

The Teixeira model was directly applied to the scattering intensity curves for the pure asphaltene, pure resin, and mixed asphaltene-resin solutions to obtain the parameters I_{0i} , ξ_i , and D_i where the subscript i is denoted by A, R, or AR, respectively. The aggregate molecular weight values for the pure asphaltene (M_A) and pure resin (M_R) solutions were determined (Equation 5) using the I_{0i} , C , and ρ_{solute} values for the pure components. Aggregate molecular weight values for the mixed asphaltene-resin solutions (M_{AR}) were determined using the same equation, except C and ρ_{solute} represented the combined asphaltene and resin solution concentration and scattering length density, respectively.

A flowchart depicting additional analyses for the mixed asphaltene-resin scattering intensity curves is shown in Figure G.2. The resin contribution to the coherent scattering in the mixed asphaltene-resin solutions was removed by direct subtraction of the appropriate resin lineshape described by Equation 1 (i.e., at the same resin concentration and solvent conditions) from the scattering intensity curves for the mixed aggregates. The residual scattering intensity curves after resin subtraction were fit to the Teixeira model to obtain the parameters I_{0Res} , ξ_{Res} , and D_{Res} . Two different molecular weight values were determined from I_{0Res} (Equation 5) by making different assumptions concerning the aggregate composition. First, the residual aggregates were assumed to consist of only asphaltene molecules. The corresponding value of the molecular weight ($M_{Res,A}$) for the residual aggregates was calculated using C and ρ_{solute} values for pure asphaltenes. The second scenario assumed that the residual aggregates consisted of a 3:1 mass ratio of resins-to-asphaltenes. The molecular weight ($M_{Res,AR}$) for the residual aggregate was calculated using values for C and ρ_{solute} that accounted for this mixture of asphaltenes and resins.

G.4 Results and Discussion

SANS scattering intensity curves were collected for three different asphaltene fractions as a function of resin concentration: B6 Whole asphaltenes in 60 % toluene, CS Whole asphaltenes in 60 % toluene, and B6 Precipitate asphaltenes in 100 % toluene. As an example, Figure G.3 provides SANS scattering intensity curves for four mixtures of B6 Whole asphaltenes (1 % wt.) in 60 % toluene with varying concentrations of B6 resins (0, 2, 6, and 10 % wt.). As shown in the figure, the scattering intensity at the highest Q-values (i.e., $Q > 0.1$) increased significantly with resin content, suggesting a decrease in the average aggregate size. This decrease in the average aggregate size does not necessarily imply that the resins are modifying the asphaltene aggregates, because pure resin solutions were also observed to contribute to the coherent scattering intensity in this Q-range. The reduction in the average aggregate size may be trivially explained by a weighting of the aggregates toward smaller molecules (i.e., resins) in solution. Bardon et al. observed similar behavior for mixtures of asphaltenes and resins extracted from Safaniya vacuum residue [34]. Furthermore, Bardon et al. compared the scattering intensity curve for the asphaltene-resin mixture to the sum of the scattering intensities for solutions of pure asphaltenes and pure resins at the appropriate concentrations. Since the sum of the pure component scattering intensities was larger than the scattering intensity of the mixture, they concluded that the resin molecules modified the asphaltene aggregates by reducing of the asphaltene aggregate size and molecular weight. With the addition of 16 % wt. resins, Bardon et al. observed a significant reduction in the asphaltene molecular weight from 105 kDa (no resins) to 14 kDa.

This study also quantifies the extent of asphaltene aggregate size reduction with the addition of resins through comparison of aggregate molecular weights; however, additional insight into the nature of the asphaltene-resin interaction is obtained through weight-averaging the summation of molecular weight values from the individual scattering components. In the earlier study, Bardon et al. assumed the residual scattering curve after subtraction of the resin scattering pattern only contained contributions from the modified asphaltene aggregates [34]. A more reasonable scenario would suggest that the residual scattering curve contains contributions from the modified asphaltenes and resin molecules intercalated into the asphaltene aggregate structure.

As previously described, additional scattering intensity curves were collected for B6 resins in 60 % toluene and 100 % toluene as a function of concentration and fit to a modified Lorentzian lineshape to model the scattering behavior over the entire Q range studied. An example fit of the scattering intensity curve for B6 resins (10 % wt.) in 60 % toluene to the resin lineshape (Equation 1) is shown in Figure G.4. A summary of the fit parameters for the remaining resin solutions in 100 % and 60 % toluene is provided in Table G.2. Since no significant low Q Porod-like upturn was observed at resin concentrations below 2 % wt, the Porod-like power law contribution was neglected in these instances. The objective of this study is to determine how the addition of resins modifies the asphaltene aggregates. The parameters shown in the table were inserted into Equation 1 to calculate the resin contribution to the coherent scattering intensity at each Q value measured for the mixed asphaltene-resin solutions. Direct subtraction of the resin contribution from the mixed asphaltene-resin scattering intensity at each Q value provided the residual scattering intensity curve used for the subsequent analyses.

An example of the scattering intensity curves for solutions obtained for B6 Whole asphaltenes (1 % wt.) and B6 resins (4 % wt.) in 60 % toluene are shown in Figure G.5. The figure contains scattering intensity curves for pure asphaltenes (Δ), pure resins (\circ), and for the mixed asphaltene-resin solution (\square). The residual scattering curve (\diamond) was generated by direct subtraction of the resin contribution from the mixed aggregates as described above. The parameters obtained by fitting the various scattering intensity curves to the Teixeira model are also shown. The correlation length of the residual aggregates (40 Å) was significantly smaller than that observed for the pure asphaltene solution (64 Å), suggesting that the addition of resins modifies the asphaltene aggregation behavior. Similar reductions in the aggregate I_0 (and M) values were also observed. This was consistent with the results previously reported by Bardon et al. [34].

A summary of the Teixeira fit parameters for all of the data collected is presented in Table G.3.

The 3:1 R:A model is consistent with the asphaltene stabilization model proposed by Leon et al. [37] (i.e., formation of an adsorbed resin layer, penetration in the asphaltene

micropores, partial dissolution of the asphaltene aggregate, and diffusion of the mixed particle into solution).

G.5 Acknowledgements

This research has been supported by PERF 97-07, Industrial Emulsion Consortium, ExxonMobil, Shell, ChevronTexaco, Ondo-Nalco, and the National Science Foundation (CTS9817127). This work benefited from the use of facilities in the Intense Pulsed Neutron Source and the Chemistry Division, which is funded by the U. S. Department of Energy, Office of Basic Energy Sciences under contract W-31-109-ENG-38 to the University of Chicago. We acknowledge the support of the National Institute of Standards and Technology, U.S. Department of Commerce, in providing the neutron research facilities used in this work. Many thanks to Pappannan Thiyagarajan and Denis Wozniak at Argonne National Laboratory and Min Lin at the NIST Center for Neutron Research for their assistance with the SANS instruments. We would also like to thank Marit-Helen Ese, Wilhelm Glomm, Matthew Smith, Tianxi Zhang, and George Blankenship for helping with the sample preparation and SANS data collection. We appreciate Darlene Mahlow at the University of Alberta, Department of Chemistry for performing elemental analyses on the asphaltene and resin samples.

G.6 References

1. R. V. Barbour, J. C. Petersen, "Molecular Interactions of Asphalt: An Infrared Study of the Hydrogen-Bonding Basicity of Asphalt," *Analytical Chemistry*, 1974, **46**(2): p. 273-277.
2. M. M. Boduszynski, J. F. McKay, D. R. Latham, "Asphaltenes, Where Are You?," *Proceedings of the Association of Asphalt Paving Technologists*, 1980, **49**: p. 123-143.

3. T. Ignasiak, O. P. Strausz, D. S. Montgomery, "Oxygen Distribution and Hydrogen Bonding in Athabasca Asphaltene," *Fuel*, 1977, **56**: p. 359-365.
4. S. E. Moschopedis, J. G. Speight, "Investigation of Hydrogen Bonding by Oxygen Functions in Athabasca Bitumen," *Fuel*, 1976, **55**: p. 187-192.
5. J. C. Petersen, "An Infra-red Study of Hydrogen Bonding in Asphalt," *Fuel*, 1967, **46**(4-5): p. 295-305.
6. V. Szewczyk, F. Behar, E. Behar, M. Scarsella, "Evidence of the physicochemical polydispersity of asphaltenes," *Rev. Inst. Fr. Pet.*, 1996, **51**(4): p. 575-590.
7. P. M. Spiecker, K. L. Gawrys, P. K. Kilpatrick, "Aggregation and solubility behavior of petroleum asphaltenes and their subfractions," *Journal of Colloid and Interface Science*, *in press*: p.
8. J. Murgich, "Intermolecular forces in aggregates of asphaltenes and resins," *Petroleum Science and Technology*, 2002, **20**(9-10): p. 983-997.
9. G. Porte, H. G. Zhou, V. Lazzeri, "Reversible description of asphaltene colloidal association and precipitation," *Langmuir*, 2003, **19**(1): p. 40-47.
10. W. R. Middleton, "Gradient Elution Chromatography Using Ultraviolet Monitors in the Analytical Fractionation of Heavy Petroleum," *Analytical Chemistry*, 1967, **39**(14): p. 1839-1846.
11. R. Miller, "Hydrocarbon Class Fractionation with Bonded-Phase Liquid Chromatography," *Analytical Chemistry*, 1982, **54**(11): p. 1742-1746.
12. J. G. Reynolds, "Characterization of Heavy Residua by Application of a Modified D 2007 and Asphaltene Separation: Effect of Solvents on Physical and Chemical Properties of Fractions Derived From Hondo 850°F Residuum," *Fuel Science and Technology International*, 1987, **5**(5): p. 593-620.
13. M. F. Ali, A. Bukhari, M. U. Hasan, "Structural Characterization of Arabian Heavy Crude Oil Residue," *Fuel Science and Technology International*, 1989, **7**(8): p. 1179-1208.
14. M. Alula, M. Diack, R. Gruber, G. Kirsch, J. C. Wilhelm, D. Cagniant, "Efficiency of Sequential Elution Solvent Chromatography-Extrography Technique for the Characterization of Hydroliquefaction and Pyrolysis Products," *Fuel*, 1989, **68**(10): p. 1330-1335.
15. S. Acevedo, B. Mendez, A. Rojas, I. Layrisse, H. Rivas, "Asphaltenes and Resins From the Orinoco Basin," *Fuel*, 1985, **64**: p. 1741-1747.

16. J. M. Swanson, "A Contribution to the Physical Chemistry of the Asphalts," *Journal of Physical Chemistry*, 1942, **46**: p. 141-150.
17. G. Hotier, M. Robin, "Action de Divers Diluants sur les Produits Petroliers Lourds: Mesure, Interpretation et Prevision de la Flocculation des Asphaltenes," *Revue de L'Institut Francais du Petrole*, 1983, **38**(1): p. 101-120.
18. A. Hirschberg, L. N. J. deJong, B. A. Schipper, J. G. Meijer, "Influence of Temperature and Pressure on Asphaltene Flocculation," *Society of Petroleum Engineers Journal*, 1984, (June): p. 283-293.
19. N. F. Carnahan, J. L. Salager, R. Anton, A. Davila, "Properties of resins extracted from Boscan crude oil and their effect on the stability of asphaltenes in Boscan and Hamaca crude oils," *Energy & Fuels*, 1999, **13**(2): p. 309-314.
20. P. M. Spiecker, K. L. Gawrys, C. B. Trail, P. K. Kilpatrick, "Effects of petroleum resins on asphaltene aggregation and water-in-oil emulsion formation," *Colloid. Surface. A*, 2003, **220**: p. 9-27.
21. H. Fordedal, Y. Schildberg, J. Sjoblom, J.-L. Volle, "Crude Oil Emulsions in High Electric Fields as Studied by Dielectric Spectroscopy. Influence of Interaction Between Commercial and Indigenous Surfactants," *Colloids and Surfaces A: Physicochemical and Engineering Aspects*, 1996, **106**: p. 33-47.
22. H. Fordedal, Ø. Midttun, J. Sjöblom, O. K. Kvalheim, Y. Schildberg, J.-L. Volle, "A Multivariate Screening Analysis of W/O Emulsions in High External Electric Fields as Studied by Means of Dielectric Time Domain Spectroscopy, II," *Journal of Colloid and Interface Science*, 1996, **182**: p. 117-125.
23. O. V. Gafonova, H. W. Yarranton, "The stabilization of water-in-hydrocarbon emulsions by asphaltenes and resins," *Journal of Colloid and Interface Science*, 2001, **241**(2): p. 469-478.
24. R. A. Mohammed, A. I. Bailey, P. F. Luckham, S. E. Taylor, "Dewatering of Crude Oil Emulsions 2. Interfacial Properties of the Asphaltic Constituents of Crude Oil," *Colloids and Surfaces A: Physicochemical and Engineering Aspects*, 1993, **80**: p. 237-242.
25. J. D. McLean, P. K. Kilpatrick, "Effects of Asphaltene Solvency on Stability of Water-in-Crude Oil Emulsions," *Journal of Colloid and Interface Science*, 1997, **189**: p. 242-253.
26. F. J. Nellensteyn, The colloidal structure of bitumens, in "The Science of Petroleum" (A. E. Dunstan and A. W. Nash, Eds.), Oxford University Press, London, 1938; pp 2760-2763.

27. J. P. Pfeiffer, R. N. J. Saal, "Asphaltic Bitumen as Colloid System," *Journal of Physical Chemistry*, 1940, **44**: p. 139-149.
28. J. A. Koots, J. G. Speight, "Relation of Petroleum Resins to Asphaltenes," *Fuel*, 1975, **54**(3): p. 179-184.
29. S. E. Taylor, "The electrodeposition of asphaltenes and implications for asphaltene structure and stability in crude and residual oils," *Fuel*, 1998, **77**(8): p. 821-828.
30. E. Rogel, "Simulation of interactions in asphaltene aggregates," *Energy & Fuels*, 2000, **14**(3): p. 566-574.
31. J. Murgich, J. Rodriguez, Y. Aray, "Molecular recognition and molecular mechanics of micelles of some model asphaltenes and resins," *Energy & Fuels*, 1996, **10**(1): p. 68-76.
32. J. Murgich, O. P. Strausz, "Molecular mechanics of aggregates of asphaltenes and resins of the Athabasca oil," *Petroleum Science and Technology*, 2001, **19**(1-2): p. 231-243.
33. J. Murgich, J. A. Abanero, O. P. Strausz, "Molecular recognition in aggregates formed by asphaltene and resin molecules from the Athabasca oil sand," *Energy & Fuels*, 1999, **13**(2): p. 278-286.
34. C. Bardon, L. Barre, D. Espinat, V. Guille, M. H. Li, J. Lambard, J. C. Ravey, E. Rosenberg, T. Zemb, "The colloidal structure of crude oils and suspensions of asphaltenes and resins," *Fuel Science & Technology International*, 1996, **14**(1-2): p. 203-242.
35. S. I. Andersen, K. S. Birdi, "Aggregation of Asphaltenes as Determined by Calorimetry," *Journal of Colloid and Interface Science*, 1991, **142**(2): p. 497-502.
36. H. W. Yarranton, H. Alboudwarej, R. Jakher, "Investigation of asphaltene association with vapor pressure osmometry and interfacial tension measurements," *Industrial & Engineering Chemistry Research*, 2000, **39**(8): p. 2916-2924.
37. O. Leon, E. Contreras, E. Rogel, G. Dambakli, S. Acevedo, L. Carbognani, J. Espidel, "Adsorption of native resins on asphaltene particles: A correlation between adsorption and activity," *Langmuir*, 2002, **18**(13): p. 5106-5112.
38. O. Leon, E. Contreras, E. Rogel, G. Dambakli, J. Espidel, S. Acevedo, "The influence of the adsorption of amphiphiles and resins in controlling asphaltene flocculation," *Energy & Fuels*, 2001, **15**(5): p. 1028-1032.

39. K. J. Leontaritis, G. A. Mansoori. *Asphaltene Flocculation During Oil Production and Processing: A Thermodynamic-Colloidal Model*. in *Proceedings of the SPE International Symposium on Oil Field Chemistry*. 1987. San Antonio, TX: Society of Petroleum Engineers.
40. H. Pan, A. Firoozabadi. *A Thermodynamic Micellization Model for Asphaltene Precipitation: Part I: Micellar Size and Growth*. in *SPE Annual Technical Conference and Exhibition*. 1996. Denver, CO.
41. A. I. Victorov, N. A. Smirnova, "Thermodynamic model of petroleum fluids containing polydisperse asphaltene aggregates," *Industrial & Engineering Chemistry Research*, 1998, **37**(8): p. 3242-3251.
42. A. I. Victorov, N. A. Smirnova, "Description of asphaltene polydispersity and precipitation by means of thermodynamic model of self-assembly," *Fluid Phase Equilibria*, 1999, **160**: p. 471-480.
43. M. Agrawala, H. W. Yarranton, "An asphaltene association model analogous to linear polymerization," *Industrial & Engineering Chemistry Research*, 2001, **40**(21): p. 4664-4672.
44. J. D. McLean, P. K. Kilpatrick, "Comparison of Precipitation and Extrography in the Fractionation of Crude Oil Residua," *Energy and Fuels*, 1997, **11**: p. 570-585.
45. T. G. Mason, M. Y. Lin, "Asphaltene Nanoparticle Aggregation in Mixtures of Incompatible Crude Oils," *Physical Review E*, 2003, **67**: p. 050401(R).
46. J. N. Roux, D. Broseta, B. Deme, "SANS study of asphaltene aggregation: Concentration and solvent quality effects," *Langmuir*, 2001, **17**(16): p. 5085-5092.
47. D. Fenistein, L. Barre, "Experimental measurement of the mass distribution of petroleum asphaltene aggregates using ultracentrifugation and small-angle X-ray scattering," *Fuel*, 2001, **80**(2): p. 283-287.
48. E. B. Sirota, "Swelling of asphaltenes," *Petroleum Science and Technology*, 1998, **16**(3-4): p. 415-431.
49. R. E. Overfield, E. Y. Sheu, S. K. Sinha, K. S. Liang, "SANS Study of Asphaltene Aggregation," *Fuel Science & Technology International*, 1989, **7**(5-6): p. 611-624.
50. D. Fenistein, L. Barre, D. Broseta, D. Espinat, A. Livet, J. N. Roux, M. Scarsella, "Viscosimetric and neutron scattering study of asphaltene aggregates in mixed toluene/heptane solvents," *Langmuir*, 1998, **14**(5): p. 1013-1020.
51. S. H. Chen, J. Teixeira, "Structure and Fractal Dimension of Protein-Detergent Complexes," *Physical Review Letters*, 1986, **57**(20): p. 2583-2586.

52. J. Teixeira, "Small-Angle Scattering by Fractal Systems," *Journal of Applied Crystallography*, 1988, **21**: p. 781-785.
53. J. Teixeira, Experimental Methods for Studying Fractal Aggregates, in "On Growth and Form: Fractal and Non-fractal Patterns in Physics" (H. E. Stanley and N. Ostrowsky, Eds.), M. Nijhoff, Dordrecht, Netherlands, 1986; pp 145-162.
54. Y. C. Liu, E. Y. Sheu, S. H. Chen, D. A. Storm, "Fractal Structure of Asphaltenes in Toluene," *Fuel*, 1995, **74**(9): p. 1352-1356.

Table G.1 Chemical composition and coherent neutron scattering length density (ρ) of asphaltenes and resins. Scattering length density calculation assumes asphaltene mass density of 1.1 g/cm³ and resin mass density of 1.0 g/cm³.

Solute	H/C	wt% N	wt% S	wt% O	ρ (\AA^{-2})
B6 Whole asphaltene	1.24	1.87	6.68	2.90	1.08E-06
B6 Precipitate asphaltene	1.22	1.93	6.33	2.81	1.12E-06
CS Whole asphaltene	1.11	1.32	0.52	1.73	1.32E-06
B6 resin	1.51	1.48	6.91	1.98	5.35E-07

Table G.2 Summary of modified Lorentzian fit parameters to pure resin scattering curves.

vol% toluene	wt% resins	I_1	n	I_0 (cm ⁻¹)	ξ (\AA)	I_{incoh} (cm ⁻¹)	R^2
100	0.5	--	--	0.048	15.6	0.0167	0.99198
100	1	--	--	0.078	15.4	0.0166	0.99545
100	2	3.15E-06	1.69	0.142	13.8	0.0164	0.99788
100	5	9.51E-06	1.84	0.275	12.0	0.0140	0.99861
100	10	4.80E-07	2.72	0.385	11.0	0.0418	0.99829
vol% toluene	wt% resins	I_1	n	I_0 (cm ⁻¹)	ξ (\AA)	I_{incoh} (cm ⁻¹)	R^2
60	0.5	--	--	0.062	15.6	0.0225	0.99338
60	1	--	--	0.087	15.3	0.0241	0.99374
60	2	5.00E-05	1.20	0.206	14.7	0.0228	0.99836
60	4	3.00E-05	1.52	0.324	12.8	0.0105	0.99892
60	6	2.00E-05	1.62	0.379	12.8	0.0103	0.99901
60	6	2.00E-05	1.77	0.419	12.1	0.0059	0.99887
60	10	7.91E-06	2.07	0.521	11.0	0.0043	0.99902

Table G.3 Summary of Teixeira fit parameters to pure resin and mixed asphaltene-resin scattering curves before and after subtraction of resin scattering contributions. (Key: B6W60 = B6 Whole asphaltenes in 60 % toluene; B6P100 = B6 Precipitate asphaltenes in 100 % toluene; CSW60 = CS Whole asphaltenes in 60 % toluene; B6R100 = B6 resins in 100 % toluene; B6R60 = B6 resins in 60 % toluene).

B6W60		Original fit to scattering curves				After subtraction of resin curves			
wt% resins	I_0 (cm ⁻¹)	D	ξ (Å)	R ²	I_0 (cm ⁻¹)	D	ξ (Å)	R ²	
0	6.2 ± 0.2	2.05 ± 0.05	64 ± 3	0.9993	6.2 ± 0.2	2.05 ± 0.05	64 ± 3	0.9993	
0.5	8.9 ± 0.5	2.01 ± 0.05	68 ± 5	0.9986	8.5 ± 0.5	2.12 ± 0.06	62 ± 5	0.9986	
1	6.7 ± 0.1	1.86 ± 0.05	66 ± 3	0.9987	6.5 ± 0.1	1.97 ± 0.05	62 ± 3	0.9987	
2	5.3 ± 0.1	1.81 ± 0.05	54 ± 3	0.9987	5.0 ± 0.1	2.02 ± 0.05	49 ± 2	0.9986	
4	3.56 ± 0.04	1.62 ± 0.05	43 ± 2	0.9993	3.19 ± 0.04	1.87 ± 0.05	40 ± 2	0.9991	
6	3.34 ± 0.04	1.63 ± 0.05	35 ± 1	0.9995	2.92 ± 0.05	1.83 ± 0.05	34 ± 1	0.9994	
10	3.32 ± 0.03	1.58 ± 0.05	28.2 ± 0.8	0.9996	2.81 ± 0.03	1.73 ± 0.05	28.9 ± 0.9	0.9996	
B6P100		Original fit to scattering curves				After subtraction of resin curves			
wt% resins	I_0 (cm ⁻¹)	D	ξ (Å)	R ²	I_0 (cm ⁻¹)	D	ξ (Å)	R ²	
0	22 ± 2	2.16 ± 0.05	109 ± 8	0.9993	22 ± 2	2.16 ± 0.05	109 ± 8	0.9993	
0.5	18 ± 1	2.01 ± 0.05	120 ± 10	0.9993	17 ± 1	2.09 ± 0.05	110 ± 10	0.9991	
2	12.7 ± 0.9	1.73 ± 0.05	120 ± 10	0.9992	11.3 ± 0.7	1.90 ± 0.05	102 ± 8	0.9991	
5	6.0 ± 0.6	1.32 ± 0.05	120 ± 20	0.9974	5.0 ± 0.4	1.64 ± 0.06	90 ± 10	0.9973	
10	4.2 ± 0.6	1.03 ± 0.05	110 ± 30	0.9979	4 ± 1	1.22 ± 0.07	120 ± 40	0.9969	
CSW60		Original fit to scattering curves				After subtraction of resin curves			
wt% resins	I_0 (cm ⁻¹)	D	ξ (Å)	R ²	I_0 (cm ⁻¹)	D	ξ (Å)	R ²	
0	8.6 ± 0.6	2.08 ± 0.07	76 ± 7	0.9980	8.6 ± 0.6	2.08 ± 0.07	76 ± 7	0.9980	
0.5	6.5 ± 0.1	1.99 ± 0.05	65 ± 2	0.9996	6.2 ± 0.1	2.12 ± 0.05	60 ± 2	0.9996	
2	4.2 ± 0.1	1.83 ± 0.05	51 ± 3	0.9989	3.8 ± 0.1	2.11 ± 0.05	44 ± 2	0.9988	
4	3.97 ± 0.04	1.70 ± 0.05	46 ± 2	0.9990	3.57 ± 0.04	1.99 ± 0.05	40 ± 2	0.9988	
6	4.06 ± 0.06	1.59 ± 0.05	41 ± 2	0.9994	3.61 ± 0.06	1.82 ± 0.05	38 ± 2	0.9993	
10	3.39 ± 0.04	1.55 ± 0.05	31 ± 1	0.9990	2.85 ± 0.04	1.73 ± 0.05	30 ± 1	0.9987	
B6R100		Original fit to scattering curves							
wt% resins	I_0 (cm ⁻¹)	D	ξ (Å)	R ²					
0.5	0.066 ± 0.001	1.05 ± 0.05	24 ± 2	0.9868					
1	0.095 ± 0.001	1.31 ± 0.05	20.6 ± 0.8	0.9941					
2	0.162 ± 0.001	1.51 ± 0.05	17.3 ± 0.5	0.9963					
5	0.300 ± 0.001	1.68 ± 0.05	14.3 ± 0.5	0.9965					
10	0.432 ± 0.002	1.66 ± 0.06	12.3 ± 0.5	0.9965					
B6R60		Original fit to scattering curves							
wt% resins	I_0 (cm ⁻¹)	D	ξ (Å)	R ²					
0.5	0.084 ± 0.001	1.10 ± 0.06	22 ± 2	0.9882					
1	0.111 ± 0.001	1.16 ± 0.05	22 ± 1	0.9931					
2	0.237 ± 0.001	1.48 ± 0.05	19.1 ± 0.5	0.9975					
4	0.343 ± 0.001	1.86 ± 0.05	13.7 ± 0.3	0.9981					
6	0.398 ± 0.001	1.93 ± 0.05	13.2 ± 0.3	0.9982					
6	0.435 ± 0.001	1.99 ± 0.05	12.2 ± 0.4	0.9976					
10	0.535 ± 0.002	2.00 ± 0.07	11.0 ± 0.4	0.9972					

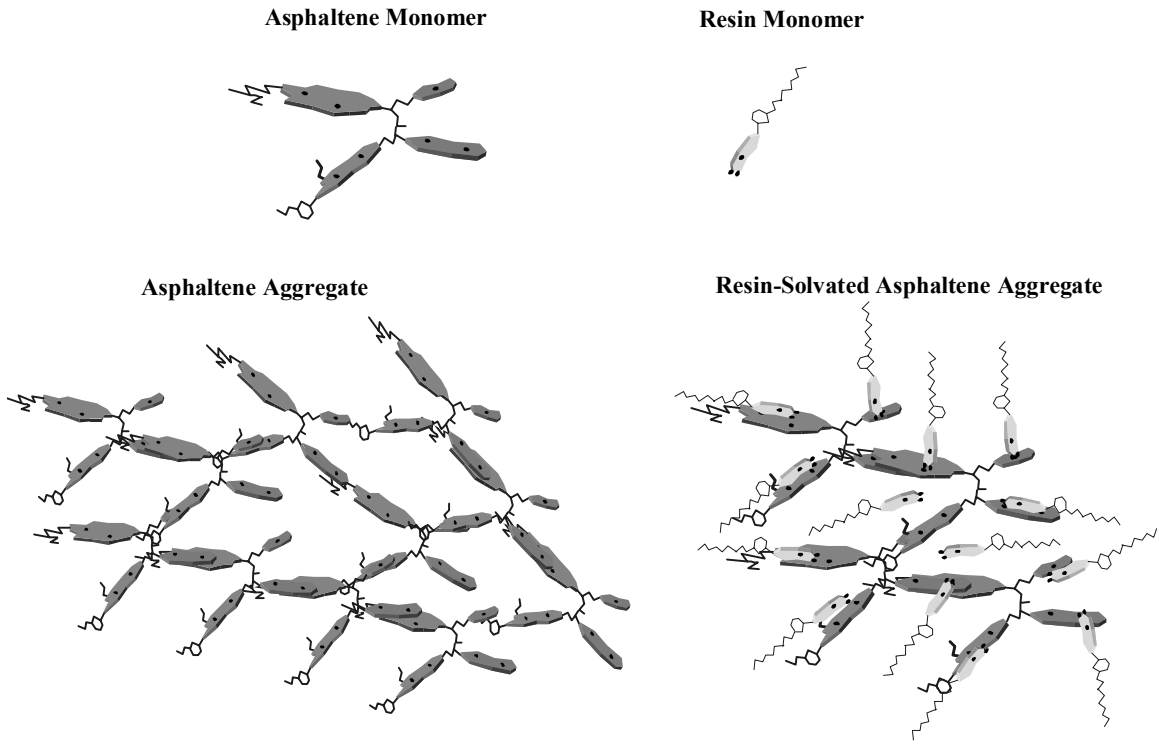


Figure G.1 Schematic illustration of an asphaltene monomer, resin monomer, asphaltenic aggregate in the absence of resins, and asphaltenic aggregate in the presence of resins.

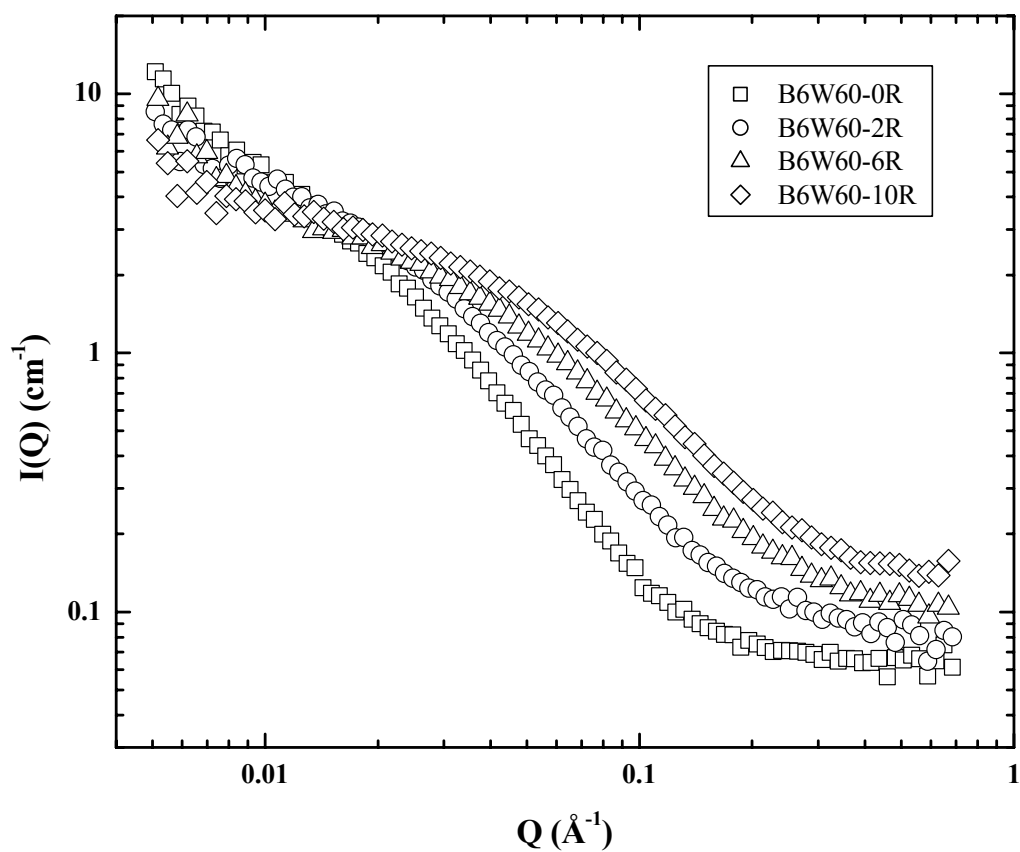


Figure G.2 SANS scattering intensity curves for B6 Whole asphaltenes (1 % wt.) in 60 % toluene with: (□) no resins; (○) 2 % wt. B6 resins; (△) 6 % wt. B6 resins; and (◇) 10 % wt. B6 resins.

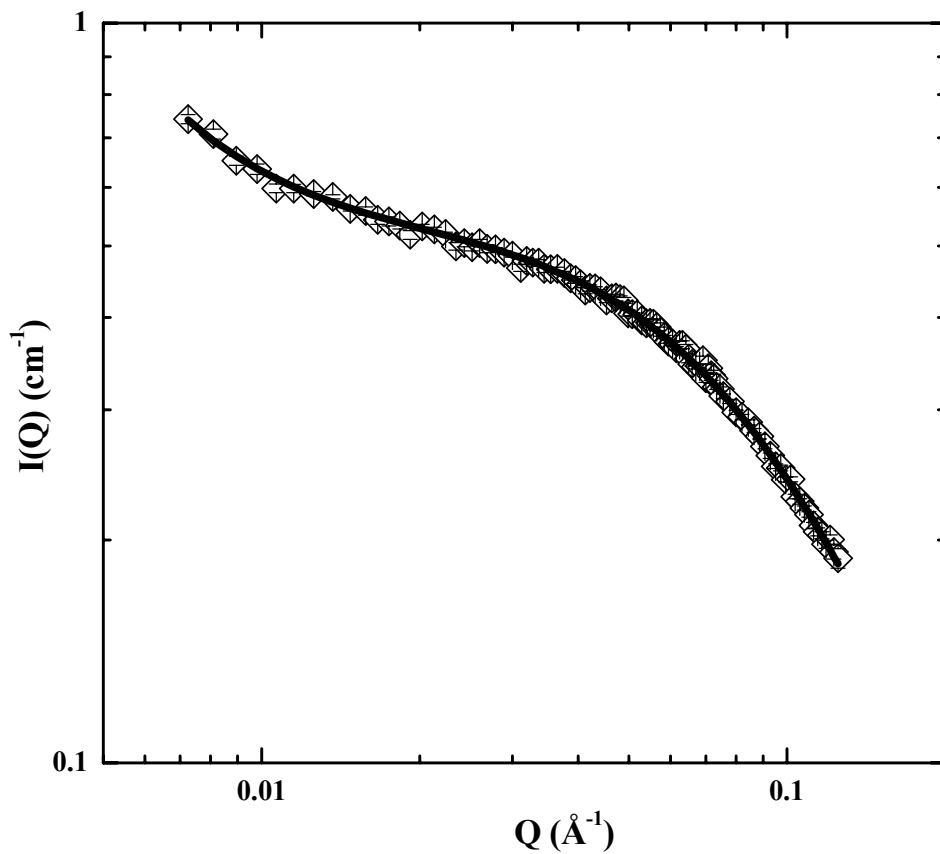


Figure G.3 Example fit of SANS scattering curve for B6 resins (10% wt.) in 60% toluene to a modified Lorentzian lineshape with additional terms to account for incoherent scattering and low Q upturn: $I_1 = 7.91\text{E-}6$; $n = 2.07$; $I_0 = 0.521 \text{ cm}^{-1}$; $\xi = 11.0 \text{ \AA}$; $\text{bkg} = 0.0043 \text{ cm}^{-1}$; $R^2 = 0.9990$. Note: Every 2nd data point displayed.

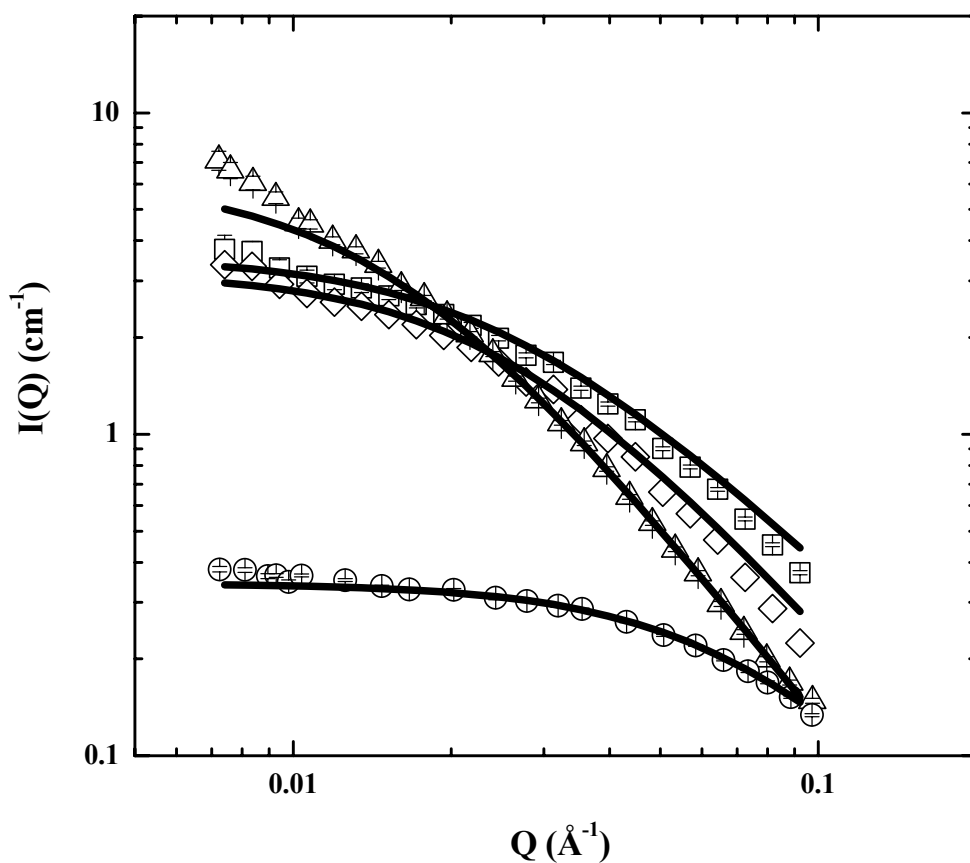


Figure G.4 SANS scattering intensity curves and Teixeira fits for solutions of B6 Whole asphaltenes (1% wt.) and B6 resins (4% wt.) in 60% toluene: (\square) Asphaltene-resin mixture, $I_{0AR} = 3.56 \pm 0.04 \text{ cm}^{-1}$, $D_{AR} = 1.62 \pm 0.05$, $\xi_{AR} = 43 \pm 2 \text{ \AA}$, $R^2 = 0.9993$; (\circ) Resin only solution, $I_{0R} = 0.343 \pm 0.001 \text{ cm}^{-1}$, $D_R = 1.86 \pm 0.05$, $\xi_R = 13.7 \pm 0.3 \text{ \AA}$, $R^2 = 0.9981$; (\triangle) Asphaltene only solution, $I_{0A} = 6.2 \pm 0.2 \text{ cm}^{-1}$, $D_A = 2.05 \pm 0.05$, $\xi_A = 64 \pm 3 \text{ \AA}$, $R^2 = 0.9993$; (\diamond) Residual scattering curve after resin subtraction, $I_{0Res} = 3.19 \pm 0.04 \text{ cm}^{-1}$, $D_{Res} = 1.87 \pm 0.05$, $\xi_{Res} = 40 \pm 2 \text{ \AA}$, $R^2 = 0.9991$. Note: Every 2nd data point displayed.

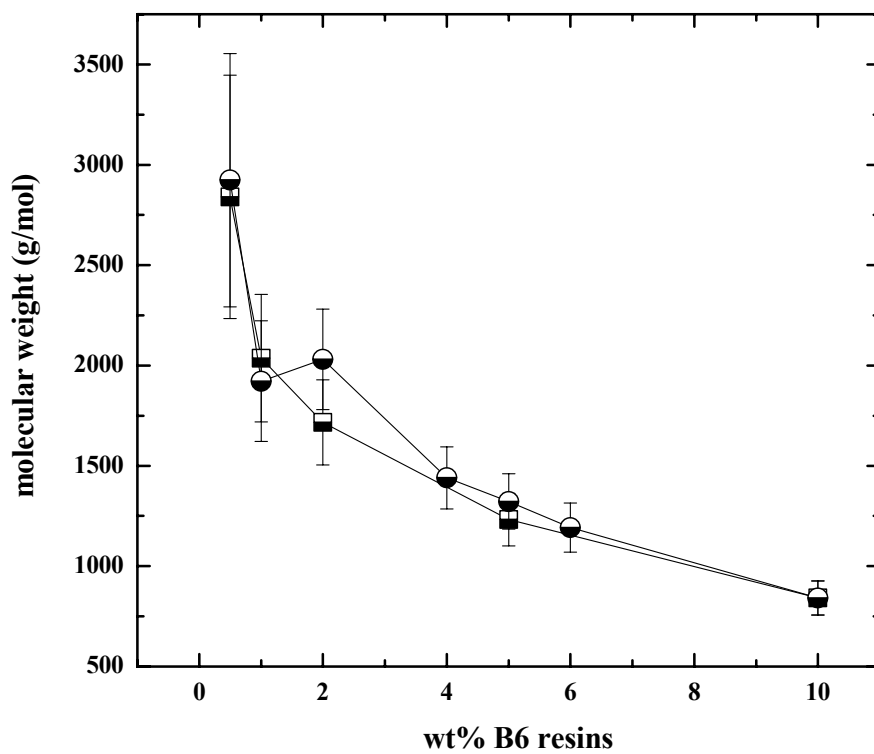


Figure G.5 Molecular weight (M_R) values for B6 resins as a function of concentration in pure toluene (■) and 60% toluene (●).

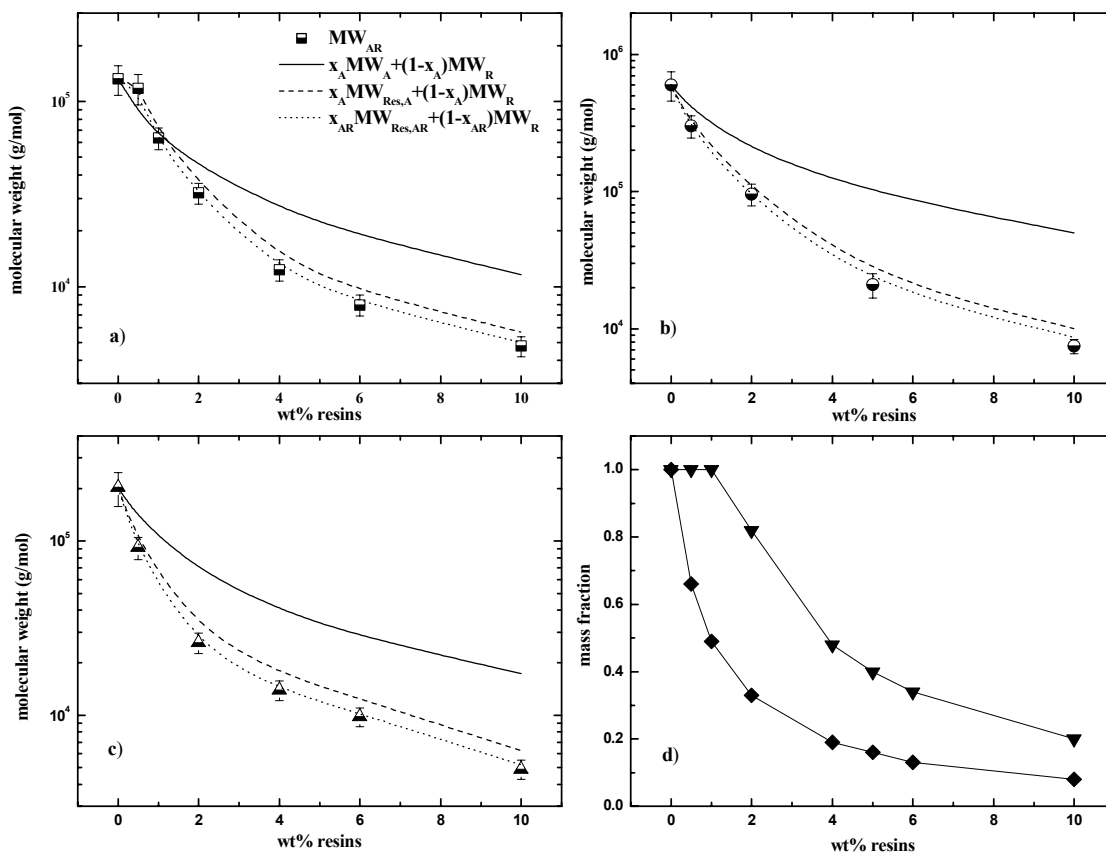


Figure G.6 Molecular weight values for solutions of asphaltenes (1% wt.) with B6 resins at various concentrations: a) B6 Whole asphaltenes in 60% toluene (■); b) B6 Precipitate asphaltenes in 100% toluene (◐); c) CS Whole asphaltenes in 60% toluene (▲). The solid, dashed, and dotted lines represent the weight-averaged summation of molecular weights for the individual scattering components by three different methods. d) Values of the asphaltene (x_A , ◆) and asphaltene-resin (x_{AR} , ▼) mass fractions as a function of resin content.

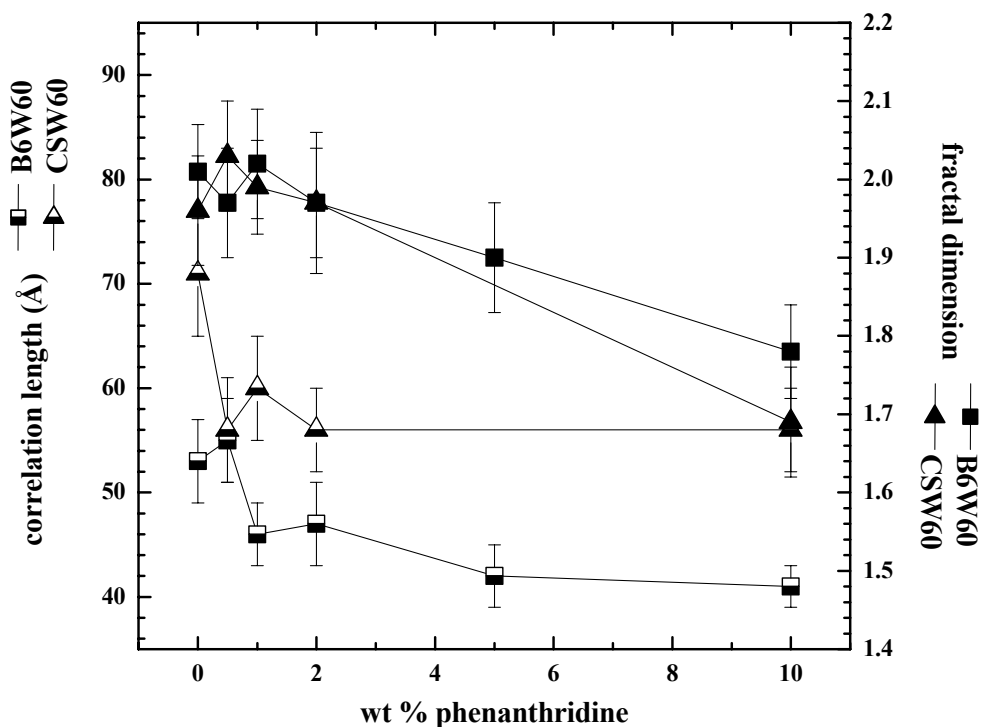


Figure G.7 Correlation length (half-filled symbols) and fractal dimension (filled symbols) values for B6 and CS Whole asphaltenes (1% wt.) in 60% toluene with various concentrations of phenanthridine added as a dopant. SANS scattering curves were collected at 80°C in 5 mm pathlength cells.

[I would like to rerun this experiment at 25°C, 2 mm using CSW60. I would also like to dope CSW60 with CA, but need to see if pure CA scatters. Ultimately, I would like to combine Figures G.7-G.8 into a single plot showing changes in ξ and D for CSW60 with PHD and CA added as dopants. This keeps the asphaltene fraction, solvent conditions, temperature, and pathlength consistent throughout the paper.]

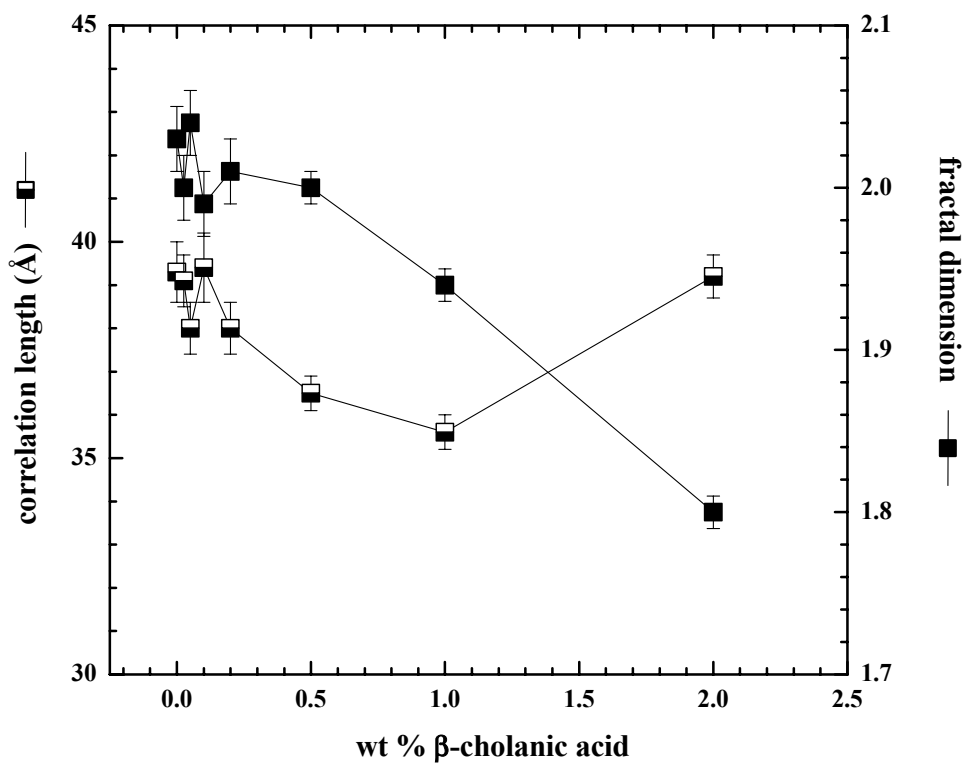


Figure G.8 Correlation length (\square) and fractal dimension (\blacksquare) values for HO Whole asphaltenes (1% wt.) in 100% toluene with various concentrations of β -cholanic acid added as a dopant.

APPENDIX H:

ASPHALTENE EMULSIONS

The following experiments were performed with Marit-Helen Ese.

Argonne Beamtime Proposal Submitted 04/15/03

ASPHALTENE AND NAPHTHENIC ACID- STABILIZED EMULSIONS

Problematic water-in-oil emulsions are frequently encountered in the production, transportation, and processing of petroleum fluids. The vast majority of these water-in-oil emulsions are stabilized by either asphaltenic films or lamellar liquid crystalline films comprised predominantly of naphthenic acids and their salts. Both types of films manifest similar mechanical and rheological properties and represent an important class of emulsion stabilization mechanisms. The oil-water interface creates a self-assembly platform onto which both asphaltenes and naphthenic acids/soaps adsorb under the appropriate conditions. We will use SANS to probe the properties of commercially available and naturally occurring naphthenic acids/soaps in bulk solution and in water-in-oil emulsions under conditions of pH, ionic strength, solvency, and concentration that have previously been determined to facilitate aggregation and emulsion formation. Preliminary SANS results for these types of emulsions show a distinct shift in the shape of the scattering curve between 0.5 and 1% wt CA that corresponds to a transition of the emulsion from a mainly asphaltene-stabilization mechanism to a mainly lamellar liquid crystalline-stabilization mechanism (see Figure 2). Appropriate contrast variation and modeling of the SANS data to a polydisperse core-shell form factor should provide information concerning the average size and film thickness of emulsion droplets. Additional SANS experiments are proposed to probe the interaction of these two mechanisms in which aggregation and emulsion stability are either enhanced or destroyed by mixing asphaltenes and naphthenates in bulk solutions or water-in-oil emulsions. For example, one set of SANS samples may consist of a 0.5% wt solution of Hondo Whole asphaltenes dissolved in 45:55 heptol with various amounts of beta-cholanic acid added. Further experiments will replace beta-cholanic acid with other model and/or crude naphthenates, such as 4-heptylbenzoic acid, deoxycholic acid, 4-pentylcyclohexane carboxylic acid, and Africa resins. One representative emulsion sample may consist of 2 mL of a 0.5% wt Hondo Whole asphaltene solution in 45:55 heptol emulsified with 2 mL of a 1%

wt solution of beta-cholanic acid in deuterated water (pH 12.0, 3.5% wt NaCl). Additional emulsion samples will vary the solution pH, type of naphthenic acid, and acid concentration. Finally, bulk solutions and emulsified mixtures of whole crude oils (Hondo and Africa) will be studied to probe the practical problem of crude oil blending to inhibit aggregate formation.

Working Equations of Polydisperse Core-Shell Model

$$I(Q) = \frac{\text{scale} \langle P(Q) \rangle}{\langle V \rangle} + \text{bkg}$$

$$\langle P(Q) \rangle = \frac{\int G(Q) f(r) [V(r)]^2 dr}{\int [V(r)]^2 f(r) dr}$$

The average particle volume is described by a Schultz distribution:

$$\langle V \rangle = \frac{4\pi}{3} \langle r^3 \rangle \quad \text{where} \quad \langle r^3 \rangle = \frac{(z+3)(z+2)}{(z+1)^2} \langle r \rangle;$$

$$\langle r_s \rangle = r_{\text{core}} + t$$

with the Schultz distribution function given by:

$$f(r) = \frac{r^z}{\Gamma(z+1)} \left[\frac{(z+1)}{r_{\text{avg}}} \right]^{(z+1)} \exp\left(- (z+1) \frac{r}{r_{\text{avg}}}\right)$$

$$z = \frac{1}{p^2} - 1; \quad 0 \leq p \leq 1$$

The polydispersity parameter, p, ranges from 0 to 1.

The form factor for monodisperse core-shell is given by:

$$G(Q) = \frac{3V_{\text{core}} (\rho_{\text{core}} - \rho_{\text{shell}}) j_1(Qr_{\text{core}})}{V_s Q r_{\text{core}}} + \frac{3(\rho_{\text{shell}} - \rho_{\text{solvent}}) j_1(Qr_s)}{Q r_s}$$

where $j_1(x) = (\sin x - x \cos x)/x^2$ and $r_s = r_{\text{core}} + t$

Assumptions:

- 1) $r_{\text{core}}/(r_{\text{core}} + t) \sim \text{constant}$.
- 2) Scale factor is correlated to SLD values and assumed unity.
- 3) Negligible interparticle correlations.
- 4) SLD values of core and solvent calculated from mass density and chemical composition.
- 5) Core radius and polydispersity known from microscopic droplet size distribution analyses.

Table H.1 Composition, Sauter mean droplet diameter, and stability of water-in-model oil emulsions. The aqueous phase consisted of brine at pH = 12 and the model oil phase consisted of 0.5 % (w/w) HO asphaltenes in 45:55 Heptane/Toluene. The volume ratio of oil: water was 1:1.

Sample	wt% CA in the emulsion	wt% asph in the oil phase	d₃₂ (μm)	Skewness about origin	% water resolved
E1	0	0.5	8.16	246	29
E2	0.025	0.5	6.49	165	57
E3	0.050	0.5	6.91	127	89
E4	0.10	0.5	20.1	1555	92
E5	1.0	0.5	7.52	256	70
E6	1.4	0.5	5.01	83	43
E7	1.0	0	5.60	113	46
E8	1.5	0	5.27	91	44

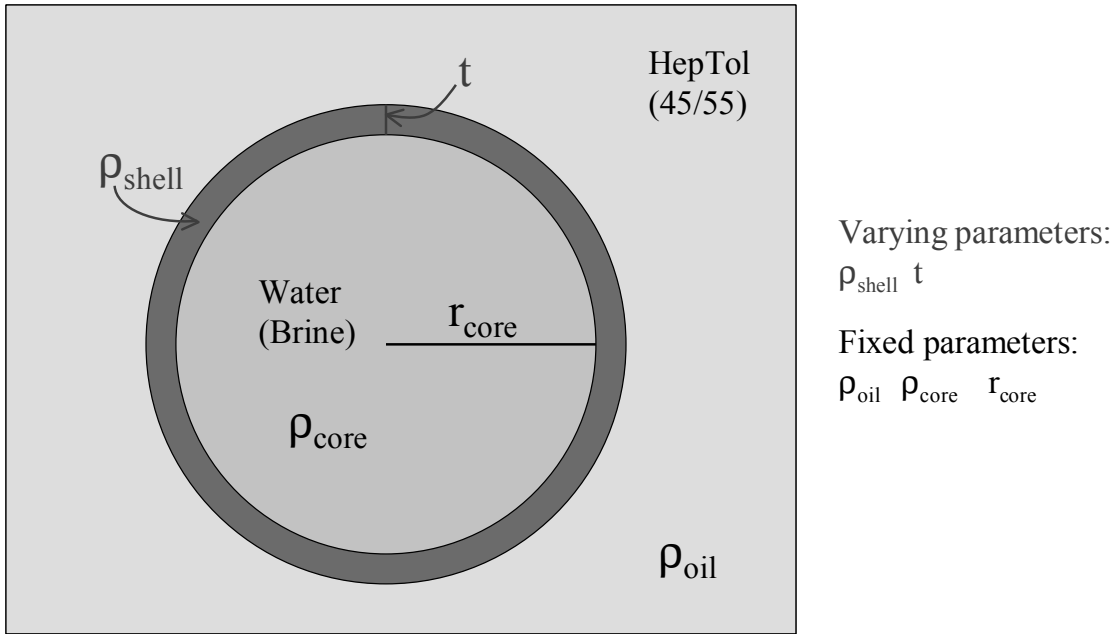


Figure H.1 Schematic representation of a water droplet in an oil continuous emulsion according to a core-shell model. Legend: r_{core} = core radius; ρ_{core} = scattering length density of water phase; t = shell thickness; ρ_{shell} = scattering length density of shell; ρ_{oil} = scattering length density of oil phase.

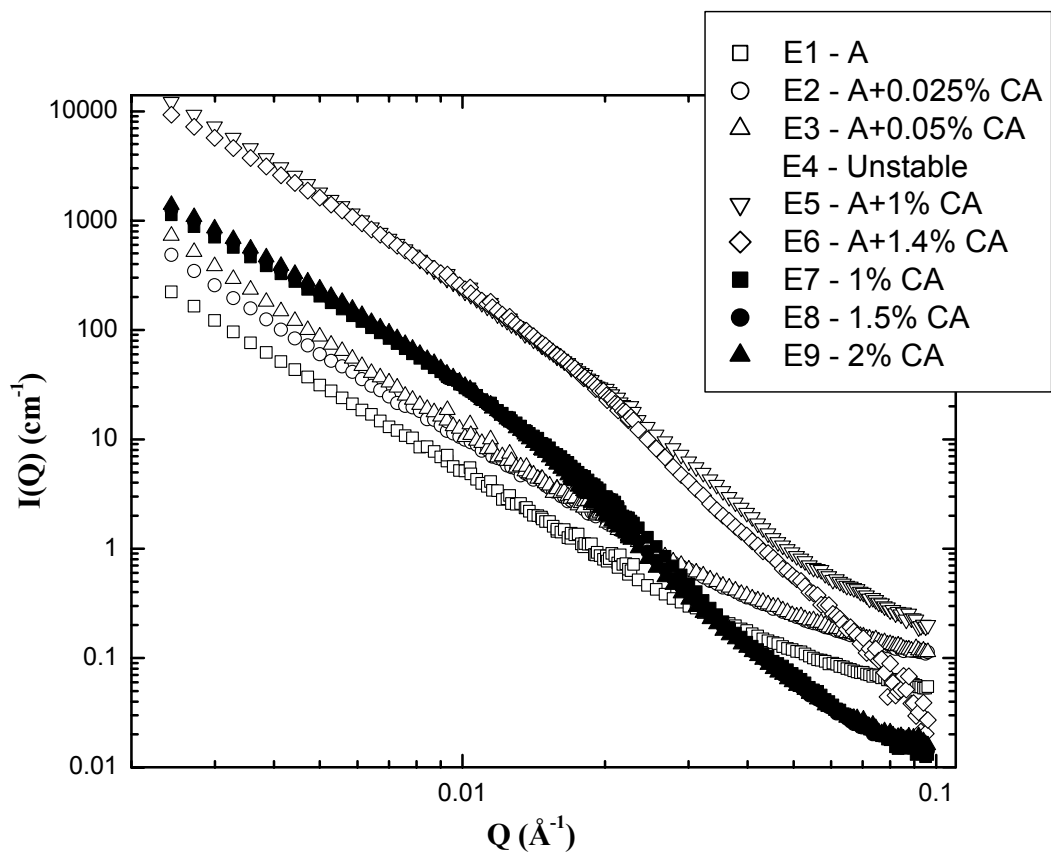


Figure H.2 SANS scattering intensity curves for mixed CA and asphaltene emulsions.

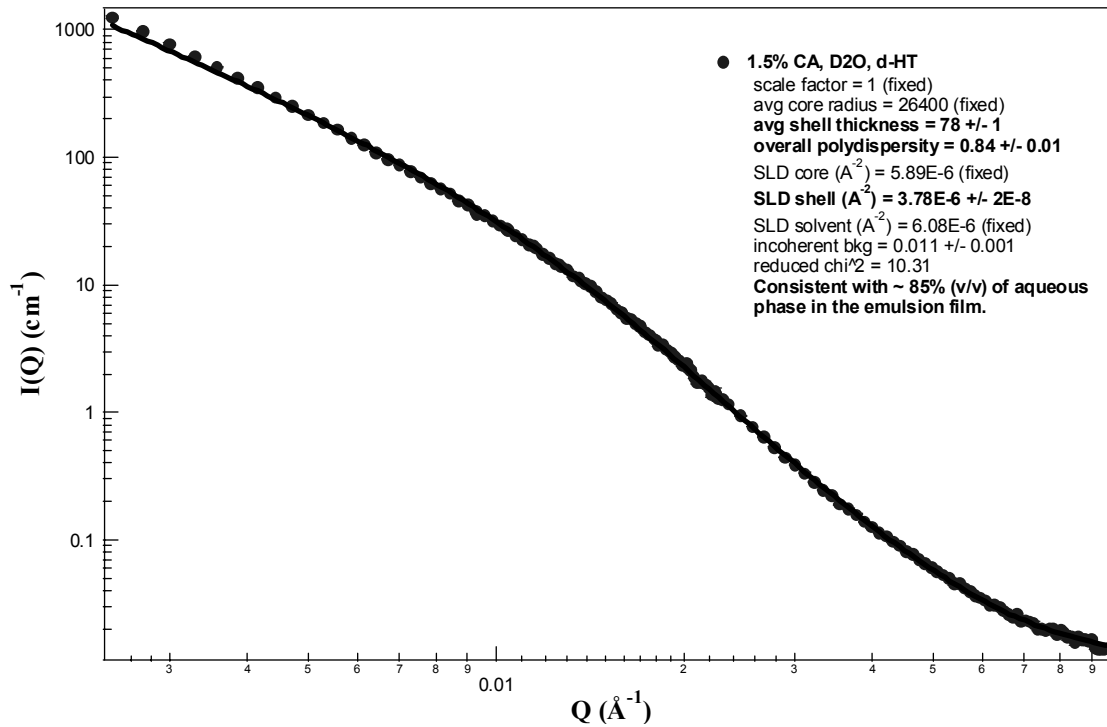


Figure H.3 Fits of emulsions E8 to a polydisperse core-shell model.

The average core radius was estimated from the Sauter mean droplet diameter. The scattering length densities of the core and oil phase were calculated from the elemental composition of the corresponding phases. The polydispersity in droplet size and thickness and scattering length density of the shell were the only varying parameters. The scattering length density of the shell was consistent with ~ 85 % (v/v) entrainment of the aqueous phase in the emulsion film.

Analysis of asphaltene emulsions is more complicated, because the scattering intensity profile consists of contributions of nanoparticle asphaltenic aggregates in the oil continuous phase and the adsorbed asphaltenic film on the surface of the water droplets. We proposed to subtract the scattering contribution of the creamed oil phase from the scattering intensity curve for the composite emulsion to isolate the scattering contributions from the adsorbed asphaltenic film only.

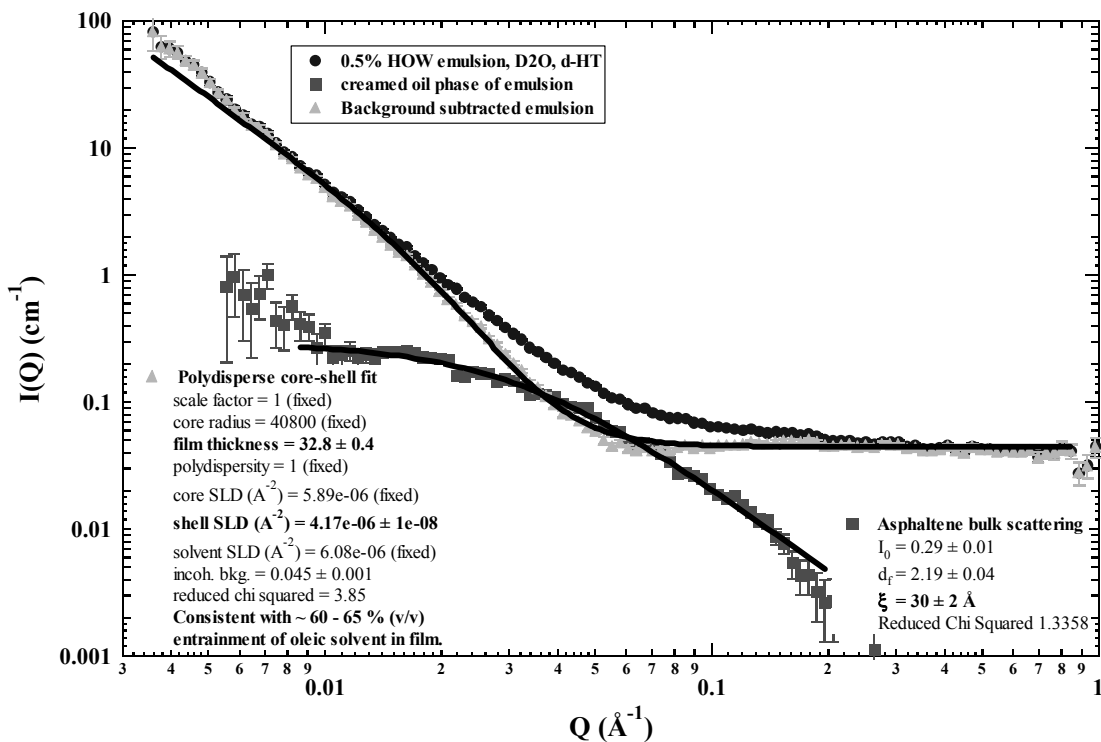


Figure H.4 Fit of the polydisperse core-shell model to emulsion E1.

The scattering length density of the shell was consistent with ~ 60 – 65 % (v/v) entrainment of the oleic solvent in the film.